## *Validation of viscous, three-dimensional flow calculations in an axial turbine cascade*

Cleak, James Gilbert Edwin

# Validation of Viscous, Three-Dimensional Flow Calculations in an Axial Turbine Cascade

*James Gilbert Edwin Cleak*

School of Engineering and Applied Science
University of Durham



A thesis submitted for the degree of
Doctor of Philosophy of the University of Durham

December 1989

## Declaration

The work contained in this thesis has not been submitted elsewhere for any other degree or qualification, and unless otherwise referenced it is the author's own work.

Dedicated to my Parents

# Validation of Viscous, Three-Dimensional Flow Calculations in an Axial Turbine Cascade

*J.G.E. Cleak*

## Abstract

This thesis presents a detailed investigation of the capability of a modern three-dimensional Navier-Stokes solver to predict the secondary flows and losses in a linear cascade of high turning turbine rotor blades. Three codes were initially tested, to permit selection of the best of the available numerical solvers for this case. This program was then tested in more detail. Results showed that although very accurate prediction of the effects of inviscid fluid mechanics is now possible, the Reynolds stress modelling can have profound effects upon the quality of the solutions obtained. Solutions using two different calculation meshes, have shown that the results are not significantly grid dependent.

The flowfield of the cascade was traversed with hot-wires to obtain measurements of the turbulent Reynolds stresses. A turbulence generating grid was placed upstream of the cascade, to produce a more realistic inlet turbulence intensity. Results showed that regions of high turbulent kinetic energy are associated with regions of high total pressure loss. Calculation of eddy viscosities from the Reynolds stresses showed that downstream of the cascade the eddy viscosity is fairly isotropic. Evaluation of terms in the kinetic energy equation, also indicated that both the normal and shear Reynolds stresses are important as loss producing mechanisms in the downstream flow.

The experimental Reynolds stresses have been compared with those calculated from the eddy viscosity and velocity fields of Navier-Stokes predictions using a mixing length turbulence model, a one equation model, and a $K - \epsilon$ model. It was found that in the separated, shear flows, agreement was poor, although the $K - \epsilon$ model performed best. Further experimental work is suggested to obtain data with which to determine the accuracy of the models within the blade and endwall boundary layers.

# Acknowledgements

I am most grateful for the interest and enthusiasm of my supervisor Dr. David Gregory-Smith. His most capable guidance, and the many useful discussions with him, have been of great benefit to me during my period of post-graduate study.

My grateful thanks are also extended to Dr. Nigel Birch, Dr. John Northall, and Dr. Peter Stow of Rolls-Royce Plc. Their helpfulness and expert advise have been greatly appreciated. I am also indebted to them for their help in exporting and running Rolls-Royce software on the Rutherford CRAY.

I would also like to thank all staff, both academic and technical, of the School of Engineering and Applied Science, for their assistance during my period as a research student. Particular thanks must go to Ian Glassford, who made pieces of experimental equipment for me with consistent care, and great attention to detail.

The financial support of Rolls-Royce Plc, and the Science and Engineering Research Council, are also gratefully acknowledged.

Finally, I would like to thank Dr. Joe Walsh for his interest and help, and for permitting me to reproduce his data within this thesis. His assistance in supplying me with the programs he used, and the discussions we have had, have been very much appreciated.

# Contents

## Chapter 4 : Apparatus and Techniques



## Chapter 5 : Experimental Results (JAW Test Case)



## Chapter 6 : Modelling Results (JAW Test Case)



## Chapter 7 : Experimental Results (JGC Test Case)

# Nomenclature

| | |
|---|---|
| $C$ | Blade chord |
| Cax | Axial chord |
| $e$ | Internal energy |
| $E$ | Total energy $= e + \frac{V^2}{2}$ |
| $E_v$ | Van Driest damping factor |
| $f$ | Body force e.g. gravity or electromagnetism |
| $h$ | Blade span |
| $H$ | Boundary layer shape factor |
| $K$ | Coefficient of thermal conductivity or turbulent kinetic energy |
| $l_0$ | Mixing length |
| $n$ | Distance from nearest solid surface |
| $P$ | Pressure |
| $P_0$ | Stagnation pressure |
| $R, Re$ | Reynolds number |
| $S$ | Blade pitch |
| $Spi$ | Stagnation pressure calibration coefficient for five hole probe |
| $U, V, W$ | Velocity components in $x, y, z$ directions |
| $u', v', w'$ | Fluctuating air velocity components |
| $V$ | Gas speed |
| $Y_s$ | Secondary loss |
| $\alpha$ | Gas angle |
| $\beta$ | Blade angle |
| $\delta$ | Boundary layer thickness |
| $\epsilon$ | Temperature or Energy dissipation rate |
| $\epsilon_{i,j}$ | Eddy viscosity calculated from $ij$ shear stress |
| $\zeta$ | Loss coefficient $= \frac{P_{01} - P_{01LOCAL}}{\frac{1}{2}\rho V_1^2}$ |
| $\mu$ | Molecular viscosity |
| $\mu_t$ | Eddy viscosity |
| $\nu$ | Kinematic viscosity $(= \frac{\mu}{\rho})$ |
| $\rho$ | Density |
| $\tau_{ij}$ | Stress in j-direction on plane Perpendicular to i-axis |
| $\omega_n$ | Normal vorticity |
| $\omega_s$ | Streamwise vorticity |

### Subscripts

| | |
|---|---|
| $ax, rad, tan$ | Axial, Radial, Tangential |
| $CAL$ | Measured during calibration |
| $i, j, k$ | Quantity in x,y or z direction or quantity stored at calculation mesh point (i,j,k) |
| 1 | Upstream or inlet |
| 2 | Downstream or exit |

# List of Figures

# Chapter 1
# Introduction

Although the gas turbine engine is popularly known as a propulsion unit for aircraft, it has also found uses as a marine power plant, and in the generation of electricity. Smaller units are now also being manufactured for application in land vehicles. Within a gas turbine engine there are in principle only three major components, a compressor, combustion chamber, and turbine. Although this conceptual engine is very simple, and avoids the reciprocating action of conventional piston engines, the actual design of all its components has proved to be very complex. Not least of these complexities is the successful aerodynamic design of the bladings which form the compressor and turbine.

The turbine's role in the engine is to extract energy from the hot gases which emerge from the combustion chamber, by expanding them to a lower temperature and pressure. In a 'turbojet' engine for aircraft propulsion applications, the turbine must supply only enough energy to drive the compressor. Such an arrangement may then be called a 'gas generator', as it produces a high speed jet of hot gas. In 'turbofan' or 'turboprop' engines, sufficient shaft power must also be available to drive the propellor or fan. In other applications, where the only desired output is shaft power, extra turbine stages are added to the gas generator to extract as much of the remaining energy as possible from the hot gases.

When high pressure ratios are required from a single axial compressor, it is desirable for different stages of the compressor to operate at different rotational speeds. Hence compressors are often split into two, or three sections, each of which is driven by a separate shaft. If heavy gear boxes are to be avoided, each shaft will require its own turbine. Hence the turbines in modern turbofan engines are often split up into 'high pressure', 'intermediate pressure', and 'low pressure' sections, which each drive their own shaft. The mechanical design of three concentric drive shafts sets a lower limit to the



inner radius of the high pressure turbine annulus. For a given overall flow area, the blade height varies inversely to the annulus radius. Hence small blade heights are common in high pressure turbine stages. Cohen *et al* (1972) have reviewed many aspects of gas turbine theory, design and operation. As they point out, there has been a trend in recent years to higher bypass ratios in turbofan engines because propulsive efficiency favours a high mass flow jet which only slightly exceeds the velocity of the surrounding fluid. Thus the mass flow rates in the turbines of modern engines are being reduced, and hence require less flow area. This compounds the effect of small blade height, and so endwall, or annulus effects have become more important.

Due to the necessity of achieving an acceptable aerodynamic design of the bladings, considerable research has been carried out into the performance of different profiles. Frequently a linear cascade, which is in effect an annulus of infinite radius, is used as a simplified test case. Gostelow (1984) has given a good review of cascade research techniques. Early studies concentrated upon the effects of different blade profiles upon the midspan flow, well away from the hub or tip of the blades. However, in recent years, the range of cascade research, has broadened to include detailed investigations of the three-dimensional flows resulting from endwall effects. These so-called 'secondary flows' lie behind the generation of 'secondary losses'. Despite their name, the 'secondary' losses may account for up to half the total losses in a low aspect ratio blade row. In a linear cascade, the primary flow direction is considered as being that which would develop with a uniform inlet flow, and blades of infinite span. The secondary flows, are then identified as being the difference between the actual flow, and the primary flow. It is with these secondary flows that the work in this thesis is primarily concerned.

Over the past decade, a program of research has been undertaken at Durham University aimed at measuring the detailed three-dimensional flow structure within turbine blade rows, and thus gaining a deeper understanding of the mechanisms of secondary loss generation. Graves (1985) presented a detailed study of a rotor blade, which revealed the major flow features that were present. A second cascade was designed and tested by Walsh (1987),

who investigated the effects of skew in the inlet endwall boundary layer upon the secondary flows and losses.

Secondary flows are of particular interest to the turbine designer, as they result from the turning of endwall boundary layer fluid through a blade row. In compressors, the adverse pressure gradient limits the amount of turning that can be achieved without serious flow separations occurring. In turbines however, the pressure gradient is favourable, and so much larger flow turning is common. This means that secondary flows are generally more powerful in turbines, than in compressors.

As secondary flows are a significant cause of losses, and other undesirable effects, there is considerable interest in developing flow models which can predict, and ultimately help the designer to reduce them. Whilst simple models may be reasonably accurate for the flow in compressors, the turbine secondary flows are so strong that they require more general techniques. Indeed nothing less than a fully three-dimensional solution of the Navier-Stokes equations seems likely to accurately predict such flows. As three-dimensional calculation methods are developed, there is a need for detailed validation of predictions, and assessment of their capabilities. It is to this task that the work in this thesis is directed. Walsh (1987) has already used his data to test two three-dimensional flow solvers, and found that although they showed considerable potential, there was a need for further development.

The current work is aimed at investigating the capabilities of 'state of the art' computer models, and identifying areas for further development. There are many possible causes of error in the numerical solutions, but it is intended to concentrate here mainly on the quality of the physical modelling. This is because numerical errors, and the benefits of particular solution techniques, are considered to be most appropriately addressed by code authors. Thus the initial work is concerned with selection of the best of the available flow solvers for further study. Where possible however, constructive criticism is also made of the solution algorithms. Having selected a flow solver, the next aim of this work is to determine the effects of, and quality of, different turbulence models within the solution procedure. Thus, in addition to the mean flow

data of Walsh (1987), detailed measurements of the turbulent flowfield within the cascade are required. It was decided to introduce a turbulence grid to the wind tunnel before undertaking a survey with hot-wires, so as to produce an inlet turbulence intensity which is more representative of conditions in a real machine.

Thus this work has two major facets, namely the testing of computational models, and the aquisition of experimental data for validation purposes. It was hoped that the advantage of one person undertaking both tasks would be the direction of experimental activity by the requirements for further test data indicated by computational results. This has proved to be the case, with a choice between investigation of the endwall, or suction surface boundary layer, being tilted in favour of the endwall by computational results. However, it is also hoped that the experimental investigation of the Reynolds stresses within the Durham turbine cascade, will be of lasting value both as a test case, and because of the insight it provides into the fundamental flow processes.

# Chapter 2
# Review of Experimental Turbine Secondary Flow Investigations

## 2.0 Introduction

This chapter aims to review experimental investigations of the three-dimensional flows in turbine cascades, and thus build an understanding of the basic flow phenomena involved. The current state of knowledge concerning loss production location, loss distribution, and possibilities for the mechanisms behind these features are described. Investigations concerning the role of turbulence in these processes are reviewed, and effects of varying inlet boundary layer thickness and skew, blade loading, and aspect ratio are discussed. The detailed aerodynamics of linear cascades is then viewed from the context of the real machine, where other effects such as radial geometry, tip leakage, Mach and Reynolds number effects, and unsteady flow, complicate the simplified cascade results. A brief description of traditional methods of modelling the secondary flows and losses is given. These start with classical secondary flow theory and loss correlations, but also include a more recent approach combining a loss model with secondary flow theory.

## 2.1 Secondary Flows

Secondary flows are formed when a non-uniform flow velocity profile is turned. In the case of a turbine cascade, the secondary flows are considered to be the difference between the actual flow direction, and the primary or ideal flow direction. The interest in these flows arises from the changes in outlet flow angle which they cause, the losses they generate (which in low aspect ratio blading may be as much as half the total losses), and the undesirable features which result from their presence within the blade passage, such as non-uniform blade loading and heat transfer 'hot spots'. Hence there is a great deal of interest in developing methods of accurately predicting such

flows, and possibly reducing them. Before this may be attempted however, experiments must be carried out to improve the physical understanding of the phenomena, and provide test cases for any models which are developed.

## 2.2 The Passage Vortex

The most dominant feature of the complex secondary flow structure in turbine cascades, is referred to as the passage vortex. This is a vortex which results from the over-turning of endwall boundary layer fluid (Figure 2.1). Within the blade passage, a pressure gradient is formed in response to the momentum of the inlet flow, giving rise to high pressure on one (pressure) surface, and low pressure on the other (suction) surface of the blade. Whilst the fluid in the endwall boundary layer is moving more slowly than the 'freestream' fluid, and hence would naturally give rise to a smaller cross-passage pressure gradient, it is forced to accept the pressures set up in the main stream as no accelerations initially exist in the spanwise direction with which to oppose them. Hence the slowly moving fluid of the endwall boundary layer is swept from pressure to suction surface, where it is obliged to move along the suction surface away from the endwall. A circulation thus develops and it is this which is termed the passage vortex. Many examples of this phenomena have been investigated, such as the works of Sjolander (1975), Langston *et al* (1977), Marchal and Sieverding (1977), and Gregory-Smith and Graves (1983). This suggests that the passage vortex formation is in essence an inviscid phenomenon, with the role of viscosity mainly limited to the production of the initial shear flow. Even in a blade row with no inlet boundary layer however, Turner (1957) has shown that secondary flows will still be formed as the boundary layer which develops within the cascade is over-turned.

## 2.3 The Horseshoe Vortex

When a cylinder is placed in the path of an endwall boundary layer,

a vortex is formed in front of it as shown in Figure 2.2. This produces two vortex legs, one either side of the cylinder, which are carried away downstream with opposite vorticities. Due to the shape of this vortex when viewed from above the endwall, it is often referred to as the horseshoe vortex, as well as the stagnation vortex. As can be seen in Figure 2.2, the horseshoe vortex is associated with two separations, which may show up on endwall flow visualisations as two distinct separation lines. Sieverding (1985b) in his excellent review of linear turbine cascade aerodynamics, devotes considerable discussion to the importance of this vortex in the cascade environment.

In a turbine cascade, a horseshoe vortex will be formed in front of each blade. Endwall visualisations by Langston *et al* (1977) and Marchal and Sieverding (1977), show that one leg of this vortex on the pressure side of the blade, crosses the passage to meet with the suction surface further into the cascade. This is called the pressure side leg of the horseshoe vortex. The other leg of the vortex, termed the suction side leg, is seen to wrap around the leading edge of the blade before meeting the suction surface. The horseshoe vortex has received considerable attention in recent years, both since it has been shown by Gaugler and Russel (1984) to be associated with a peak in endwall heat transfer, and as the pressure side leg is seen to cross the passage, rotating in the same sense as the passage vortex. Since the flow behind the pressure side leg separation line is highly over-turned and is clearly part of the passage vortex (see for example Langston *et al* (1977)), this begs the question; 'does the horseshoe vortex initiate the passage vortex'? The answer is not entirely obvious. Turner (1957) has shown that passage vortices may be formed in the absence of horseshoe vortices, which might suggest that the latter are relatively unimportant. However the situation is complicated by the fact that it is generally agreed that fluid from the pressure side leg of the horseshoe vortex, emerges in the passage vortex core e.g. Langston (1980) and Moore and Smith (1984). The fate of the suction side leg of the horseshoe vortex is rather less clear however. Langston *et al* (1977) thought that it remained in the suction surface/endwall corner, whereas Marchal and Sieverding (1977) found it to emerge on the midspan side of the passage

vortex in their cascade. Sieverding (1985b) suggests that the suction side leg of the horseshoe vortex is convected around the passage vortex on the basis of the work of Moore and Smith (1984), who followed this fluid by a technique of ethylene detection. Hence the final location of the suction leg of the horseshoe vortex is thought to be dependent upon the strength of the passage vortex, and is thus influenced by many factors.

In consideration of this model of the simultaneous evolution of both passage and horseshoe vortices, it seems likely that the horseshoe vortex will have little bearing upon the passage vortex other than to alter locally the rotational velocity of the fluid near the main vortex core where the pressure side leg is to be found. Such a view is expressed by Sieverding (1985b).

## 2.4 Corner Vortices

Endwall flow visualisations may show the existence of a three-dimensional separation line running downstream from the point where the crossflow first meets the suction surface. This then follows a path very close to the suction surface (see for example Marchal and Sieverding (1977)). A similar line may be observed rising slightly above the endwall on the blade suction surface. These are the separation and reattachment lines of the passage vortex which cannot completely follow the perpendicular junction of blade and endwall. A vortex is often found between these two lines, rotating in the opposite sense to the passage vortex. This is probably best illustrated by Gregory-Smith and Graves (1983). Sieverding (1985b) refers to an endwall visualisation taken by Belik (1975) showing this separation line to originate where the crossflow interferes almost perpendicularly with the suction surface, and presents the interesting suggestion that a counter vortex may be formed by a stagnation process similar in nature to that which forms the horseshoe vortex. He also comments that a similar counter vortex may be formed in the pressure side/endwall corner as a result of downwash of the pressure surface boundary layer. This effect is not generally reported in the literature however, possibly owing to the probable small size of such a vortex.

Whatever the precise cause of the suction side/endwall counter vortex, it is often associated with a non-negligible loss core (see Gregory-Smith and Graves (1983), Langston et al (1977)). It is worth noting however, that real gas turbines do not have perpendicular endwall/blade junctions, but will either present a fillet radius or tip gap, either of which will modify the observed flow.

## 2.5 The Endwall Boundary Layer

The state of the endwall boundary layer within the blade row has not yet been entirely resolved. Senoo (1958) found that the boundary layer at the throat of a high turning nozzle cascade was laminar and independent of the state and thickness of the inlet boundary layer. He suggested that this was a relaminarisation effect produced by the strong favourable pressure gradient in turbines. Langston *et al* (1977) in their pioneering paper on secondary flow structures within the blade row, found the inlet boundary layer to be completely removed from the wall by the powerful passage vortex, and rolled up into a loss core. On the basis of this experience they then suggested that Senoo had observed a new boundary layer, formed downstream of the separation of the inlet boundary layer. Whilst most workers have found this new endwall boundary layer too thin to determine its state, Belik (1977) measured the wall shear stress along the centreline of two high turning nozzle cascades with film gauges. He found that the shear stress increased rapidly to a maximum near the point of greatest streamwise pressure gradient. By measuring endwall boundary layer noise, he confirmed that this position was close to the start of a laminar boundary layer. Further evidence for the state of the endwall boundary layer has recently been presented by Harrison (1989). Using film gauges he found that large areas of the endwall boundary layer in a high turning rotor cascade were laminar. This was found to mainly occur in the region of growth of a new endwall boundary layer.

Hence, although there is not yet much information available, the body of evidence seems to be indicating that the thin boundary layer which forms

downstream of the inlet boundary layer separation, is probably laminar within the blade passage on the pressure side. It is however worth noting, that Harrison (1989) found the boundary layer near to the suction surface to be indeterminate from the overall loss core, and to be turbulent.

## 2.6 Distribution of Losses

There are typically three distinct loss cores downstream of turbine cascades. The first is the 'corner' loss on the endwall between successive passage vortices, which is probably aided by the development of the suction side/endwall counter vortex. Another loss core is associated with the passage vortex and is composed of fluid from the inlet boundary layer, with extra losses from the passage walls which are fed into it within the blade row. The third loss core is again in a counter-rotating region between successive passage vortices, but this time it is not adjacent to the endwall. This vortex is generally identified with the shed vorticity of classical secondary flow theory. Such a distribution is evident in the works of Langston *et al* (1977), Gregory-Smith *et al* (1987), Walsh and Gregory-Smith (1987), and Zunino *et al* (1987), all of whom were investigating high turning rotor cascades. These give particularly noticeable manifestations of the various loss features, due to the powerful secondary flows which result from their high turning. The work of Walsh and Gregory-Smith (1987) was concerned with testing the effects of three levels of skew in the inlet boundary layer. For the case of positive skew, where the secondary flows are inhibited, the spatial distinction between the loss cores described above is quite remarkable, particularly in the plane just upstream of the trailing edge. From this distribution of losses, it appears that a significant proportion of secondary loss is produced by the action of the passage vortex on the suction surface. This sweeps low momentum boundary layer fluid into the main flow to form the third of the above loss cores. A similar process occurs with the new boundary layer on the endwall, with some loss collecting in the endwall/suction surface corner.

The position of the passage vortex in the exit plane has obvious

implications for the outlet flow angle distribution of the blade row, but it is not easily predicted. The passage vortex convects itself (Gregory-Smith and Graves (1983)) towards the suction surface, and may then move up the suction surface away from the endwall. The extent of this migration is determined primarily by the strength of the passage vortex, and thus depends upon many parameters such as the blade turning, and inlet boundary layer thickness.

## 2.7 Growth of Losses

Most workers appear to find that the secondary losses are fairly constant up to the position of maximum suction side velocity, and thereafter increase more rapidly (see for instance Langston *et al* (1977), Marchal and Sieverding (1977)). However, a notable exception to this type of loss growth was given by Gregory-Smith and Graves (1983), who found a fairly steady increase throughout their cascade, with a large jump at the trailing edge due to the addition of blade boundary layer losses. Looking closely at the loss curve however, there may also be a more rapid increase in the last 25% of the cascade which is not picked up by the particular axial planes which have been traversed. Certainly in the work of Walsh and Gregory-Smith (1987), who investigated the effects of inlet skew in a very similar blade row, the rate of loss production is seen to rise sharply in the latter half of the cascade. Some of this loss might be accounted for as boundary layer loss which is not covered by the traverses further upstream, but is convected into the mainstream by the passage vortex to add to the losses measured by traverses further downstream. However, another possible explanation might be deduced from the work of Moore (1985). He presented three-dimensional Navier-Stokes calculations of the loss in the cascade of Langston *et al* (1977), and a geometrically similar cascade which was investigated by Moore and Adhye (1985). The latter cascade had an inlet boundary layer which was almost twice the thickness of that in the tests of Langston *et al* (1977). He shows that although the net loss (see section 2.8) measured and predicted for the two cascades is similar, the losses are predicted to be produced earlier in

the cascade with the thicker inlet boundary layer. Experimental information is not available to test this conclusion, but it would fit in with the early loss development observed by Gregory-Smith and Graves (1983), as their cascade had an unusually thick inlet shear layer.

## 2.8 Inlet Boundary Layer Thickness

The thickness of the inlet endwall boundary layer has been varied by many investigators. Marchal and Sieverding (1977) showed that varying the inlet boundary layer thickness from 8.5% to 31.5% span in a linear cascade of nozzle blades, did not alter the rise in loss produced across the cascade. Furthermore they showed that this was true independently for the losses due to the blade boundary layers ('profile losses') and the secondary losses. The more usual loss coefficient is defined relative to some reference pressure (typically inlet freestream stagnation pressure), and hence gives non-zero values of loss at the inlet plane due to the presence of the endwall boundary layer. This type of coefficient then varies with inlet boundary layer thickness, giving rise to a non-constant loss. Marchal and Sieverding defined their loss coefficient relative to the inlet plane mass averaged total pressure in order to overcome this problem. The coefficient they used then gives a measure of loss production by the cascade, and this is often referred to as the 'net' loss.

The work of Gregory-Smith and Graves (1983), tested three inlet boundary layer thicknesses varying from 23% to 42% span in a high turning rotor cascade. They also concluded that 'the effect of varying inlet boundary layer thickness is small on the net increase of loss across the blade row'. Atkins (1987) presents results of varying the inlet boundary layer thickness in a turbine rotor cascade, over a range of displacement thicknesses from 0 to 2.1% of axial chord (approximately corresponding to a range of 99% thicknesses from 0 to 16%). Six different boundary layer thicknesses were tested, and he also concluded that the rise in loss produced across the cascade was constant with respect to this parameter, even down to zero inlet boundary

layer thickness. However, a slightly different result has been presented by Wolf (1961). He shows that for very thin inlet boundary layers, less loss is incurred. He plots a graph showing the net loss rising with inlet boundary layer thickness, until a critical value is reached, whereafter the net loss remains constant. Wolf suggests that this critical inlet boundary layer thickness is that just sufficient to cause complete removal of the inlet boundary layer from the endwall by the action of secondary flow.

Unfortunately none of the above references contain information about the strength of the vortex produced by the different upstream boundary layers, such as the mass averaged kinetic energy of the secondary velocities. One might expect that if the passage vortex is mainly formed from the over-turning of inlet boundary layer fluid, then thickening of this shear layer would result in a greater mass of fluid being subjected to increased deflection, and hence greater secondary kinetic energy. Some support for this view may be found in the viscous three-dimensional calculations of Moore (1985). He showed that whilst varying the inlet boundary layer thickness produced no change in net loss for the cascade of Langston *et al* (1977), the predicted secondary kinetic energy was greatly effected. A thicker inlet boundary layer was shown to produce stronger secondary flows.

One effect that variations in upstream boundary layer thickness are reported to produce, is the differing radial extent of the passage vortex, and the distance from the endwall of its centre. Bailey (1980) showed that a reduction of inlet boundary layer thickness moved the passage vortex closer to the endwall in a linear nozzle cascade, and Gregory-Smith and Graves (1983) showed that a thickened inlet boundary layer resulted in a larger loss zone extending further from the endwall.

## 2.9 Inlet Boundary Layer Skew

Skew is introduced in the endwall boundary layers of real machines, as the fluid emerges from the stationary hub into the rotating blade row. In contrast to the effect of boundary layer thickness, the level of skew present

has been shown to produce profound changes in the secondary flows and losses which develop. Boletis (1984) incorporated some skew tests in his very extensive investigation of the flowfield in annular cascades. Using low aspect ratio high turning nozzles, he found the introduction of skew was significant, and led to the intensification of the secondary flows. Walsh (1987) presents detailed measurements of the secondary flow development in a linear cascade of high turning rotor blades, under three different inlet skew conditions. He also found that the type of skew naturally present in a turbine rotor cascade, caused significant intensification of all secondary flow features, leading to increased secondary kinetic energy and net losses. Walsh (1987) also tested an unusual type of skew for his blade, such that inlet boundary layer fluid contained momentum in a direction opposing the endwall crossflow which generally develops. He found that the flowfield was greatly altered by this inlet condition. The horseshoe vortex pressure side leg penetrated further into the blade passage before meeting the suction surface. The area of endwall covered by 'new' endwall boundary layer fluid was reduced, and the secondary kinetic energy and secondary loss were also seen to decrease.

## 2.10 Passage Aspect Ratio

Variation of blade height was shown by Bailey (1980) to have little effect on the secondary flows in a turbine vane passage, even with a change in aspect ratio from 1.87 to 0.617. In his review Dunham (1970) points out that varying blade height whilst keeping chord and inlet boundary layer thickness constant, suggests that the overall cascade loss is inversely proportional to aspect ratio. However, if span and inlet boundary layer thickness are constant, and blade chord is varied, little change in loss is evident. This might be explained if one considers the overall cascade loss to be composed of three components; an inlet boundary layer 'loss', an extra secondary loss, and a

profile loss. Then, for a linear cascade;

$$\overline{Loss} = \frac{InletLoss + SecondaryLoss}{PassageArea} + \left(\frac{ProfileLoss}{UnitSpan}\right) * \frac{Span}{PassageArea}$$
$$= \frac{InletLoss + SecondaryLoss}{Span * Pitch} + \left(\frac{ProfileLoss}{UnitSpan}\right) * \frac{1}{Pitch}$$

Thus varying the span independently of everything else will result in an inverse relationship between average loss and span (and hence aspect ratio). If the chord is varied independently of everything else, then the test becomes one of varying cascade Reynolds number. Hence if the various losses are not strongly dependent on Reynolds number in the range covered, there may be little effect. This does of course also assume that there is no variation in secondary loss with pitch to chord ratio. The effect of the blade pitch upon the secondary loss is not obvious however. Dunham (1970) comments that most workers assume that secondary loss depends upon the blade turning, and not the pitch, when defining loss correlations. Unfortunately, no experimental evidence is presented in support of this assumption. However, classical secondary flow theory (section 2.15) suggests that the secondary vorticity depends upon the blade turning, but that the secondary velocities that it produces are also dependent upon the passage area (and hence the pitch). Thus, the blade chord seems to have no major influence upon the magnitude of the secondary losses.

Atkins (1987) varied the aspect ratio of a linear cascade of turbine blades in the range 0.36 to 1.44 and observed no effect on the average losses. This change in aspect ratio was achieved by variations in blade span only. However, the result does serve to show that the concepts of a two-dimensional profile loss and net secondary loss remain valid even when the entire blade is swept by secondary flow at very low aspect ratios.

## 2.11 Downstream Loss Growth

Most workers find that the losses continue to grow downstream of the blade row, due to the growth of the endwall boundary layer, and the

mixing of non-uniform flows (e.g. Binder and Romey (1983), Harrison (1989), Gregory-Smith and Graves (1983), Langston *et al* (1977)). Perhaps the most comprehensive piece of work on the processes of downstream loss generation has been provided by Moore and Adhye (1985) and Moore *et al* (1986). In the first paper, Moore and Adhye (1985) traversed four planes from 96% to 140% of an axial chord from the leading edge, of a linear cascade which was a replica of that used by Langston *et al* (1977). They showed that more than one third of the losses occurred downstream of the trailing edge in their cascade. The rise in loss was found to be almost exactly matched by a reduction in secondary kinetic energy, with most of this being lost by the dissipation of radial velocities. This seems a little strange, as viscous dissipation must be occurring in the endwall boundary layer. In a later paper, Moore *et al* (1986) measured the Reynolds stresses at one of the downstream planes, and combined these with the earlier measurements of mean velocities, in order to calculate the rates of turbulent deformation work. They found that two terms could act to produce increases in the mean kinetic energy of the primary flow; a deformation work term involving the streamwise normal stress, which produced mean kinetic energy from turbulent kinetic energy, and a reversible pressure work term which could exchange mean kinetic energy between its three components. These two mechanisms offset the 30% of the loss production rate which was due to shear in the endwall boundary layer. The rest of the loss was found to be balanced by the action of the other turbulent stresses, giving a complete picture of the downstream flow.

## 2.12 Turbulence Measurements

When Sieverding (1985b) wrote his review, he concluded that little was then known about the structure of turbulence in turbine cascade flows. Since that time, however, the literature has expanded, giving rise to a clearer understanding of the flow physics. Priddy and Bayley (1988) showed that in a high speed turbine rotor cascade, the freestream turbulence intensity reduced in accordance with the rising mean flow velocity. Thus the absolute

magnitude of the turbulent fluctuations was found to remain constant in this area. Bailey (1980) measured the turbulent flow in a cascade of inlet guide vanes. He found maximum turbulence intensities of 4% of local velocity, and large regions of the passage vortex to exhibit freestream turbulence levels. He then suggested that laminar flow calculations would prove to be accurate tools for predicting the flow in turbine cascades. A contrasting result was reported by Sharma *et al* (1985). They set out to investigate the unsteady flow in a one and a half stage model turbine. The flow downstream of the first stator was found to be steady, with only small variations due to the presence of the downstream rotor. Measurements of turbulence in the gap between the first stator and the rotor, showed the passage vortex to be turbulent, with intensities of up to 28% of axial velocity present. Downstream of the rotor, the flow was found to be highly unsteady, and typical turbulence intensities in the wake and vortex regions reached 41% of axial velocity.

The work of Moore *et al* (1986) showed that at 10% of an axial chord downstream of a replica of the cascade used by Langston *et al* (1977), the turbulence intensities reached peaks of 25% of upstream velocity. They showed that although only 23% of the total loss could be accounted for directly as turbulent kinetic energy, the turbulence was of major significance in the loss generation process downstream of the cascade. The cross-passage/radial shear stress was shown to be twice as large as the other two, and was considered to be important in the mixing out of radial velocities. It was also shown that the normal stresses played a major part in the conversion between mean and turbulent kinetic energy. In particular, the streamwise stress was found to strongly produce mean flow kinetic energy from turbulent energy as the mixing process accelerated the turbulent, high loss, low velocity regions. Direct viscous action was found to be relatively insignificant as a loss production mechanism.

Perhaps the most detailed investigation of turbulence within a blade passage has been provided by Zunino *et al* (1987). They investigated the flow in a high turning steam turbine rotor cascade. At a position close to the passage throat, they found that high turbulence (12% of upstream velocity)

was associated with the three loss cores (section 2.6). At the downstream location (20% of an axial chord from the trailing edge), turbulence intensities were found to have risen to peak values of 15% of upstream velocity. The turbulent kinetic energy was found to account directly for only 10% of the total loss, but the authors expressed the opinion that this reflected a near balance between the generation and dissipation of turbulence, rather than indicating large quantities of direct viscous dissipation of mean velocities. Another detailed investigation of a linear turbine rotor cascade was presented by Gregory-Smith *et al* (1988). They found peak turbulence intensities of 29% of upstream velocity in the vortex core, but still only 17% of the loss could be accounted for as turbulent kinetic energy. They also found that regions of high loss were associated with high turbulent kinetic energy. Downstream of the cascade, they found that the wake turbulence dissipated whilst the overall turbulent kinetic energy continued to rise. A short spectral survey of the turbulence, indicated that a dominant frequency was present in the energy spectrum, and it was postulated that this might be associated with a periodic shedding of the passage vortex from the passage. No other data seems to be available with which to compare this however. A recent paper by Hebert and Tiederman (1989), showed turbulence intensities of 18% of upstream velocity, to be associated with the passage vortex, and 32% with the separation of the passage vortex from the blade suction surface at exit from a turbine stator. This is somewhat in contrast with the results of Bailey (1980) mentioned previously.

In conclusion, it appears that significant turbulence levels are present in the secondary flow regions of most turbine cascades. This implies that the action of the secondary flow in rolling up the endwall boundary layer, and its interaction with the blade passage boundary layers, results in significant turbulence generation. This process is believed to account for the majority of the secondary losses in such cascades. The fact that the losses are not manifested as an equal rise in turbulent kinetic energy, is probably due to the rate of viscous dissipation of the turbulence almost matching its rate of production. The turbulence levels in rotor cascades are likely to be greater

than those in inlet guide vanes, as the turning angles are generally much larger giving rise to more powerful secondary flows, and the fluid acceleration is less. As the turbulent stress distribution has already been shown to be very complex (see for example Zunino *et al* (1987)), there is a need for test data with which to validate turbulence models for use in the computation of these flows. Also, the above studies were generally for low freestream turbulence levels (Zunino *et al*, Gregory-Smith *et al*, Moore *et al*, and Sharma *et al*, all had inlet turbulence intensities $\leq 1\%$ ). Hence data concerning the effect of variations in inlet turbulence intensity would be valuable.

## 2.13 Summary of 3-D Linear Turbine Cascade Aerodynamics

From the above discussion, quite a detailed description of the three-dimensional flow in a linear turbine cascade can be formed. The endwall boundary layer incident onto the blade leading edges rolls up into a horseshoe vortex. The pressure side leg of this vortex then crosses the passage, forming a separation line which is a distinct feature of endwall flow visualisations. A passage vortex forms under the action of the cross-passage pressure gradient on the endwall boundary layer fluid. The strength of the passage vortex is greatly influenced by the blade turning angle, and is hence powerful in the high turning cascades of turbines. The passage vortex sweeps the endwall boundary layer towards the suction surface, and rolls it up into a loss core. This may then move up the suction surface if the secondary flows are very strong. A new boundary layer forms on the endwall, and is kept very thin by the sweeping action of the passage vortex. It appears to be generally laminar on the pressure side of the blade passage, undergoing transition towards the trailing edge. On the suction side of the passage, the endwall boundary layer is indistinguishable from the overall loss core, and is turbulent. High loss regions appear to be associated with the separation of the passage vortex from the passage surfaces, and these loss cores are observed to be highly turbulent.

## 2.14 Real Turbines

In a real machine, the flow is much more complex than that in the simple test cases which have been considered above. Rotor blades are often unshrouded, and thus over-tip leakage flows develop. Dishart and Moore (1989) showed that the loss due to tip leakage may be very significant. In a replica of Langston's cascade, with a tip gap 2% of blade height, and a very thin inlet boundary layer, they measured greater losses than were found in the same cascade with no tip gap and a very thick inlet boundary layer.

Modern turbines often contain transonic blading. Although there will be losses associated with the shock waves which must be present, Denton and Cumpsty (1987) suggest that these will be small as the shocks are weak and oblique. It is the effect on the boundary layers caused by these shocks, which they considered to be more important. The high speeds typical in modern turbines, may also cause other differences when compared with the simplified flows in low speed cascades. Perdichizzi (1989) found the passage vortex to move closer to the endwall and grow weaker as the Mach number was increased from 0.3 to 1.2. The radial geometry of real machines also results in modified flow features. Boletis (1984), investigated the flow through an annular cascade which used the same blade profile as that of Marchal and Sieverding (1977). The effect of radial pressure gradient was found to be significant. Low momentum fluid migrates from casing to hub under the action of this pressure gradient, which is formed in response to the swirl of the fluid about the axial direction. This low momentum transport was found in the blade boundary layers, and the wake, and resulted in greater losses at the hub than the tip. Perhaps the most daunting aspect of real turbomachines, when compared with simple cascade tests, is the unsteady nature of the flow within them. The works of Sharma *et al* (1985), and Hebert and Tiederman (1989), suggest that the flow through a blade row will resemble the familiar steady flow pattern when upstream blade wakes impinge on the blades, but is markedly different when they enter mid-passage. The flowfield is thus highly unsteady and continuously oscillates between the two

extreme cases described.

In recent years, some attempts have been made to control the secondary flows in isolated, steady flow cascades, e.g. Boletis (1984), Atkins (1987), Dominy and Harding (1989). These tests generally aim to contour the geometry in such a way as to reduce blade loading near the endwalls, and hence lead to less over-turning of the endwall boundary layers. There has been a certain amount of success in these approaches, but the three-dimensional design of geometries to achieve these results is far from simple. This is one of the areas where modern three-dimensional flow solvers might be expected to make advances.

## 2.15 Secondary Flow Theory

Although the details of secondary flows are very complex, it was mentioned previously that the formation of the dominant passage vortex, is essentially an inviscid phenomenon. Viscous effects are required to produce the inlet boundary layer, but thereafter inviscid fluid mechanics will produce secondary flow. This was realised in the 1950's, and attempts were made to predict secondary flows using inviscid vorticity equations. The solution of Squire and Winter (1951), who derived an equation for the downstream vorticity resulting from a given upstream normal vorticity, heralded the start of secondary flow theory in turbomachines.

A similar solution was derived in a different way by Hawthorne (1951). He showed that the equation for the streamwise component of vorticity for steady, inviscid, incompressible flow in the absence of body forces was:

$$\left(\frac{\omega_s}{V}\right)_2 - \left(\frac{\omega_s}{V}\right)_1 = -2\int_1^2 \frac{\nabla P_0}{\rho}\frac{\sin\phi}{V^2}\,d\theta \qquad (2.1)$$

where

$\omega_s = streamwise \quad component \quad of \quad vorticity$

$V = velocity \quad magnitude$

$P_0 = stagnation \quad pressure$

$\rho = density$

$\phi = angle \quad between \quad endwall \quad and \quad normal \quad to \quad Bernoulli \quad surface$

$\theta = angle \quad of \quad turning \quad of \quad fluid \quad through \quad the \quad bend$

A solution of this equation assuming no change in $\phi$, an axial velocity ratio of unity, and small deflection, is:

$$\omega_{s_2} - \omega_{s_1} = -2\omega_{n_1}\theta_{12} \tag{2.2}$$

Here

$\omega_{n_1} = normal \quad component \quad of \quad vorticity \quad at \quad inlet$

$\theta_{12} = total \quad angle \quad of \quad turning \quad of \quad the \quad cascade$

This work has been considerably extended by a number of researchers, and a good review of the subject has been given by Horlock and Laksminarayana (1973).

Although the above work was based on vector analysis and vorticity equations, an alternative approach was suggested by Came and Marsh (1974) based on Kelvin's Circulation Theorem. This analysis is more easily visualised, and the authors clearly described the three streamwise vorticity components to be found downstream, namely distributed secondary vorticity (the passage vortex), trailing filament, and trailing shed vorticity. Trailing shed vorticity arises from the spanwise change in circulation around the blades, whereas trailing filament vorticity is the result of vortex filaments on the suction surface arriving at the trailing edge before the corresponding filament on the pressure surface. Hence the filament is stretched in the wake and together with the trailing shed vorticity, forms a vortex sheet.

Once the streamwise vorticity at the passage outlet has been determined, the flow is solved for by introducing a stream function. Gregory-Smith (1984) has given a good account of secondary flow theory, and the extent

of the work covered gives a clear indication of the effort which has been expended on this approach. Indeed, secondary flow theory has met with considerable success in cascades of small turning, where the underlying assumptions of the theories are not invalidated. However, in the case of many modern turbine cascades, the turning is so severe that the endwall boundary layer is completely removed from the endwall. The assumption of no rotation of Bernoulli surfaces is then obviously in error. Glynn (1982) has proposed a method of streamline tracing, in an attempt to address this problem.

Perhaps one of the most valuable contributions that secondary flow theory can make, is in the understanding of cascade flow phenomena, rather than numerically exact flow predictions. For instance Marsh (1976), used his theory to show that the effect of compressibility on secondary vorticity, was much more important in compressors than turbines. However, the need for a fast design tool, to aid secondary loss estimation in the early stages of design is still accute. It seems likely that secondary flow theory, which does contain at least some of the flow physics, will provide a better basis for such a model than simple correlations.

## 2.16 Secondary Loss Prediction

In order to enable loss estimation in a turbomachine design, a number of correlations have been developed. Dunham (1970) reviewed several such loss prediction techniques and found them to give significantly different results. Dunham thus produced his own correlation, based on the Ainley and Mathieson (1951) blade loading parameter. The secondary loss is then described as :-

$$Y_s = \frac{\overline{\overline{P_{01} - P_{02}}}}{P_{02} - P_2} = \frac{c}{h}\left(\frac{\cos\alpha_2}{\cos\beta_1}\right)\left(\frac{C_L}{s/c}\right)^2 \frac{cos^2\alpha_2}{cos^3\alpha_m} f\left(\frac{\delta_1}{c}\right) \qquad (2.3)$$

where

$$C_L = \frac{2s}{c}(tan\alpha_1 - tan\alpha_2)cos\alpha_m$$

and

$$f\left(\frac{\delta_1}{c}\right) = 0.0055 + 0.078\left(\frac{\delta_1}{c}\right)^{\frac{1}{2}}$$

with $c$ = blade chord, $h$ = blade height, $\alpha_2$ = outlet gas angle, $\beta_1$ = inlet blade angle, $s$ = blade pitch, $\alpha_m$ = vector mean gas angle = $tan^{-1}(\frac{1}{2}(tan\alpha_1 + tan\alpha_2))$, and $\delta_1$ = boundary layer displacement thickness.

The physical basis for such correlations must be derived from the results of cascade tests. Most authors appear to regard the blade loading, and a length ratio term which is associated with the secondary loss, to be of greatest significance. Dunham (1970) has tried to also incorporate the inlet boundary layer thickness, as well as the aspect ratio in his correlation, since he observed that it is variation in blade height which causes changes in secondary loss and not variations in the chord. Thus the assumption that the losses depend upon aspect ratio is over-simplified, and he suggested that this was due to the importance of the inlet boundary layer.

More recent correlations have been reviewed by Sieverding (1985a). Whilst he points out that these now usually take only their physical basis from cascade data, and rely upon real turbine performance measurements for evaluation of the constants, a disturbing lack of agreement between methods is still apparent.

In reality all correlations must rely upon geometrical similarity between blades, and so their use as an innovative design tool is questionable. They do still find application in early design stages however, as they are easily evaluated, and do not require detailed knowledge of the blade profile.

A more realistic secondary loss model has been provided by Gregory-Smith (1982). With a knowledge of the flow physics obtained from the experimental investigations of the 1970's (e.g. Langston *et al* (1977), Marchal and Sieverding (1977)), he was able to design a simple model for the endwall losses in turbine cascades. He used secondary flow theory to calculate the exit vorticity, and solved this for secondary flow velocities using numerical solutions of the equation for secondary flow stream function produced by Glynn and Marsh (1980). Secondary losses were assumed to be composed

of three components, the upstream boundary layer which is shed downstream as a loss core, the new skewed boundary layer which forms on the endwall behind the separation line of the inlet boundary layer, and an extra secondary loss due to the passage vortex and its interaction with the boundary layers. The loss core was assumed to be triangular in shape and had the same mass flow and kinetic energy deficit as the inlet boundary layer. It was centred at a distance from the endwall equal to the inlet boundary layer thickness. The new endwall boundary layer was assumed to be turbulent, and to start at the passage throat. A two-dimensional calculation was performed along the passage centreline, ignoring the effect of skew. For the extra secondary loss, a relationship with secondary kinetic energy seems plausible, and the extra secondary loss was assumed to be equal to the secondary kinetic energy. All three components were then simply added to give the total loss, which could be presented as a function of distance from the endwall. Reasonable results were found for several turbine blade rows.

Work is currently in progress at Durham University (Gregory-Smith and Okan (1989)) to develop the above loss model in conjunction with the streamline tracing secondary flow theory of Glynn (1982), so as to produce a fast calculation method for the secondary flows and losses in a proposed blade row, without the need for a detailed knowledge of the blade profile.

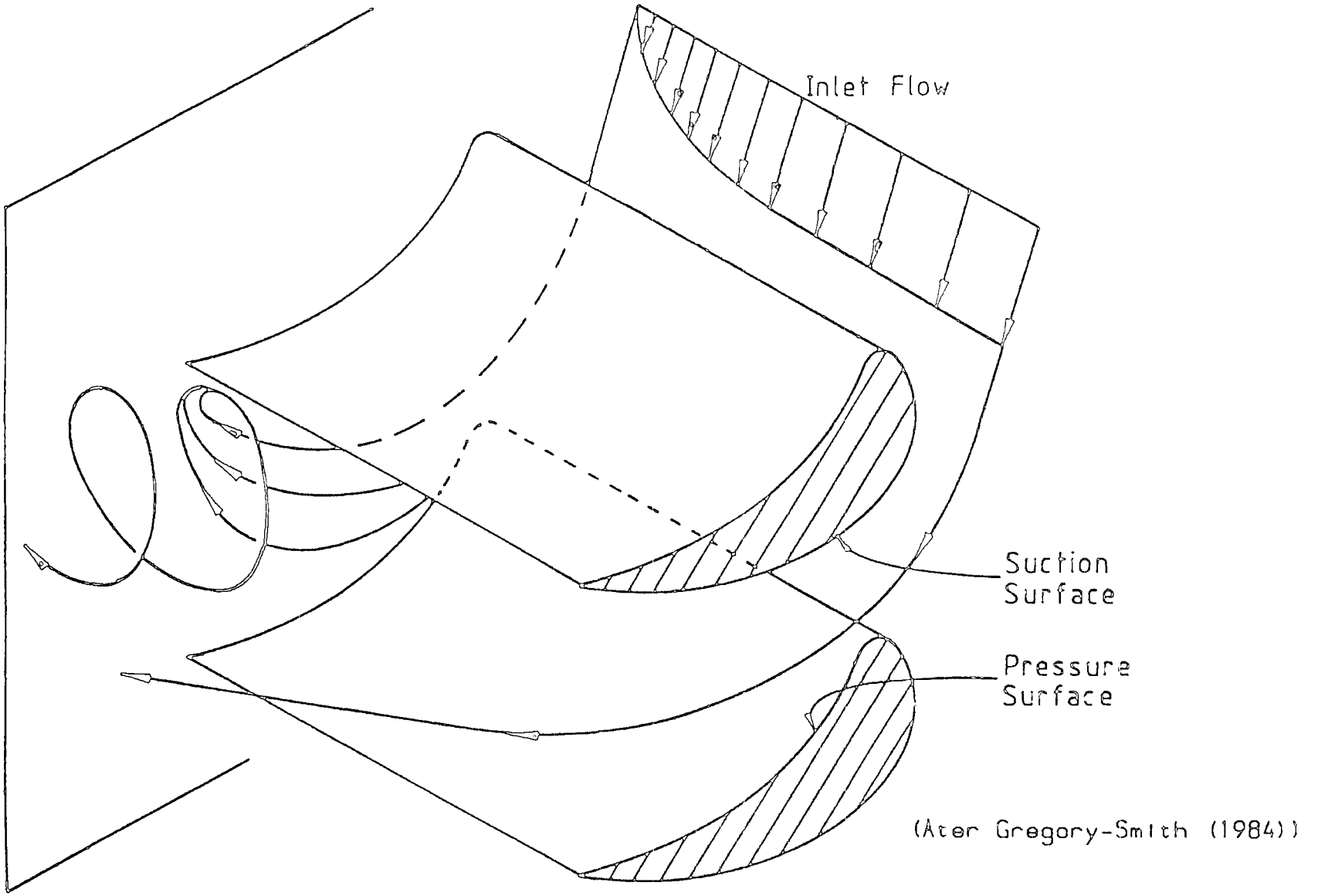


FIGURE 2.1 : The Passage Vortex

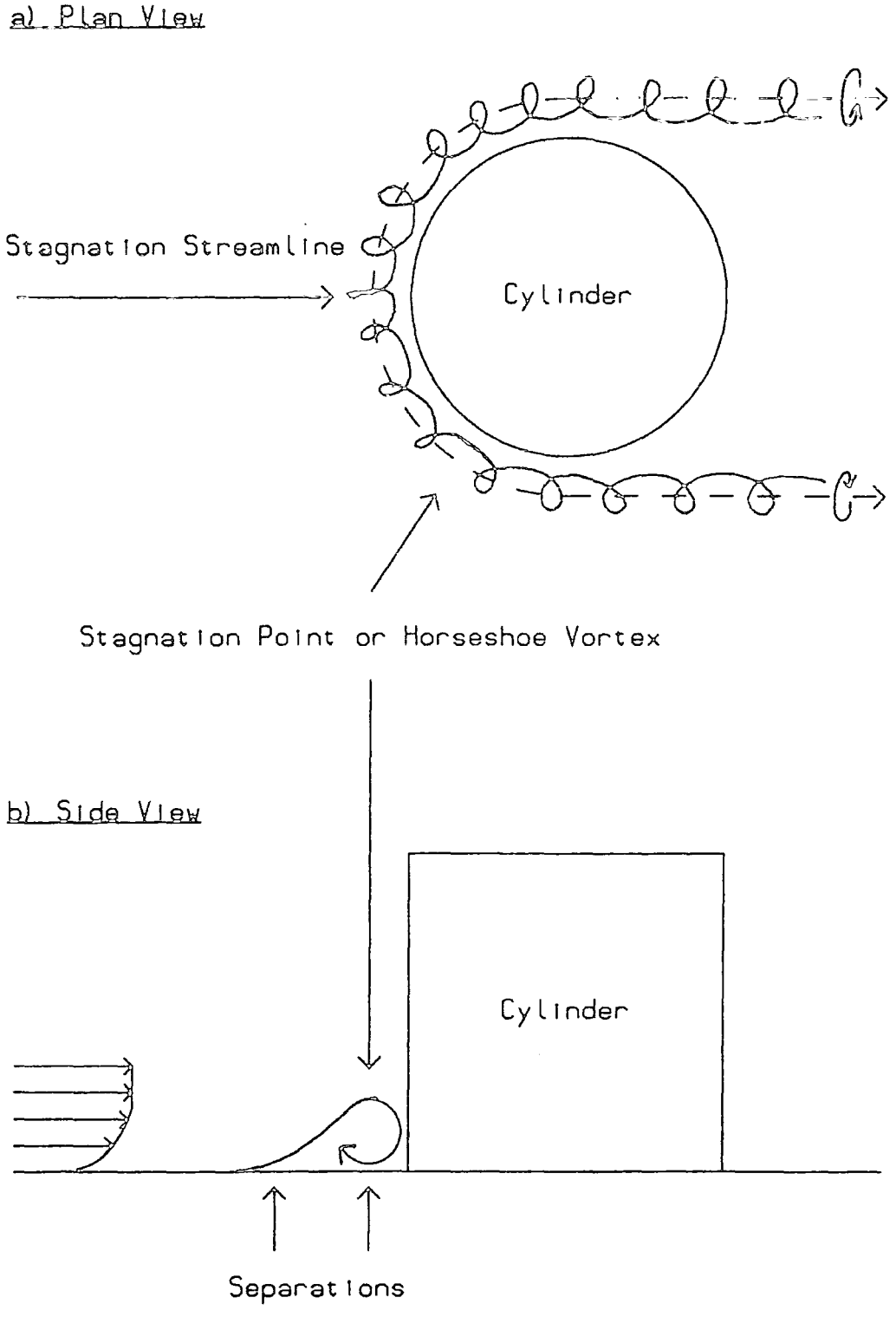


FIGURE 2.2 : Horseshoe Vortex in Front of a Cylinder

# Chapter 3
# Computational Fluid Dynamics and Secondary Flow Simulations

## 3.0 Introduction

This chapter aims to describe the modern application of computational fluid dynamics in turbine technology, with particular emphasis on the state of three-dimensional Navier-Stokes solvers. The basic equations, methods of solution, examples of codes, and some of the problems of these techniques are described. Finally the problem of closure of the Navier-Stokes equations is discussed, and a very brief introduction to the modelling of turbulence within turbomachinery calculations is given.

## 3.1 Computational Fluid Dynamics and Secondary Flows

The early approaches to the modelling of endwall flows in turbomachinery aimed to generalise two-dimensional boundary layer theory to cope with cross-flows. These are considered to be the components of flow perpendicular to the assumed streamwise direction outside the boundary layer. For small cross-flows it was found that the boundary layer could be accurately represented by an equivalent two-dimensional power law velocity profile, and a polar plot of the cross-flow versus 'streamwise' components. Langston (1980) quotes Johnston (1960) as modelling the polar plot with a triangular representation. However this could not adaquately describe the over and under-turning found in the endwall flow of cascades. Langston (1980) states that after much research, it was concluded that no general cross-flow profile existed. Thus in the absence of a universal profile, an integral boundary layer calculation technique could not be general enough to cope with new geometries. Hence as computer power has increased, integral techniques have been abandoned in favour of differential methods. Indeed generally the methods which have been developed to calculate the flows within turbomachines have been governed by

the computational power available to the modellers. Early inviscid methods included singularity approaches for two-dimensional flows. However, the rapid development of computer hardware has led to ever more general calculations.

## 3.2 The Quasi-Three-Dimensional Approach

Wu (1952) proposed a method of tackling the three-dimensional flow problem by calculating the flow on two intersecting families of stream surfaces. The first set are blade to blade surfaces and are generally known as S1 stream surfaces. The other surfaces which lie between the blades, extend from hub to tip and are approximately aligned with the flow direction. The solution of the flow on these S2 surfaces, is referred to as a through-flow calculation. Stow (1985) points out that although Wu's theory can predict the complete three-dimensional flow in the cascade by using an iterative procedure which links the calculations on the two families of surfaces, most workers have not done so. Instead they use the concept of the two families of surfaces, but with only one S2 surface (e.g. Jennions and Stow (1985a,b)). The S1 surfaces are then taken as surfaces of revolution. This is often referred to as the 'quasi-three-dimensional' model as it can cope with varying radial blade sections, and contracting or diverging annulus geometry, but makes no allowance for the endwall effects such as secondary flows. However such methods are used at present by engine manufacturers, and so are worthy of mention. Streamline curvature and stream function techniques for the S1 surfaces are used in these design systems. Such calculations usually incorporate a viscous boundary layer model for the blade to blade calculations. These models generally rely upon correlations for the prediction of transition and are hence limited to calculations at, or near, the design incidence. Trailing edges also present a problem, and are usually modelled with a cusp. Hence there is interest in more general viscous analyses in two dimensions (e.g. Davis *et al* (1988)), as well as fully three-dimensional calculations. These offer the exciting prospect of tailoring blade row geometries in all three dimensions, so as to achieve more favourable downstream conditions.

Dunham (1986) has strongly supported the continued development of computational fluid dynamics (CFD) for turbomachinery analysis. He convincingly argues that advances in CFD in the past have been closely followed by advances in engine design, and moreover, result in less problems requiring solution on the test bed.

## 3.3 The Governing Equations of Fluid Mechanics

The full set of governing equations of a fluid flow may be obtained by considering flow through a small volume fixed in space, or the motion of a small fluid element. An excellent account of the derivation has been given by Anderson (1986). The conservation form of the governing equations derived from consideration of a volume fixed in space, maybe written in matrix form as :-

$$\frac{\partial U}{\partial t} + \frac{\partial F}{\partial x} + \frac{\partial G}{\partial y} + \frac{\partial H}{\partial z} = \frac{\partial R}{\partial x} + \frac{\partial S}{\partial y} + \frac{\partial T}{\partial z} + J \tag{3.1}$$

$$U = \begin{pmatrix} \rho \\ \rho u \\ \rho v \\ \rho w \\ \rho E \end{pmatrix}, \quad J = \begin{pmatrix} 0 \\ \rho f_x \\ \rho f_y \\ \rho f_z \\ \rho(u f_x + v f_y + w f_z) \end{pmatrix}$$

$$F = \begin{pmatrix} \rho u \\ \rho u^2 + p \\ \rho v u \\ \rho w u \\ \rho u(E + p/\rho) \end{pmatrix}, \quad G = \begin{pmatrix} \rho v \\ \rho u v \\ \rho v^2 + p \\ \rho w v \\ \rho v(E + p/\rho) \end{pmatrix}, \quad H = \begin{pmatrix} \rho w \\ \rho u w \\ \rho v w \\ \rho w^2 + p \\ \rho w(E + p/\rho) \end{pmatrix}$$

$$R = \begin{pmatrix} 0 \\ \tau_{xx} \\ \tau_{xy} \\ \tau_{xz} \\ R_5 \end{pmatrix}, \quad S = \begin{pmatrix} 0 \\ \tau_{yx} \\ \tau_{yy} \\ \tau_{yz} \\ S_5 \end{pmatrix}, \quad T = \begin{pmatrix} 0 \\ \tau_{zx} \\ \tau_{zy} \\ \tau_{zz} \\ T_5 \end{pmatrix}$$

$$R_5 = K\frac{\partial \epsilon}{\partial x} + u\tau_{xx} + v\tau_{xy} + w\tau_{xz}$$

$$S_5 = K\frac{\partial \epsilon}{\partial y} + u\tau_{yx} + v\tau_{yy} + w\tau_{yz}$$

$$T_5 = K\frac{\partial \epsilon}{\partial z} + u\tau_{zx} + v\tau_{zy} + w\tau_{zz}$$

where

$$E = total\ \ energy = e + (u^2 + v^2 + w^2)/2, \qquad e = internal\ \ energy$$

$$u, \quad v, \quad w = velocity\ \ components\ \ in\ \ x, \quad y, \quad z\ \ directions$$

$$K = coefficient\ \ of\ \ thermal\ \ conductivity$$

$$f_x, \quad f_y, \quad f_z = body\ \ forces\ \ e.g.\ \ gravity/electromagnetism$$

$$\epsilon = temperature$$

$$\tau_{ij} = stress\ \ in\ \ j\ \ direction,\ \ exerted\ \ on\ \ plane\ \ perpendicular\ \ to\ \ i-axis$$

The matrices F, G, H, are called the flux vectors, and J represents a source term which might include terms to cope with blade row rotation, or body forces due to gravitational or electromagnetic potentials. The solution vector is U. The five equations written in these matrices are the continuity equation, the three Navier-Stokes momentum equations (one for each component), and an energy equation. The equation of state of a perfect gas is then used to close the system. These equations are a set of coupled non-linear partial differential equations for which no general analytic solution is known. The equations can have very different behaviour depending upon their coefficients. If there exist surfaces within the flowfield upon which the solution is at best indeterminate, the equations are said to be hyperbolic. These surfaces are called characteristic surfaces and if they are real, they bound the region which is influenced by the point in the flowfield under consideration. If the characteristic surfaces form a plane in the flowfield the equations are said to be parabolic, and if they are imaginary, then the equations are elliptic. In this last case each point in the flowfield influences all other points. The notation arises from the mathematics of conic sections, which are described by similar equations.

If the viscous stress terms involving derivatives with respect to x are ignored, the Navier-Stokes equations become 'parabolised'. A familiar example of parabolic equations is provided by the boundary layer equations, which are obtained when velocities normal to a surface are considered to be small. Due to their parabolic nature, flow governed by these equations may be solved by calculating conditions at a downstream location from those existing upstream. Hence the calculation may start from upstream boundary conditions, and march downstream in steps, calculating the flow as it proceeds (e.g. Patankar and Spalding (1972)). This is called space marching. By contrast, subsonic steady flow exhibits elliptic behaviour where the solution at any point in the flowfield effects that at any other point, be it upstream or downstream. This means that the solution must be calculated simultaneously for all points, from boundary conditions defined all around the region to be modelled. An example of an elliptic calculation procedure has been given by J.G. Moore (1985a).

## 3.4 Euler Solvers and Time Marching

In numerical solutions for the flow through a particular geometry, the result is a set of numbers which are values of the flow variables at particular discrete points within the region of interest. Hence a grid is set up over the calculation domain to define these calculation points. Clearly the number of points required for three-dimensional calculations will be much greater than that needed to describe a two-dimensional flow. In a solution of the full governing equations (often called the Navier-Stokes equations by the CFD community) it might be necessary to store five variables, two or more turbulence quantities, and possibly other quantities relating to coordinate transformations. As this information must be stored at each point in the flowfield, it is not surprising that the first three-dimensional methods attempted to solve only the inviscid governing equations (called the Euler equations) rather than the full Navier-Stokes equations. These equations are easily obtained from equation (3.1) by setting the right hand side to zero (the

source vector J may be retained if required). This neglects all the viscous terms, and greatly simplifies the simulation task. The Euler equations are parabolic in time, regardless of the type of flow. Thus it is possible to solve them by defining some initial starting guess, and marching forwards in time until the steady boundary conditions cause the solution to settle to a steady state. This method is called 'time marching' and has been widely used in turbomachinery applications, and CFD in general. As an example, the following simple equation is considered:-

$$\frac{\partial u}{\partial t} = \frac{\partial^2 u}{\partial x^2} \tag{3.2}$$

The derivatives may be approximated by a truncated Taylor series to form finite difference equations. If a forward difference is used for the time derivative, and a central difference for the space derivative, a finite difference version of equation (3.2) may be written as :-

$$\frac{u_i^{n+1} - u_i^n}{\Delta t} = \frac{u_{i+1}^n - 2u_i^n + u_{i-1}^n}{(\Delta x)^2} \tag{3.3}$$

Here superscripts relate to the time step number, and subscripts to the grid point locations (e.g. Figure 3.1). As all the values on the right hand side of equation (3.3) are written in terms of the current time step, the value of $u_i^{n+1}$ may be calculated directly from this one equation. This then, is an explicit technique. It is worth noting at this point, that equation (3.3) is not an exact representation of equation (3.2), (unless $\Delta x$ and $\Delta t$ tend to zero). Hence, when performing CFD calculations, the equations which are actually solved are not the governing equations, but an approximate representation of them, and this can have significant effects upon the results.

In equation (3.3) it would be better to write the spatial derivative in terms of average properties between times $n$ and $n+1$. Then :-

$$\frac{u_i^{n+1} - u_i^n}{\Delta t} = \frac{1}{2}\left(\frac{u_{i+1}^{n+1} + u_{i+1}^n - 2u_i^{n+1} - 2u_i^n + u_{i-1}^{n+1} + u_{i-1}^n}{(\Delta x)^2}\right) \tag{3.4}$$

Clearly this equation cannot be solved directly for $u_i^{n+1}$. In this case the finite difference equations must be constructed for each point in the flowfield,

to give a set of simultaneous linear equations. These may then be solved for the new values at each point in the flowfield, simultaneously. Equation (3.4) is an example of the Crank-Nicolson form of time marching and is one example of an implicit method. In general it is found that implicit methods are much more stable than explicit techniques, which are forced to use small time steps if divergence of the solution is to be avoided. Hence long computer running times are required to advance an explicit scheme through a given time interval. Implicit schemes allow much larger time steps, but involve more calculation and hence computer time per time step. As implicit methods are considerably more complex to set up and program, most authors of Euler solvers have adopted explicit techniques. McNally and Sockol (1985) cite Gopalakrishnan and Bozzola (1972) as applying an explicit finite difference scheme (MacCormack's algorithm) to a transonic compressor cascade. This algorithm has also been adopted by Chima (1985), and Shang *et al* (1980). Implicit techniques are more popular for full Navier-Stokes solutions (e.g. Briley and McDonald (1977)).

A slightly different approach which is widely used for internal flow calculations is the finite volume technique. This is obtained by integrating the governing equations over local control volumes surrounding each grid point. In the numerical solution, the integration of fluxes over the surface of the control volume is approximated by a summation over the number of cell faces (usually six in three dimensions) of the average flux through a face multiplied by the area of that face. Denton (1985a) describes such a method, and points out that its popularity in internal flow calculations, arises from its ability to conserve automatically quantities such as mass flow. This results from the fact that any error causing say outflow from one control volume, will cause an equal inflow to another. Denton's scheme is very well known and has been in use for some years, the original method being reported by Denton (1975). Another example of an explicit time marching code utilising finite volumes, is described by Arts (1984).

Time marching Euler solvers have the ability to cope with transonic flows and are hence very attractive for turbomachinery applications, the shock

waves appearing naturally within the solution. Denton (1985a) argues that a calculation method should be simple, as a complex code will only be understood and used by its author. The range of reported applications of Denton's code (and modifications to it) must lend some support to this opinion (e.g. Sato *et al* (1986a,b), Atkins (1987), Walsh (1987)).

## 3.5 Time Marching Stability, Accuracy, and the CFL Condition

As mentioned before, explicit time marching schemes are generally less stable than implicit methods. Indeed generally there is no guarantee that finite difference equations will be accurate or stable under all conditions. Two sources of error are those errors in representing the governing equations in finite difference or finite volume form (called the discretisation error), and the round off error due to repetative calculations to only a finite number of significant figures. If the governing equations are linear, a general error analysis method (the von Neumann stability method) may be applied to obtain a stability limit for the scheme. If such an analysis is applied to the first order wave equation

$$\frac{\partial u}{\partial t} + \frac{\partial u}{\partial x} = 0 \tag{3.5}$$

using first order accurate differences (discretisation errors of order $\Delta x$, $\Delta t$), the stability condition is found to be

$$c\frac{\Delta t}{\Delta x} \leq 1 \tag{3.6}$$

This is the famous Courant - Friederics - Lewy condition (CFL condition) which is taken as the stability limit for explicit time marching schemes. In reality, since the fluid mechanics equations are non-linear, the above stability method may not be applied, and the CFL condition gives only an approximate guide to the stability limit of the scheme. Anderson (1986) illustrates the physical significance of the CFL condition with the aid of a simple example. Considering a second order wave equation he shows that if the CFL condition is precisely satisfied, the characteristic lines running through a given point to

be evaluated exactly bound those points used in the finite difference equation by which it is calculated. If the CFL condition is exceeded, then conditions at a point are evaluated from conditions at other points which do not cover the full range of space which should influence it. This under-couples the flowfield and leads to instability. Conversely, if the CFL condition is easily satisfied (i.e. $\Delta t$ is very small), then the calculation of the value at a point is influenced by a much greater region of space than is physically the case. This procedure is stable but unrealistic, and can produce inaccurate results. Hence it is generally desirable to use time steps which closely approach the CFL condition.

### 3.6 Decoupling, Oscillations, and Smoothing

Other problems which often occur in CFD are related to the discrete nature of the solutions. For example, consider a one-dimensional conservation equation for a quantity $\psi$:-

$$\frac{\partial \psi}{\partial t} + a\frac{\partial \psi}{\partial x} = 0 \tag{3.7}$$

One finite difference equation which might be written as an approximation to this equation is :-

$$\frac{\psi_i^{n+1} - \psi_i^n}{\Delta t} = -a\frac{(\psi_{i+1}^n - \psi_{i-1}^n)}{2\Delta x} \tag{3.8}$$

This procedure would then allow oscillations such as those in Figure 3.2 to exist without damping them. This is often a problem in solutions if nothing is done to counteract it, but causes particular difficulties near shock waves. Denton (1985b) states that it is usual to have to add damping or smoothing terms to the equations in order to prevent 'wiggles' occurring around shock waves which might otherwise influence a large part of the flow. In reality entropy is produced at shock waves, but computationally the shocks are often spread over several grid points and require extra 'numerical' entropy production to produce the correct downstream flow. This must be added carefully to avoid damaging the whole flow prediction. Some natural 'numerical viscosity'

exists in the finite difference equations due to the truncation errors. The particular form this takes will depend upon the type of differencing used. For instance the right hand side of equation (3.8) should really be a series, with

$$\left(\frac{\partial \psi}{\partial x}\right)_i^n = \frac{\psi_{i+1}^n - \psi_{i-1}^n}{2\Delta x} - \left(\frac{\partial^3 \psi}{\partial x^3}\right)_i^n \frac{(\Delta x)^2}{6} + \ldots \qquad (3.9)$$

Here the first neglected term in equation (3.8) is dependent upon $(\Delta x)^2$. Thus finer grids produce more accurate results. Denton (1985a) advocates the use of fine meshes rather than higher order accurate equations, in order to achieve reliable solutions. It is also apparent that the error term depends upon the third derivative of the conserved quantity. This term is analogous to the form of the viscous terms in the Navier-Stokes equations. Thus 'inviscid solutions' will often generate numerical losses which are convected and effect the downstream flowfield just as real viscous losses do.

If oscillations develop within the solution, they may be damped by the addition of extra terms to the equations which introduce viscous type derivatives. The finite difference equations for these terms then introduce strong coupling of the solution on odd and even grid points, damping oscillations. Unfortunately they may also adversely effect the accuracy of the solution, as the equations then effectively describe a more viscous fluid. Generally it is found sufficient to smooth solutions with fourth order derivatives except in shock waves, where second order terms are required. Such smoothing techniques, or their equivalent, are generally employed in time marching methods (e.g. Dawes (1983), Denton (1985a), Chima (1985), Chew and Birch (1987), Dawes (1987), Davis *et al* (1988)).

## 3.7 Acceleration Techniques For Time Marching Solutions

Due to the limits imposed on explicit algorithms by stability requirements, significant expertise has developed in the acceleration of the convergence of the schemes. The most obvious acceleration technique is to use different time steps for each control volume. This destroys the physical meaning of the transients in the solution, but if a steady state solution is required this

is unimportant. Most authors offer the user a choice between uniform, and local time steps. Spatially varied time steps may also be used to increase the 'robustness' of a method. If the local time step is made inversely dependent upon the local rate of change of variables, then local instabilities are restricted. This can prevent a calculation failing in the early stages when large transients are occurring, and is recommended by Denton (1985b).

Another technique which has been shown to be very effective, is multigrid. This groups blocks of control volumes together to perform initial 'coarse grid' calculations, moving on to the refined grid after the initial large transients in the flowfield have been washed out to the boundaries. In some schemes (e.g. Denton (1985b), Chima (1985)) the calculations on both grids are performed in parallel. Denton (1985b) suggests that spatially varied time steps can yield 50% savings in CPU time, whereas multigrid may increase convergence speed by a factor of five.

One particular point of interest for time marching algorithms, is that they usually perform badly in low speed flows. This is because they solve for density, which is almost constant at low Mach numbers. This problem can be overcome without seriously compromising accuracy, by modelling the flow with the maximum Mach number scaled to 0.3. Such practise is recommended by Birch (1989a). However, methods of modifying algorithms to cope with low speed flows have also been developed by some workers, such as the use of pseudo-compressibility.

## 3.8 Calculation Grids

The choice of grid upon which to perform computations is not trivial. Many turbomachinery blade rows exhibit high turning or stagger, and a simple square ('H'-type) grid will result in highly sheared cells (Figure 3.3). Denton (1985b) describes how such sheared cells will increase numerical errors. Considering a simple difference representation, he shows that derivatives with respect to $x$ will be poorly evaluated from the four points shown in Figure

3.3 since

$$\frac{\partial \psi_P}{\partial x} = \frac{(\psi_E - \psi_W)}{2\Delta s}\frac{1}{\sin\theta} - \frac{(\psi_N - \psi_S)}{2\Delta y}cot\theta \qquad (3.10)$$

If $\theta$ is small, $\frac{\partial \psi}{\partial x}$ becomes the difference of two large numbers which are only approximately evaluated with finite differences.

One alternative to accepting the numerical errors associated with sheared grids is to develop a much more complex grid system. Although this has been done by several authors of two-dimensional methods (e.g. Delaney (1982), Chima (1985), Davis *et al* (1988)), such techniques have been less widely adopted in three-dimensional calculations owing to the increased complexity, and computation requirments. However, with grid generation techniques remaining an active area of research in CFD in general, this may change in the future. An attractive method is to solve an elliptic equation to transform a uniform mesh in one coordinate system, to a body fitted mesh in the physical coordinates. Chima (1985), and Davis *et al* (1988), use a Poisson equation to generate a 'C' grid, which certainly contains cells which are much more orthogonal than those which are typical of simple meshes. Taking the idea of coordinate transformations a stage further, the governing equations may be transformed into a 'computational' coordinate system, in which the mesh is uniform. Dawes (1983) describes a two-dimensional implicit method which works on a uniform mesh in the computational plane. However, McNally and Sockol (1985) point out that in three-dimensional calculations, nine or more metric derivatives need to be stored at each grid point, in addition to the flow variables. Hence such techniques are not so common for three-dimensional methods.

As mentioned earlier, the finite difference equations will not be an exact representation of the governing equations. The approximation may be made more accurate however, by using more grid points in the finite difference equations. Usually codes are either first or second order accurate (depending upon whether the error term is of order $\Delta x$ or $(\Delta x)^2$). Sometimes authors will point out that their scheme is second order accurate if it is applied on a smoothly varying mesh (e.g. Dawes (1987)). This arises from neglecting

non-uniform mesh spacing when evaluating the fluxes at a cell boundary from values stored at adjacent cell centres. Such schemes then are prone to give grid dependent solutions, where the use of a carelessly (or inexpertly) constructed mesh might yield very poor predictions, even though the code can be very accurate when applied to a suitable mesh (e.g. Birch (1989a)). Hence the use of transformed equations in a uniform computational plane, might prove to be worthwhile, since it allows the accurate use of simple algorithms, despite the additional storage requirements and transformational complexity.

## 3.9 Pseudo Viscous Approximations

Although Euler solvers have been widely used to model blade row aerodynamics, they do have some limitations. In compressor cascades the growth of boundary layers may have a significant effect on the 'freestream' flow by effectively decreasing the passage area. Gostelow (1984) points out that differences between early British and American cascade tests, resulted from the inclusion of the endwall boundary layer blockage in the British case, whereas these boundary layers were removed in the American work. Another problem with inviscid methods has been identified by Stow (1985). When considering models of the effect of skew in the inlet boundary layer, he shows that inviscid calculations can perform badly as they do not account for the change in boundary layer profile from the inlet boundary to the leading edge. In reality viscous effects can be significant in such a boundary layer, resulting in a different profile entering the blade row from that measured upstream. Hence Stow concludes that care must be taken when using an inviscid calculation to simulate the effects of an inlet boundary layer.

Denton (1985a) describes a method of transpiring fluid through solid surfaces so as to displace the freestream flow by the displacement thickness of the boundary layer as calculated with a simple two-dimensional boundary layer method. He shows that this technique gives more realistic results than a completely inviscid solution in the case of compressor cascades and transonic

fans. A different approach to the simulation of viscous effects in Euler solvers, is to incorporate viscous force terms in the source vector J, as body forces. Denton (1985a) describes such a technique where the magnitude and distribution of the force are chosen 'empirically' by the user to produce good agreement with real flows. Denton himself clearly states that such a model is grossly simplified compared with even the simplest Navier-Stokes solver, but nevertheless reports improved results with the use of this technique. Gregory-Smith (1989) has compared results of Denton's scheme, with those of a state of the art implicit time marching Navier-Stokes solver due to Dawes (1986). The two schemes produce results of comparable quality in this case. However it should be remembered that as soon as empirical constants are introduced into calculations, the methods are strictly limited to the range over which those constants have been determined. Hence Navier-Stokes solvers are still an attractive development as they should offer the possibility of off-design analysis (assuming empirical constants in the turbulence models are adaquately defined). However, Denton (1985a) comments that it is likely to be some time yet before turbulence models are sufficiently accurate to give absolute predictions of aerodynamic loss.

## 3.10 Time Marching Navier-Stokes Solvers

For viscous solutions the full Navier-Stokes equations are solved. The solution procedures are essentially the same as those for the Euler equations. Examples of explicit time marching Navier-Stokes solvers have been reported by Chima (1985), Davis *et al* (1988) in two dimensions, and Shang *et al* (1980) in three dimensions. Such algorithms suffer badly as a result of the CFL condition as fine meshes are required to resolve shear layers. Hence Denton (1987) suggests that implicit methods with bigger time steps are much more attractive for viscous analyses than for Euler solvers. Examples of implicit codes have been reported by Briley and McDonald (1977), Dawes (1983), Dawes (1987), Chew and Birch (1987), and Choi and Knight (1988). Viscous time marching schemes should in principle be able to solve for trailing

edge flows. However, in practise instabilities may occur and Stow *et al* (1987) suggest that it is usually necessary to smooth this region. This smoothing must be very carefully formulated if information concerning aerodynamic loss is to be retained. All the viscous methods suffer from the same grid and instability problems discussed for Euler solvers. Smoothing is required and this is normally a mixture of second and fourth order differences. A further application of time marching, is to compute the unsteady flow through blade rows, and blade row interaction. This would require time accurate calculations and is a major incentive to the continued development of time marching algorithms.

## 3.11 Pressure Correction Techniques

A completely independent approach to flow modelling which has developed alongside time marching is the method of pressure correction. The technique was originally developed to deal with flows in which viscous effects are significant, before the computational power became available to perform three-dimensional time marching Navier-Stokes calculations. However the method has been developed to such an extent as to rank alongside time marching as a major CFD technique. As mentioned previously, the boundary layer equations are parabolic in space, thus permitting solution by marching downstream from an inlet boundary. The early pressure correction methods were developed to solve the more general problem of parabolised Navier-Stokes equations, which are obtained by neglecting the streamwise viscous diffusion terms. However the concept has been extended to a wider range of flows as greater computer power has become available.

## 3.12 The Parabolic Approximation and Pressure Correction

The fully parabolic methods require some extra assumption beyond the neglect of streamwise viscous diffusion. This might be obtained by assuming knowledge of the primary flow direction so that convective derivatives and

viscous terms can be ignored in the transverse momentum equations. However the method of Patankar and Spalding (1972) utilises a different approach. The pressure field is initially guessed, and then the momentum equations are solved to give a first approximation to the velocity field at a particular plane. Corrections are then made to the pressure field and velocity field so as to satisfy the continuity equation over the plane. Approximate relations between the pressure corrections and velocity corrections are introduced from consideration of the momentum equations. These are substituted into the continuity equation to obtain a set of simultaneous equations for the pressure corrections on the plane being considered. The additional parabolising assumption is the assumed knowledge of the pressure gradient in the marching direction. Patankar and Spalding (1972) firstly calculate this by consideration of the overall mass flow through the plane and the use of a separate pressure correction. The solution may then be marched downstream from an inlet boundary. Only one such marching sweep is required. Such parabolic techniques are computationally efficient, but cannot cope with reverse flow, upstream transmission of pressure, and streamwise viscous transport of momentum. Another example of a parabolic method has been presented by Lawrenz (1984).

## 3.13 Partially Parabolic Pressure Correction Methods

A further generalisation of the range of flows which may be calculated can be obtained with the aid of a partially parabolic calculation procedure. This uses a parabolic technique to obtain an estimate of velocities and pressures, and then sets up a three-dimensional pressure correction equation based upon the divergence of the momentum equations. The whole procedure can then be iterated until the pressure corrections become small. Such methods thus allow for the upstream transmission of pressure. Pratap and Spalding (1976), and Moore and Moore (1979) have described the detailed application of partially parabolic techniques. Dodge (1977) splits the velocity into viscous and potential parts $\mathbb{U}$ and $\nabla\phi$. $\mathbb{U}$ is obtained from marching the momentum equations, and $\phi$ is updated after each full sweep by solving a

three-dimensional elliptic equation obtained from continuity. An approximate relation between pressure and $\phi$ then enables the pressure field to be updated.

Although all partially parabolic calculations involve iteration of the scheme, with multiple marches through the flowfield, convergence is usually rapid and only a few 'passes' are required when compared with the thousands of iterations which might be necessary in a time marching solution. The method of Moore and Moore (1979) also iterates on each marching plane to ensure convergence of the momentum and continuity equations. Partially parabolic techniques are more general than parabolic calculations, and have been applied to turbomachinery flow problems (e.g. Pouagare and Delaney (1986)). They require greater storage and calculation facilities than fully parabolic methods, but still cannot describe reverse flow phenomena such as the horseshoe vortex.

## 3.14 Fully Elliptic Solutions by Pressure Correction

Although partially parabolic methods have been used for turbomachinery flow calculations, the full description of a subsonic flow is an elliptic problem. The advantages of an elliptic calculation procedure over a partially parabolic method, are that mass, and viscous transport can be transmitted upstream. Thus in the turbomachinery environment, the elliptic methods can cope with reverse flow phenomena such as the horseshoe vortex (even the passage vortex may appear to cause reverse flow if a very poorly aligned mesh is used). As an elliptic method implies simultaneous solution over the entire flow region, such calculations place greater demands upon the storage and processing power of computer hardware, and have only become realistic in the past decade. Two main methods of interest which have been developed for turbomachinery flow analysis, are those of Moore and Moore (1985), and Hah (1984). Both methods utilise finite volume approaches, and solve a fully elliptic equation for pressure corrections. The method of Hah (1984) may be applied to both steady and unsteady flows, whereas that of Moore and Moore is designed to solve for steady flows only. Both codes have been used

to model the flow described by Langston *et al* (1977), and results have been compared by Moore (1985). The performance of these methods is very encouraging, with secondary flow phenomena being reasonably predicted in both cases. Detailed differences between these two codes include the discretisation technique, and the turbulence model used to simulate turbulent stresses on the control volume surfaces. Hah uses an two equation (k-$\epsilon$) model to evaluate evaluate a turbulent viscosity, whereas Moore and Moore use a simple Prandtl mixing length model.

Of particular interest for the work presented in this thesis, is the calculation technique of Moore and Moore (1985). The method has been described in detail by J.G. Moore (1985a,b), and is based upon Patankar's SIMPLER algorithm. The basic calculation procedure is outlined below :-

1. Initial 3D estimate of flowfield.
2. Calculate effective viscosity with turbulence model.
3. Calculate density from the gas law (perfect gas).
4. Calculate velocity field from the momentum equations.
5. Use approximate relation between pressure corrections and velocity corrections (obtained from consideration of the form of the momentum equations) to form a pressure correction equation from the continuity equation.
6. Solve the set of simultaneous equations for the pressure corrections.
7. Update the velocity and pressure fields.
8. Solve the energy equation for rothalpy and calculate the temperatures, entropy, etc.

The calculation is then repeated from step two, until the pressure corrections become acceptably small. In the above sequence the velocity field is calculated explicitly from existing conditions. If this calculation is performed implicitly, the procedure is similar to Patankar's SIMPLE algorithm. This improves convergence of the velocity field, but can lead to divergence of the pressure field. Significant under relaxation is then required to maintain stability. Hence the procedure which has been adopted alternates between explicit and implicit velocity calculations on successive iterations. To maintain

stability, the pressure field is not updated on iterations where the momentum equations are implicitly solved. This then is the final algorithm which is similar to Patankar's SIMPLER algorithm. Discretisation uses linear variations of velocities and pressures between grid points, thus giving the scheme second order accuracy.

The advantage of pressure correction methods is that they can be very efficient, requiring a few lengthy iterations, compared with the multiple quick iterations of explicit time marching procedures. Since few iterations are required, with a significant proportion of the time being spent on matrix operations, the use of linear variations of quantities is relatively insignificant in terms of computation time. This results in greatly improved capacity to cope with distorted grids, and can produce accurate solutions on fairly coarse meshes.

## 3.15 Upwinding, Accuracy and Stability

In the past pressure correction techniques have often used upwind differencing to obtain well posed equations for control volumes drawn around the grid points. In an excellent lecture, J.G. Moore (1985b) describes how such a procedure introduces large quantities of numerical viscosity into the calculation, which can be of similar magnitude to the physical viscous effects. Hence the calculation of losses with such a technique produces spurious results. A different approach is then proposed, based upon the use of upwinded control volumes. Such upwinded momentum control volumes are used by Moore and Moore (1985) in their calculations. They are determined such that they approximately follow the local flow direction, and so may change shape as the solution progresses. The effect of upwinding control volumes is shown by J.G. Moore (1985b) to eliminate artificial viscosity or numerical mixing, but she also shows that on a grid that is not well aligned with the local flow direction, the technique does result in some artificial cross-convection of conserved quantities. Hah (1984) also recognised the problem of upwinding. His approach was to use a higher order accuracy differencing scheme which is

more stable than simple central differencing. However, he still has to resort to upwind differences when the stability limit for a given cell is exceeded. Stow (1985) has stressed the importance of such methods of eliminating numerical viscosity in calculations. Loss is an important parameter, and he comments that before it is possible to validate turbulence models for the calculation of losses, grid independence from numerical viscosity must be achieved. Hah and Leylek (1987) investigated the effect of grid refinement upon results produced by Hah's code with four different grid sizes. They plotted loss against the inverse of the total number of grid points, and showed that substantial grid independence was achieved with the use of one hundred thousand points in a turbine nozzle row. Moore (1985), comparing losses calculated for the Langston cascade with those presented by Hah (1984), suggests that Hah's method still includes some numerical mixing. It is this numerical mixing which is reduced by refinement of the calculation mesh, so the number of grid points required to achieve low numerical error will vary from algorithm to algorithm. Although smoothing does not appear to be so generally applied to pressure correction techniques, the earlier comments about decoupling and oscillations do still apply, and damping may be required in certain areas.

### 3.16 Code Validation & Pressure Correction Versus Time Marching

Validation of methods is clearly an important exercise for establishing the strengths and weaknesses of different methods and their capabilities. The validation process is not trivial as fully three-dimensional flows are being computed. Hence there is a need for detailed test cases. The cascade of Langston *et al* (1977) has proved a popular choice for code authors. Hah (1984), Moore (1985), and Choi and Knight (1988) have presented results of modelling this flowfield. Although specific differences do exist in the quality of solutions, there is no major difference between the results of all three methods, and certainly no large discrepancy is apparent between time marching and pressure correction solutions. Kirtley *et al* (1986) also concluded that no significant difference existed between the quality of results obtained

from time marching and partially parabolic pressure correction, using both algorithms on the same calculation grid. The results of Northall *et al* (1987), who modelled the VKI annular turbine cascade tested by Boletis (1984), showed that the Moore's code can produce good predictions of blade row loss production with a fairly modest grid (21420 points). Although this is a triumph for the numerical accuracy of the procedure, it was necessary to know in advance where the transition of blade boundary layers occurred. Thus as the numerical accuracy of algorithms increases, so the relative importance of turbulence modelling will rise, and it is this concern to which much of the work in this thesis will be directed.

## 3.17 Turbulence Modelling

Although the Navier-Stokes equations (equation (3.1)) should describe the full turbulent motion of a fluid (provided that the smallest eddy scales are orders of magnitude greater than the molecular mean free path), in practise calculation grids cannot be made fine enough to do so. Thus the equations are Reynolds averaged (i.e. time averaging of turbulent fluctuations) so as to maintain time dependent terms for gross unsteadiness within the flow, but describe the effects of turbulent motions with a suitable model.

For a laminar flow, the viscous stress terms in equation (3.1) may be written as :-

$$\tau_{ij} = \mu \left( \frac{\partial U_i}{\partial x_j} + \frac{\partial U_j}{\partial x_i} \right) - \frac{2}{3} \mu \frac{\partial U_k}{\partial x_k} \delta_{ij} \tag{3.11}$$

where the summation convention is in operation, and $\delta_{ij}$ is the Kronecker delta. In a turbulent flow, the Reynolds averaged Navier-Stokes equations will include extra terms due to momentum transfer by the turbulent motions. These extra terms are the components of the Reynolds stress tensor

$$\tau_{ij}^{T} = -\rho \overline{u_i' u_j'} \tag{3.12}$$

where $u_i'$, $u_j'$ are fluctuating turbulent velocities such that $\overline{u_i'} = \overline{u_j'} = 0$. Although it is possible to write down transport equations for the Reynolds

stresses, these introduce extra source terms involving triple correlations. Again transport equations can be written for the triple correlations, but this merely introduces higher order correlations, and so the process can be repeated. This is called the problem of closure, and at some stage it is necessary to model the correlations in some way. Generally turbulence models attempt to describe the components of the Reynolds stress tensor directly.

Most models employed in turbomachinery calculations to date have been of first order closure, and use the Boussinesq eddy viscosity concept :-

$$\mu_t = \frac{-\rho\overline{u_i' u_j'}}{\left(\frac{\partial U_i}{\partial x_j} + \frac{\partial U_j}{\partial x_i}\right)} \tag{3.13}$$

This assumes that the turbulent stresses depend upon the mean rate of strain in the same way as the molecular viscous stresses do. The effective viscosity which is the sum of the molecular and turbulent viscosities, is then substituted into equation (3.11) in order to account for the turbulent stresses. It is worth noting at this point, that the eddy viscosity hypothesis is in reality erroneous, as it tries to compare the interactions of turbulent eddies with those of molecules. This cannot be corrrect since the mean free path between eddies is not necessarily negligible compared with the flow dimensions, and the eddies do not transfer momentum by a series of discrete collisions as molecules do.

The simplest form of turbulence model specifies the eddy viscosity algebraically. The concept of a mixing length was introduced by Prandtl as an analogy to the mean free path of molecular interactions. Hence the mixing length is related to the eddy viscosity by the formula :-

$$\mu_t = \rho l_0^2 \left[\frac{\partial \overline{U_i}}{\partial x_j}\left(\frac{\partial \overline{U_i}}{\partial x_j} + \frac{\partial \overline{U_j}}{\partial x_i}\right)\right]^{\frac{1}{2}} \tag{3.14}$$

Prandtl suggested that within the boundary layer the mixing length was directly proportional to the distance to the wall, and further out was proportional to the boundary layer thickness. Von Karman suggested the following relation for the mixing length in a simple two-dimensional boundary layer, from similarity considerations

$$l_0 \quad \alpha \quad \left(\frac{\frac{\partial \overline{U}}{\partial y}}{\frac{\partial^2 \overline{U}}{\partial y^2}}\right) \tag{3.15}$$

However, the mixing length model, which is used here for work with the code of Moore and Moore (1985), follows Prandtl's suggestion and hence the mixing length is specified by the equation :-

$$l_0 = MIN(KnE_v \quad , \quad \lambda\delta) \tag{3.16}$$

where $n$ is the distance to the nearest solid boundary, $\delta$ is the shear layer thickness, $K, \lambda$ are constants (0.41, 0.08), and $E_v$ is the Van-Driest damping factor, used to cope with near-wall effects. The specification of the shear layer thickness, $\delta$, is difficult, and will be discussed in later chapters as appropriate. In the freestream, where no shear layer can be identified, a constant mixing length is assumed. This can be specified directly by the user, or it is calculated from the inlet turbulence intensity and a characteristic length scale.

The eddy viscosity has also been modelled by assuming a link with turbulent kinetic energy, and solving a transport equation for this quantity. Prandtl proposed :-

$$\mu_t = C_\mu \rho K^{\frac{1}{2}} l \tag{3.17}$$

where $K$ is the turbulent kinetic energy, $l$ is a length scale, $C_\mu$ is a constant. Thus there are a set of turbulence models called one-equation models in which a differential equation is solved for the transport of turbulent kinetic energy, and the length scale is specified algebraically. Such a model is described by Birch (1989b), and will be considered in more detail later. In two-equation models, a transport equation is also solved for the length scale (e.g. Hanjalic and Launder (1972)). Usually the transport equation solves for the dissipation rate $\epsilon$, which implies a length scale. Hence such models are frequently referred to as $K - \epsilon$ models.

Although the complexity of the above models for turbulent stresses is rapidly increasing (the $K-\epsilon$ model involves solution of two differential transport equations), they are all still bound to the concept of an eddy viscosity. To move away from the limitations of such an unphysical assumption, it is

necessary to model the components of the Reynolds stress tensor directly. Such a model has been proposed by Launder *et al* (1975). However McNally and Sockol (1985) comment that although the recent focus of modelling has shifted to Reynolds stress models, at present they show little or no advantage over simpler treatments. This is especially true of separated flows. One problem is that the validation of the models is itself difficult, due to the numerical viscosity effects which are often present in CFD calculations.

Certainly the modelling of turbulence in turbomachinery flows is a formidable task. McNally and Sockol (1985) suggest that good flow predictions should be possible for turbomachinery components using only simple turbulence models, as the motion is essentially pressure driven. Whilst this may be true for the basic flow patterns, it seems doubtful that losses will be so easily evaluated. This is because the losses are really a small part of the total flow energy. Even if the small flow perturbations caused by turbulence effects seem inconsequential as far as mean velocities are concerned, that does not necessarily imply that losses will be similarly unaffected. Indeed experimental evidence supports the natural expectation that turbulence is important in the loss production process. Hence the level of turbulence modelling that will be required to obtain realistic predictions of aerodynamic loss, is at present unclear. It is hoped that the work presented in this thesis will help to, at least partially, clarify the situation.

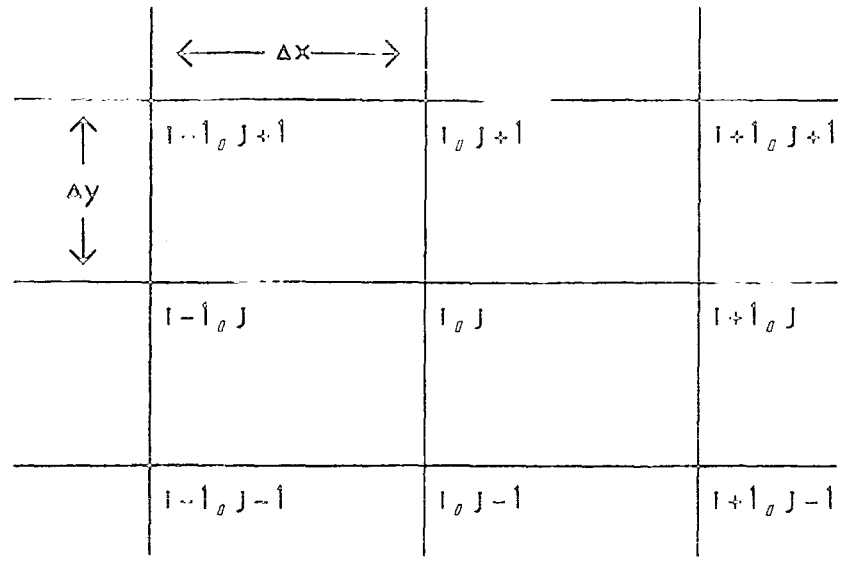


FIGURE 3.1 : Calculation Grid Point Arrangement

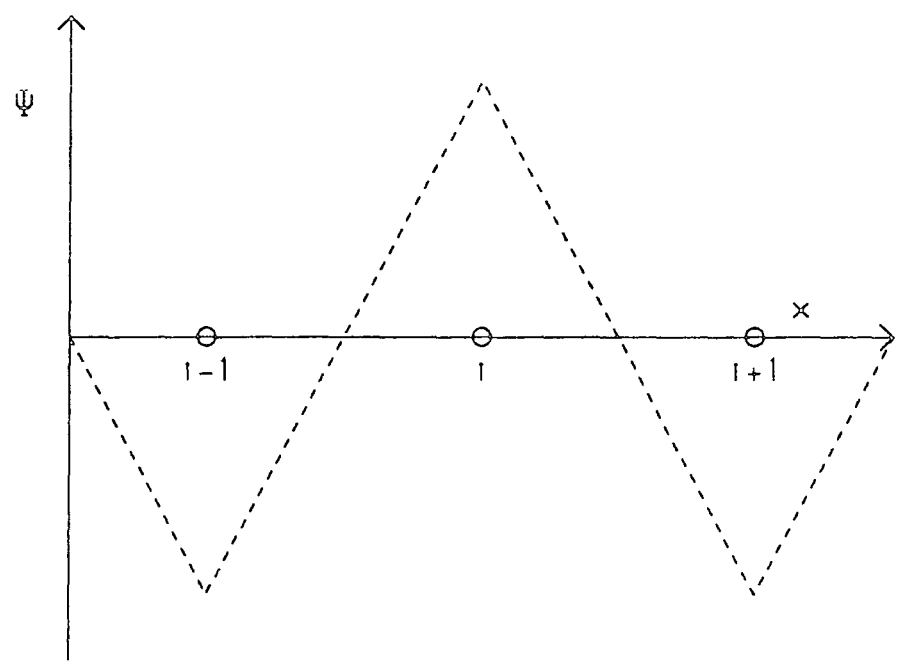


FIGURE 3.2 : Decoupling of Odd/Even Point Solutions

a) A Skewed Calculation Mesh

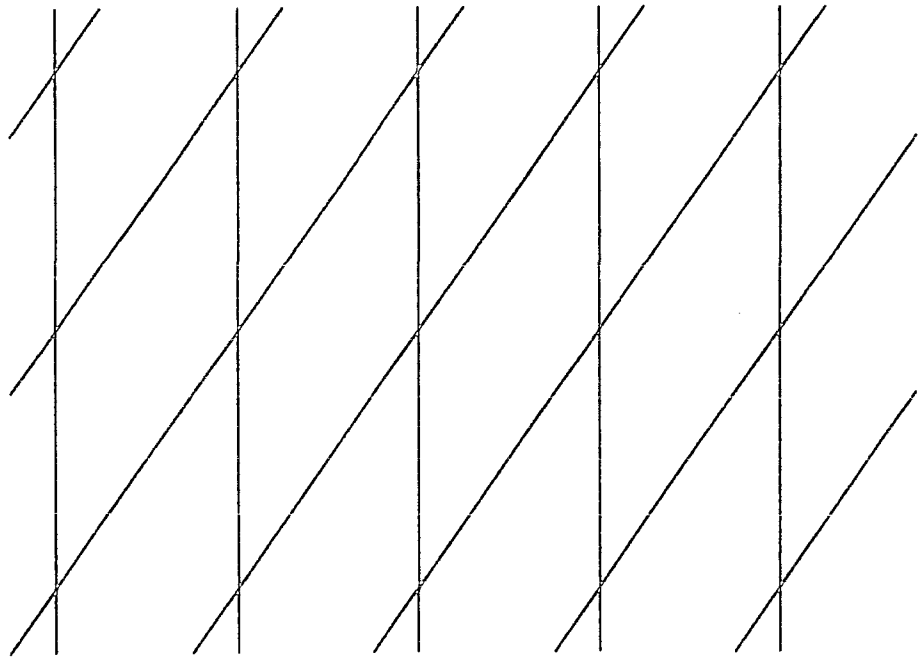

b) The Numerical Problem

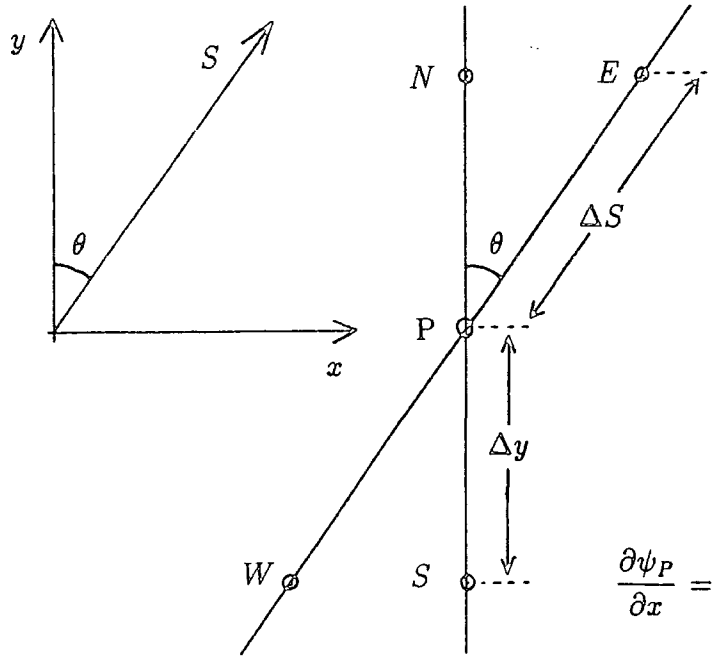


$$\frac{\partial \psi_P}{\partial y} = \frac{\psi_N - \psi_S}{2\Delta y}$$

$$\frac{\partial \psi_P}{\partial s} = \frac{\psi_E - \psi_W}{2\Delta s}$$

$$\frac{\partial}{\partial s} = \frac{\partial}{\partial x} sin\theta + \frac{\partial}{\partial y} cos\theta$$

$$\frac{\partial \psi_P}{\partial x} = \frac{\psi_E - \psi_W}{2\Delta s} \frac{1}{sin\theta} - \frac{\psi_N - \psi_S}{2\Delta y} cot\theta$$

FIGURE 3.3 : Numerical Effect Of Skewed Calculation Mesh

# Chapter 4
# Apparatus and Techniques

## 4.0 Introduction

This chapter describes the apparatus and techniques used to obtain the experimental data presented in this thesis. A brief description is given of the large scale, low speed turbine cascade and its associated wind-tunnel. A review is made of the instrumentation employed to obtain test data from the cascade, and techniques of data aquisition and analysis are also discussed, together with considerations of experimental accuracy. The cascade facility and several experimental techniques had already been used for research prior to this project, hence detailed discussion will be restricted to developments introduced since then.

As well as the experimental techniques, some information is also given about the facilities used to run and assess three-dimensional, viscous Navier-Stokes calculations of the flow in the Durham cascade.

## 4.1 The Durham Cascade Facility

As this project forms part of a continuing program of turbomachinery research at Durham University, much of the apparatus and experimental techniques have been inherited from previous workers. Graves (1985) investigated the secondary flows in a linear cascade of turbine blades mounted on the exit of a low-speed wind tunnel which remains largely unchanged. The tunnel is supplied by a dual entry centrifugal fan, which blows air down a short parallel walled section, before allowing it to diffuse through gauzes into a large settling chamber. The air is then accelerated through a contraction, and finally passes through a honeycombe flow straightener before entering the parallel walled working section. The cascade is mounted at the end of this section, and exhausts to atmosphere. Walsh (1987), modified the working section to include a moving wall (achieved by use of a belt on driven rollers)

which he used to investigate the effects of skew in the inlet boundary layer, upon the development of secondary flows in a second turbine cascade. All work presented in this thesis will be concerned with the flow through this more recent cascade (which Walsh termed the 'JAW' cascade).

Since testing with this facility is restricted to low speed (incompressible) flow, excessive suction surface diffusion results from the use of a blade profile designed for transonic conditions (e.g. Graves (1985)). Hence a notable feature of this cascade is that it was designed to give aerodynamic similarity to a typical high pressure turbine blade section, rather than be an exact geometrical copy. Although full details of the cascade are given by Walsh (1987), the design parameters are reproduced below :-

Table 4.1 : Cascade Design Data

| | |
|---|---|
| Flow Inlet Angle (degrees) | 42.75 |
| Blade Exit Angle (degrees) | −68.8 |
| Blade Chord (mm) | 224 |
| Axial Chord (mm) | 181 |
| Blade Span (mm) | 400 |
| Blade Pitch (mm) | 191 |
| Zweifel loading coefficient | 0.97 |
| Cascade Reynolds Number | $4 * 10^5$ |

A right handed cartesian coordinate system is defined for the cascade, with radial coordinates increasing from zero at one endwall (such that in Figure 4.1 the positive radial direction is out of the paper). This axis system which is aligned with the scales drawn in Figure 4.1, is referred to as 'cascade coordinates' in this thesis. The 'hot-wire coordinates' which are drawn in Figure 4.1 refer to the coordinate system in which turbulent Reynolds stresses are measured using a hot-wire anemometry technique discussed in section 4.4. This 'hot-wire' coordinate system is aligned with the midspan flow direction at each tangential position.

## 4.2 Turbulence Grid

The level of freestream turbulence which develops naturally in most wind tunnels is less than one percent of mean velocity. The Durham tunnel was reported by Gregory-Smith *et al* (1988) to be at the high end of this range, with an intensity of approximately one percent.

Several factors made an investigation of the effects of increasing this freestream level seem worthwhile. The turbulence intensities typical of a modern gas turbine are larger than those which are present in most wind tunnels, and so a test with a turbulence grid placed upstream of the cascade would be more realistic. Also the effect of the freestream level upon the flows and losses is not fully understood. It seems likely that an increased turbulence would promote earlier transition of boundary layers. As discussed previously, the blade profile used in this work was redesigned to give a smaller amount of suction surface diffusion when run at low speeds. Despite this, however, a small laminar separation bubble was observed on the suction surface of the blade at approximately 80% of an axial chord from the leading edge (Walsh (1987)). Hence an increased level of freestream turbulence could eliminate the separation bubble completely, promoting a smooth transition from the laminar to turbulent states. This would make a more interesting comparison with the results of Gregory-Smith *et al* (1988), who thought that the higher turbulence in their cascade, and in particular the presence of a dominant frequency in the energy spectrum, could be due to a gross unsteadiness resulting from the presence of a large separation bubble on the suction surface of their blade.

In order to determine the freestream turbulence intensity that would be required to eliminate the laminar separation bubble on the blade's suction surface, several runs were undertaken with a quasi three-dimensional computer code, based on the streamline-curvature technique. Details of the method have been presented by Morgan (1984), and by Jennions and Stow (1985a, 1985b). Results of three calculations are shown in Figure 4.2, where the intermittency of the boundary layer (i.e. the proportion of the time that the boundary layer is turbulent) is plotted against the distance along the suction

surface from the leading edge. A vertical jump from an intermittency of zero to one indicates the presence of a separation bubble. Hence the results show that a freestream turbulence intensity of 4% should be sufficient to promote a smooth transition from the laminar to turbulent states. In order to give a margin for error, it was decided to design the turbulence grid to give an intensity of 5% at inlet to the cascade.

The aerodynamic design of a suitable geometry is not straight-forward, as the limitations imposed by the rig in which the grid is to be mounted, force a compromise to be reached with the desirable properties of such a device. An excellent account of these aerodynamic factors influencing grid design has been given by Roach (1987). Additional factors due to the rig, included the moving belt on one endwall, which meant that if the grid was to be mounted within a distance of $1200mm$ of the cascade, it could not be supported from one side. Also the large inlet angle of the Durham cascade results in significantly varying distances between the grid and the cascade, if the grid is mounted perpendicularly to the tunnel. As the turbulence decays with downstream distance, this would cause greater turbulence intensities to be received by the uppermost blade passages. However, mounting the grid parallel to the cascade to overcome this problem, results in a deflection of the flow as it passes through the bars. A large distance to the cascade is then required to allow the flow to regain as much uniformity as possible before inlet. A large distance between the grid and the cascade is also desirable in order to prevent significant decay of the turbulence within the blade passage, as well as allowing time for individual jets (emerging from the open spaces between bars) to mix fully, thus promoting isotropic conditions. However, for a given intensity at inlet, the diameter of the bars comprising the grid increases with the distance to the cascade. The grid must not present so much blockage as to exceed the fan's capability to run the tunnel at the required Reynolds number, but too large a pitch results in big jets (which take longer to mix) and hence less isotropy of the inlet turbulence. Also the grid should have enough bars to act like a grid, and not individual obstructions (in the extreme case there would be just one bar vertically and

one bar horizontally).

The initial design was based upon data from a paper by Bains and Peterson (1950). The best solution to the problem was felt to be a grid of one inch diameter bars, mounted upstream of the belt at a distance of $1400mm$ from the cascade. The bars were mounted parallel to the cascade at a spacing of $80mm$ in the horizontal direction. Since the grid is at an angle to the incoming flow, and all the design data was based upon grids mounted perpendicularly to the flow, it was decided to open up the spacing to a distance of $\frac{80mm}{\cos 42.75^{\circ}}$ in the direction parallel to the cascade, so as to present a 'vertical' spacing of $80mm$. The bars were made of aluminium tubing, and were mounted through holes cut in the tunnel. On the sides of the tunnel, two aluminium plates drilled with one inch holes at the required spacing were fixed, and used as templates for drilling into the wood. On the top and bottom of the tunnel, machined aluminium blocks with the required inclined holes were mounted, and also used as templates for drilling. The bars were held in tension between these aluminium fixtures, by large nuts threaded onto their ends. The resulting grid is shown in Figure 4.3 viewed from the side of the tunnel, and in Figure 4.4 viewed from the cascade inlet position. The designed conditions at inlet to the cascade have been estimated with the methods reported by Roach (1987) and are shown below :-

Table 4.2 : Predicted Inlet Turbulence Characteristics

| | Streamwise Direction | Orthoganol Directions |
|---|---|---|
| Turbulence Intensity | 4.6% | 4.1% |
| Macro/Integral Scale | $38mm$ | $19mm$ |
| Micro/Dissipation Scale | 4-$5mm$ | $3mm$ |

To determine the distortion to the mean flow produced by the grid, several measurements of total pressure were made, vertically downwards through the tunnel, and horizontally from endwall to endwall. Figure 4.5 shows some measurements taken with the five hole probe at midpitch of

slot 1. It can be seen that with the grid as designed, the flow just beyond the endwall boundary layer has suffered less loss than that towards midspan. It appears that a sort of 'jet' flow is occurring at the edge of the grid. The reason for this is that the grid was designed for the tunnel width of $400mm$ existing at inlet to the cascade. The moving belt facility was designed to grow a skewed boundary layer (Walsh (1987)). Hence a false wall was fitted extending slightly upstream of the belt, with an adjustable bleed-off duct, to allow the removal of the incoming boundary layer. The width of the upstream tunnel is $460mm$, and the grid thus left a gap of $100mm$ between the last bar and the wall of the tunnel on this side. As the grid was only $15cm$ upstream of the false wall, it was thought that adjusting the bleed-off duct to produce zero incidence onto the false wall, would yield a uniform flow through the grid. However, as the results in Figure 4.5 show, this is clearly not the case.

To remedy this problem, it was decided to fit an extra bar to the grid near the endwall. This was initially chosen to equalise the blockage which the grid presented in this region, to that elsewhere. However, this design condition was found to be inadaquate, and so some trial and error was necessary before a satisfactory solution was obtained. This consisted of a bar of diameter $\frac{5}{16}$ inch, placed at $25mm$ from the endwall. The resulting radial total pressure profile at midpitch of slot 1 is also shown in Figure 4.5, together with that measured by Walsh (1987) before introduction of the grid. Whilst the extra bar has produced an acceptable inlet boundary layer, it is clearly different from that reported by Walsh (1987). The new boundary layer is actually thinner than the old. This might indicate that a 'jet' flow still exists at the start of the false wall, but is slowed by the growth of of a boundary layer on it.

The vertical traverse from top to bottom of the tunnel also revealed a change in total pressure, with more energy towards the top of the tunnel. This may be because the grid is angled to the flow, hence causing an upward deflection, and a higher static pressure towards the top of the tunnel. Then the velocity with which the flow traverses the grid, would reduce towards

the top of the tunnel, resulting in less loss in this region. The magnitude of the variation in stagnation pressure across the traversed blade row is approximately 1%. Although this situation is not ideal, no attempt was made to correct it as the only obvious solution would be to remount the turbulence grid perpendicularly to the flow. As discussed previously, this approach would introduce other difficulties. Thus no simple solution to the problem seemed possible.

## 4.3 Five Hole Probe Measurement Technique

Several traverses have been made with a five hole probe during this project, using a technique set up by Graves (1985). Measurements were taken with the probe inserted through slots cut in one endwall, such that data could be collected on planes of constant axial location (Figure 4.1). The probe was made of $0.5mm$ hypodermic tubing, and being of the cobra type could be rotated about a perpendicular axis without disturbing the position of its measuring volume. Freedom of movement in the radial and tangential positions was provided by the traverse gear (Figure 4.6) which also incorporated a rotary mount, allowing rotation about a spanwise axis.

A calibration technique proposed by Schaub *et al* (1964) was employed to avoid the necessity of nulling the probe head at each traverse point (indeed it was not possible to null in the pitchwise sense). By measuring the pressure on each of the five tubes of the probe, and the dynamic head detected by a reference pitot-static tube placed upstream of the cascade, it was possible to deduce the flow velocity, direction, and loss of stagnation pressure from the calibration maps.

Throughout the work presented in this thesis, use was made of a computerised data aquisition system which consisted of a Cifer microcomputer, and a specially made data aquisition unit. This allowed automatic reading of up to eight voltages, and provided an output which was used to control a valve selection box. Thus different combinations of the pressures on the five hole probe could be selected, and fed into a differential pressure transducer. A

second transducer constantly monitored the output of the upstream reference pitot-static tube. Potentiometers served as positional transducers, leaving only the angular setting of the probe, and the settings on a signal conditioner to be entered manually for each point. In practise these were rarely varied, and tests in the microcomputer programs warned the operator if the voltages on any of the digital to analogue converters were out of range. The Cifer microcomputer converted readings of voltages into pressures and stored these on a floppy disk for later analysis by software run on the University's mainframe service.

Having set the traverse gear at a particular slot location, the probe was used to obtain measurements of the flow at previously determined points in the flowfield. By traversing outwards from the endwall in the radial direction, the tangential location remained unaltered for long periods, and hence unused areas of the slot could be sealed with masking tape. This was most important for the early slots, where the higher than atmospheric pressure causes significant outflow through exposed passages. Unused slots were always kept sealed with special T-shaped wooden fillers, which maintained a reasonably smooth surface on the remote end-wall.

Although this technique had been successfully used at Durham for several years, it was not trouble-free. Walsh (1987) reported that significant losses were measured in regions expected to be governed by potential flow. No satisfactory explanation could be found for this and so the early stages of this project were spent investigating the problem.

Throughout the work undertaken with the five hole probe, regular checks were made of the validity of its calibration. This was achieved by inserting the probe in the working section upstream of the cascade. The mounting for this was comprised of two rotary mounts and a right angled bracket, which permitted rotation of the probe head in two directions. Thus data could be collected for the probe head set at different angles, and later run through the analysis program to recover the flow velocity, direction, and loss (which should always be zero).

An initial check of the probe calibration revealed satisfactory measurement of angle and velocity, but a variation in the returned value of

stagnation pressure equal to three percent of the inlet dynamic head. Further investigation identified the data aquisition system as the source of this problem, with significant noise levels present in the signal from the pressure transducers. The easiest way to reduce the effects of noise, was to take more samples of each pressure and average. Thus the minimum number of samples was increased from twenty to two hundred. After this the system examined the mean and variance of the data, to determine whether more readings were required. If so one hundred samples were added before repeating the check. A maximum of one thousand samples was specified to avoid system lock-up in highly turbulent regions. To eliminate effects of vibration from the rig, the bench on which the instrumentation was mounted was vibrationally isolated from the floor. Software on the microcomputer was modified to correct each reading of pressure for variations in upstream dynamic pressure, to achieve 'standardised' data.

Testing of the modified system showed the measurement of stagnation pressure to be an order of magnitude more accurate. Having developed the reliability of the system pressure measurement, a re-calibration of the probe utilising this methodology appeared desirable.

The five hole probe was calibrated in the range $\pm 30°$ yaw and $\pm 30°$ pitch, with data values spaced at intervals of two degrees. Bi-cubic spline surfaces were fitted to the data and the quality of the fit determined by inspection. Satisfactory fits were then incorporated in the analysis program, to give a description of the probe head's response. Use of this calibration improved measurements of stagnation pressure, but did not entirely eliminate the apparent losses which were recovered from data collected at midpitch of the midspan positions. These spurious losses were found to increase with slot number, and will be discussed in detail in Chapter 5.

## 4.4 X-Probe Hot-Wire Anemometry Technique

The flowfield in the cascade has also been traversed using a hot-wire method similar to that described by Graves (1985). This combined

information obtained from two traverses using x-wire probes (DISA 55P53 and DISA 55P54), to measure five of the six independent components of the Reynolds stress tensor, as well as the mean velocity components.

The hot-wires were run by DISA 55M01 constant temperature bridges, working at an overheat ratio of 0.8. Although Yavuzkurt (1984) has shown that real-time data reduction techniques are generally more accurate than time averaging of the hot-wire signals, the later technique was adopted as the necessary equipment was readily available. Bridge outputs were calibrated against flow velocity, with the probe placed at midspan of slot 10, between the blade wakes. It was decided to linearise these signals, as it is more accurate to do so in highly turbulent regions, where the slope of the calibration graph is not really constant over the range covered by the instantaneous velocity vector. Fourth order polynomial fits have been shown by Bruun *et al* (1988) and Swaminathan *et al* (1986) to give an accurate representation of the calibration data, and so two Prosser 6130 linearisers were used to produce voltages proportional to flow velocity (Figure 4.7). These were then passed through Prosser 6141 signal conditioners, which removed most of the steady voltage levels, and amplified the remaining signals to give stronger fluctuating information. The outputs were passed into two units; a DISA 52B25 turbulence processor which was set to evaluate the correlation between them, and a circuit specially made to determine the mean and root mean square levels of the signals. Voltages from this circuitry, the two positional transducers, and a differential pressure transducer (connected to the upstream reference pitot-static tube), were transformed to integers by analogue to digital converters in the data aquisition unit, before downloading to the controlling microcomputer.

The same traverse gear served for both hot-wires and pressure probes, and the hot-wire probe supports were designed to keep the position of the measuring volume constant when rotating about the spanwise direction. Hence the probes could be aligned with the local yaw angle, determined from a previous pressure probe traverse. This was the system used by Graves (1985) and Walsh (1987) to obtain data from the first Durham turbine cascade.

Although there is not a great deal of literature presenting turbulence measurements in the swirling, three-dimensional flows of cascades, an apparent discrepancy existed between results obtained at Durham and those of other workers. Sieverding (1985b) commented on the opposing results of Bailey (1980) who found turbulent stresses to be insignificant in large regions of the secondary flow, and Gregory-Smith and Graves (1983) who measured peak local turbulence intensities of 30% in the vortex core. This dilemma persisted with results of Walsh (1987) showing 92% of the loss in the Durham cascade to be manifested as a rise in turbulent kinetic energy, whilst Moore *et al* (1986) found this ratio to be 23%, and Zunino *et al* (1987) only 10%.

Indeed the work of Zunino *et al* (1987) presented another dilemma. As they used a twin traverse x-wire method, their results should have shown similar quality to those obtained at Durham. Although their analysis method was different, following an unlinearised approach proposed by Majola (1974), this should not have accounted for the superior quality of their shear stress measurements. As both workers used calibrations against mean velocity only, ignoring the effects of the thermal inertia of the wire-prong system (described by Perry (1982)), this could not be responsible for the differing results. Thus although comparison between traverses with hot-wires and five hole probes showed Durham's mean flow data to be correct, some doubt was cast on the accuracy of fluctuating measurements.

Investigation of the hot-wire system was approached from two fronts. The electronic signal path was examined for integrity at each stage, and the analysis equations were thorougly checked. Two problems have been identified. In the analysis described by Graves (1985), all the complex equations for the response of a hot-wire are 'correct', but the recovery of the root mean square of the fluctuating velocity from the voltages measured is not. The circuitry which measured signal r.m.s. was not A.C. coupled and so included the mean voltage which emerged from the signal conditioner

$$MEAN = (\overline{E} - Offset) * Gain \tag{4.1}$$

thus the measured Root Mean Square voltage

$$RMS = \sqrt{(\overline{e'^2} * Gain^2) + MEAN^2} \tag{4.2}$$

which is not the same as equations 2, 4 pp 181, 182 of Graves' thesis (1985). Unfortunately the error term this produced was quite smoothly varying as it depended upon the values of offsets and gains applied by the signal conditioners. Hence contour plots of turbulence quantities did not show obvious discontinuities.

The hot-wire data obtained from the first Durham cascade has been re-analysed and published by Gregory-Smith *et al* (1988). Many of the afore-mentioned discrepencies have thus been eliminated, although the turbulence levels found in the Durham cascade were still higher than those observed elsewhere.

It had been hoped that re-analysis of the experimental data would produce much clearer pictures of the shear stresses working on the fluid. These however did not materialise, and so another source of inaccuracy in fluctuating quantities had to be sought. This was found to reside in the electronics used to measure signal mean and r.m.s. values. Whilst the circuit diagrams showed no fault, and the unit should in principle have produced the desired outputs, it was not sufficiently accurate to preserve the integrity of shear stress information. Errors resulted from the use of noisy operational amplifiers, not enough trim circuits, and D.C. coupling of the r.m.s. measurement. Although mathematically there is no apparent advantage in measuring the r.m.s. of either a D.C. or A.C. coupled signal, the D.C. coupled method produces a larger error when there is a certain level of uncertainty inherent in the data. Some time was devoted to re-building the mean/r.m.s. measuring unit which resulted in greatly increased accuracy as indicated by tests with a sinusoidal signal generator over a frequency range of $1Hz$ to $40kHz$. An amplifier was also built to boost the output of the turbulence processor, which was generally very small. The combination of these measures was found to achieve the desired accuracy, and in particular produce clearly defined shear stress distributions.

Fluctuating data from the hot-wire system described above was determined in the coordinates described by the probe and two perpendicular directions. Due to the omission of one of the six independent components of the Reynolds stress tensor ($\overline{v'w'}$) the experimental measurements cannot be determined in another set of axes. Thus as it was intended to compare hot-wire information with that obtained from computational models, it was considered preferable to align all measurements at a particular tangential coordinate, with the midspan flow angle, rather than the local flow angle at each radial station as had been the case in the previous work of Gregory-Smith *et al* (1988). This reduces the accuracy of the analysis equations, but some testing showed that the system could cope adaquately with the misalignment range involved.

Improvements in the accuracy of measurements, resulted in reliable convergence of the higher order analysis proposed by Gregory-Smith, and already incorporated in the mainframe software by Graves (1985). Hence all data presented in this thesis results from the application of this method.

## 4.5 Rotatable Single Wire Technique

A new hot-wire anemometry technique has been developed, as an investigation of the state of the flow very close to the endwall was required. A method was needed which could determine the mean flow velocity, and show whether the new, highly skewed, boundary layer which forms after the inlet boundary layer has been swept from the endwall, is in a laminar or turbulent state. As a minimum distance for readings of one millimeter from the endwall was desired, the x-probe method could not be used. Hence a single wire approach was required.

The basic concept of the method utilises the fact that most of the effective cooling velocity comes from the velocity component perpendicular to the wire. This is especially true of gold-plated wires, where the effects of the thermal conductivity of the wire supports, are greatly reduced, by keeping them away from the sensing length (Perry (1982)). Hence if several readings

are taken at a point, with a single wire set at various angles, the individual mean velocity components, and some of the components of the Reynolds stress tensor, may be found.

Since a close approach to the wall was required, it was decided to rotate the wire in a plane parallel to the endwall. This is most easily achieved by using a right-angled probe, mounted from the remote endwall. By ensuring that the wire was on the line of the main probe support, it could be rotated about the spanwise direction without disturbing its position. This method naturally offered itself to being mounted on the existing traverse gear, with the probe support entering the tunnel through the slots already provided (Figure 4.1). However, as a much finer degree of accuracy was required for positioning the probe in the radial direction, a standard DISA 55E40 traversing mechanism was also fixed onto the rotary mount in Figure 4.6, by means of a specially made boss. This was designed such that the probe support passed through the centre of the rotary mount. The DISA traversing mechanism incorporated a potentiometer which was used as a positional transducer for measurements by the data aquisition system. A diagram of the probe support is shown in Figure 4.8.

The probe support was used to hold DANTEC 55P04 gold plated wire probes, which were run at an overheat ratio of 0.8, by a DISA 55M01 constant temperature bridge. Fourth order polynomials were fitted to probe calibration data, and their coefficients set on a Prosser 6130 lineariser so as to produce a voltage proportional to flow velocity (Figure 4.7). The probes were calibrated in the working section of another wind tunnel, in order to obtain calibration data down to a minimum velocity of four meters per second.

When traversing, the signal from the lineariser was passed through a signal conditioner to amplify the fluctuating component, before being fed into the unit used to give steady output voltages equal to the mean and root mean square levels of the input signal. These outputs were measured by the data aquisition unit and passed to the Cifer microcomputer which was used to control the experiments, and log data onto a floppy disk for later analysis on the University's mainframe machine. At each point in the flowfield, the

recorded data consisted of the probe's position, the number of wire angles for which the flow was measured, and then for each of these, the turret angle setting, the offset and gain applied by the signal conditioner, the measured mean and r.m.s. voltages, and the upstream dynamic head.

The method used to run the experiments was similar to that of the five hole probe and x-wire measurements. The controlling microcomputer guided the operator with a question and answer approach, which prompted for the atmospheric conditions, in order to calculate the inlet dynamic head required for constant Reynolds number operation. The program then read in reference voltages from the positional transducers when placed at known positions. In the radial direction a piece of shim material was used to place the probe protector pin at a known distance from the endwall. The extension of the probe protector pin from the wire was found beforehand with the aid of a travelling microscope. The sensitivities of the positional transducers were measured separately, and imbedded in the Cifer programs. The program then asked if the upstream pressure transducer needed to be calibrated, and would take the user into a routine to do this, if required. Values for the sensitivity of the wire, and the settings on the signal conditioner were also required before the main loop was entered and a prompt given for the next probe position to be entered.

The probe was traversed radially outwards from the endwall, keeping exposed areas of the slot covered with masking tape. When the probe was set at the correct position, the user was asked to align it as well as possible with the flow (i.e. rotate until a maximum output from the mean voltage measurement was obtained). The turret setting angle, and signal conditioner settings were manually entered, before the system measured the upstream flow velocity, and the local mean and r.m.s. effective cooling velocities. These were displayed on the microcomputer screen, and if acceptable, the program would prompt for the turret setting angle to be set to a new value. After entering the signal conditioner settings (if changed) the system would measure the flow again. When all the required angles had been recorded, the next position in space was requested.

The details of the analysis of the single wire data are presented in Appendix A, so a brief summary of the procedure will suffice here. Firstly the program calculated the mean and r.m.s. cooling velocity for each rotational setting at a given point. These were corrected according to the upstream velocity, so that they corresponded to an arbitrary 'standard day' velocity of 19.1 $ms^{-1}$. Although the analysis could cope with the probe being set at arbitrary angles (provided the velocity vector was within the probe's acceptance cone), and any number of angles greater than two, in practice only five angles were set for each position. These were at 0°, ±20°, ±40°, to the direction which was estimated to be streamwise. Since only three angular settings were required to solve the equations, redundant information was obtained from the five orientations recorded. The equations were represented in the analysis program in matrix form, and solved by a least squares method in NAG subroutine F04AMF. This also allowed a confidence interval to be calculated for each solution. The flow was solved for $\overline{U}, \overline{V}, \overline{W^2}, \overline{u'^2}, \overline{v'^2}, \overline{u'v'}$ in the probe's coordinates (for the sake of the accuracy of the response equations used) and then rotated to cascade coordinates for storage. The radial normal stress $\overline{w'^2}$ was not measured, and so was assumed to be equal to the average of $\overline{u'^2}$ and $\overline{v'^2}$. Although this will obviously be erroneous close to the wall, where large radial velocity fluctuations will be damped, it was thought to be a preferable assumption to that of assuming zero radial turbulence, as the probe was to be traversed radially from 1 to 10$mm$ from the endwall.

## 4.6 Spectral Analysis of Hot-Wire Signals

A short spectral survey of the flowfield was undertaken in order to determine whether or not there were any dominant frequencies present. A Le Croy model 9400 digital oscilloscope was borrowed for this purpose, as it had the capability of performing fast Fourier transforms on input signals over a wide range of frequencies. The transforms were averaged over two hundred samples, to give a smoother spectrum. The display on the screen of the oscilloscope was then dumped to a plotter for later presentation. The

width of the individual 'frequency bins' for which a power was calculated, was typically $1Hz$ for a low range spectrum (0 to $200Hz$) and $200Hz$ for a bigger spectrum (0 to $20kHz$).

The single wire probe was used as a signal source, and its output linearised to provide a voltage proportional to flow velocity, before connecting to the digital oscilloscope.

## 4.7 Flow Visualisation

A relatively fast means of gaining some qualitative information concerning a three-dimensional flow, is by use of some form of flow visualisation. Walsh (1987) described a method suitable for use in the low speed cascade, whereby a mixture of diesel oil and 'Dayglo' pigment (in a ratio of three to one by weight) is painted onto the surfaces of the blades and endwall. After running the tunnel for some time, fine dry patterns are left on these surfaces, and photographs taken. This effectively gives a picture of the streamlines in the limit as the wall is approached, and clearly shows any lines of separation of the flow from the surface.

## 4.8 Surface Pressure Distributions

The central blades in the cascade were fitted with pressure tappings at several spanwise distances from the endwall. All tappings at a particular fraction of chord, were drilled into the same piece of tubing cast under the blade's surface, and so all except one had to be covered with tape when measuring the surface pressure distribution at a given radial distance. The axial locations of the pressure tappings are shown in Figure 4.1. A series of distributions at different radial coordinates is useful, as it builds up an effective picture of the variations in lift on the aerofoil, due to the action of the secondary flows. The pressures were connected to a multi-tubed inclined manometer and read manually with the tunnel running at constant Reynolds number.

Although it is almost impossible to assess the overall accuracy of experiments which have a very complicated sequence of data processing, with a correspondingly large number of potential sources of error, it is important to gain some idea of the uncertainty of the results.

The positional accuracy with which the five hole probe and x-wires were located in the flowfield, was estimated to be $\pm 0.5mm$ in both radial and tangential coordinates. For the single wire, the same tolerance is appropriate for the tangential direction, but the probe was located more accurately radially, with an estimated error of $\pm 0.1mm$. The upstream dynamic head was constantly monitored in all experiments, and kept within two percent of the value required to run the cascade at its standard Reynolds number.

The accuracy of the data aquisition system for voltage measurement, was regularly checked by comparing the output for a given test signal, with that obtained on a digital multimeter. This was also monitored during runs to ensure that the system was always performing well. The linearisers, signal conditioners, and mean/r.m.s. unit, were also checked at regular intervals for satisfactory operation.

When using an intrusive technique to measure a fluid flow, care must be taken to try and minimise the disturbance which the probe support induces at the measurement location. The 'cranked' design of the probe's used in this work was intended to ensure that this was the case. Also, the five hole probe was never used to record the flow within two diameters of its head from the endwall, as this would have caused distortion of the streamlines, and hence invalidated the calibration technique.

In the case of a hot-wire, close approach to a solid boundary will generally result in an over estimation of the velocity (Wills (1962)). This is due to the cooling influence of the wall (assumed at lower temperature than the wire) on the fluid immediately surrounding the wire. However, Oka and Kostić (1972) used a standard DISA wire of diameter $5\mu m$ in their work on wall proximity effects. They commented that the distance from the wall at

which the increased cooling becomes detectable, decreases with flow velocity. The maximum range therefore occurs when there is zero flow, and was found to be $1mm$. Hence, as similar wires were used in this work, with a closest approach of $1mm$ and non-zero flow speeds, wall interference effects may be assumed to be insignificant.

In the case of pressure probes the accurate calibration of pressure transducers is clearly important. A subroutine was added to the programs running on the Cifer microcomputer, to enable interactive calibration of the transducers. The system measured the voltage output from the transducer, and requested that the pressure read from a micromanometer, be typed in. The user could keep taking more readings, until the error determined by a least squares fit to the calibration data was acceptably small. The micromanometer was also monitored during traverses, to validate the readings of pressure displayed by the microcomputer. The accuracy of individual pressure measurements was estimated to be $\pm 0.05 mm H_2O$.

An indication of the overall performance of the five hole probe technique was given by the regular probe calibration checks. These returned measurements of flow angle to within $\pm 0.2°$ and velocities to within $\pm 0.2$ $ms^{-1}$ when mounted in the calibration position upstream of the cascade. However, at a slot location there are also other sources of error, including the alignment accuracy between traverse gear and cascade, the action of turbulence to cause the over-reading of individual pressures, and Reynolds number effects. Thus the total error applicable to angle measurements might be as great as $\pm 1°$. A detailed consideration of problems concerning loss measurement will be given in Chapter 5.

An obvious source of inaccuracy in the use of hot-wires, arises from the quality of their calibration. The error in calibrations generally increases with decreasing velocity, due to inaccurate reading of the dynamic pressure on a micromanometer. Using the methods proposed by Yavuzkurt (1984), the calibration error typical of this work was found to be within one percent over the velocity range encountered.

Throughout the hot-wire anemometry work presented in this thesis,

care was taken to try and minimise the effects of wire contamination due to dust. The inlet to the fan was filtered (Walsh (1987)), which greatly reduced the problem, but after a long run the sensors did show reduced sensitivities. It might be tempting to allow the wire to reach an equilibrium state of dirtiness, and calibrate it without cleaning. Whilst this would probably produce reasonable mean flow results, the frequency response of the devise would be seriously impaired, and so fluctuating data would be correspondingly de-valued. Hence a point in the flowfield was chosen, and at the end of each tangential station the probe was returned to this position to check that its sensitivity was still unaltered. If a slight drop in sensitivity was observed the probe was removed, cleaned, returned and re-tested. If the probe had been very dirty, the data recorded since its previous check, would have to be repeated.

The x-probes were tested for angular response, by placing them at the midpitch, midspan position of slot 10, and recording outputs for misalignment angles in the range $-20°$ to $+20°$. The velocity measurements obtained, were found to be consistent to within $\pm 0.5\ ms^{-1}$, and the angles to $\pm 2°$. The sum of the normal Reynolds stresses $(\overline{u'^2} + \overline{v'^2} + \overline{w'^2})$ was consistent to $\pm 1$ $(ms^{-1})^2$. Although these results seem quite satisfactory, Yavuzkurt (1984) has shown that the measurements of mean velocity and second order correlations, using a time averaging technique with a slant wire in a two dimensional flat plate boundary layer, are in error by approximately 5%. Hence, due to the similarity of the basic systems, and in the absence of any other evidence, it will be assumed that this is a valid estimate of the errors to be expected from the x-wires.

As mentioned previously, the single wire method utilises a least squares solution, which enabled the computation of confidence intervals. For a 99% confidence interval, the typical errors to be associated with each quantity are tabulated below :-

Table 4.3 : Errors for the Rotatable Single Wire Method

| Quantity | Error |
|---|---|
| Streamwise Mean Velocity $\bar{U}$ | $\pm 0.5\ ms^{-1}$ |
| Cross-Passage Mean Velocity $\bar{V}$ | $+0.5\ ms^{-1}$ |
| Radial Mean Velocity $\bar{W}$ | $\pm 1.2\ ms^{-1}$ |
| Streamwise Root Mean Square Velocity $\sqrt{\overline{u'^2}}$ | $\pm 6$ % |
| Cross-Passage Root Mean Square Velocity $\sqrt{\overline{v'^2}}$ | $\pm 11$ % |
| Streamwise/Cross-Passage Velocity Correlation $\overline{u'v'}$ | $\pm 40$ % |

## 4.10 Computational Facilities for Navier-Stokes Calculations

As a large proportion of this project involves the running and analysis of numerical calculations of the flow in the Durham cascade, significant computational power was required. For three-dimensional calculations, the memory and time requirements are too great to be handled by most mainframe services, and so a grant was obtained for use of the SERC supercomputing facilities at the Rutherford Appleton Laboratory. Batch jobs were submitted to a Cray X-MP/48 (4 processors, 8 Megawords) machine from an account on an IBM CMS service which is used as a front-end. This was accessed from Durham via JANET (the Joint Academic NETwork).

Enormous quantities of information are obtained from one such calculation, and so a program was written to interpolate out planes of data corresponding to the cascade traverse slots, for transmission to Durham. Solution convergence could then be determined by examining this data, and the details supplied by the calculation procedure itself, before deciding whether or not to accept the full three-dimensional output.

## 4.11 Output Processing

The method of presentation of three-dimensional flow data is clearly important, if comprehension of the principal phenomena is to be easily attained. The methods used to present the experimental data obtained by

Walsh (1987) were plots of contours, and vectors, on planes of constant axial location (traverse slots). Pitch and mass averaging of this data was also performed, and overall mass averages were manually plotted to show the development of quantities such as loss, against axial distance through the cascade. Hence some programs were available, designed to work on the data from one traverse plane, and produce the type of output described above.

Whilst these facilities were perfectly adaquate for the assessment of hard won traverse data, they were not intended to produce rapid descriptions of the full three-dimensional solutions emerging from a numerical calculation procedure. Hence a more powerful output processing package was required, both to ensure satisfactory solution convergence, and to produce output which directly compared accepted solutions with the corresponding experimental data.

It would be nice to be able to produce 'three-dimensional images' of the flow field on a piece of paper. Graphics packages are becoming available which will certainly improve the options of data presentation for future workers (e.g. UNIRAS), but for the duration of this work GHOST80 was still the main graphics library available on the University's mainframe service. Hence it was decided to develop facilities based on the same type of output as that produced by Walsh (1987), but with much greater flexibility and data handling capabilities.

Two main programs have been produced. They both work on up to four datasets, each of which can contain data for any number of the eleven traverse slots. The first program produces plots of contours and vectors ('area plots') for a traverse plane chosen interactively by the user, and displays data from hot-wires, pressure probes, and numerical Navier-Stokes solvers, side by side. The actual data which is displayed is also interactively chosen by the user. This gives a basically qualitative comparison of output.

For exacting quantative assessment, a second code was developed. This program, also run interactively, accepts the same input data types as the 'areaplotter', and rapidly produces tabular and graphical output of pitch and mass averaged quantities. Graphs are also plotted of certain mass averaged quantities versus axial distance through the cascade. The graph

showing the growth of loss was found to be particularly useful, as an aid to assessing the convergence of numerical solutions.

The total pressure loss coefficient is defined as :-

$$\xi = \frac{P_{O1} - P_O}{\frac{1}{2}\rho V_1^2} \tag{4.3}$$

where subscript '1' refers to conditions upstream of the cascade. A similar expression defines the static pressure coefficient.

Data was integrated in the tangential direction, to obtain a pitch averaged value (for each radial location) :-

$$\overline{\xi(z)} = \frac{\int V_{ax}(y,z)\,\xi(y,z)\,dy}{\int V_{ax}(y,z)\,dy} \tag{4.4}$$

where $V_{ax}(y,z)$ is the axial velocity at that point in the flowfield.

In the case of the yaw angle :-

$$\overline{\epsilon(z)} = tan^{-1}\left(\frac{\overline{V_{tan}(y,z)}}{\overline{V_{ax}(y,z)}}\right) = tan^{-1}\left(\frac{\int V_{ax}(y,z)\,V_{tan}(y,z)\,dy}{\left(\int V_{ax}(y,z)\,dy\right)^2}\right) \tag{4.5}$$

Secondary velocity components were defined by the difference between the local flow velocity, and that at midspan. The turbulent kinetic energy was defined as :-

$$Turbulent \quad KE = \frac{(\overline{u'^2} + \overline{v'^2} + \overline{w'^2})}{V_1^2} \tag{4.6}$$

to give a coefficient comparable with the loss coefficient.

Within the blade passage, experimental data is normally available only over a limited range between the blades since the probes are unable to approach the solid surfaces very closely. Walsh (1987) extrapolated data values from the two tangential locations nearest to the blade, onto the blade surface for the purposes of pitch averaging. This was found to produce large changes in the results obtained, and so the data in this thesis was integrated only over the range traversed. Hence the pitch averaged values obtained for positive quantities such as loss, will be an under-estimate of the true value within the blade passage.

Up and downstream of the cascade, traversing generally extends over more than one pitch to give some indication of the flow repeatability from

passage to passage. Data such as this was averaged first over a region from the 'left hand' edge of the traverse plane to a location one pitch on from that, and then from the 'right hand' edge back to a location one pitch from it. The two values for the pitch averaged quantity thus obtained, were then averaged.

Once data had been pitch averaged for each radial location, the results were integrated in the radial direction to obtain an area average. All integrations were performed using a four point quadrature integration scheme.

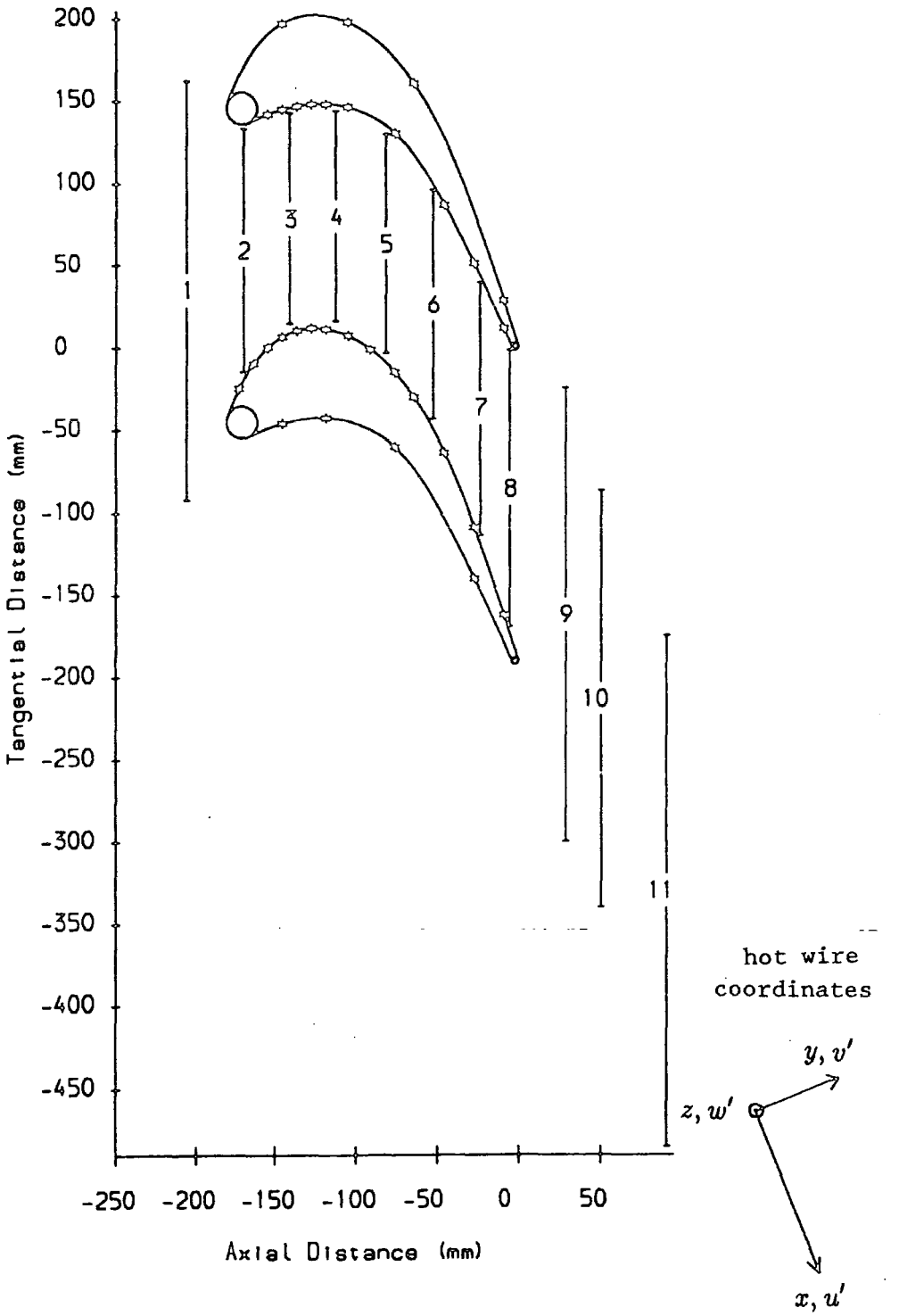


FIGURE 4.1 : Traverse Slots & Pressure Taps

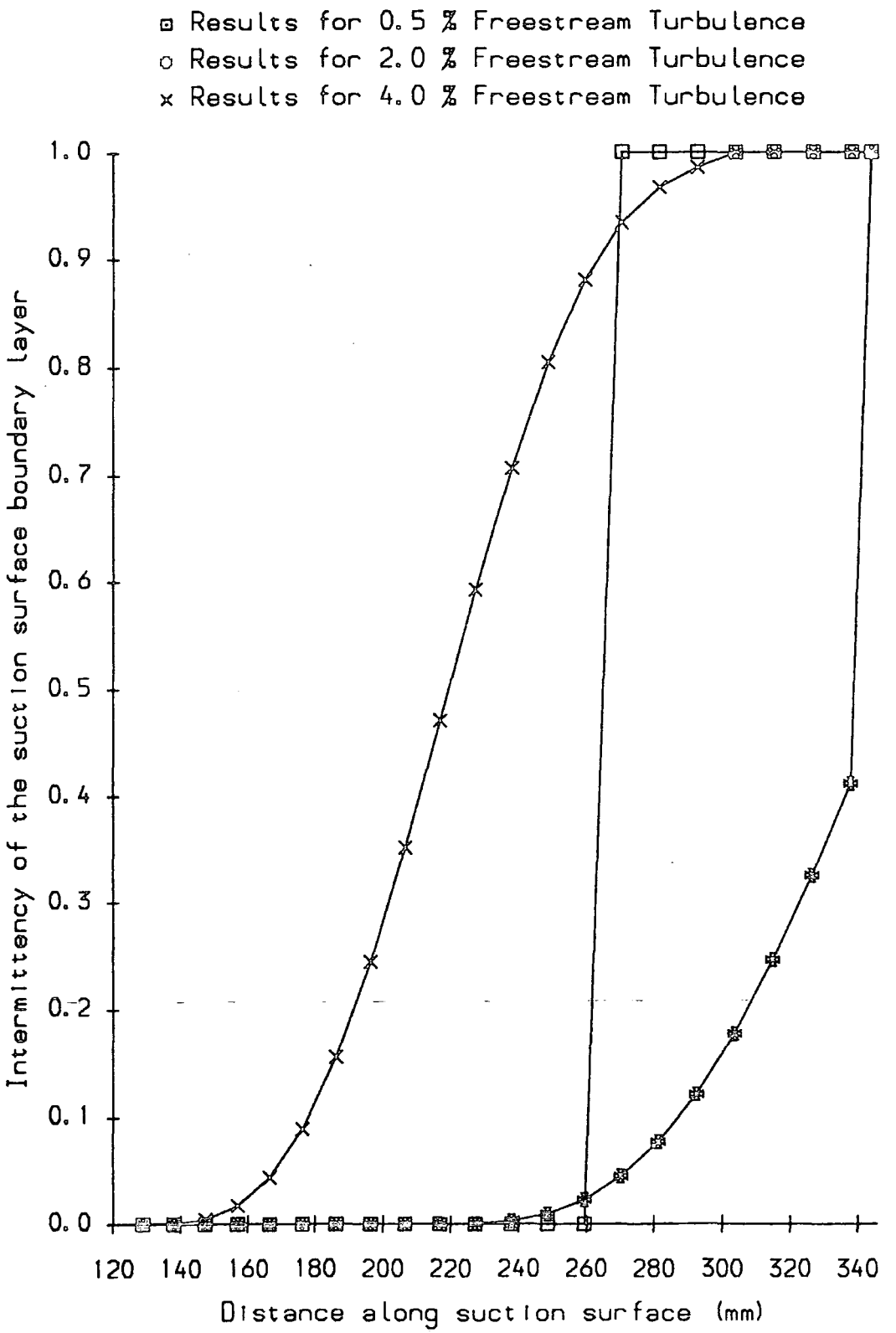


FIGURE 4.2 : Predicted Boundary Layer Transition

FIGURE 4.3 : Turbulence Grid Viewed From the Tunnel Side

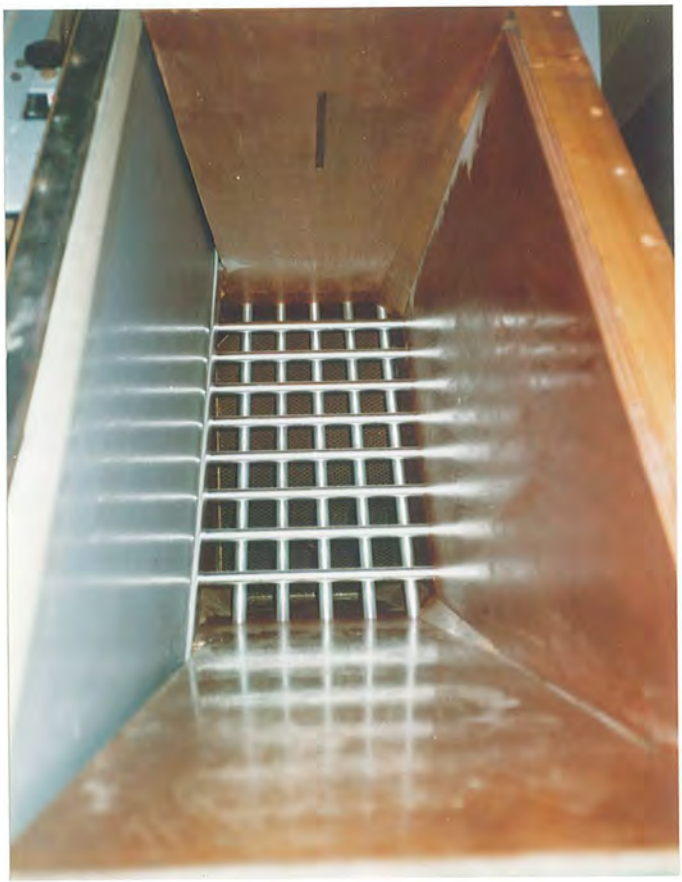

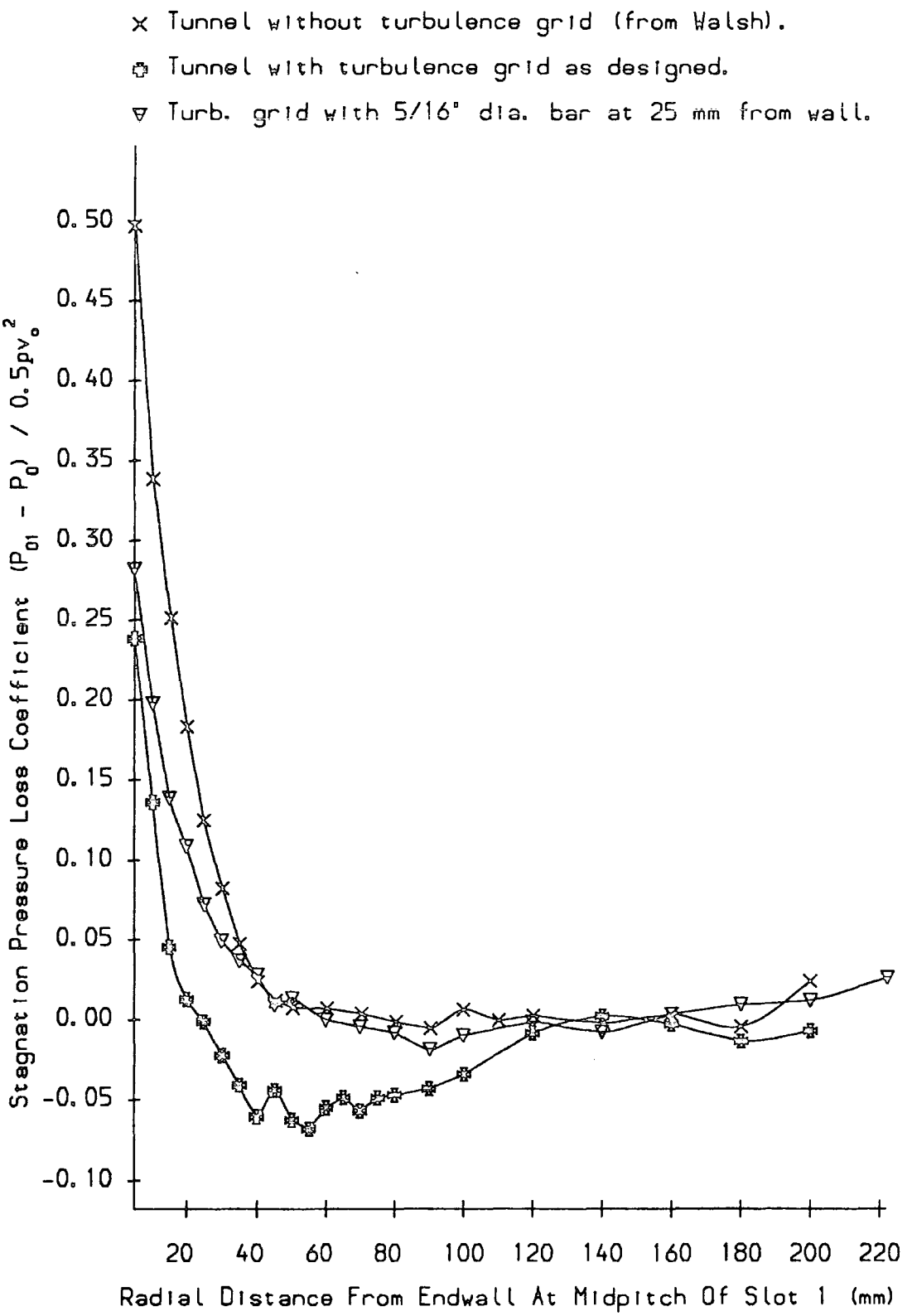


FIGURE 4.5 : Inlet Boundary Layer Profiles

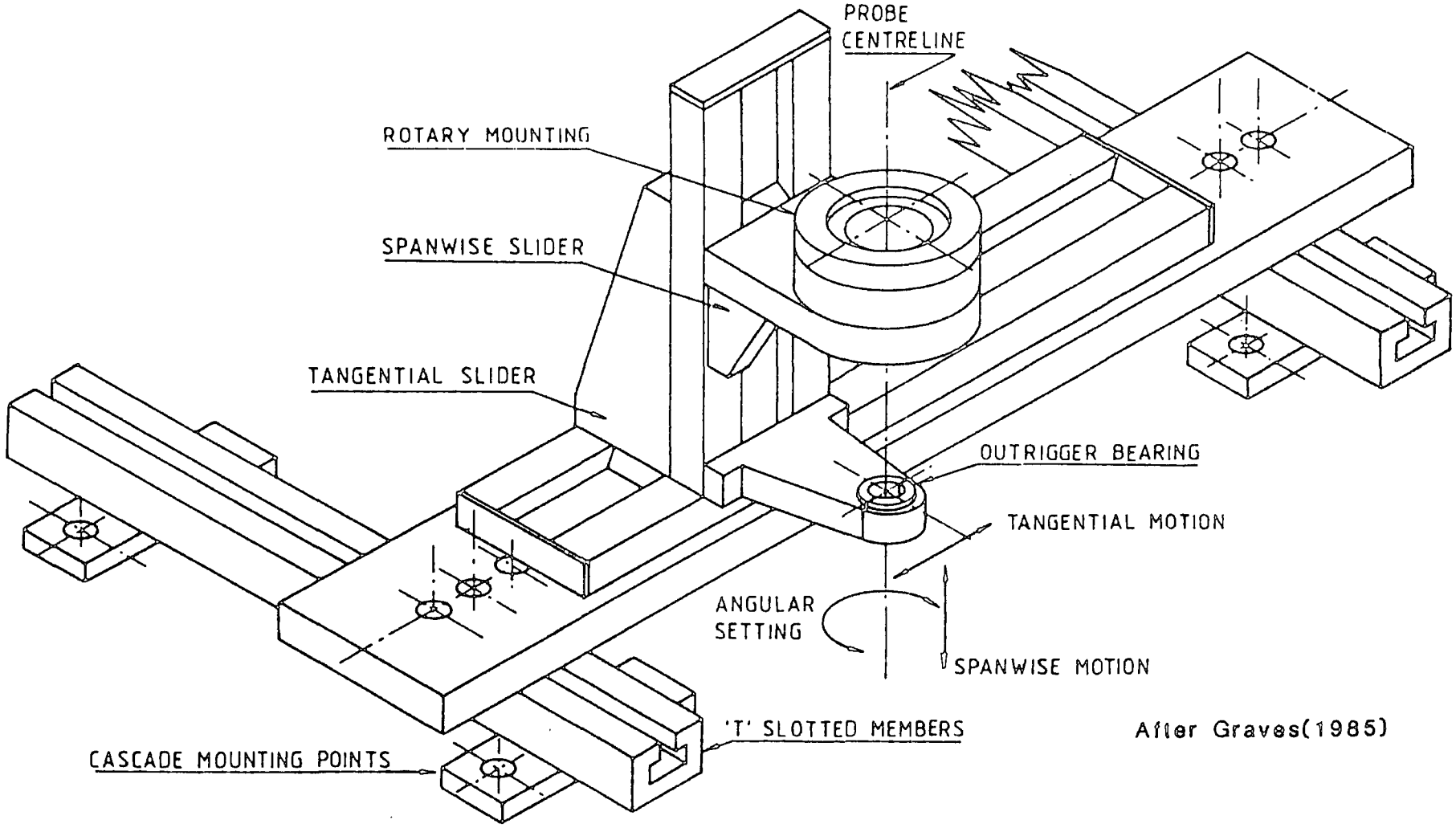


FIGURE 4.6 : Traverse Gear

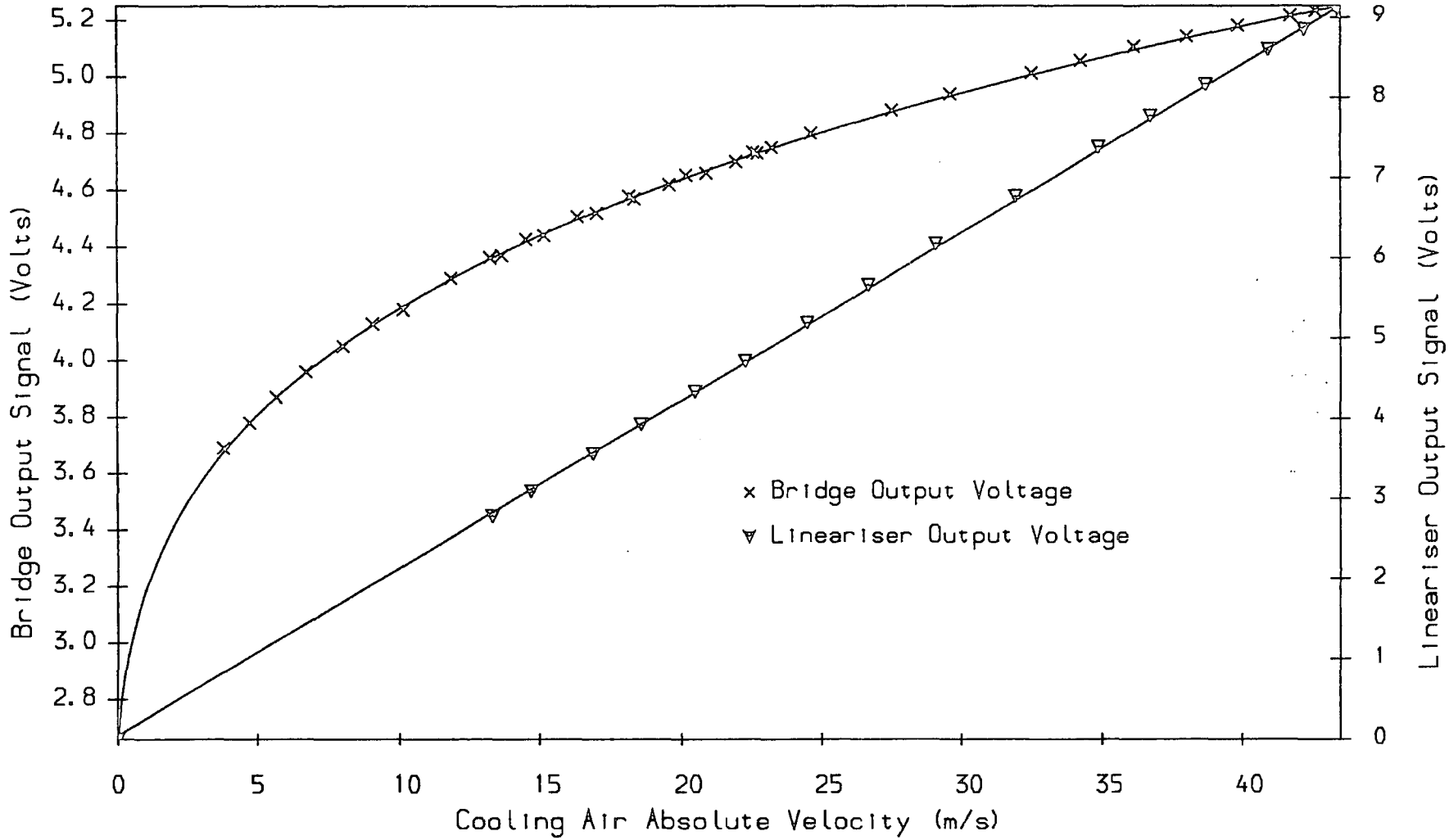


FIGURE 4.7 : A Typical Hot-Wire Calibration

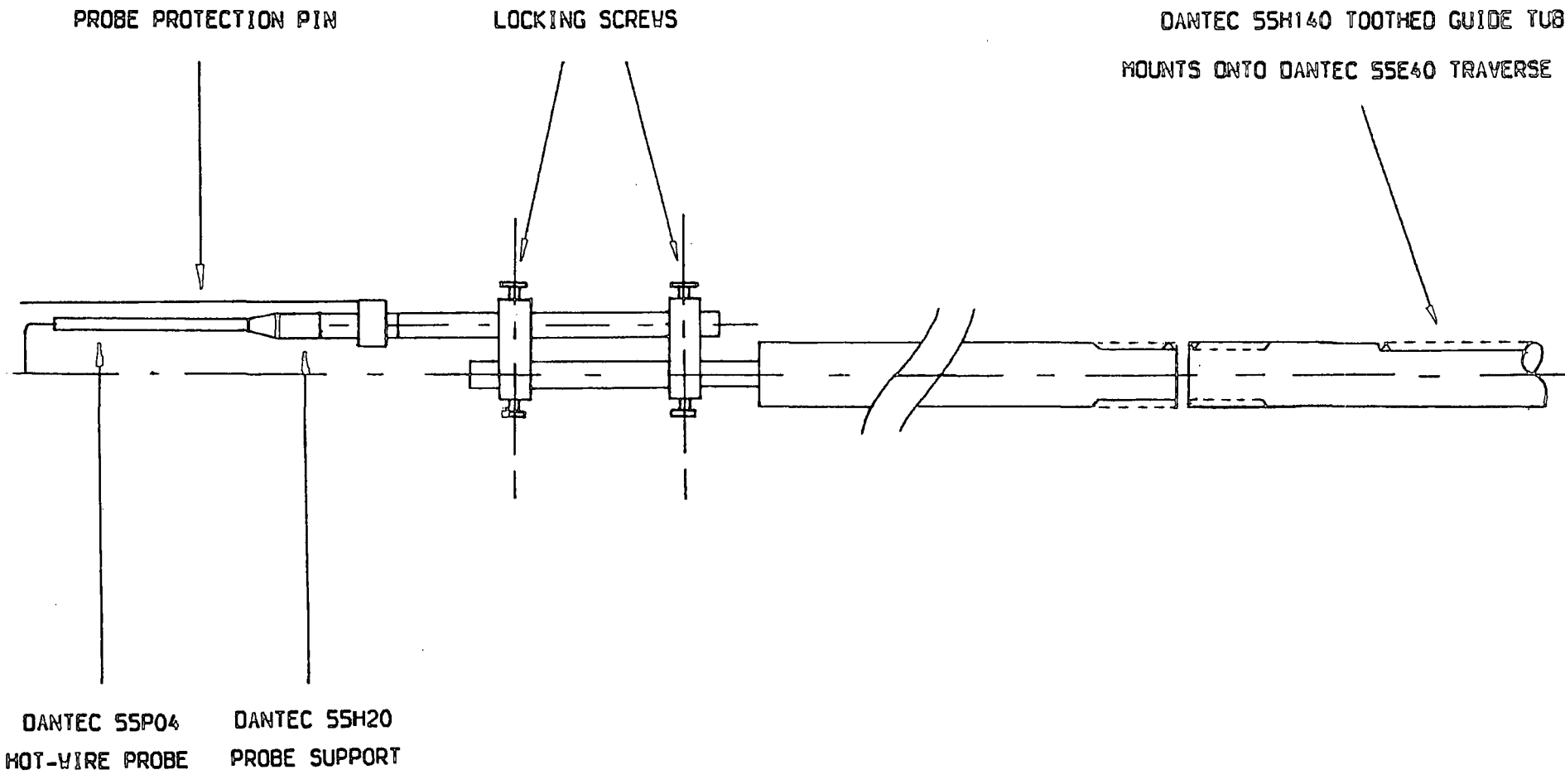


FIGURE 4.8 : Rotatable Single Wire Probe Support

# Chapter 5
# Experimental Results (JAW Test Case)

## 5.0 Introduction

This chapter aims to describe the initial dataset used for comparison with flow models. Much of this data was collected and presented by Walsh (1987). In addition, three new traverses have been made to provide greater detail of the flow development in the latter half of the blade row, and downstream of the trailing edge. A problem with the five hole probe measurement technique has been investigated, and this will be discussed in detail. Since the majority of experimental data which is available for this test case originated from Walsh (1987), it will be referred to as the 'JAW' test case in this thesis.

## 5.1 The Walsh Data

The JAW turbine cascade at Durham, was constructed by Walsh to allow investigation of the effects of skew in the inlet boundary layer upon the secondary flows and losses. He presented results of traverses at slots 1, 3, 5, 8, 10 for three separate skew levels. One of the skew levels he tested was that of zero skew. This data, for the case of a colateral inlet boundary layer, will be used in this work as a test case for three-dimensional calculations. The flow in the JAW cascade was found to develop into the usual features of passage vortex, endwall counter vortex, and suction surface counter vortex. The aspect ratio of the blading is such that the secondary losses are of comparable magnitude to the profile losses. This also means that the midspan flow is essentially two-dimensional, which makes identification of three-dimensional flow features a simple matter of comparison with midspan conditions. Thus the data constitutes a very useful test for flow models. Although the linear cascade does not contain any radial pressure gradients, the flow is still very complex, and provides a difficult case to predict.

Since the flow was found to develop rapidly between slots 5, 8, and 10, it was decided to traverse some intermediate slots. This would also provide an introduction to the traversing and data analysis techniques.

## 5.2 Errors in Loss Measurements

As discussed previously in section 4.3, certain problems had been encountered with the measurement of losses using the calibrated five hole probe technique. Walsh (1987) reported that significant losses were measured in regions expected to be governed by potential flow. Some time was thus spent investigating the accuracy of pressure measurements, and improvements were then made to the system, culminating in a new calibration of the five hole probe. Despite efforts to improve the accuracy of individual pressure measurements, and the new calibration of the five hole probe, the problems with loss measurement were not entirely eliminated. A traverse of slot 7, analysed with the new calibration, revealed that an average loss of 0.05 appeared to be present in freestream areas. Analysing the raw pressure data with the old probe calibration (as used by Graves (1985), and Walsh (1987)), suggested that this freestream loss was 0.1. Hence it was clear that an error in the measurement technique was present which was somehow related to the probe calibration.

The problem of non-zero freestream loss persisted in traverses of slots 9 and 11. Analysis with the new probe calibration suggested that the freestream loss was 0.06 in both cases, whereas this value was approximately 0.1 when the old calibration was used. Generally, data had been corrected for spurious freestream losses, by simply subtracting this apparent loss from the values of the total, and static pressure coefficients at all points on the traverse plane (a process which will be referred to as 'constant loss correction' in this thesis). However, after traversing slot 11, it became clear that data analysed with the new probe calibration, and corrected in this way, consistently produced lower mass averaged losses than data which had been analysed by Walsh with the old probe calibration. In Figure 5.1, the results of plotting mass averaged

losses from Walsh (1987) with new values obtained for slots 7, 9, 11 are plotted under the heading 'mixed calibrations - constant loss correction'. It is clear that the curve for loss growth through the cascade thus obtained, is somewhat unbelievable, with the losses apparently falling between slots 10 and 11. This aroused some concern about the validity of the treatment adopted for the spurious freestream losses, and so an investigation into the origins of the problem was undertaken.

## 5.3 Properties of the Spurious Losses

As Walsh had found that the magnitude of the freestream losses appeared to increase with slot number (and hence velocity), an initial test was undertaken to determine the effect of velocity on measured losses. The five hole probe was mounted downstream of the cascade whilst the tunnel velocity was varied. Results are shown in Figure 5.2(a), which shows that despite some random uncertainty in the measurements, there is no significant velocity effect over the range of velocities encountered in the cascade. This is encouraging as it tends to discount the possibility of a Reynolds number effect.

A second concern was whether or not the spurious losses were sensitive to the incidence of the flow onto the probe. With the five hole probe mounted downstream of the cascade, and the tunnel running at constant speed, the angle of the probe head to the flow was varied. Results are shown in Figure 5.2(b), where it is possible to see that although a significant 'freestream loss' is indicated, it does not appear to vary much with changing angle of incidence. This is important as all results have been collected using a non-nulling technique. Hence, if the error in total pressure measurement was to vary with flow incidence, accurate correction of the data would be very difficult. Also this evidence also suggests that the problem is not a Reynolds number effect. Hodson and Dominy (1988) have shown that low Reynolds number effects are associated with separation of the flow from the probe head, and hence are sensitive to flow incidence.

A final test was undertaken to confirm that the spurious losses were independent of absolute velocity magnitude. The reference pitot tube and the five hole probe were mounted upstream of the cascade, and the losses recorded. Then the five hole probe was moved to slot 10 (where the velocity is increased by a factor of approximately 1.8) leaving the pitot-static probe upstream, and more measurements taken. Finally the pitot-static probe was mounted alongside the five hole probe at slot 10, giving a measurement at the high end of the range of velocities encountered in the cascade. In each case the probes were placed in 'potential flow areas' and should have detected no losses. Results are shown in Figure 5.2(c). It can be seen that although there is a bias error in loss measurement of approximately 0.015, it is when there is a difference in velocity between the reference pitot-static probe and the five hole probe that large losses are calculated. This seems odd, but the position is clarified by Figure 5.3. In Figure 5.3(a) the apparent losses at midspan of slot 3 are plotted as a function of tangential distance. As the velocity on the suction side of the passage is higher than that on the pressure side, the loss appears to fall when moving from one to the other. However, it is the loss coefficient which is being considered. If the loss coefficient is redefined as the loss in stagnation pressure between the upstream pitot-static probe and the five hole probe, divided by local rather than upstream dynamic head, a different picture emerges. This new loss coefficient is plotted against tangential distance for the midspan data at slot 3 in Figure 5.3(b). Here the error in total pressure measured by the five hole probe appears to be a constant fraction of local dynamic head (the random errors increase towards the pressure side of the passage as the denominator becomes small).

## 5.4 Proposed Explanation of Apparent Freestream Losses

The five hole probe calibration technique used at Durham, calculates losses from the formula :-

$$P_0 - P_{0_{LOCAL}} = (P_0 - P_c) - (P_c - P_i)Spi \tag{5.1}$$

where

$P_0 = upstream \quad stagnation \quad pressure$

$P_c = pressure \quad on \quad central \quad tube \quad of \quad 5 \quad hole \quad probe$

$P_i = pressure \quad on \quad left \quad or \quad right \quad hand \quad tube,$

$whichever \quad is \quad at \quad lower \quad pressure$

$Spi = stagnation \quad pressure \quad calibration \quad coefficient, \quad which$

$is \quad a \quad function \quad of \quad yaw \quad and \quad pitch \quad angles$

Examination of data shows that the value of $P_0 - P_c$ does not account for the apparent losses which are calculated in freestream areas. Thus the error must arise in the term $(P_c - P_i)Spi$. If one considers a nulled probe head, then as the velocity increases (without loss), $P_c$ will be the full stagnation pressure, which is constant. However, the pressure on the left or right hand tube, $P_i$, is the local stagnation pressure less some proportion of the dynamic pressure. Hence $(P_c - P_i)$ increases with increasing velocity. This suggests that the source of error in loss measurement may be a constant error in the stagnation pressure calibration $Spi$, which is amplified at higher speeds by an increased value of $P_c - P_i$. The calibration of $Spi$ is defined as :-

$$Spi = \frac{P_{0_{LOCAL}} - P_c}{P_c - P_i} \tag{5.2}$$

Here $P_{0_{LOCAL}}$ is measured by a pitot tube during calibration. The only obvious way in which a systemmatic error could have entered the calibration is if the pitot tube recorded a different value of total pressure to that incident on the five hole probe. Then :-

$$P_{0_{TRUE}} = P_{0_{CAL}} + \eta \tag{5.3}$$

where $\eta$ is a constant error. Substituting in equation (5.2) yields :-

$$Spi^{TRUE} = Spi^{CAL} + \frac{\eta}{(P_c - P_i)_{CAL}} \tag{5.4}$$

The loss coefficient is normally calculated from the formula :-

$$\frac{P_0 - P_{0_{LOCAL}}}{\frac{1}{2}\rho V_0^2} = \frac{(P_0 - P_c) - (P_c - P_i)Spi}{\frac{1}{2}\rho V_0^2} \tag{5.5}$$

Thus substituting for $Spi$ from equation (5.4) gives :-

$$\begin{aligned} \text{true loss} \\ \text{coefficient} \end{aligned} = \frac{(P_0 - P_c) - (P_c - P_i)Spi^{CAL} - \frac{(P_c - P_i)}{(P_c - P_i)_{CAL}}\eta}{\frac{1}{2}\rho V_0^2} = \begin{aligned} \text{usual loss} \\ \text{coefficient} \end{aligned} - \frac{(P_c - P_i)}{(P_c - P_i)_{CAL}} \frac{\eta}{\frac{1}{2}\rho V_0^2} \tag{5.6}$$

For a given angle of incidence, $P_c - P_i$ is a constant fraction of the local dynamic head, i.e. :-

$$P_c - P_i = A(\theta)\frac{1}{2}\rho V^2 \tag{5.7}$$

where $A$ is a function of incidence angle $\theta$. Substituting into equation (5.6), the error term becomes :-

$$\frac{P_c - P_i}{(P_c - P_i)_{CAL}} \frac{\eta}{\frac{1}{2}\rho V_0^2} = \frac{V^2}{V_{CAL}^2} \frac{\eta}{\frac{1}{2}\rho V_0^2} \tag{5.8}$$

This formula is then independent of flow incidence angle $\theta$, and only depends upon the ratio of local to upstream velocity. This explains why the error term is roughly constant if the loss coefficient is defined relative to local dynamic head (see Figure 5.3). It also explains why the errors detected using the new five hole probe calibration are lower than those obtained with the old calibration. The new calibration was performed at a higher velocity than the old calibration.

Thus the above explanation of the source of the spurious freestream losses, appears to fit the observed properties of the phenomenon. The error in total pressure introduced during calibration, is assumed to be due to a small variation in stagnation pressure between the tunnel centre (where the five hole probe was located), and the tunnel side (where the pitot tube was mounted). The magnitude of the error $\eta$ deduced from freestream data at slots 7, 9, 11 analysed with the new calibration, is approximately $0.7mmH_2O$ (=3.2% $\frac{1}{2}\rho V_0^2$). This value for $\eta$ may be used to correct $Spi$, to produce a calibration which should give zero freestream loss, regardless of velocity (in the limited range of the cascade). Results of such an analysis are shown in Figure 5.1 under the heading 'corrected new calibration - no loss correction'. Also shown is a re-analysis of all the data using the new five hole probe calibration, with constant loss correction (i.e. subtraction of the freestream

loss from the total and static pressure coefficients at each point on a traverse plane). This is headed 'new calibration - constant loss correction'. It may be seen from Figure 5.1 that the results of using a 'constant loss correction', or the 'corrected new calibration' are very similar outside of the blade row where velocities are fairly even over a traverse plane. Within the blade row however, the results are quite different due to the high cross-passage pressure gradients.

If the error $\eta$ could be accurately deduced, a corrected probe calibration would be attractive, but unfortunately this is not the case. Figure 5.4 shows a comparison between the midspan losses at slot 5 obtained from the old calibration with constant loss correction, the new calibration with constant loss correction, and the corrected new calibration with no loss correction. The loss should be close to zero at all tangential locations (the data does not reach the blade boundary layers). The old calibration gives a loss which increases as the velocity increases, moving from the pressure surface to the suction surface. The corrected calibration with no loss correction, over compensates for velocity effect, and gives a loss which decreases with velocity. The flattest curve is actually that obtained from analysis with the new calibration and constant loss correction. Thus it was decided to use this data for further work. The good agreement between results downstream of the cascade obtained with a corrected calibration, or the new calibration and constant loss correction, allows reasonable confidence in the data in this region. Within the blade row the mass averaged loss is always suspect, as the entire passage area is not covered by the measurements. Hence accepting a constant loss correction, which is clearly not correct for slots with large velocity gradients, does not seem to be a great sacrifice. It should be realised that the correction, whilst being very significant for the mass averaged loss, is small when compared with the losses found within the loss core, and hence contour plots of losses on a traverse plane are little effected by it.

Returning to Figure 5.1, there is a surprisingly large discrepancy between the analyses using the new and old calibrations with constant loss correction. The reason for the discrepancy was found to be mainly due to

the choice of fluid which was assumed to be 'loss free' for deduction of a loss correction. At slots 1, 3, 5 Walsh had chosen the midspan data to be free of loss. At slots 8 and 10 however, an area had been used. In re-analysing the data an area has always been used, though not necessarily the same area as that chosen by Walsh. This then was the major source of difference between mass averaged losses calculated by Walsh, and those presented in this work. These differences highlight the difficulty of correcting data for the errors in loss measurement. Some experimentation using different freestream areas to deduce the loss correction for each traverse plane, indicated the uncertainty in mass averaged loss resulting from the choice of this 'freestream area'. Figure 5.13 shows the final loss growth curve to be used for validation of calculation codes, with error bars indicating the probable uncertainty at each slot. It is possible for losses apparently to decrease within the blade row, as traverses do not extend to the blade surfaces.

For the remainder of this thesis it will be assumed that all five hole probe measurements are analysed with the new calibration, and corrected for apparent freestream losses by constant loss correction.

## 5.5 Slot 7 Traverse (87% Cax)

Results of a five hole probe traverse of slot 7, are shown in Figure 5.5. The measurement locations can be deduced from the position of the secondary velocity vectors presented in Figure 5.5(e). Although the data is only plotted up to a radial distance of $150mm$ from the endwall, measurements were made all the way to midspan at $200mm$. In Figure 5.5(a), the static pressure coefficient contours, show the minimum pressure to be located near the centre of the passage vortex, and away from the suction surface. This effect was observed by Langston *et al* (1977) in their endwall pressure distribution. It is clear that the vortical motion of the secondary flow has a profound impact upon the pressure distribution in its locality. The yaw angle contours shown in Figure 5.5(b) indicate the magnitude of the flow angle variation caused by the passage vortex, with over-turning of 20° occurring close to the endwall. In

Figure 5.5(c) large pitch angles are also evident, reaching a peak of 60° near to the suction surface. The loss contours in Figure 5.5(d) indicate that the endwall boundary layer has been swept towards, and up, the suction surface by the strong secondary flows. Freestream fluid has been brought into the endwall region on the pressure side of the passage. The secondary velocity vectors indicate that the vortex centre is approximately half way between its positions at slots 5 and 8, which were reported by Walsh (1987). There is some evidence of a counter vortex on the midspan side of the passage vortex, towards the suction surface, but this is not well covered by the range of the traverse. Hence the streamwise vorticity, which is calculated using the method of Gregory-Smith *et al* (1987) and non-dimensionalised by upstream velocity and the cascade pitch, does not detect this counter vorticity, and is dominated by the presence of the passage vortex.

The pitch averaged results in Figure 5.6, show that at this stage the secondary flow effects extend from the endwall to $70mm$ radially. The yaw angle plot indicates strong over-turning within $30mm$ radially, and the loss coefficient shows that the loss core is not yet detached from the endwall. There is a peak in loss at $60mm$ from the endwall, where the passage vortex separates from the suction surface, but this is not yet dominant. The peak develops rapidly between slots 7 and 8 to produce a distinct loss core. Similarly the secondary kinetic energy is greatest near to the endwall at slot 7, but also develops to give a distinct peak at $60mm$ from the endwall at slot 8. The mass averaged results (Figure 5.13) show that whilst the secondary kinetic energy is almost fully developed at slot 7, the loss rises rapidly from its value of 0.07 to reach 0.1 by slot 8.

## 5.6 Downstream Flow Development

Figure 5.7 shows the results of a traverse of slot 9 (116% Cax). This can be compared with Figures 5.9 and 5.11, which show results for slots 10 (data from Walsh (1987)) and 11 respectively. Slot 10 is 128%, and slot 11 is 152% of an axial chord downstream of the leading edge. As the flow

procedes from slots 9 to 11, the blade wakes broaden, and the peak loss within them decreases from approximately 0.8 to 0.5. The static pressure over the plane becomes more even, and radial velocities are progressively reduced, as evidenced by the pitch angle contours. The blade wake within $75mm$ of the endwall is gradually convected into the loss core by the passage vortex, and the counter vorticity which is shed within the blade wake is convected around the passage vortex. This is most clearly shown by the vorticity contours which steadily decay downstream. Despite the continuous sweeping of the blade wake near to the endwall into the loss core, another significant loss core emerges, on the endwall between successive passage vortices. This is probably caused by an accumulation of endwall boundary layer loss in the region of the endwall counter vortex, with additional losses due to the action of this vortex upon the endwall.

Pitch averaged results for slots 9, 10, and 11, are shown in Figures 5.8, 5.10, and 5.12 respectively. In each case the two curves were obtained by integrating the traverse data over a distance of one pitch, in one case incorporating only the left hand blade wake, and in the other only the right hand wake. This gives an indication of the flow repeatability from passage to passage, which is observed to be fair. As the flow develops downstream of the cascade, the over-turning on the endwall is decreased by the growth of the endwall counter vortex, but the under-turning peak of the passage vortex appears to remain unchanged. The loss core spreads slightly further from the endwall, and the secondary kinetic energy reduces.

The quantitative developments of the downstream mass averaged properties are presented in Table 5.1. Also, Figure 5.13 shows the development of loss, and secondary kinetic energy. From these graphs it can be seen that the secondary kinetic energy appears to decay steadily downstream of the cascade, whilst the loss rises more rapidly between slots 9 and 10 than between slots 10 and 11. This is slightly different to the results of Moore and Adhye (1985) who found that the loss rose quite steadily downstream of their cascade, and was matched by an equal decay of secondary kinetic energy. However Moore *et al* (1986), showed that this was the result of an

incidental balance between losses generated in the endwall boundary layer, and mean kinetic energy created from turbulent kinetic energy.

Table 5.1 : Downstream Development of Cascade Losses

| JAW TEST CASE | Slot 9 | Slot 10 | Slot 11 |
|---|---|---|---|
| Loss Coefficient | 0.183 | 0.196 | 0.212 |
| - Midspan Loss Coefficient | 0.088 | 0.090 | 0.097 |
| = Gross Secondary Loss | 0.095 | 0.106 | 0.115 |
| - Inlet Loss | 0.042 | 0.042 | 0.042 |
| = Net Secondary Loss | 0.053 | 0.064 | 0.073 |
| Secondary KE Coefficient | 0.049 | 0.043 | 0.030 |
| Secondary KE Coefficient + Loss Coefficient = | 0.232 | 0.239 | 0.242 |
| Mixed Out Loss Coefficient | 0.234 | 0.239 | 0.243 |
| - Midspan Mixed Out Loss Coefficient | 0.089 | 0.095 | 0.104 |
| = Gross Mixed Out Secondary Loss | 0.145 | 0.144 | 0.139 |
| - Inlet Loss | 0.042 | 0.042 | 0.042 |
| = Net Mixed Out Secondary Loss | 0.103 | 0.102 | 0.097 |

The mixed out loss was calculated at each of the downstream planes as an attempt to remove the dependency of the loss on downstream distance. The calculation is described by Moore and Adhye (1985). The mixed out loss in Table 5.1 rises from slots 9 to 11, due to an apparent increase in the midspan coefficient. The secondary loss rises slowly as secondary kinetic energy is lost, and a new boundary layer develops on the endwall. However, the mixed out secondary loss is observed to be approximately constant at each downstream slot and might even reduce slightly. This must be due to the streamwise turbulence acting to convert turbulent kinetic energy to primary kinetic energy, and/or the reversible pressure work term discussed by Moore *et al* (1986), acting to convert secondary kinetic energy to primary kinetic energy. The combination of these effects must be matching or slightly exceeding the rate at which the endwall boundary layer produces extra loss. The mixed out loss is well represented by the sum of the loss and the

secondary kinetic energy, a result which was also found by Moore and Adhye (1985).

## 5.7 Overall Flow Features

The data discussed in this chapter (JAW test case) constitutes a difficult test case for flow models, as the secondary flows are quite powerful. The endwall boundary layer is strongly over-turned, and eventually is entirely removed from the endwall, being shed downstream as a loss core. Freestream fluid is introduced next to the endwall, but is prevented from developing into a significant boundary layer within the blade row. Instead it is continuously swept to the passage suction side, and replaced by new freestream fluid.

The losses are seen to rise rapidly in the latter half of the cascade, in accordance with other rotor cascades (e.g. Langston *et al* (1977)). As the flow at midspan is essentially two-dimensional, it should be possible to distinguish between the quality of modelling of blade boundary layers, and secondary flow effects.

Finally, Figure 5.14 shows a plot of the blade static pressures, which were measured and presented by Walsh (1987). As the endwall is approached, the deviation of the suction surface pressures from those at midspan increases. The loading is progressively reduced at the leading edge, and increased towards the trailing edge, where low pressures result from the proximity of the passage vortex. In particular, within $35mm$ of the endwall, there is a significant adverse pressure gradient, on the suction surface in the last 20-30% of an axial chord. This may contribute to the rapid rise in loss in this region. The variation in blade loading is also of interest for blade stress analysis. As the surface pressures are influenced by secondary flows, they will constitute a useful test for three-dimensional calculations.

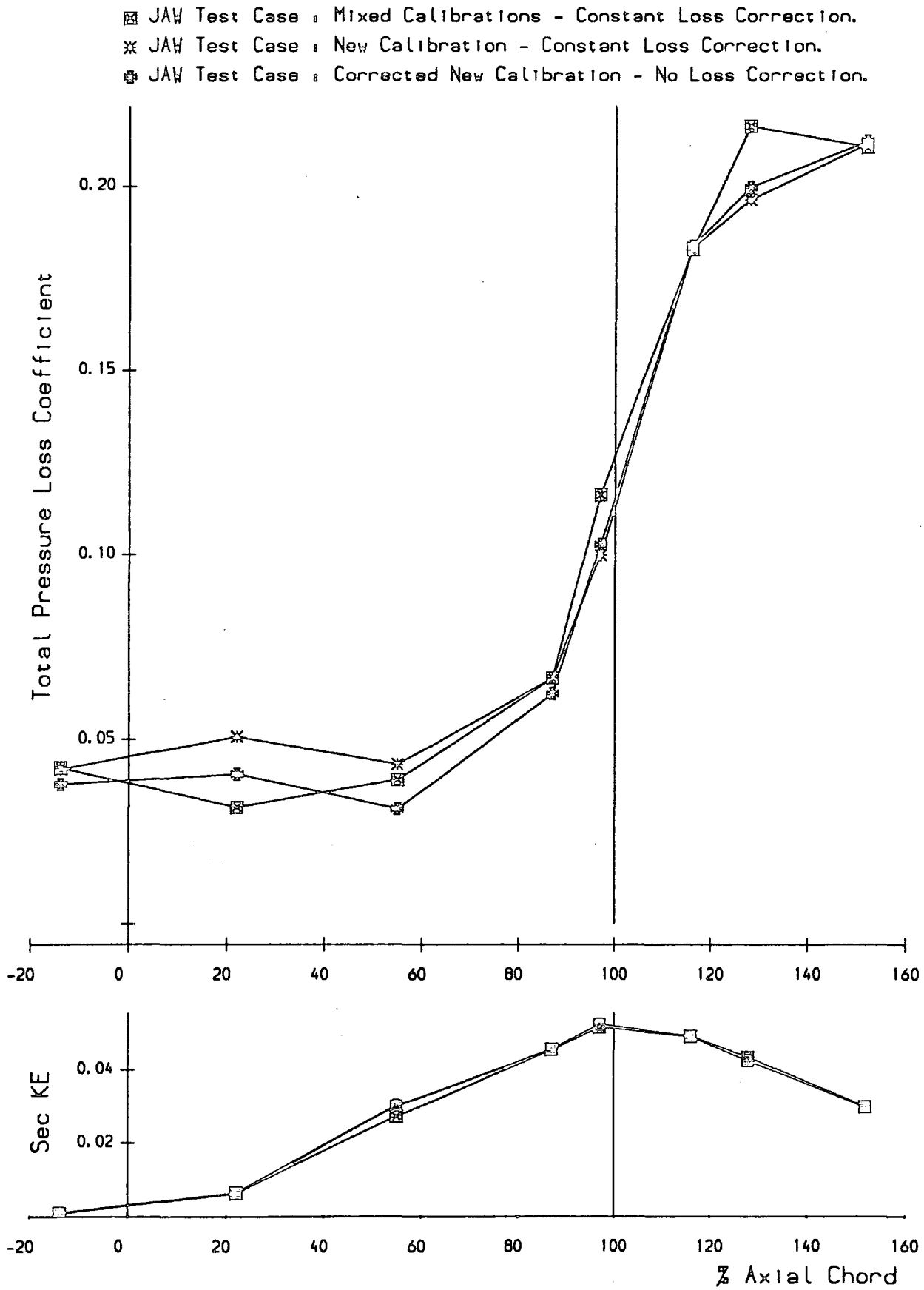


FIGURE 5.1 : Mass Averaged Loss & Secondary Kinetic Energy

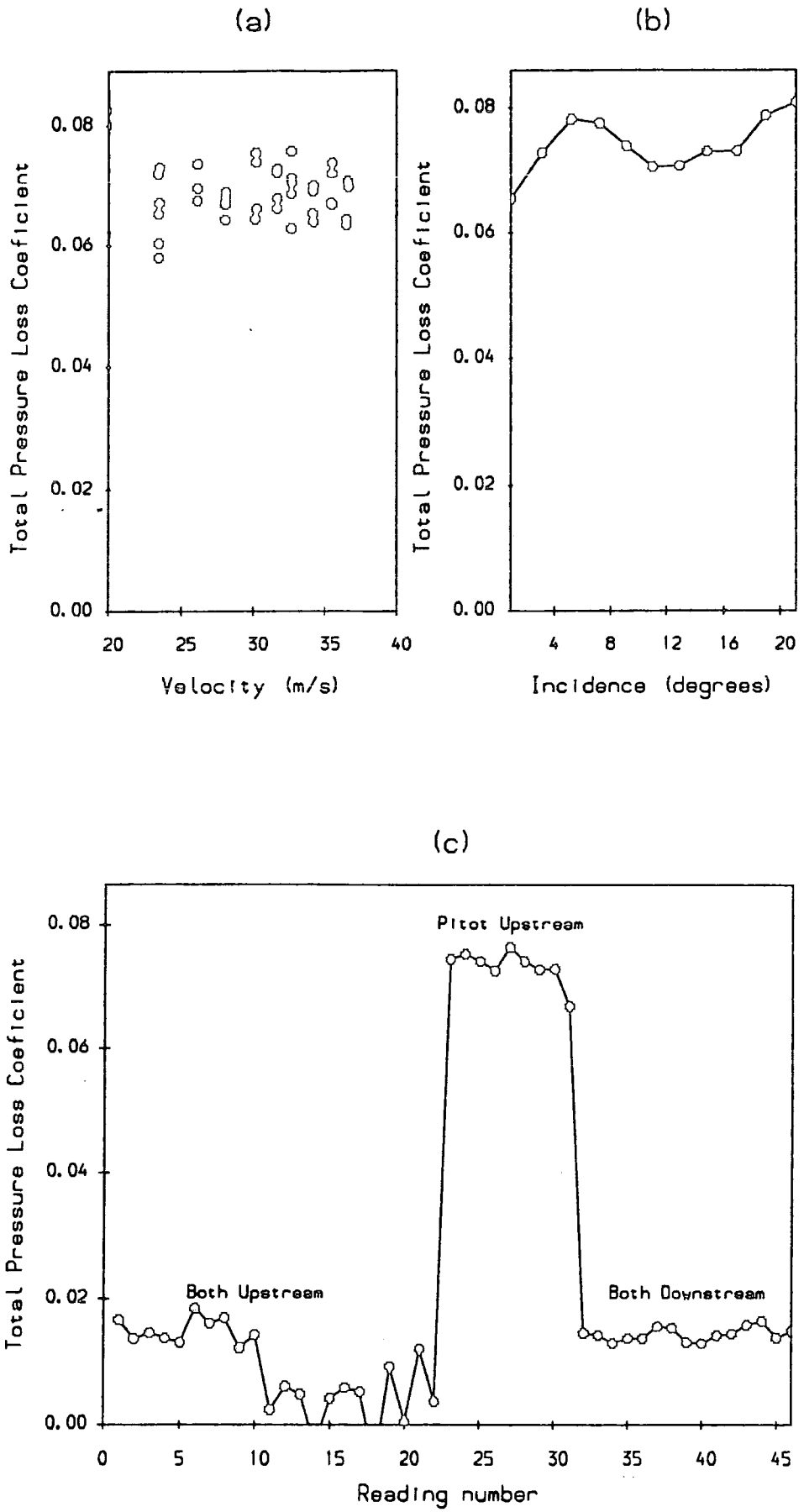


FIGURE 5.2 : Behaviour of Spurious Freestream Losses

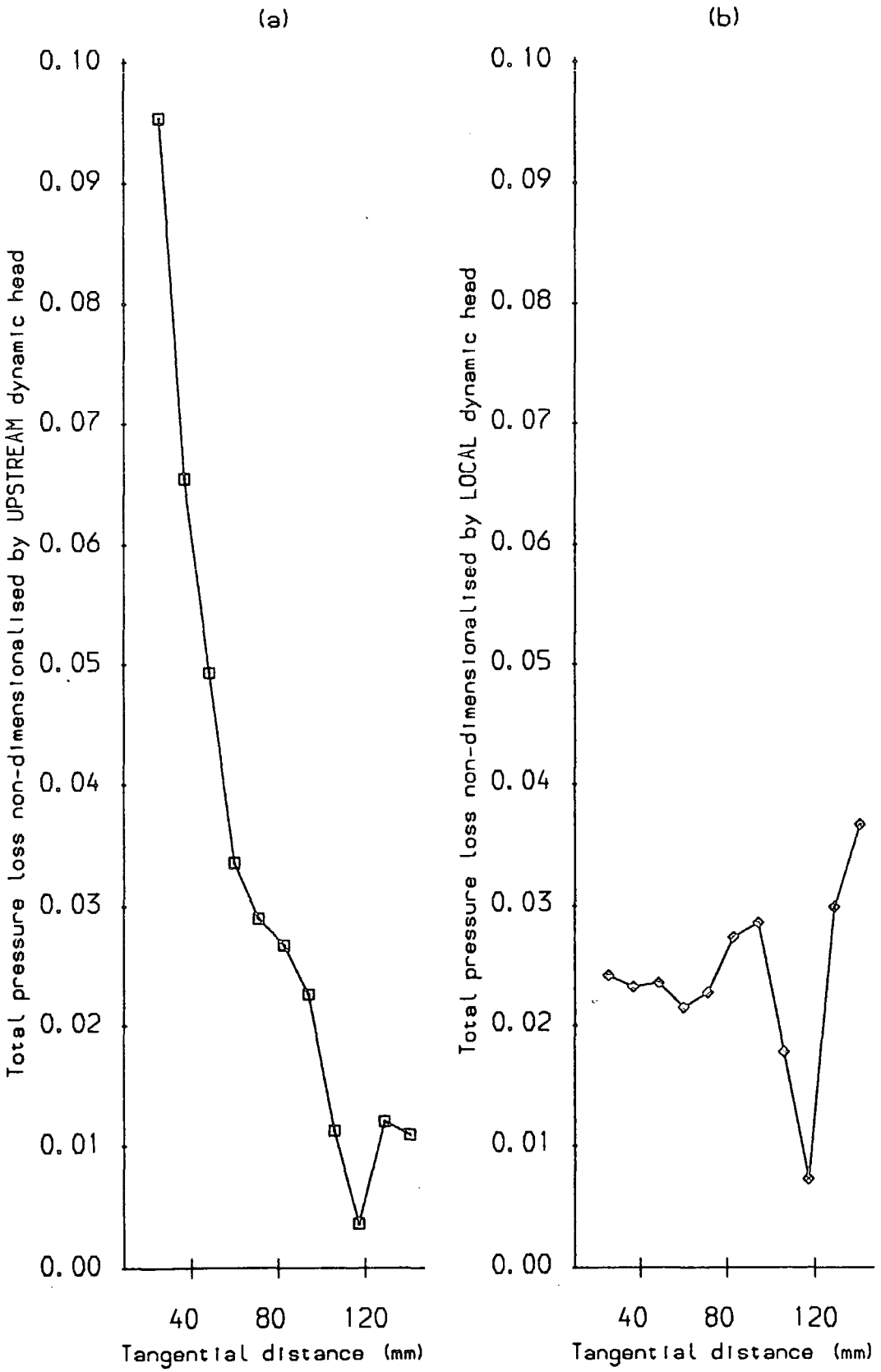


FIGURE 5.3 : Apparent Losses at Midspan of Slot 3

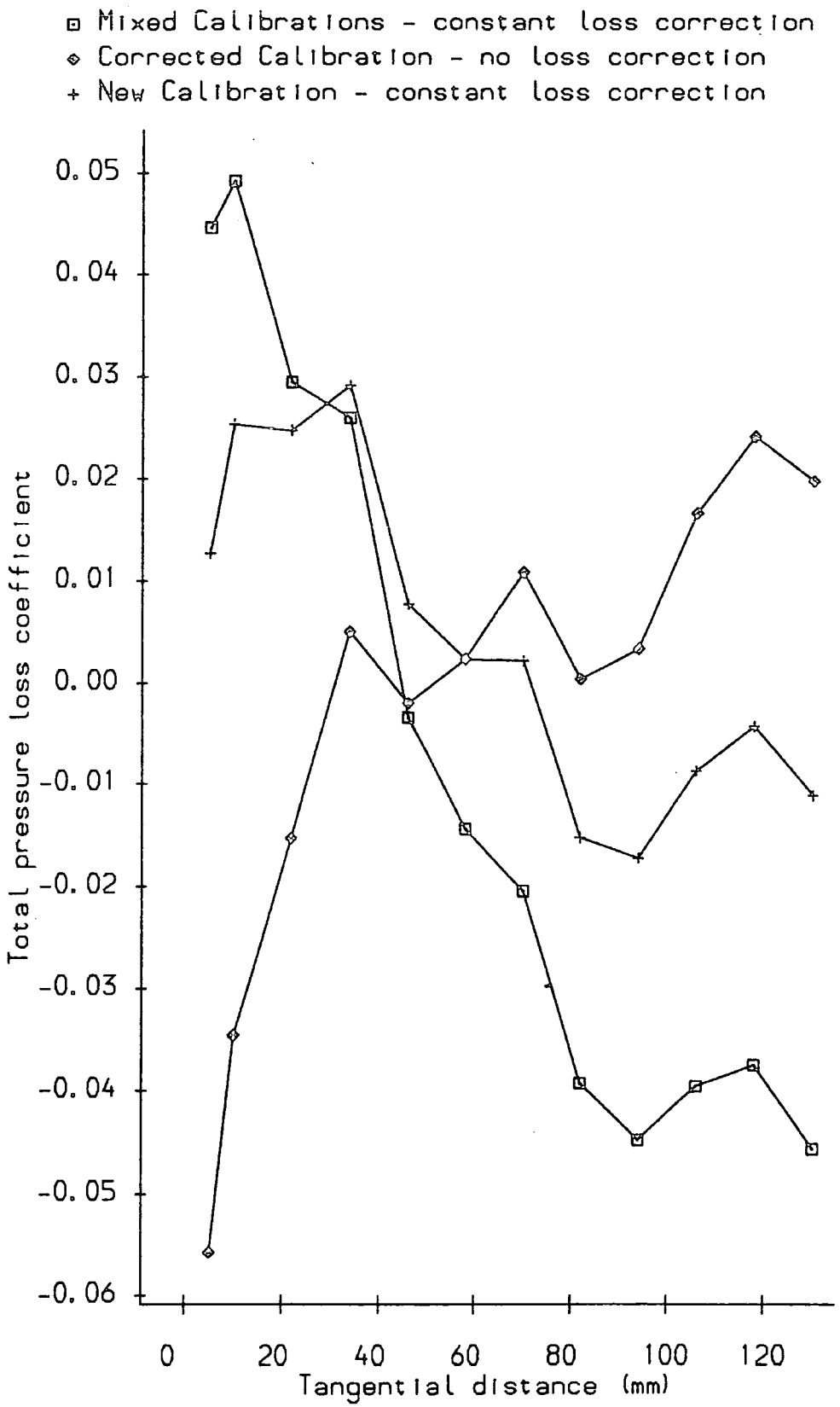


FIGURE 5.4 : Midspan Losses at Slot 5

Five Hole Probe Measurements (JAV Test Case).

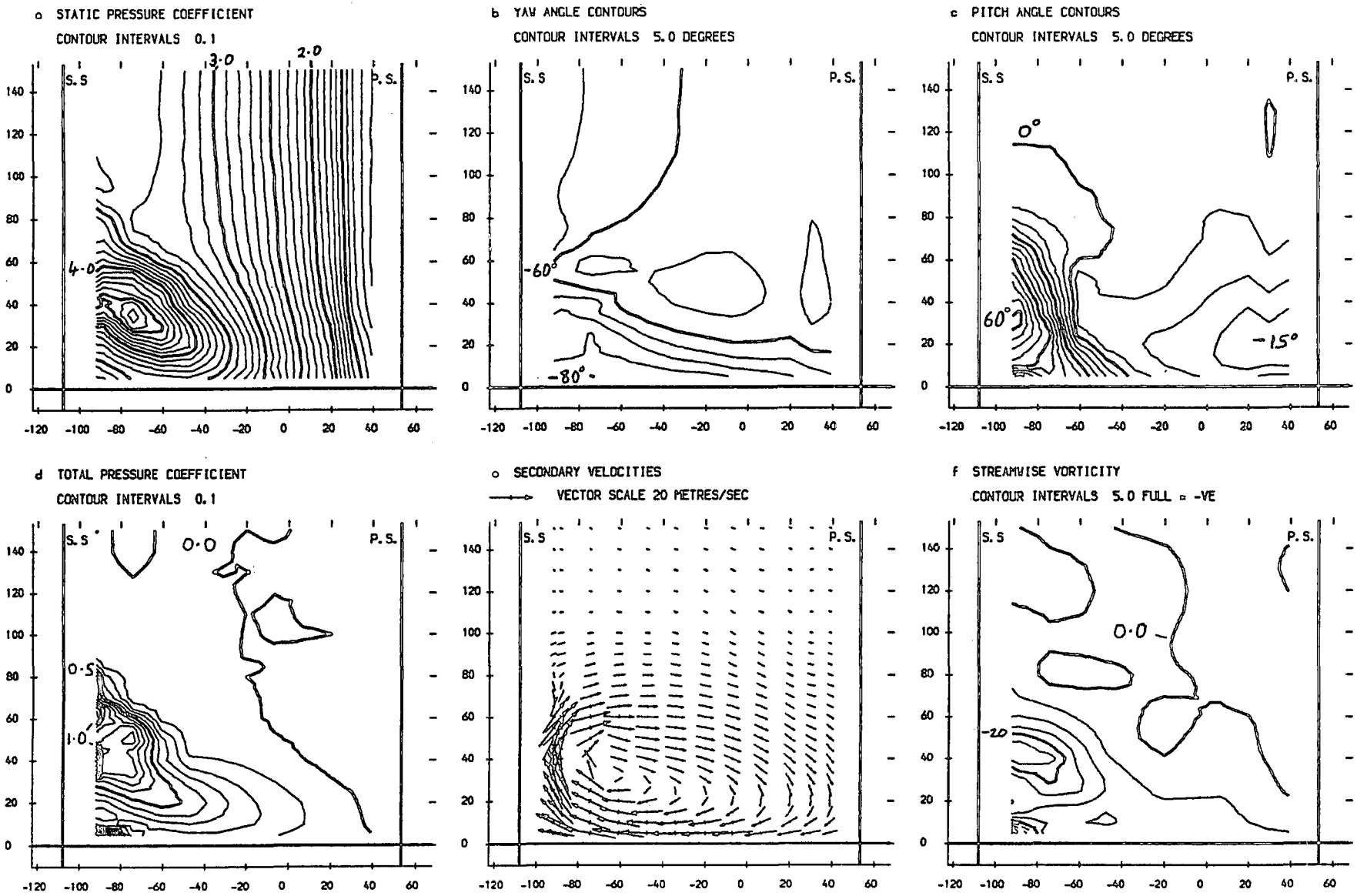


FIGURE 5.5 : Area Plots For Slot 7

Five Hole Probe Measurements (JAW Test Case).

a) Yaw Angle (Degrees)

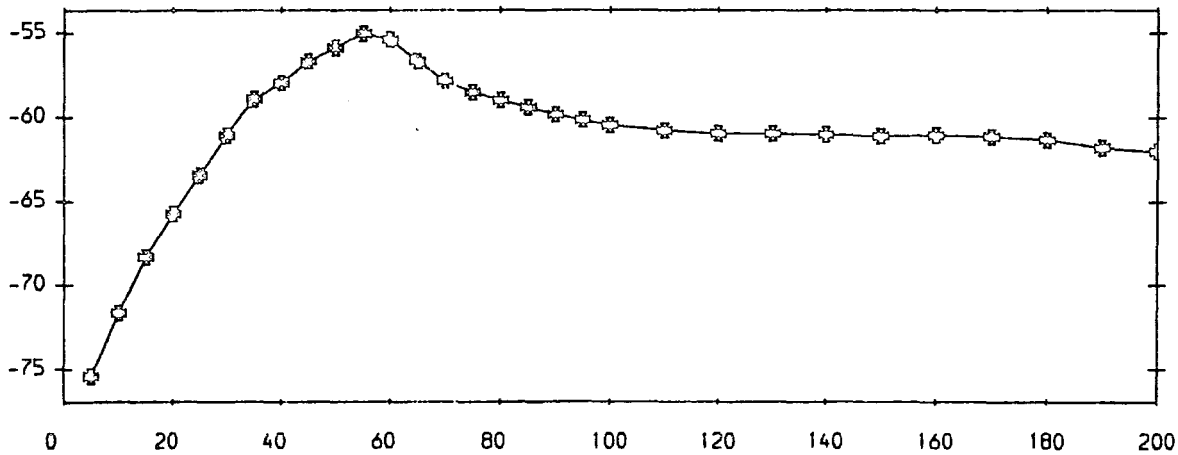


b) Total Pressure Loss Coefficient

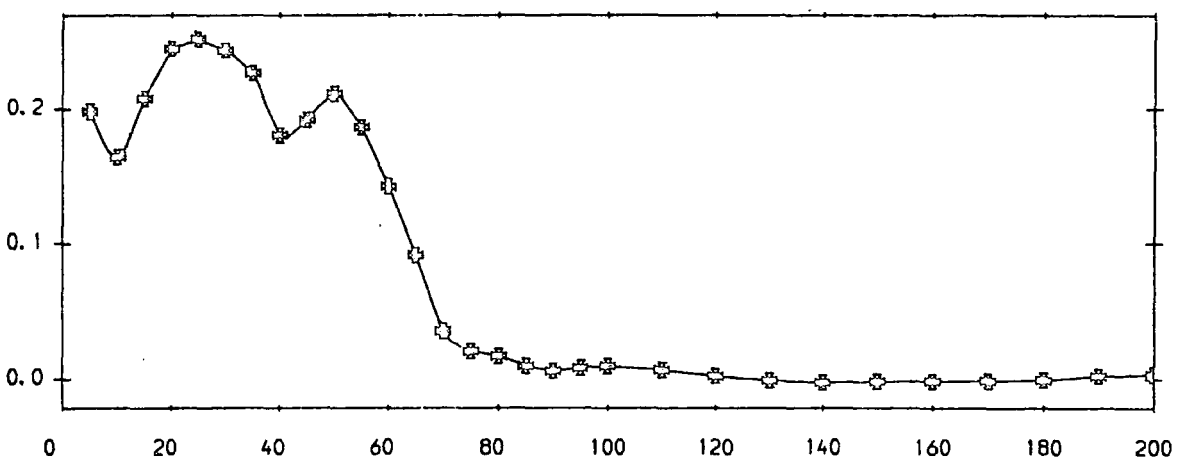


c) Secondary Kinetic Energy Coefficient

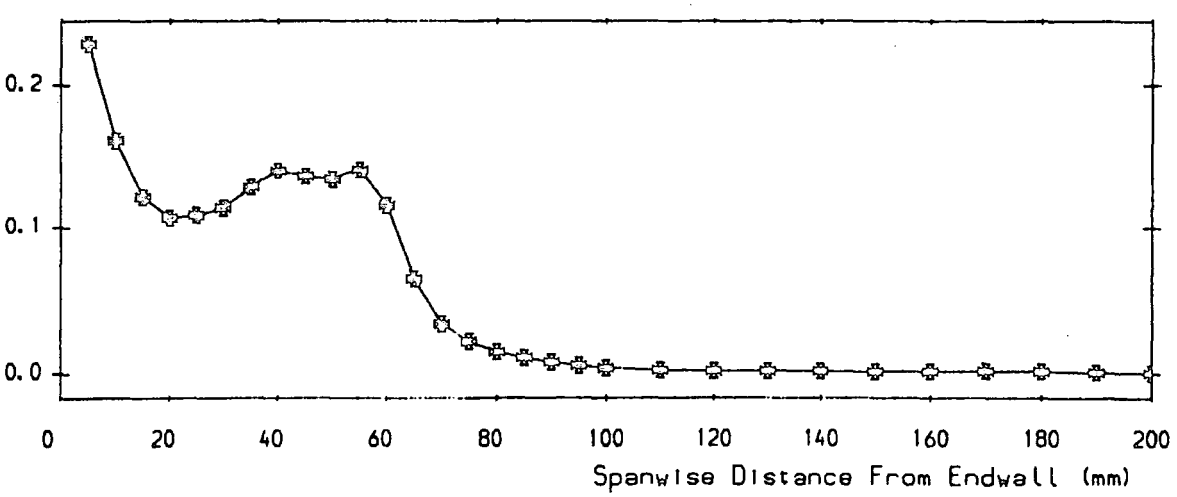


FIGURE 5.6 : Pitch Averaged Results For Slot 7

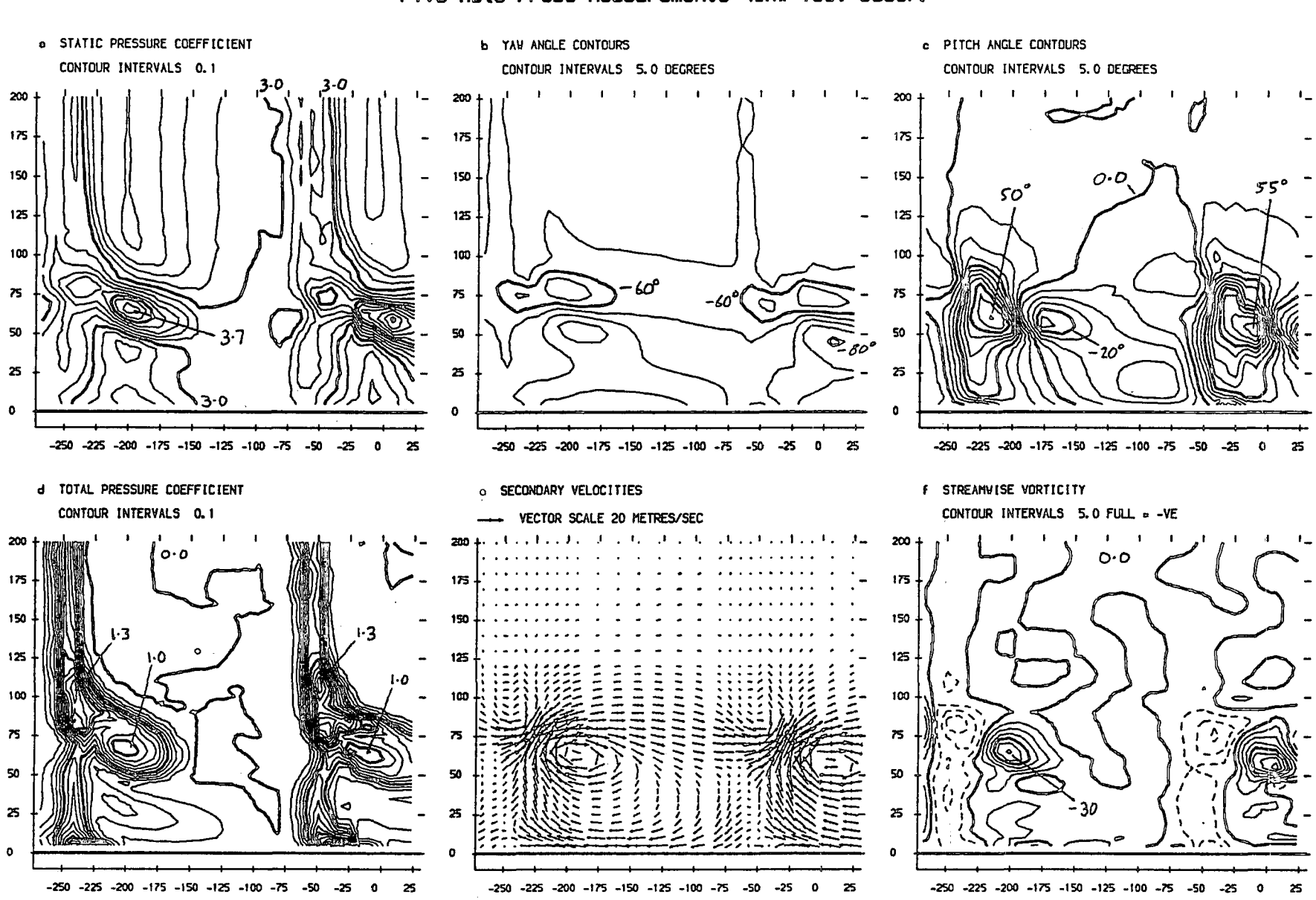


FIGURE 5.7 : Area Plots For Slot 9

⁂ 5 Hole Probe Measurements (JAW Test Case, Right Hand Wake).
✿ 5 Hole Probe Measurements (JAW Test Case, Left Hand Wake).

a) Yaw Angle (Degrees)

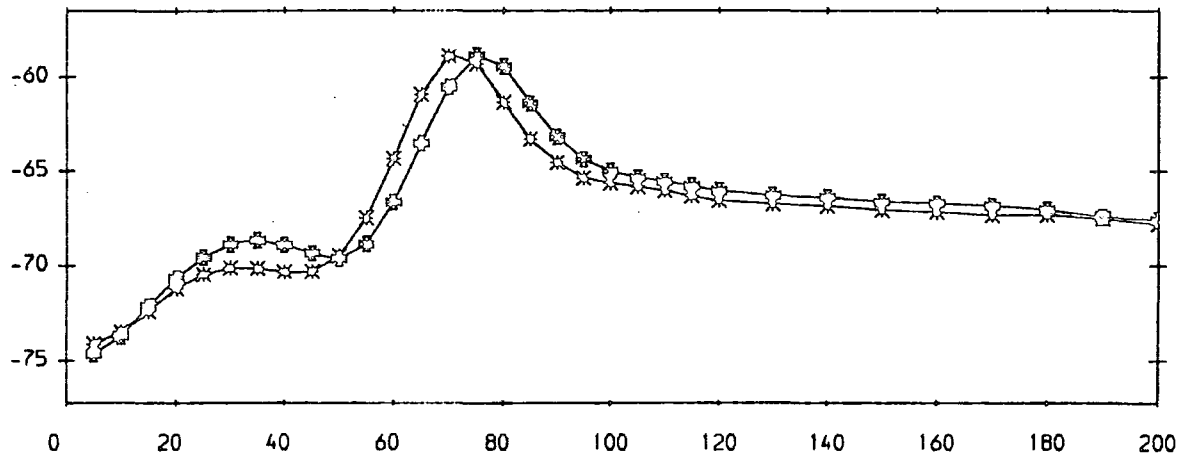


b) Total Pressure Loss Coefficient

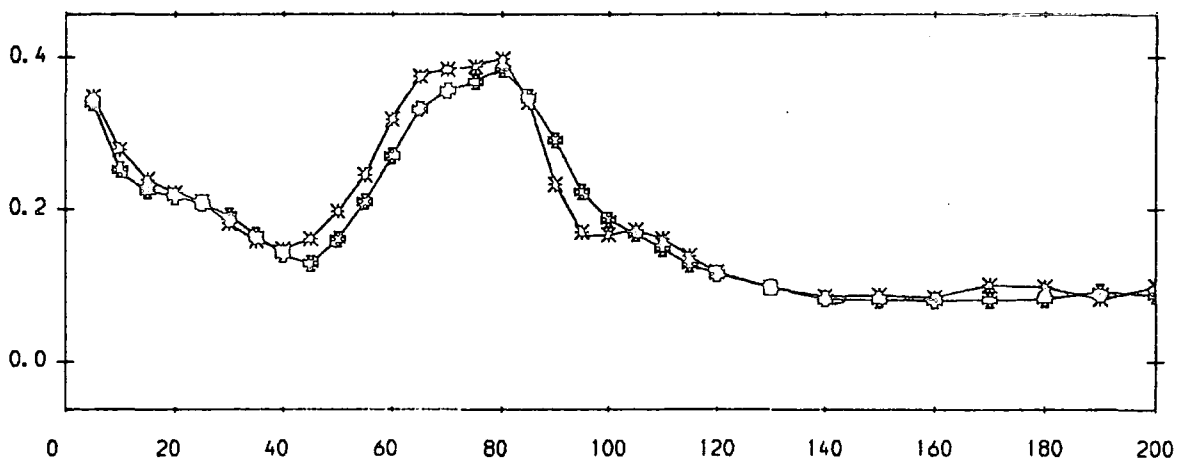


c) Secondary Kinetic Energy Coefficient

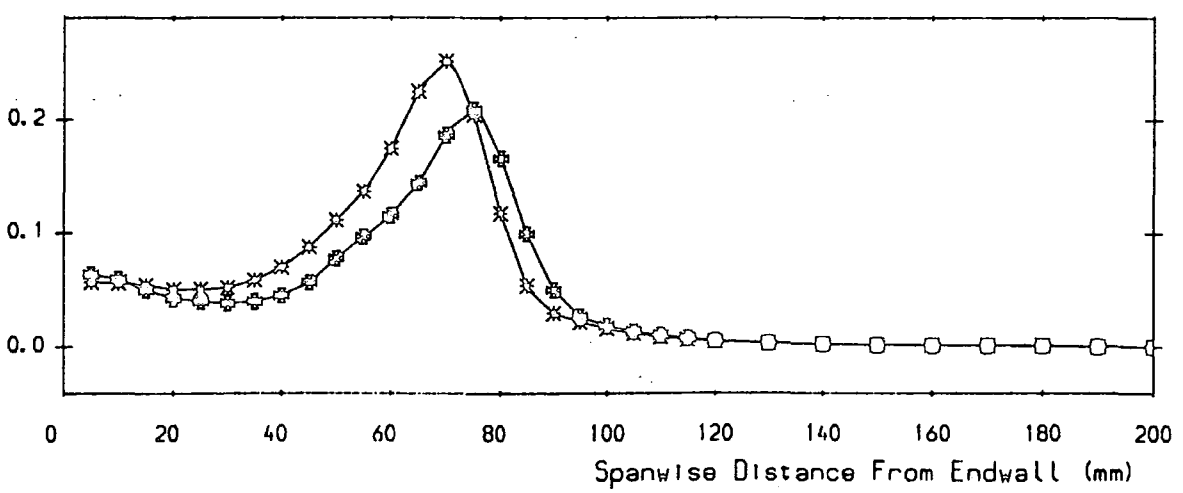


FIGURE 5.8 : Pitch Averaged Results For Slot 9

Five Hole Probe Measurements (JAV Test Case).

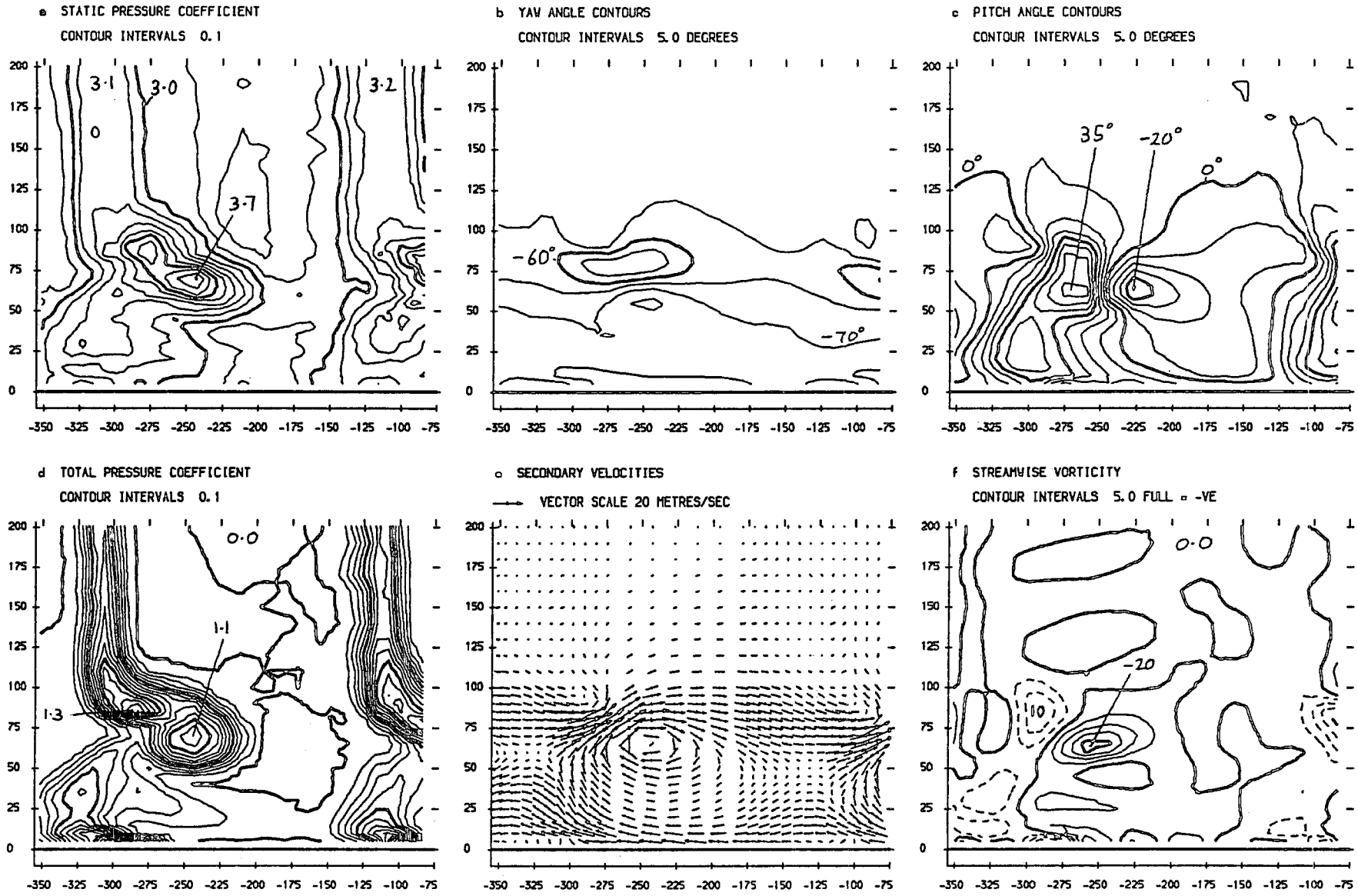


FIGURE 5.9 : Area Plots For Slot 10

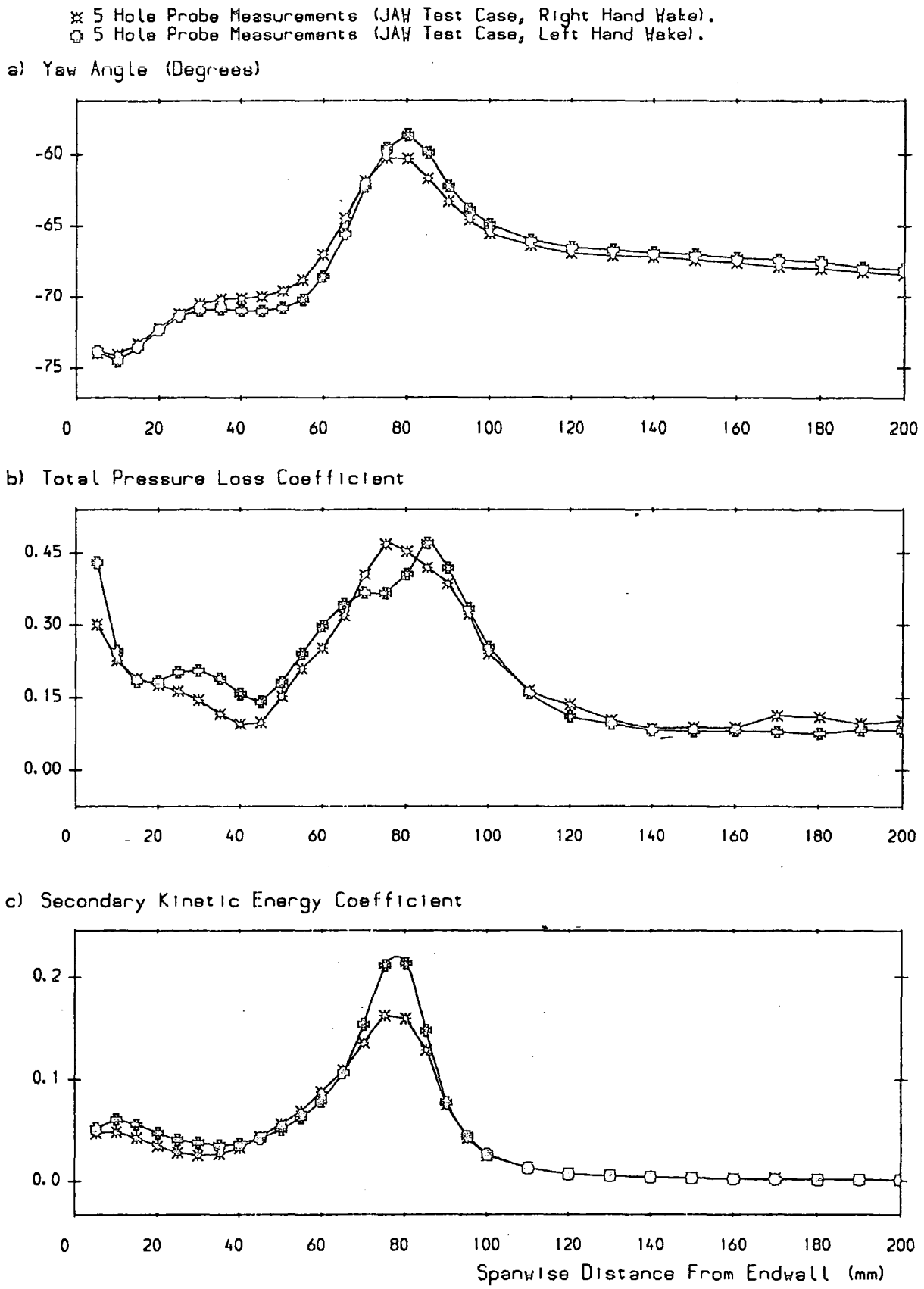


FIGURE 5.10 : Pitch Averaged Results For Slot 10

Five Hole Probe Measurements (JAW Test Case).

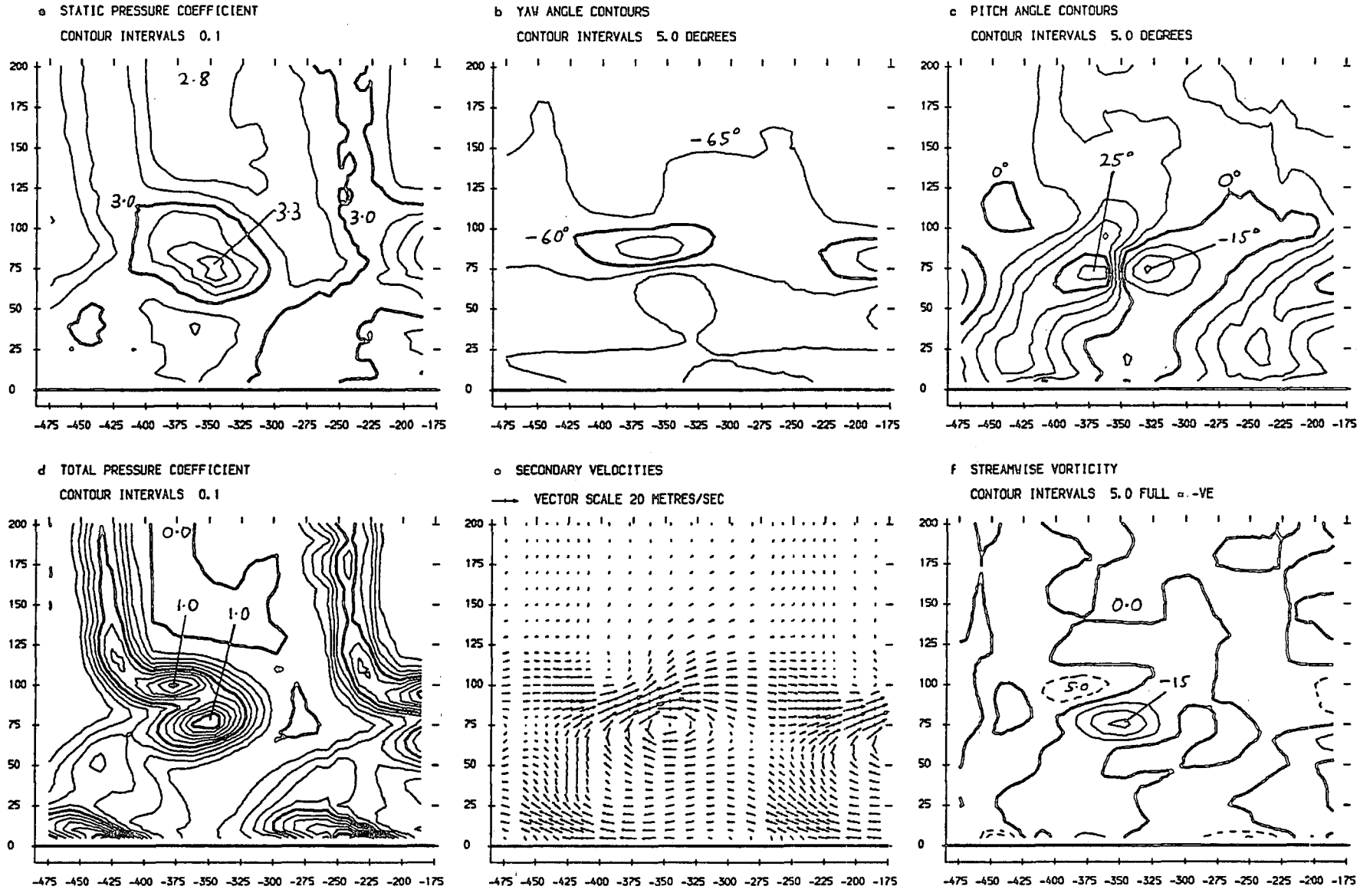


FIGURE 5.11 : Area Plots For Slot 11

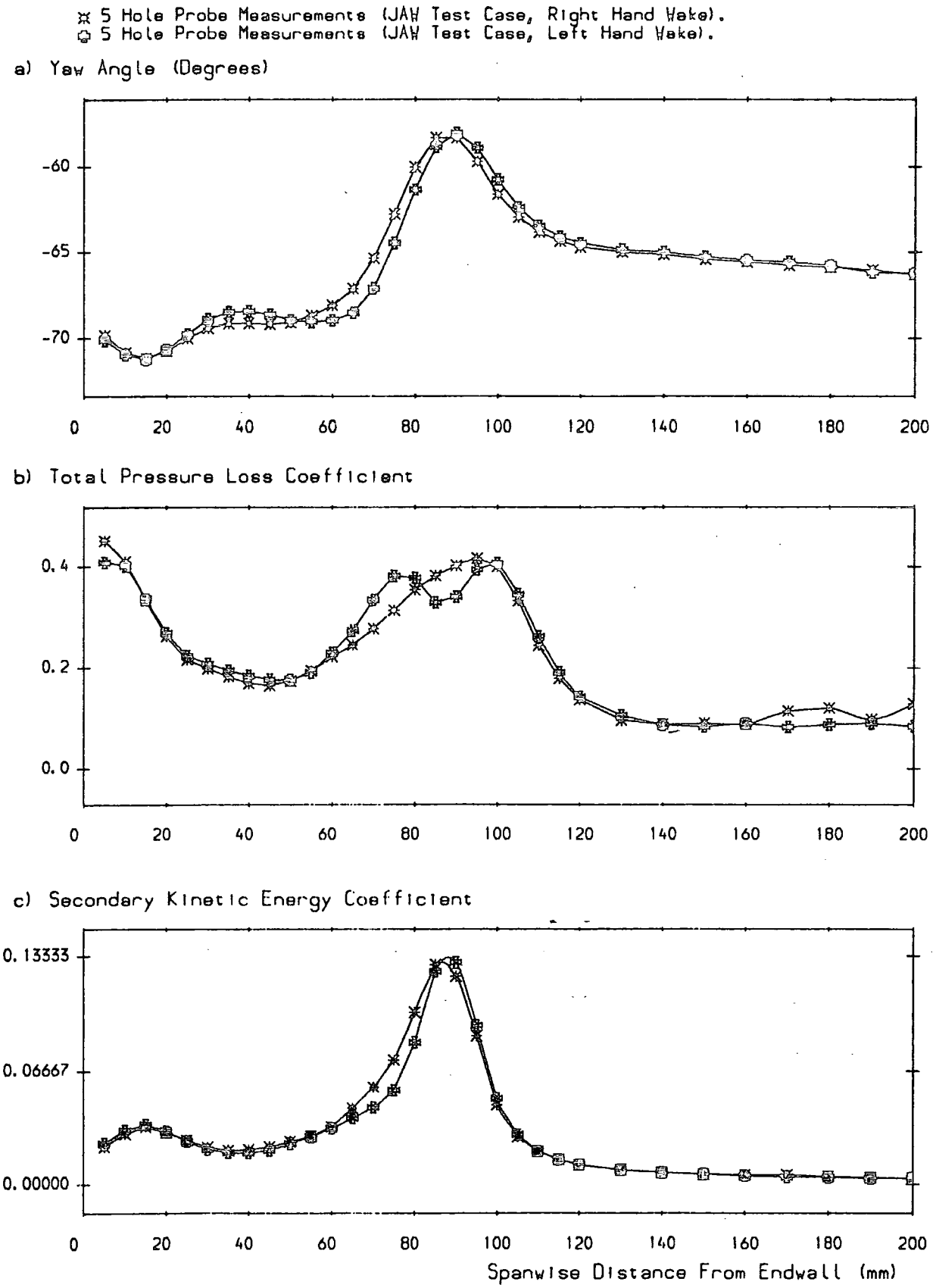


FIGURE 5.12 : Pitch Averaged Results For Slot 11

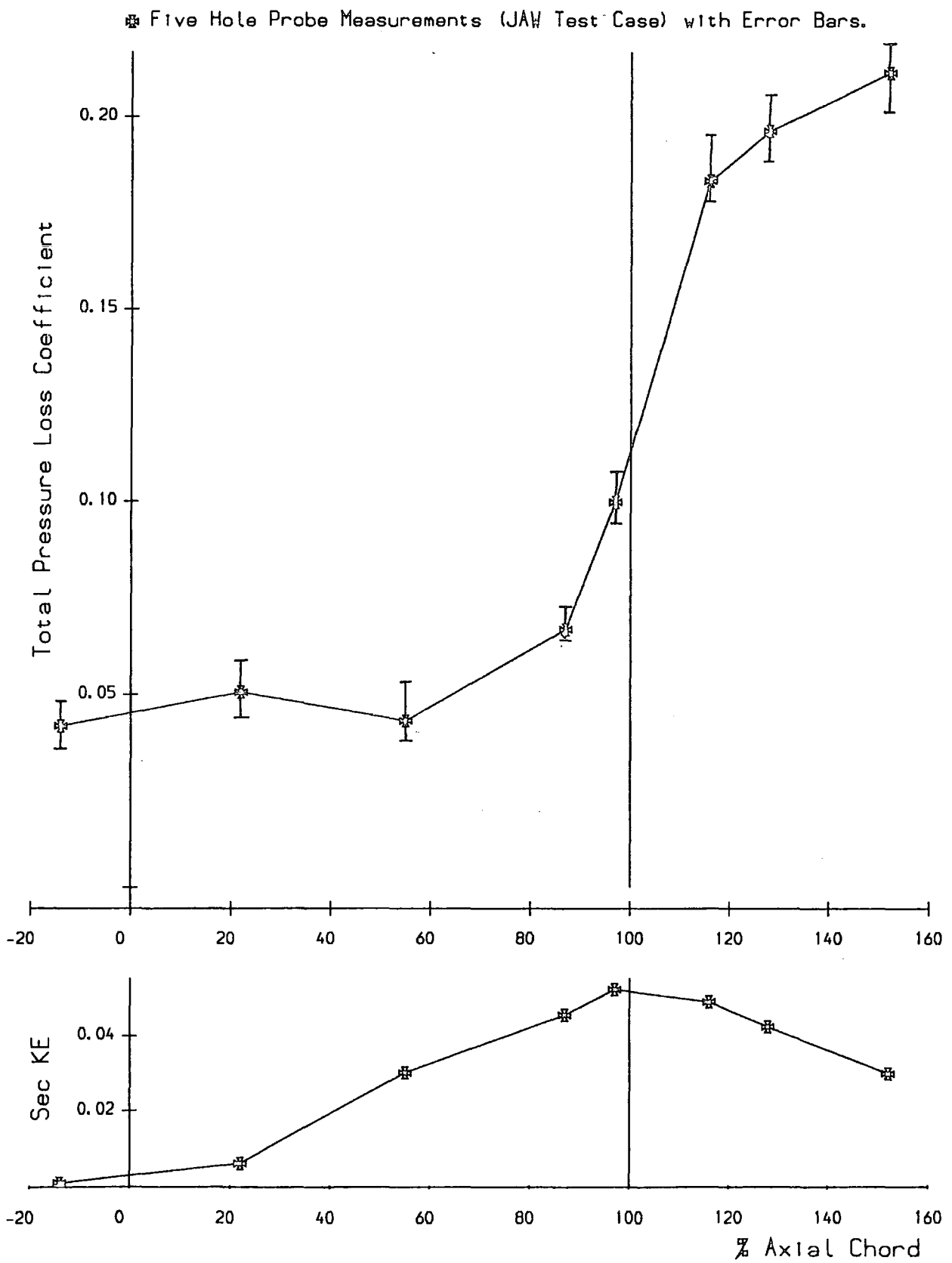


FIGURE 5.13 : Mass Averaged Loss & Secondary Kinetic Energy

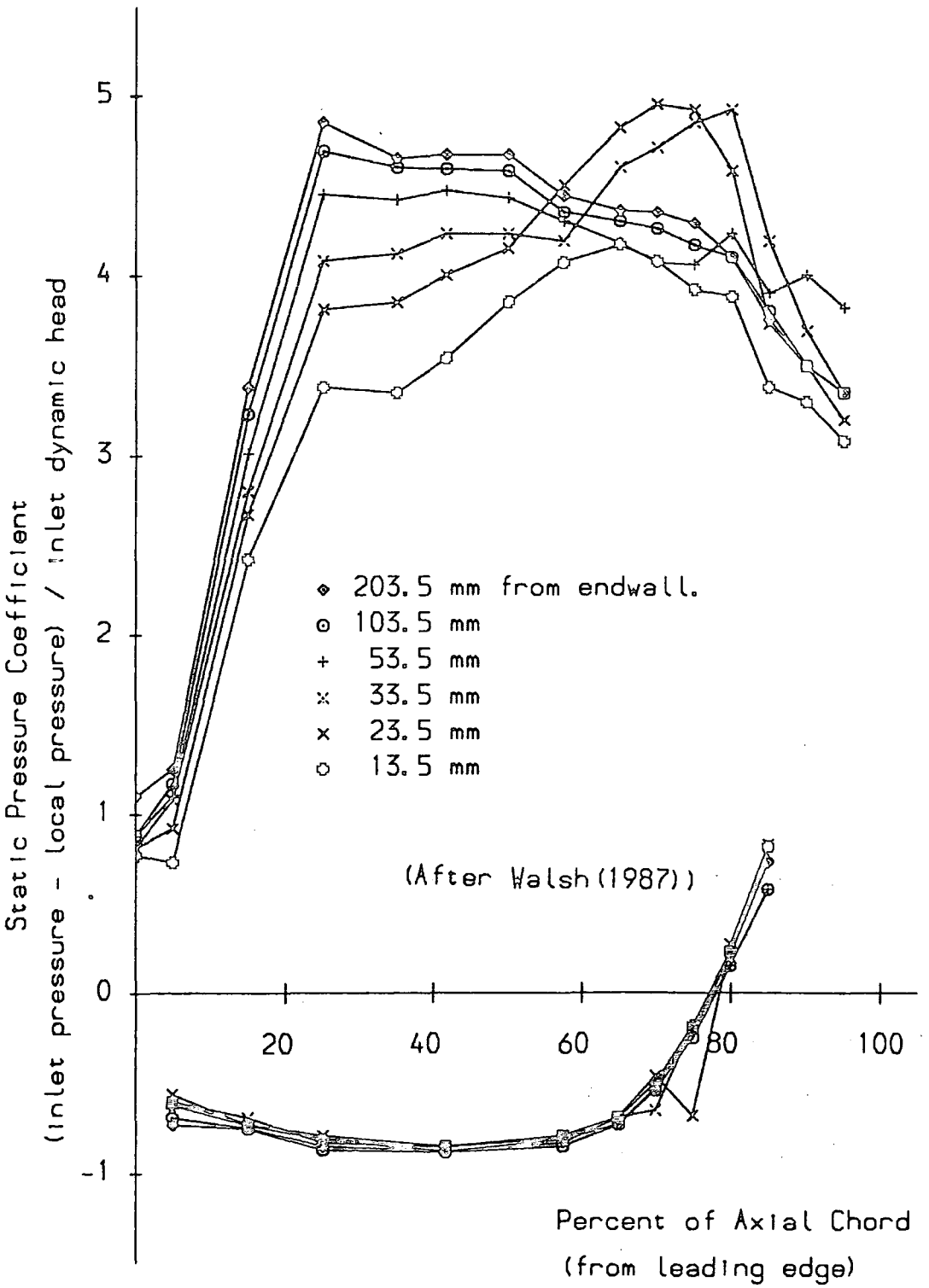


FIGURE 5.14 : Static Pressures (JAH Test Case)

# Chapter 6
# Modelling Results (JAW Test Case)

## 6.0 Introduction

This chapter describes results of modelling the JAW test case (experimental data described in Chapter 5). Three Navier-Stokes solvers are compared, and some comments are made about the various algorithms. The most accurate code for this case (the elliptic flow model of Moore and Moore (1985)) is then tested in more detail. The effects of the turbulence model, and benefits of improved versions of it are tested and discussed. Also results of calculations on two different meshes are compared, to determine the 'grid dependence' of the results.

## 6.1 Three Calculation Codes

The Navier-Stokes methods which are compared in this study are version 5 of the Moore Elliptic Flow Program (MEFP), and two time marching codes. The Moore's pressure correction algorithm has already been described in Chapter 3, but significant features of the implementation include second order accurate finite volume formulation, upwinded control volumes for reduced numerical mixing, and smoothing only applied when absolutely necessary. The grid system maps the blade onto a box and so some grid points appear inside the blades. Whilst this might seem wasteful, it makes the calculation of tip leakage flows particularly simple. The grid used in this study is shown in Figure 6.1(a), and consists of 47 x 25 x 17 points in the axial, tangential, and radial directions respectively. The two-dimensional mesh is simply stacked to form a three-dimensional mesh. A total of 19975 points is thus used to model half the cascade span. A smoothing program was used in an attempt to produce more orthogonal cells, and this causes the unusual kinks in the repeating boundary. This mesh will be referred to as the 'coarse mesh' in further work with the Moore code.

The first of the time marching codes is called ANSI, and is an explicit method which was developed at the Massachusets Institute of Technology. Significant features include finite difference formulation of first order accuracy, and fourth order smoothing. The grid system employed by the scheme is sophisticated, and incorporates 'O', 'C', and 'H' lines to give high definition of the blade boundary layers. This system is described by Norton *et al* (1984) in a paper concerning an implicit version of the code. The grid used in this study is shown in Figure 6.1(b) and consists of 56 x 28 x 18 points. A total of 28224 points was thus used to model half the cascade span.

The second time marching code which is tested is called VICTA, and at the time of testing was in an early stage of development at Rolls Royce. The program is a finite volume formulation of second order spatial accuracy, and employs second order smoothing to damp out oscillations. The grid system is a simple 'H' grid, and in this study 50 x 23 x 17 points were used to model half the cascade span. Thus a total of 19550 points were used, and the resulting two-dimensional mesh is shown in Figure 6.1(c). At the time the calculation was performed, no turbulence model had been coded into VICTA, so an inviscid run is described. For the other two codes, mixing length turbulence models were available. As Walsh (1987) reported a laminar boundary layer from the leading edge to 80% of an axial chord on the suction surface of the blade, both the MEFP and ANSI runs were set up to allow for this feature. Both codes were run turbulent, but with a laminar block specified as shown in Figure 6.2(a). This extends from inlet to 80% of axial chord in the axial direction, right across the blade pitch, and from 10% to 50% span in the radial direction (a midspan symmetry condition is used for the linear cascade). Values of turbulent viscosity are forced to be zero in this region, which is referred to as 'laminar block A' in this thesis.

## 6.2 Comparison of Results for the Three Codes

Plots of the results at slot 7 (87% Cax) are presented in Figure 6.3(a-l). The location of the calculation grid points show that as intended

the three codes have a similar density of points in the secondary flow region. Also, the grid spacings reduce as solid boundaries are approached, with ANSI giving the best resolution of the blade boundary layer region as expected. Results for flow quantities may be compared with the experimental results in Figure 5.5. All the calculations appear to under-predict the static pressures towards the pressure side of the passage, but most noticable is the oscillatory behaviour of the ANSI results in the boundary layer regions. The MEFP results seem reasonable, although the depression in static pressure caused by the vortical motion of the secondary flow is not captured. VICTA appears to have rather too much secondary flow with a large scale depression in the static pressure contours, which are generally too low. The secondary velocity vectors (Figure 6.3(g-i)) confirm these impressions, and show that MEFP has produced a vortex which is too weak, and which has not migrated towards the suction surface in the way that the real passage vortex is observed to do. The vortex produced by ANSI is the weakest of the three and again has not migrated towards the suction surface. VICTA predicts the strongest secondary flow, but the tangential positioning of the vortex is incorrect, remaining in mid-passage. Comparing the results of the loss predictions it is immediately clear that MEFP is the best 'conserver of total pressure'. The ANSI prediction is obviously erroneous, particularly in the blade boundary layer areas. Most of the passage is covered with loss, which increases towards the suction side. This large loss production on the suction side of the passage is also evident in the VICTA prediction. However VICTA is being run inviscid. Therefore any loss in excess of that present in the inlet boundary layer, must be attributed to numerical errors alone, rather than a combination of these, real effects, and errors in the turbulence model.

Similar comments may be made about the solutions at other locations. Figure 6.4 shows results at slot 10 (128% Cax), which may be compared with the experimental data in Figure 5.9 (from Walsh (1987)). The repeating boundary condition has been used to extend the modelling results to cover the same range as the experimental data. Clearly the best solution is produced by MEFP, although the vortex is not correctly placed, and the blade wakes

contain too much loss. The ANSI solution is dominated by loss which covers most of the flow area. The dashed contours indicate regions of total pressure gain, which are certainly produced by numerical errors. The VICTA solution has also produced a large amount of numerical loss, although quite a strong passage vortex is also predicted. However, the shape and location of this vortex are not representative of the experimental results.

Mass averaged quantities are presented in Figure 6.5. The best prediction of loss is given by MEFP, although it is itself producing at least 50% too much. VICTA produces a large steady increase in loss, which is purely numerical. ANSI is struggling with large losses produced early in the cascade and convected downstream. It also predicts far too little kinetic energy of the secondary flow. MEFP gives a more realistic prediction, but is only producing half of the observed value. VICTA however predicts far too much secondary kinetic energy. This might be expected if the inviscid run had contained little numerical error, but it is difficult to interpret this result when such large levels of numerical viscosity appear to be present.

Figure 6.6 shows results of performing a mass average of the losses, but first forcing all negative losses (energy gains) to be set to zero. Comparing with Figure 6.5 it is clear that ANSI has produced very large total pressure losses and gains in the leading edge region. The fact that the loss reduces downstream of the cascade suggests that significant total pressure gains are also being generated in this region. The mass flow plot also shows that ANSI is having difficulties in the leading edge region.

## 6.3 Interpretation of the Comparative Study

In order to attempt to understand the ANSI results some two-dimensional runs were undertaken. With the grid shown in Figure 6.1(b), large errors were again produced at the leading edge, giving an overall loss prediction eight times that measured experimentally. Also the blade surface pressure distribution was poorly predicted. Using a two-dimensional mesh with five times as many grid points as used previously, reduced the loss to 2.4

times the experimental loss, and gave a much improved pressure distribution. Also, running the code at an elevated Mach number such that the Mach number at exit was raised from 0.11 to 0.3 was found to improve convergence (this is because the code solves for density changes which are very small in a low speed flow). The strong influence of grid refinement upon the quality of the results, suggests that truncation errors are having significant effects. Where the grid spacing changes rapidly serious errors might be entering the first order discretisation. In the grid used for the three-dimensional run the grid spacing expanded by as much as fifty times when passing from the 'C' grid to the 'H' grid. It was therefore felt that ANSI should be modified to perform weighted averages so as to achieve second order spatial accuracy. Unfortunately such modifications to the software were beyond the scope of this project. However, Birch (1989a) has since shown that approaching the problem from a different direction, ANSI can give high quality results if the mesh is carefully constructed so as to avoid rapid changes in cell size.

The VICTA result cannot be explained in the same way as the ANSI case. Firstly the code is second order accurate, and so should not suffer so greatly from rapid changes in grid spacing, and in any case these were avoided when setting up the mesh. Secondly the loss growth curve is observed to rise steadily, even upstream of the cascade. It thus seems likely that VICTA is dominated by excessive smoothing, as apart from truncation errors this is the only other possible source of loss production in an inviscid solution. Reducing the smoothing by a factor of two was found to reduce the loss by almost as much. However the smoothing factors cannot be reduced much further as the solution then becomes unstable. A second problem was found with the method of calculating the time steps. VICTA contained five separate options for calculating time steps, and they were found to have a very significant effect upon the results of the calculation. Thus it seems that changing the time step changes the level of smoothing within the calculation. It was found that VICTA solves equations such as :-

$$\Delta\rho = \Delta t\,[-\,\nabla\,.\rho V] + Smoothing \tag{6.1}$$

Clearly the relative significance of the smoothing term will vary with the time step ($\Delta t$). This makes the use of locally varying time steps interfere with the uniformity of smoothing over the grid. The smoothing factors must then be raised to cope with the largest time steps leaving many cells with far greater smoothing than is necessary. As the smoothing in VICTA is of second order, the smoothing terms look like viscous terms in the equations and generate numerical losses. Thus it would be preferable to multiply the smoothing term by $\Delta t$ in equation (6.1), and then evaluate an optimum range of smoothing factors. With the implementation tested here, the optimum smoothing factors depend upon $\Delta t$, and are thus highly grid dependent. Also a fourth order smoothing option as used in ANSI, might be of benefit.

The MEFP result is obviously the most realistic of the three predictions. Comparison with some earlier results presented by Walsh (1987) on a mesh of only 8398 points, showed that the solution was not significantly grid dependent. Thus it seemed that the Moore's code was the most appropriate of the available models for further investigation.

## 6.4 Moore Code (Version 5) 'Laminar' Run

Although MEFP proved to give the best prediction of the flowfield for this case, some problems remained. The vortex was not found to move towards and up the suction surface as happens in the experiment. Also the losses were over-predicted, and the secondary kinetic energy was under-predicted. Since in a turbulent run it is not clear whether excess losses are a result of numerical error, or inaccurate turbulence modelling, it was decided to perform a laminar calculation of the flowfield. However, as the trailing edge flow is unsteady and turbulent, the calculation procedure would probably have difficulty in controlling it with only laminar viscosity. Thus the turbulence model was left on for a region containing the blade boundary layers downstream of 80% axial chord, and the blade wake as shown in Figure 6.2(b). However the secondary flow region was still essentially laminar, and so this will be referred to as a 'laminar' run. The results of such a calculation

should reveal whether the apparent damping of the secondary flow in the previous calculation, was a result of numerical viscosity, or an over-active turbulence model.

Figure 6.7(a-l) shows results of the two Moore code calculations and corresponding experimental data (from Walsh (1987)) at slot 8 (97% Cax). The yaw angle contours show that the 'laminar' run captures more of the under-turning at $70mm$ from the endwall than the turbulent run with laminar block A. Similarly the static pressure contours show that the depression in static pressure resulting from the presence of the passage vortex, is much better modelled with the laminar flowfield. The most striking change is apparent in the secondary velocity vectors (Figure 6.7(g-i)). With the secondary flow region modelled as turbulent, the vortex remains close to the endwall and centred at mid-passage. However, with a laminar secondary flow region the vortex is convected in a most convincing manner towards and up the suction surface. The loss contours show that the laminar run has more areas of total pressure generation than the turbulent run with laminar block A. However two distinct loss cores are emerging, and as described in Chapter 2, this is a characteristic feature of turbine secondary flows. Pitch averaged results at slot 8 for the two MEFP solutions and experiment, are shown in Figure 6.8. The turbulent run with laminar block A fails to capture the under-turning of the flow at $60mm$ from the endwall, but predicts the over-turning nearer to the wall quite well. It also fails to predict the secondary kinetic energy peak at $60mm$ from the endwall, and this results in less radial convection of the loss core than is experimentally observed. In contrast, the 'laminar' run produces too much secondary kinetic energy and thus exhibits a strong under-turning peak at $70mm$ from the endwall. The loss core is also convected radially from the endwall. The low loss at $30mm$ from the endwall results from the negative loss present in the contour plot (Figure 6.7(l)) and is thus a product of numerical error. However, one might expect a laminar run generally to under-predict loss.

The 'laminar' run results at slot 10 (128% Cax) are presented in Figure 6.9(a-f). These may be compared with the 'turbulent run with

laminar block A' results in Figure 6.4, and the experimental results of Walsh (1987) reproduced in Figure 5.9. The calculation grid locations show that the blade wakes are fairly well covered. The wakes are similar to those in the turbulent run with laminar block A, as both calculations used the turbulence model in this region. However the loss core is better defined and contains the two peaks that are characteristic of turbine cascades. The passage vortex is also better positioned in the 'laminar' run. Comparing the results of the 'laminar' run with experiment, it can be seen that the static pressure contours are no longer in such good agreement as they were at slot 8 (Figure 6.7). The depression in static pressure resulting from the rotation of the passage vortex is not captured. Also there is a difference between the predicted and measured midspan static pressure coefficient. This is a common feature in all the Moore code runs, and is thought to result from a difference in incidence between experiment and modelling. The models were all run at the design incidence of 42.75°, whereas the pitch averaged flow angle at slot 1 presented by Walsh (1987) was approximately 46°. Hence the experiment operates at a slightly lower mass flow rate than intended, but with the design inlet dynamic head. This tends to result in the modelling predicting a higher velocity, and lower static pressure downstream of the cascade. Also the modelling slightly over-predicts the exit angle, which produces similar effects. The pitch and yaw angles are more realistically modelled, however.

Mass averaged loss and secondary kinetic energy for the two runs are compared with experiment in Figure 6.10. The 'laminar' run reduces the loss, although it is still greater than that measured experimentally. Both runs produce too large a jump in loss across the trailing edge of the blade, possibly indicating numerical error or an over-active turbulence model in the trailing edge region. The most striking change is in the secondary kinetic energy. The laminar flowfield produces too much secondary kinetic energy within the blade passage. This is encouraging since the true secondary flow is probably turbulent (e.g. Gregory-Smith *et al* (1988), Zunino *et al* (1987), Moore *et al* (1986)). If the laminar calculation had failed to over-predict the secondary kinetic energy, it would indicate that numerical errors were

hindering the calculation. This does not appear to be the case within the blade passage. However the large drop in secondary kinetic energy across the trailing edge might be associated with numerical and/or turbulence modelling problems in this region.

The blade static pressures are presented in Figure 6.11 for the turbulent run with laminar block A, and Figure 6.12 for the 'laminar' run. These may be compared with the experimental pressures shown in Figure 5.14 (from Walsh (1987)). The turbulent run with laminar block A, models the unloading of the first half of the blade as the endwall is approached, but fails to capture the low pressure suction peaks in the second half of the blade passage. These result from the proximity of the passage vortex, and thus the turbulent flowfield with its weak vortex positioned at mid-passage, fails to predict this feature. The 'laminar' run produces an over energetic vortex, and thus over-predicts the suction surface peaks. In both results large spikes can be seen in the trailing edge region. These are associated with modelling problems in this area, with flow remaining attached for too long, and thus experiencing severe acceleration around the trailing edge.

**Table 6.1 : MEFP (Version 5) Losses at Slot 10**

| JAW TEST CASE | Experiment | MEFP Turbulent + Lam Block A | MEFP 'Laminar' Run |
|---|---|---|---|
| Mixed Out Loss Coefficient | 0.239 | 0.344 | 0.328 |
| - Midspan Mixed Out Loss Coefficient | 0.095 | 0.175 | 0.167 |
| = Gross Mixed Out Secondary Loss | 0.144 | 0.169 | 0.161 |
| - Inlet Loss | 0.040 | 0.037 | 0.036 |
| = Net Mixed Out Secondary Loss | 0.102 | 0.132 | 0.125 |
| Secondary KE Coefficient | 0.043 | 0.018 | 0.042 |
| Net Secondary Loss (= Loss - Midspan Loss - Inlet Loss) | 0.064 | 0.109 | 0.074 |

Table 6.1 presents an analysis of the losses at slot 10 from the two MEFP calculations and experiment. It is clear that most of the error in

predicting overall loss is due to a poor prediction of profile loss. The values for net mixed out secondary loss are too large, but not excessively so. It is also interesting that the values of net mixed out secondary loss from the two MEFP calculations are similar. This suggests that making the flowfield laminar, reduces the net secondary loss, but results in an almost equal rise in secondary kinetic energy, and this can be seen to be approximately the case in Table 6.1. The fact that the 'laminar' run produces 68% of the net secondary loss that the turbulent run produced, suggests that its turbulent blade boundary layer from 80% of axial chord onwards, is an important region for the production of secondary losses, as laminar losses are likely to be much smaller than turbulent losses (Moore *et al* (1986) have shown this to be true downstream of a turbine cascade).

## 6.5 Conclusions of Work with Version 5 of the Moore Code

The comparison between the results of the turbulent run with laminar block A, and a similar run by Walsh (1987) on a much coarser grid of 8398 points (c.f. 19975 points used here), shows that the results from the Moore code are not very grid dependent. This suggests that the second order accuracy of the scheme is generally controlling truncation errors well. In some areas there may be localised problems however. The breakdown of losses in Table 6.1 shows that most of the excess loss is produced in the calculation of profile loss, and Figure 6.10 indicates that much of this over-prediction occurs in the trailing edge region. Thus a calculation on a finer mesh would be a useful test of the grid dependence of the results around the trailing edge.

The magnitude of the change in secondary kinetic energy, and positioning of the vortex when the secondary flow region is specified as laminar is surprising. It is not clear whether the changes result from the whole passage vortex being laminar, or if it is just the laminar modelling of the new endwall boundary layer that has most effect. It is possible that the new endwall boundary layer which forms after the inlet boundary layer has been

removed from the endwall, is in a laminar state within the blade passage (e.g. Harrison (1989)). Hence a turbulent run was proposed, with laminar block A, and a new laminar block running from 25% to 100% axial chord in the axial direction, right across the pitch in the tangential direction, and from 0 to 1% span in the radial direction. This new laminar block will be referred to as 'laminar block B' in this thesis, and is shown in Figure 6.2(c).

## 6.6 Version 7 of the Moore Code

As the software used in this work is in a continual state of development, new versions became available during the period in which the modelling was undertaken. Cleak *et al* (1989) have described results obtained with an intermediate version (version 6) of the Moore code. However, to avoid confusion, all new results described hereafter will be assumed to have been obtained using version 7 of the code (i.e. the MEFP algorithm as implemented within version 1 of the Rolls Royce Computational Fluid Dynamics System).

The only changes between version 5, and version 7 of the Moore code which are of significance in this work are the changes made to the turbulence model, and to the subroutine which adds in the pressure corrections to the pressure field. Some problems had been encountered in previous work with oscillations developing in the pressure field across the trailing edge plane. In Figure 6.7(d,f) it is possible to see some oscillatory behaviour in the static pressures towards the pressure side of the passage. The only fix available previously was to smooth the pressure field (this was not used with the version 5 results presented here, but was used by Cleak *et al* (1989) when working with version 6 of the program). Whilst this technique removes pressure oscillations, it also compromises the quality of total pressure conservation. Since the initial guess of the flowfield does not contain pressure oscillations, these must be introduced by the pressure corrections. Thus a better fix would be to smooth the pressure corrections, which should become small at convergence. However the upwinded control volume technique (described by J.G. Moore (1985b)) which helps to reduce numerical mixing within the Moore

code, makes this difficult since the points at which the pressure corrections are stored can move around during the calculation. Thus a simpler fix was provided by J.G. Moore as a new option when calling the subroutine. Any significant oscillations in the pressure field are simply clipped to prevent them from growing large. This has been found to be quite an effective method of stabilising the calculations for the Durham test case.

The basic mixing length turbulence model has been described in Chapter 3, and the mixing length is specified by equation (3.16). The mixing length model was really developed with a view to two-dimensional, attached boundary layers, and its implementation in a three-dimensional separated shear flow is difficult. Within such flows, the mixing length is proportional to the shear layer thickness, $\delta$. Specification of this shear layer thickness is rather arbitrary, and is achieved by looking at gradients of a shear layer parameter $S$, where for incompressible flow $S$ takes the form of a non-dimensional loss of total pressure. This is defined such that $S$ has a value of one on walls, and zero in the freestream.

In version 5 of the Moore code, a search was made along each of the grid directions (forwards and backwards), looking at gradients of the shear layer parameter until some arbitrary cutoff value signified the edge of the shear layer. The shear layer thickness was thus obtained by summing distances during the search. The values obtained from the searches in three directions were then averaged. However the authors noticed that with the model set up in this way, blade wakes appeared to mix out more rapidly than occurred in experiment. Thus the model was modified to only search along the direction with the biggest gradient of the shear layer parameter. The value so obtained was then taken to be the shear layer thickness at that point. This tends to reduce the shear layer thickness, $\delta$, and thus also the mixing length which is proportional to it. Thus the turbulent stresses are then generally smaller, and so wakes are found to mix out more slowly, achieving better agreement with experimental measurements.

## 6.7 Coarse Grid Results (MEFP Version 7)

Initial work with version 7 of the Moore code used the same 'coarse' calculation mesh as used previously and shown in Figure 6.1(a). One of the results of the work with version 5 of the code was the decision to perform a run with an extra laminar block. This is called laminar block B, and is shown in Figure 6.2(c). It is intended to simulate crudely the effects of a possible laminar endwall boundary layer downstream of the separation of the inlet boundary layer. However, as the turbulence model has been changed, it is also necessary to repeat a run for comparison with version 5. Thus a run with laminar block A was also undertaken as well as the run with laminar blocks A and B. A final run was made with the flowfield specified as completely turbulent in order to determine the capabilities of the program as a purely predictive tool (i.e. if no previous knowledge of transition locations is assumed). Firstly however, the comparison is made between results obtained with versions 5 and 7 using laminar block A.

Figure 6.13 shows results for the three version 7 runs at slot 8 (97% Cax). Results for the turbulent run with laminar block A may be compared with the equivalent run using version 5 of the program shown in Figure 6.7. Looking at the yaw angle contours it is clear that the revised turbulence model is allowing more secondary flow to develop, and the results from version 7 compare better with the experimental results which are also shown in Figure 6.7. Comparing static pressure contours (Figures 6.7(d,e) and 6.13(e)) it can be seen that the depression in static pressure caused by the vortical motion is better modelled in version 7 with the revised turbulence model. The secondary velocity vectors (Figures 6.7(g,h) and 6.13(h)) show the passage vortex to be more energetic in version 7, and to have moved slightly further away from the endwall and towards the suction surface. This movement is not as great as that observed experimentally, but is more realistic than the version 5 result, where the passage vortex remained centred at mid-passage and too close to the endwall. The loss contours from version 7 also indicate improvements, and do not include the negative losses which can be seen

at the edge of the suction surface boundary layer in the version 5 result. Flow quantities at slot 10 (28% Cax downstream) for the version 7, version 5, and experimental results, are presented in Figures (6.15(b,e), 6.4(a,d) and 5.9(e,d) respectively. It can be seen that the version 7 result produces a more energetic and better positioned passage vortex, which results in improved loss core definition. Looking at the secondary kinetic energy development in Figure 6.17, it is clear that the version 7 result with the revised turbulence model, allows the secondary kinetic energy to develop to a much more realistic level than occurred previously with version 5. Also the loss can be seen to grow more in the latter half of the cascade in the version 7 result, rather than the steady growth which was evident in version 5. The jump in loss across the trailing edge has also reduced slightly, although it is still too large. However, downstream of the cascade the loss appears to develop more realistically in version 7, and indeed it was this objective which motivated the changes to the turbulence model.

The above discussion of the comparison of versions 5 and 7 of the Moore code, shows that reducing the turbulent stresses by modifying the definition of the shear layer thickness, has produced improved secondary flow predictions. This is consistent with the results of the version 5 'laminar' run discussed previously. The extent of the sensitivity of the secondary flow prediction to the turbulence model is perhaps surprising, and suggests that great care should be taken when attempting to model such complex flows with simple turbulence models.

Comparison of the three version 7 runs is made at slot 8 in Figure 6.13. The yaw angle contours indicate that the secondary flow becomes more powerful as the flowfield is made to contain progressively more laminar regions. However, the inclusion of laminar block A does not cause large changes to the turbulent solution, as the flow is still turbulent from the endwall to $40mm$ radially in this case. In contrast, the addition of laminar block B results in surprisingly large changes, and appears to over-predict the secondary flow when compared with the experimental results in Figure 6.7. The static pressure contours also indicate a stronger passage vortex.

Comparing secondary velocity vectors for the three runs (Figure 6.13(g-i)) it is clear that laminar block A makes little difference to the secondary flow development as intended (it was included to aid the prediction of profile loss). However laminar block B (the laminar endwall from 0 to $4mm$ radially) results in greater migration of the passage vortex, leaving it realistically located, although the magnitude of the secondary velocities appears to be a little too large. The loss contours reveal the benefit of laminar block A; as compared with the turbulent run it produces a thinner suction surface boundary layer. The three runs produce similar loss cores on the suction surface at approximately $70mm$ from the endwall. Addition of laminar block B increases the size of this loss core slightly, as fluid from the suction surface boundary layer within $70mm$ from the endwall is convected into it more rapidly by the passage vortex.

Pitch averaged results at slot 8 are presented in Figure 6.14. There appears to be a constant error in yaw angle of approximately 2°, which might be associated with numerical problems in the trailing edge region. The run with laminar block B produces a slightly larger under-turning peak than the other two runs, which produce very similar yaw angles. The addition of laminar block B also convects loss radially in a more realistic manner. At midspan the turbulent run produces twice as much loss as the other two runs which each include laminar block A. The secondary kinetic energy peak at $60mm$ from the endwall is over-predicted by the run with laminar block B, but in general the shape of the curve is better modelled by it.

Results downstream of the cascade at slot 10 are presented in Figure 6.15. These may be compared with the experimental results in Figure 5.9. The run with laminar block B produces slightly improved positioning of the passage vortex. The loss contours show that the addition of laminar block A has reduced the loss in the blade wakes, but it is still too great. The most interesting change is that the addition of laminar block B has resulted in a more clearly defined loss core at coordinate (-250,70). This is probably composed mainly of inlet boundary layer loss, and compares quite well with experiment.

Pitch averaged results at slot 10 are presented in Figure 6.16. Again there appears to be a constant error in yaw angle of approximately 2°. The run with laminar block B produces too much over-turning at approximately $50mm$ from the endwall. However its representation of the loss distribution is quite good, if the error in midspan prediction is subtracted from all the radial points. The turbulent run produces approximately 50% more profile loss than the other two, but they still produce twice as much as measured experimentally. All three runs appear to have a peak in secondary kinetic energy at $70mm$ from the endwall, but the calculation grid is too coarse to locate it more accurately than this. The run with laminar block A, and the turbulent run, produce approximately the correct magnitude of this peak, but also predict a second peak at $15mm$ from the endwall. This unrealistic feature is not produced by the run with laminar block B, but the peak at $70mm$ from the endwall is over-predicted by it.

The development of mass averaged loss and secondary kinetic energy for the three version 7 runs and experiment, is shown in Figure 6.18. As laminar blocks are added to the flowfield the loss is steadily reduced, although all the runs predict too much loss. The turbulent run, and the run with laminar block A, predict similar levels of secondary kinetic energy which are quite realistic. This similarity is expected since the secondary flow region was mainly turbulent in both cases. However the secondary kinetic energy is not seen to decay downstream of the cascade in a realistic manner. The laminar block B, produces a significant increase in secondary kinetic energy and thus predicts too much, although the rate of its decay downstream appears to be more realistic. Table 6.2 presents a breakdown of losses at slot 10 for the three version 7 runs and experiment. As mentioned in previous analyses of losses, the net mixed out secondary loss is quite well represented by the sum of net secondary loss and secondary kinetic energy at a particular downstream distance. The net mixed out secondary loss is similar for the two runs which included laminar block A. This appears to indicate that the addition of laminar block B reduces the loss (presumably due to less endwall loss growth) but produces an almost equal rise in secondary kinetic energy.



All three runs predict too much profile loss. Apparently the turbulent run predicts less mixed out secondary loss than the other two. This is a little surprising as the addition of laminar block A was intended to only effect the profile loss. Thus a similar prediction of secondary loss was expected from the turbulent run and the run with laminar block A only. Perhaps the breakdown of losses is becoming slightly inaccurate with such large profile losses present in the solution. In general however, all three runs appear to give reasonable estimates for the mixed out secondary loss.

Table 6.2 : MEFP (Version 7) Flow at Slot 10

| JAW TEST CASE | Experiment | MEFP Turbulent | MEFP Turb + Lam Block A | MEFP Turb + Lam Blocks A+B |
|---|---|---|---|---|
| Mixed Out Loss | 0.239 | 0.397 | 0.342 | 0.321 |
| - Midspan Mixed Out Loss | 0.095 | 0.269 | 0.183 | 0.168 |
| = Gross Mixed Out Sec. Loss | 0.144 | 0.128 | 0.159 | 0.153 |
| - Inlet Loss | 0.040 | 0.040 | 0.038 | 0.037 |
| = Net Mixed Out Sec. Loss | 0.102 | 0.088 | 0.121 | 0.116 |
| Secondary KE | 0.043 | 0.045 | 0.050 | 0.064 |
| Net Secondary Loss (=Loss - Midspan Loss - Inlet Loss) | 0.064 | 0.045 | 0.070 | 0.047 |
| Midspan Mixed Out Angle | −67.5° | −69.1° | −69.3° | −69.2° |

The mixed out flow angle is less accurate in all three runs than might have been expected, and this could be associated with numerical problems in the trailing edge region. However, as discussed in Chapter 5, the raw pressure probe data of Walsh (1987) has been re-analysed in order to resolve some problems with the measurement of losses. When analysing data, it is often necessary to add a constant to the yaw angles in order to account for small misalignments of the fine cranked end of the probe. These are determined before and after the traverse by checking the probe's response in a known flow. This does not effect the quality of pressure or velocity magnitude measurements, as it is purely concerned with relating the angle

of the probe to the cascade axis system, after the calibration maps have determined the angle, velocity, and pressure of the flow onto the probe head. When re-analysing the data, the value of this correction was not incorporated, and so the value of mixed out flow angle presented at slot 10 by Walsh was $-68.2°$ which is different to the value of $-67.5°$ presented in Table 6.2. However, a difference of $1°$ in yaw angle is still apparent between experiment and the MEFP predictions.

## 6.8 Conclusions of Coarse Grid Runs of MEFP (Version 7)

The above discussion of results of modelling the endwall flow as laminar within 1% span, and downstream of the inlet boundary layer separation line (laminar block B), showed that this produces large changes to the flowfield. In particular too much secondary kinetic energy was produced, whereas the run with only laminar block A predicted approximately the correct amount. This contrasts with the results of the run with laminar block A on version 5 of the program where only half of the observed secondary kinetic energy was generated. The reason for the change in results between versions 5 and 7 was the changes made to the turbulence model discussed in section 6.6. Thus if a run could be performed on version 5 of MEFP (the source code is no longer available), with laminar blocks A and B, it is possible that approximately the correct level of secondary kinetic energy would be produced. The revised turbulence model for separated shear flows in version 7 does produce a more realistic growth of loss downstream of the cascade. However this alone might not be considered to be sufficient justification for the rather arbitrary changes to the turbulence model. Thus some questions arose which directed further experimental work. Firstly it would be desirable to know what the state of the new endwall boundary layer really is (i.e. laminar or turbulent). Secondly a comparison between experimental measurements of the Reynolds stresses within the flow, with those predicted by the turbulence model, would clearly indicate the accuracy of the model within the separated three-dimensional shear flows.

The run with a fully turbulent flowfield predicts too much profile loss. Thus there is clearly a need to develop models of transition, if the Navier-Stokes solvers are not to be tied to transition correlations as are currently used in many of the boundary layer calculations which are coupled to two-dimensional inviscid solvers. The use of such correlations would limit the application of the codes to design incidence, and is thus undesirable.

All the runs undertaken so far have produced too much loss in the trailing edge region. This is a difficult area of the flowfield to model, but a run on a finer mesh would help to indicate if numerical problems in this region could be reduced with the use of more grid points.

## 6.9 Fine Grid Results (MEFP Version 7)

A second calculation mesh was produced for use with the Moore code, and is shown in Figure 6.19. This has 60 x 36 x 30 points in the axial, tangential and radial directions respectively. A total of 64800 points is thus used to model half the cascade span. This mesh will be referred to as the 'fine' mesh in this thesis, and contains 3.2 times as many points as does the 'coarse' mesh used previously.

Two fine grid runs were undertaken, one with a fully turbulent flowfield, and another incorporating laminar block A, as shown in Figure 2.2(a). A comparison between the two fine mesh results at slot 8 (97% Cax) is made in Figure 6.20. These results may be compared with the equivalent coarse mesh runs, shown in Figure 6.13. In general the effect of grid refinement is quite small. The pressure surface boundary layer is thinner when more points are placed in it, but the level of grid refinement is not sufficient to change greatly the suction surface boundary layer thickness. The loss core is perhaps slightly better defined by the fine mesh, and the static pressure contours are more tightly closed around the passage vortex. Surprisingly, the oscillatory behaviour in the static pressure field on the pressure side of the passage, is slightly worse in the fine grid calculations.

Results of calculations on the fine mesh at slot 10 (128% Cax) are

presented in Figure 6.21. The static pressure contours may be compared with the experimental results in Figure 5.9. The fine mesh helps to capture the static pressure depression in the centre of the passage vortex. Although equivalent coarse mesh results are not presented, this feature was not modelled so well by them. The midspan pressures are different from those measured experimentally, probably due to the experiment running at a slightly different incidence, as mentioned previously. The secondary velocity vectors are very similar in comparable results with coarse or fine grids. The fine grid slightly reduces the loss within the blade wakes but also makes them significantly thinner. However there is still too much profile loss. Mass averaged loss and secondary kinetic energy for the two fine grid runs are presented in Figure 6.22. This may be compared with Figure 6.18 which shows the results obtained with the coarse calculation mesh. Clearly the main effect of grid refinement is to reduce the jump in loss produced across the trailing edge of the cascade to quite a realistic level. The prediction of secondary kinetic energy is very little changed however.

**Table 6.3 : MEFP (Version 7) Fine Mesh Flow at Slot 10**

| JAW TEST CASE | Experiment | MEFP Turbulent | MEFP Turb + Lam Block A |
|---|---|---|---|
| Mixed Out Loss Coefficient | 0.239 | 0.337 | 0.290 |
| - Midspan Mixed Out Loss Coefficient | 0.095 | 0.192 | 0.138 |
| = Gross Mixed Out Secondary Loss | 0.144 | 0.145 | 0.152 |
| - Inlet Loss | 0.040 | 0.038 | 0.036 |
| = Net Mixed Out Secondary Loss | 0.102 | 0.107 | 0.116 |
| Secondary KE Coefficient | 0.043 | 0.050 | 0.049 |
| Net Secondary Loss (= Loss - Midspan Loss - Inlet Loss) | 0.064 | 0.057 | 0.065 |
| Midspan Mixed Out Flow Angle | −67.5° | −68.7° | −68.9° |

Table 6.3 presents a breakdown of losses at slot 10 for the two fine mesh runs. This can be compared with Table 6.2 for the equivalent coarse

mesh results. The biggest change is clearly in the prediction of profile loss which is much improved with the fine calculation mesh. The predictions of net secondary loss and secondary kinetic energy are also quite good. The fine grid has also reduced the exit flow angle slightly, so that comparison with Walsh's experimental value of $-68.2°$ shows less discrepancy.

Following Hah (1987), Figure 6.23 presents graphs of mixed out loss versus the inverse of the number of grid points used in the calculation mesh. Hah tested four separate grids with his pressure correction code, and found a linear relationship for this type of plot. Here, a linear relationship is assumed with no justification other than Hah's result. However the resulting graphs are interesting. The plot for the 'vorticity ML' results concerns results discussed in the next section, and so should be ignored here. Looking at the graph for a fully turbulent flowfield in Figure 6.23, it appears that the mixed out loss which would be obtained with an infinitely fine mesh is approximately 0.31. This is greater than the experimental value due to errors in turbulence modelling, most obviously by assuming completely turbulent blade boundary layers. The graph for a turbulent flowfield with laminar block A, is significantly lower than that obtained with a fully turbulent flowfield, and suggests that an infinitely fine mesh would yield a mixed out loss of 0.27 when using this flow regime. It is clear that the graphs for the turbulent run, and the turbulent run with laminar block A, are almost parallel. This suggests that refining the grid makes very little difference to the loss calculated within the blade boundary layers between zero and 80% axial chord.

In general, the results of modelling with the fine calculation mesh show that localised improvements may be made to the flow in the trailing edge region by using more grid points, but otherwise the solutions are remarkably grid independent. This is a result of the use of second order spatial accuracy, and is a very attractive feature in a calculation scheme.

## 6.10 Vorticity Function Search for Shear Layer Thickness

A new option for determining the shear layer thickness to be used in separated regions has recently been provided by J.G. Moore. This uses a different definition for the shear layer parameter, $S$, which is based on vorticity rather than total pressure loss. The motivation behind the introduction of this option, was that the shear layer parameter as defined previously, could sometimes lead to the detection of shear layers where none existed. This occurred if a spurious value of pressure existed within the flowfield. Thus it is hoped that the new vorticity based search for shear layer thickness will be less prone to error, and yield more smoothly varying values for the mixing length.

Two runs have been performed using this new search procedure for shear layer thickness. These are turbulent runs with laminar block A (Figure 6.2(a)) on both the coarse and fine calculation meshes. The use of the new turbulence modelling option is indicated by the inclusion of 'vorticity ML' in the headings of diagrams, to remind the reader of the vorticity based determination of the mixing length. Figure 6.24 presents results at slot 8 (97% Cax) for the new turbulence model with laminar block A on coarse and fine grids. These may be compared with Walsh's experimental results which are reproduced in Figure 6.7. The static pressure contours show that the depression at the centre of the vortex is better modelled with the fine grid. This also helps to draw the contour lines for a value of 3.5 closer together at midspan, achieving better agreement with experiment. Comparing with equivalent fine mesh results using the standard mixing length model and laminar block A in Figure 6.20, shows that the new turbulence model results in improved static pressure definition. The secondary velocity vectors indicate good agreement between the coarse and fine mesh solutions, and are quite a good representation of Walsh's experimental results (Figure 6.7). The loss contours show that the fine grid produces a slightly better representation of the suction surface boundary layer and is generating a secondary loss core which exhibits many of the experimental characteristics. Pitch averaged

results at slot 8 are presented in Figure 6.25. Again there is a small error in midspan angle as discussed previously. However the general representation of the secondary flow effects is very good. Both coarse and fine grids produce broadly similar results except that perhaps surprisingly, the coarse grid predicts generally less loss than the fine grid at this position. The secondary kinetic energy has not migrated radially as far as the experimental results indicate, and there is a corresponding lack of radial convection of loss.

Results of the coarse and fine grid runs at slot 10 are shown in Figure 6.26(a-l). Experimental results from Walsh (1987) are also plotted in Figure 6.26 for clarity. The yaw angle contours show that the fine grid slightly improves the coarse grid results, and is in good agreement with the experimental results. The fine grid also produces a better representation of the static pressures than the coarse grid, and is also superior to the standard mixing length model fine grid results in Figure 6.21. The secondary velocity vectors indicate broad similarities between the fine and coarse grid solutions, and are quite a good model of the experimental results. However the main benefits of the new turbulence model are evident in the loss contours. The coarse grid produces results of similar quality to those produced by the standard mixing length model on the fine grid (Figure 6.21). The fine grid 'vorticity ML' results are remarkable. The blade wakes are approximately the correct width, although they still contain too much loss. However, the loss core definition is excellent and compares very well with experiment.

Pitch averaged results at slot 10 are presented in Figure 6.27. Again there is a small constant error in yaw angle, but the general distribution is very good. The loss core is also well defined by both runs, and the fine grid run now produces less loss at midspan than the coarse grid run. The secondary kinetic energy distribution is quite well modelled, although both runs appear to be producing too much. Mass averaged results are presented in Figure 6.28. Both runs indicate a decrease in loss between slots 2 and 3 due to generation of total pressure gains by numerical error. However, in general both runs produce a better prediction of loss than previously obtained. The coarse grid produces a total loss which is comparable to that produced by the

fine grid previously (Figure 6.22). The fine grid with vorticity based mixing length apparently predicts the correct loss. However, both runs over-predict secondary kinetic energy.

Table 6.4 presents a breakdown of losses at slot 10 for the two vorticity based mixing length runs and experiment. This may be compared with results of the fine mesh run with laminar block A and the standard turbulence model, shown in Table 6.3. The coarse grid with the vorticity based mixing length model produces the same overall loss as the fine grid with the standard turbulence model. The fine grid run with the vorticity based turbulence model produces a much improved prediction of profile loss and also models the secondary loss quite well. The exit angle of $-68.8°$ is only $0.6°$ different from Walsh's experimental value of $-68.2°$, and overall the predictions seem to be remarkably good.

**Table 6.4 : MEFP (Version 7 Vorticity ML) Results at Slot 10**

| JAW TEST CASE | Experiment | Coarse Mesh Lam Block A | Fine Mesh Lam Block A |
|---|---|---|---|
| Mixed Out Loss Coefficient | 0.239 | 0.291 | 0.256 |
| - Midspan Mixed Out Loss Coefficient | 0.095 | 0.136 | 0.110 |
| = Gross Mixed Out Secondary Loss | 0.144 | 0.155 | 0.146 |
| - Inlet Loss | 0.040 | 0.038 | 0.037 |
| = Net Mixed Out Secondary Loss | 0.102 | 0.117 | 0.109 |
| Secondary KE Coefficient | 0.043 | 0.053 | 0.053 |
| Net Secondary Loss (= Loss - Midspan Loss - Inlet Loss) | 0.064 | 0.062 | 0.055 |
| Midspan Mixed Out Flow Angle | $-67.5°$ | $-69.1°$ | $-68.8°$ |

Returning to Figure 6.23, the benefits of the new turbulence model become clear. It appears that with an infinitely fine mesh, the correct loss would be predicted. However, this only indicates that the average level of Reynolds stress modelling over the whole flow area is correct, and does not prove it to be correctly distributed.

The blade static pressure distributions for the fine mesh run are presented in Figure 6.29. This can be compared with the experimental results in Figure 5.14 (from Walsh (1987)) and the two version 5 MEFP results in Figures 6.11 and 6.12. All the MEFP results indicate higher static pressure on the suction surface for the first 50% of axial chord, than was measured experimentally. The reason for this is not clear, but could possibly be associated with the experiment running at a higher incidence ($\alpha_1 = 46°$) than the calculations ($\alpha_1 = 42.75°$). In general, the new turbulence model run on the fine grid with laminar block A, produces quite a realistic prediction of the variation in loading caused by the passage vortex. In particular, it is much better than the coarse grid with laminar block A result from version 5 using the standard mixing length model, which did not detect these peaks in the suction surface pressure coefficient. The pressures in Figure 6.29 are also more realistic than those predicted by the laminar run on version 5, which over-predicted the suction surface peaks.

## 6.11 Conclusions

The results presented in this chapter have shown that it is possible to obtain very good three-dimensional flow predictions with a 'state of the art' Navier-Stokes solver. Of the three codes tested here, the pressure correction method of Moore and Moore (1985) proved to be the most accurate for this case. However, the author would not wish to imply that pressure correction methods are in general superior to time marching techniques. Kirtley *et al* (1986) have tested a pressure correction technique and a time marching technique on the same case, and found no clear advantage of one over the other. The pressure correction technique used here was more suited to the low speed flow than the time marching techniques which were tested, but its main advantages were in its numerical discretisation. The use of second order spatial accuracy greatly reduces the grid dependence of the scheme. Some localised problems have been found in the trailing edge region, but otherwise the secondary flow appears to be quite well represented with

relatively few grid points. Figure 6.30 shows a plot of the trailing edge region of the coarse and fine meshes which were tested, and corresponding midspan velocity vectors for the two runs with laminar block A. The flow with the fine grid is very smooth with only a small recirculation area behind the trailing edge. The coarse mesh does not have so many control volumes in this region, and so is unable to contain the trailing edge effects to such a small region. The grid is basically too coarse to cover adaquately the rapidly varying flow. Hence more numerical errors are produced which are convected downstream. Another feature of the Moore code which helps to produce good flow predictions, is the upwinded control volume technique described by J.G. Moore (1985b). This helps to avoid numerical viscosity in the formulation, which is an essential feature of a program which is intended to predict aerodynamic loss.

Some problems have been observed with the prediction of static pressures, and it was suggested that these might be associated with the modelling and experiment operating at slightly different inlet angles. To test this, a final calculation was performed on the fine mesh, using the vorticity based search for shear layer thickness, and incorporating laminar block A as shown in Figure 6.2(a). This run was set up to the measured inlet angle, and thus the flow entered the calculation region at 45.9°. The general flow prediction was found to be very similar to that produced by the same run with the design inlet angle of 42.75°. Figure 6.31 presents results of these two runs at slot 10. The vortex predictions and loss distribution look very similar in the two runs, but there is a clear difference in static pressure over the axial plane. Comparing with Walsh's experimental results, which are reproduced in Figure 5.9, it can be seen that the static pressure is now in better agreement with the experiment, although the magnitude of variation within the wake and vortex are not captured.

Pitch averaged results at slot 10 for the two runs and experiment, are presented in Figure 6.32. The results are very similar, except that the correct inlet angle appears to produce slightly more radial convection, achieving better agreement with experiment particularly for the secondary kinetic energy. Mass

averaged results are presented in Figure 6.33, and show that the two runs produce broadly similar results. An increase in inlet angle might be expected to result in slightly greater loss, as is suggested by the modelling results, since the flow is turned through a greater angle in this case.

Table 6.5 presents mass averaged quantities at slot 10 for the two runs and experiment. Clearly the two runs produce similar predictions for loss and flow angle. Indeed inspection of the pitch averaged yaw angles showed that good agreement was achieved between the two solutions by slot 4 (38% Cax).

Table 6.5 : Mass Averaged Results

| JAW TEST CASE | Experiment | MEFP Fine Mesh Vorticity ML Inlet = 42.75° | MEFP Fine Mesh Vorticity ML Inlet = 45.9° |
|---|---|---|---|
| Mixed Out Loss Coefficient | 0.239 | 0.256 | 0.265 |
| - Midspan Mixed Out Loss Coefficient | 0.095 | 0.110 | 0.107 |
| = Gross Mixed Out Secondary Loss | 0.144 | 0.146 | 0.158 |
| - Inlet Loss | 0.040 | 0.037 | 0.036 |
| = Net Mixed Out Secondary Loss | 0.102 | 0.109 | 0.122 |
| Secondary KE Coefficient | 0.043 | 0.053 | 0.050 |
| Net Secondary Loss (= Loss - Midspan Loss - Inlet Loss) | 0.064 | 0.055 | 0.068 |
| Midspan Mixed Out Flow Angle | −67.5° | −68.8° | −68.7° |

Finally Figure 6.34 presents a plot of the blade static pressure distributions predicted by the fine mesh run at the correct inlet angle. This may be compared with that predicted by the equivalent run at the design inlet angle (Figure 6.29) and the experimental results (Figure 5.14). Since the static pressure coefficient is generally reduced by the greater inlet angle, it is seen to be in worse agreement with experiment than that produced previously. However, it is felt that the five hole probe measurements are probably a more accurate test of the codes performance than the surface pressure coefficient.

It is however interesting that the change in inlet angle predicts the slight increase in pressure coefficient at 25% axial chord which was observed in the measurements.

Despite the excellent predictions which have been obtained, more work is needed to both validate the program, and extend its usefulness. The turbulence model which is employed within the solution procedure has been shown to have profound effects upon the quality of the resulting secondary flow predictions. This is somewhat in contrast to the view which is sometimes expressed, which argues that since the flow is primarily pressure driven, the turbulence model is not likely to produce major changes to the flowfield. Here it has been found that the turbulence model can have a very significant effect upon the amount of secondary kinetic energy which is produced, and thus the final location of the passage vortex. Seemingly arbitrary changes to the mixing length model in areas which are not close to solid boundaries, have been found to produce significantly different results. Thus it seems that there is a need for experimental Reynolds stress data with which to validate the turbulence models which are used in such flow calculations. It should be stressed that the fact that such a study can be contemplated is a tribute to the accuracy of the numerical solution procedure, as otherwise numerical viscosity would swamp the effects of the turbulence model.

As many turbomachinery blade boundary layers undergo transition, a turbulence model which accurately predicts this phenomena would be very useful. Such models are currently appearing in Navier-Stokes solvers, and so tests of their accuracy are now required. If more general turbulence models can be developed, they will greatly extend the predictive capabilities of the Navier-Stokes methods, as it seems that they are now the most restrictive part of such solutions.

Finally it is worth recording the calculation times which are involved for the runs which have been presented. The solutions generally require forty passes of the calculation procedure as described in Chapter 3 to achieve good convergence. This requires approximately one hour of CPU time on a CRAY XMP-48, with 2.3 Mega Words of storage for a 'coarse' grid solution (19975

points). The 'fine' grid solutions (64800 points) required over three hours of CPU time and 5.5 Mega Words of storage. Clearly running such calculations is expensive. Also, a significant amount of the user's time is required to set up the input data for the program. Whilst this will become much easier with greater automation, it is clear that running such calculations is not a trivial matter. Thus there is still a need for rapid, simple calculation techniques which can give an estimation of secondary flow effects in the early design stages.

The fine grid solutions were seven times more expensive to run than the coarse grid calculations, and the resulting solutions were so large as to be difficult to handle. Also, as far as secondary flow predictions are concerned, there is not a great deal of advantage in using the fine grid, its benefits being mainly restricted to the calculation of profile loss. Therefore it was decided to perform all future runs on the coarse calculation mesh, as shown in Figure 6.1(a).

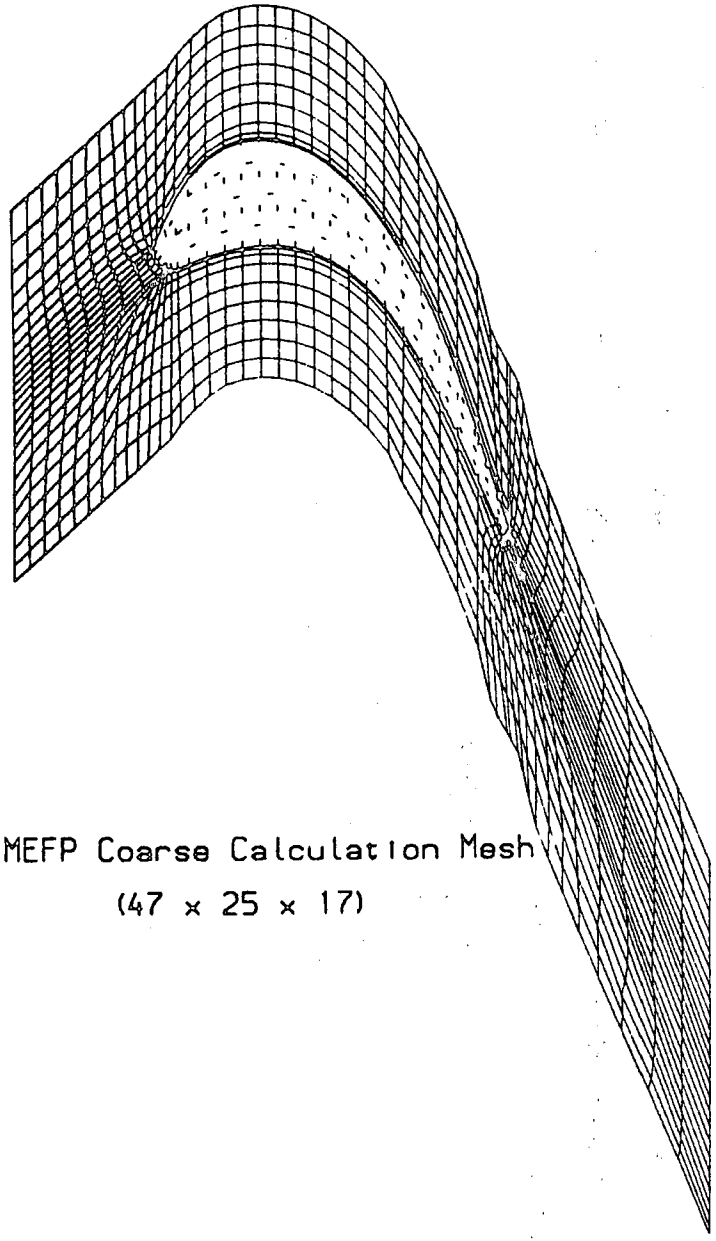

MEFP Coarse Calculation Mesh
(47 x 25 x 17)

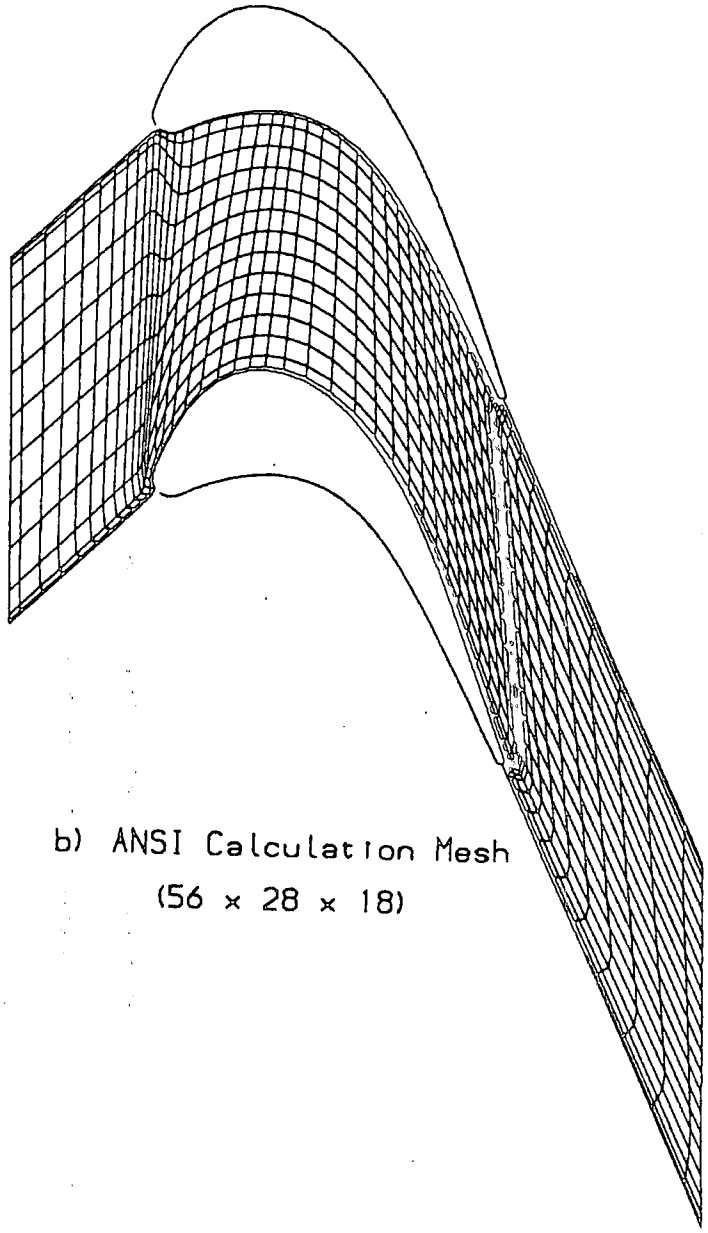

b) ANSI Calculation Mesh
(56 x 28 x 18)

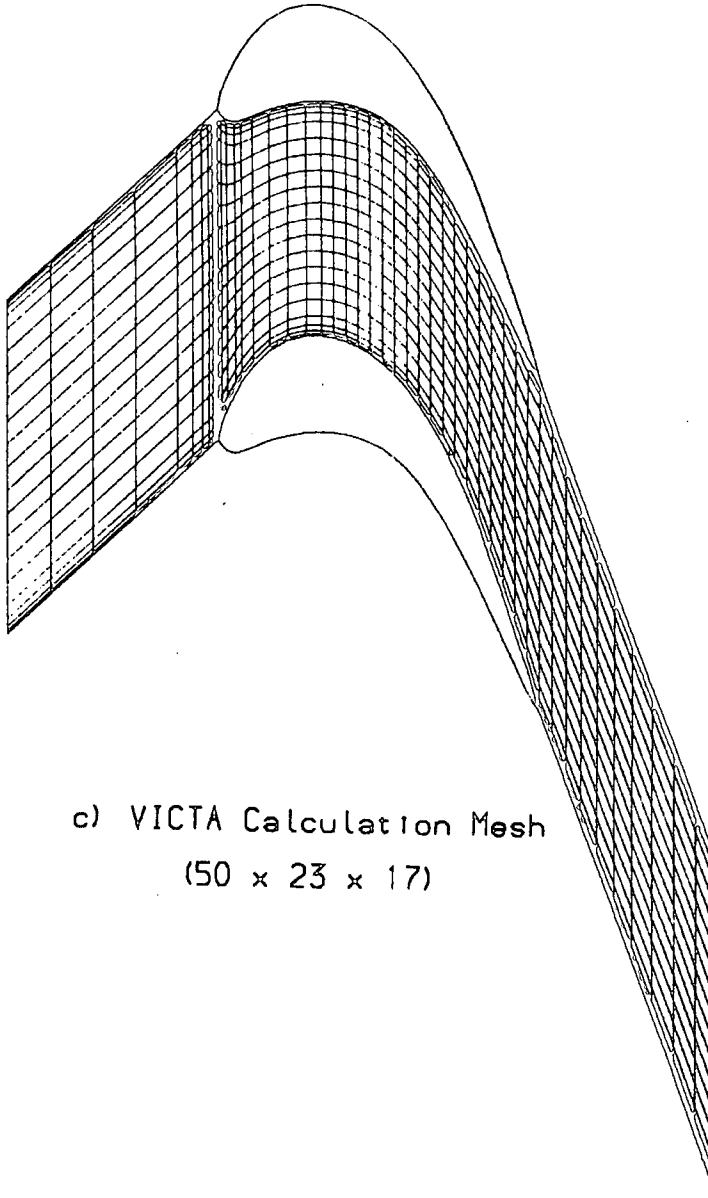

c) VICTA Calculation Mesh
(50 x 23 x 17)

FIGURE 6.1 : Calculation Meshes for Comparison of Three Codes

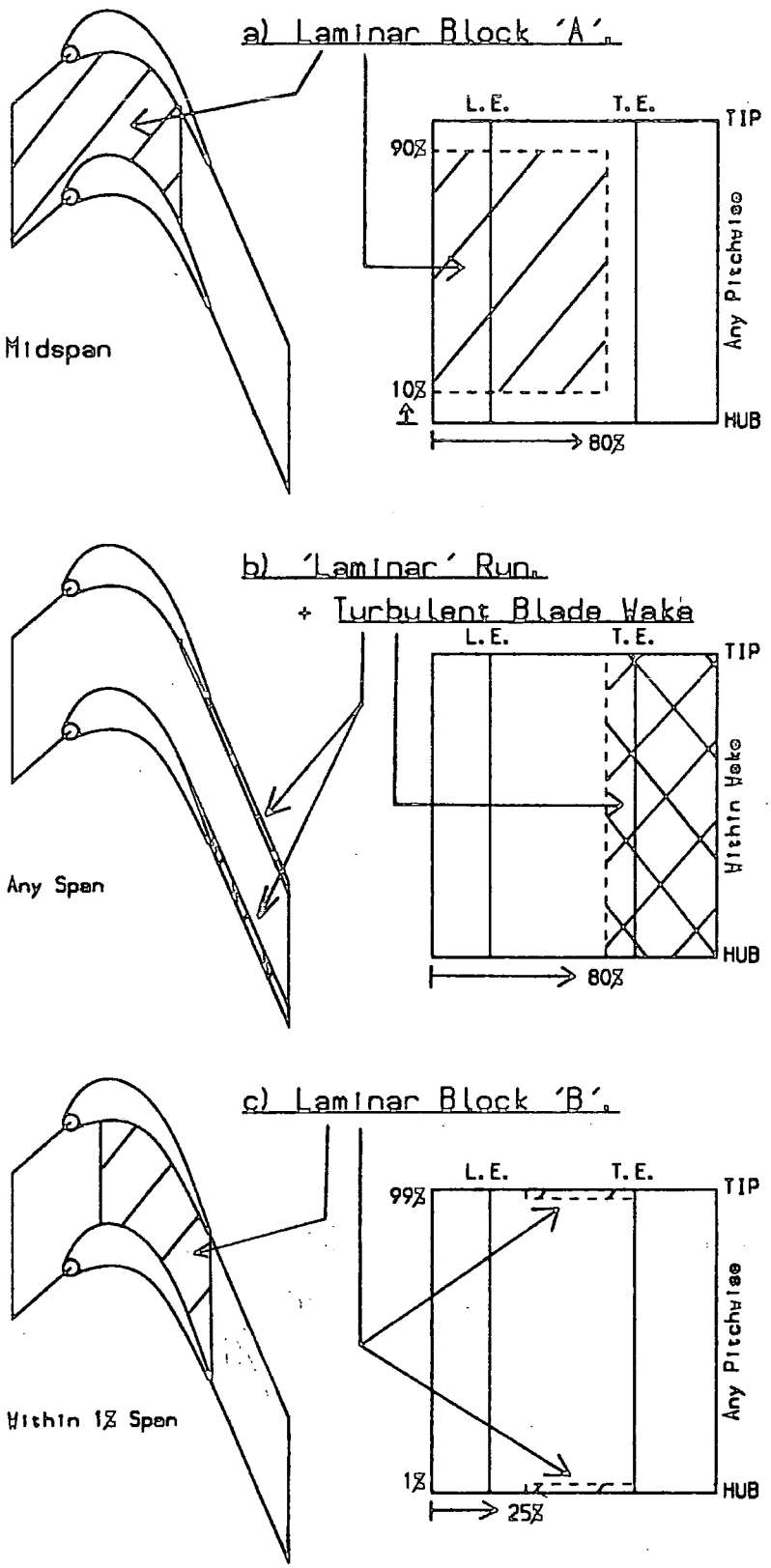


FIGURE 6.2 : Laminar Blocking Arrangements

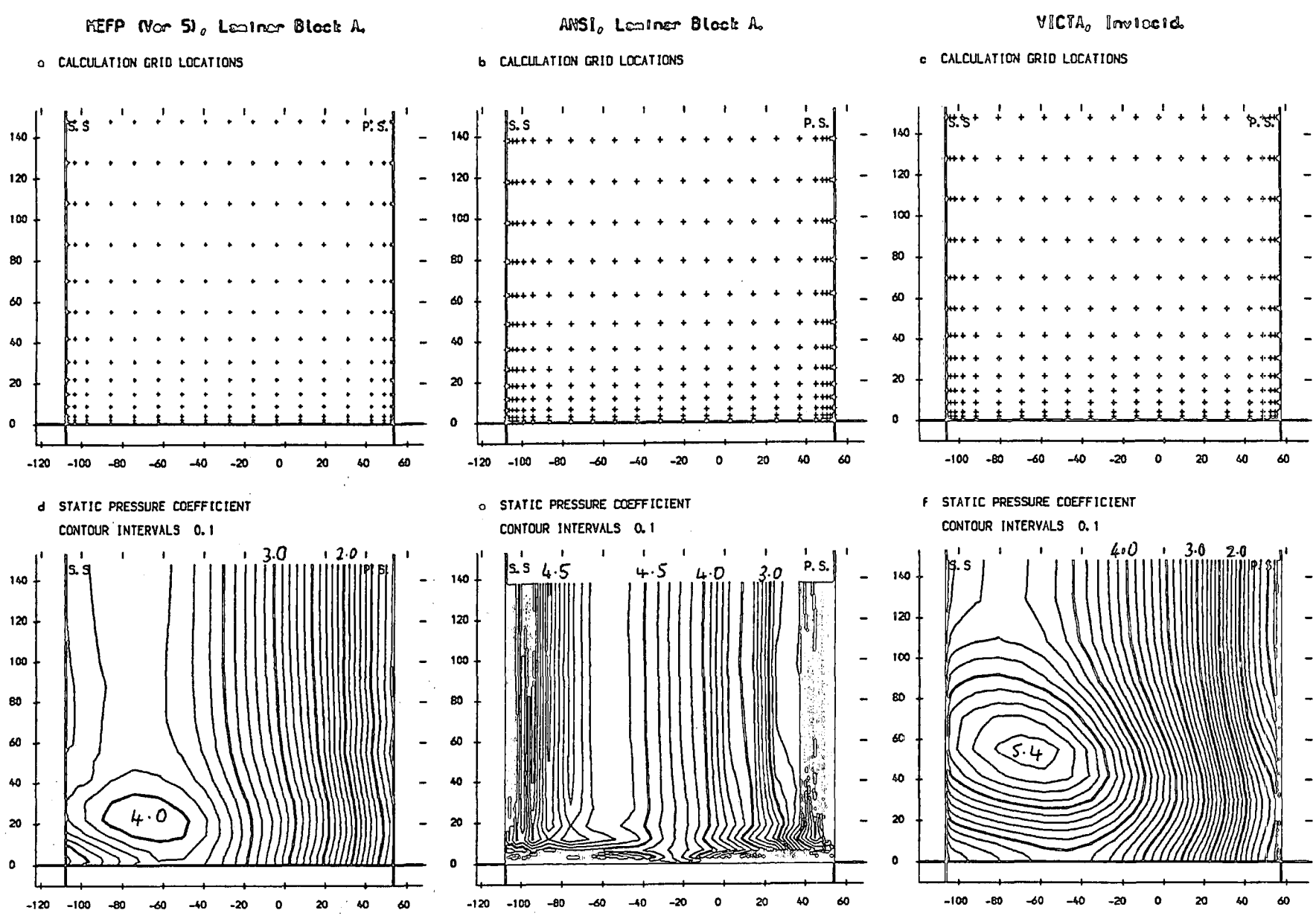


FIGURE 6.3 (a-f) : Area Plots For Slot 7

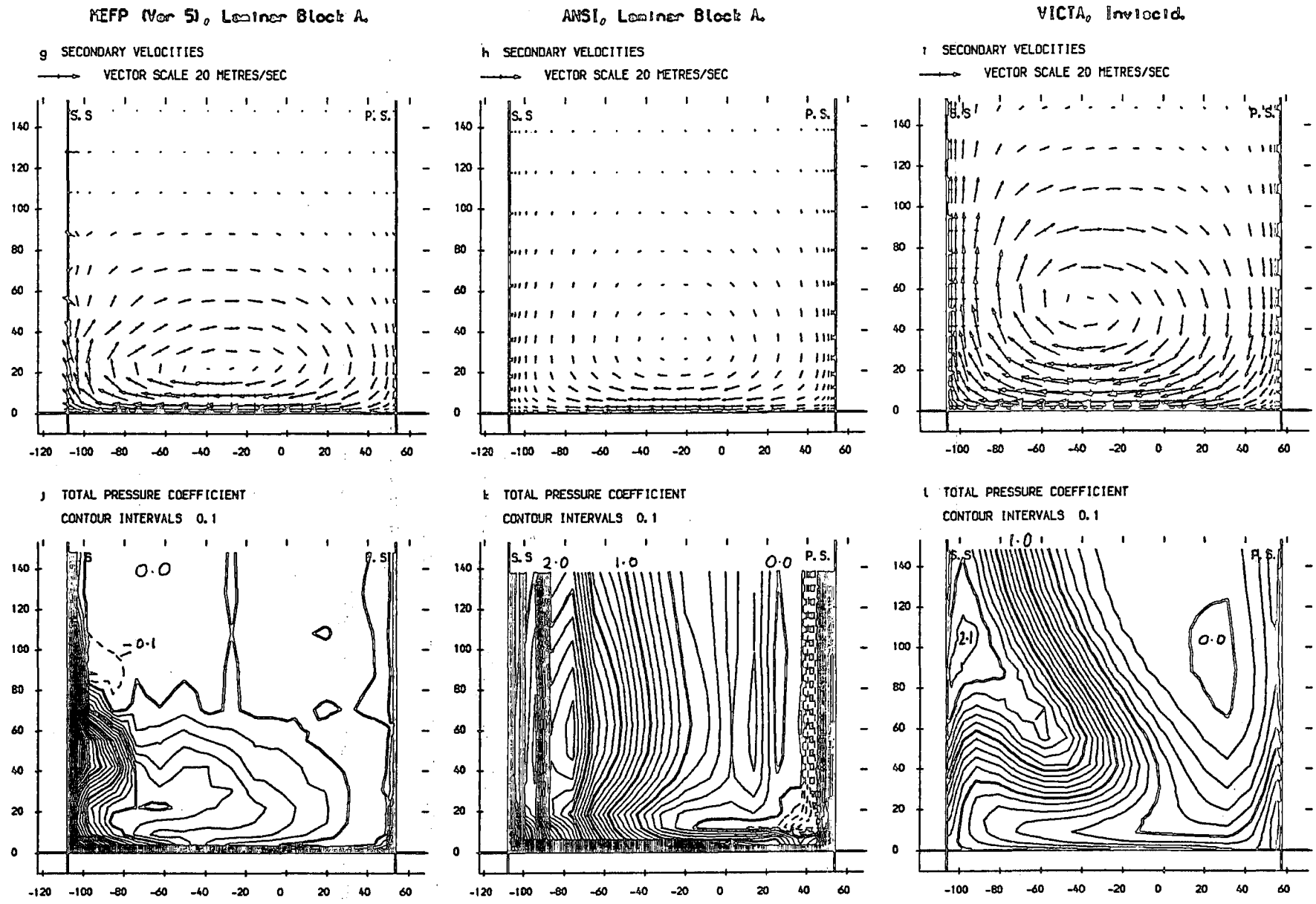


FIGURE 6.3 (g-l) : Area Plots For Slot 7

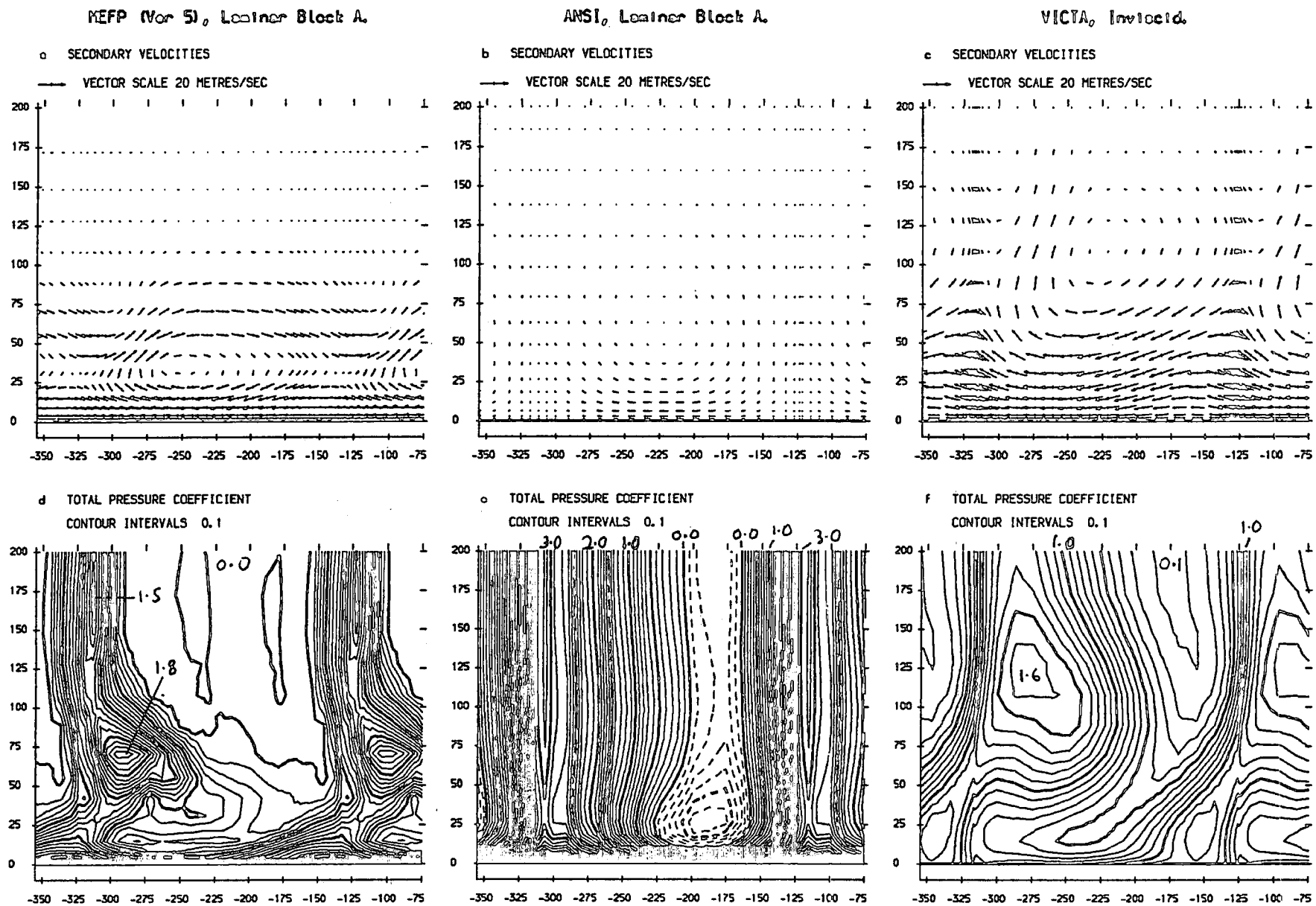


FIGURE 6.4 (a-f) : Area Plots For Slot 10

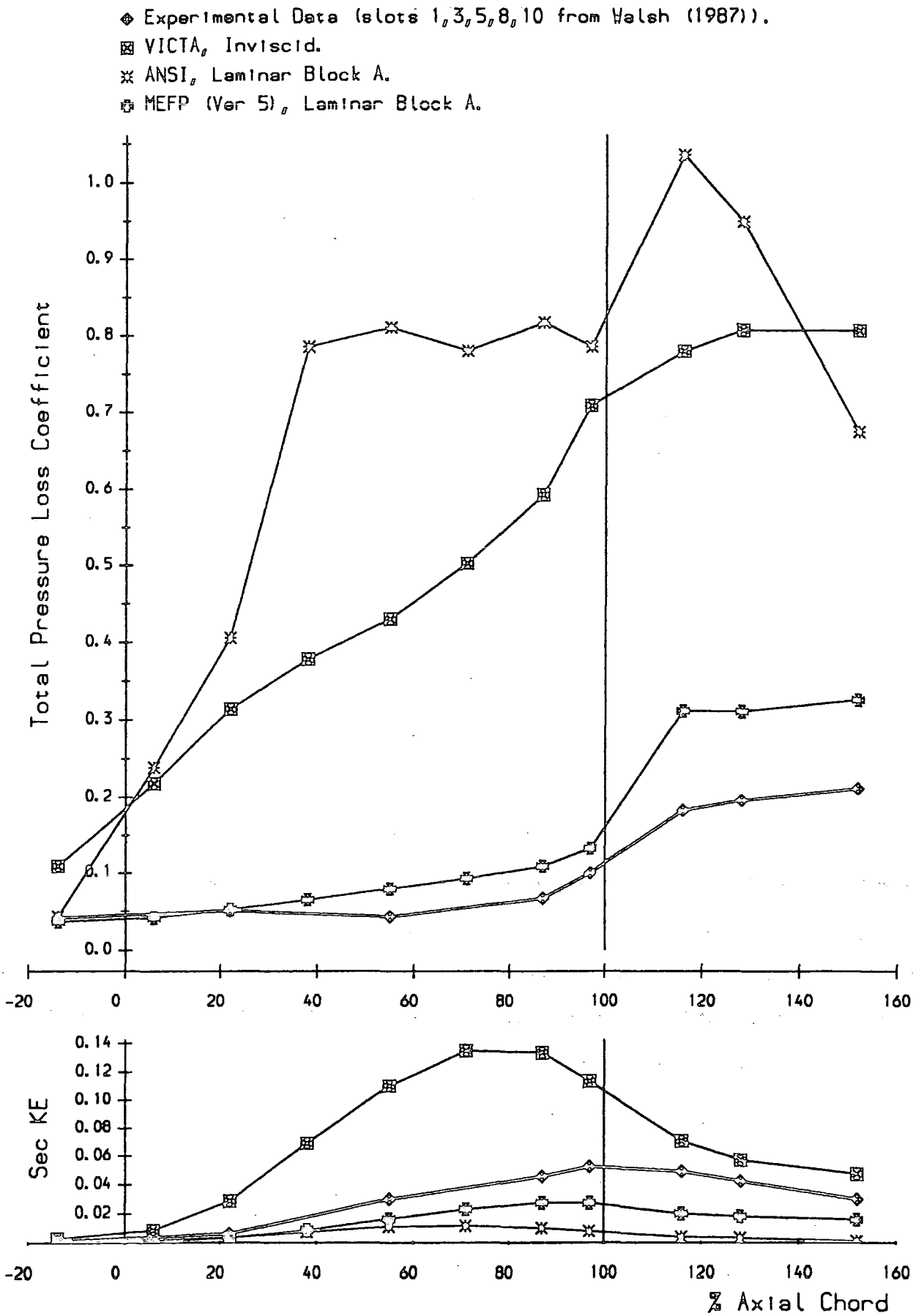


FIGURE 6.5 : Mass Averaged Loss & Secondary Kinetic Energy

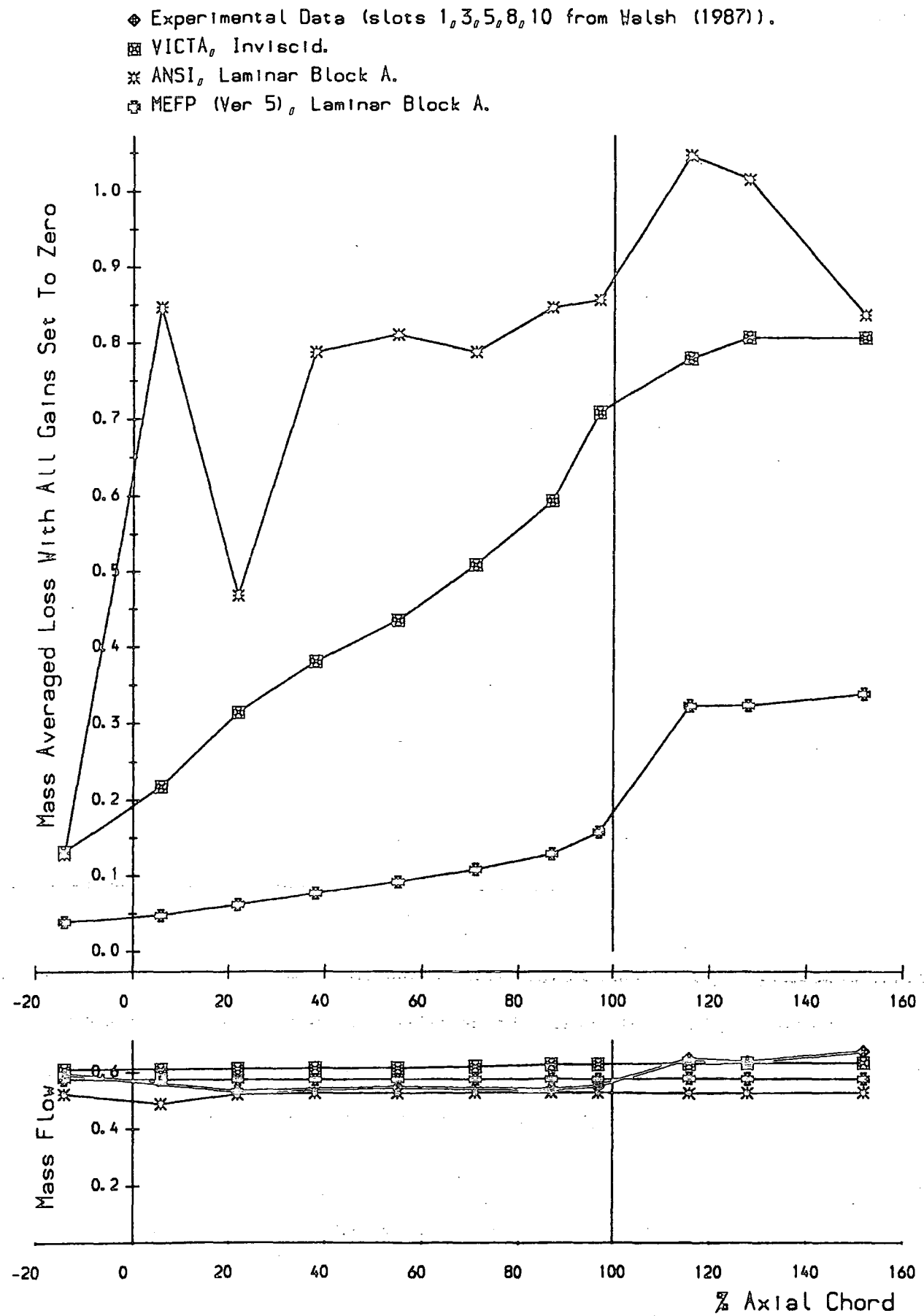


FIGURE 6.6 : Mass Averaged (+ve) Loss & Total Mass Flow

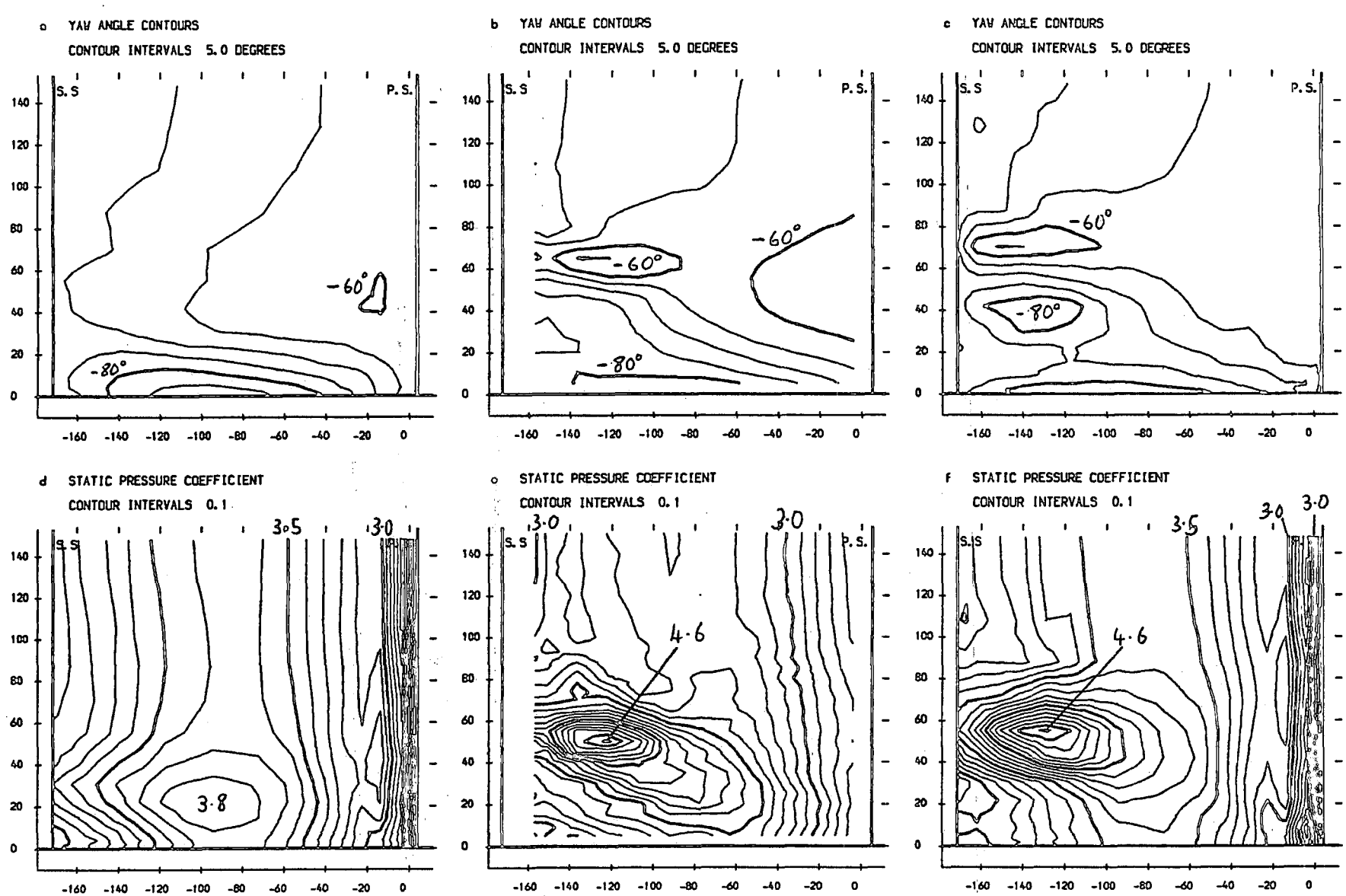


FIGURE 6.7 (a-f) : Area Plots For Slot 8

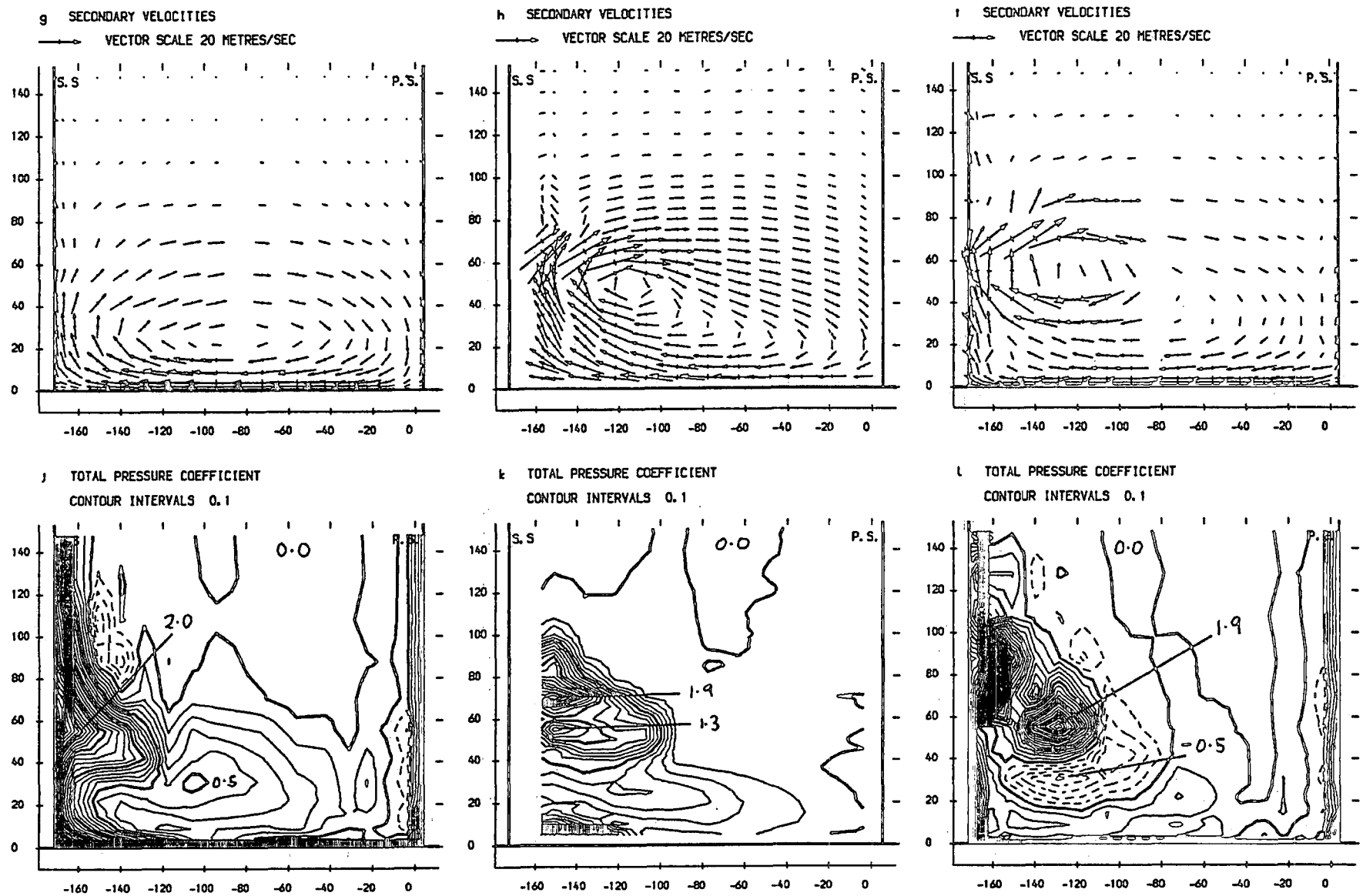


FIGURE 6.7 (g-l) : Area Plots For Slot 8

▦ Experiment (from Walsh (1987)).
⁜ MEFP (Ver 5), Turbulent + Laminar Block A.
○ MEFP (Ver 5), 'Laminar' Run (with Turbulent Blade Wakes).

a) Yaw Angle (Degrees)

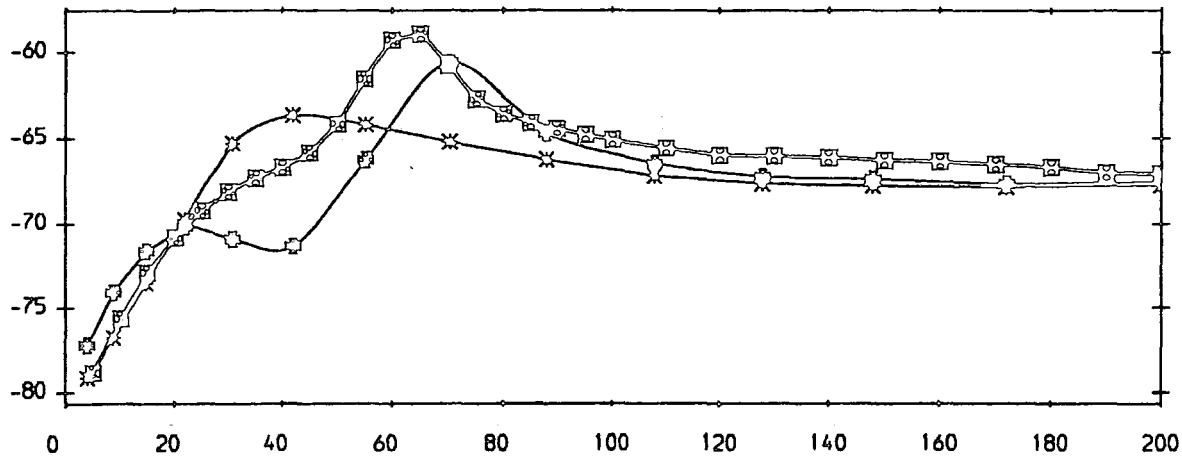


b) Total Pressure Loss Coefficient

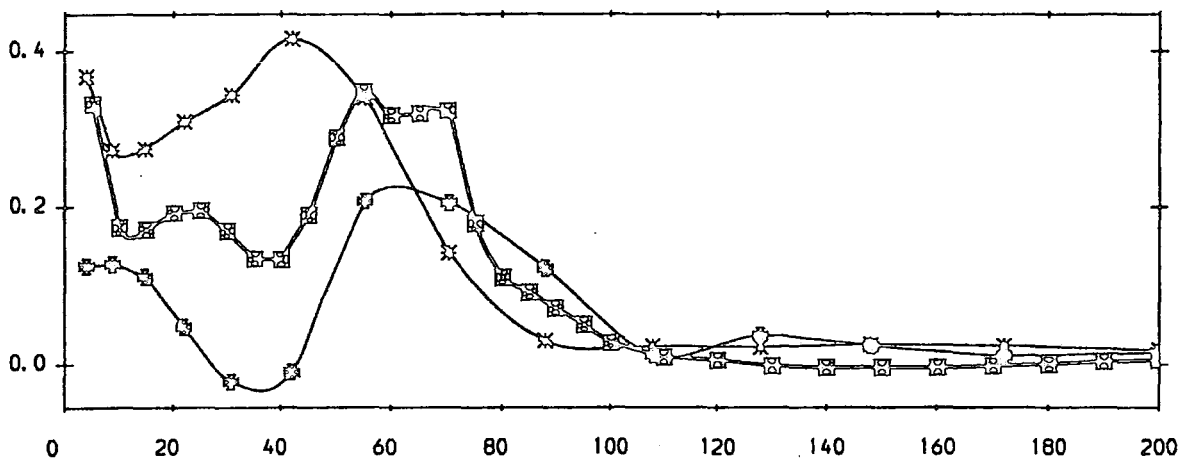


c) Secondary Kinetic Energy Coefficient

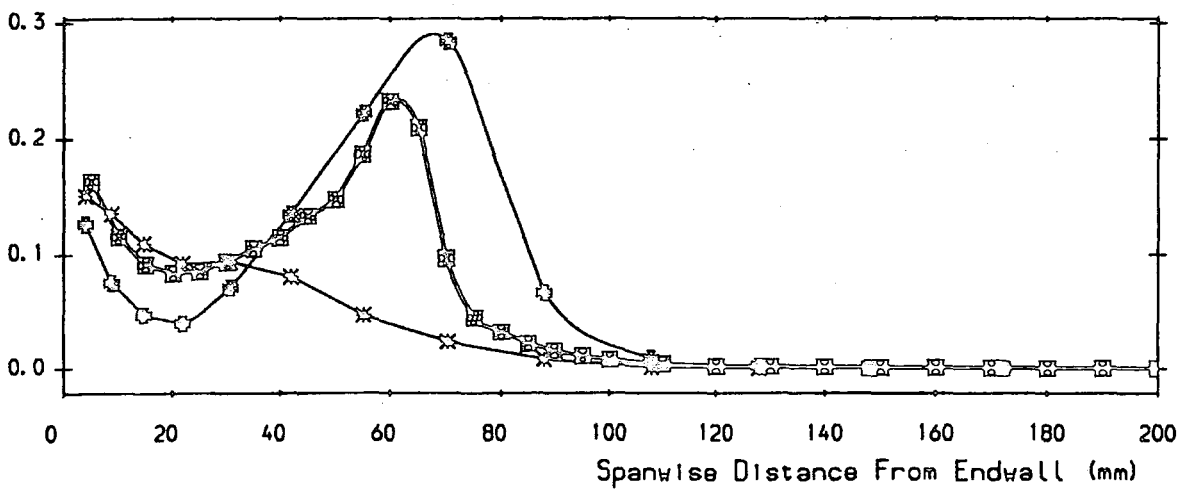


FIGURE 6.8 : Pitch Averaged Results For Slot B

MEFP (Ver 5)₀ 'Laminar' Run (with turbulent blade wake).

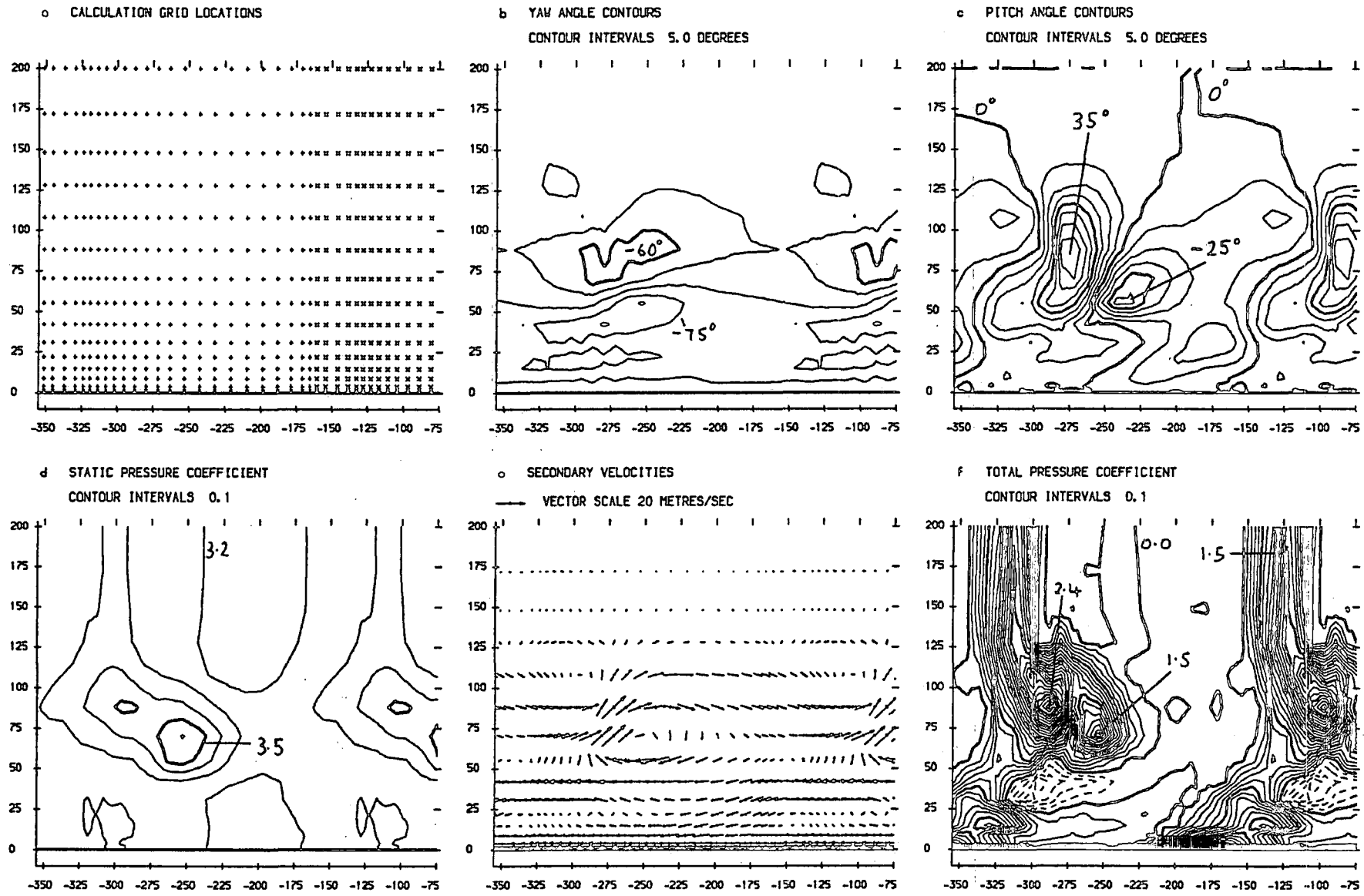


FIGURE 6.9 (a-f) : Area Plots For Slot 10

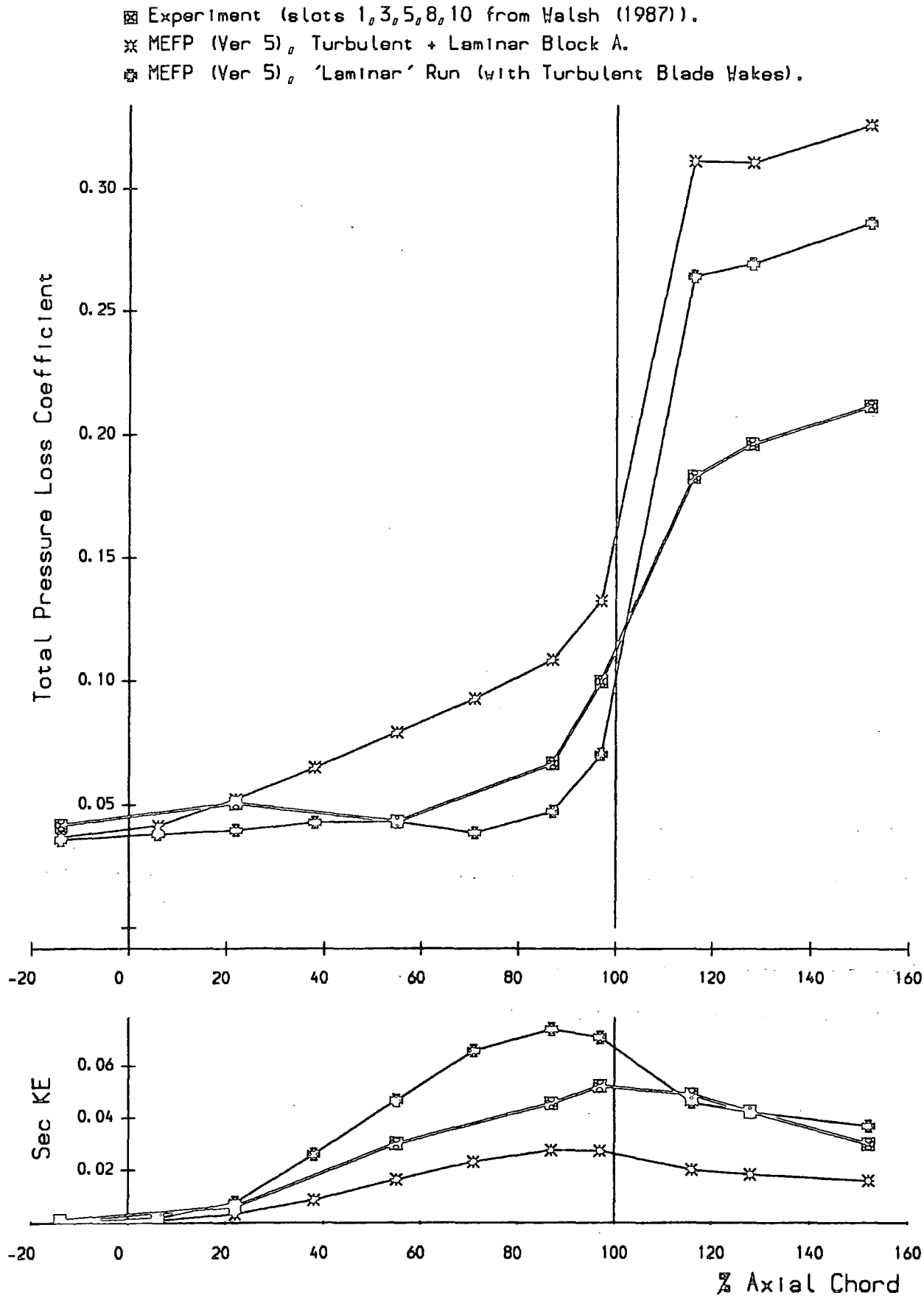


FIGURE 6.10 : Mass Averaged Loss & Secondary Kinetic Energy

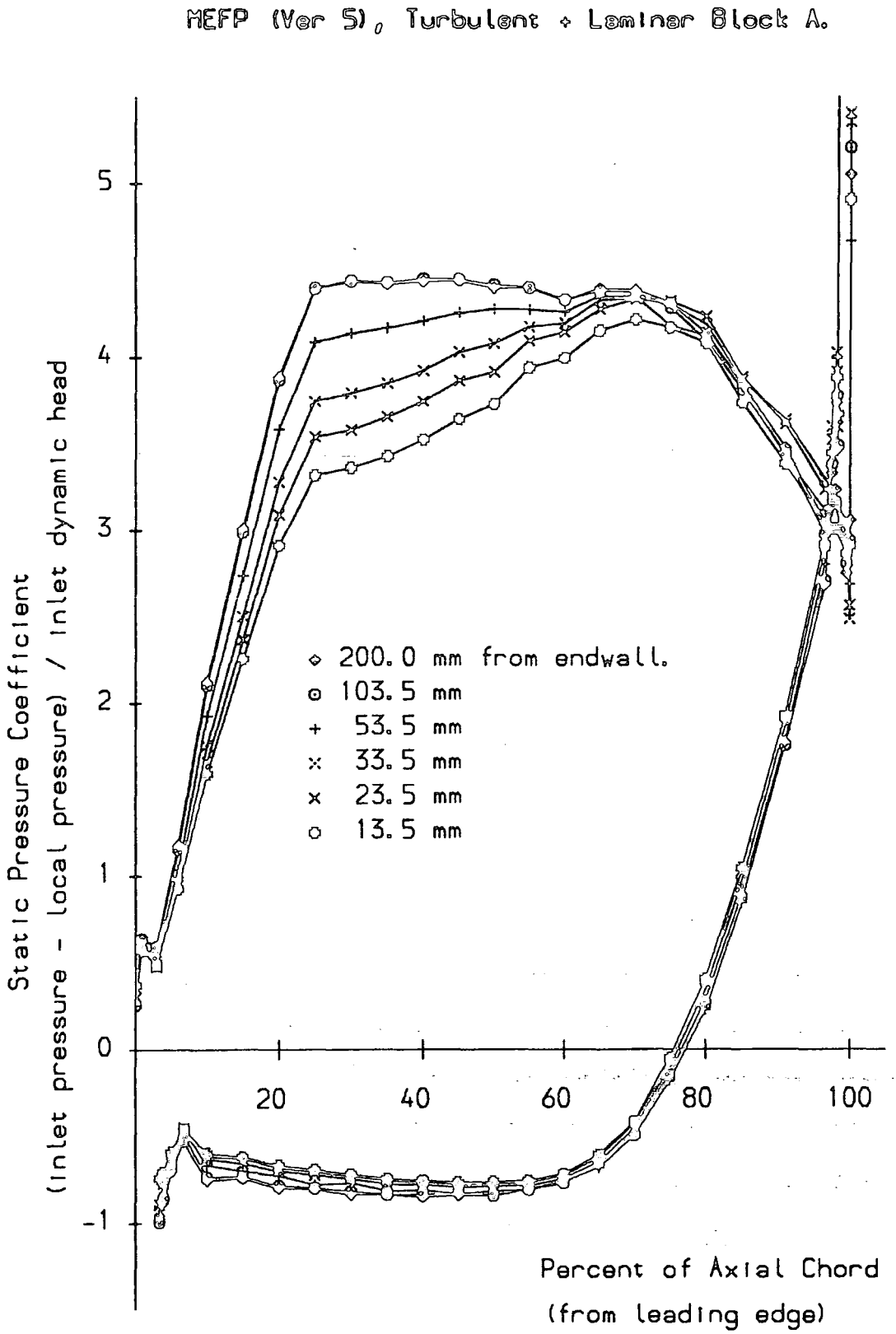


FIGURE 6.11. Blade Static Pressure Distributions

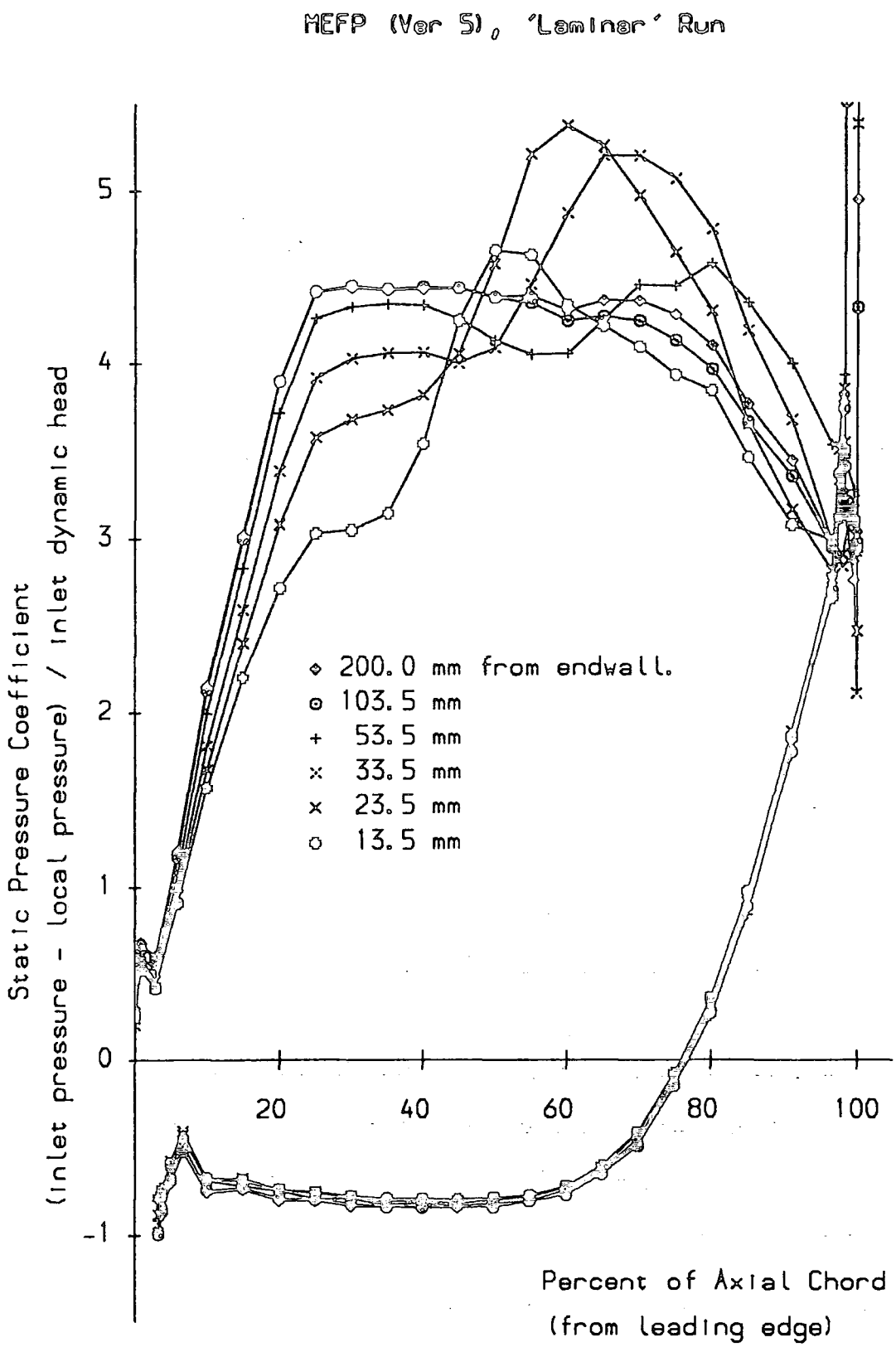


FIGURE 6.12, Blade Static Pressure Distributions

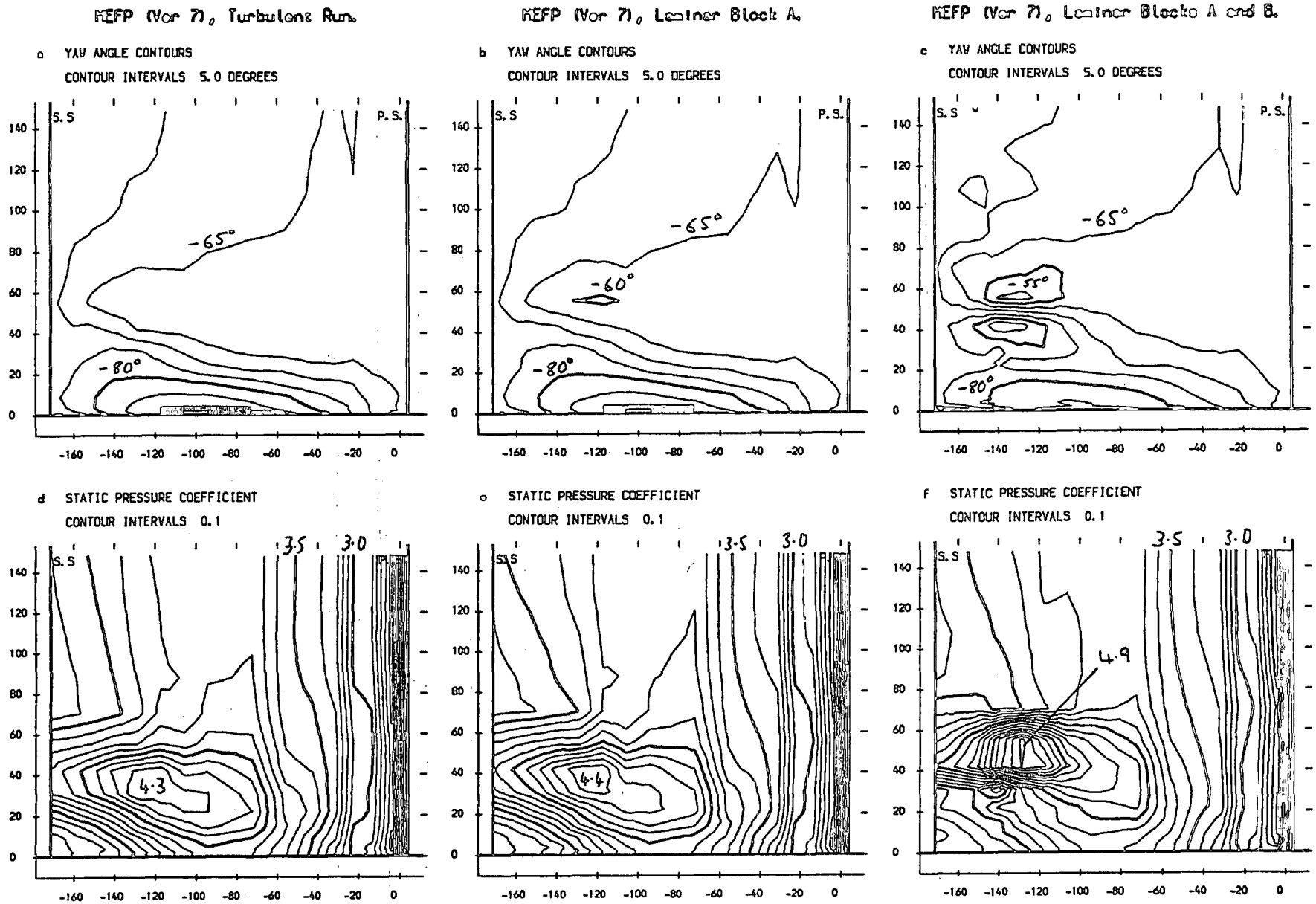


FIGURE 6.13 (a-f) : Area Plots For Slot 8

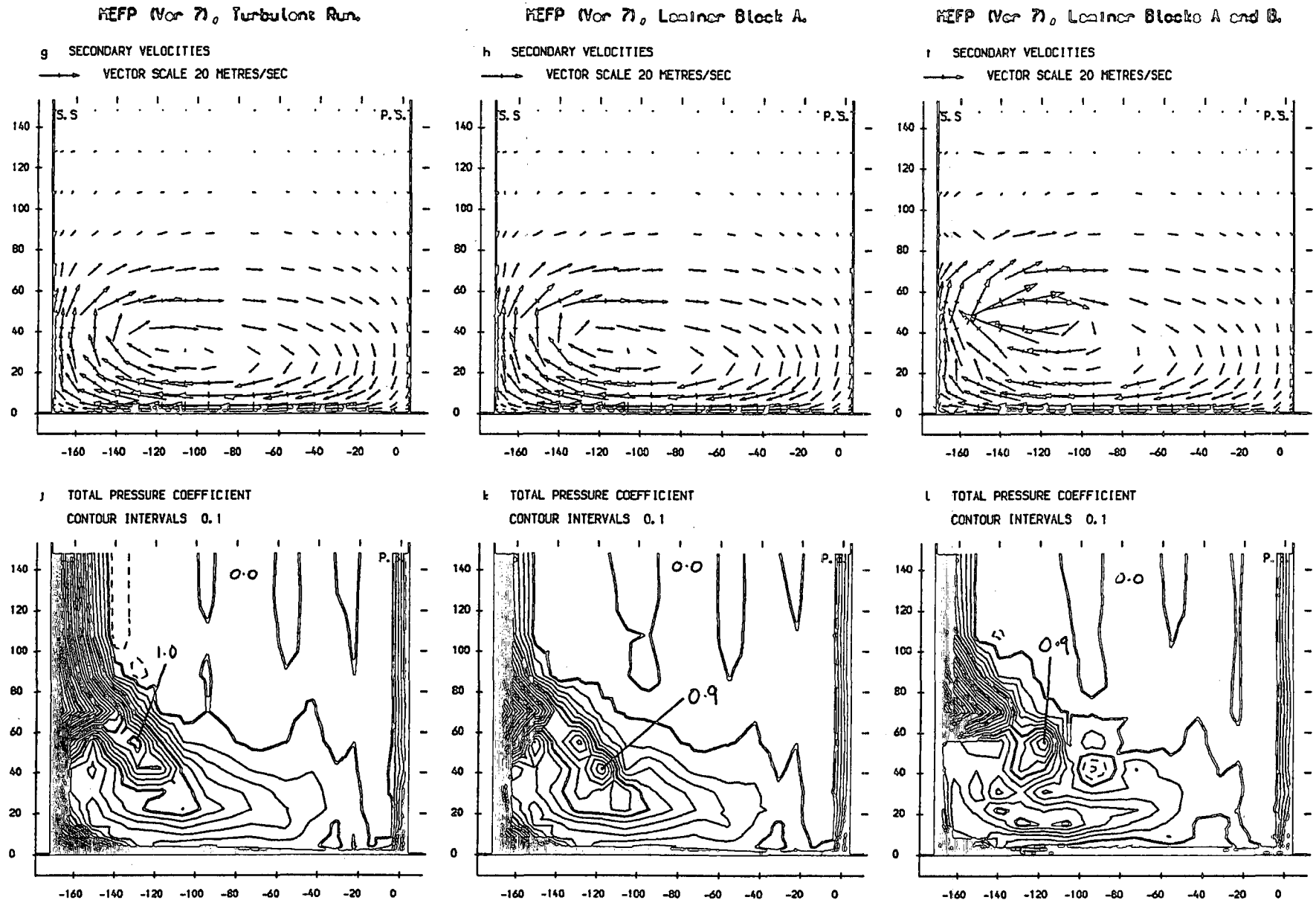


FIGURE 6.13 (g-l) : Area Plots For Slot 8

◆ Experiment (from Walsh (1987)).
▣ MEFP (Ver 7), Turbulent with Laminar Blocks A and B.
✳ MEFP (Ver 7), Turbulent with Laminar Block A.
❁ MEFP (Ver 7), Turbulent Run.

a) Yaw Angle (Degrees)

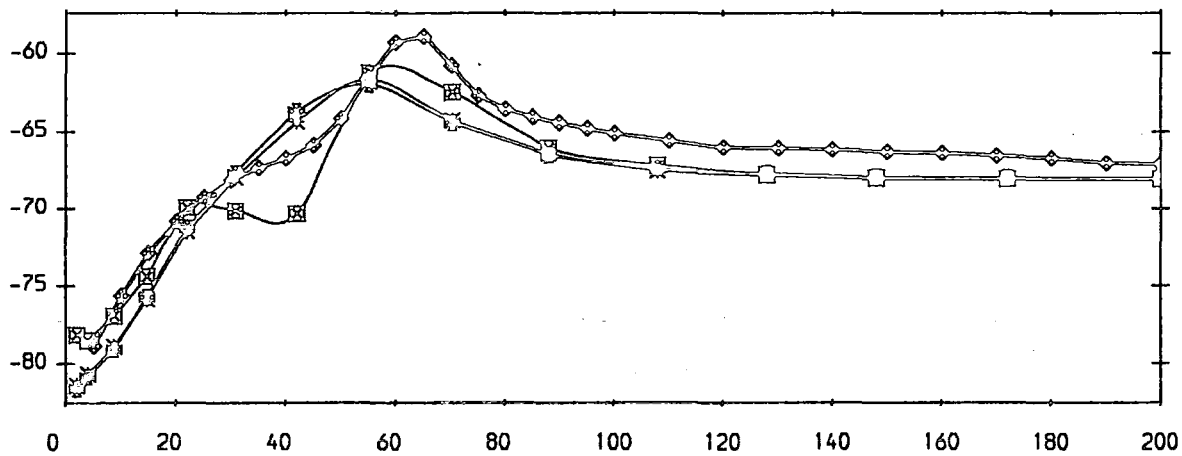


b) Total Pressure Loss Coefficient

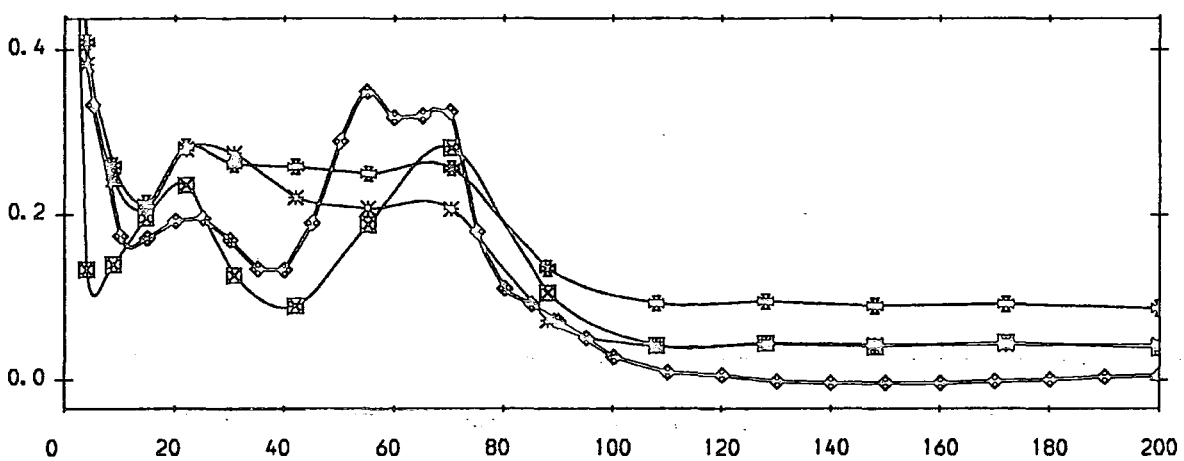


c) Secondary Kinetic Energy Coefficient

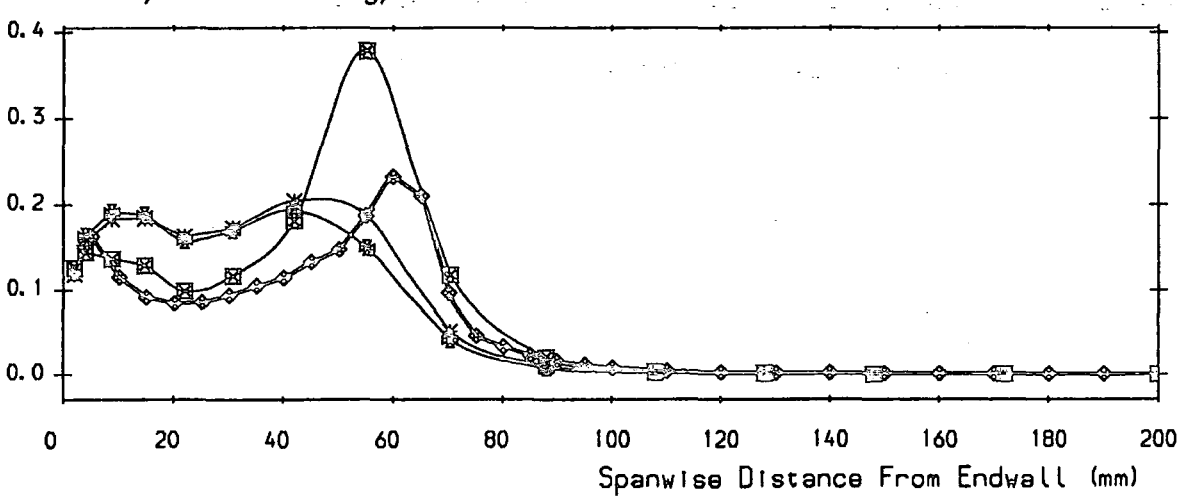


FIGURE 6.14 : Pitch Averaged Results For Slot B

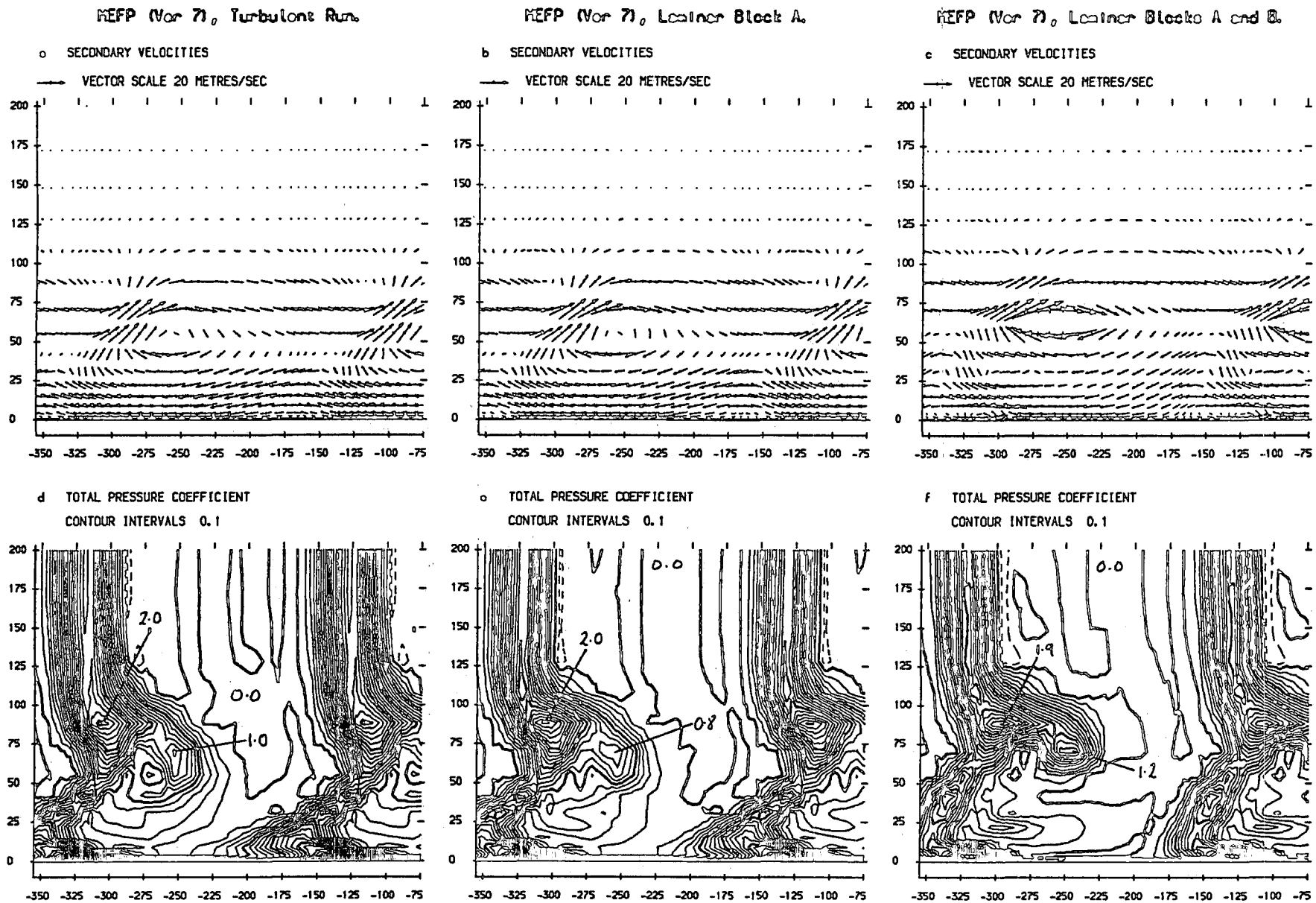


FIGURE 6.15 (a-f) : Area Plots For Slot 10

◆ Experiment (from Walsh (1987)).
▣ MEFP (Ver 7), Turbulent with Laminar Blocks A and B.
✳ MEFP (Ver 7), Turbulent with Laminar Block A.
❁ MEFP (Ver 7), Turbulent Run.

a) Yaw Angle (Degrees)

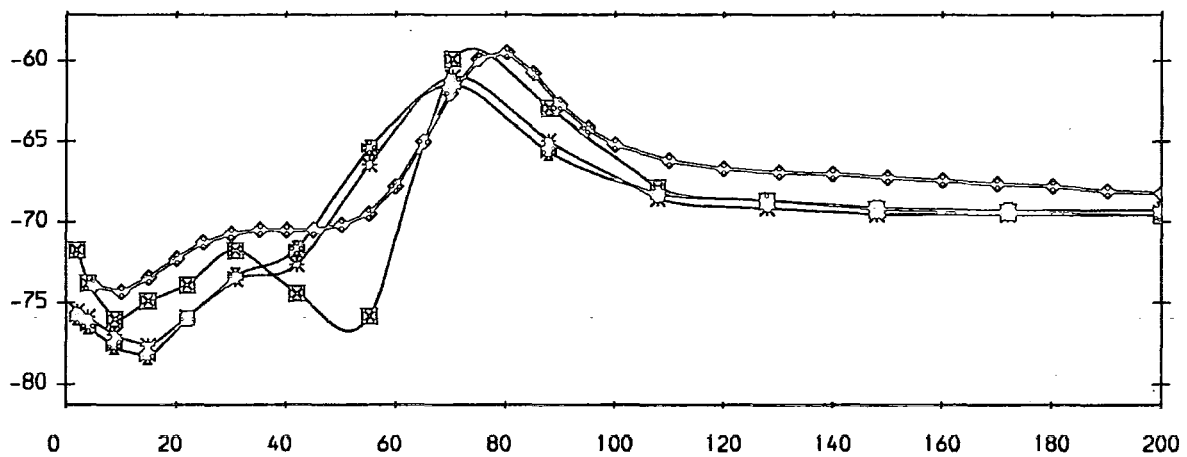


b) Total Pressure Loss Coefficient

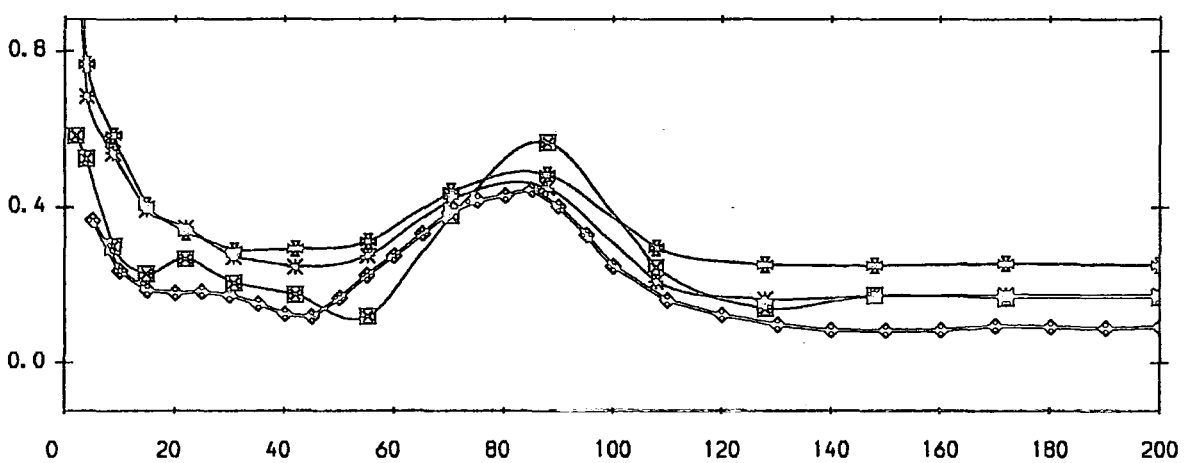


c) Secondary Kinetic Energy Coefficient

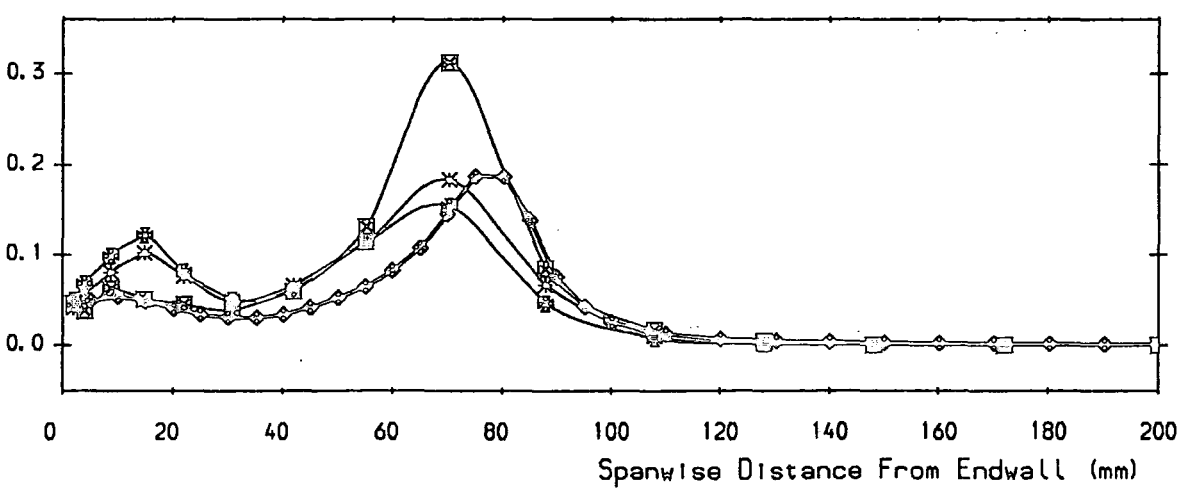


FIGURE 6.16 : Pitch Averaged Results For Slot 10

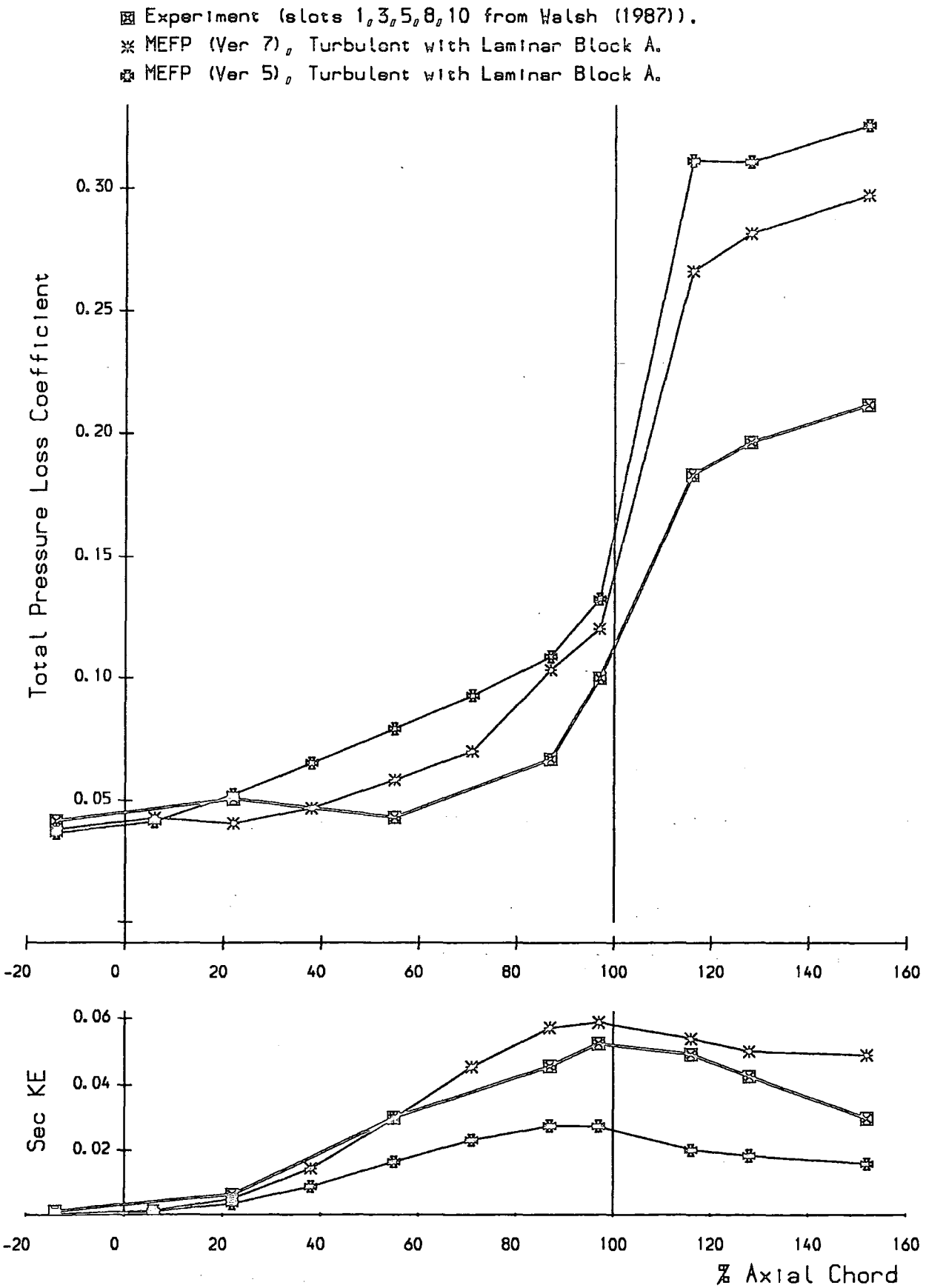


FIGURE 6.17 : Mass Averaged Loss & Secondary Kinetic Energy

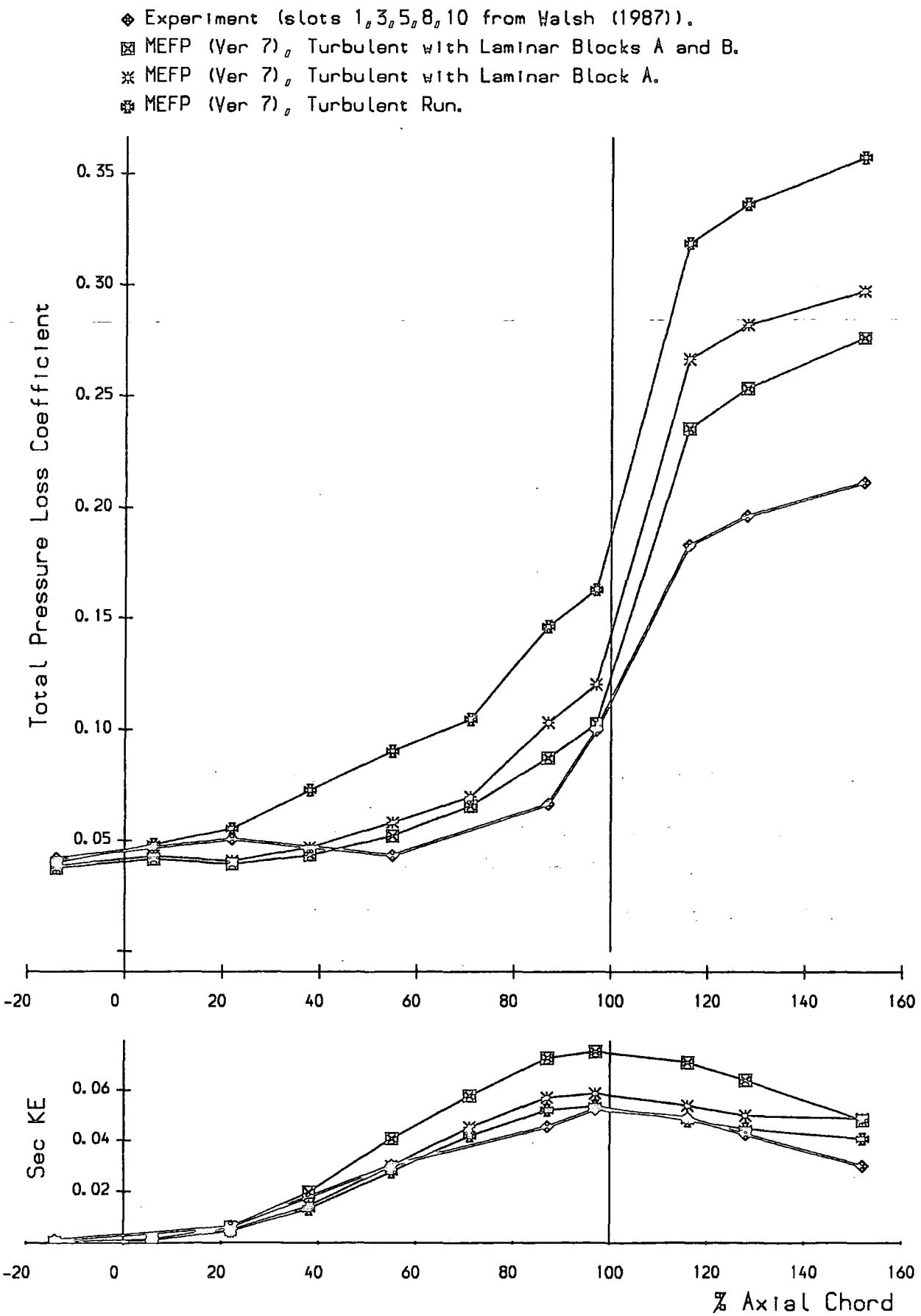


FIGURE 6.18 : Mass Averaged Loss & Secondary Kinetic Energy

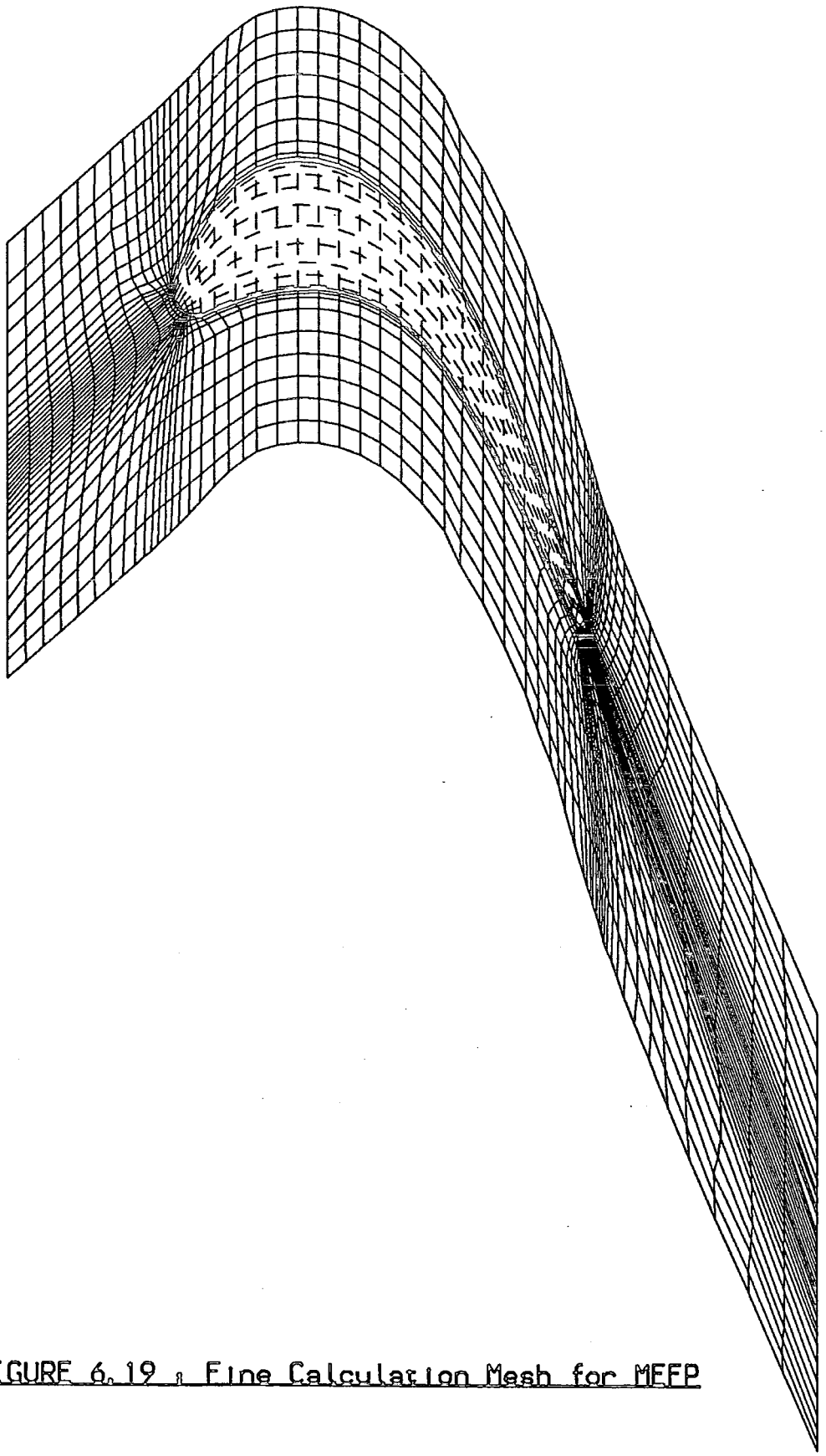

FIGURE 6.19 : Fine Calculation Mesh for MFFP

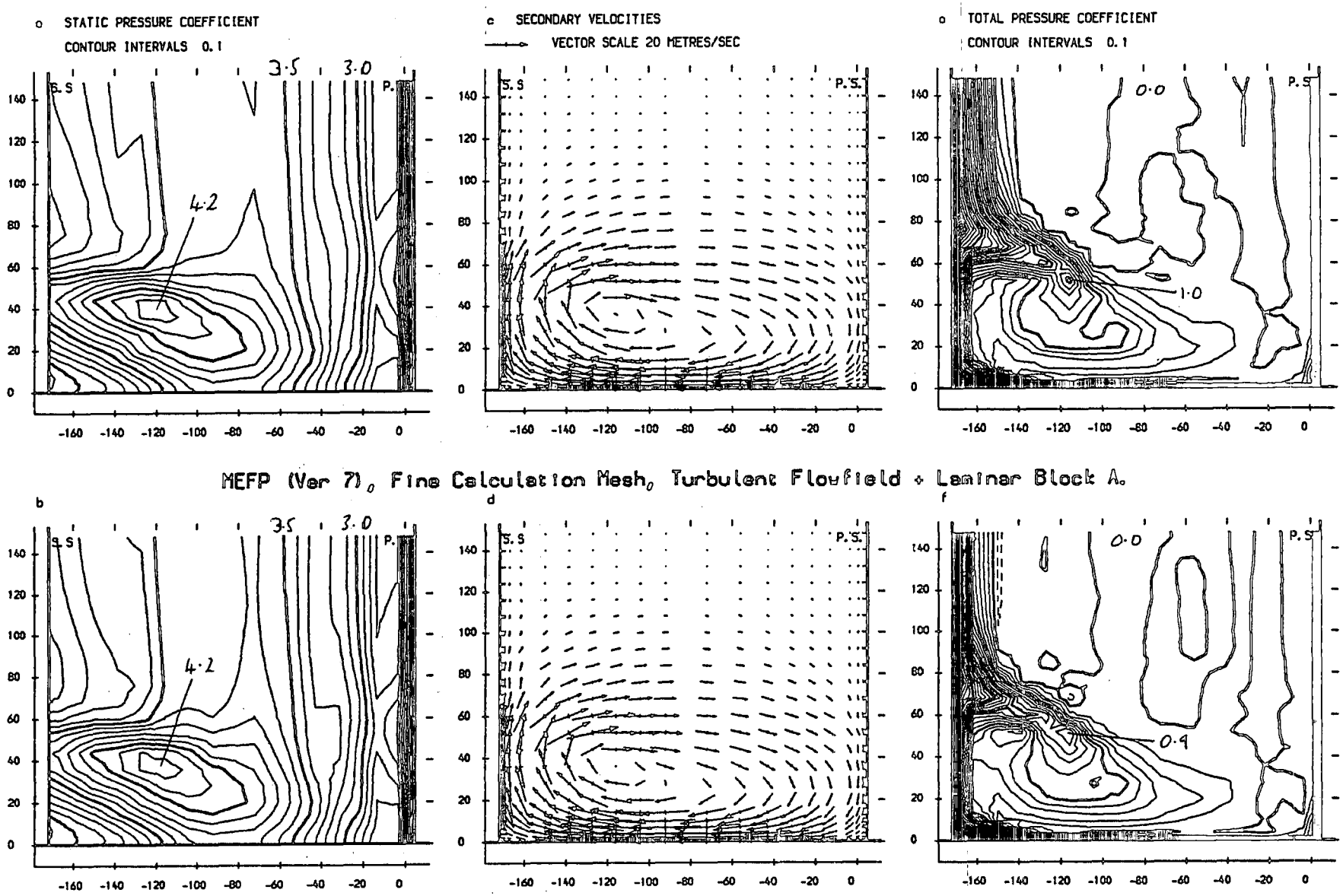


FIGURE 6.20 (a-f) : Area Plots For Slot 8

MEFP (Ver 7)₀ Fine Calculation Mesh₀ Fully Turbulent Flowfield.

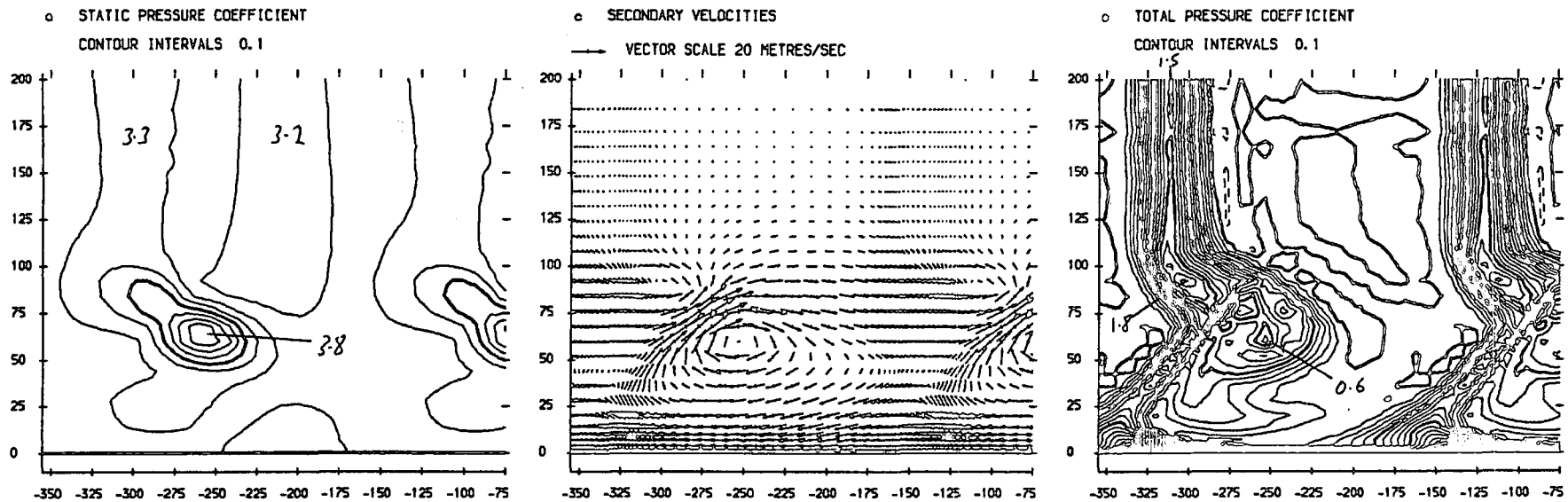


MEFP (Ver 7)₀ Fine Calculation Mesh₀ Turbulent Flowfield + Laminar Block A.

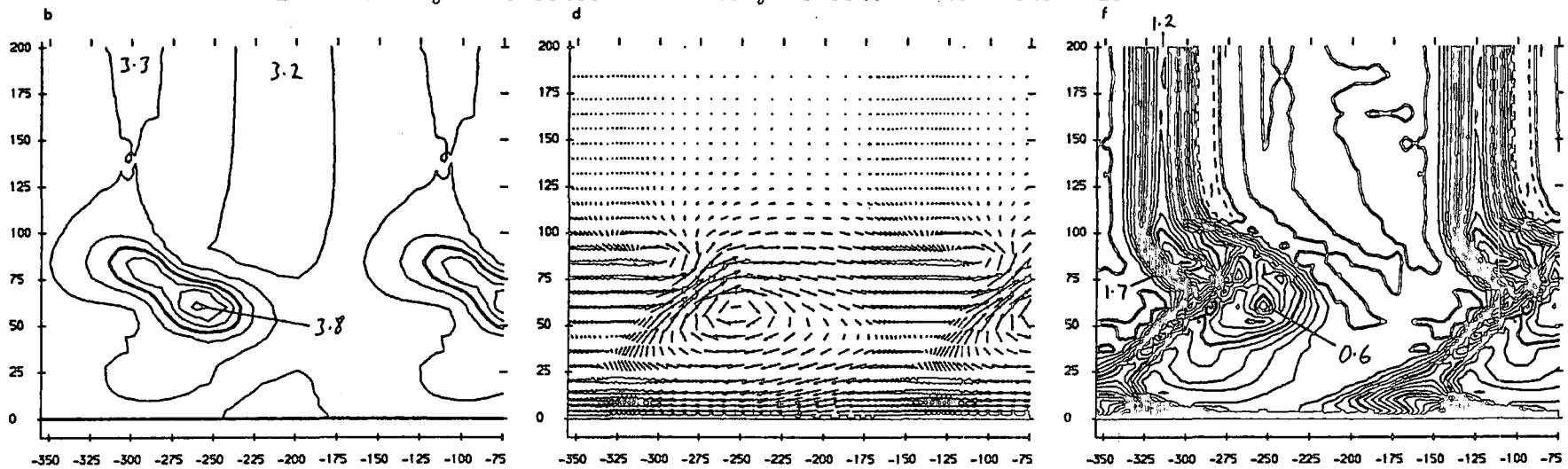


FIGURE 6.21 (a-f) : Area Plots For Slot 10

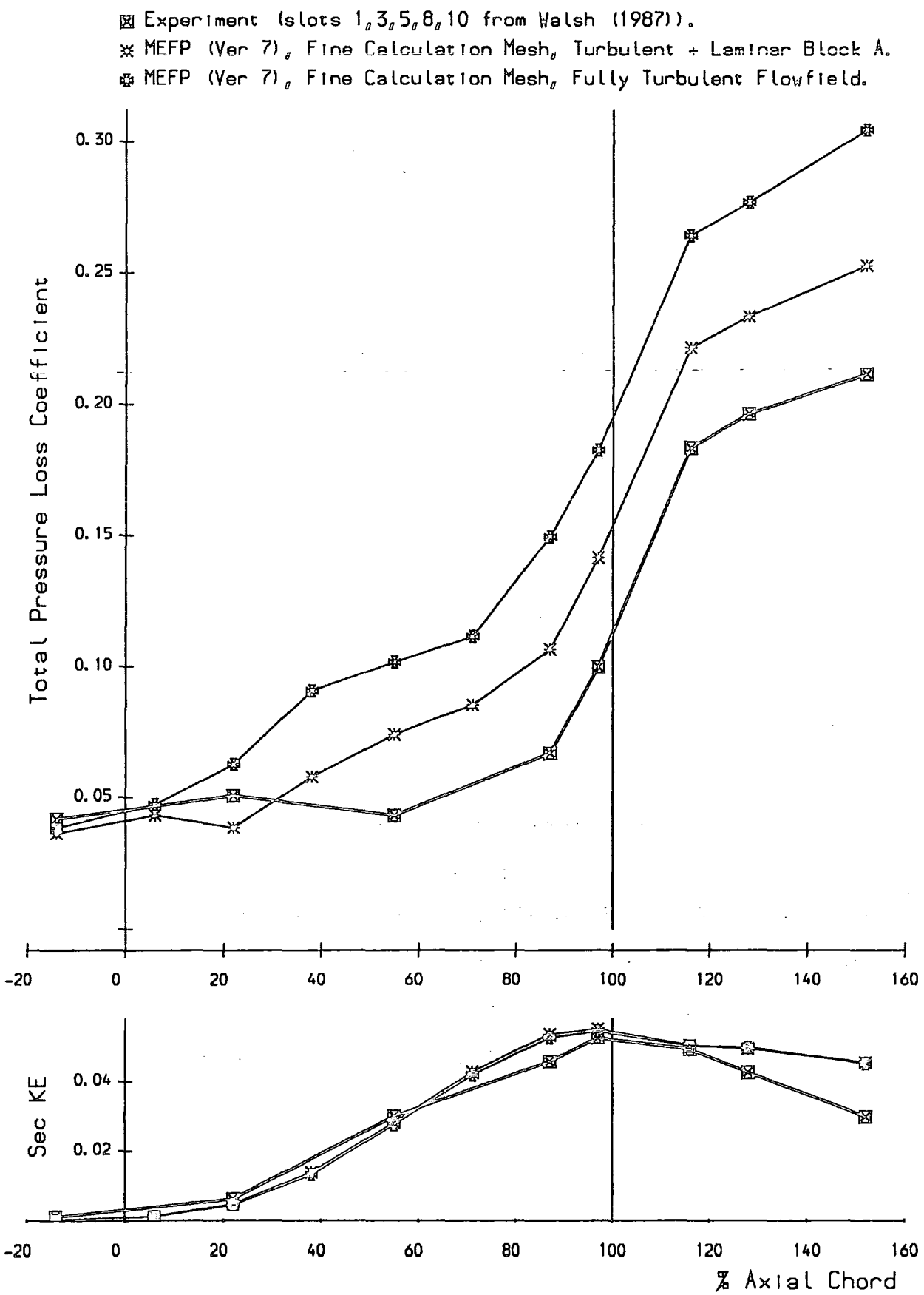


FIGURE 6.22 : Mass Averaged Loss & Secondary Kinetic Energy

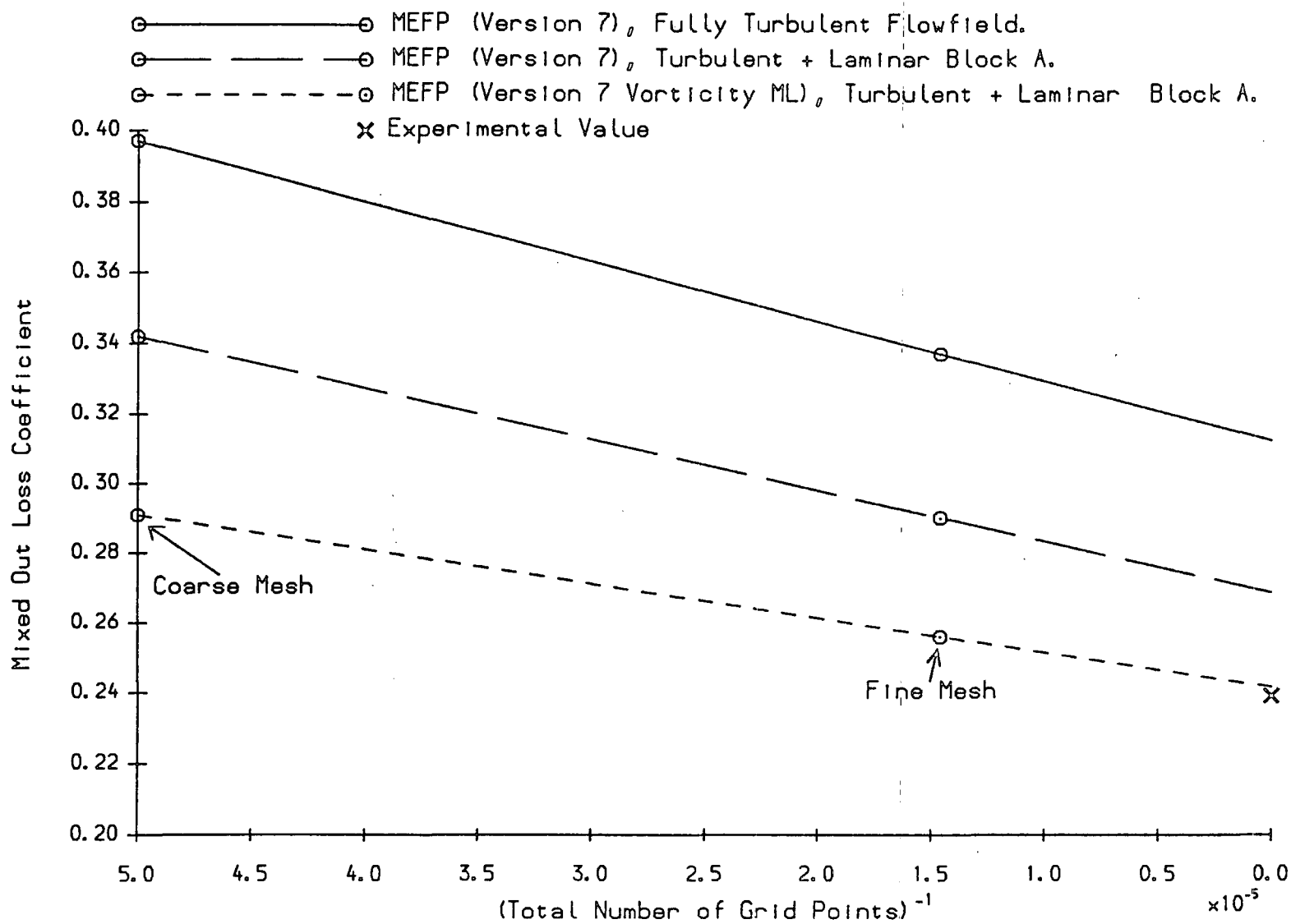


FIGURE 6.23 : Influence of Mesh Refinement and Turbulence Modelling on Loss Prediction

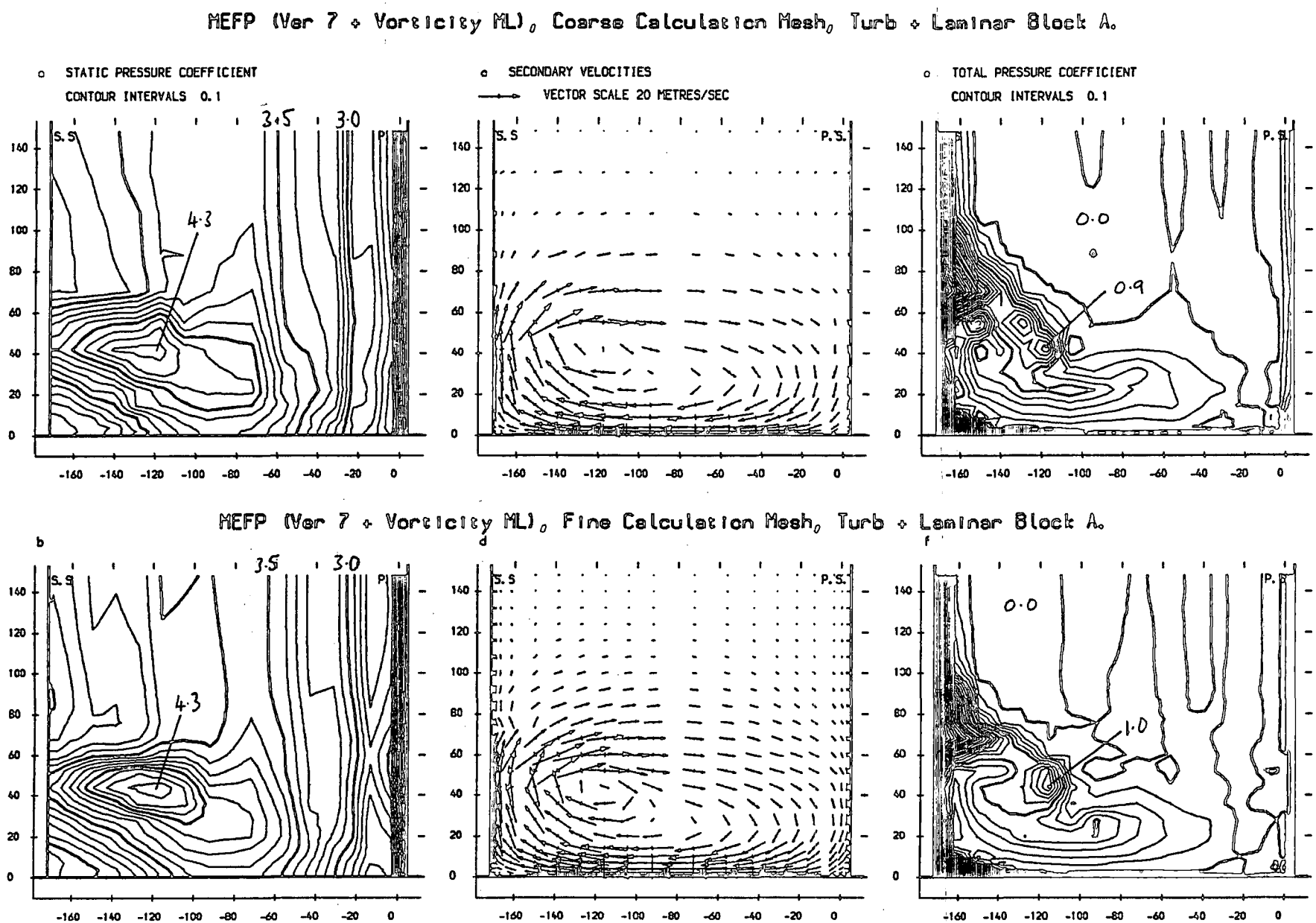


FIGURE 6.24 (a-f) : Area Plots For Slot 8

⊠ Experiment (from Walsh (1987)).
※ MEFP (Ver 7 Vorticity ML), Coarse Mesh, Turb + Laminar Block A.
⊛ MEFP (Ver 7 Vorticity ML), Fine Mesh, Turb + Laminar Block A.

a) Yaw Angle (Degrees)

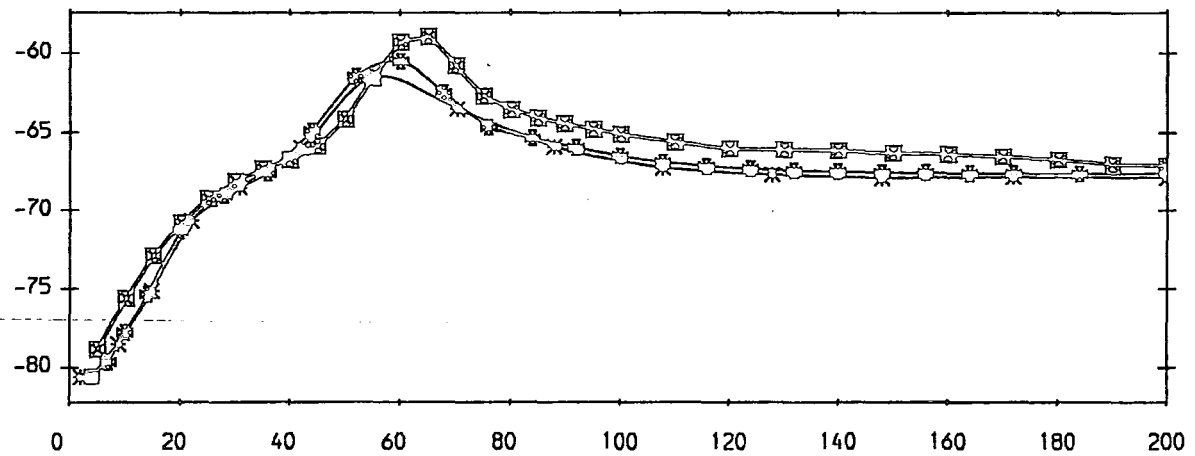


b) Total Pressure Loss Coefficient

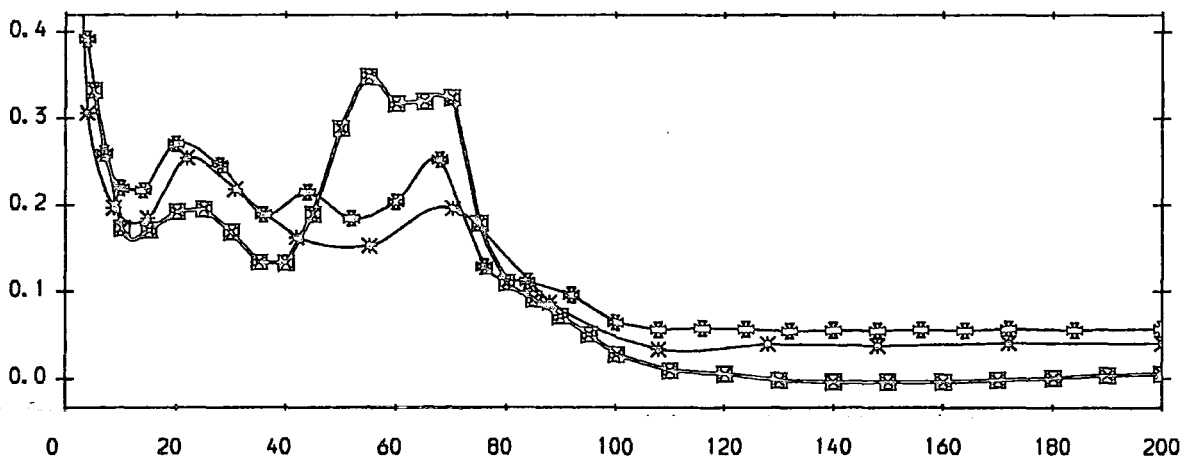


c) Secondary Kinetic Energy Coefficient

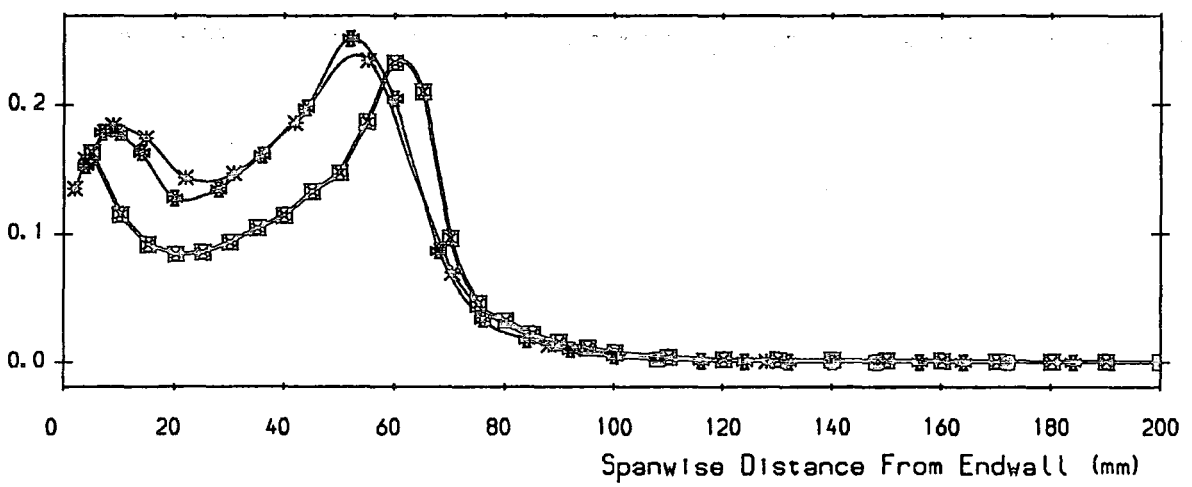


FIGURE 6.25 : Pitch Averaged Results For Slot B

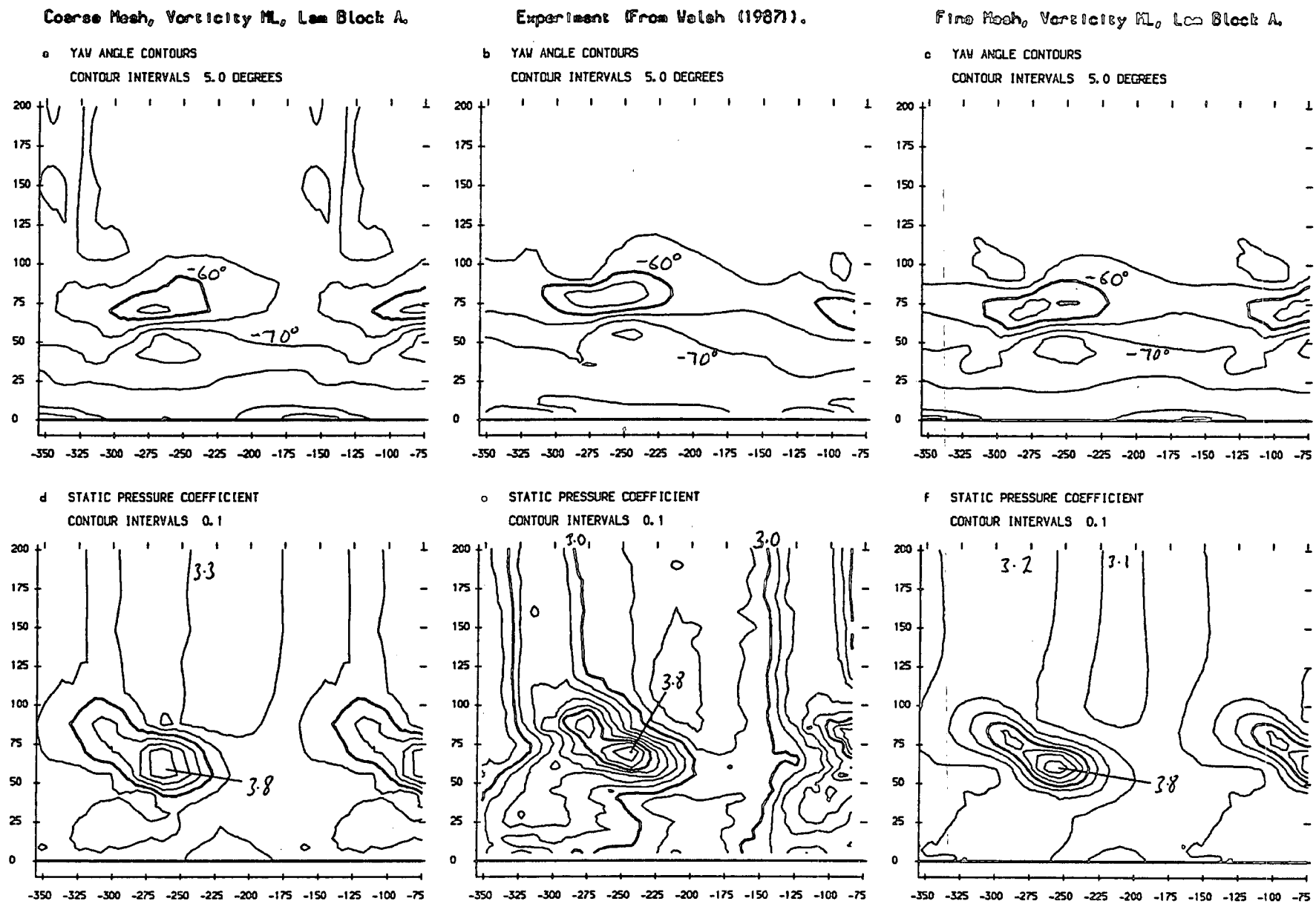


FIGURE 6.26 (a-f) : Area Plots For Slot 10

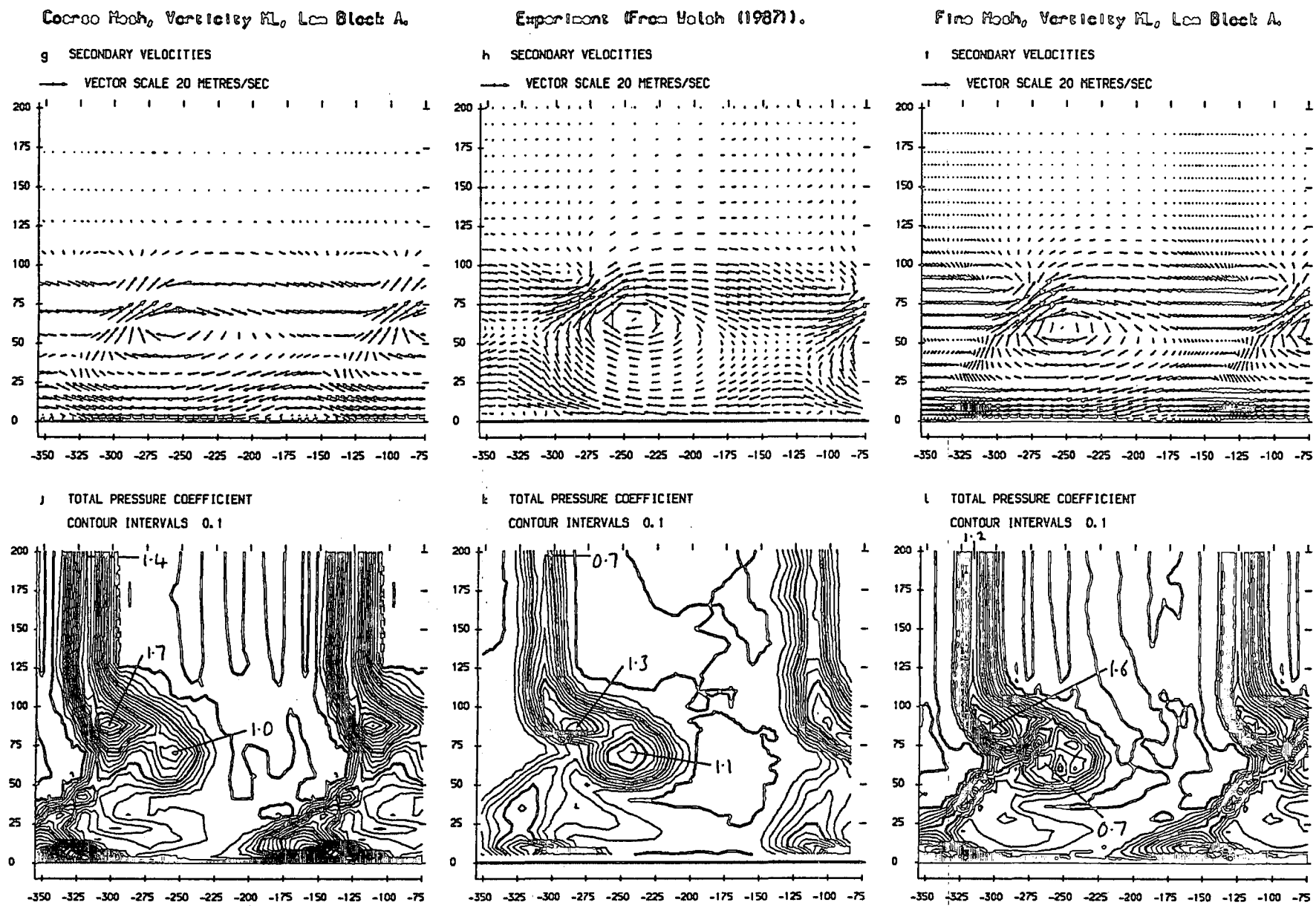


FIGURE 6.26 (g-l) : Area Plots For Slot 10

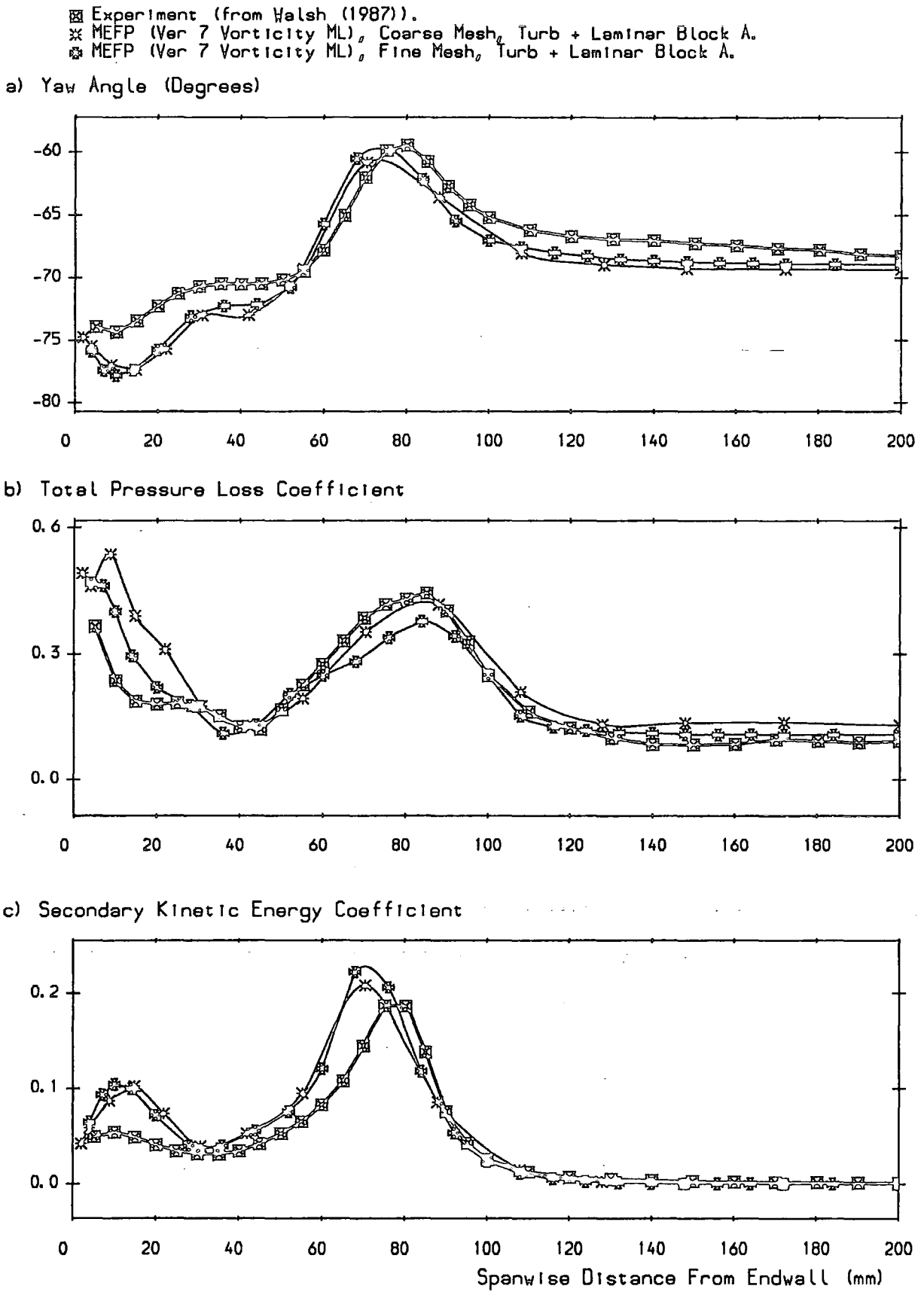


FIGURE 6.27 : Pitch Averaged Results For Slot 10

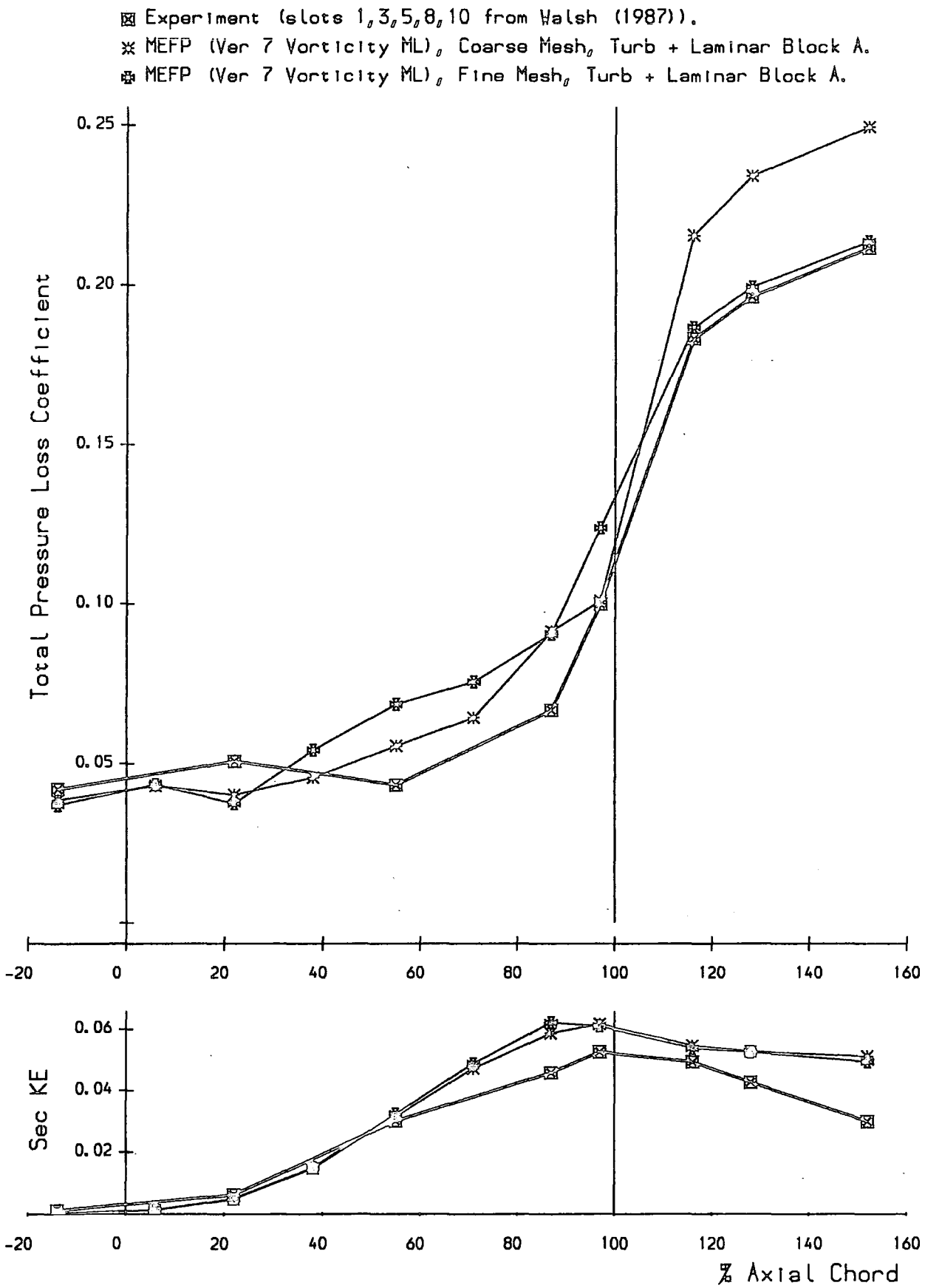


FIGURE 6.28 : Mass Averaged Loss & Secondary Kinetic Energy

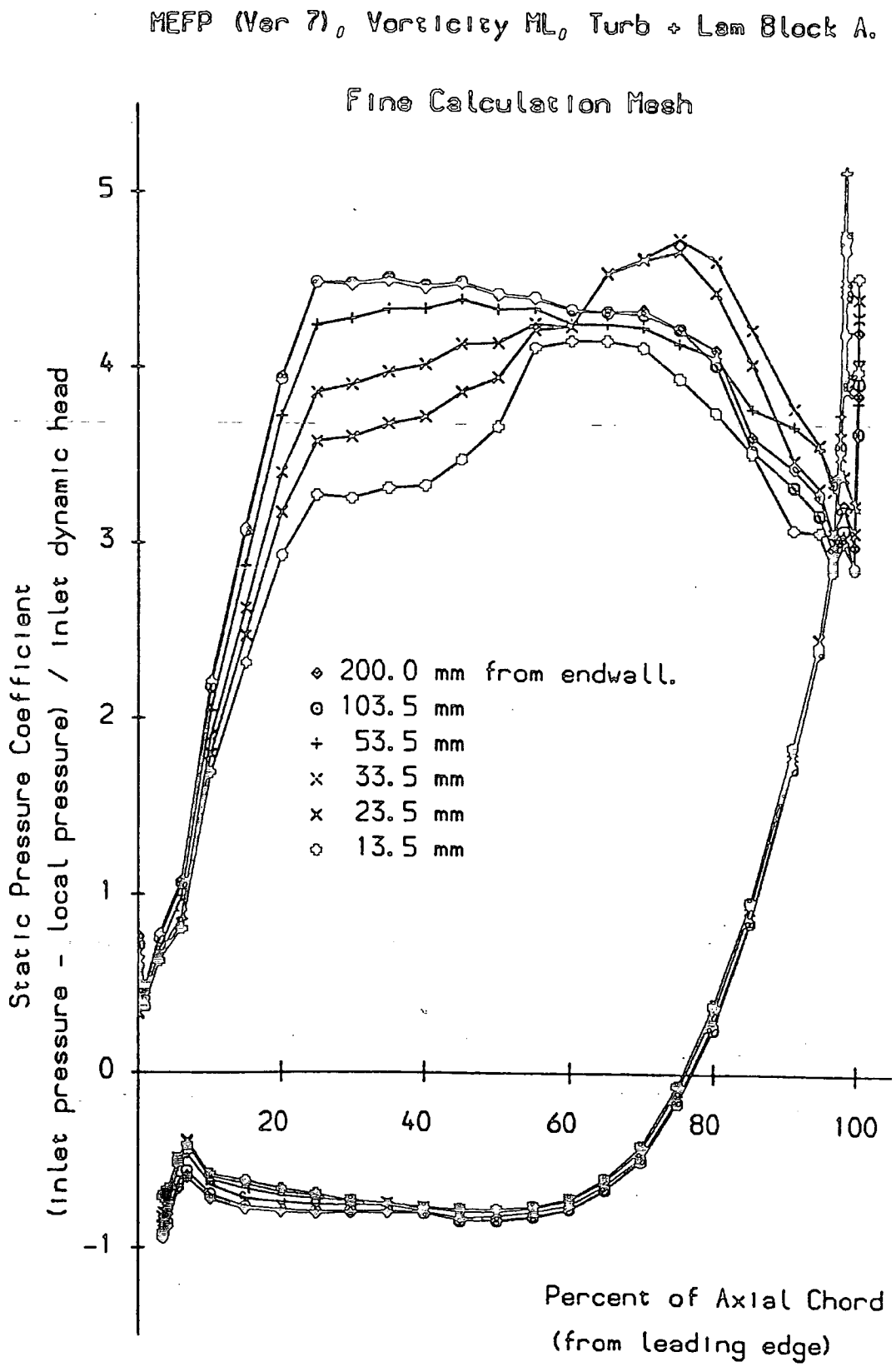


FIGURE 6.29 : Blade Static Pressure Distributions

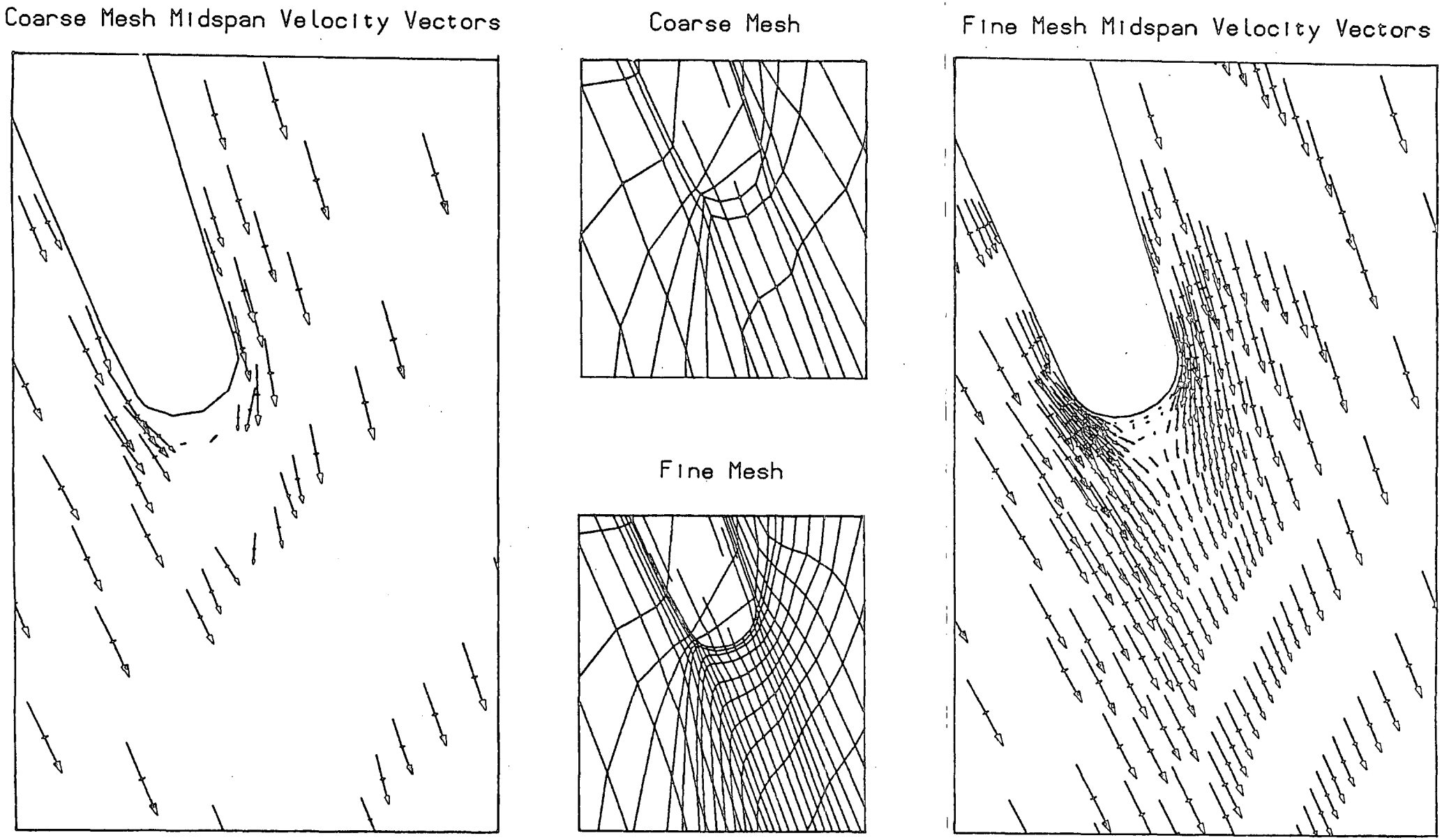


FIGURE 6.30 : Comparison of Coarse and Fine Mesh Trailing Edge Flows (Laminar Block A)

Fine Mesh$_0$ Vorticity ML$_0$ Laminar Block A$_0$ Inlet Angle = 42.75 Degrees

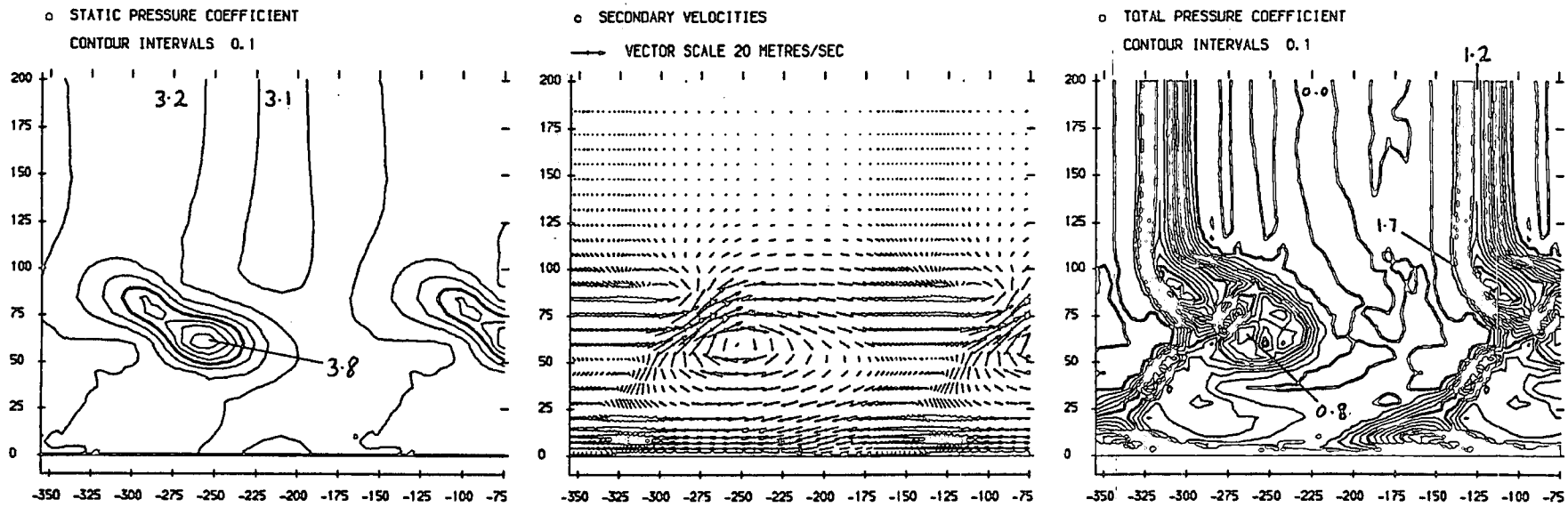


Fine Mesh$_0$ Vorticity ML$_0$ Laminar Block A$_0$ Inlet Angle = 45.90 Degrees

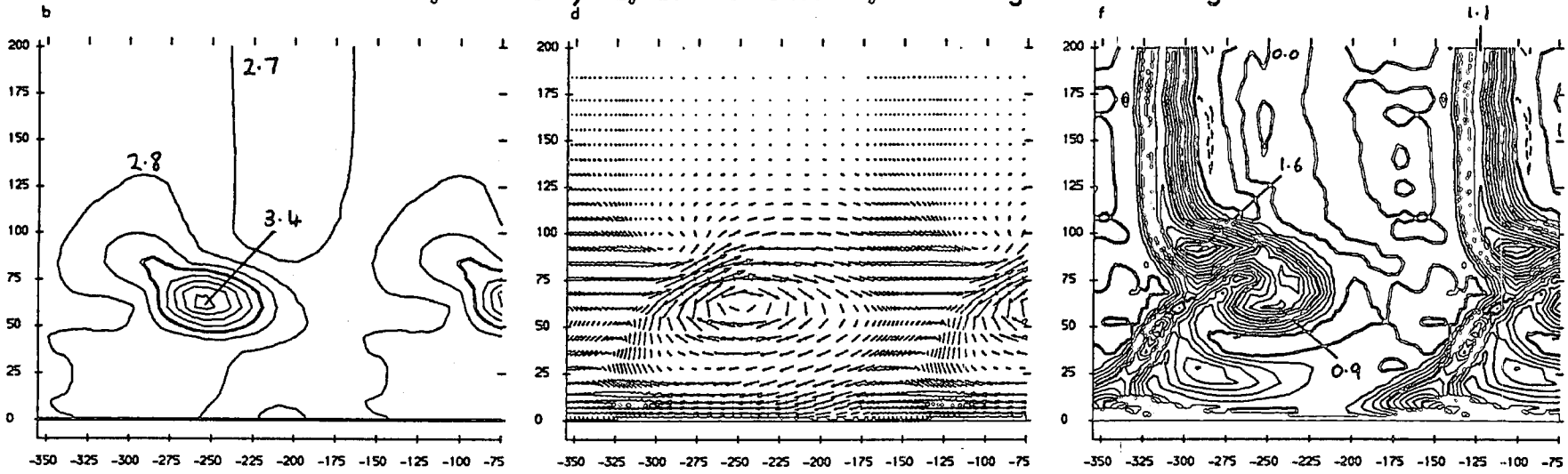


FIGURE 6.31 (a-f) : Area Plots For Slot 10

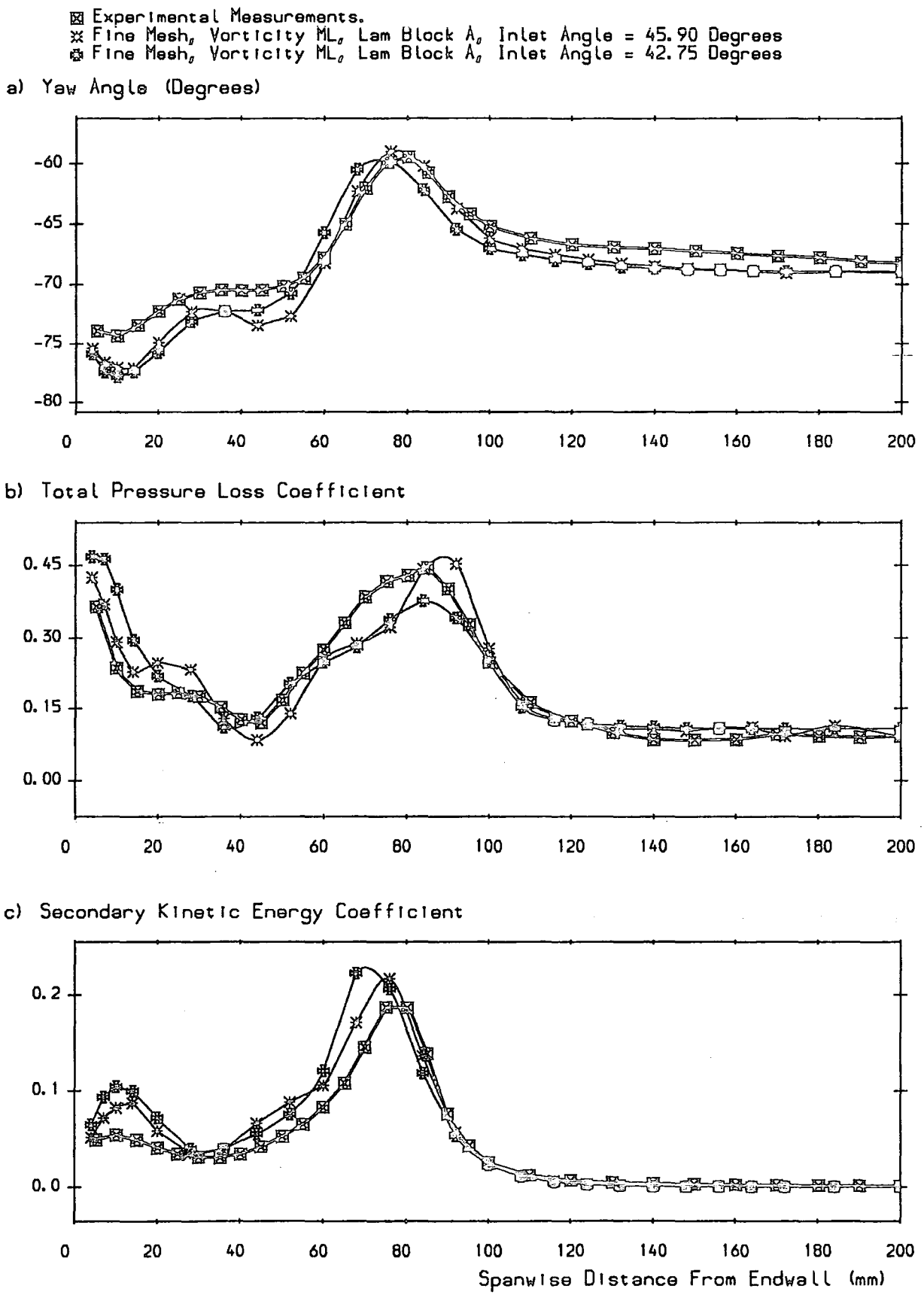


FIGURE 6.32 : Pitch Averaged Results For Slot 10

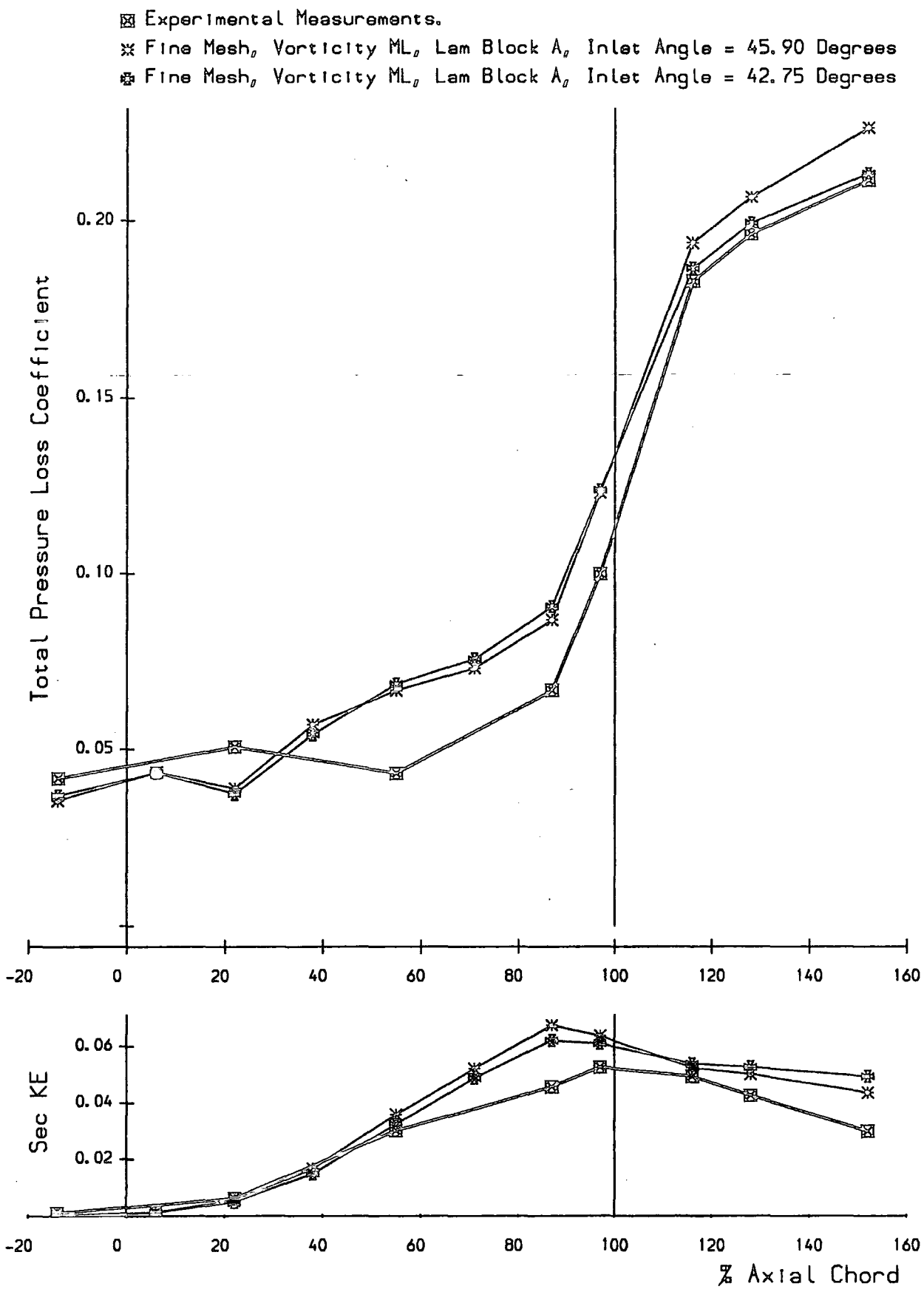


FIGURE 6.33 : Mass Averaged Loss & Secondary Kinetic Energy

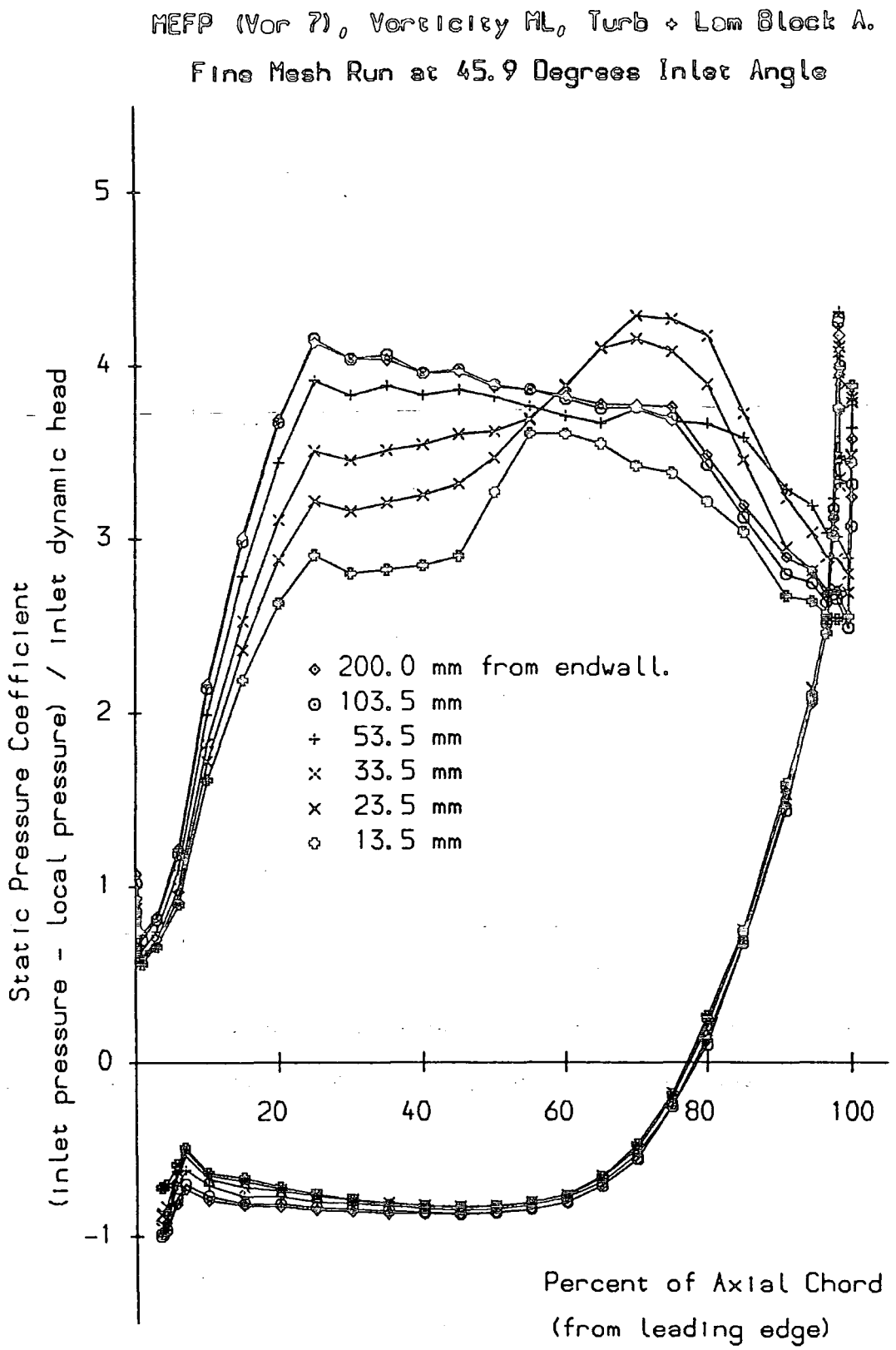


FIGURE 6.34 : Blade Static Pressure Distributions

# Chapter 7
# Experimental Results (JGC Test Case)

## 7.0 Introduction

This chapter describes experimental measurements of the flow in the Durham turbine cascade, with a turbulence generating grid mounted upstream in the working section of the wind tunnel. As the introduction of the turbulence grid changed the inlet flow to the cascade, experimental measurements obtained with it in place will be referred to as the 'JGC' test case in this thesis. Flow visualisation, blade surface pressures, and five hole probe traverses at slots 1 and 10 are compared with results obtained by Walsh (1987) for the 'JAW' test case. Results of using the x-probe hot-wire anemometry technique (section 4.4) to investigate the turbulent flow through the cascade are presented. Some calculations are then made from the data to determine eddy viscosities, and the contribution of the Reynolds stresses to the loss production process downstream of the cascade. Traverses using the rotatable single wire technique (section 4.5) to make measurements close to the endwall are also presented. Finally, results of a brief spectral survey of the turbulence within the flowfield are described.

## 7.1 Mean Flow Measurements

As discussed in Chapter 4, a turbulence grid was designed and fitted to the wind tunnel in order to raise the inlet turbulence level to 4.5%. There were two motivations for this change. Firstly the natural turbulence level which develops in the wind tunnel was reported by Gregory-Smith *et al* (1988) to be approximately 1.4%, which is smaller than the turbulence levels which are likely to exist in a real machine. Secondly, a small laminar separation bubble was reported by Walsh (1987) on the suction surface of the blade, and it was thought that this might be eliminated with a higher freestream turbulence. This would then make interesting comparison with the results

of Gregory-Smith *et al* (1988). They thought that the high turbulence levels in their cascade, and in particular the presence of a dominant frequency in the energy spectrum, could be the result of a large separation bubble on the suction surface of their blade. Hence, having fitted the turbulence grid, surface flow visualisation was used to test for the elimination of the suction surface separation bubble, and identify any major changes in the flowfield. Figure 7.1(a) shows the endwall flow visualisation result. This may be compared with the colateral case shown in Figure 5.19 of Walsh's thesis (1987), which is the equivalent result with no turbulence grid ('JAW' test case). There is very little difference between the 'JAW' and 'JGC' test case results. The only clear change is that the separation line of the horseshoe vortex lies closer to the blade leading edge in the 'JGC' test case. This is because the introduction of the turbulence grid thinned the inlet boundary layer at inlet to the cascade, as discussed in Chapter 4. Thus the viscous drag of the freestream fluid on the fluid close to the wall was increased. This tends to delay stagnation of the streamlines, and pull the horseshoe vortex closer into the obstruction which causes it. In an inviscid calculation, the horseshoe vortex can cause reverse flow to occur as far back as the inlet plane, even when this is some distance upstream.

The suction surface flow visualisation, shown in Figure 7.1(b), may be compared with the result for the 'JAW' test case shown in the colateral case of Figure 5.20 of Walsh's thesis. Again the two results are very similar, except that the vertical line in Walsh's result, which marked the position of the laminar separation bubble, is not present in Figure 7.1(b). Thus it is concluded that the higher inlet turbulence intensity has succeeded in suppressing the laminar separation bubble, and has forced the suction surface boundary layer to undergo smooth transition further upstream.

Measurements of the blade surface pressures are presented in Figure 7.2, which may be compared with Walsh's results for the 'JAW' test case which are reproduced in Figure 5.14. The new measurements indicate that the surface pressures from $50mm$ from the endwall to midspan, are almost identical in the first half of the blade passage. This was not the case in the

'JAW' test case, possibly indicating a slight radial variation in inlet conditions. The unloading of the blade in the first half of the cascade, as the endwall boundary layer is penetrated, is slightly reduced in the 'JGC' test case. This is probably because the endwall boundary layer at inlet to the cascade was thinner in this case. Also the peaks in the pressure coefficient which result from the action of the passage vortex on the suction surface, are reduced. This may indicate some reduction of the secondary flow intensity. However, the overall shape and positioning of various features, are very similar between the two results.

Results of a five hole probe traverse at slot 1 (14% upstream of the leading edge) are presented in Figure 7.3. Also plotted are results from Walsh (1987) for the 'JAW' test case. The yaw angle contours indicate the upstream effect of the blades, and are very similar for the two tests. The distortion of the yaw angles close to the endwall, is perhaps slightly reduced in the 'JGC' test case, possibly indicating a smaller horseshoe vortex. Static pressure contours also support the apparent similarity of the upstream flow for the two tests. However, the stagnation pressure loss coefficient contours reveal that the endwall boundary layer is thinner in the 'JGC' test case. As discussed in Chapter 4, this is believed to result from a 'jet' flow close to the endwall downstream of the turbulence grid. This is slowed by viscous interaction with the endwall, to form the observed boundary layer profile at inlet to the cascade. Table 7.1 presents details of the inlet boundary layer evaluated from pitch averaged results at slot 1 for the 'JAW' and 'JGC' test cases.

**Table 7.1 : Inlet Boundary Layer Characteristics**

| All Values are in $mm$ | 'JAW' Test Case | 'JGC' Test Case |
|---|---|---|
| 99% Thickness ($\delta$) | 39.0 | 37.4 |
| Displacement Thickness ($\delta^*$) | 5.6 | 4.2 |
| Momentum Thickness ($\theta$) | 3.2 | 2.2 |
| Shape Factor ($H = \delta^*/\theta$) | 1.8 | 1.9 |

The 'JGC' shape factor seems large for a turbulent boundary layer, but this is not a result of introduction of the turbulence grid as it was also large in the 'JAW' test case. Perhaps there may be some source of unsteadiness in the upstream flow which is causing the unusual boundary layer development. Pitch averaged results at slot 1 are presented in Figure 7.4 together with Walsh's results for the 'JAW' test case. There is some difference in the yaw angle within $20mm$ of the endwall, possibly indicating changes in the size of the horseshoe vortex. However, the main difference is in the loss distribution, which indicates the thinner endwall boundary layer in the 'JGC' test case.

Results of a five hole probe traverse at slot 10 (128% Cax) are presented in Figure 7.5. This may be compared with results obtained by Walsh (1987) for the 'JAW' test case, which are reproduced in Figure 5.9. The static pressure contours indicate less depression of static pressure in the vortex core for the 'JGC' test case. This also appears to produce a generally lower midspan static pressure. Also the yaw and pitch angles indicate slightly less secondary flow activity in the 'JGC' case, although the general shape and positioning of the features are similar to those measured previously by Walsh. The loss contours also look very similar, and appear to contain almost identical loss peaks. The secondary velocity vectors indicate that whilst the passage vortex location has not changed, it is slightly weaker. This is also illustrated by the lower values of streamwise vorticity contours, which were calculated using the method of Gregory-Smith *et al* (1987).

Figure 7.6 presents pitch averaged results at slot 10 for the 'JAW' and 'JGC' test cases. There is some discrepancy in the midspan flow angle for the two runs, which indicates the difficulty of relating probe angles to cascade coordinates. However the main difference in the yaw angle plot is the smaller magnitude of the over and under-turning in the 'JGC' test case. This is highlighted by the secondary kinetic energy curve which shows the 'JGC' test case to have a significantly smaller amount of secondary kinetic energy than the 'JAW' test case. However, losses in both cases are very similar, with the loss core in the 'JAW' test case being slightly bigger. This

is probably because it contains more inlet boundary layer loss than the 'JGC' test case. Figure 7.7 presents a plot of loss growth through the cascade for both tests. It is clear that although the inlet loss is lower in the 'JGC' test case the rise in loss across the cascade is approximately the same as for the 'JAW' test case. Also the secondary kinetic energy plot clearly shows a reduction in levels between the 'JAW' and 'JGC' test cases.

Table 7.2 : Mass Averaged Five Hole Probe Data

| | 'JAW' Test Case (from Walsh) | 'JGC' Test Case |
|---|---|---|
| Loss Coefficient (Slot 10) | 0.196 | 0.182 |
| - Midspan Loss Coefficient (Slot 10) | 0.090 | 0.097 |
| = Gross Secondary Loss (Slot 10) | 0.106 | 0.085 |
| - Inlet (Slot 1) Loss | 0.042 | 0.027 |
| = Net Secondary Loss (Slot 10) | 0.064 | 0.058 |
| Secondary KE Coefficient (Slot 10) | 0.043 | 0.026 |
| Sec KE + Loss Coefficients (Slot 10) | 0.239 | 0.208 |
| Mixed Out Loss Coefficient | 0.239 | 0.211 |
| - Midspan Mixed Out Loss Coeff | 0.095 | 0.100 |
| = Gross Mixed Out Secondary Loss | 0.144 | 0.111 |
| - Inlet (Slot 1) Loss | 0.042 | 0.027 |
| = Net Mixed Out Secondary Loss | 0.102 | 0.084 |
| Midspan Mixed Out Flow Angle | $-67.5°$ | $-66.7°$ |

Table 7.2 presents a breakdown of mass averaged quantities for both the 'JAW' and 'JGC' test cases. The introduction of the turbulence grid has possibly increased the profile loss slightly. However, as the accuracy of total pressure measurements is $\pm 0.005$, the increase of 0.007 is barely significant. The net secondary loss appears to have reduced slightly with the introduction of the grid, but again the comment about the accuracy of loss measurement applies. The rise in loss produced by the cascade (slot 10 loss minus slot 1 loss) is 0.154 for the 'JAW' test case, and 0.155 for the 'JGC' test case.

It can be seen in table 7.2 that there is quite a large drop in secondary kinetic energy between the 'JAW' and 'JGC' test cases. As mentioned in previous analyses, the mixed out loss is well represented by the sum of the loss coefficient and the secondary kinetic energy coefficient at a particular downstream plane. Hence the net mixed out secondary loss is lower in the case of the 'JGC' test, as less secondary kinetic energy was produced. There appears to be a small discrepancy in exit flow angle between the two tests of 0.8°. However, this is well within the experimental uncertainty of the measurements, which was estimated as ±1° for the five hole probe.

It might seem sensible that raising the inlet turbulence intensity, would tend to create more dissipation of the secondary flow, and hence result in a lower value of secondary kinetic energy. However, it could also be that the main effect is the differing thickness of the inlet boundary layer. Classical secondary flow theory suggests that reducing the inlet boundary layer thickness will result in less secondary kinetic energy at exit. As discussed in section 2.8, many workers have varied only the boundary layer thickness at inlet to their cascades, and have found that the rise in loss produced by the cascade was approximately constant. Although these workers did not present the resulting values of secondary kinetic energy, Moore (1985) has presented results of modelling the effects of varying inlet boundary layer thickness. He found that varying the inlet boundary layer thickness for the cascade of Langston *et al* (1977), results in a constant net loss, but different secondary kinetic energy. Similarly Figure 7.8 presents a plot of mass averaged loss and secondary kinetic energy for the Durham cascade, resulting from two runs of the Moore code (version 7). These two runs used the standard mixing length model, with laminar block A as described in Chapter 6 and shown in Figure 6.2(a). The only difference between the runs is the inlet boundary layer thickness, which has been tailored to fit the 'JAW' test case in one run, and the 'JGC' test case in the other. Clearly both runs predict a similar growth of loss across the cascade, but the secondary kinetic energy is considerably reduced in the 'JGC' test case with the thinner inlet boundary layer. Comparing with Figure 7.7 which shows the experimental results, it

can be seen that the prediction for secondary kinetic energy reduction is quite realistic. Thus the change in secondary kinetic energy is thought to be a result of thinning the inlet boundary layer, rather than raising the freestream turbulence.

The work of Harrison (1989) implies that a significant proportion of secondary loss might be generated by turbulent and viscous action on the endwall and suction surface. It might also seem logical that the overall loss could depend upon the magnitude of secondary velocities near to these surfaces. Thus the invariance of cascade loss with inlet boundary layer thickness, could indicate that the secondary flow near the solid surfaces is not greatly altered by the thickness of the inlet shear layer, even if the overall secondary kinetic energy changes. This suggestion will be investigated further, later in this chapter.

## 7.2 Hot-Wire Measurements at Slot 1 (-14% Cax)

Results of using the x-probe hot-wire anemometry technique (section 4.4) to traverse the flow at slot 1 are presented in Figures 7.9 (a-k). The yaw angle contours may be compared with those measured by the five hole probe, shown in Figure 7.3(b). The agreement between the two techniques is quite good. However the pitch angle contours indicate a region of high pitch angle at midspan in front of one of the blades. Although equivalent five hole probe results are not presented, they did not detect this feature. Hence it seems sensible that such an unlikely result, only found in front of one of the blades, and not detected by a more accurate measurement technique, should be attributed to experimental error. The secondary velocity vectors indicate that there is little secondary flow upstream of the blades, although the potential effect of the blades is clearly manifested in the total velocity magnitude contours. Measurements of turbulence quantities are shown in Figure 7.9 (f-k). It should be stressed that the scales for the contour plots are magnified compared with those for subsequent plots of the flow further downstream. The $\overline{u'v'}$ correlation shows very little activity except in the region

in front of the blades and next to the endwall which is probably associated with the horseshoe vortex. The $\overline{u'w'}$ correlation reveals generally negative values (positive shear stress) in the endwall boundary layer, which is to be expected of a colateral boundary layer flow. Values of turbulent kinetic energy rise as the endwall is approached, but only reach a value of 0.016, which is approximately 5% of the loss coefficient value of 0.31 (Figure 7.3(f)). The turbulence intensities show that the turbulence at midspan is fairly isotropic, and has an intensity of approximately 4.2% which is close to the design value of 4.5%. However the characteristics are quite different within the endwall boundary layer. The streamwise turbulence intensity ($\sqrt{\overline{u'^2}}$) increases most, to reach a level of approximately 8% of upstream velocity at $5mm$ from the endwall. The cross-passage turbulence intensity ($\sqrt{\overline{v'^2}}$) also rises within the boundary layer, but not as rapidly as the streamwise turbulence. The radial turbulence hardly changes as the endwall is approached, except for a small area which might be associated with the horseshoe vortex.

Pitch averaged results at slot 1 are compared with results of the five hole probe traverse in Figure 7.10. There appears to be a constant difference in yaw angle of approximately 0.6°, which is well within the estimated uncertainty of the results. The turbulent kinetic energy is much smaller than the loss (there is a factor of ten difference in scale for the two curves), and the secondary kinetic energy is also very small at this stage.

## 7.3 Hot-Wire Measurements at Slot 5 (55% Cax)

Results of a traverse of slot 5 with the x-probes, are presented in Figure 7.11 (a-k). The secondary velocity vectors reveal the passage vortex in a relatively early stage of development. It is located closer in to the endwall and suction surface than the vortex measured by Walsh (1987) for the 'JAW' test case. This might be due to the thinner inlet boundary layer in this work. The yaw angle contours show that the main secondary flow effects are still confined quite close to the endwall at this stage. Also it is clear that the yaw angles vary rapidly within $20mm$ of the endwall, indicating that the

endwall flow is highly skewed. The total velocity magnitude does not appear to decrease very much in this region however. The turbulence quantities are now very different to those at slot 1. Significant shear stresses are developing within the secondary flow, and the turbulent kinetic energy rises to 10-20% of inlet dynamic head in the endwall/suction surface corner. This corresponds to the region of separation of the passage vortex from the endwall. Comparing with the magnitude of the loss levels which Walsh measured at slot 5 for the 'JAW' test case, the turbulent kinetic energy only accounts directly for approximately 10-20% of the loss in the passage vortex. The turbulence intensities are also rising to values of 20% of inlet velocity. Thus there appears to be significant turbulence generation within the endwall region over the first half of the blade passage. Hence it seems likely that the process of formation of the passage vortex is giving rise to significant generation of turbulence. Gregory-Smith *et al* (1988) found similar turbulence levels within the secondary flow region of their rotor cascade. However the freestream turbulence intensity in their test was only 1.4% of upstream velocity. Thus it appears that the higher inlet turbulence intensity in this test has had little effect upon the turbulence levels which are generated within the secondary flows. The $\overline{u'v'}$ correlation (streamwise/cross-passage) is positive throughout the traverse, corresponding to negative values of shear stress. This is to be expected away from the suction surface boundary layer as the cross-passage pressure gradient gives rise to a large velocity gradient in the tangential direction (Figure 7.11(e)). Within the suction surface boundary layer, the shear stress should be positive, but the traversing does not approach the suction surface closely enough to show this. The $\overline{u'w'}$ correlation shows a sign change across the vortex region, but at this stage generally exhibits lower levels than the $\overline{u'v'}$ correlation.

Pitch averaged results for slot 5 are shown in Figure 7.12. It is clear that most of the secondary flow activity is still concentrated near to the endwall at this stage. The over-turning close to the endwall is very large, and is accompanied by a peak in turbulent kinetic energy. However, beyond $40mm$ radially, the flow is essentially undisturbed by the secondary flows.

Figure 7.13 (a-h) presents results of traversing close to the endwall using the rotatable single wire technique described in section 4.5. The grid of measurement locations shows that the traversing was extended to $10mm$ from the endwall to provide some overlap with the x-probe measurements. The yaw angle contours agree well with those shown in Figure 7.11(b), and indicate a very large degree of skew in the endwall flow. The total velocity magnitude contours also tie up quite well with the x-probe measurements, and show that the velocity hardly varies between 1 and $10mm$ from the endwall. Thus any normal concept of a boundary layer must be confined to within $1mm$ of the endwall (0.25% span) at this stage. The turbulence quantities, $\overline{u'v'}$, $\sqrt{\overline{u'^2}}$, $\sqrt{\overline{v'^2}}$ all agree well with the x-probe measurements, and indicate that freestream turbulence levels are being brought into the endwall region on the pressure side of the passage. This does not show that the endwall flow is laminar, but as high turbulence levels are not being generated on the pressure side of the passage, it is possible that there is a very thin laminar boundary layer in this region. Harrison (1989) found the endwall boundary layer to be laminar over a large proportion of the endwall, towards the pressure side of the passage in his turbine cascade. However, if such a laminar boundary layer exists here it must be extremely thin. As the measurement technique could only solve for the square of radial velocity, all spanwise velocities are taken as positive, and hence the secondary velocity vectors appear to point in the wrong direction radially, towards the pressure side of the passage. The radial turbulence intensity was not measured by the single wire, and so the turbulent kinetic energy is calculated by assuming that the radial turbulence intensity is equal to the average of the streamwise and cross-passage intensities. This is probably reasonably accurate away from the endwall, but becomes less so on close approach to it. However, the turbulent kinetic energy contours appear to agree reasonably well with the corresponding x-probe measurements in the region $5 - 10mm$ from the endwall. They also clearly indicate that the flow on the suction side of the passage is quite turbulent, but to the pressure side there are only freestream turbulence levels.

## 7.4 Hot-Wire Measurements at Slot 8 (97% Cax)

Results of an x-probe traverse at slot 8 are presented in Figure 7.14. By this stage the secondary flow effects extend to at least $100mm$ from the endwall. The centre of the passage vortex has moved up and away from the suction surface compared with its position at slot 5. However it is still approximately $15mm$ closer to the endwall than it was in the 'JAW' test case. The passage vortex is generally quite turbulent with individual turbulence intensities reaching 20% of inlet velocity. Near to the suction surface, at about $60mm$ from the endwall there appears to be a region of considerable turbulence activity. This corresponds to the region in which the passage vortex separates from the suction surface, and so might include turbulence which has been convected from the suction surface boundary layer/passage vortex interaction. The $\overline{u'w'}$ correlation shows a rapid sign change in this separation region, but is generally quite small elsewhere. The $\overline{u'v'}$ correlation is still generally positive, although the velocity magnitude contours indicate that the cross-passage velocity gradient has largely disappeared. Significant $\overline{u'v'}$ shear stress is associated with both the passage vortex core, and the suction surface separation. Indeed in the separation region the velocity magnitude contours indicate that the sign of the correlation is opposite to that which would be expected from a Boussinesq eddy viscosity model. The streamwise turbulence is also large over the whole of the suction surface. This may be linked with deceleration of the suction surface flow towards the trailing edge, particularly close to the endwall, where the surface pressure coefficient peaks (Figure 7.2) indicate that quite severe deceleration might be occurring. This could be a significant process behind the rapid rise in loss which is usually observed in the latter half of rotor cascades (e.g. Langston *et al* (1977)).

Pitch averaged results at slot 8 are presented in Figure 7.15. Comparing with the results at slot 5 shown in Figure 7.12, it can be seen that the secondary flow has spread radially from the endwall. There is still quite a large over-turning of the flow within $40mm$ of the endwall, but a significant under-turning peak is now also evident at $60mm$ radially. The turbulent

kinetic energy has formed a distinct core, and the secondary kinetic energy exhibits a sharp peak at approximately $55mm$ from the endwall.

The endwall flow measurements obtained with the single wire technique, are presented in Figure 7.16. Again agreement with the x-probe measurements in the region $5 - 10mm$ from the endwall is reasonable. The yaw angle contours indicate that the level of skew in the endwall flow is now very much reduced from that which was observed at slot 5. However, the total velocity is still almost constant up to $1mm$ from the endwall, although a sharp reduction in velocity is apparent in the endwall/suction surface corner, which is probably associated with the counter vortex to be found in this region. This is accompanied by a region of intense negative $\overline{u'v'}$ correlation, which would agree with an eddy viscosity concept. The endwall flow appears to be generally more turbulent at slot 8, and this is in keeping with the results of Harrison (1989) who observed transition of the endwall flow occurring upstream of the trailing edge in his cascade.

## 7.5 Hot-Wire Measurements at Slot 10 (128% Cax)

Figure 7.17 presents results of an x-probe traverse at slot 10. Mean flow data can be compared with corresponding five hole probe results for the 'JGC' test case, which are shown in Figure 7.5. The pitch and yaw angle contours generally compare very well, as do the secondary velocity vectors. The loss core and blade wakes show up clearly in the total velocity magnitude contours as areas of velocity deficit. They are also clearly apparent in the turbulence quantities. The streamwise and cross-passage turbulence intensities reach maximum values of 20% of upstream velocity. The radial turbulence intensity has grown larger than the other two, to peak at 30% of upstream velocity within the loss core. The turbulent kinetic energy is concentrated in the passage vortex, with relatively low levels within the blade wake. This is consistent with the results of Gregory-Smith *et al* (1988) who observed that the wake turbulence appeared to dissipate rapidly downstream of their cascade, whilst the turbulence levels within the loss core were maintained.

Both the shear stresses which are measured with the x-probe technique, appear to change sign across the loss core. The $\overline{u'v'}$ shear stress also changes sign across the wake, in keeping with the sign of the velocity gradients and a positive eddy viscosity. However most of the passage vortex now exhibits negative $\overline{u'v'}$ correlation values. Thus the correlation has changed sign between slots 8 and 10. This is somewhat surprising, and so terms in the shear stress convection equation were approximately evaluated at slot 8. Details are presented in Appendix B, but it was found that the convection equation does appear to support a change in sign of the $\overline{u'v'}$ correlation between slots 8 and 10. As mentioned earlier, the dominant velocity gradient within the blade passage is imposed by the large turning angle of the blade and its associated cross-passage pressure gradient. This tends to result in positive values of the $\overline{u'v'}$ correlation within the blade passage. Downstream however, the velocity gradients in the passage vortex are only a result of the vortex motion, and its interaction with the flow from adjacent blade passages. As the secondary flow regions are generally areas of velocity deficit (as indicated in the total velocity magnitude contours), the shear stresses will tend to change sign across them, as observed. Some support for the change in sign of the $\overline{u'v'}$ shear stress as the flow proceeds downstream may be gained from the published literature. Moore *et al* (1986) found negative values of the $\overline{u'v'}$ correlation within the loss core downstream of their cascade. Zunino *et al* (1987) found positive values in the loss core with negative values in the suction surface corner, at a plane across the throat of their cascade. Unfortunately they did not show shear stress measurements downstream.

Comparing the turbulence levels found here with those of other workers, Zunino *et al* (1987) found slightly lower turbulence levels in the vortex core (turbulent kinetic energy approximately 0.06-0.07) but the levels on the endwall were a little higher. Gregory-Smith *et al* (1988) seem to have slightly higher turbulence levels downstream of their cascade, particularly in the cross-passage direction. They thought that these high levels might be associated with the large laminar separation bubble on their blade, or the large suction surface diffusion. Both of these effects were reduced in this test, and so

might explain the slightly lower turbulence levels here. Moore *et al* (1988) found generally similar turbulence levels within the loss core to those reported here. However their wake turbulence was somewhat larger, and this may be because their measurement plane was closer to the trailing edge (10% Cax downstream) than slot 10 (28% Cax downstream).

Pitch averaged results at slot 10 are also presented in Figure 7.18, together with the five hole probe data. There is some small disagreement in midspan angle, but in general the agreement between the two measurement techniques is good. This is also evident in the secondary kinetic energy curve, giving confidence in the results obtained. The turbulent kinetic energy and loss distributions are clearly correlated, but the turbulent kinetic energy is much smaller than the loss (the curves are plotted on different scales).

Endwall flow data at slot 10 obtained with the single wire technique, is shown in Figure 7.19. The yaw angles indicate the presence of the small counter vortex on the endwall at tangential coordinates -100 and -300. Some evidence for this may also be seen in the secondary velocity vectors, although the positive radial velocities can make interpretation difficult. The total velocity magnitude contours are beginning to indicate the growth of a more usual type of boundary layer flow, although it is still only a few millimetres thick. The turbulence quantities also indicate that the endwall flow is quite turbulent. This agrees with the results of Harrison (1989), who found the endwall boundary layer to be turbulent downstream of his cascade. In particular here, the streamwise turbulence is rising to considerable levels near the endwall. This is to be expected of a turbulent colateral boundary layer flow.

## 7.6 Turbulent Kinetic Energy, Secondary Kinetic Energy, and Loss

The results of the x-probe traverses were mass averaged over the traverse planes. Figure 7.20 shows a graph of mass averaged turbulent kinetic energy coefficient, and secondary kinetic energy coefficient at the various axial positions through the cascade. Also shown are the results of five hole probe

traverses for the 'JAW' test case (no turbulence grid) and the 'JGC' test case. It is clear that the turbulence grows steadily through the cascade, but at a much lower level than the loss. Indeed at slot 10 the turbulent kinetic energy (0.029) only accounts directly for 16% of the loss (0.182). Moore *et al* (1986) found that 23% of the loss in their cascade appeared as turbulent kinetic energy, whereas Zunino *et al* (1987) found this ratio to be 10%, and Gregory-Smith *et al* (1988) 17%. Thus the value found here appears to be in accord with other results. Zunino *et al* (1987) expressed the opinion that although only a small fraction of the loss could be accounted for directly as turbulent kinetic energy, this did not indicate that some process other than the turbulent stresses was causing the development of loss. Instead they believed that the rate of viscous dissipation of the turbulence approximately matched the rate of its generation, thus preventing any large build up of turbulent kinetic energy.

Returning to Figure 7.20, it can be seen that the secondary kinetic energy is considerably reduced in the 'JGC' test case. As discussed previously, this is believed to be a result of the thinner inlet boundary layer in this case. The agreement between results at slot 10 obtained with the five hole probe, and the hot-wire measurements, also serves to give confidence in the accuracy of the results. As mentioned previously many workers have found that the net cascade loss is not very dependent upon the inlet boundary layer thickness. Also it appears that the changes between the 'JAW' and 'JGC' test cases, and modelling results, suggest that the kinetic energy of the secondary flow is quite strongly dependent on the endwall boundary layer at inlet. This is a little surprising as it might be thought that the magnitude of secondary velocities close to solid surfaces would contribute to the secondary loss. Indeed Gregory-Smith (1982) recognised this in his loss model. The downstream loss was modelled as the sum of three components. These were the inlet boundary layer loss, the loss due to the growth of a new boundary layer on the endwall, and an extra secondary loss. This extra secondary loss was assumed to be equal to the secondary kinetic energy predicted by classical secondary flow theory. Figure 7.21 presents contours of secondary

kinetic energy at slots 5, 8, 10 for the 'JAW' test case (from Walsh (1987)) and the 'JGC' test case. Two sets of contour intervals are used. The broken contours cover the range 0.0 to 0.1, and are in steps of 0.02. The full contours cover the full range of data values, and are in steps of 0.1. At slot 5, the contours show the majority of the secondary kinetic energy to be located in a region near to the endwall. Very close to the endwall, there is more secondary kinetic energy in the 'JAW' test case, with the thicker inlet boundary layer. As the vortex rotates, and convects the inlet boundary layer up the suction surface, the secondary kinetic energy contours are also convected. By slot 8 there is a clear secondary kinetic energy core, centred at the position where the passage vortex separates from the suction surface. Some more secondary kinetic energy has also developed on the endwall. Although there is generally more secondary kinetic energy in the 'JAW' test case than in the 'JGC' test case, the values close to the endwall are almost identical, and on the suction surface similar levels also seem likely. By slot 10 there is a distinct secondary kinetic energy core, which is centred between the centre of the passage vortex and the counter vortex which is associated with the blade shed vorticity (as described by Walsh and Gregory-Smith (1989)). The levels of secondary kinetic energy near to the endwall are not very different between the two cases, when compared with the magnitude of the levels which are seen in the secondary kinetic energy core. Thus it seems that the effect of the inlet boundary layer thickness is to determine the amount of secondary kinetic energy which is initially imparted to the endwall boundary layer. This is rolled up into a core, which is convected up the suction surface. Thus the secondary kinetic energy levels close to much of the suction surface and endwall, might be little effected in the latter half of the blade passage by the thickness of the endwall boundary layer at inlet.

## 7.7 Frequency Spectra

As described in section 4.6, a spectral analysis of hot-wire signals was performed at various locations in the flowfield. Two typical curves are shown

in Figure 7.22. These show the power density of the hot-wire signal versus frequency. Both curves were obtained at slot 8, Figure 7.22(a) being for a wire placed in the high turbulence region near the suction surface separation line (coordinate (-140,65) in Figure 7.14(h)). The second curve shows the spectrum over a much smaller frequency range at midspan and mid-pitch of slot 8. In the suction surface separation region, there is a steady decay in power density over the frequency range $0 - 20kHz$, with no dominant frequencies being detected. In the second curve however, the turbulence levels are generally much lower, and there is a clear peak at $15.2Hz$. This peak was detected at all points in the flowfield where it was not swamped by higher turbulence levels, and was found both upstream and downstream of the cascade. This unexpected feature was not detected by Walsh (1987) in the earlier Durham turbine cascade described by Graves (1985). It is possible that the cause of the discrete frequency is an organ resonance in the wind tunnel. For a sound speed of $340ms^{-1}$, and a frequency of $15.2Hz$, a wavelength of $22.5m$ would be expected. The length of the wind tunnel is almost exactly $5.6m$ from the fan to the cascade, which supports the idea of a quarter wavelength at $15.2Hz$ with an anti-node at the cascade exit. In none of the measurements was any evidence found for an energy peak at $32.5Hz$ as detected by Gregory-Smith *et al* (1988). They observed this peak only in the high turbulence regions of the flow downstream of their cascade. Their blade had similar inlet and outlet angles to the blade used here, similar overall dimensions, and was run at an identical Reynolds number. However their blade had a large suction surface diffusion from about 50% axial chord with an associated laminar separation bubble. As mentioned previously, they also found slightly larger turbulence levels downstream of their cascade particularly in the cross-passage direction. This might be associated with the large suction surface diffusion present in their cascade. Thus it seems possible that an instability due to the large diffusion, or the separation bubble may have effected their flow.

## 7.8 Eddy Viscosities and Dissipation Rates

Since all the turbulence models which are tested in this thesis use the Boussinesq eddy viscosity hypothesis, it was decided to calculate eddy viscosities ($\epsilon_{ij}$) from the experimental shear stresses, as defined by:-

$$\epsilon_{ij} = \frac{-\rho\overline{u_i' u_j'}}{\frac{\partial \overline{U_i}}{\partial x_j} + \frac{\partial \overline{U_j}}{\partial x_i}} \tag{7.1}$$

Clearly before the eddy viscosities may be calculated, the partial derivatives of velocity must be determined. This calculation was based upon the method described by Gregory-Smith *et al* (1987) for obtaining vorticity from experimental data. Bi-cubic splines were fitted to the data, and used to evaluate gradients of velocity and stagnation pressure in the radial and tangential directions. Axial gradients were then calculated using the incompressible Helmholtz equation. The continuity equation enabled determination of the final partial derivative, and these could then be rotated to the hot-wire coordinates in which the Reynolds stresses were measured. The inverse procedure of determining the components of the Reynolds stress tensor in cascade coordinates was not possible, as one of the shear stresses ($\overline{v'w'}$) was not measured. Since the above method requires a measurement of total pressure over the traverse plane, the calculations could only be performed for traverses of slots 1 and 10 where five hole probe results were available. Over large regions of the flowfield, the denominator in the eddy viscosity definition approaches zero. Thus the calculation procedure was forced to yield a value of zero for eddy viscosity when the denominator fell below a cut-off value, and the shear stress was also small. If the shear stress was not small, but the denominator approached zero, then interpolation between neighbouring points was performed. Thus the final results should be treated with some caution.

The experimental measurements of two of the shear stresses ($\overline{u'v'}$, and $\overline{u'w'}$) are compared with eddy viscosities calculated from them in Figure 7.23. Also shown are the measurements of turbulent kinetic energy. The eddy viscosities are divided by the laminar viscosity, and show maximum levels of

around 2000. The calculations from both shear stresses produce most eddy viscosity in the loss core region, where the turbulent kinetic energy is highest. Both shear stresses yield similar values in this region, and the $\overline{u'v'}$ calculation also shows some eddy viscosity within the wake. The $\overline{u'w'}$ calculation was too poorly conditioned to detect such a level of eddy viscosity in the wake. Thus it appears that at slot 10, an isotropic eddy viscosity is a reasonable approximation. However as mentioned previously, at slot 8 the $\overline{u'v'}$ shear stress implies a negative value of eddy viscosity in some regions. Thus the application of an eddy viscosity model within the blade passage may be less realistic.

The partial velocity derivatives may also be used to calculate terms in the kinetic energy equation for the flow of a turbulent fluid (Hinze (1975), p72). Terms for the production of turbulent kinetic energy are evaluated from the Reynolds stress measurements via the equation:-

$$-\rho \quad \overline{u_i' u_j'} \quad \frac{\partial \overline{U_i}}{\partial x_j} \tag{7.2}$$

The rate of viscous dissipation of mean flow kinetic energy may also be determined by the equation:-

$$\mu \left[ \frac{\partial \overline{U_i}}{\partial x_j} + \frac{\partial \overline{U_j}}{\partial x_i} \right] \frac{\partial \overline{U_i}}{\partial x_j} \tag{7.3}$$

The rates of dissipation of mean flow energy are made dimensionless by dividing by the inlet dynamic head, and multiplying by the ratio of axial chord to axial velocity. This expresses the rates as 'the fraction of inlet dynamic head which would be lost if the rate were to be maintained over a distance of one axial chord, whilst travelling at the axial velocity'. This is consistent with the definition used by Moore *et al* (1986) in their work on turbulence effects downstream of a turbine cascade.

The rate of dissipation of mean flow energy by molecular viscosity is plotted in Figure 7.23(f). The corresponding total dissipation rate due to the five terms of the Reynolds stress tensor which were measured is shown in Figure 7.23(g). It can be seen that the dissipation rate due to the five terms of the Reynolds stress tensor which were measured, is generally

two orders of magnitude greater than that due to molecular viscosity. The contributions of the individual components of the Reynolds stress tensor to the overall dissipation rate, are shown in Figure 7.23(h-l). By far the largest rates are produced by the normal stresses in the cross-passage and spanwise directions. These can either act to extract energy from the mean flow, or return turbulent kinetic energy to the mean flow. The streamwise normal stress has only a minor effect, as the streamwise velocity gradient downstream of the cascade is small. This may not be the case within the blade passage, where there is strong acceleration of the flow. The $\overline{u'v'}$ shear stress produces some dissipation of the mean flow energy within the loss core and blade wake regions, but the $\overline{u'w'}$ stress has only a small effect. Shear stresses are usually dissipative, acting to produce turbulent kinetic energy from mean flow energy, since they normally change sign with velocity gradient. The dissipation rates shown in Figure 7.23 have been mass averaged over the traverse plane, and the results are presented in Table 7.3.

**Table 7.3 : Mass Averaged Dissipation of Mean Flow K.E.**

| 'JGC' Test Case | % $\frac{1}{2}\rho V_0^2 \cdot \frac{V_{ax}}{C_{ax}}$ |
|---|---|
| Rate of Viscous Dissipation | 0.02 |
| Total Rate of Turbulence Production (less $\overline{v'w'}$ term) | 1.92 |
| Rate of Turbulence Production by $\overline{u'^2}$ | 0.13 |
| Rate of Turbulence Production by $\overline{v'^2}$ | -0.06 |
| Rate of Turbulence Production by $\overline{w'^2}$ | 0.67 |
| Rate of Turbulence Production by $\overline{u'v'}$ term) | 1.05 |
| Rate of Turbulence Production by $\overline{u'w'}$ term) | 0.13 |

It is clear that the viscous dissipation of mean flow kinetic energy is much smaller than that due to turbulent energy production. The net rate of production due to the $\overline{v'^2}$ component is small and negative, despite the high local values which were apparent in Figure 7.23(k). However the radial normal stress $\overline{w'^2}$ does have a significant net effect, although not as large as that due to the $\overline{u'v'}$ shear stress. Contour plots of the partial velocity

derivatives at slot 10 in both cascade, and hot-wire coordinates are presented in Appendix C for the convenience of those who may be interested.

Detailed comparison of the effects of the individual Reynolds stresses may be made with results presented by Moore *et al* (1986) for the flow downstream of their turbine cascade. This was a replica of the cascade investigated by Langston *et al* (1977), although the inlet boundary layer was thicker in the work of Moore *et al* (1986). General agreement is found with results presented here, except for the $\overline{u'^2}\frac{\partial \overline{U}}{\partial x}$ term which they found to be significant. However their measuring plane was closer to the trailing edge than slot 10 (10% Cax as compared with 28% Cax). This may mean that streamwise gradients were greater in their work, due to the flow being less mixed. The overall dissipation rate given in Table 7.3 may be compared with the rate of loss production at slot 10 if it is assumed that in Figure 7.20 the gradient of the loss growth curve downstream of the cascade is the same for the 'JAW' and 'JGC' test cases. The loss coefficient growth rate is 7.9% per axial chord, whereas the total rate of turbulence production is only 1.92% per axial chord. However this excludes two components which Moore *et al* (1986) found to be significant. As the $\overline{v'w'}$ shear stress was not measured in this work its effects could not be determined. Moore *et al* (1986) found this stress contributed 31% of the total loss production rate in their cascade. Also no estimate has been made of the effect of $\overline{u'w'}$ in the near wall region. Again Moore *et al* (1986) suggested that this was significant, contributing 30% to the total rate. Thus even though these contributions may be relatively smaller here, due to the higher aspect ratio and traverse plane location, the value presented in Table 7.3 seems reasonable. The fact that the turbulent kinetic energy does not appear to be growing as rapidly as the loss, suggests that it is being rapidly dissipated by viscous action.

Hence it appears that downstream of the cascade, loss is produced principally by turbulent Reynolds stresses, and that direct viscous action is almost negligible. Unfortunately the equivalent calculations cannot be made at slots 5 and 8, as the necessary total pressure traverses are not available. The results of Moore *et al* (1986) suggest that downstream of the cascade,

approximately 60% of the loss is produced away from the endwall in the shear layers. The results found here do not appear to disagree with this conclusion. However within the blade passage, where significant losses may also be generated on the suction surface, the relative importance of the loss production due to the separated shear layers may be reduced.

## 7.9 Conclusions

Analysis of mean flow results appears to indicate that the higher freestream turbulence in this test has little effect upon the secondary loss or kinetic energy of the secondary flow. This may be because the fluid in the loss core originates in the inlet boundary layer, where turbulence levels are less influenced by the freestream turbulence intensity. However changes were observed between the level of secondary kinetic energy which was produced by the 'JAW' and 'JGC' test cases. This is thought to be a result of differing inlet boundary layer thickness in this case as compared with the 'JAW' test case. Also the increased inlet turbulence does successfully suppress the small laminar separation bubble which previously existed on the blade's suction surface. Thus the suction surface boundary layer now undergoes transition earlier, apparently leading to slightly greater profile loss.

High turbulence energy is associated with the loss core and passage vortex region, and also where separation lines on the endwall and suction surface feed loss into the main flow. The streamwise/radial shear stress $\overline{u'w'}$ changes sign across the position of the suction surface separation line. Within the blade passage the streamwise/cross-passage shear stress $\overline{u'v'}$ is generally negative in the loss core due to the strong cross-passage velocity gradient. Downstream of the cascade it responds to local velocity gradients within the secondary flow and is thus observed to have changed sign over much of the loss core. This change in sign from the flow within the blade passage to the flow downstream is supported by consideration of the shear stress transport equation. Spectral studies indicate no unusual features of the turbulence except that there is a low frequency organ resonance within the wind tunnel.

Where the turbulence was high, no dominant frequencies were found. This contrasts with the results reported by Gregory-Smith *et al* (1988), who found a low frequency peak downstream of their cascade. The lack of such a feature in this study, might be due to the lower suction surface diffusion of the blade tested here, or the absence of the large separation bubble which was associated with this diffusion.

Traverses close to the endwall show that the new endwall boundary layer which forms behind the separation line of the inlet boundary layer, must be extremely thin within the blade passage. Towards the suction side of the passage the endwall flow appears to be generally turbulent, but towards the pressure side freestream levels of turbulence are observed. Hence the new endwall boundary layer might be laminar towards the pressure side of the blade passage. This would agree with the results of Harrison (1989) who observed a laminar flow over a large area of the endwall in his cascade. Also as the flow proceeds downstream, the endwall region becomes more turbulent until at slot 10 a turbulent boundary layer across the whole pitch seems likely. This again would fit in with Harrison's results. Also the yaw angles at slot 5 show the endwall flow to be very highly skewed, varying by 5° per millimeter. By slot 8 this skew has reduced to approximately 1° per millimeter. Such a boundary layer flow may well prove difficult to model.

The rate of dissipation of mean kinetic energy by turbulent and viscous action has been calculated at slot 10. The results suggest that turbulence is an important loss producing mechanism downstream of the cascade. Comparing with the results of Moore *et al* (1986) it appears that loss production in separated regions away from the endwall is important in the downstream flow. However within the blade passage where loss will also be produced on the suction surface, the relative significance of the separated shear layers may be smaller. It would be very interesting to calculate rates of dissipation at slots 5 and 8 from the Reynolds stress measurements. This would require five hole probe traverses at these locations and so unfortunately cannot be carried out here due to lack of time.

Contours of shear stress, turbulent viscosity, and turbulent kinetic

energy have been presented. These may be compared with predictions of turbulence models within Navier-Stokes solvers, and were the major objective of this study. However, although an isotropic eddy viscosity concept may be a reasonable approximation downstream of the cascade, the rapid change in sign in $\overline{u'v'}$ from slots 8 to slot 10 indicates that it s application within the blade passage may be less realistic. Indeed there are areas at slot 8 where the $\overline{u'v'}$ shear stress implies a negative eddy viscosity. Also an eddy viscosity model does not attempt to account for the effects of the normal stresses. As seen at slot 10, these can make some significant overall contributions to loss production, and locally their effects can be very large. Within the blade passage, where the normal rates of strain are large, the normal stresses may have important effects. In particular the streamwise normal stress could be significant in this region, tending to keep losses low at first, where the suction flow accelerates, and then acting to produce turbulence rapidly as the flow decelerates. An experimental investigation of the Reynolds stresses in the suction surface boundary layer, and the rate at which they produce loss would therefore be a very interesting, and valuable contribution.

a) Endwall Flow

b) Suction Surface Flow

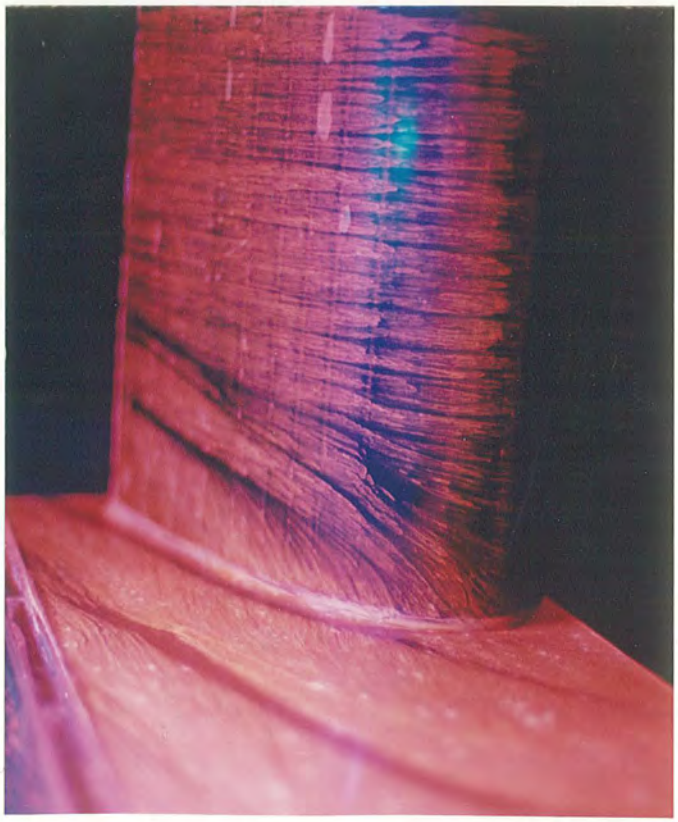

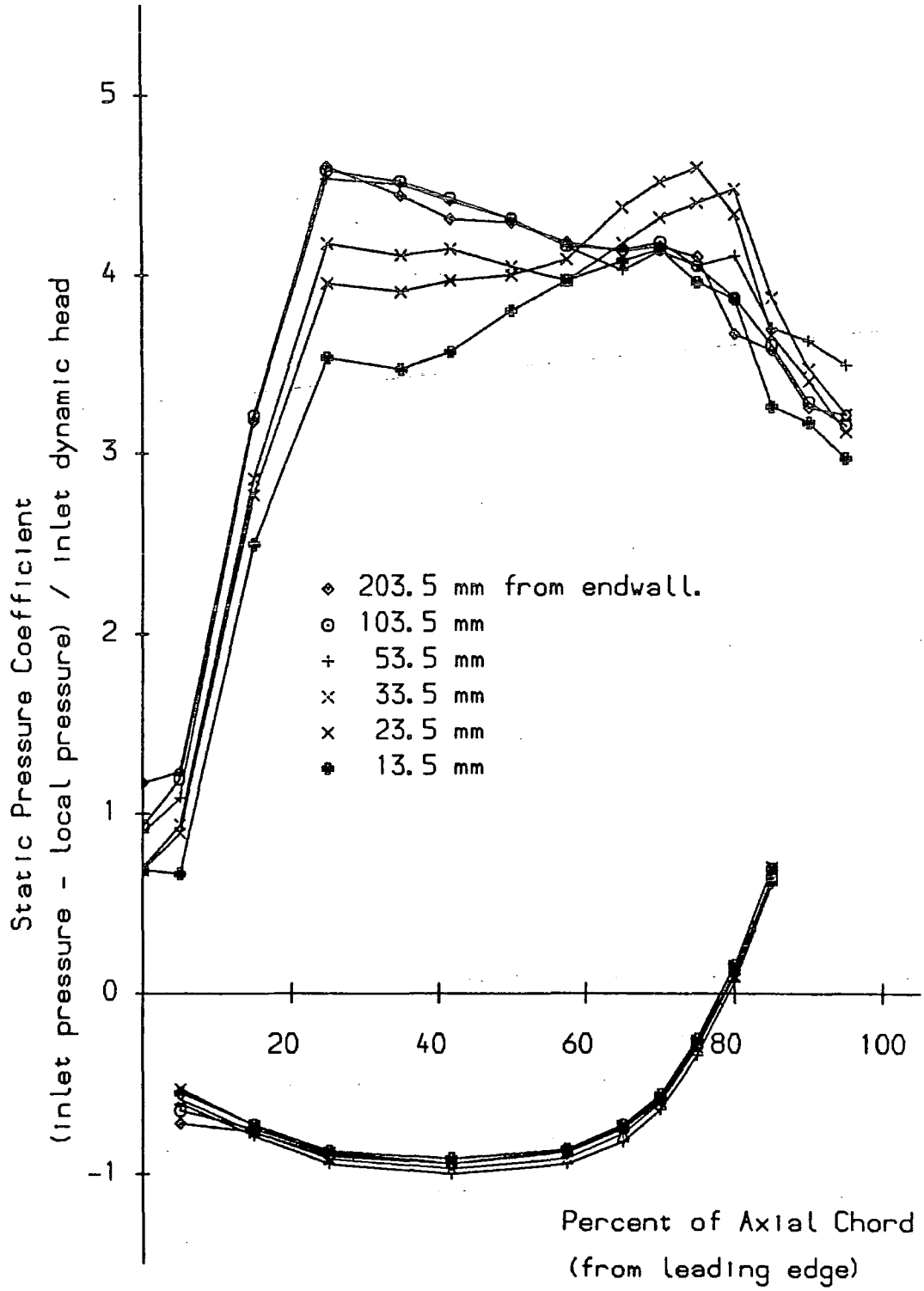


FIGURE 7.2 : Static Pressures (JGC Test Case)

Five Hole Probe Measurements (JAV Test Case, from Walsh (1987)).

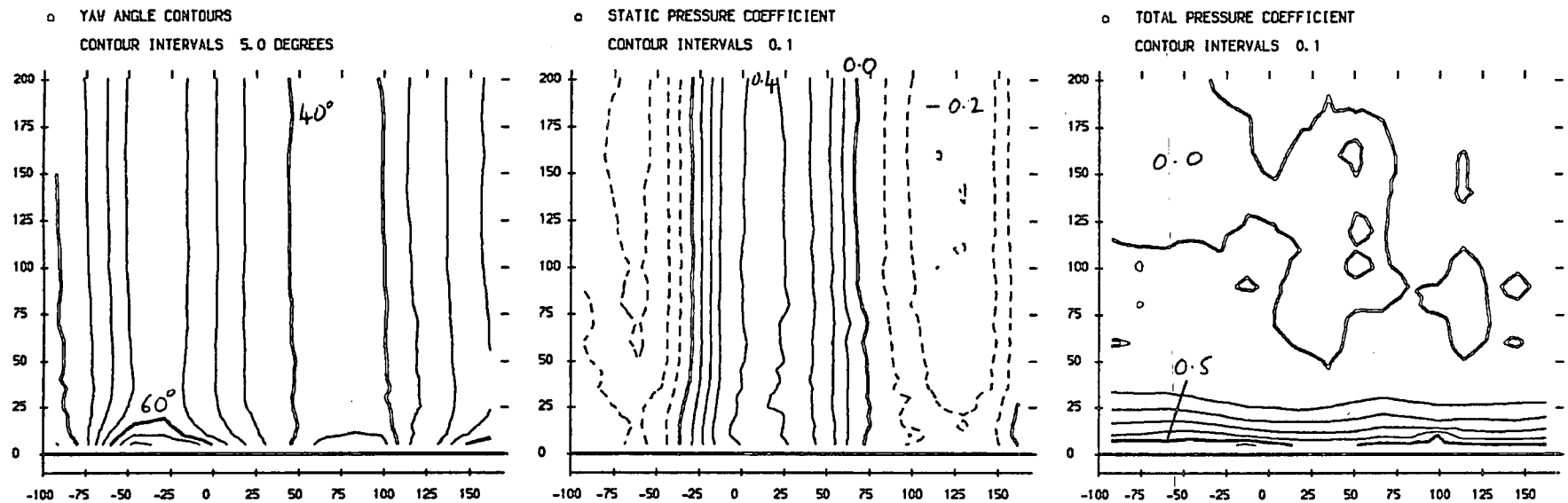


Five Hole Probe Measurements (JGC Test Case).

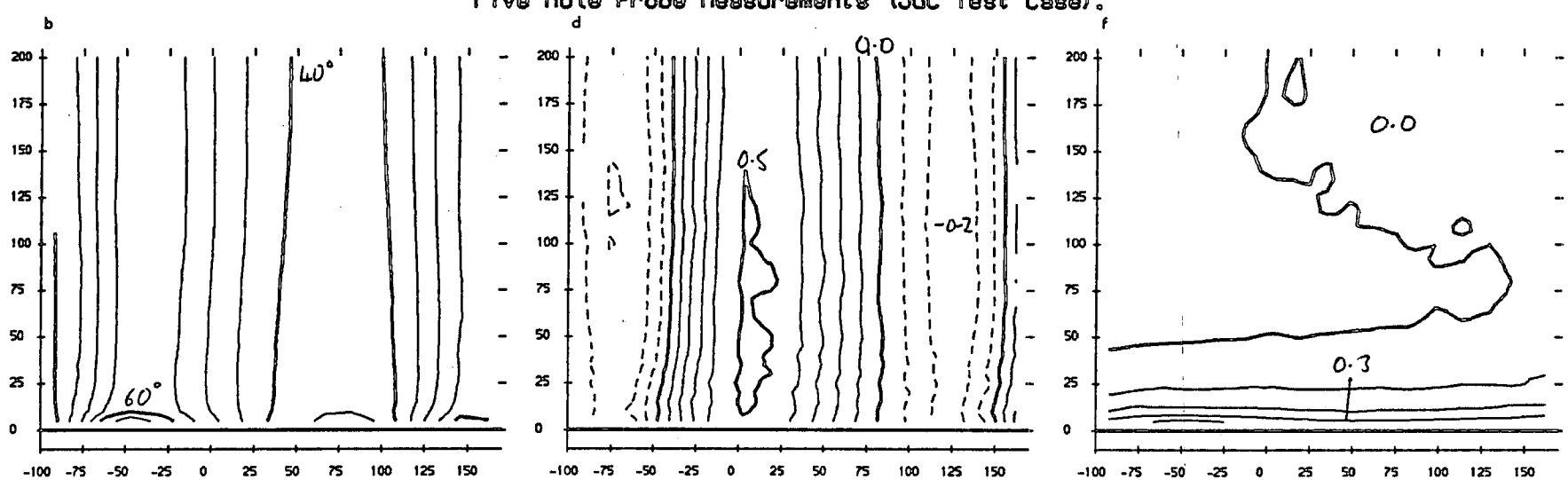


FIGURE 7.3 (a-f) : Area Plots For Slot 1

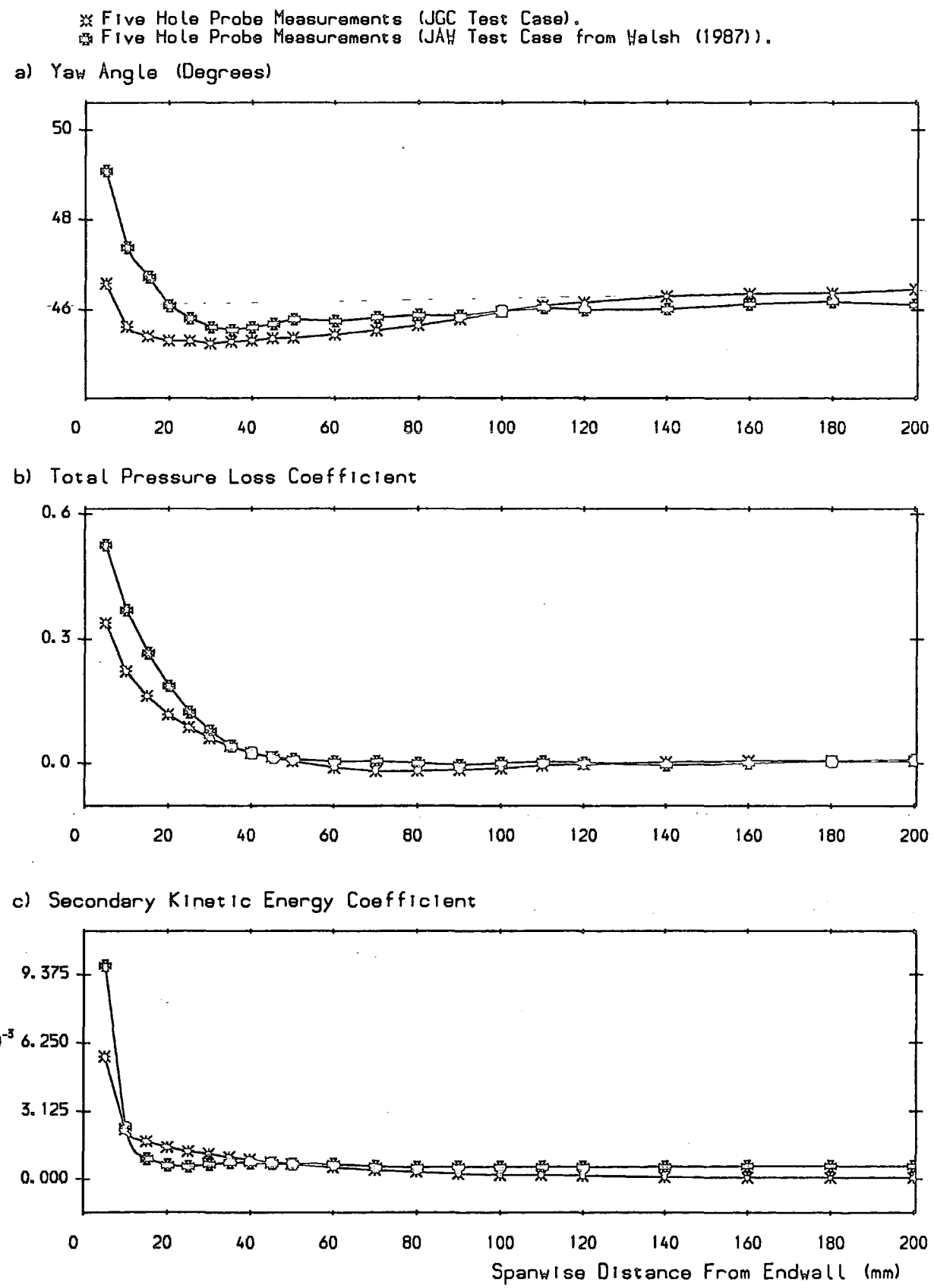


FIGURE 7.4 : Pitch Averaged Results For Slot 1

Five Hole Probe Measurements (JGC Test Case).

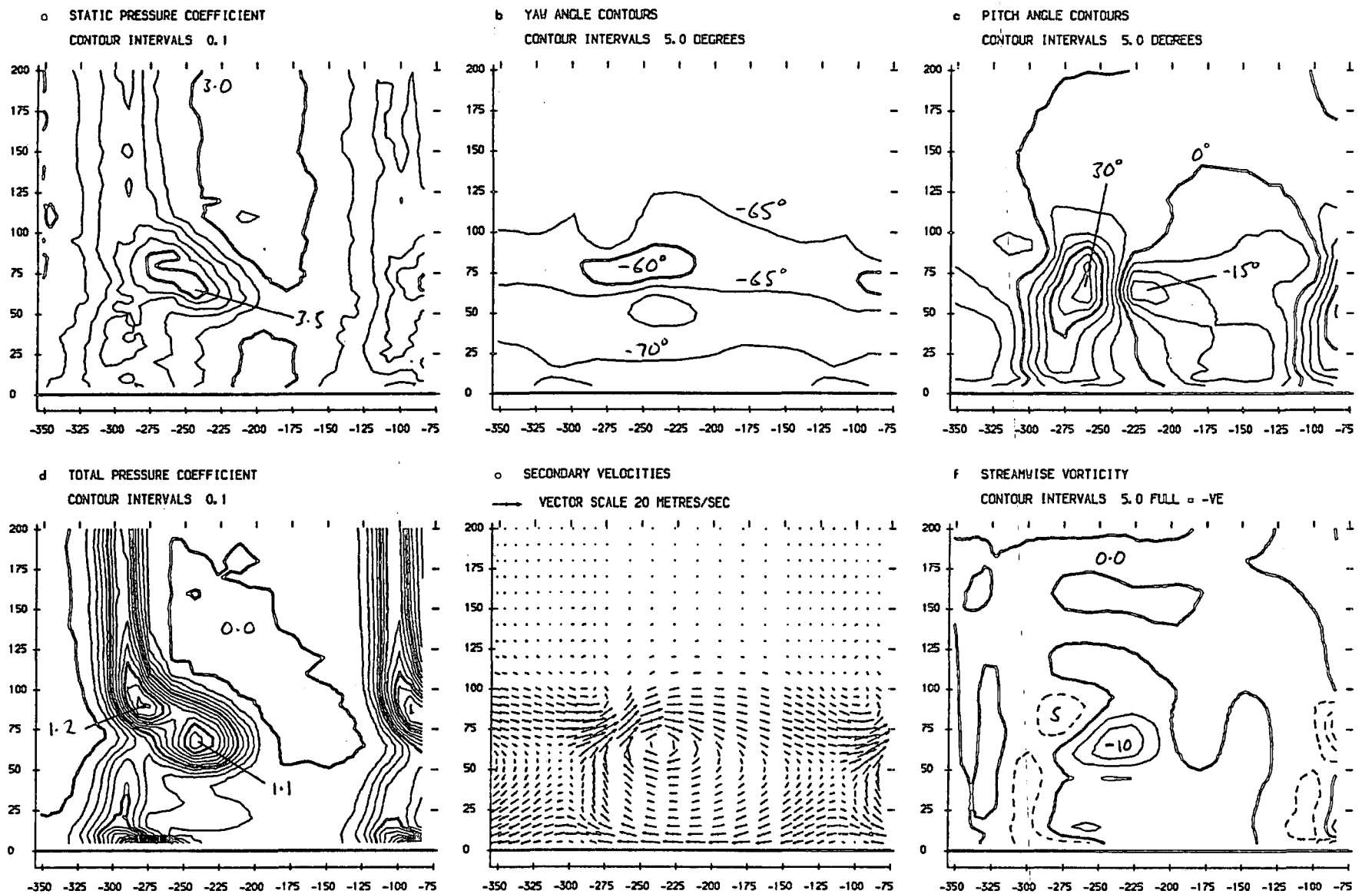


FIGURE 7.5 (a-f) : Area Plots For Slot 10

⁂ Five Hole Probe Measurements (JGC Test Case).
⁂ Five Hole Probe Measurements (JAW Test Case from Walsh (1987)).

a) Yaw Angle (Degrees)

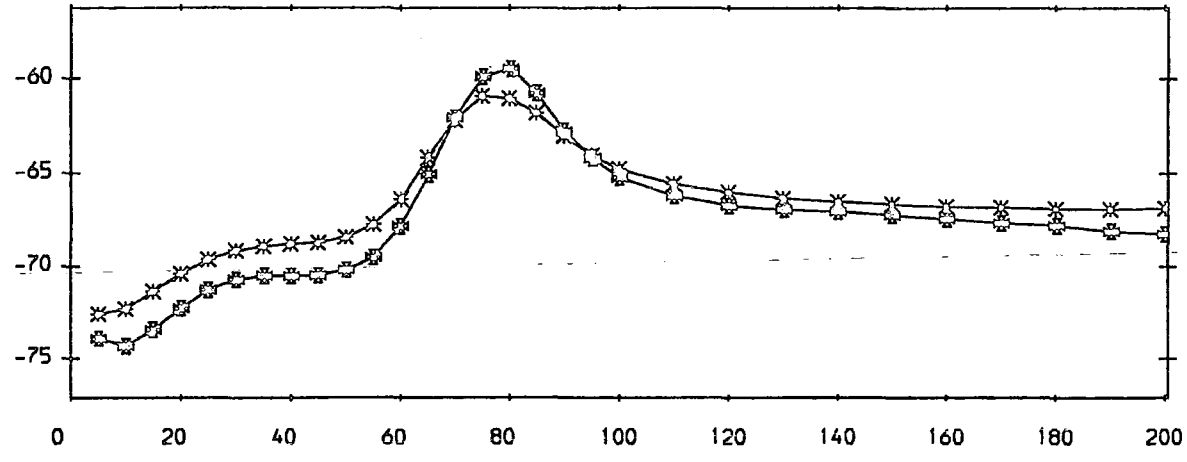


b) Total Pressure Loss Coefficient

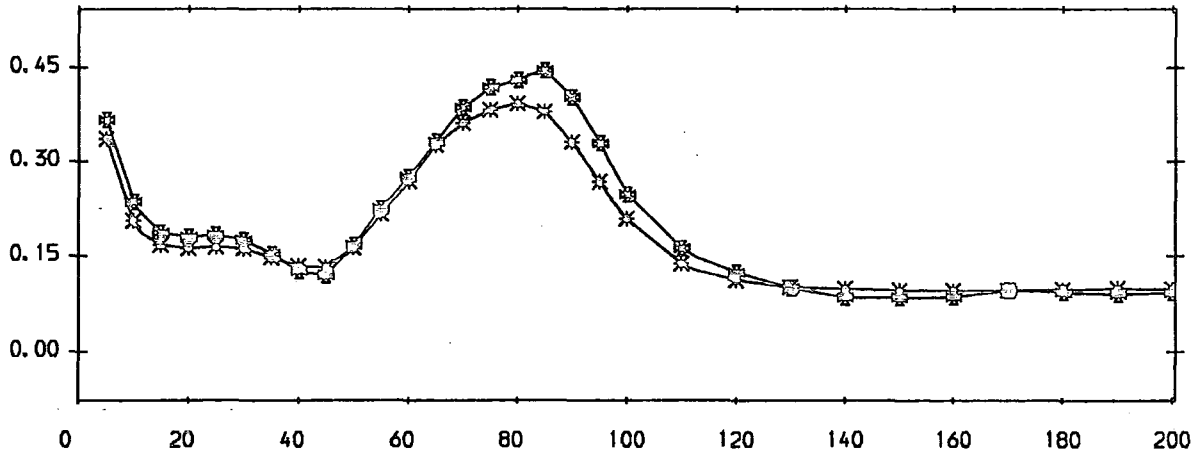


c) Secondary Kinetic Energy Coefficient

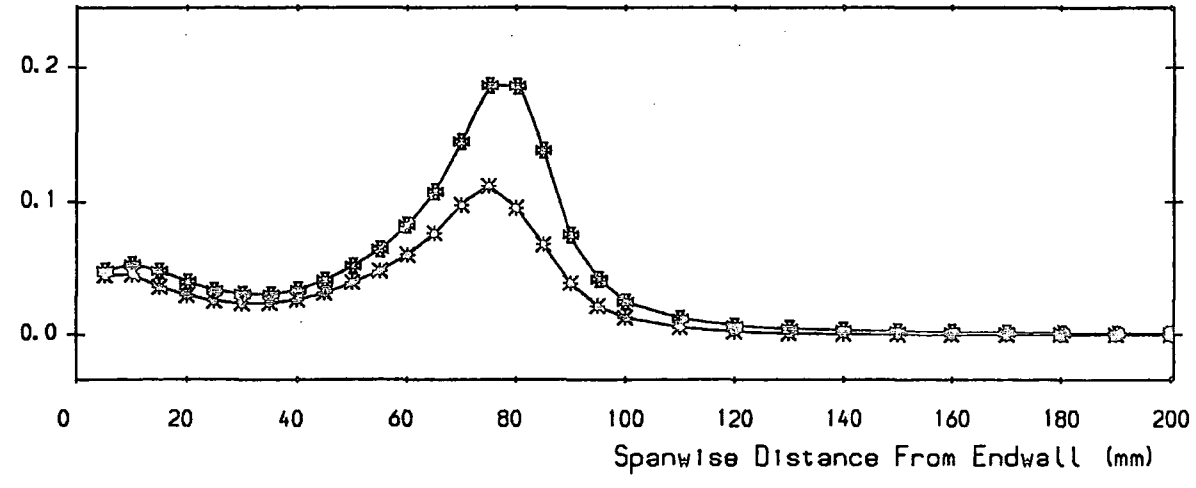


FIGURE 7.6 : Pitch Averaged Results For Slot 10

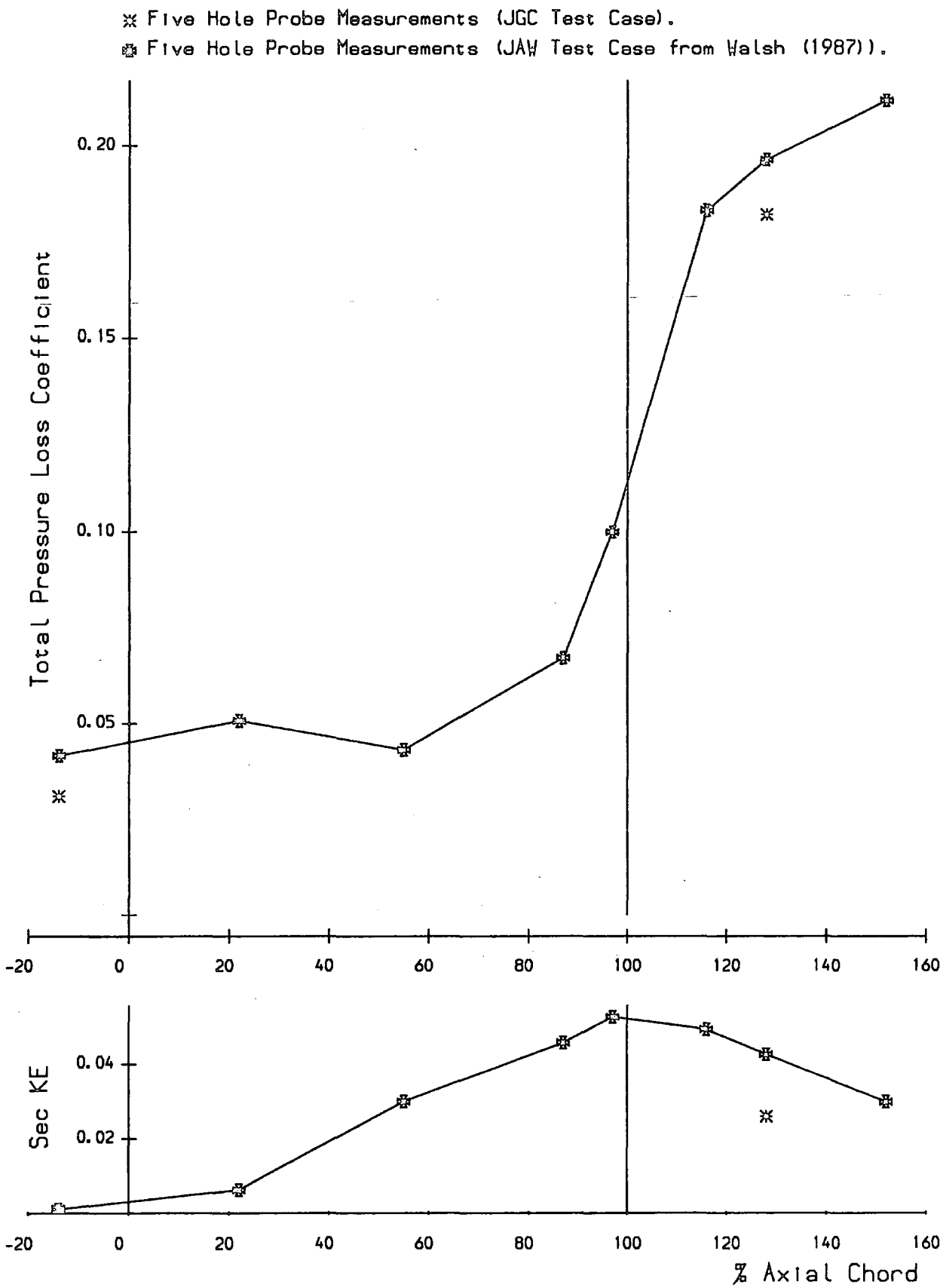


FIGURE 7.7 : Mass Averaged Loss & Secondary Kinetic Energy

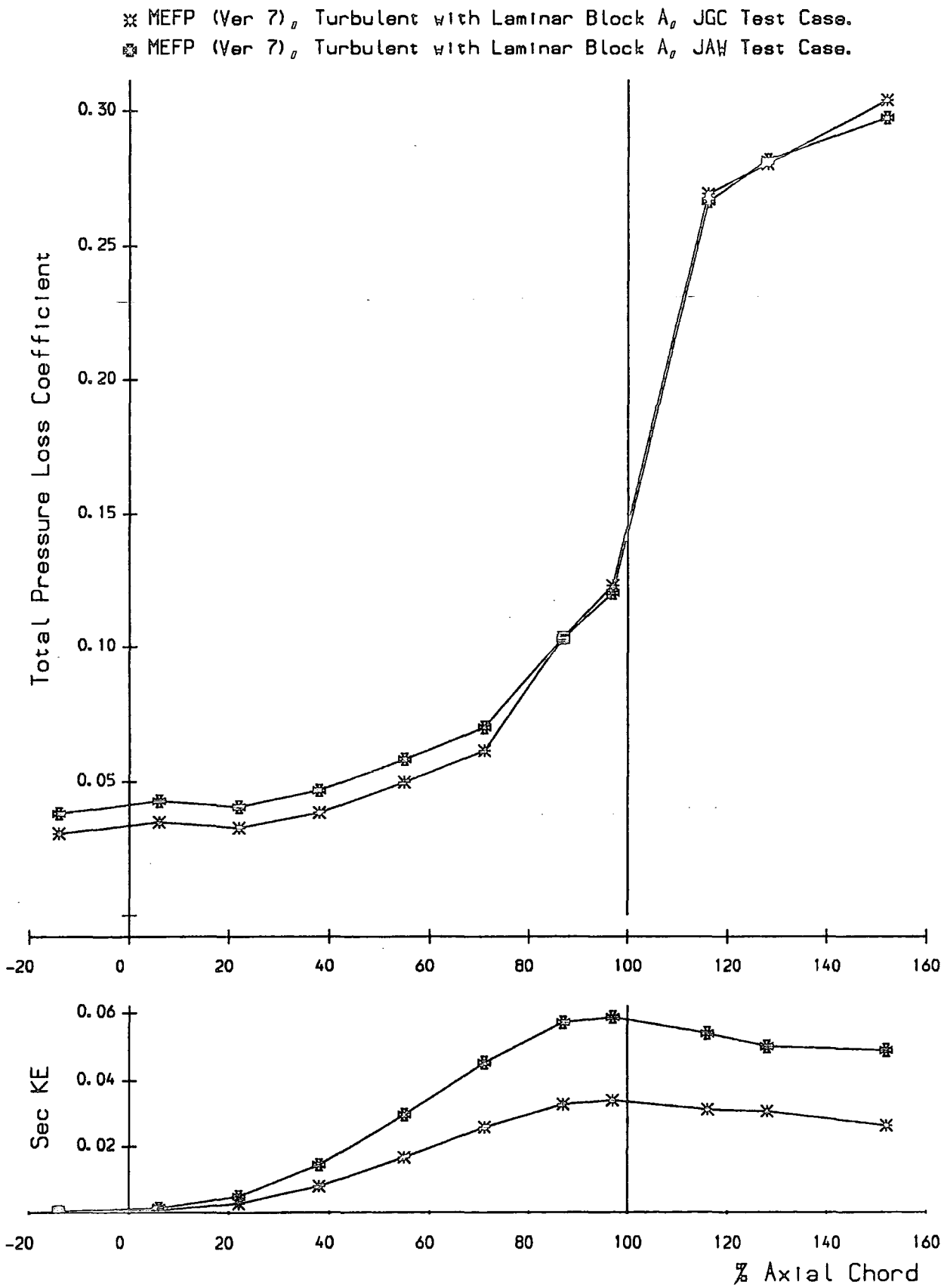


FIGURE 7.8 , Mass Averaged Loss & Secondary Kinetic Energy

Hot-Wire Anemometry (X-Probe) Measurements

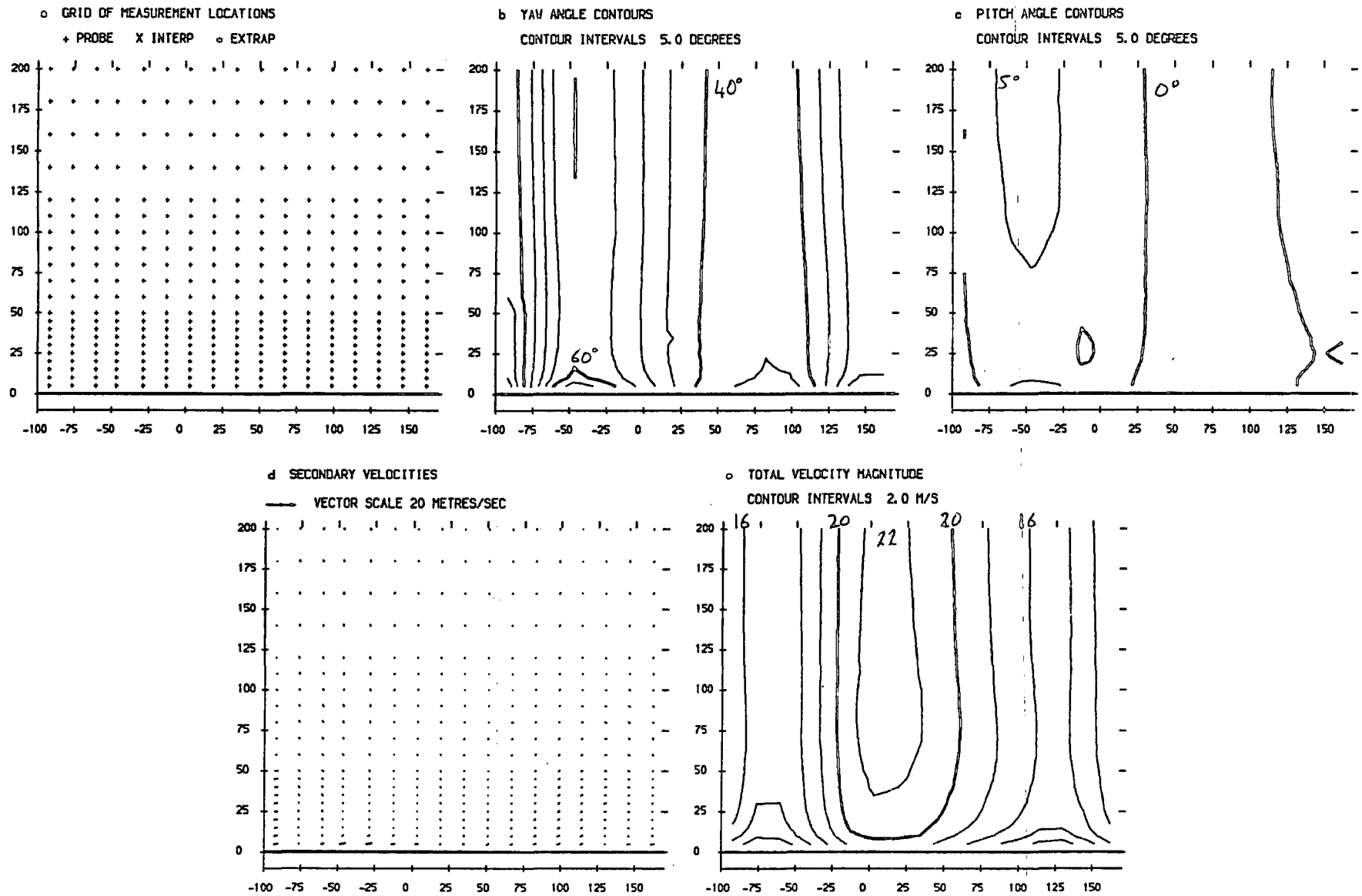


FIGURE 7.9 (a-e) : Area Plots For Slot 1

Hot-Wire Anemometry (X-Probe) Measurements

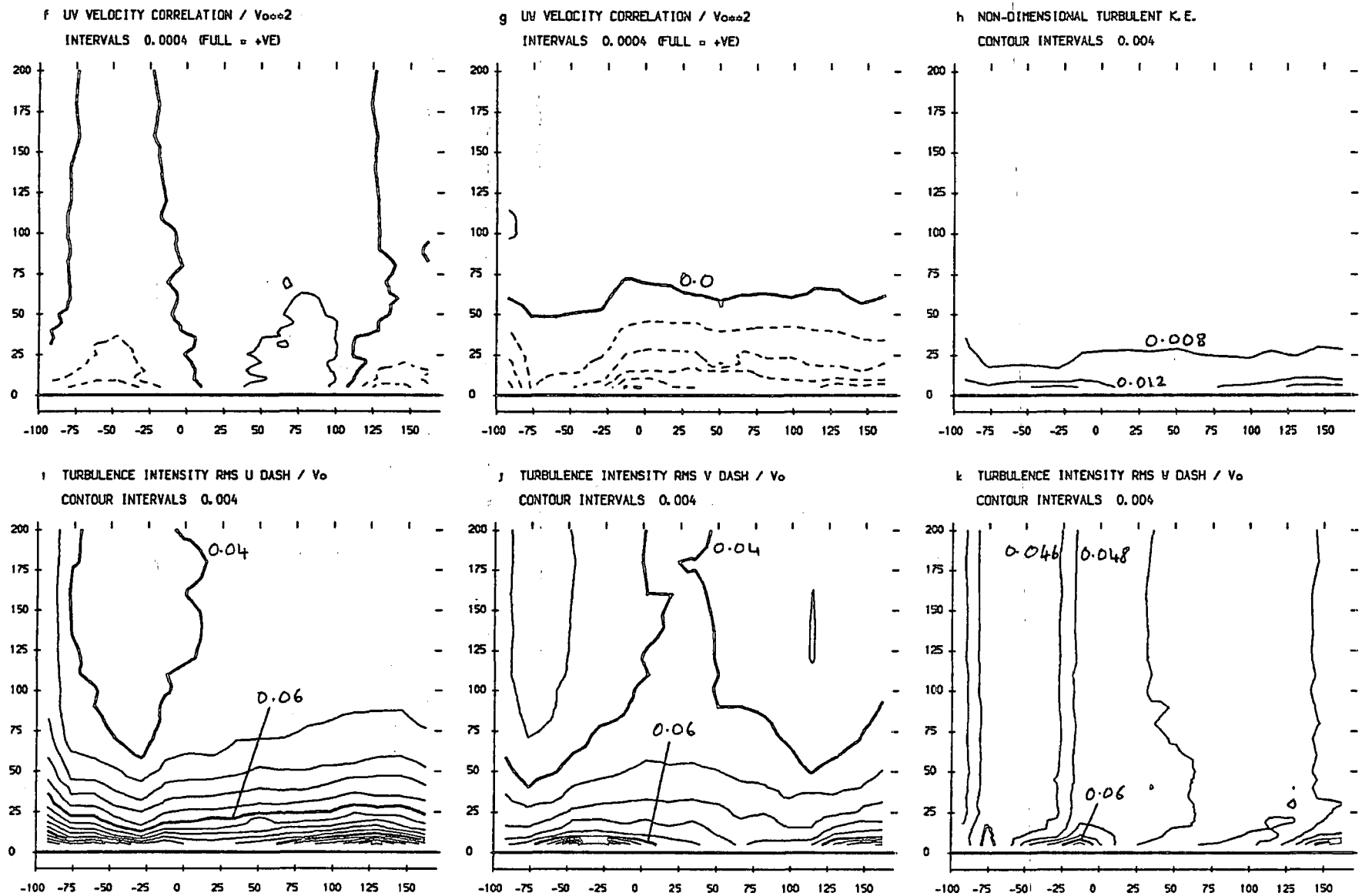


FIGURE 7.9 (f-k) : Area Plots For Slot 1

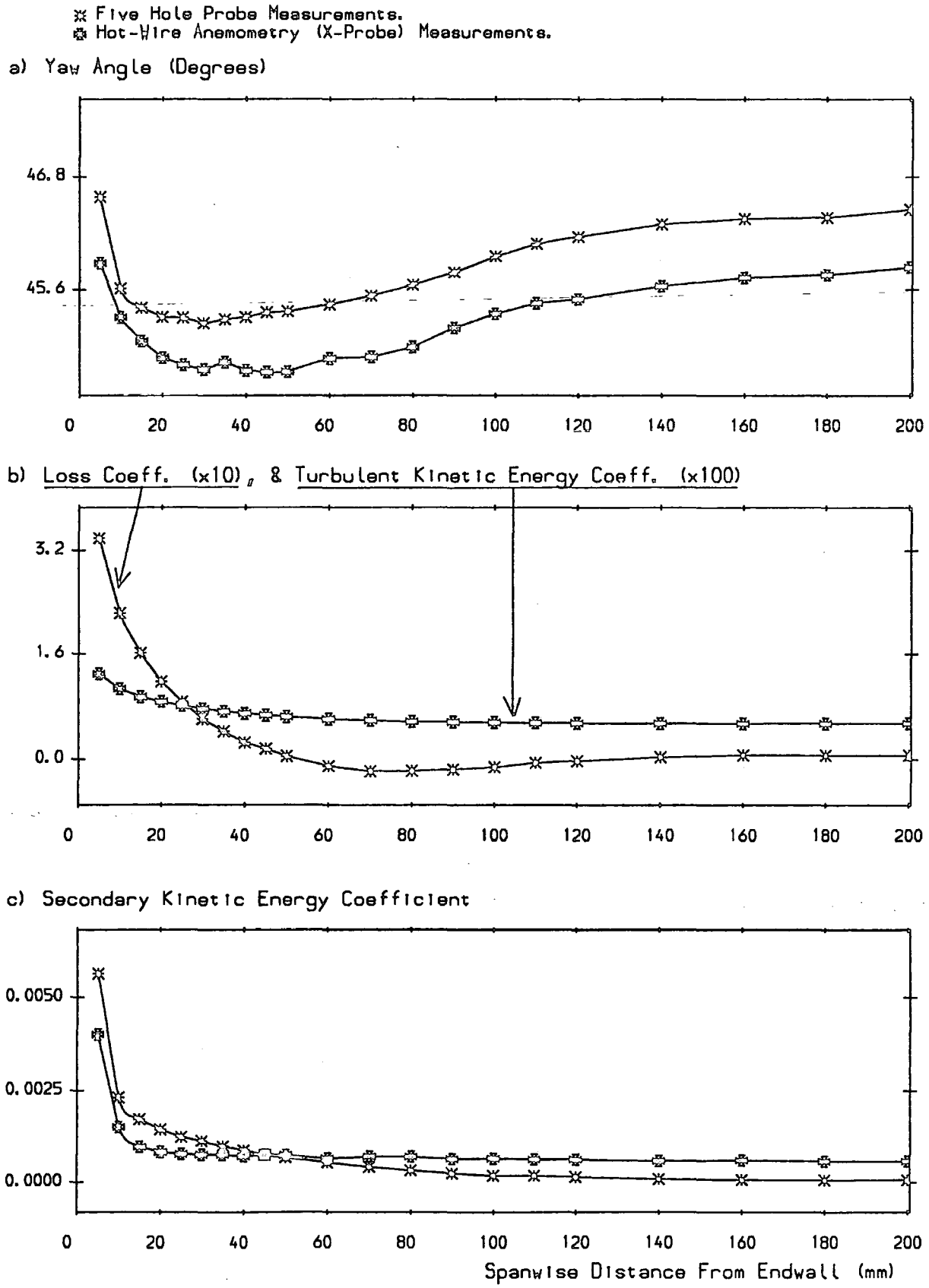


FIGURE 7.10 : Pitch Averaged Results For Slot 1

Hot-Wire Anemometry (X-Probe) Measurements

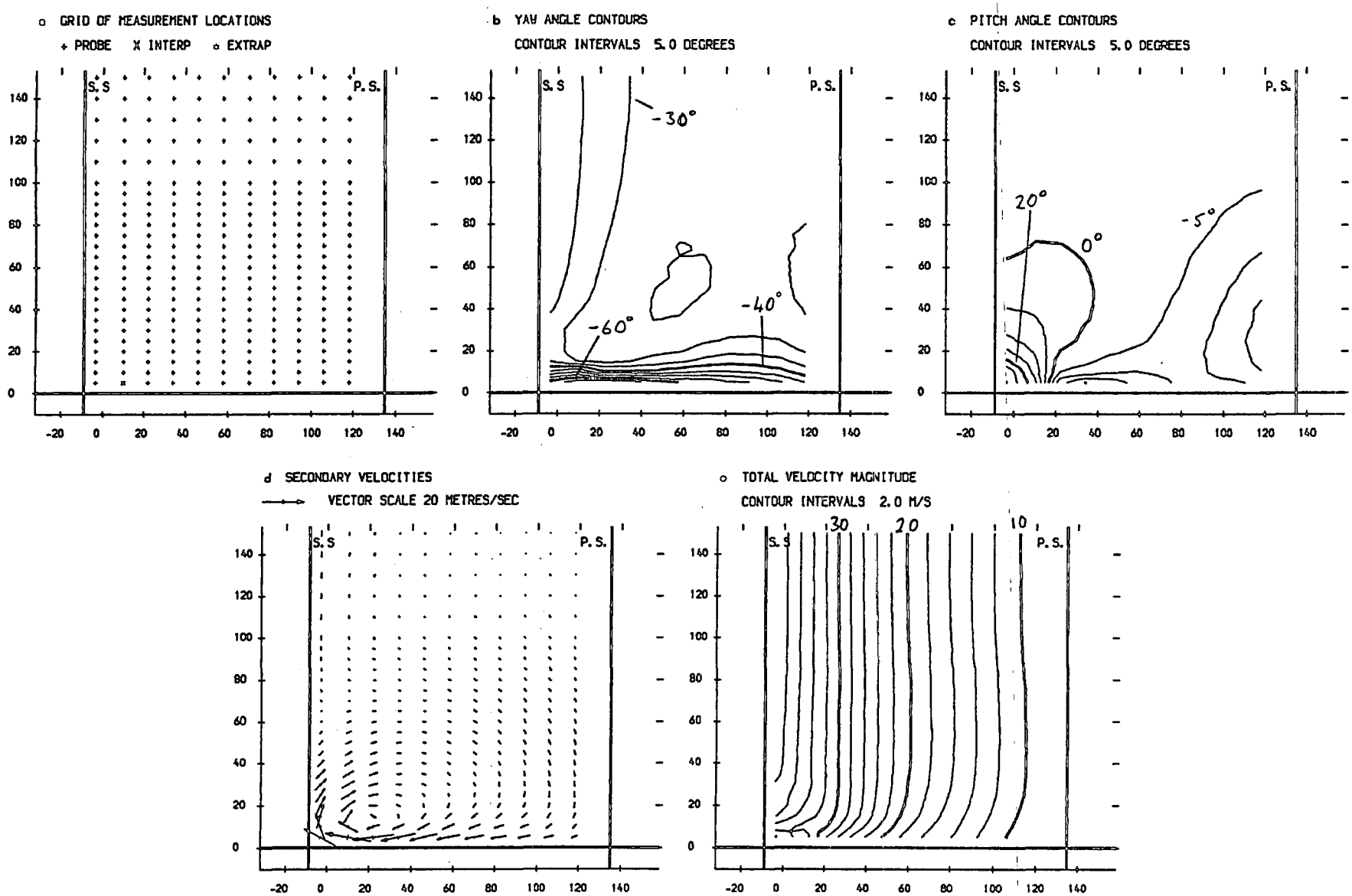


FIGURE 7.11 (a-e) : Area Plots For Slot 5

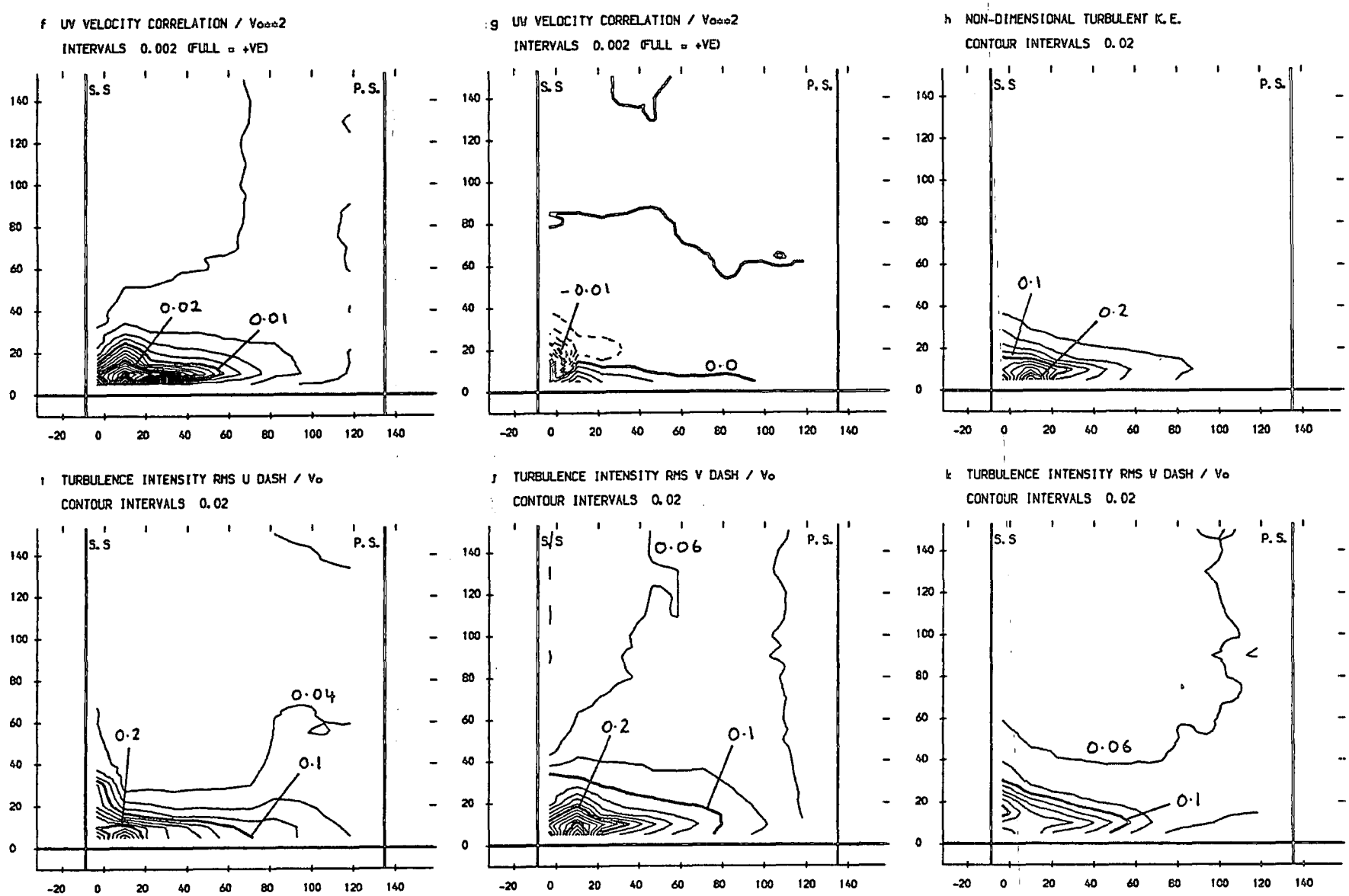


FIGURE 7.11 (f-k) : Area Plots For Slot 5

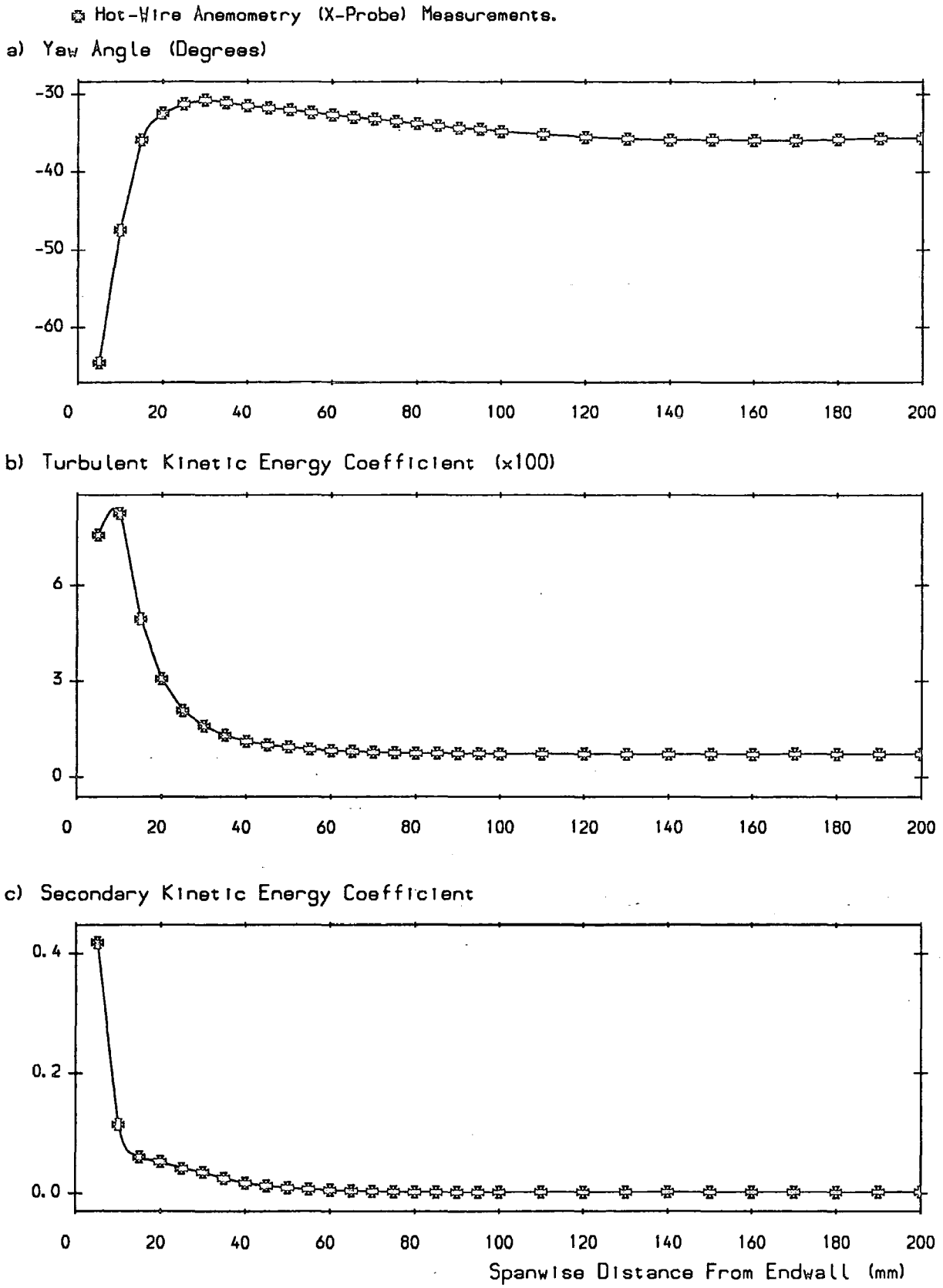


FIGURE 7.12 : Pitch Averaged Results For Slot 5

# Rotatable Single Wire Endwall Flow Measurements

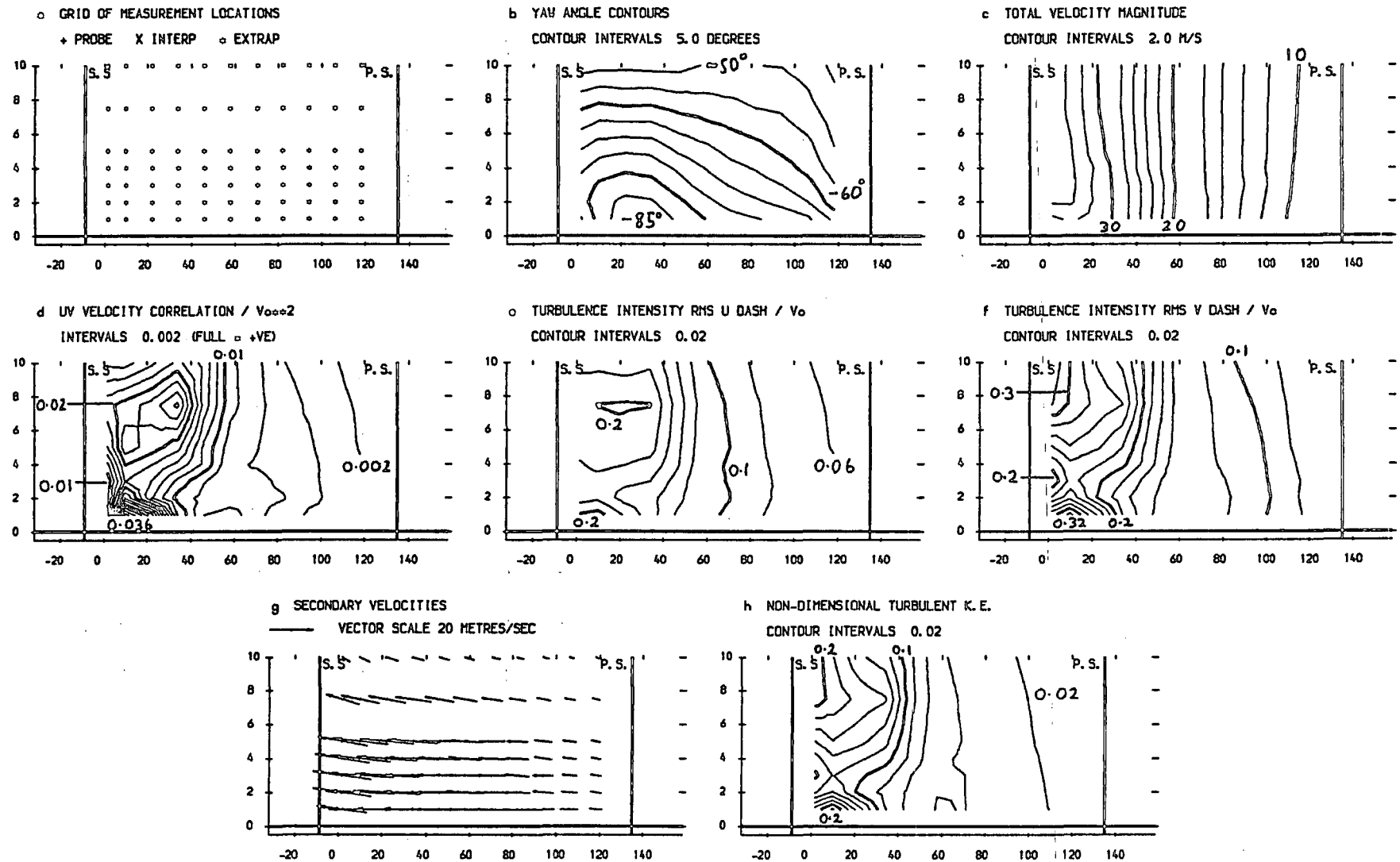


FIGURE 7.13 (a-h) : Area Plots For Slot 5

Hot-Wire Anemometry (X-Probe) Measurements

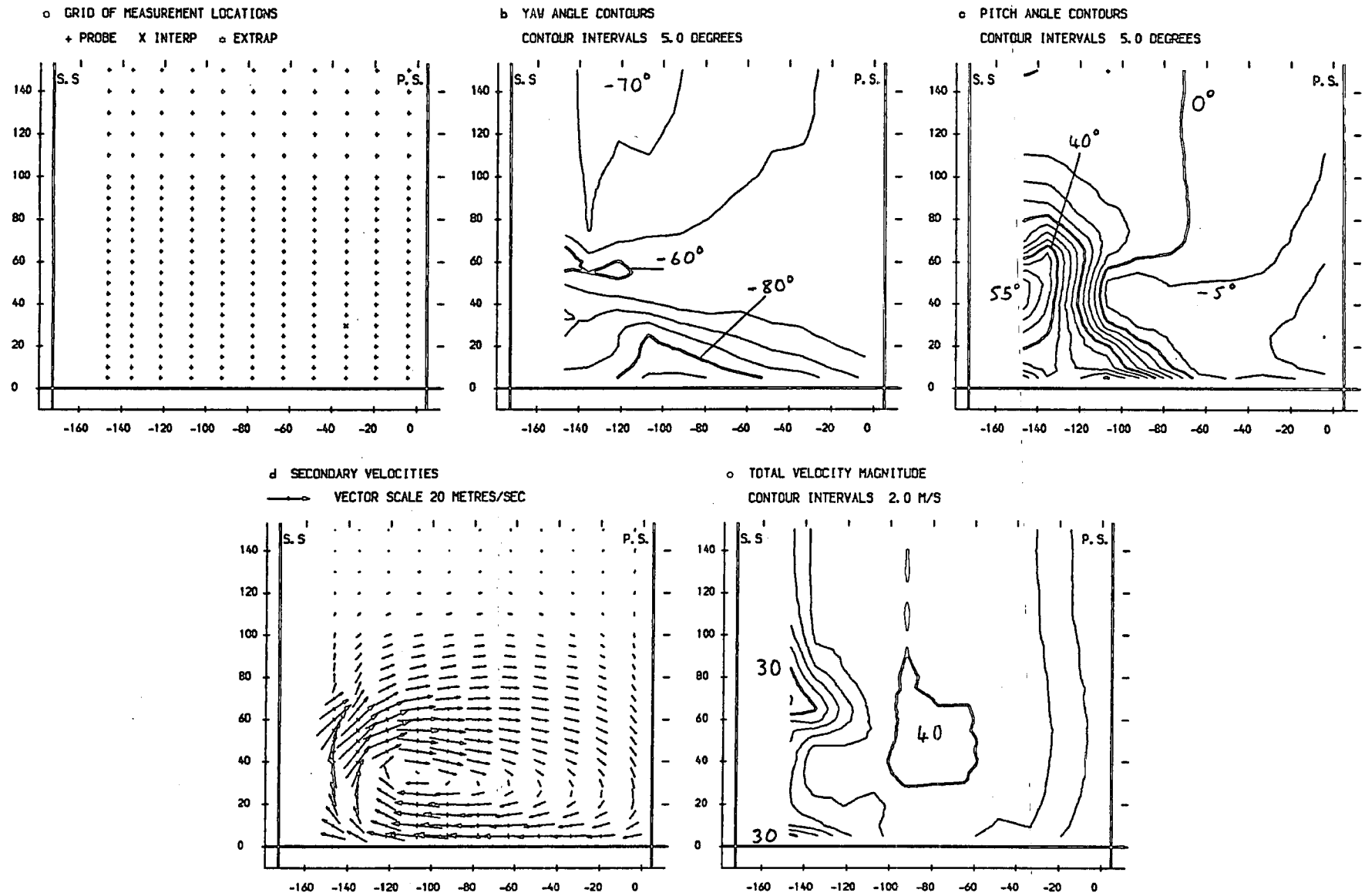


FIGURE 7.14 (a-e) : Area Plots For Slot 8

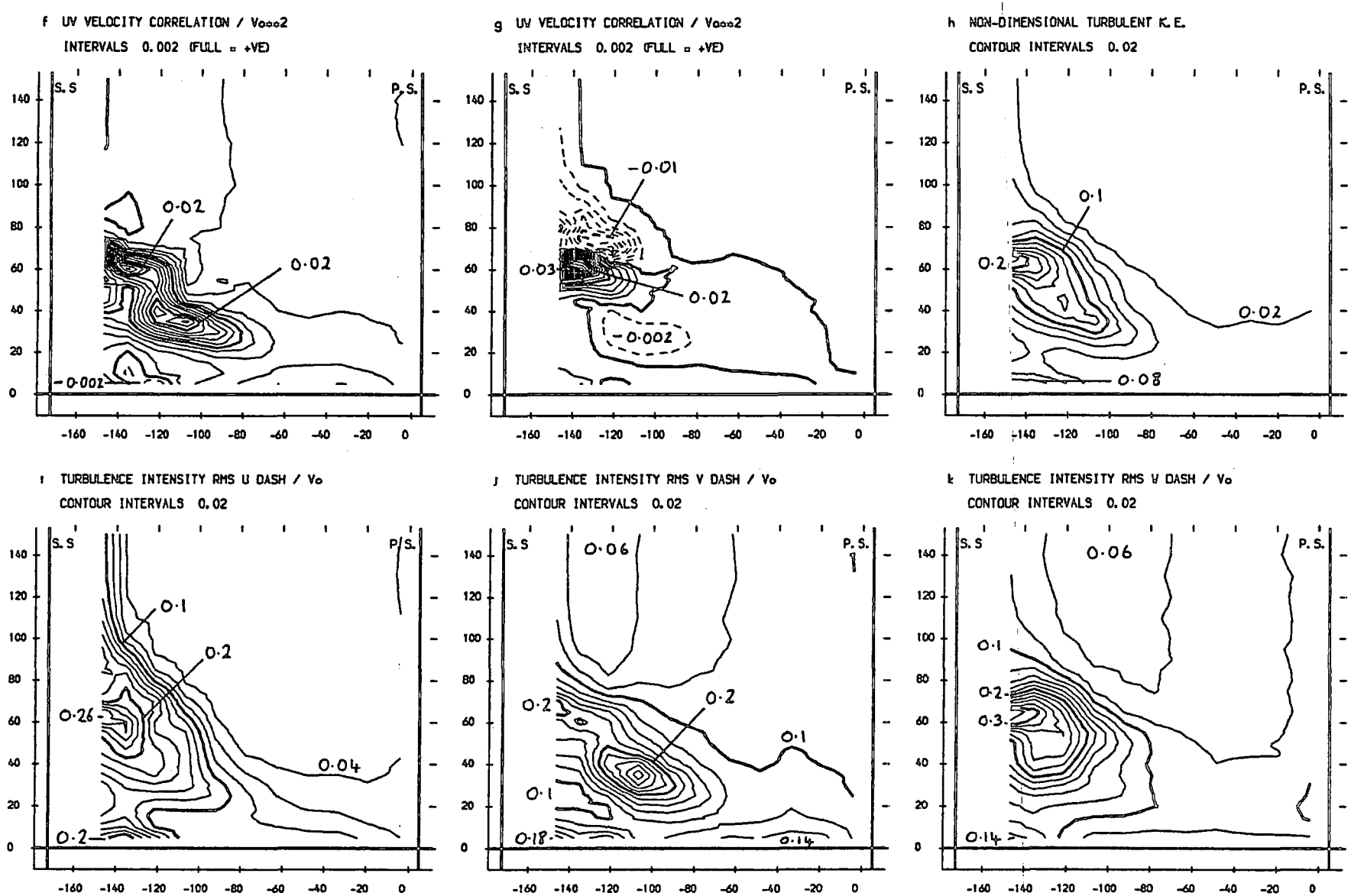


FIGURE 7.14 (f-k) : Area Plots For Slot 8

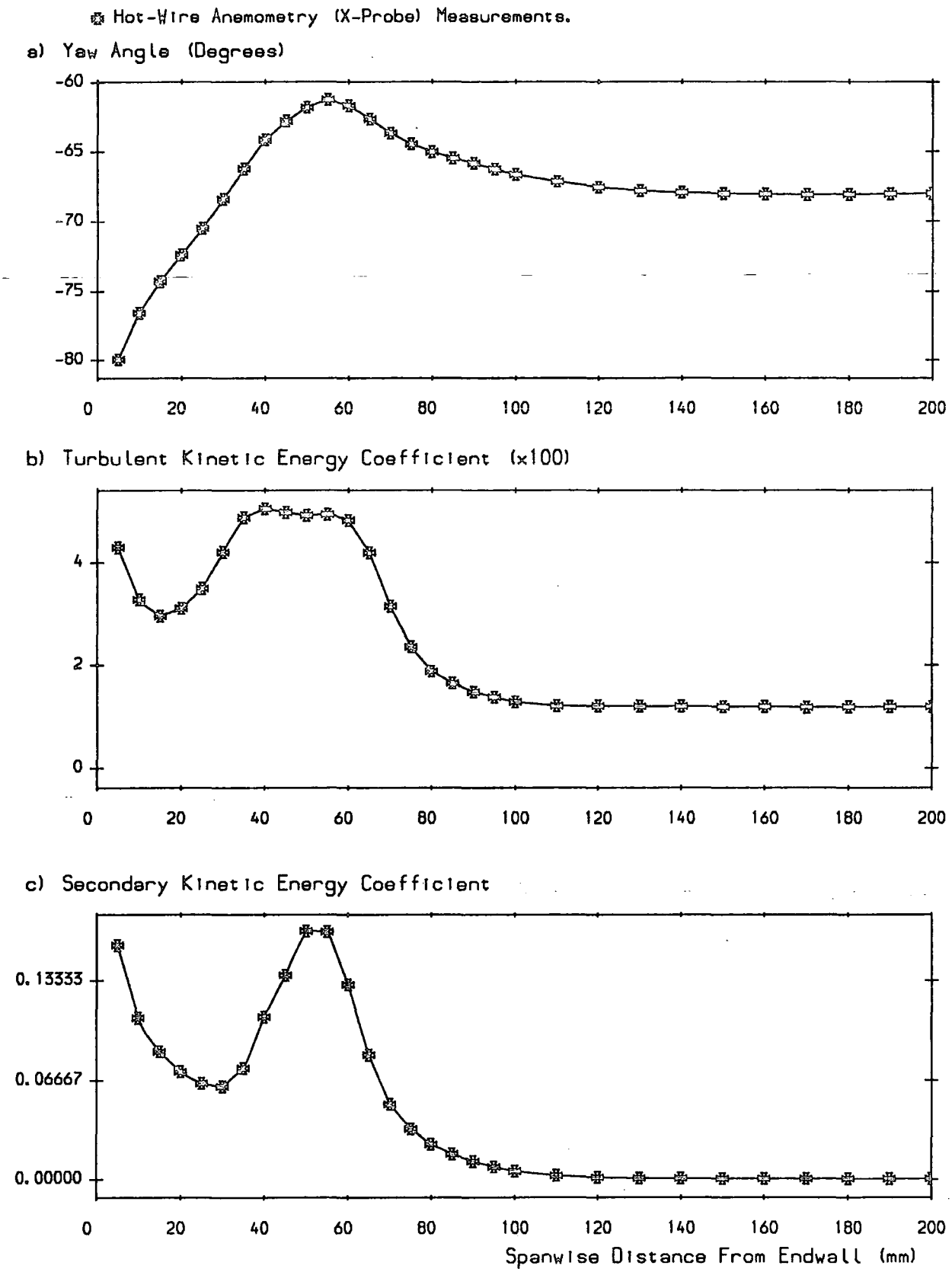


FIGURE 7.15 : Pitch Averaged Results For Slot 8

# Rotatable Single Wire Endwall Flow Measurements

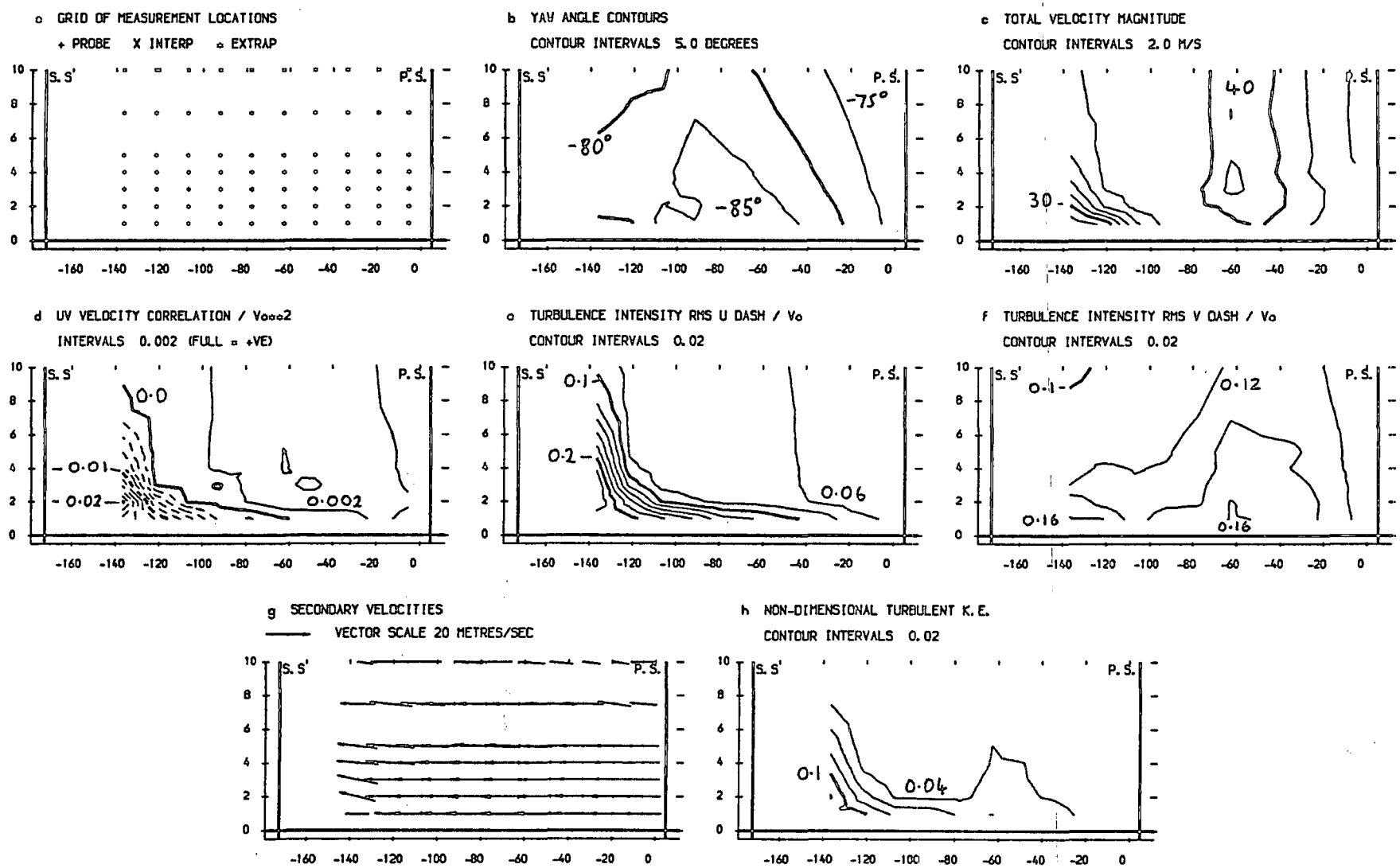


FIGURE 7.16 (a-h) : Area Plots For Slot 8

Hot-Wire Anemometry (X-Probe) Measurements

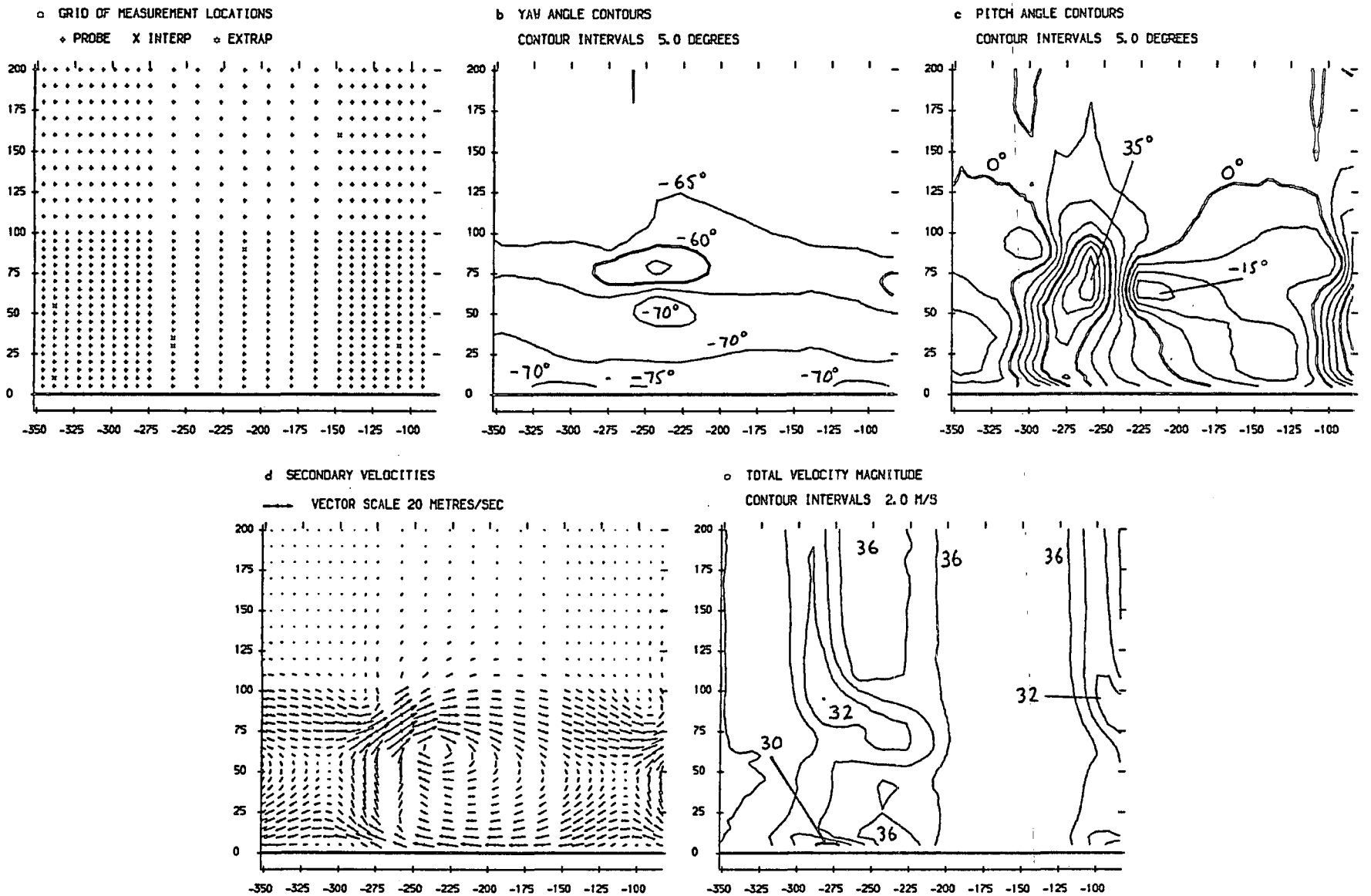


FIGURE 7.17 (a-e) : Area Plots For Slot 10

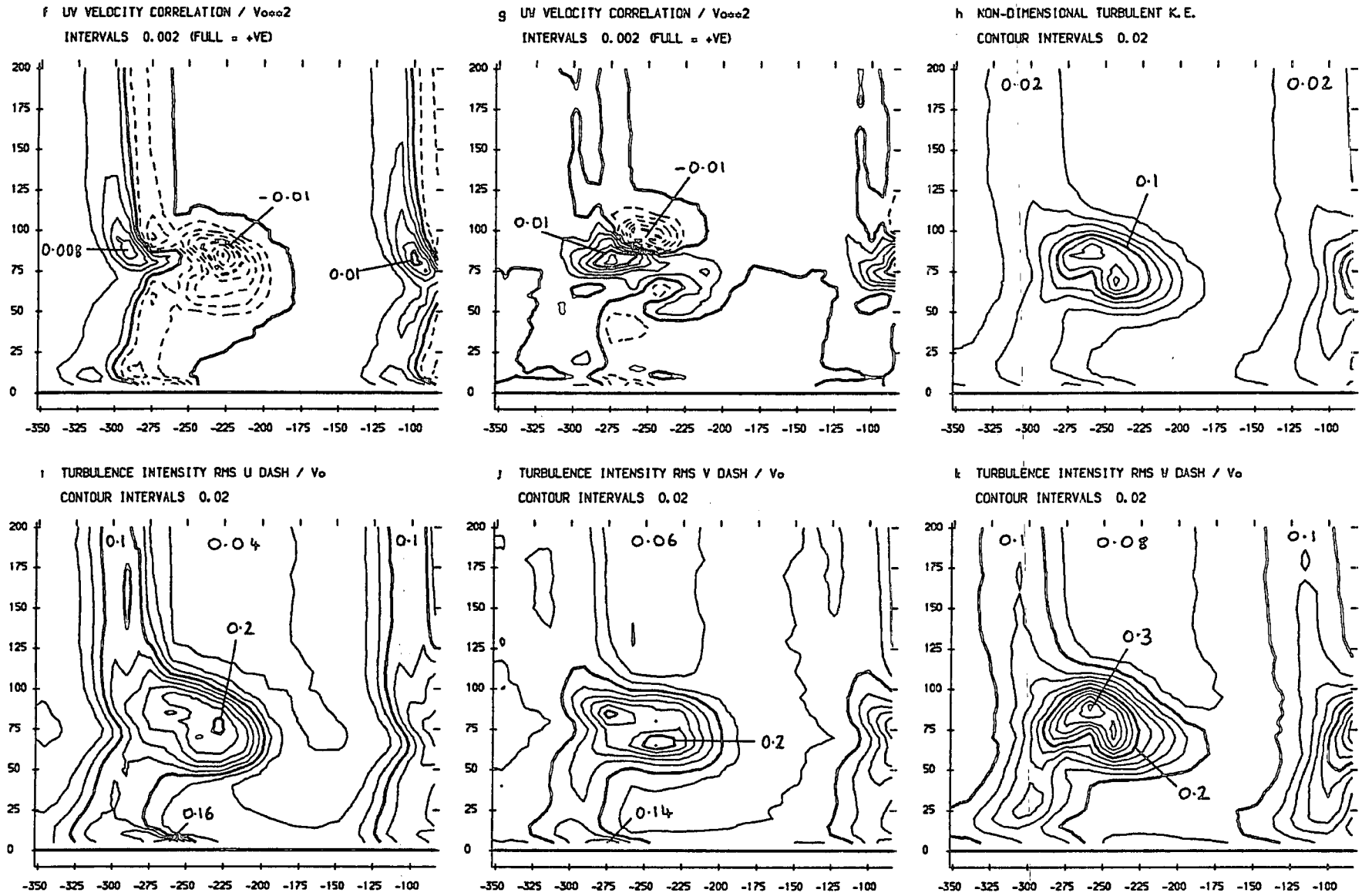


FIGURE 7.17 (f-k) : Area Plots For Slot 10

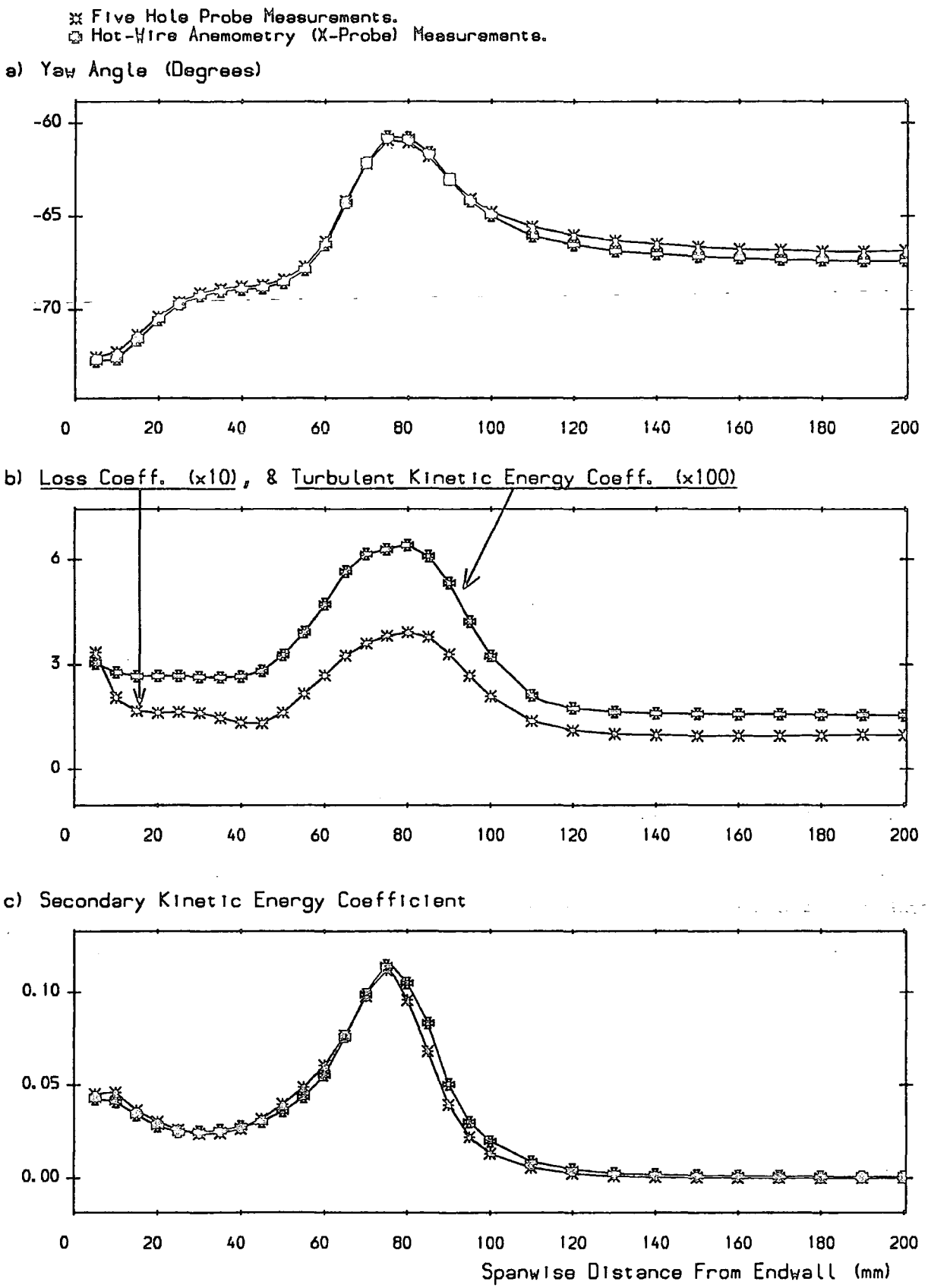


FIGURE 7.18 : Pitch Averaged Results For Slot 10

# Rotatable Single Wire Endwall Flow Measurements

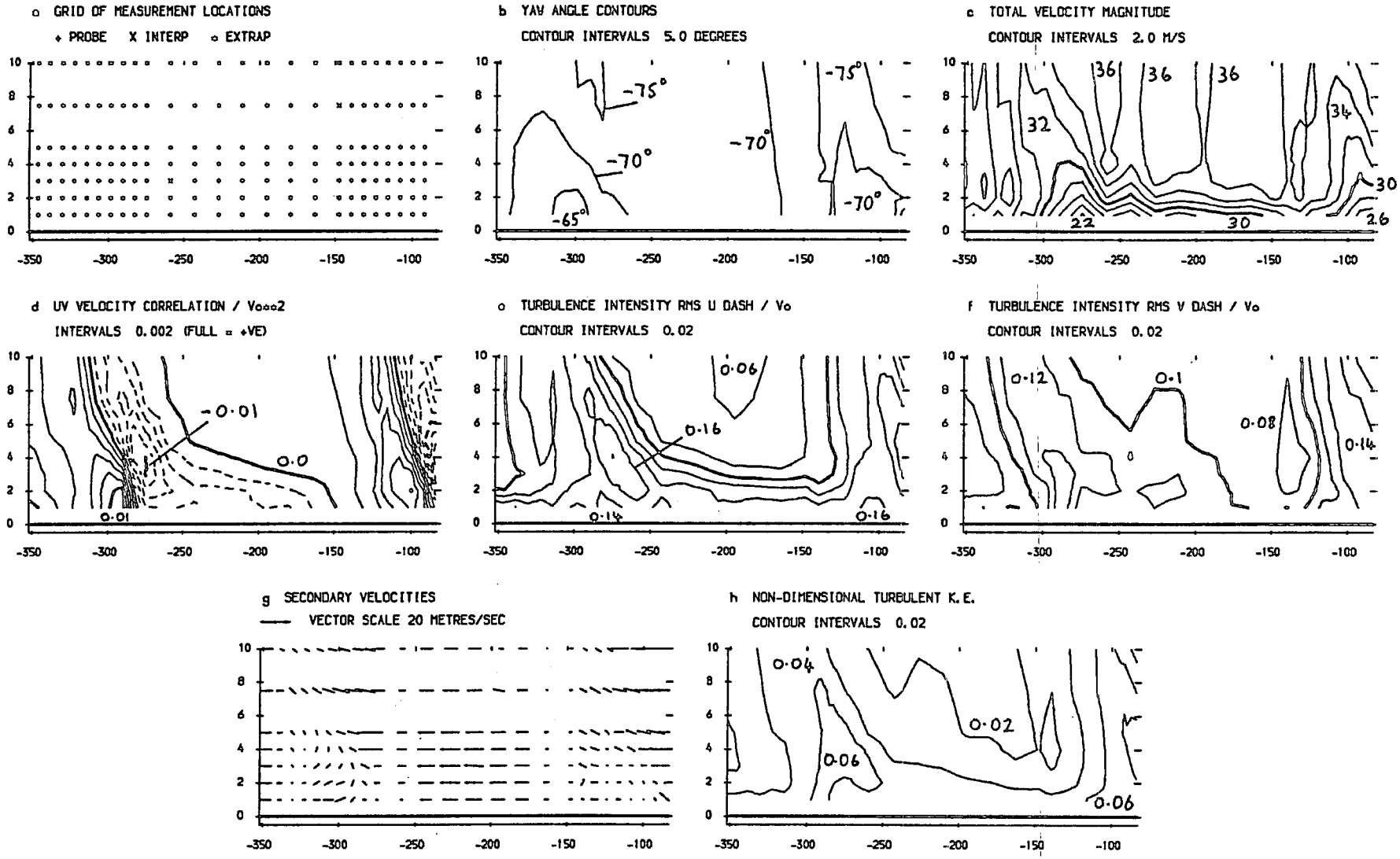


FIGURE 7.19 (a-h) : Area Plots For Slot 10

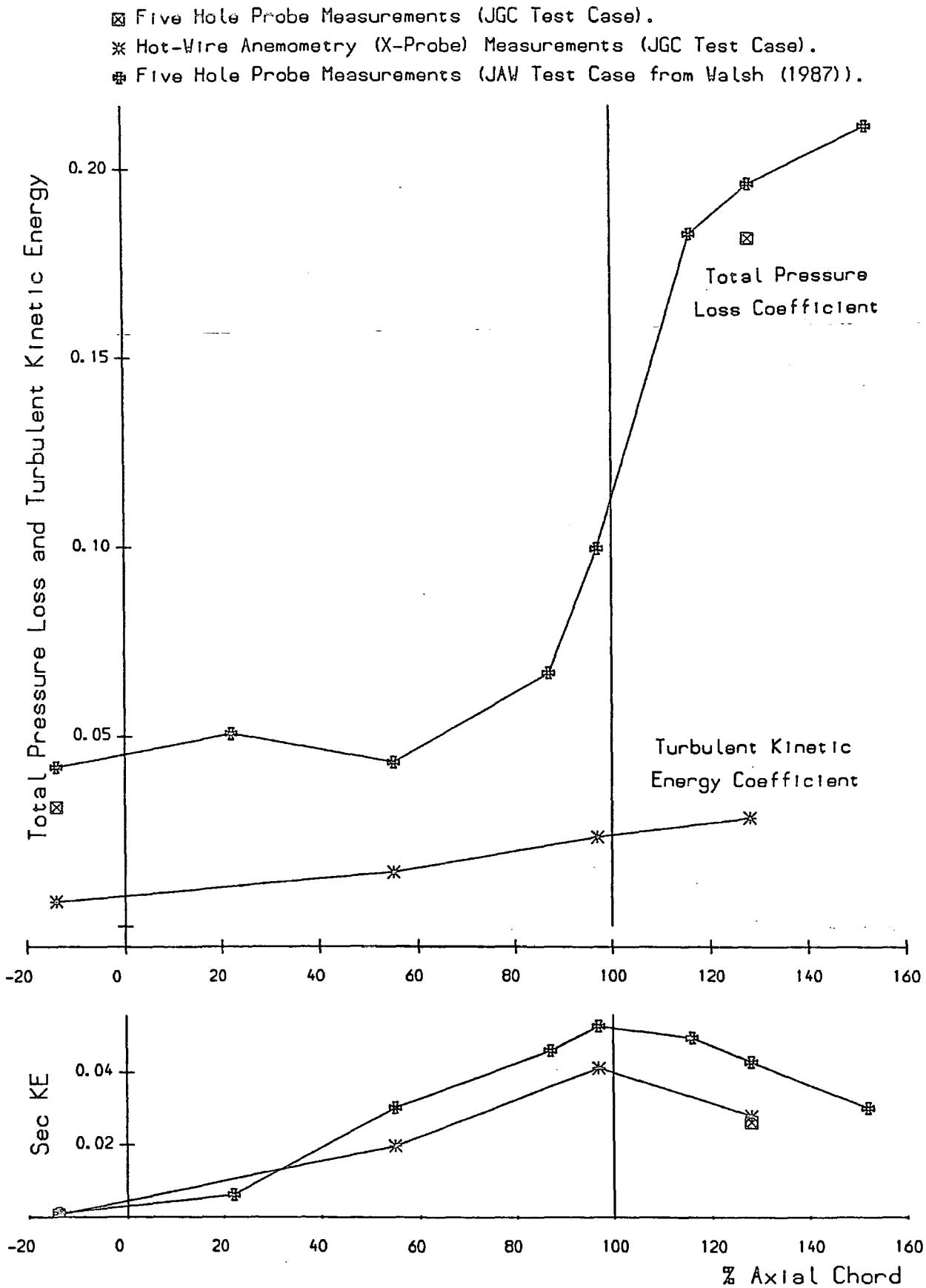


FIGURE 7.20 : Mass Averaged Loss & Secondary Kinetic Energy

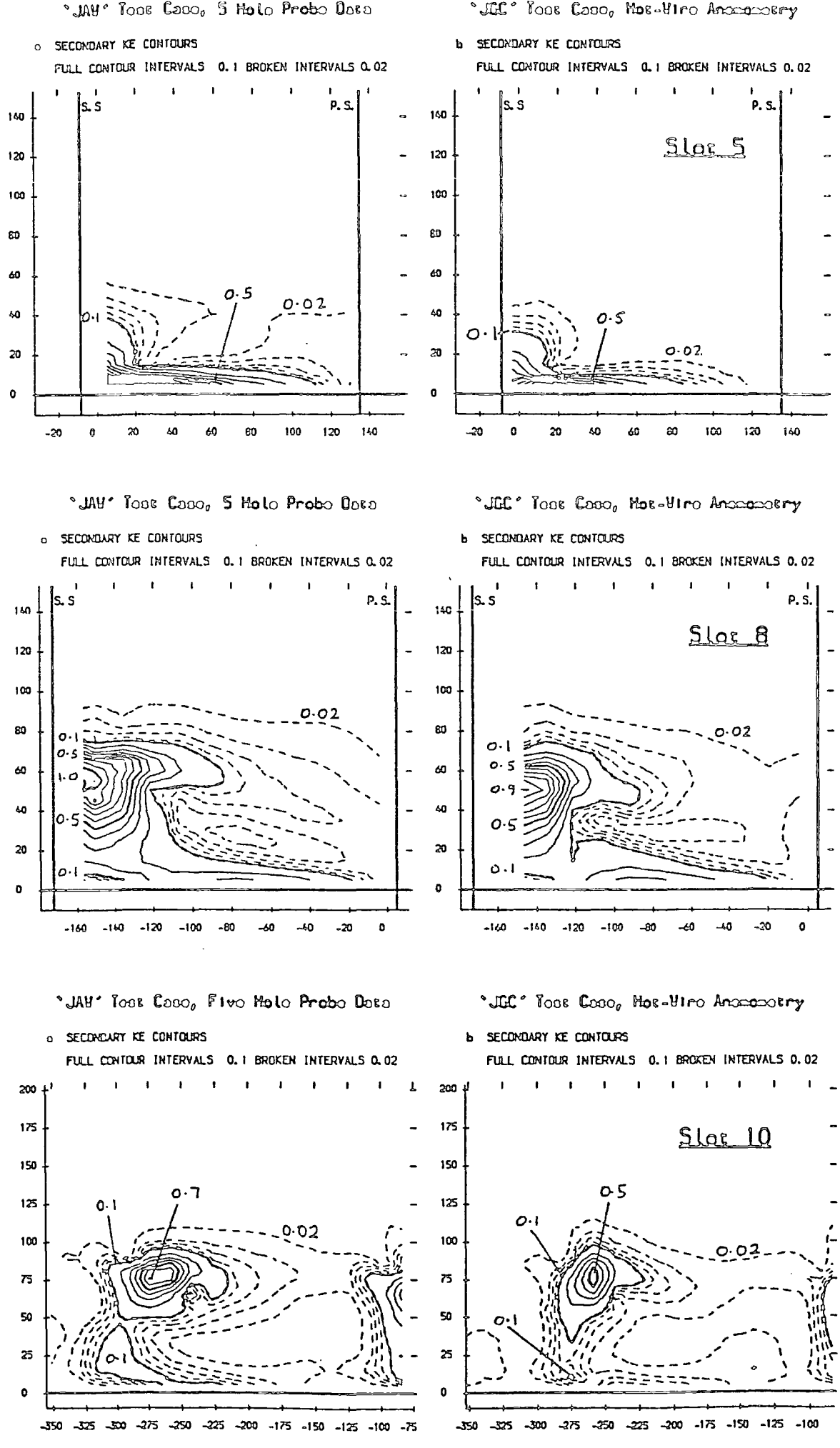


FIGURE 7.21 : Secondary Kinetic Energy Contours

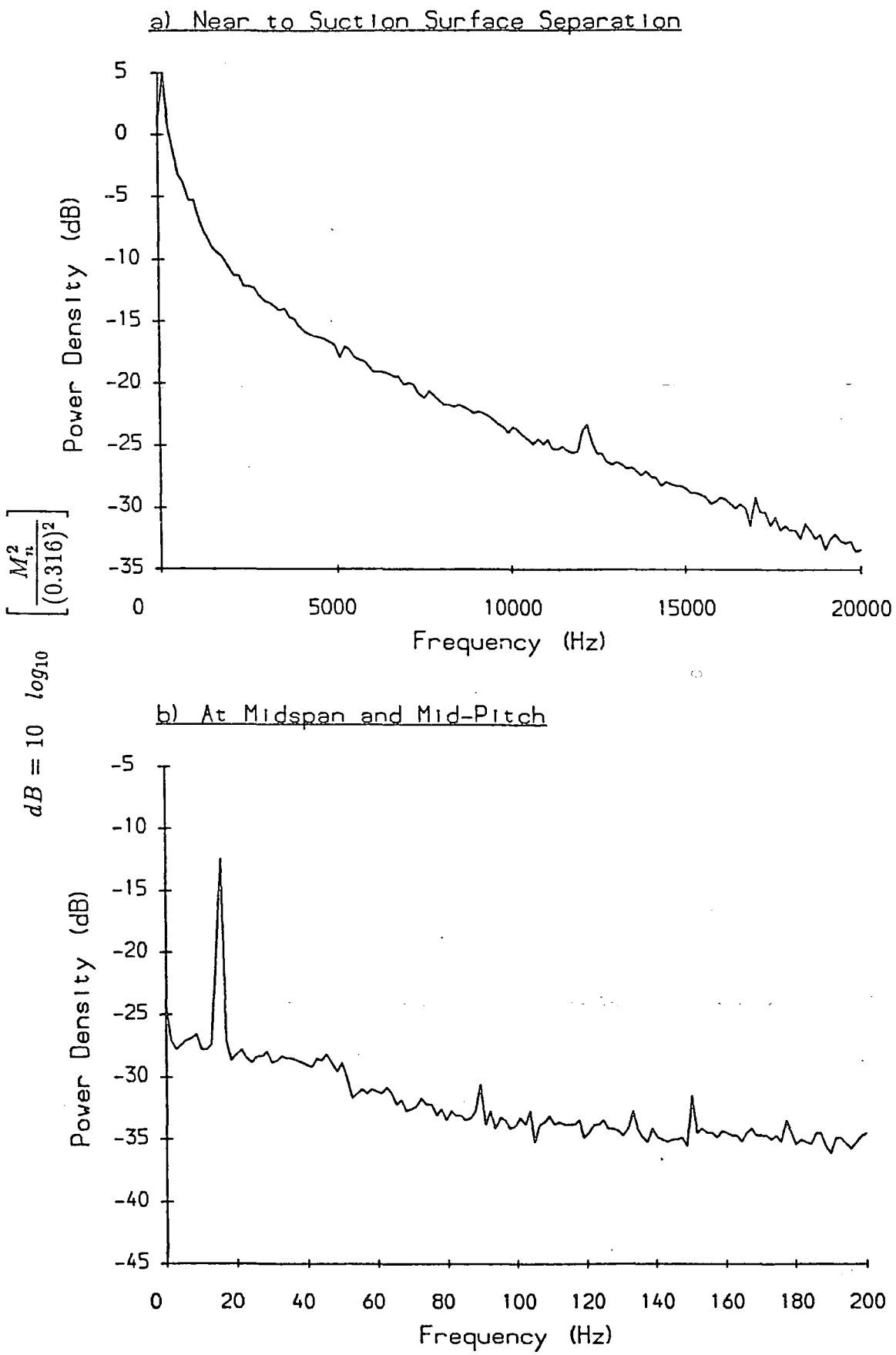


FIGURE 7.22 : Turbulence Spectra at Slot 8

Calculated Eddy Viscosities and Dissipation Rates for 'JGC' Test Case

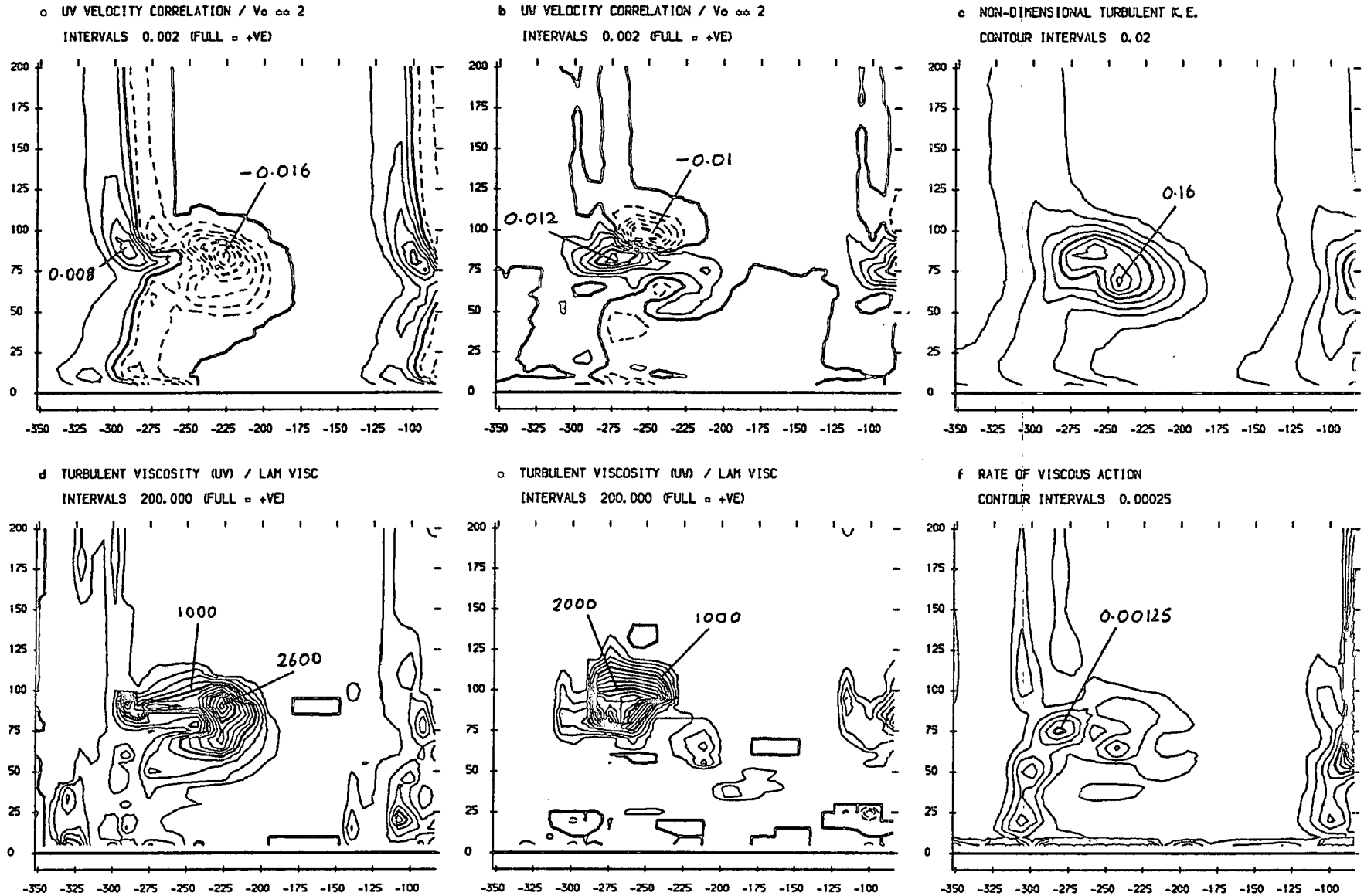


FIGURE 7.23 (a-f) : Area Plots For Slot 10

Calculated Eddy Viscosities and Dissipation Rates for 'JGC' Test Case

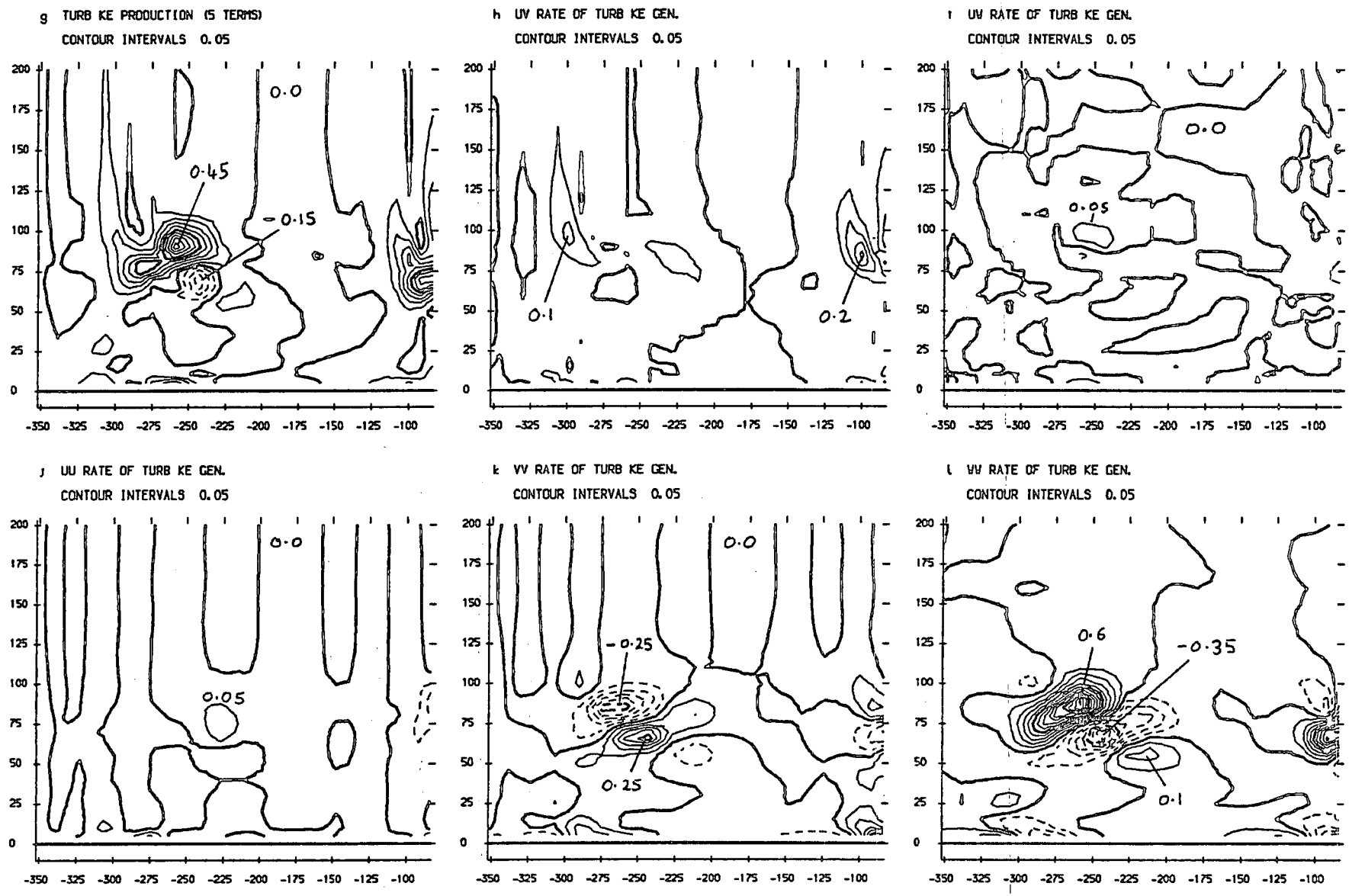


FIGURE 7.23 (g-l) : Area Plots For Slot 10

# Chapter 8
# Modelling Results (JGC Test Case)

## 8.0 Introduction

This chapter describes results of modelling the 'JGC' test case (experimental data described in Chapter 7). The pressure correction code of Moore and Moore (1985) is tested with three different turbulence models. Resulting predictions for the Reynolds stresses are calculated from the predicted velocity and turbulent viscosity fields, and are compared with the results of hot-wire anemometry traverses. Where appropriate, eddy viscosities and turbulent kinetic energy are also compared with experiment. All the Navier-Stokes calculations presented in this chapter were run on the coarse mesh (Figure 6.1(a)), and used version 7 of the Moore code (as described in Chapter 6).

## 8.1 Standard Mixing Length Model Mean Flow Results

Three runs have been performed using the Moore code, with the standard mixing length turbulence model as described in Chapter 6. The three runs differed in the regions of the flowfield in which the turbulence model was allowed to operate. The first run assumed that the flow was turbulent everywhere, the second incorporated laminar block A (Figure 6.2(a)), and the third included both laminar blocks A and B (Figures 6.2(a), 6.2(c)).

Figure 8.1 shows pitch averaged results at slot 1 (-14% Cax) for the three calculations and experiment. There is a systemmatic difference in yaw angle due to the experiment operating off the design incidence of 42.75°. The effects of the model running at a slightly different inlet angle are discussed in Chapter 6, and were not found to be very significant for the general secondary flow development. The loss curve indicates that all three runs have conserved total pressure well from the inlet boundary to slot 1, and have the correct inlet boundary layer profile. Although the secondary kinetic energy measured experimentally appears larger than that modelled, this is due to some radial

variation in the inlet flow angle, and the levels are in any case very small.

Results at slot 5 (55% Cax) are presented in Figure 8.2 (a-l). These may be compared with the hot-wire measurements shown in Figure 7.11. The yaw angle contours indicate that the distribution in each of the three runs is similar at this stage, but that compared with the experimental results, the flow is generally over-turned by approximately 5°. This is rather surprising. Comparing yaw angles measured by Walsh (1987) for the 'JAW' test case, with those obtained from hot-wire traverses of the 'JGC' test case, reveals a systemmatic difference of approximately 2.4°. This might be attributed to experimental error as no change in midspan angle was expected from introduction of the turbulence grid (which is the difference between the 'JAW' and 'JGC' test cases). Although the equivalent results for the 'JAW' test case have not been presented, a similar difference existed between measured and predicted yaw angles. The run described in Chapter 6, which had the upstream flow set at the experimental inlet angle, also shows this discrepancy, thus eliminating the inlet angle as a possible cause. It is not clear why such a difference should exist between measured and predicted values. It is perhaps worth bearing in mind however, that at this stage in the cascade the flow is being turned very rapidly. Thus agreement between experiment and modelling might be obtained by looking at predicted data on an axial plane only slightly upstream of slot 5. Despite these problems with the midspan flow angles, the over-turning on the endwall appears to be quite well modelled by all three runs, as is the distribution of total velocity. However, the secondary velocity vectors indicate that the vortex is not centred in the correct place in any of the predictions, although the run with laminar block B ('laminar endwall') is perhaps showing some signs of shifting the vortex centre towards the suction surface.

Although no measurements of loss are available at slot 5, the predicted losses are presented in Figures 8.2(j-l). It is clear that the loss is still confined quite closely to the endwall at this stage. Some significant loss is also appearing on the suction surface, but the fully turbulent run shows this to be quite uniform in radial distribution, indicating that it is purely

profile loss, and not a result of the secondary flows interacting with the blade boundary layer. Also freestream fluid has been brought into the endwall region on the pressure side of the passage. This is in keeping with the results of the endwall boundary layer traverse discussed in Chapter 7.

Figure 8.3 presents pitch averaged results at slot 5. Here the systematic difference in yaw angle is very clear. As discussed above, 2.4° of this might be attributed to experimental error, but the origin of the remaining discrepancy is unclear. The loss coefficient and turbulent kinetic energy show the secondary flow effects to be confined quite close to the endwall at this stage. Also reasonable agreement is apparent between the predicted and measured secondary kinetic energy, although the vortex migration observed in the vector plots for the run with laminar block B produces the best results.

Results at slot 8 (97% Cax) are presented in Figure 8.4(a-l). This may be compared with the hot-wire results shown in Figure 7.14. The yaw angles indicate that the under-turning at $50mm$ from the endwall is not correctly modelled by any of the calculations. However they all predict the over-turning near to the endwall more accurately. The total velocity magnitude contours indicate good agreement with experiment, and are similar in each case. In the turbulent run, the suction surface boundary layer is clearly thicker than for the two runs which included laminar block A. However it is not as large as that indicated by the experimental results. This is surprising, and the experimental boundary layer does seem very thick. This may be a result of the very accute angle of the blade to the axial traverse plane at this location. Any misplacement of the axial location of the probe, will appear to be magnified when viewed in a plot such as Figure 7.14. It is also clear that the low velocity region associated with the convected inlet boundary layer fluid forms slightly further from the endwall in the run with laminar block B than in the other two. This is more realistic, and indicates a more energetic passage vortex in this case. The secondary velocity vectors confirm this and show the vortex to be quite realistically located in the run with laminar block B. Less convection is apparent for the other two runs. The loss contours indicate that the suction surface boundary layer is much

thicker in the turbulent run than in those which incorporated laminar block A. Again the run with laminar block B appears to be slightly more realistic than the other two, and predicts a distinct loss core forming away from the suction surface, with a second core located in the region where the passage vortex separates from the blade. Although equivalent experimental results are not available, this has been seen previously to be a characteristic feature of turbine rotor blade secondary flows.

Pitch averaged results at slot 8 are presented in Figure 8.5. The yaw angles show good agreement with experiment at midspan. Agreement is also good within $20mm$ of the endwall, where the flow is strongly over-turned. However, the under-turning at about $60mm$ from the endwall is less well modelled. The run with laminar block B appears to produce the best radial positioning, but fails to predict the magnitude of the under-turning. The loss coefficient shows that the effect of laminar block B is to encourage radial migration of loss. A peak is forming at about $55mm$ from the endwall, which is associated with the suction surface separation, and convected inlet boundary layer fluid. The hot-wire measurements also indicate that this is a region of high turbulent kinetic energy. None of the runs predict the secondary kinetic energy peak at $55mm$ from the endwall exactly, but the run with laminar block B is closer to the experiment in this respect.

Results at slot 10 (128% Cax) are presented in Figure 8.6(a-r). These may be compared with the five hole probe results shown in Figure 7.5, and the hot-wire anemometry results in Figure 7.17. The yaw angles compare well with experiment except within the blade wake where the flow appears to be over-turned. This is associated with numerical problems in the trailing edge region, and can be alleviated with a finer calculation mesh, and modifications to the mixing length calculation as described in Chapter 6. The pitch angles are reasonably modelled in all the calculations, but the run with laminar block A captures the negative pitch angle peak best. The static pressure contours show that the modelling predicts too low a static pressure over the traverse plane. This was discussed in Chapter 6, and was found to result from the incorrect inlet flow angle employed in the modelling, since

the experiment is actually running slightly off-design. Despite this, the total velocity magnitude contours agree reasonably well with experiment, but all show too much reduction of velocity within the blade wake. The secondary velocity vectors show that the run with laminar block B has achieved the best passage vortex position, with the other runs locating it too close to the endwall. The loss contours all indicate too much loss within the blade wake as discussed in Chapter 6, but reasonable predictions appear to be obtained for the loss core.

Pitch averaged results at slot 10 are presented in Figure 8.7. There is a systemmatic difference in yaw angle between experiment and modelling, and as discussed in Chapter 6 this results from numerical problems in the trailing edge region. However, if this discrepancy was subtracted from the experimental curve at all radial locations, good agreement would be obtained with the prediction which incorporated laminar block B. The other two runs do not convect the vortex so far from the endwall, and hence locate the under-turning peak at $55mm$ radially rather than at the experimental position of $75mm$. The loss curve indicates the over-prediction of profile loss in all the runs, but is otherwise reasonable. If the midspan loss is subtracted from all the modelling results at each radial position, then the two runs which did not include laminar block B, produce a reasonably sized loss core, but located too close to the endwall. The run with laminar block B produces better radial positioning, but smooths out the loss curve a little. The secondary kinetic energy curves all appear to generally indicate over-prediction at this stage. This is because the secondary kinetic energy generally does not decay downstream of the cascade in a realistic manner. Again the run with laminar block B appears to produce the most realistic prediction in terms of radial distribution.

## 8.2 Standard Mixing Length Model Mass Averaged Results

The mass averaged loss, and secondary kinetic energy for the three runs and experiment, are presented in Figure 8.8. The predicted loss reduces

as laminar blocks are added to the flowfield, but is generally too large. Also the secondary kinetic energy increases with increasing laminar regions. It is interesting that for this test case the run with laminar block B appears to give the best prediction of secondary kinetic energy, particularly as the values measured within the blade passage did not cover the full flow area, and so must be assumed to be too small. For the 'JAW' test case the run with laminar block B appeared to over-predict secondary kinetic energy. However, generally the code has performed very well, and has managed to predict the reduced levels of secondary kinetic energy resulting from the thinner inlet boundary layer in this case.

Table 8.1 presents mass averaged quantities at slot 10. Whilst all the runs predict too much profile loss, the predictions of net secondary loss are quite good. The sum of secondary kinetic energy and loss gives a reasonable prediction of the mixed out loss, as observed in previous chapters.

**Table 8.1 : Mass Averaged Results**

| JGC TEST CASE | Experiment | MEFP Turbulent | MEFP Turb + Lam Block A | MEFP Turb + Lam Blocks A+B |
|---|---|---|---|---|
| Loss (Slot 10) | 0.182 | 0.323 | 0.280 | 0.254 |
| - Midspan Loss (Slot 10) | 0.097 | 0.248 | 0.184 | 0.176 |
| = Gross Sec. Loss (Slot 10) | 0.085 | 0.075 | 0.096 | 0.078 |
| - Inlet (Slot 1) Loss | 0.027 | 0.032 | 0.031 | 0.030 |
| = Net Sec. Loss (Slot 10) | 0.058 | 0.043 | 0.065 | 0.048 |
| Secondary KE (Slot 10) | 0.026 | 0.028 | 0.031 | 0.033 |
| Sec KE + Loss (Slot 10) | 0.208 | 0.351 | 0.311 | 0.287 |
| Mixed Out Loss | 0.211 | 0.370 | 0.324 | 0.299 |
| - Midspan Mixed Out Loss | 0.100 | 0.264 | 0.191 | 0.185 |
| = Gross Mixed Out Sec. Loss | 0.111 | 0.106 | 0.133 | 0.114 |
| - Inlet (Slot 1) Loss | 0.027 | 0.032 | 0.031 | 0.030 |
| = Net Mixed Out Sec. Loss | 0.084 | 0.074 | 0.102 | 0.084 |
| Midspan Mixed Out Angle | −66.7° | −69.2° | −69.3° | −69.3° |

The fully turbulent run under-predicts the secondary loss. The other

two runs which include laminar block A predict more secondary loss. This is because the subtraction of profile loss was correct for the turbulent run, but leaves an extra secondary loss due to the growth of a turbulent suction surface boundary layer within $40mm$ of the endwall for those runs which included laminar block A. The best prediction appears to be produced by the run with both laminar blocks A and B, although the degree of agreement is probably slightly fortuitous.

### 8.3 Calculation of Shear Stresses

As it was shown in Chapter 6 that the turbulence modelling employed within a solution can have major effects upon the quality of the secondary flow predictions, it was considered desirable to compare the shear stresses used by the code directly with experiment. The shear stresses applied to the sides of control volumes are approximately in a streamwise coordinate system, as the grid lines are intended to roughly follow the two-dimensional flow direction. Thus shear stresses computed in hot-wire coordinates (which are aligned with the midspan streamwise direction) should be similar to those which are employed within the Navier-Stokes predictions. The Moore code was thus made to dump out the eddy viscosity field calculated by the mixing length turbulence model on the last iteration of each solution. With the aid of the subroutine used in Chapter 7 to calculate eddy viscosities, and developed by Gregory-Smith *et al* (1987), it was possible to calculate partial velocity derivatives from the axial planes of data. The method uses bi-cubic spline surface fits to determine gradients of velocity and stagnation pressure on a traverse plane, and then uses the incompressible Helmholtz equation and the continuity equation to find the axial gradients of velocity. The axial planes of data were interpolated from the three-dimensional solutions, to correspond to the axial traverse planes. The three Reynolds shear stresses ($\overline{u'v'}, \overline{u'w'}, \overline{v'w'}$) were then calculated from the equation:-

$$\overline{u_i' u_j'} = -\frac{\mu_t}{\rho}\left(\frac{\partial \overline{U_i}}{\partial x_j} + \frac{\partial \overline{U_j}}{\partial x_i}\right) \tag{8.1}$$

The first two stresses $\overline{u'v'}$, and $\overline{u'w'}$ may be directly compared with the experimental results presented in Chapter 7. The third stress was not measured experimentally, but was calculated for the predictions as it has been found by Moore *et al* (1986) to be important for the secondary flows.

## 8.4 Standard Mixing Length Model Shear Stresses

Results of calculating the shear stresses at slot 5 (55% Cax) for the three predictions using the mixing length turbulence model are presented in Figure 8.9. The definition of the laminar blocks shows up in these plots, with laminar block A eliminating turbulence effects above approximately 10% span from the endwall, and laminar block B within 1% span of the endwall. These distances may not be quite the same as those given in the definition of the laminar blocks, as the eddy viscosities are stored within the Moore code at cell centres, but had to be interpolated to cell corners for this calculation of stresses. The turbulent run shows that significant $\overline{u'v'}$ shear stress is predicted by the mixing length model on the suction surface, but that this is not effected by the secondary flow as the radial distribution is almost uniform. In the runs with laminar block A, the shear stress only appears within $55mm$ of the endwall, and so is allowed to contribute to the secondary loss when the midspan loss is subtracted from the total loss. This is certainly not a predictive capability of the code, and is the result of user intervention. The turbulence model was left on in this region as it was felt that the passage vortex would probably cause more rapid development of the suction surface boundary layer close to the endwall. However the modelling does not produce much radial variation of shear stress (Figure 8.9(a)), and thus the effect of laminar block A is to allow a poor prediction of the suction surface boundary layer to appear in the final solution as part of the secondary loss. This effect shows up in the mass averaged results at slot 10, as can be seen in the difference between predictions of the net secondary loss by the turbulent run, and the run with laminar block A. There is a region of positive $\overline{u'v'}$ correlation near to the suction side of the passage. This agrees

with the sign of the experimental measurements shown in Figure 7.11, but does not capture the magnitude of this shear stress which is associated with the passage vortex.

The $\overline{u'w'}$ correlation may also be compared with experimental measurements in Figure 7.11. A small negative region is located in the endwall/suction side region of the passage in the turbulent run and the run with laminar block A. Experimentally the stress was measured as positive in this area, but the modelling has not predicted the correct location of the passage vortex. The run with laminar block B, allows larger over-turning to develop very close to the endwall, and this appears to be encouraging the passage vortex to migrate towards the suction surface/endwall corner as it is seen to do experimentally. This also appears to be starting to convect the $\overline{u'w'}$ shear stress onto the suction surface and is thus approaching a more realistic solution than the other two predictions. Unfortunately, experimental data is not available with which to compare the $\overline{v'w'}$ predictions. A small area of negative $\overline{v'w'}$ correlation is predicted by the turbulent run in the endwall/suction surface corner. However, the run with laminar block B appears to have less of this negative region, and instead is producing a small intense positive region on the suction surface of the blade at about $15mm$ from the endwall. The contours of eddy viscosity, show that this is associated with a peak in the turbulent viscosity calculated by the mixing length model. It is surprising that addition of laminar block A changes the eddy viscosities from those present in the turbulent run, and this may be an indication of the sensitivity of the calculation to small changes in the flowfield. However the turbulent viscosities only reach values of 100 times the molecular viscosity. Calculations of eddy viscosities from the experimental data downstream of the cascade showed peak values of 2000 within the loss core.

Results at slot 8 (97% Cax) are presented in Figure 8.10(a-l), and may be compared with the experimental results in Figure 7.14. The $\overline{u'v'}$ correlation shows large negative values all over the suction surface. Whilst these cannot be seen in the experimental results, the sign is consistent with a boundary layer on the suction surface, which the experiment did not

approach closely enough to measure. These contours are related to the total velocity magnitude contours shown in Figure 8.4(d-f). The region of negative $\overline{u'v'}$ in the suction surface/endwall corner was measured by the single wire probe. However the general sign of $\overline{u'v'}$ in the loss core region was found experimentally to be positive at slot 8. As discussed in Chapter 7, this is a legacy of the strong cross-passage velocity gradient which exists upstream, and the experimental shear stress is rapidly decaying towards values of the opposite sign at slot 10. However at slot 8, a negative eddy viscosity would be required to predict $\overline{u'v'}$, so the mixing length model could not be expected to model this feature.

The $\overline{u'w'}$ correlation predicts a sign change across the suction surface separation region of the correct sign, but the levels are much too low. Indeed the model generally fails to identify the magnitude of the turbulent stresses within the three-dimensional flow of the passage vortex. On the endwall, both the runs which did not include laminar block B, predict significant negative values of $\overline{u'w'}$. Whilst the sign is consistent with the growth of an endwall boundary layer, the x-probe measurements which extended to $5mm$ from the endwall, did not detect this feature. Thus too much loss is probably being produced on the endwall by both of these runs. However, the run with laminar block B almost eliminates this shear stress, which is consistent with the lower levels of secondary loss predicted by this run, than by the run with only laminar block A.

The $\overline{v'w'}$ correlation shows generally positive values on the endwall. This is consistent with a boundary layer growth from pressure to suction side of the passage. However this region is very thin and rapidly changes sign. On the suction surface negative values exist in the region where the passage vortex sweeps flow radially from the endwall. This is also consistent with a boundary layer growing up the suction surface away from the endwall. However a region of positive $\overline{v'w'}$ is identified within the secondary flow. Whilst no experimental measurements exist with which to compare this prediction, the model is clearly indicating that the $\overline{v'w'}$ stress is the largest of the three shear stresses within the passage vortex. Moore *et al* (1986) found this to be true in the flow

downstream of their cascade, and showed that there the $\overline{v'w'}$ correlation was the largest contributor to loss production.

Contours of eddy viscosity, although still not identifying very large values within the passage vortex, do show a peak in the suction surface separation region. Also the two runs which do not include laminar block B, show an area of high eddy viscosity on the endwall towards the suction side of the passage. Although as seen above, this results in rather large values of $\overline{u'w'}$, an increase in eddy viscosity in this region seems likely as the turbulent kinetic energy contours (Figure 7.14) indicate increased turbulence activity. The run with laminar block B eliminates this feature entirely. As discussed in Chapter 7, a laminar flow over a large proportion of the endwall on the pressure side of the passage seems likely, but towards the suction side the flow is generally turbulent. Thus allowing laminar block B to extend right across the pitch, is a rather crude model of the endwall flow.

Results at slot 10 (128% Cax) are presented in Figure 8.11, and may be compared with the experimental results in Figure 7.17. As the calculation of velocity gradients did not force a repeating condition in the pitchwise direction, the extension of the data to cover the same range as the experimental data has resulted in some problems for the contour plotting routine. Thus in places the contours may seem slightly different in one wake from those in the other. The $\overline{u'v'}$ correlation shows reasonable values within the wake, but this is aided by the prediction of too large a velocity deficit in this region. None of the runs identify the magnitude of the stress associated with the separated secondary flows. The $\overline{u'w'}$ correlation is confined predominantly to the endwall region where it clearly indicates growth of an endwall boundary layer across the whole pitch. The experimental values may possibly indicate that the stress extends a little too far from the wall, but do not really approach closely enough to validate the predictions. Again the mixing length model clearly identifies the $\overline{v'w'}$ correlation as being the most significant within the passage vortex. A clear sign change is evident across the region where the passage vortices from neighbouring passages interact. The positive band by the endwall which is predicted by the run with laminar

block A, seems unlikely, particularly as the pitch averaged curves (Figure 8.7) do not indicate it to have more over-turning in this region than the other two runs. Hence this feature is thought to probably result from surface fitting problems near to the endwall when calculating the partial velocity gradients. This is supported by the fact that the eddy viscosities do not indicate any larger values in this region for this run than for the other two.

The eddy viscosities may be compared with those calculated from the experimental shear stresses and shown in Figure 7.23. The loss core is obviously identified as a region of high eddy viscosity, but the peak values of about 150 do not approach those calculated from experiment which rise to values of 2000 or more. The eddy viscosity is also too small within the wake. This indicates the problem of using such a simple turbulence model within such a complex flow. In some regions significant turbulence generation takes place. In these areas the constants in the model would need to be adjusted to produce realistic values of the eddy viscosity. However in other regions the turbulence does not increase so much and so a modified turbulence model would then over-predict the stresses there. Thus a model which solves a turbulent kinetic energy transport equation becomes attractive.

## 8.5 Discussion of Mixing Length Model Results

The under-prediction of the turbulent stresses within the secondary loss core by the mixing length model is consistent with the low rate of decay of secondary kinetic energy downstream, which is seen in all the Moore code predictions. However, the loss growth curve is seen to rise fairly realistically downstream. As it is known that a significant proportion of the downstream loss growth results from the action of the turbulent stresses within the secondary flow, this suggests that too much loss is being produced by the mixing out of the wake and/or the growth of an endwall boundary layer (numerical error is of course a third possibility, but it is felt that the code has already shown itself to be sufficiently good at conserving stagnation pressure to neglect this here). This is supported by approximately correct

stress levels within the wake but larger velocity gradients there, and the apparently large $\overline{u'w'}$ in the endwall region. Thus it does not seem that the modelling of loss development downstream of the cascade can be considered to be realistic.

It is curious that the code has been shown to be capable of producing reasonably good secondary loss predictions for this cascade. Publications have also shown this for other cases. Moore (1985) produced good predictions of loss in the Langston cascade, whilst Northall *et al* (1987) showed good results for the annular cascade of Boletis (1984), which used the same blade profile as that tested by Marchal and Sieverding (1977). Also Walsh (1987) found that using a very crude calculation mesh, the relative change in secondary loss due to skew in the inlet boundary layer was well predicted by the code. It seems possible that this loss is a result of sweeping loss produced on the suction surface (possibly by a slightly over-active boundary layer model) into the main flow. The extent of this removal would then depend to some extent upon the power of the passage vortex. If loss is rapidly swept away from the suction surface in the secondary flow region, the increased shear will produce new loss more rapidly. Thus subtraction of the profile loss from the overall loss downstream of the cascade, will appear to leave some extra 'secondary loss'. Indeed this may be a reasonable model of some of the real effects which are present. It is possible that a significant proportion of secondary loss results from the passage vortex introducing high velocity fluid close to the suction surface, and thus increasing the shear in part of the blade boundary layer. However the experimental data presented here cannot validate this suggestion. It would clearly be helpful to know the rate at which loss is being produced by the stresses within the passage vortex. As discussed in Chapter 7 this would require a total pressure traverse at slots 5 and 8. It is possible that the net effect of the stresses within the experimental shear flow is almost zero, which would help to explain the apparently good secondary loss predictions. However if this is the case, it must surely be due to a fortuitous combination of effects, and the generality of a model which fails to identify the true physical processes must then be questioned.

## 8.6 One Equation Turbulence Model

The Navier-Stokes solver which is tested here, is continuously being developed. One of the directions in which progress is being made, is in the application of more sophisticated turbulence models within the solution procedure. Birch (1989b) has given a thorough account of the models currently available. At present these are all still limited by a Boussinesq eddy viscosity hypothesis, but the new models use the Prandtl-Kolmogorov formula to relate the eddy viscosity to the turbulent kinetic energy and a length scale via:-

$$\nu_T = K^{\frac{1}{2}} l \tag{8.2}$$

Here $K$ is the turbulent kinetic energy, and $l$ is a length scale proportional to that of the energy containing motions. In a one equation model, a transport equation is solved for the turbulent kinetic energy, and the length scale is specified algebraically. In Birch's one equation model the turbulent kinetic energy formula takes the form:-

$$\frac{DK}{Dt} = \frac{\partial}{\partial x_j}\left[(\nu + \nu_T)\frac{\partial K}{\partial x_j}\right] + \nu_T\left[\frac{\partial \overline{U_i}}{\partial x_j}\left(\frac{\partial \overline{U_i}}{\partial x_j} + \frac{\partial \overline{U_j}}{\partial x_i}\right)\right] - \left[\frac{C_1}{C_2}\nu_T + C_3\nu\right]\frac{K}{l^2} \tag{8.3}$$

where $\nu_T$ is the eddy viscosity and $C_1$, $C_2$, $C_3$ are constants.

Birch also uses a damping factor to help with near wall effects, so that the eddy viscosity is calculated from the formula:-

$$\nu_T = C_2 K^{\frac{1}{2}} l\left[1 - e^{-\frac{C_4 n K^{\frac{1}{2}} l}{\nu}}\right] \tag{8.4}$$

where $C_4$ is also a constant, and $n$ is the distance to the nearest wall.

The dissipation length scale is then specified algebraically. In order to account for transition, a constant in the definition of the dissipation length is adjusted according to the maximum turbulent kinetic energy within the boundary layer. This is an important consideration in turbomachinery applications, where blade boundary layers may often be transitional. Beyond any identifiable boundary layers, the mixing length is adopted as the dissipation length scale, and calculated in the same way as that for the mixing length model described in Chapter 3 and 6.

## 8.7 One Equation Turbulence Model Mean Flow Results

The one equation model has been run on the coarse calculation mesh for the 'JGC' test case. Results at slot 5 (55% Cax) are presented in Figure 8.12(a-f). The static pressure contours indicate the strong cross-passage pressure gradient that exists within the blade passage. This is also evident in the total velocity contours. Comparing these with experimental results in Figure 7.11, good agreement is observed, although the suction surface boundary layer is perhaps slightly thicker in the modelling. The yaw angle contours again show the 5° discrepancy which was observed with the mixing length results. The over-turning near to the endwall is reasonably modelled, but the pitch angles are clearly inaccurate. This is because the passage vortex is unrealistically located at mid-passage. The loss contours are similar to those predicted by the mixing length model, except that the suction surface boundary layer is clearly thicker here.

Results at slot 8 (97% Cax) are presented in Figure 8.13(a-f). Here the static pressure contours clearly indicate quite a weak passage vortex and are rather reminiscent of the type of results obtained with version 5 of the Moore code which incorporated an earlier version of the mixing length model (Figure 6.7(d)). The yaw angle contours are reasonable, but do not capture the under-turning at $60mm$ from the endwall which appears in the experimental results (Figure 7.14). It can also be seen that the pitch angle contours are in poor agreement with experiment. The secondary velocity vectors do not predict enough convection of the passage vortex, which has been seen previously (Chapter 6) to be a characteristic feature of an over-active turbulence model. Also the loss contours and total velocity magnitude contours indicate that the suction surface boundary layer is rather too thick.

Pitch averaged results at slot 8 are presented in Figure 8.14. The results of another run, using a $K-\epsilon$ turbulence model are also shown, but should be ignored here as they will be discussed later. The yaw angle plot shows that the one equation model is failing to predict the radial migration of the passage vortex. The loss curve indicates that the one equation model

produces a similar level of midspan loss as the fully turbulent mixing length run (Figure 8.5). However the secondary kinetic energy at $55mm$ from the endwall is not captured by the one equation model.

Results at slot 10 (128% Cax) are presented in Figure 8.16(a-f) and may be compared with five hole probe results in Figure 7.5 and hot-wire anemometry results in Figure 7.17. The static pressure contours indicate little variation over the flow area, which is supported by the rather weak passage vortex. The yaw angle contours fail to identify the under-turning peak properly, but do not show the same magnitude of variation of yaw angle within the wake as was apparent in the mixing length model results (Figure 8.6). The pitch angles are rather unrealistic, in keeping with the poor prediction of the passage vortex. The loss contours show the blade wake to be too wide, and contain too much loss. However, the depression in velocity magnitude within the wake is better modelled by the one equation model than it was by the mixing length model (Figure 8.6).

Pitch averaged results at slot 10 are presented in Figure 8.16. The yaw angles again show some discrepancy at midspan which is probably associated with trailing edge modelling problems. Also it is clear that the prediction of the over and under-turning is not very realistic. The loss plot shows that too much profile loss is predicted by the one equation model, but that this is no worse than results obtained with the mixing length model and laminar block A. However, if the over-prediction of profile loss is subtracted from all points then the secondary loss core can be seen to be too small, as is the loss produced on the endwall. Also the secondary kinetic energy is rather unrealistic, predicting too much near to the endwall, and not enough at $75mm$ radially.

The mass averaged loss and secondary kinetic energy for the one equation model and experiment are plotted in Figure 8.17. The model predicts a smooth growth of loss through the cascade with a large jump across the trailing edge. Downstream the loss does not grow very rapidly, which is probably related to the lower loss production observed on the endwall in the pitch averaged plot at slot 10 compared with the mixing length model.

The overall loss appears to be comparable to that produced by the mixing length model with laminar block A, which is encouraging since no specification of transition had to be included here. However the secondary kinetic energy is too small, and might be considered similar to results obtained with version 5 of the program with an earlier version of the mixing length model (Figure 6.10).

Mass averaged results at slot 10 (128% Cax) are presented in Table 8.2 together with the five hole probe measurements, and the results of a run using a $K-\epsilon$ turbulence model to be discussed later. The results in Table 8.2 indicate that although the one equation model predicts too much loss, most of this is profile loss, and the prediction of secondary loss is too small by a factor of 50%. This is most surprising, given the good secondary loss predictions which have previously been obtained with the mixing length model.

**Table 8.2 : Mass Averaged Results**

| JGC TEST CASE | Experiment | MEFP One Equation Model | MEFP $K-\epsilon$ Model |
|---|---|---|---|
| Loss (Slot 10) | 0.182 | 0.272 | 0.378 |
| - Midspan Loss (Slot 10) | 0.097 | 0.212 | 0.268 |
| = Gross Sec. Loss (Slot 10) | 0.085 | 0.060 | 0.110 |
| - Inlet (Slot 1) Loss | 0.027 | 0.036 | 0.031 |
| = Net Sec. Loss (Slot 10) | 0.058 | 0.024 | 0.069 |
| Secondary KE (Slot 10) | 0.026 | 0.015 | 0.010 |
| Sec KE + Loss (Slot 10) | 0.208 | 0.296 | 0.388 |
| Mixed Out Loss | 0.211 | 0.297 | 0.399 |
| - Midspan Mixed Out Loss | 0.100 | 0.219 | 0.274 |
| = Gross Mixed Out Sec. Loss | 0.111 | 0.078 | 0.125 |
| - Inlet (Slot 1) Loss | 0.027 | 0.036 | 0.031 |
| = Net Mixed Out Sec. Loss | 0.084 | 0.042 | 0.094 |
| Midspan Mixed Out Angle | $-66.7°$ | $-68.7°$ | $-69.0°$ |

## 8.8 One Equation Turbulence Model Reynolds Stresses

The shear stresses have been calculated from the one equation model solution, using the method described in section 8.3. Figure 8.18 (a-e) presents results at slot 5 (55% Cax). These may be compared with the experimental results in Figure 7.11, and the mixing length model results in Figure 8.9. The $\overline{u'v'}$ correlation shows some negative values near to the suction surface as would be expected for the boundary layer flow. These values are rather less than those predicted by the turbulent mixing length model run. However, the one equation model also predicts positive values beyond the suction surface boundary layer, due to the cross-passage velocity gradient. These are unrealistically large, and extend right across the span. The model also fails to identify the intense shear stress within the passage vortex that was observed experimentally. The $\overline{u'w'}$ correlation predicts some negative values at about mid-pitch on the endwall. This is consistent with the growth of an endwall boundary layer. Also the $\overline{v'w'}$ correlation shows positive values immediately next to the endwall, but these rapidly change to negative values further away. Again the activity is centred at mid-pitch, whereas experimentally the turbulence activity was found to be confined to the suction side of the passage. The turbulent viscosity can be seen to attain appreciable levels on the whole suction side of the passage, and it is these that result in the significant $\overline{u'v'}$ correlation predictions in this region. Also a peak is identified with the passage vortex, but this is centred very much at mid-passage.

The turbulent kinetic energy shows that the one equation model is predicting too much turbulence on the suction surface. This is probably because the strong curvature and acceleration within the blade passage interact selectively with particular components of the Reynolds stress tensor to promote anisotropy. In particular the streamwise normal stress will act to convert turbulent energy to mean flow energy, which may explain why the one equation model is over-predicting the suction surface turbulence. Also some turbulent kinetic energy is associated with the passage vortex, but this does not approach the levels which are generated within the real secondary flow.

Results at slot 8 (97% Cax) are presented in Figure 8.19(a-e). These may be compared with the experimental results in Figure 7.14, and the mixing length model results in Figure 8.10. A large suction surface boundary layer is now in evidence and is associated with significant negative $\overline{u'v'}$ correlation. This is not too much greater than the levels which are predicted by the fully turbulent mixing length run. However the one equation model also predicts some significant $\overline{u'v'}$ correlation near to the pressure surface. The values very near to the surface are positive, in keeping with a boundary layer flow. However just beyond this boundary layer significant negative values appear.

The $\overline{u'w'}$ correlation shows very little activity, even on the endwall which explains the lower endwall loss growth observed in the pitch averaged plots. This is probably more realistic than the mixing length model results. The one equation model also identifies significant $\overline{v'w'}$ correlation with the passage vortex on the suction side of the passage. In this respect it is in reasonable agreement with the mixing length model results. The turbulent viscosity indicates fairly uniform activity over the flowfield, and does not identify any significant peak with the passage vortex. This is also shown by the turbulent kinetic energy contours which do not identify the turbulence generation which has occurred within the secondary flow.

Results at slot 10 (128% Cax) are presented in Figure 8.20(a-e) which may be compared with Figure 7.17 and 8.11. The $\overline{u'v'}$ correlation shows a similar level of activity within the wake to that predicted by the mixing length model with turbulent flowfield, and this is reasonably realistic. However the $\overline{u'w'}$ correlation shows much lower values on the endwall than were observed from the mixing length model. The experiment does not approach the endwall closely enough to validate this prediction, but as discussed earlier, the mixing length values were thought to be too large. However the high shear stress values which are associated with the passage vortex are not captured by the modelling. The $\overline{v'w'}$ correlation is something of an exception to this. Although the real values might be much higher, significant levels of $\overline{v'w'}$ are predicted by the one equation model and these are clearly associated with the secondary flow. The turbulent viscosity rises to a peak of 250 times the

laminar viscosity in this region. This does not compare with the magnitude of turbulent viscosities within the secondary flow which were calculated from the experimental measurements (Figure 7.23), but the values within the wake appear reasonable. It is interesting to see that the turbulent kinetic energy is over-predicted within the wake. Gregory-Smith *et al* (1988) found that the wake turbulence dissipated rapidly downstream of their cascade, and the levels measured here (128% Cax) are quite low. Examination of the prediction at slots 9 and 11 shows that the model does predict dissipation of the wake turbulence so that by slot 11 (152% Cax) the predicted levels are similar to those measured at slot 10 (128% Cax). Despite this high wake turbulence, the model again fails to identify the turbulence levels within the three-dimensional separated flow of the passage vortex.

## 8.9 Discussion of One Equation Turbulence Model Results

Clearly the one equation model requires further development if it is to improve upon results obtained with the mixing length model. One encouraging aspect of the model is its transition modelling capability, and the profile loss predicted by it is between that obtained from the mixing length model with a fully turbulent flowfield, and with laminar block A (Figure 6.2(a)). However the one equation model does not identify the turbulent kinetic energy production within the passage vortex, and generally produces too much turbulent viscosity over the flowfield. The model may benefit from adjustment of constants based upon experience with test cases such as this one. Birch (1989b) has also suggested that it be modified to cope with the effects of streamline curvature. This seems very important, particularly if the model is to be used on a wide variety of blade types.

The observed inaccuracy of the one equation model in predicting secondary losses is interesting. In previous experience with the mixing length model it appeared that the secondary loss was generally reasonably well modelled. However looking back to the first two runs which used version 5 of the Moore code (Figure 6.10), it can be seen that the loss remains almost

constant up to 80% of axial chord in the 'laminar' run. This was because the only region in which the turbulence model operated in this run was in the blade boundary layers from 80% axial chord to the trailing edge, and in the blade wake. Yet this run still managed to produce good secondary loss predictions (Table 6.1). This indicates that the mixing length model produces a large proportion of its secondary loss through the interaction of the passage vortex with the suction surface boundary layer in the final 20% of axial chord, and by interaction of neighbouring passage vortices downstream of the trailing edge. Some support for this is provided by the shear stresses presented in Figures 8.9 and 8.10. At slot 5 (Figure 8.9) the shear stresses within the suction surface flow are virtually unaffected by the passage vortex. By slot 8 however (Figure 8.10) significant distortion of the $\overline{u'v'}$ correlation by the secondary flow is clear. It could be that the one equation model is over-damping the turbulence in the near-wall region, thus preventing the secondary flow influence on the flow in these areas from having so much effect. There certainly seems to be cause for some concern, when changing the turbulence model can lead to such large changes in the predictions of losses.

## 8.10 $k - \epsilon$/Mixing Length Hybrid Model

Instead of specifying the dissipation length scale $l$ algebraically, as is the case in the one equation turbulence model, a separate transport equation may be solved for it. As the turbulent kinetic energy $K$ is already being solved for, the second equation may solve for any $K^a l^b$ where $a$ and $b$ are constants. At high turbulence Reynolds numbers the energy dissipation rate, $\epsilon$, is given by:-

$$\epsilon = \frac{K^{\frac{3}{2}}}{l} \tag{8.5}$$

hence many two-equation models solve for $\epsilon$ and are thus known as $K - \epsilon$ models. The restriction of high turbulence Reynolds number means that the model does not perform well near walls. Although versions of the $K - \epsilon$

model exist which are intended to extend right up to the wall, the gradients of $K$ and $\epsilon$ become very steep, and thus require a large number of grid points to be adaquately represented in a discretised solution procedure. This is very expensive in three dimensions, and thus it becomes desirable to use a separate model for the flow close to the walls.

In the model tested here, which is described by Birch (1989b), the standard mixing length model is employed within the boundary layers. Clearly there must be some interface between the grid cells in which the $K-\epsilon$ model is used, and those in which the mixing length model operates. This is allowed to vary as the calculation proceeds, and is based upon a turbulence Reynolds number as defined by:-

$$R_y = \frac{K^{\frac{1}{2}} n}{\nu} \tag{8.6}$$

where $n$ is the distance to the nearest wall. In the solution presented here, the boundary was set so that the $K-\epsilon$ model operated when $R_y$ exceeded a value of 400. Boundary conditions are also set at the interface to ensure a continuous eddy viscosity, and local equilibrium such that the dissipation rate $\epsilon$, matches the rate of turbulence production.

The standard high Reynolds number $K-\epsilon$ model equations are then used:-

$$\frac{DK}{Dt} = \frac{\partial}{\partial x_i}\left[\left(\nu + \frac{\nu_T}{\sigma_K}\right)\frac{\partial K}{\partial x_i}\right] + \nu_T \frac{\partial \overline{U_i}}{\partial x_j}\left[\frac{\partial \overline{U_i}}{\partial x_j} + \frac{\partial \overline{U_j}}{\partial x_i}\right] - \epsilon \tag{8.7}$$

and

$$\frac{D\epsilon}{Dt} = \frac{\partial}{\partial x_i}\left[\left(\nu + \frac{\nu_T}{\sigma_\epsilon}\right)\frac{\partial \epsilon}{\partial x_i}\right] + C_1\left(\frac{\epsilon}{K}\right)\nu_T \frac{\partial \overline{U_i}}{\partial x_j}\left[\frac{\partial \overline{U_i}}{\partial x_j} + \frac{\partial \overline{U_j}}{\partial x_i}\right] - C_2\left(\frac{\epsilon^2}{K}\right) \tag{8.8}$$

where $\sigma_K$, $\sigma_\epsilon$, $C_1$, $C_2$ are constants. The Prandtl-Kolmogorov formula (equation 8.2) is then used with equation (8.5) to express the eddy viscosity in terms of $K$ and $\epsilon$.

## 8.11 Results of a $k-\epsilon$/Mixing Length Hybrid Model Run

The hybrid $K-\epsilon$/mixing length model has been run on the coarse calculation mesh for the 'JGC' test case. As the mixing length model operates

within the blade boundary layers, they were forced to be laminar up to 80% of axial chord beyond 10% span from the endwall (this is like laminar block A, except that the $K-\epsilon$ model operates away from the boundary layers).

Results at slot 5 (55% Cax) are presented in Figure 8.21 which may be compared with the experimental data in Figure 7.11, and the one equation model results in Figure 8.12. Generally the mean flow results appear similar to those obtained with the one equation model and indicate a weak passage vortex centred at mid-passage. This results in unrealistic pitch angles. The yaw angles again indicate a discrepancy with the experiment results, and this has been found in all the MEFP predictions at slot 5. The turbulent blade boundary layer within 10% span, is clearly evident in the loss contours which also indicate that the inlet boundary layer has been swept to the suction side of the passage.

The predicted turbulence quantities may be compared with results of the one equation turbulence model in Figure 8.18, the mixing length model in Figure 8.9, and the experimental results in Figure 7.11. The results are quite remarkable. The turbulent viscosity contours immediately indicate that the $k-\epsilon$ model is predicting significant turbulence generation within the secondary flow. The turbulent kinetic energy contours show that the model is predicting approximately the correct level of turbulent kinetic energy, and even possibly too much. This is in sharp contrast with the results of the one equation model which failed to identify this feature. The prediction of significant eddy viscosity then has a significant impact upon all the shear stresses. The $\overline{u'v'}$ correlation shows the negative values within the suction surface boundary layer which are predicted by the mixing length model. Beyond this however, there is significant positive $\overline{u'v'}$ correlation. This is in agreement with the experiment, but indicates rather too large an area to be associated with these high values with the stress not being confined as closely to the endwall/suction surface corner as it is in the experiment. The $\overline{u'w'}$ correlation shows negative values on the endwall which is consistent with the growth of an endwall boundary layer. This does not however fit the experimental observation of mainly positive values down to $5mm$ from the

endwall. Also the $\overline{v'w'}$ correlation is predicted to have a large effect right across the pitch and this is strongly linked to the passage vortex. The one equation model also detected some of this feature, whereas the mixing length model had much less $\overline{v'w'}$ at this stage. In particular the run with laminar block B almost eliminated it. It could be that this stress is keeping the passage vortex from migrating in the one and two equation model solutions.

Results at slot 8 (97% Cax) are presented in Figure 8.22(a-k) which may be compared with the experimental results in Figure 7.14. The static pressure contours are quite similar to those predicted by the one equation model (Figure 8.13) except that here there is generally lower static pressure over the axial plane. The passage vortex and yaw and pitch angles also look very similar to those predicted by the one equation model, and show the vortex to be rather weak, and 'glued' to the endwall in a way which is becoming a familiar indication of over-active turbulence modelling away from the boundary layers. However, the total velocity magnitude contours and the loss contours indicate larger peaks where the passage vortex separates from the suction surface.

The turbulent viscosity again shows higher values within the secondary flow than have been detected by the other models. The turbulent kinetic energy identifies a peak in the region where the passage vortex separates from the suction surface and the general distribution appears to be good. Another peak in turbulent kinetic energy is predicted in the endwall/suction surface corner, and is clearly associated with the passage vortex separation from the endwall. This was observed in the experiment, but the predicted level appears to be too high. A similar feature is predicted in the endwall/pressure surface corner due to separation of the passage vortex from the pressure surface. This feature was not detected experimentally, although Marchal and Sieverding (1977) did observe a small counter vortex in this region. Also generally higher turbulence levels appear to be associated with the pressure surface than were observed experimentally.

The shear stresses generally agree in sign and location with predictions by the other models, but show larger values due to the larger predictions

of turbulent viscosities. In particular significant $\overline{u'v'}$ correlation is associated with the suction surface boundary layer, significant $\overline{u'w'}$ correlation with the endwall boundary layer, and large $\overline{v'w'}$ correlation with the passage vortex.

Figure 8.23(a-k) presents results at slot 10 (128% Cax) which may be compared with the experimental results in Figures 7.5 and 7.17. The static pressure indicates little variation over the axial plane, and this is unrealistic, although a similar result was obtained with the one equation model (Figure 8.15). The yaw and pitch angles indicate rather less secondary flow than was measured experimentally or predicted by any of the other runs. This is confirmed by the rather weak passage vortex shown by the secondary velocity vectors, which has clearly not been convected to the correct location. The loss contours indicate too much loss within the blade wake, and indeed also have some loss in areas which would be expected to be governed by potential flow. However more loss appears to be associated with the secondary flow than was the case in the one equation model run (Figure 8.15). The total velocity magnitude contours indicate similar results to the one equation model, and in particular predict less velocity deficit within the blade wake than the mixing length model (Figure 8.6). However, in general the secondary flow prediction is not of such high quality as that produced by the mixing length model.

The turbulent kinetic energy contours indicate that the $k-\epsilon$ model is predicting too much turbulence within the wake. The one equation model also showed this (Figure 8.20) but examination of the predicted results at slots 9 and 11 shows that the $K-\epsilon$ model initially predicts much higher levels than the one equation model. However, it also dissipates these more rapidly, so that the levels predicted by the two models at slot 11 are comparable. It has been shown experimentally by Gregory-Smith *et al* (1988) that the wake turbulence dissipates rapidly, whilst the levels within the secondary flow remain. Since the turbulence levels within the wake are predicted to be quite high by the $K-\epsilon$ model, the levels within the secondary flow region are also large. However the high turbulence region which is associated with the secondary flow is not as large as that measured experimentally (Figure

7.17) which suggests that either the production is under predicted, or the dissipation is over predicted, within the secondary flow downstream of the cascade. However the prediction of secondary flow turbulence is superior to that produced by the one equation model (Figure 8.20). The turbulent viscosity indicates slightly higher levels within the wake than those predicted by the one equation model (please note that the contour intervals here are different from those employed in the plot of experimental results in Figure 7.23), and reaches higher levels than any of the other models within the secondary flow. However the location of this high turbulent viscosity is a little suspect, although it is possible that if the $\overline{v'w'}$ stress had been measured experimentally, it might have suggested high eddy viscosity in this region.

As a result of the high turbulence within the wake the $\overline{u'v'}$ correlation is over-predicted there. However high positive $\overline{u'v'}$ is also associated with the secondary flow which is more realistic. The negative values within the loss core are not well modelled however. The $\overline{u'w'}$ correlation, which is generally the least active of the three, shows negative values on the endwall, indicating the growth of a boundary layer there. The localised intense values within the secondary flow are not predicted. The $\overline{v'w'}$ stress again predicts large values associated with the secondary flow. These values are larger than those predicted by any of the other models tested here, and there is clearly a need for experimental measurements with which to validate them.

## 8.12 $k-\epsilon$/Mixing Length Hybrid Model Mass Averaged Results

Pitch averaged results at slot 8 are presented in Figure 8.14 together with the results from the one equation model, and the experimental hot-wire measurements. In terms of yaw angle and secondary kinetic energy, the two turbulence models perform fairly similarly, and both fail to identify the under-turning peak at $55mm$ from the endwall. However the $K-\epsilon$/mixing length model clearly predicts more loss than the one equation model in the secondary flow region. This correlates moderately well with the experimental turbulent kinetic energy curve, which is a reasonable indicator of loss distribution.

The pitch averaged results at slot 10 (Figure 8.16) indicate that the $K-\epsilon$/mixing length hybrid model is predicting even less secondary flow than the one equation model at this stage. Both the runs are predicting too much profile loss, but if this is subtracted at all radial points, the hybrid model is producing more secondary loss than the one equation model. The one equation model indicates more secondary kinetic energy than the hybrid model, particularly on the endwall, which is probably because of its lower prediction of the shear stresses there.

The growth of loss and secondary kinetic energy for the one equation model, the hybrid $K-\epsilon$/mixing length model, and experiment is shown in Figure 8.17. Clearly both models predict too little secondary kinetic energy, with the hybrid $K-\epsilon$/mixing length model performing slightly worse in this respect. The hybrid model also predicts much more loss than the one equation model. However much of this is produced across the trailing edge and is associated with problems with the mixing length model in this region. The one equation model clearly does much better in this respect. Generally the losses up to slot 6 produced by the hybrid model (with laminar blades up to 80% axial chord and beyond 10% span) are less than those produced by the one equation model. Thereafter the hybrid model (and probably the mixing length part of it) produces loss more rapidly. Also downstream it is clear that the hybrid model predicts more growth of loss than the one equation model. This is probably associated with the larger shear stress observed on the endwall, and the associated growth of an endwall boundary layer.

## 8.13 Conclusions

Mass averaged quantities are presented in Table 8.2 for the $K-\epsilon$/mixing length model, and the one equation model. It can be seen that although the $K-\epsilon$/mixing length hybrid model over-predicts the loss, most of this appears as profile loss and the prediction of secondary loss is reasonable. In particular, comparing with the results of the mixing length run with laminar block A in Table 8.1, it can be seen that the predictions of net

secondary loss are very similar. However less mixed out secondary loss is predicted by the $K-\epsilon$/mixing length model, as the secondary kinetic energy was under-predicted by it. Thus it might seem that the shear stresses within the secondary flow have had a relatively minor effect compared with those in the boundary layers. Also experience with the mixing length model suggests that it produces most secondary loss within the suction surface boundary layer in the final 20% of axial chord. Unfortunately it is not possible to validate this model with the data available here, and further experimental work is required.

Generally however, the results of the $K-\epsilon$ calculation appear to be encouraging. The two transport equations succeed in capturing more of the secondary flow turbulence behaviour than either of the other models tested here. The quality of the secondary flow prediction is clearly impaired by the one equation model and the $K-\epsilon$ model. However this should not be considered to be too discouraging as results in Chapter 6 showed similar behaviour with an earlier version of the mixing length model. The mixing length model thus benefits from its longer period of implementation, and correspondingly finer tuning. It seems that a combination of the $K-\epsilon$ model for the separated flows, with a one equation model for the boundary layers, could eventually capture more of the flow physics than the mixing length model and thus be correspondingly more generally applicable. However the one equation model needs to be carefully validated before being used to replace the mixing length model. A treatment of the effects of streamline curvature within the one equation model seems almost essential for suction surface boundary layer calculations. This might also be a general problem resulting from the use of a Boussinesq eddy viscosity hypothesis within a highly curved channel. The validity of such an isotropic assumption is highly questionable in these circumstances. Leschziner (1989) suggests that such flows should be modelled with a Reynolds stress model. However he admits that the use of such models within three-dimensional flows is still in early days, and that the development of good turbulence models is likely to be slow, thus retarding the progress of CFD as a truly predictive technique.

◈ Five Hole Probe Measurements.
⊠ MEFP Turbulent + Laminar Blocks A+B, Mixing Length Model.
※ MEFP Turbulent + Laminar Block A, Mixing Length Model.
⊕ MEFP Turbulent Flowfield, Mixing Length Model.

a) Yaw Angle (Degrees)

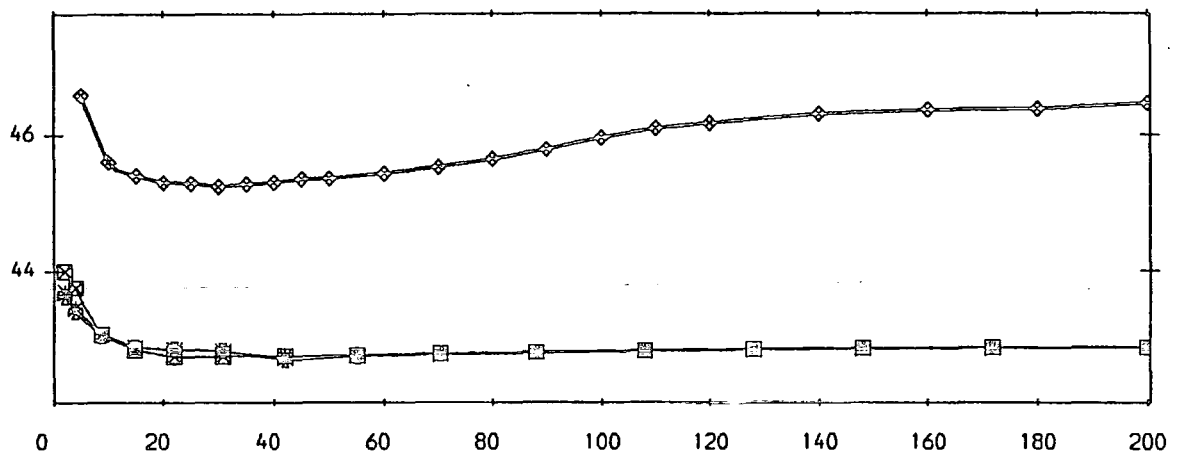


b) Total Pressure Loss Coefficient

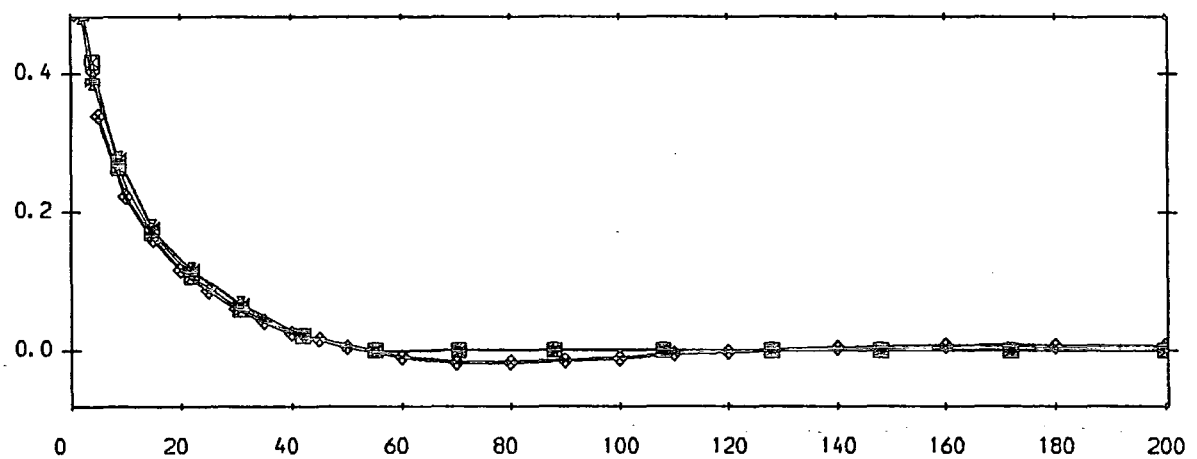


c) Secondary Kinetic Energy Coefficient

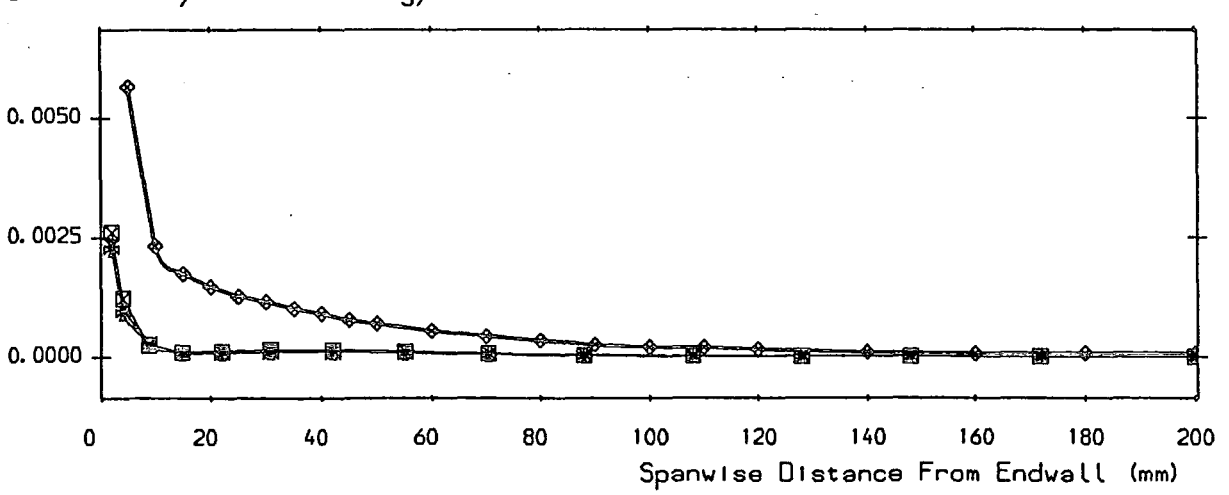


FIGURE 8.1 : Pitch Averaged Results For Slot 1

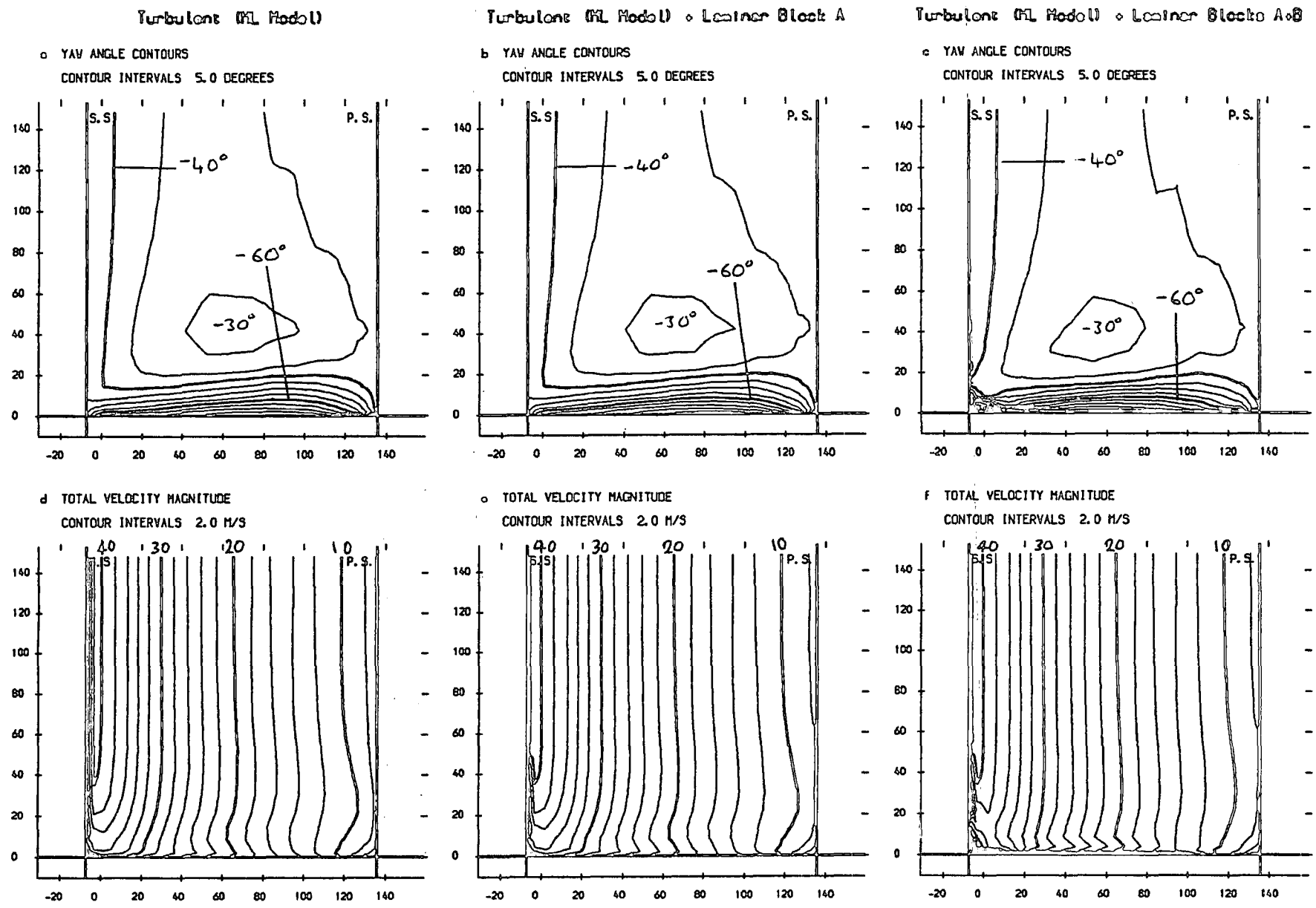


FIGURE 8.2 (a-f) : Area Plots For Slot 5

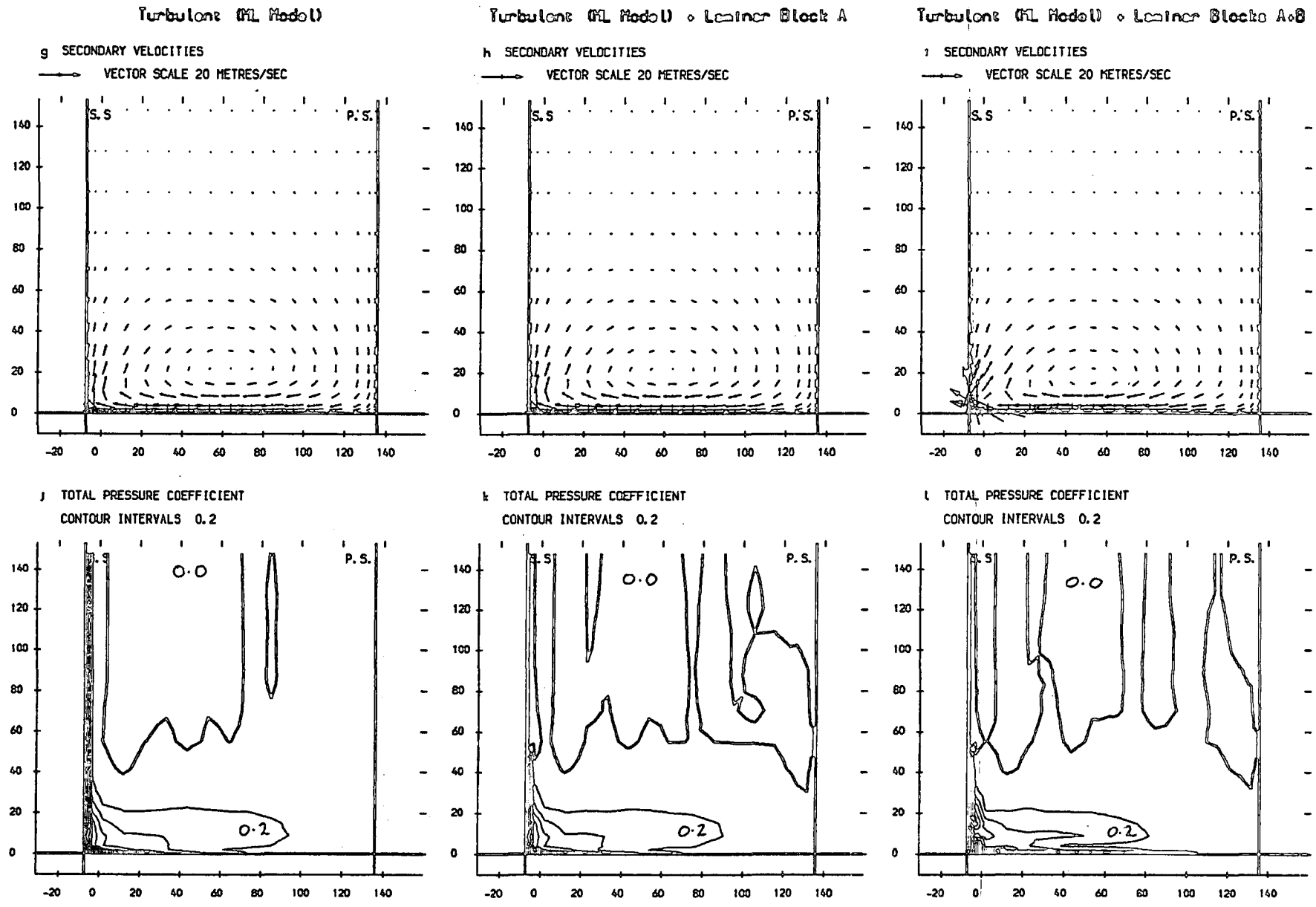


FIGURE 8.2 (g-l) : Area Plots For Slot 5

◈ Hot-Wire Anemometry Measurements.
⊠ MEFP Turbulent + Laminar Blocks A+B, Mixing Length Model.
✳ MEFP Turbulent + Laminar Block A, Mixing Length Model.
✙ MEFP Turbulent Flowfield, Mixing Length Model.

a) Yaw Angle (Degrees)

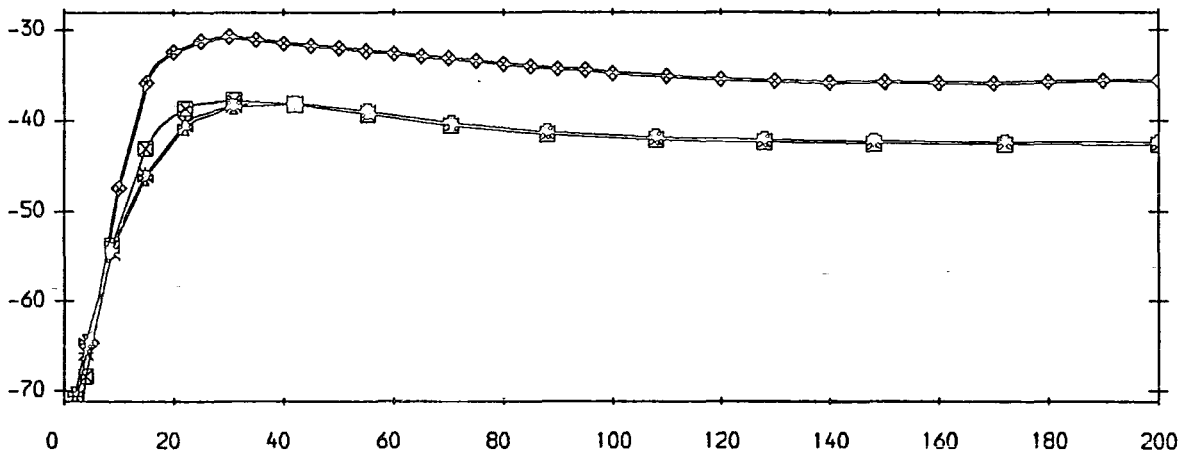


b) Loss Coeff. (x10), & Turbulent Kinetic Energy Coeff. (x100)

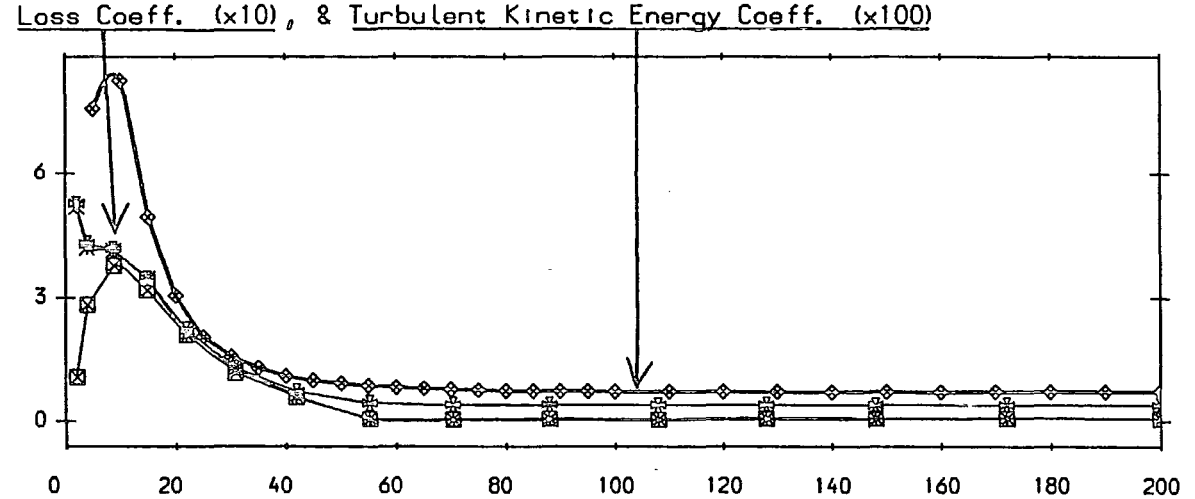


c) Secondary Kinetic Energy Coefficient

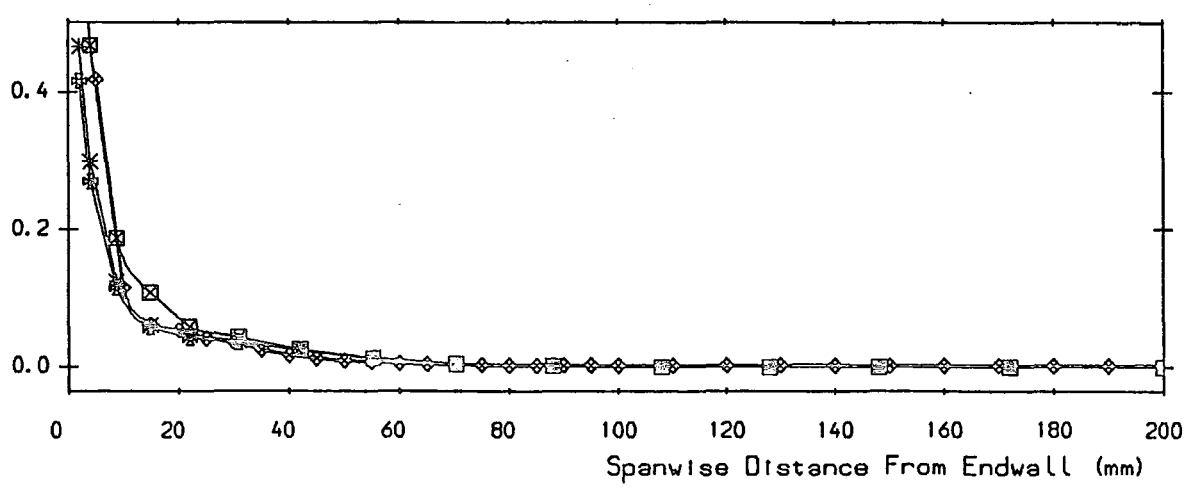


FIGURE 8.3 : Pitch Averaged Results For Slot 5

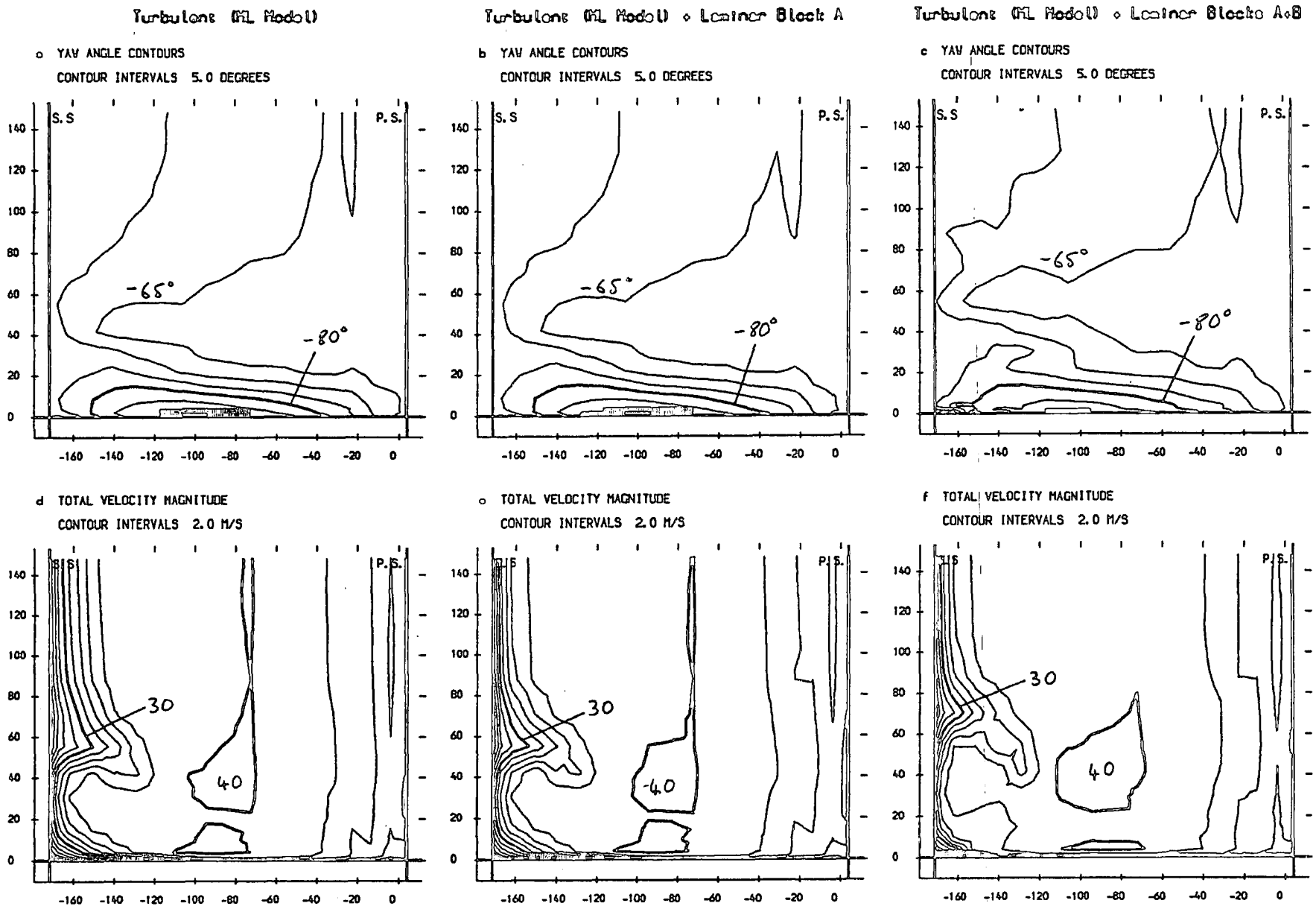


FIGURE 8.4 (a-f) : Area Plots For Slot 8

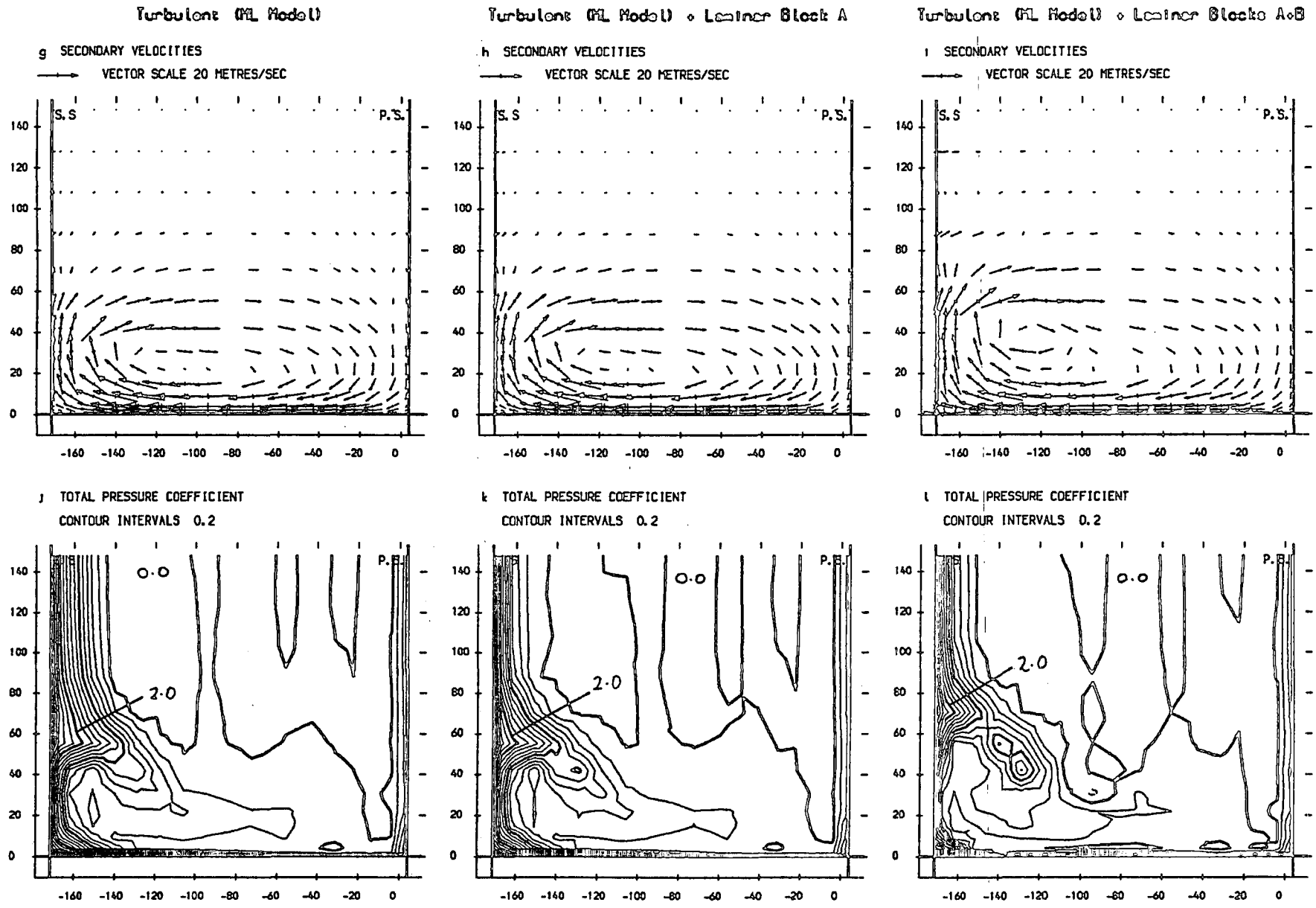


FIGURE 8.4 (g-l) : Area Plots For Slot 8

◆ Hot-Wire Anemometry Measurements.
⊠ MEFP Turbulent + Laminar Blocks A+B, Mixing Length Model.
※ MEFP Turbulent + Laminar Block A, Mixing Length Model.
❋ MEFP Turbulent Flowfield, Mixing Length Model.

a) Yaw Angle (Degrees)

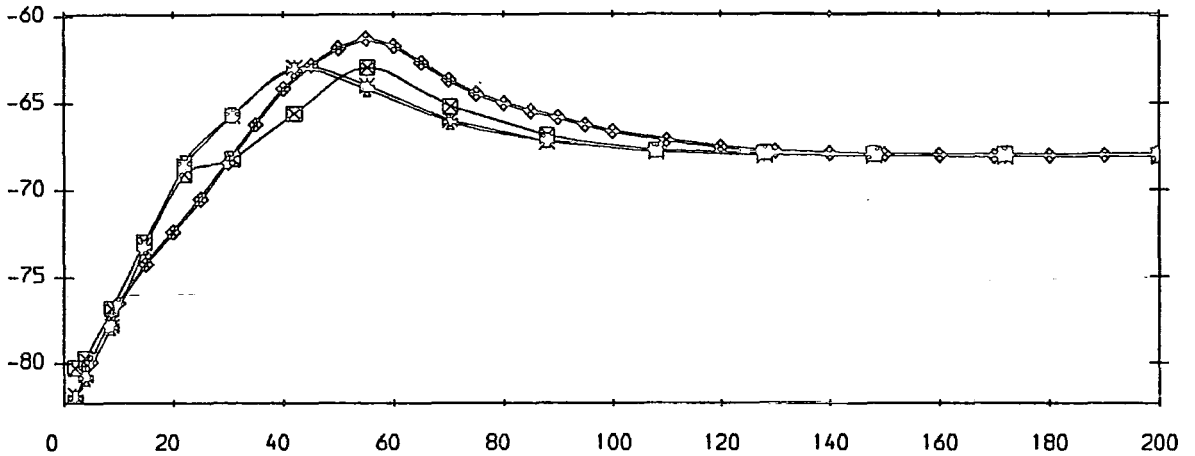


b) Loss Coeff. (x10), & Turbulent Kinetic Energy Coeff. (x100)

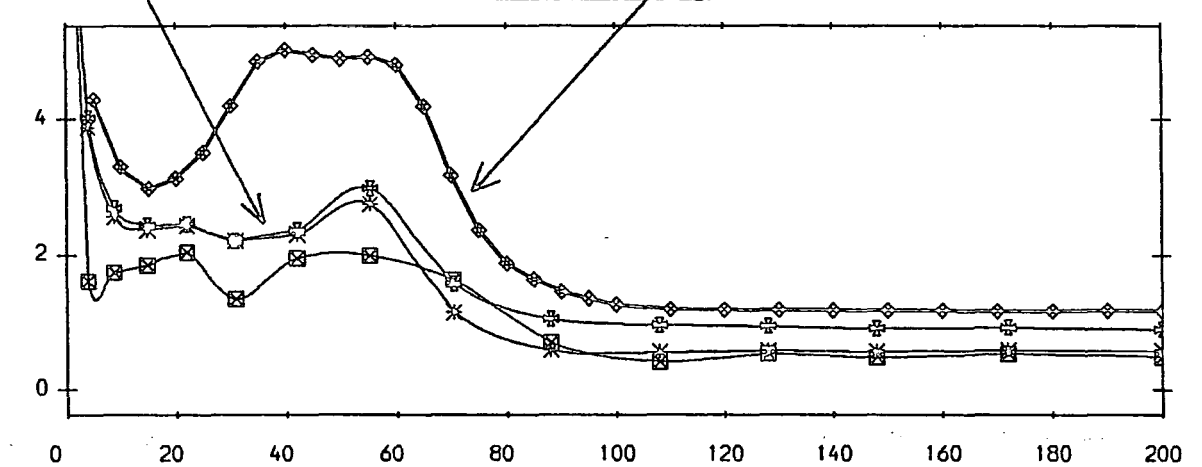


c) Secondary Kinetic Energy Coefficient

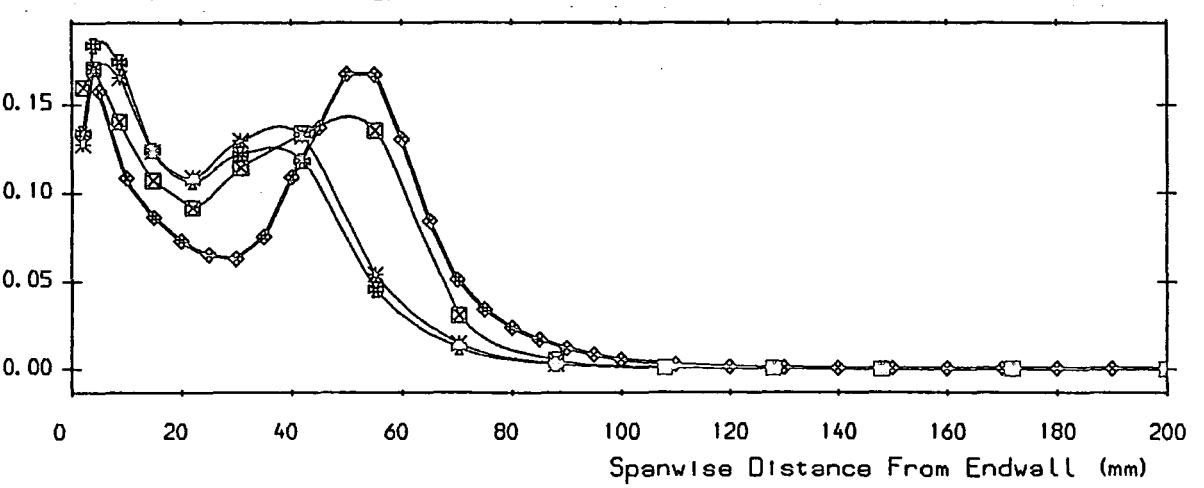


FIGURE 8.5 : Pitch Averaged Results For Slot 8

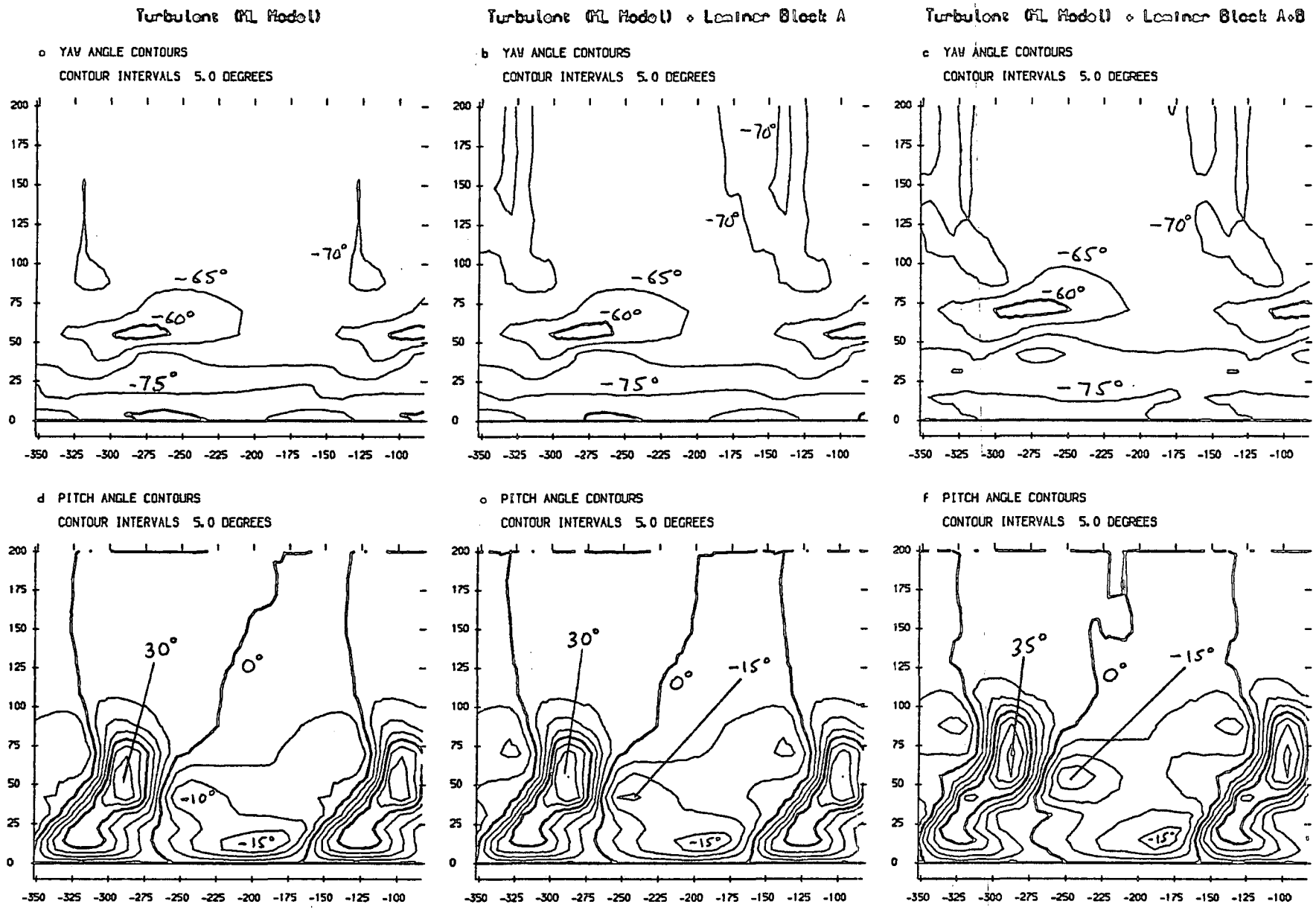


FIGURE 8.6 (a-f) : Area Plots For Slot 10

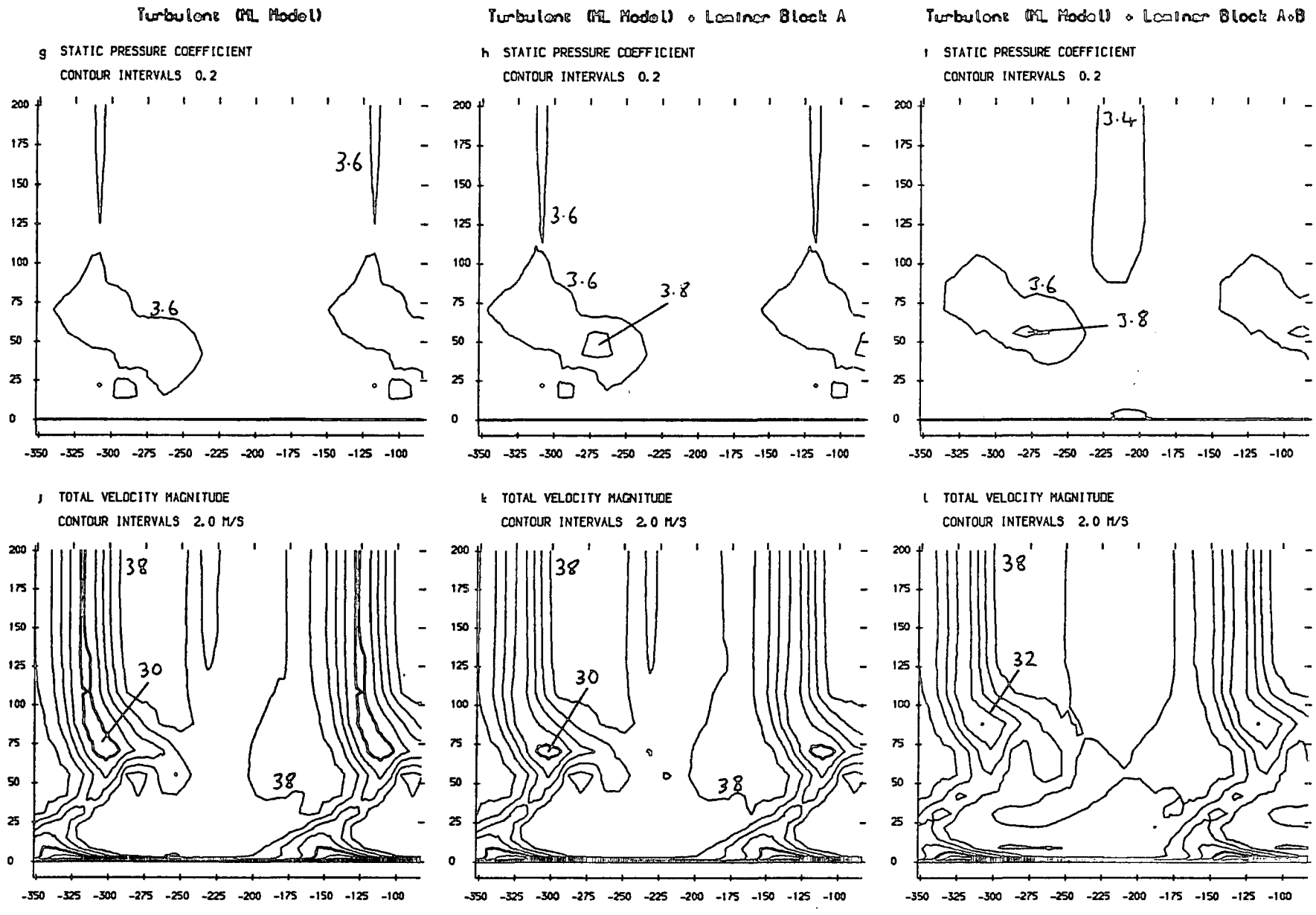


FIGURE 8.6 (g-l) : Area Plots For Slot 10

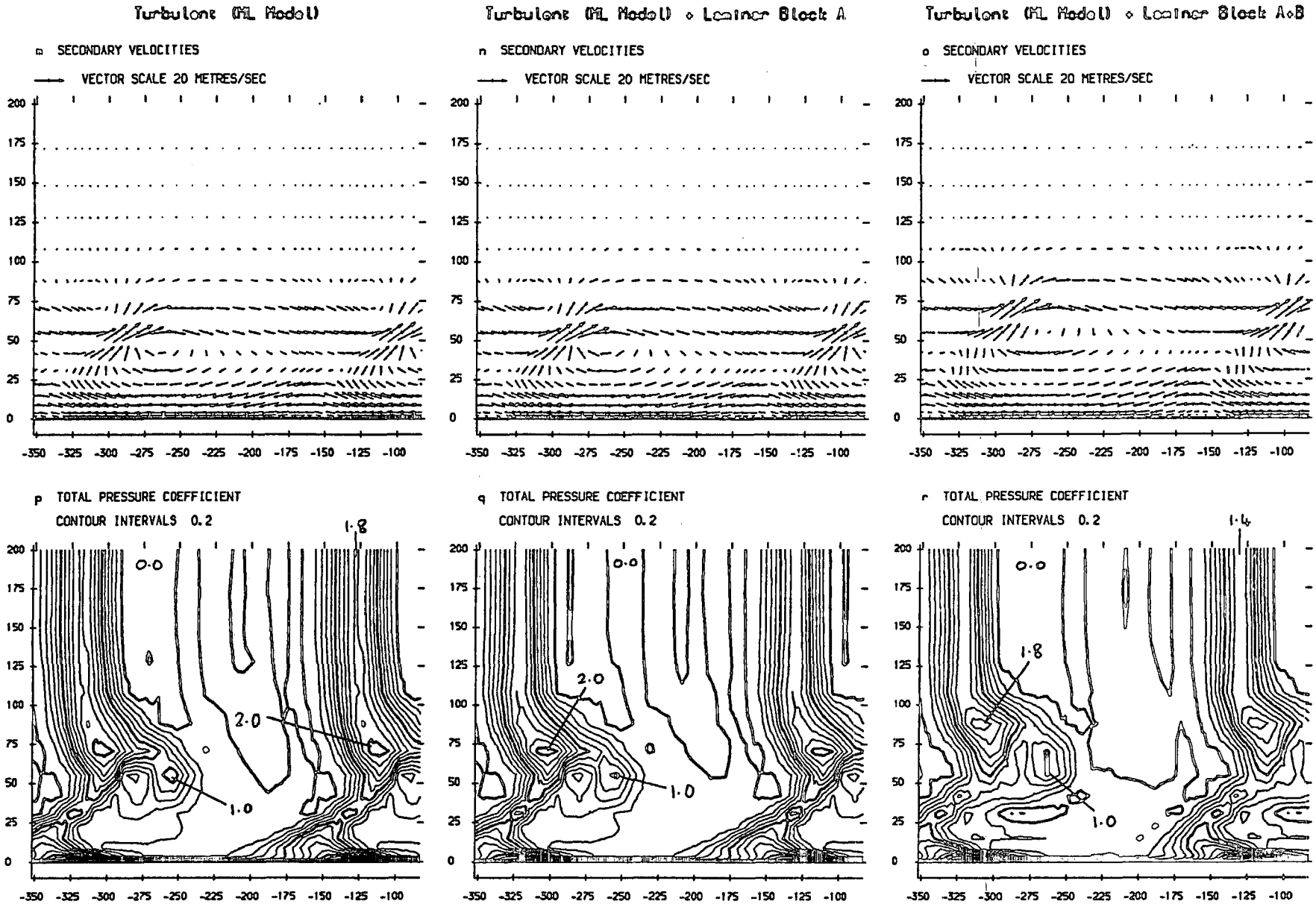


FIGURE 8.6 (m-r) : Area Plots For Slot 10

◆ Five Hole Probe Measurements.
⊠ MEFP Turbulent + Laminar Blocks A+B, Mixing Length Model.
✳ MEFP Turbulent + Laminar Block A, Mixing Length Model.
❋ MEFP Turbulent Flowfield, Mixing Length Model.

a) Yaw Angle (Degrees)

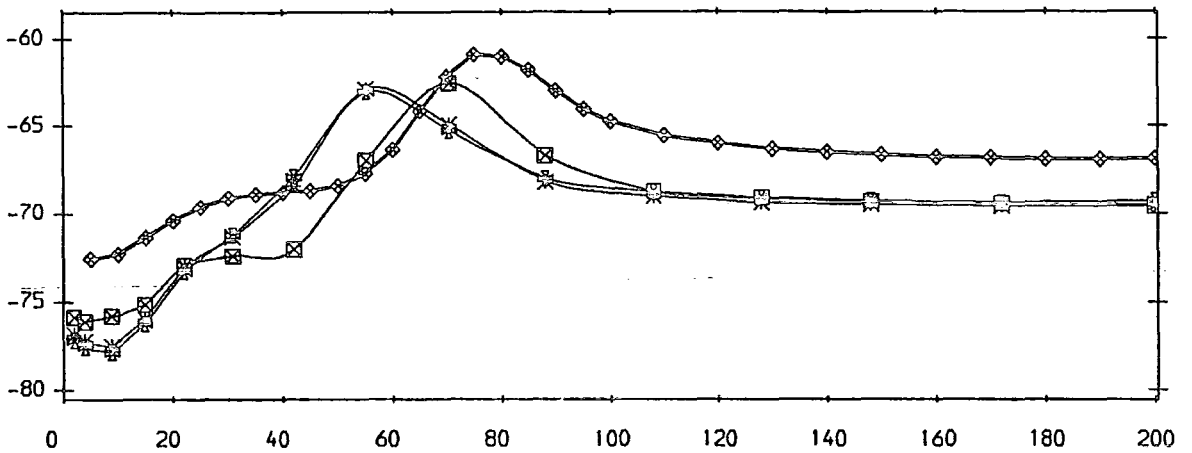


b) Total Pressure Loss Coefficient

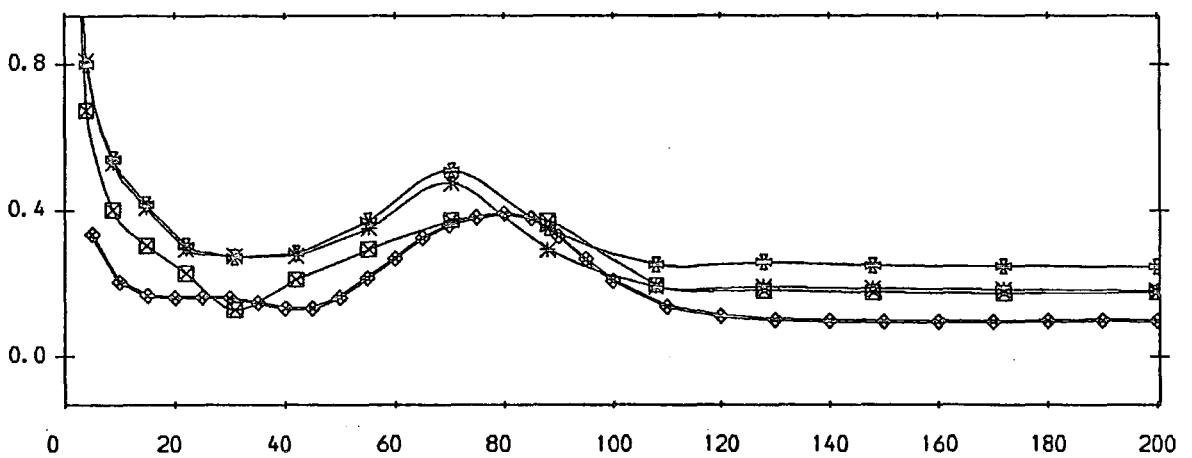


c) Secondary Kinetic Energy Coefficient

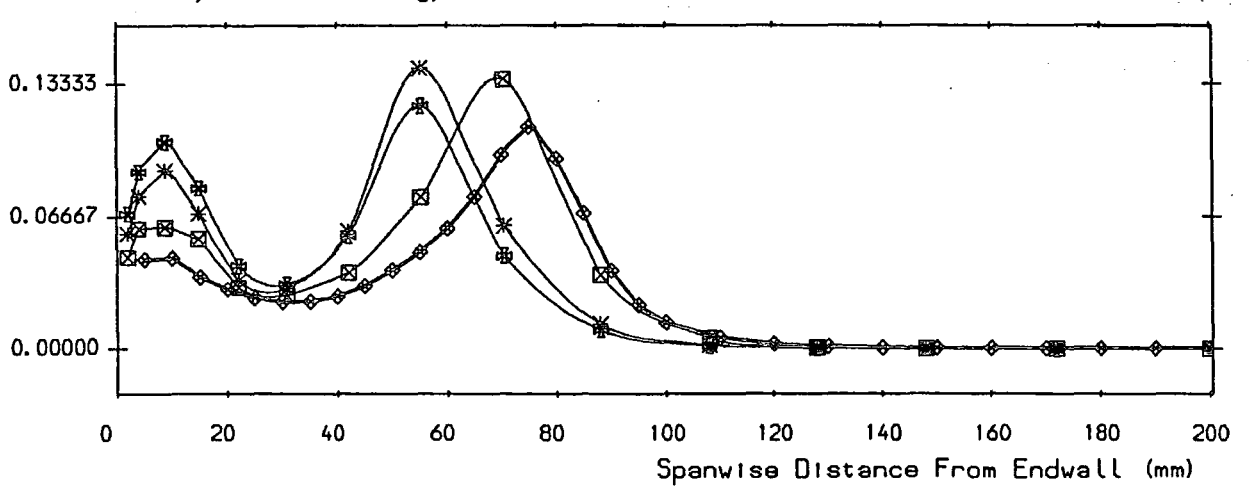


FIGURE 8.7 : Pitch Averaged Results For Slot 10

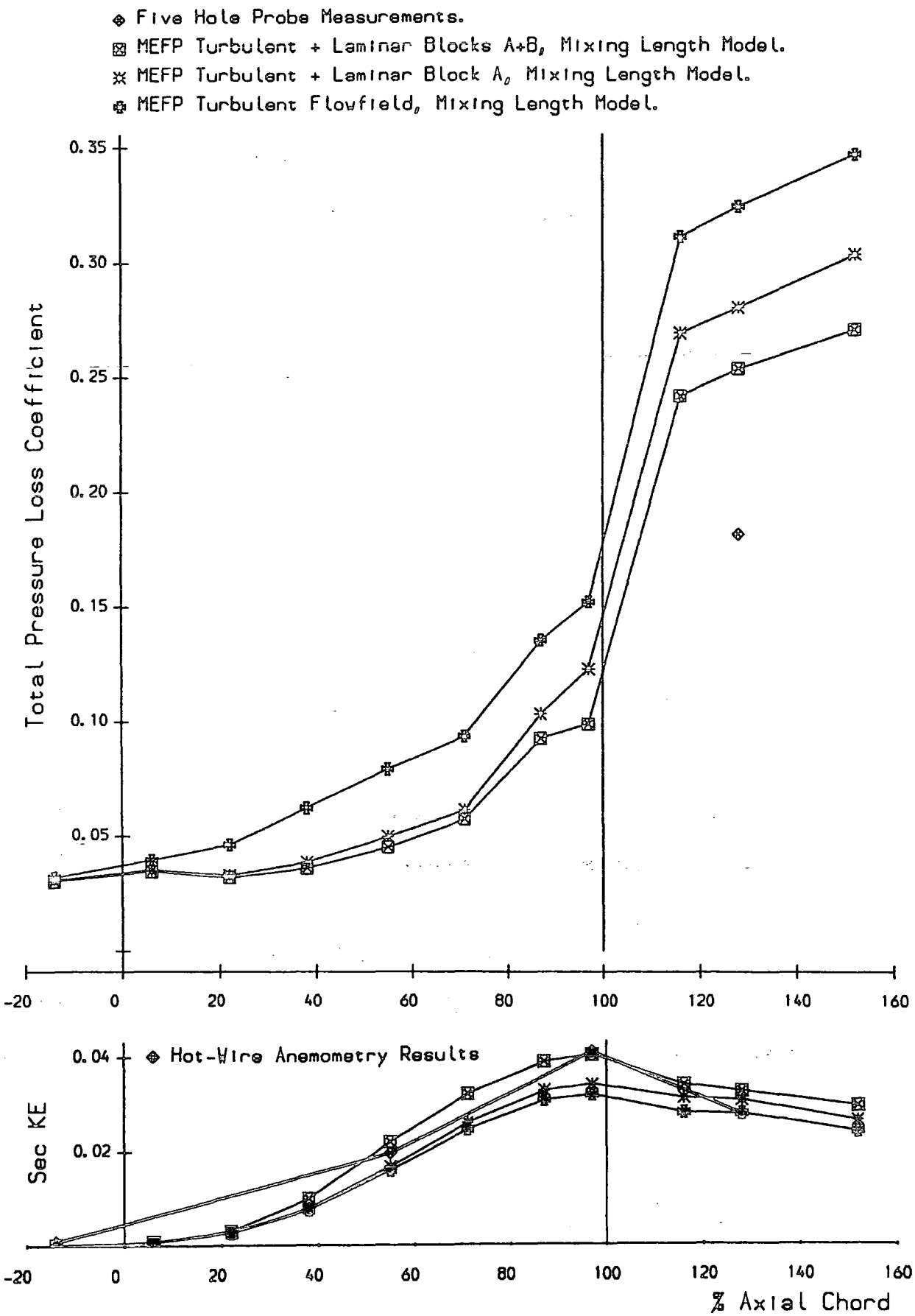


FIGURE 8.8 : Mass Averaged Loss & Secondary Kinetic Energy

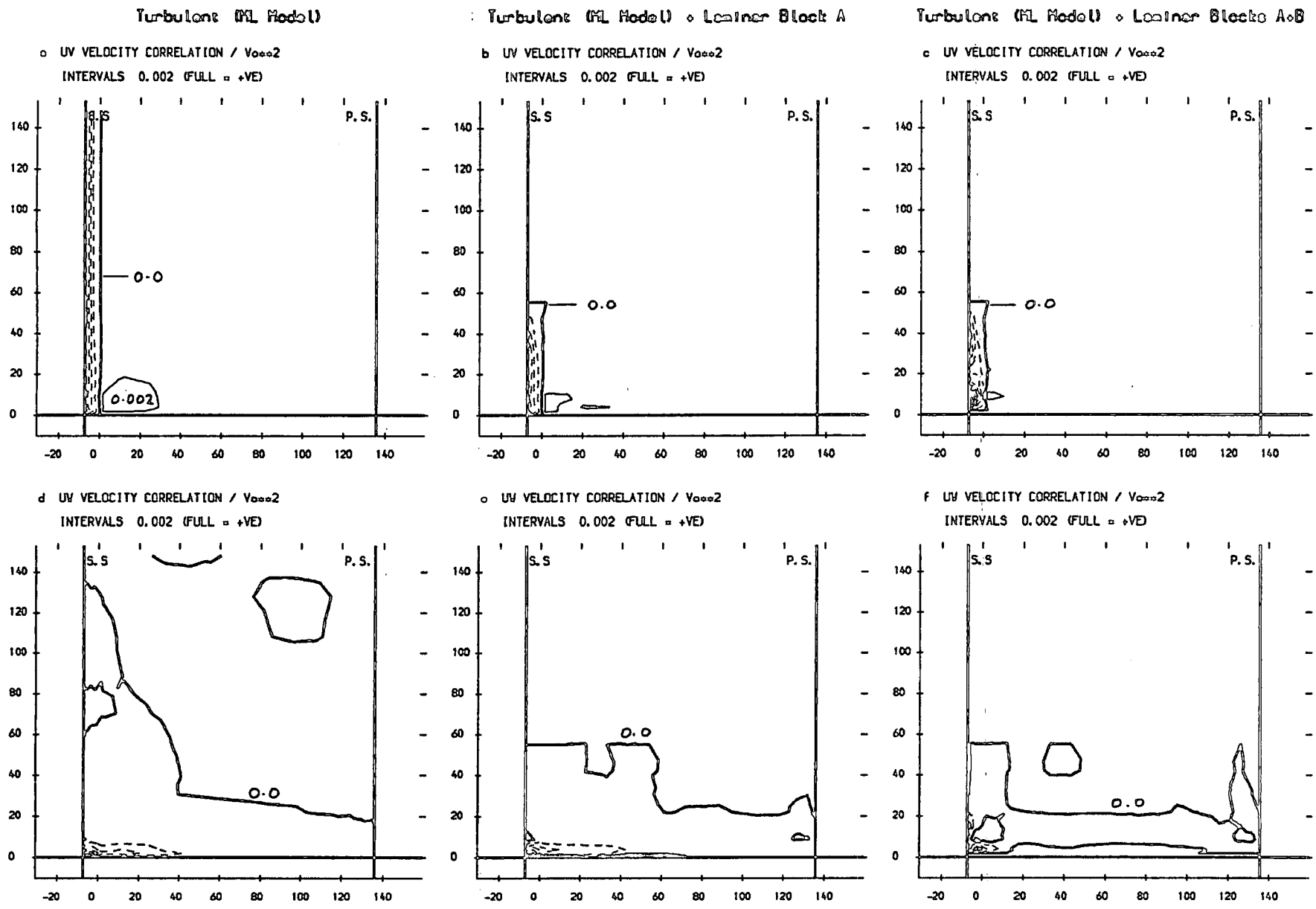


FIGURE 8.9 (a-f) : Area Plots For Slot 5

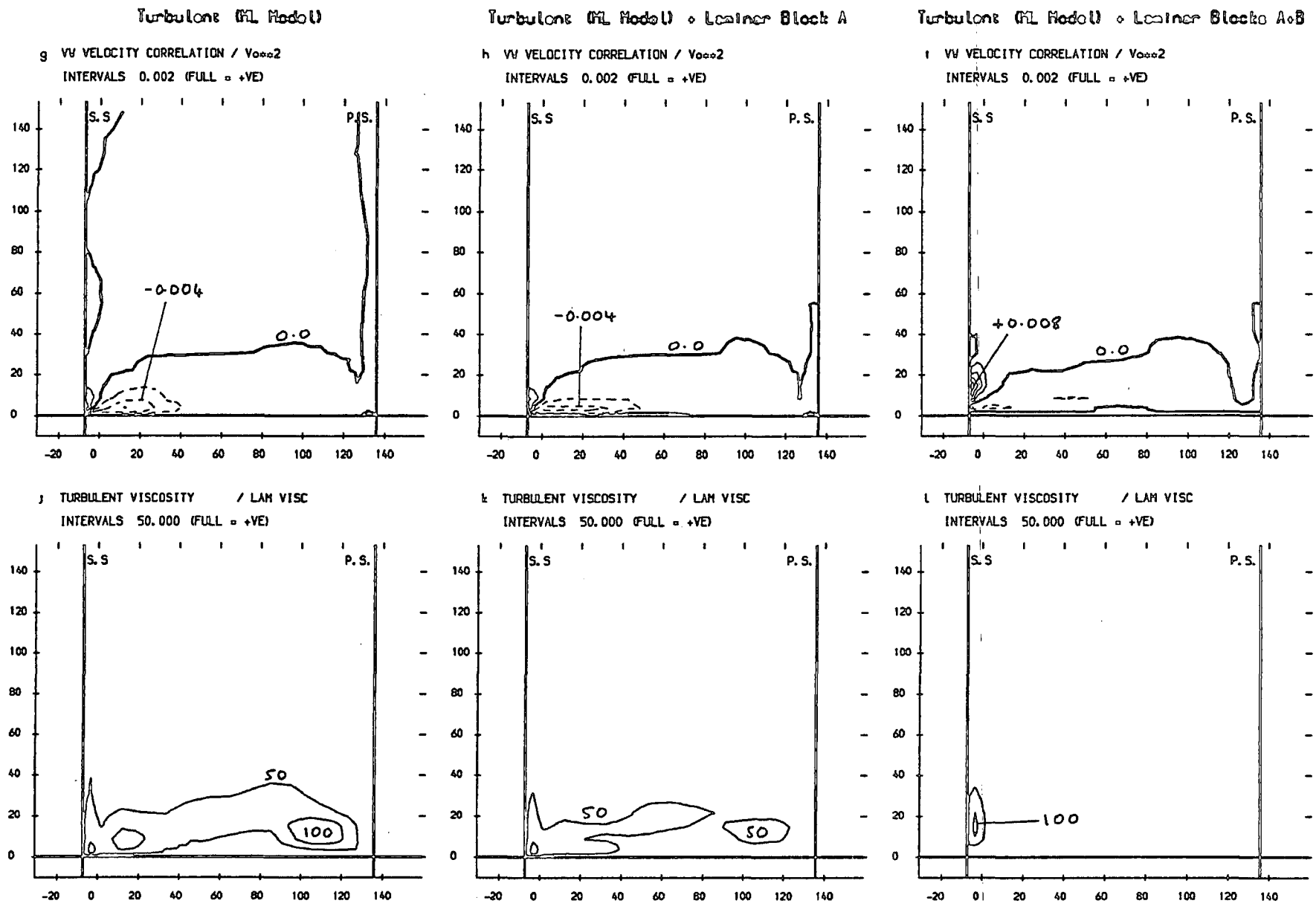


FIGURE 8.9 (g-l) : Area Plots For Slot 5

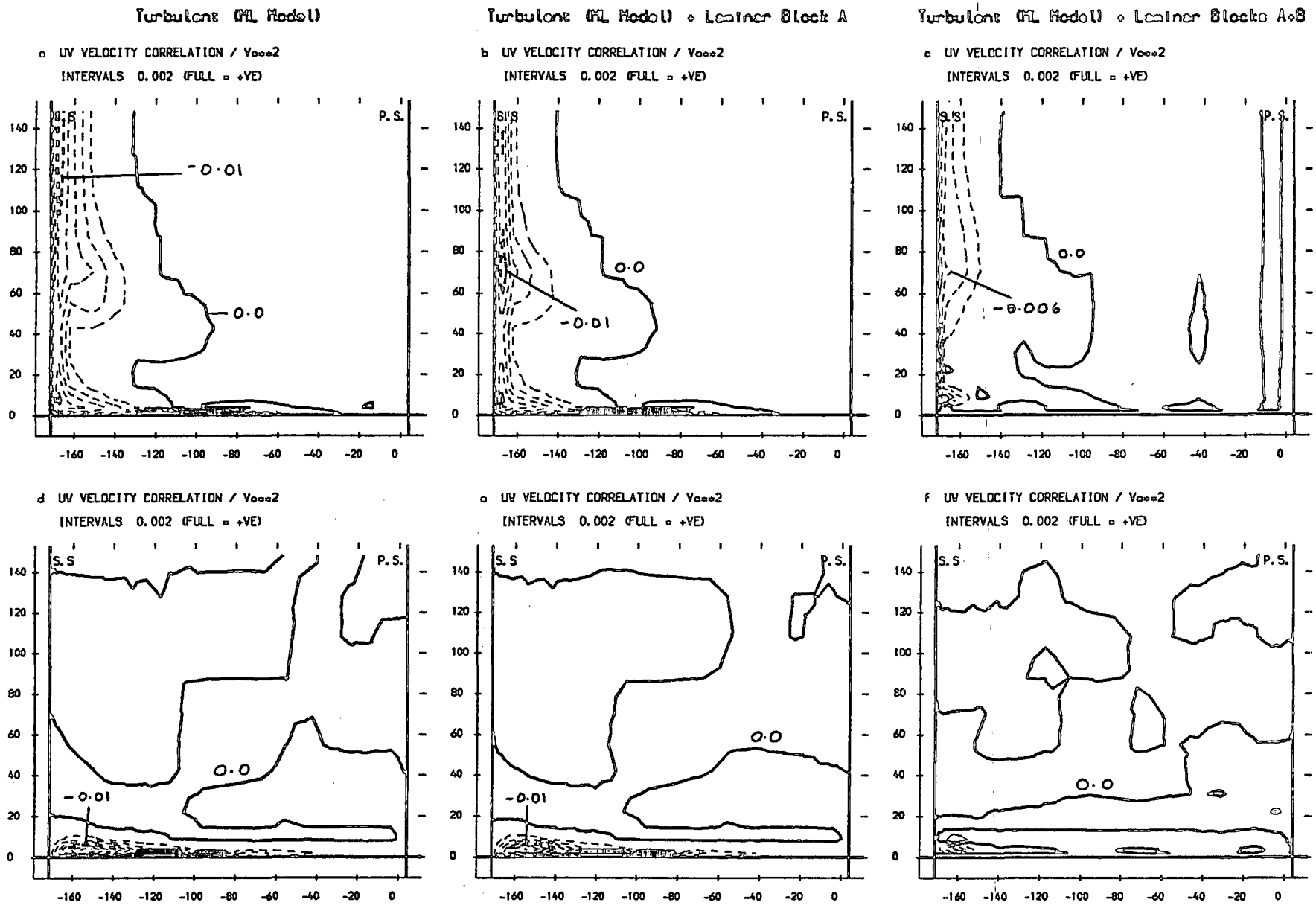


FIGURE 8.10 (a-f) : Area Plots For Slot 8

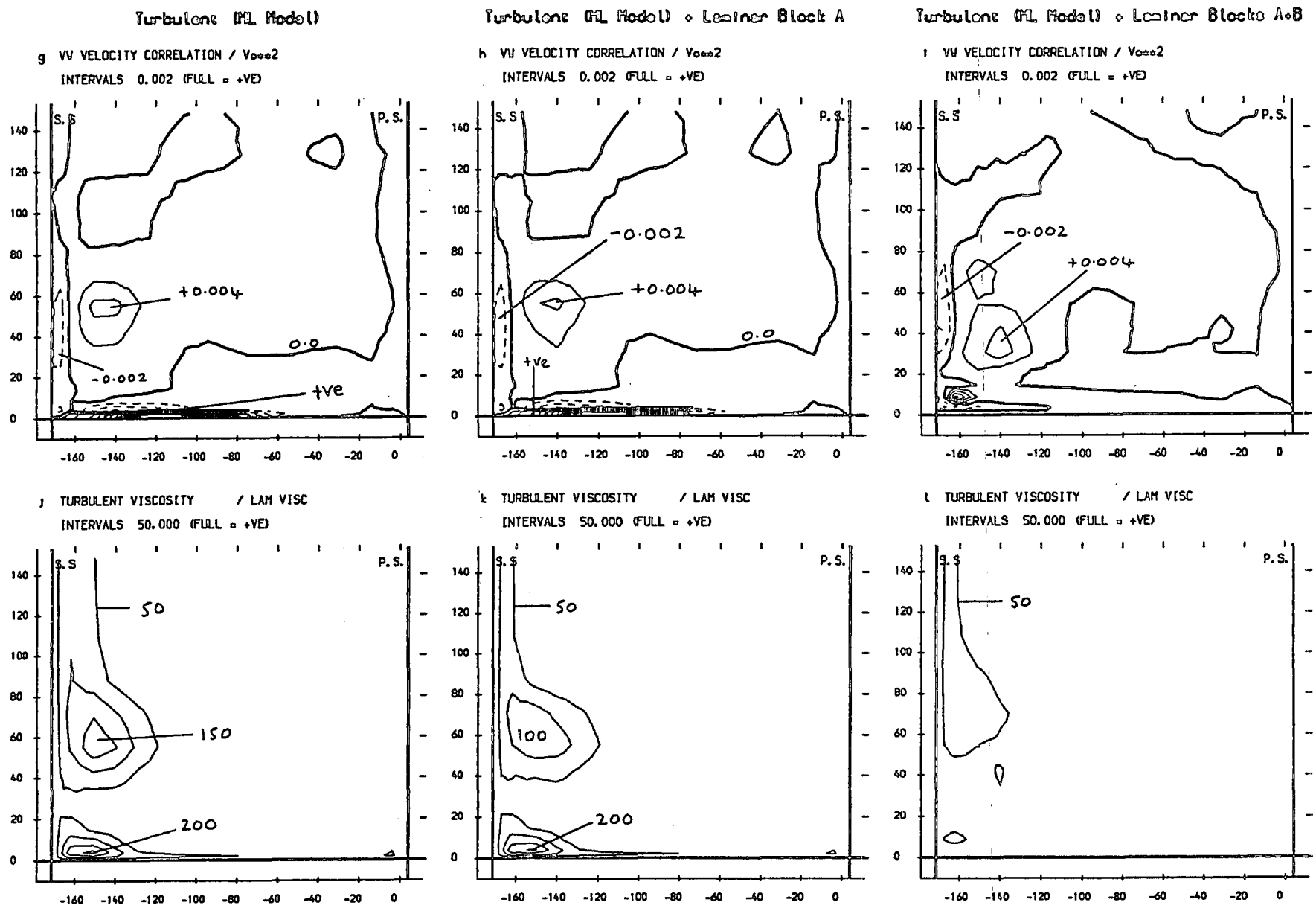


FIGURE 8.10 (g-l) : Area Plots For Slot 8

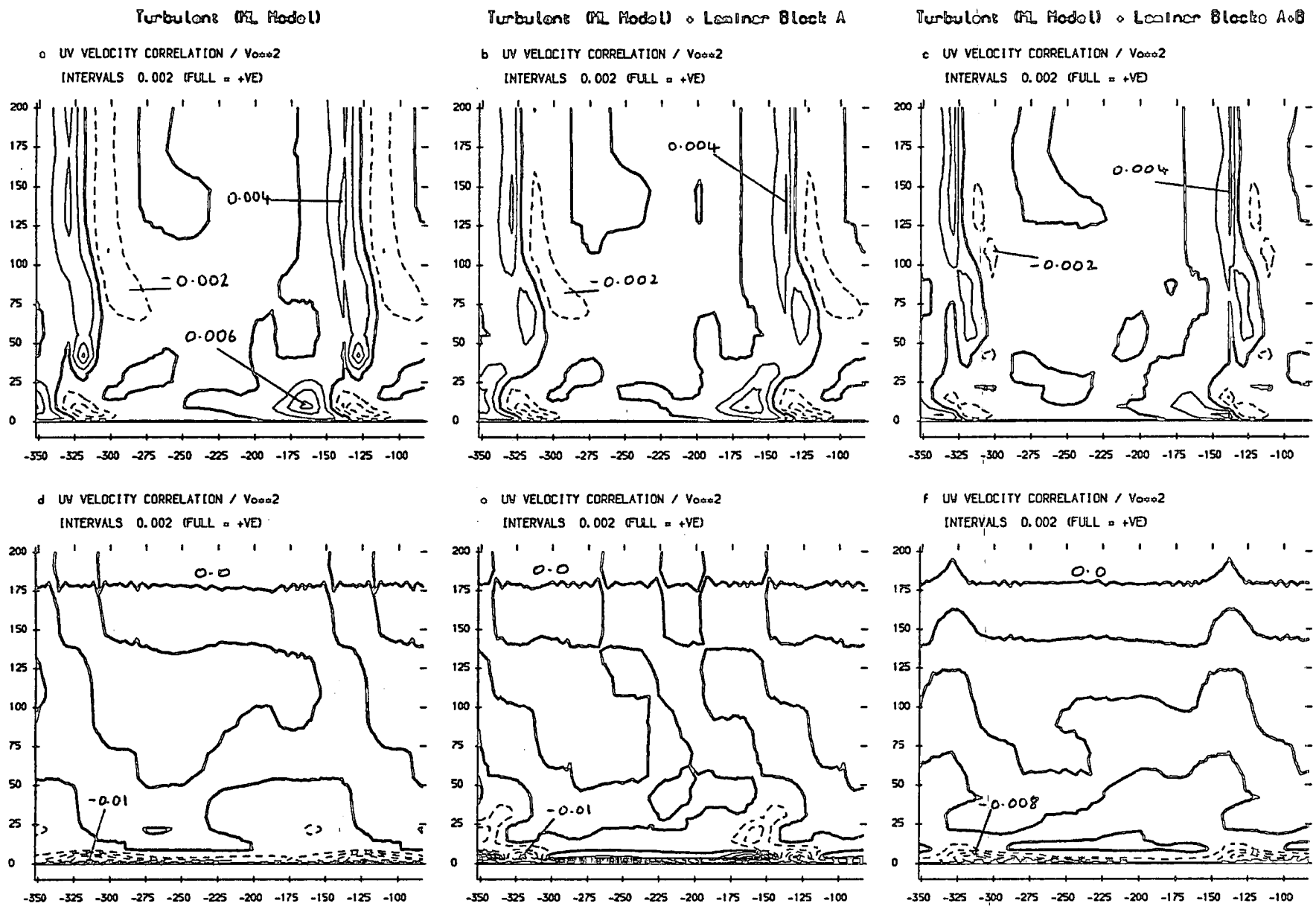


FIGURE 8.11 (a-f) : Area Plots For Slot 10

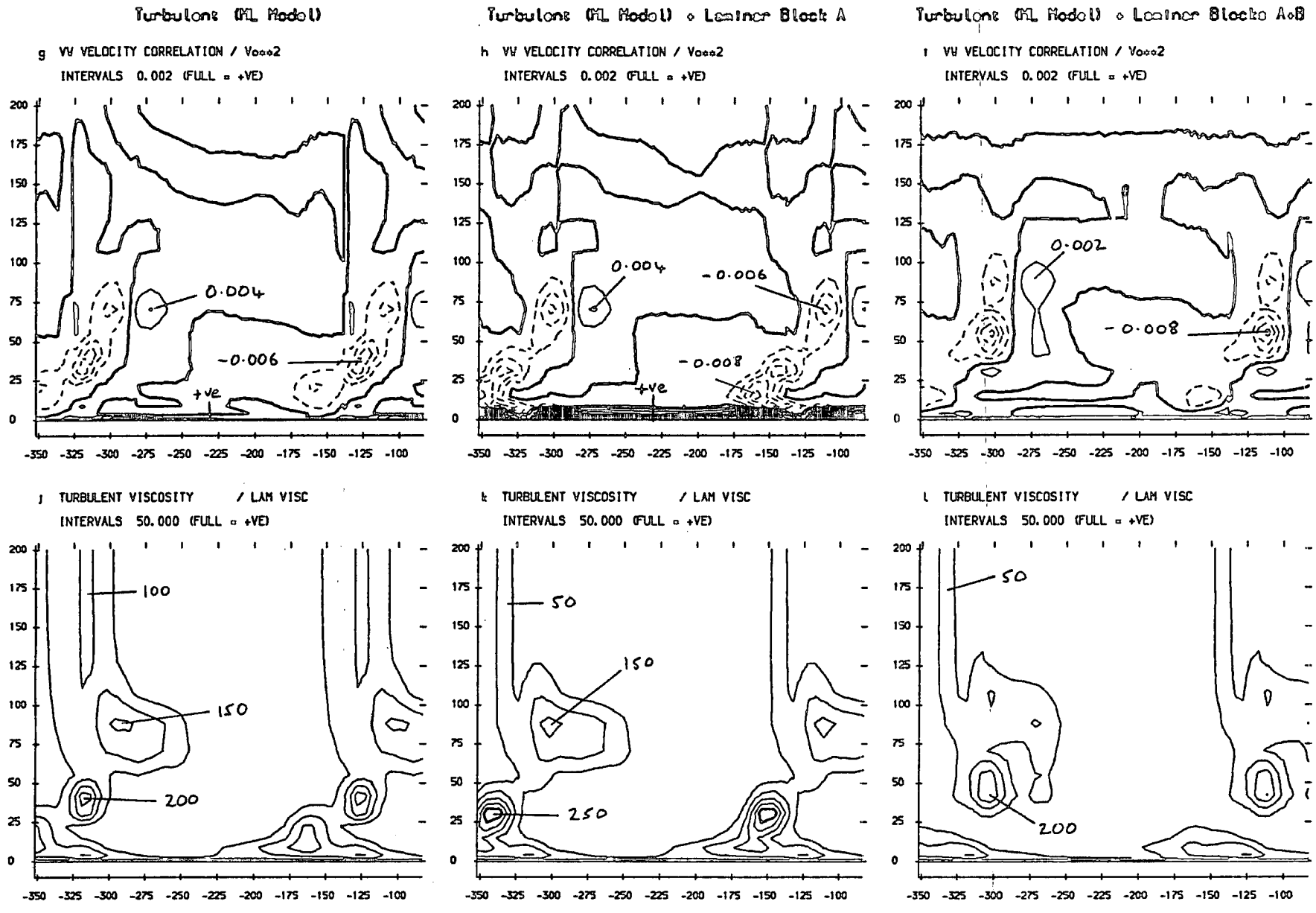


FIGURE 8.11 (g-l) : Area Plots For Slot 10

# One Equation Turbulence Model Results (Turbulent Flowfield)

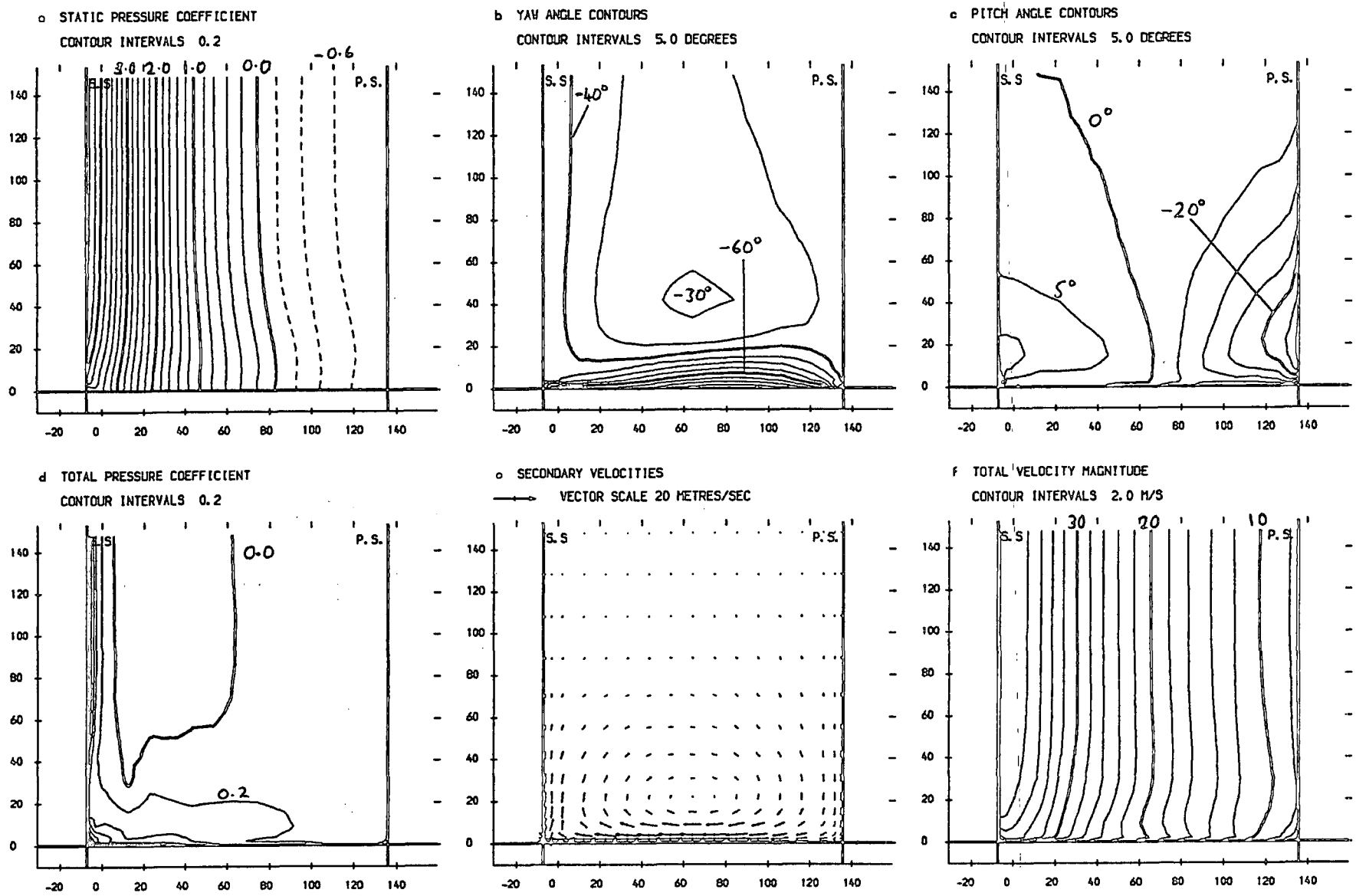


FIGURE 8.12 (a-f) : Area Plots For Slot 5

# One Equation Turbulence Model Results (Turbulent Flowfield)

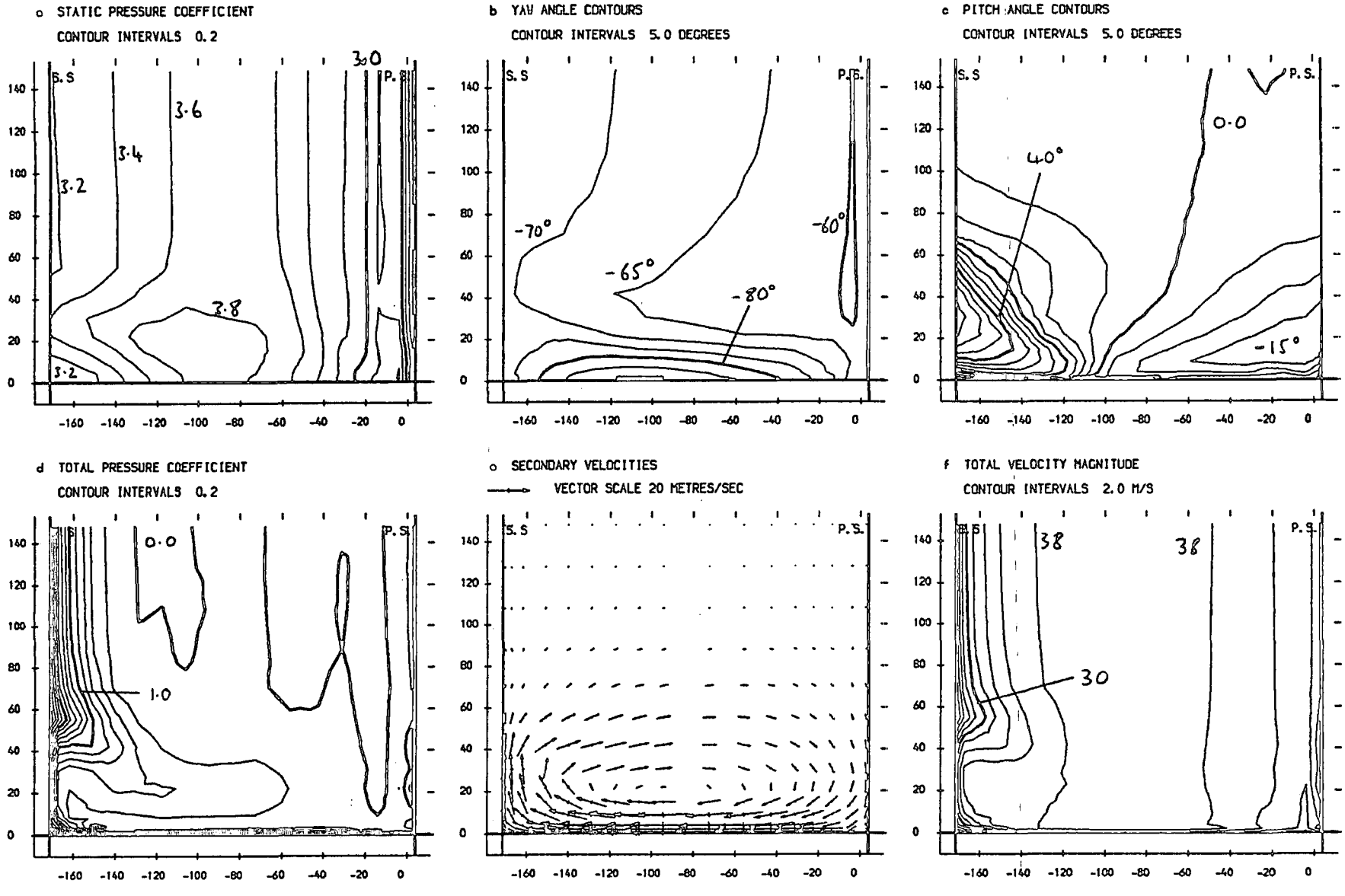


FIGURE 8.13 (a-f) : Area Plots For Slot 8

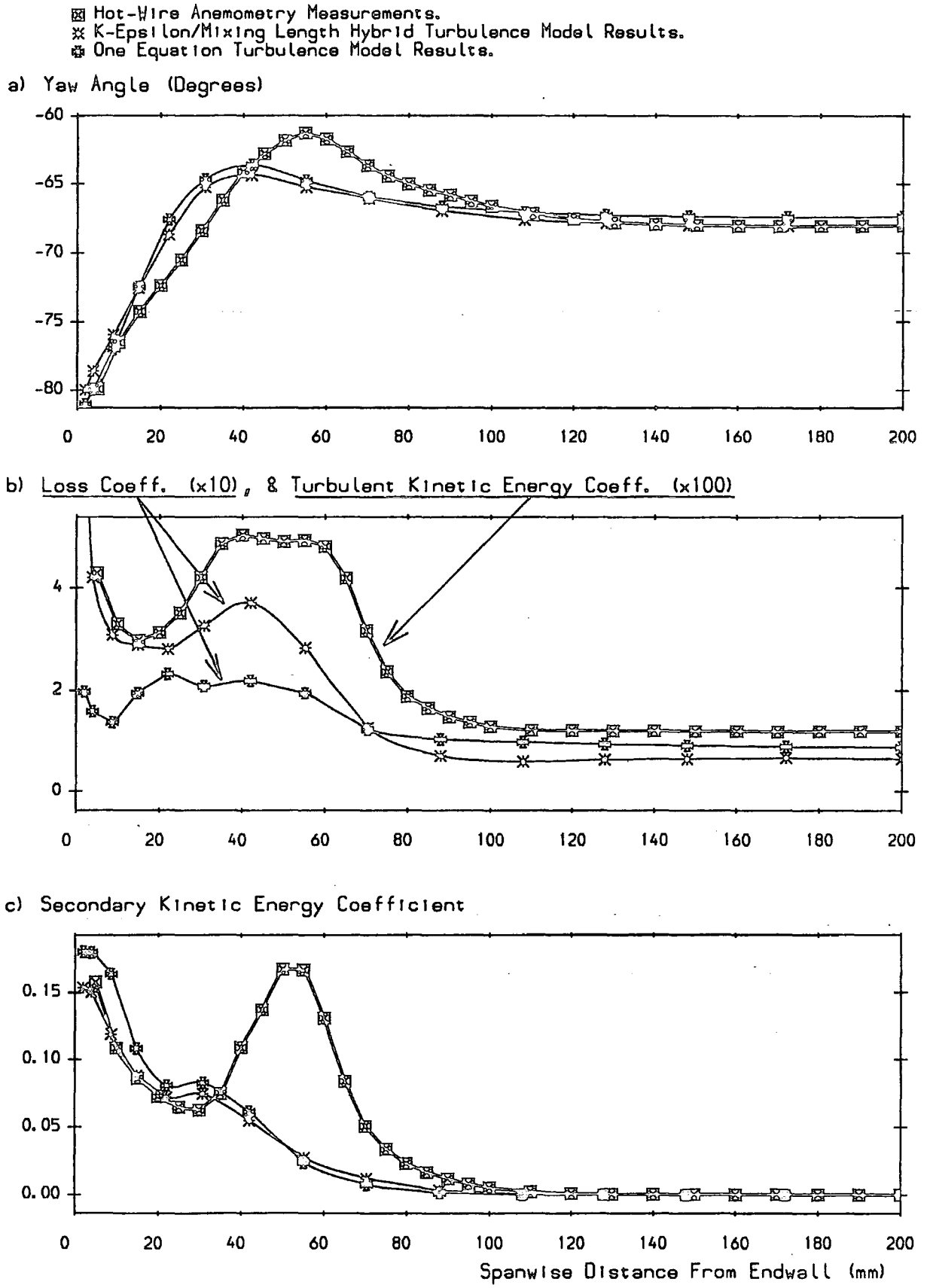


FIGURE 8.14 : Pitch Averaged Results For Slot 8

# One Equation Turbulence Model Results (Turbulent Flowfield)

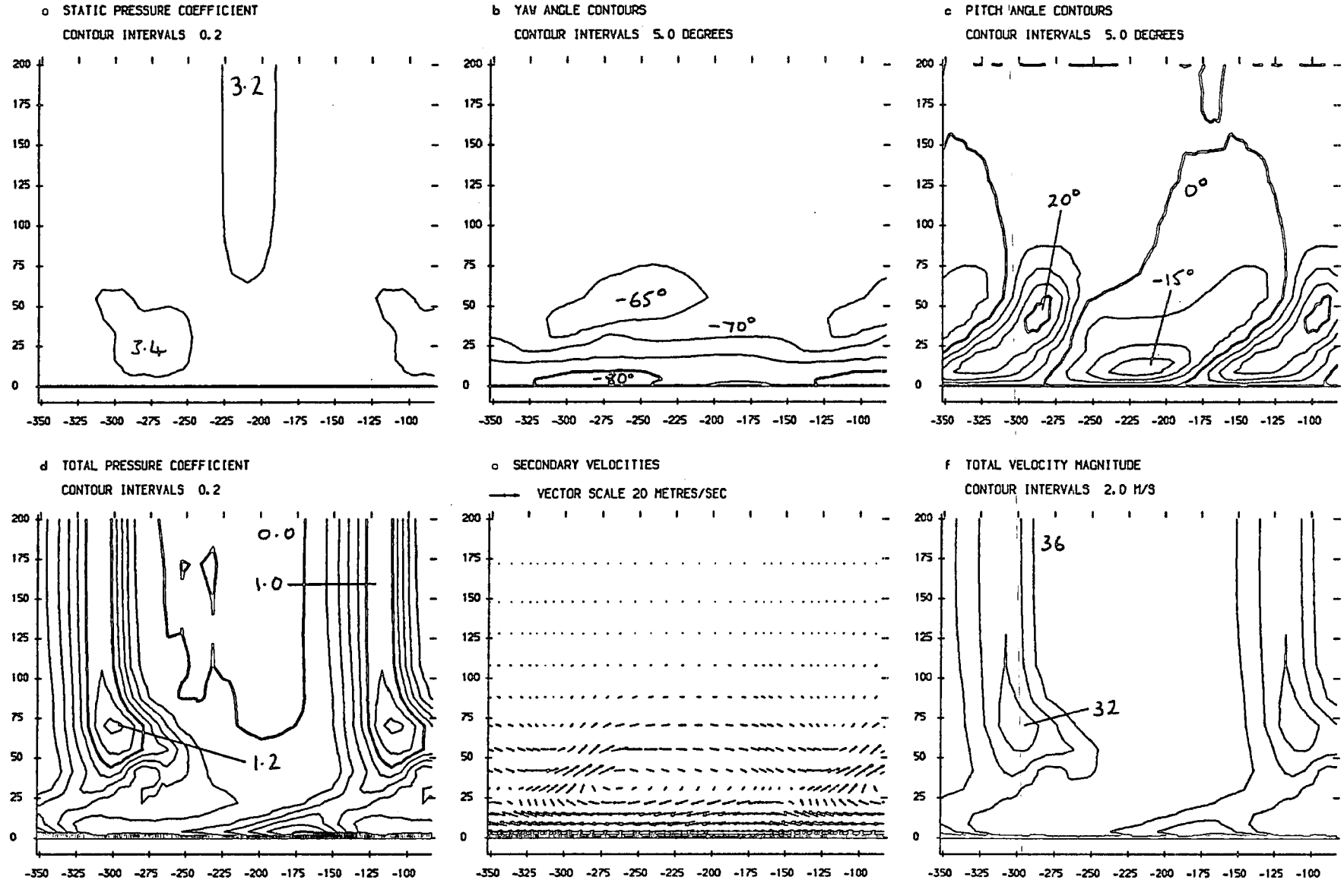


FIGURE 8.15 (a-f) : Area Plots For Slot 10

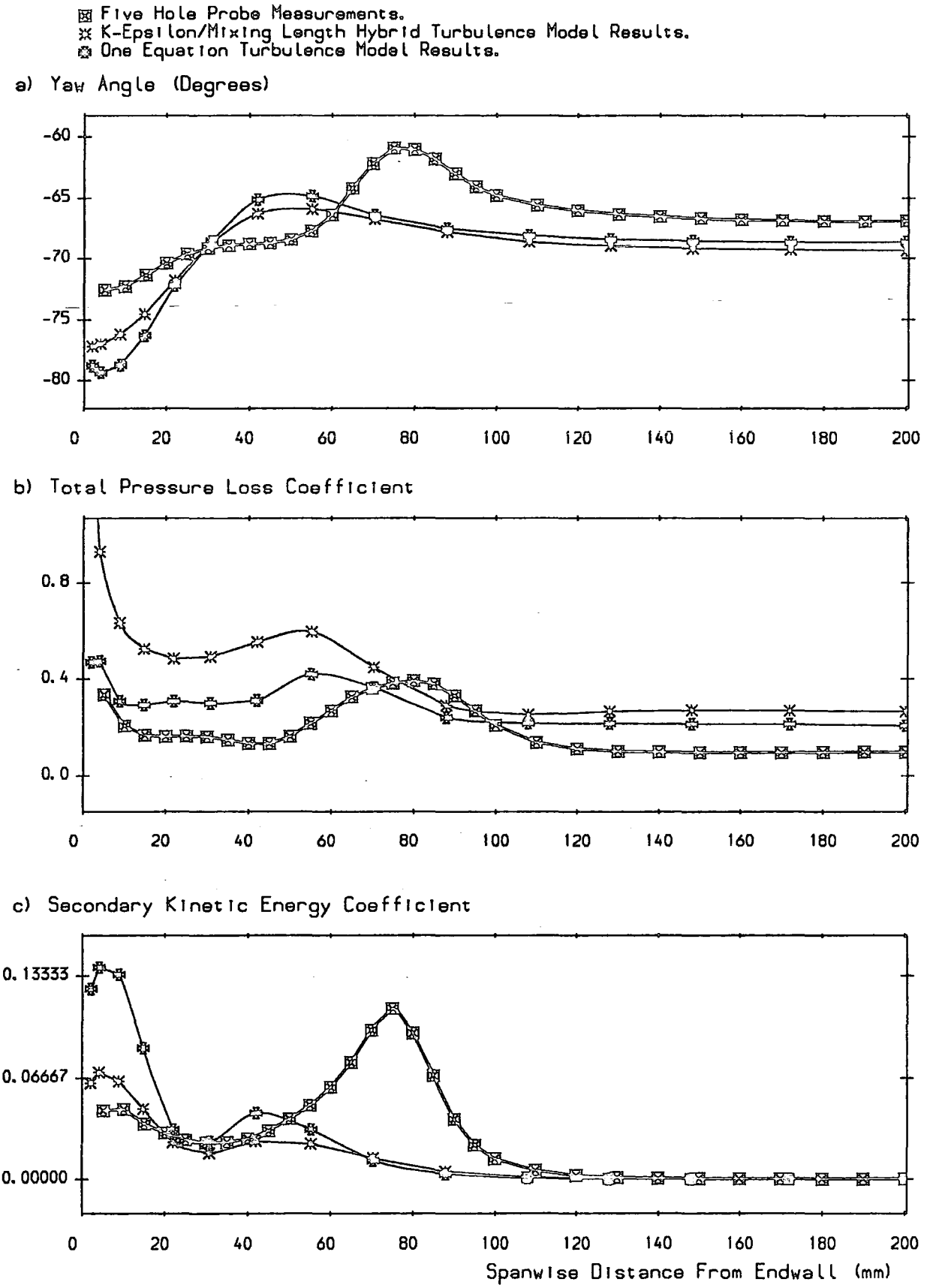


FIGURE 8.16 : Pitch Averaged Results For Slot 10

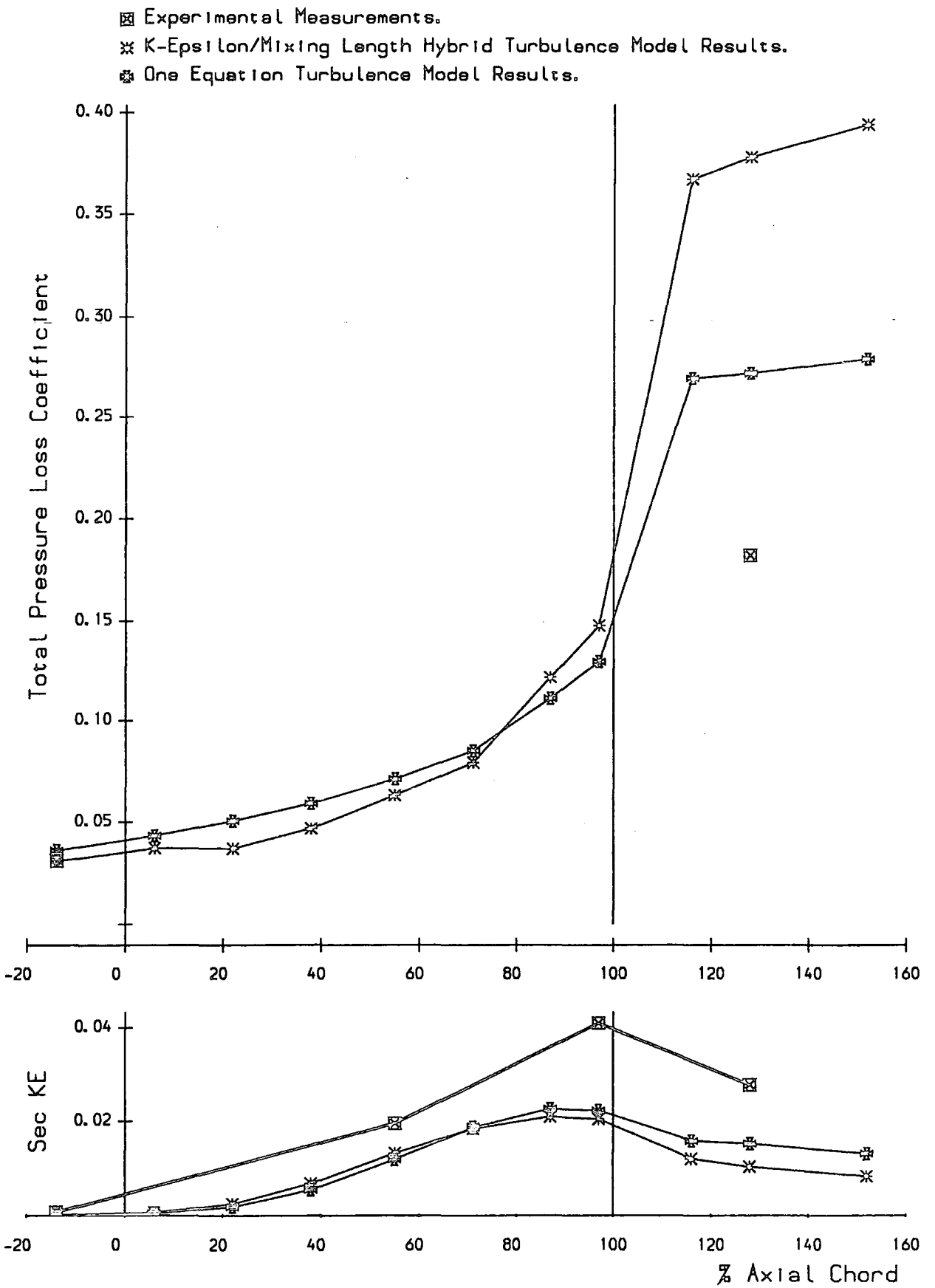


FIGURE 8.17 : Mass Averaged Loss & Secondary Kinetic Energy

One Equation Turbulence Model Results (Turbulent Flowfield)

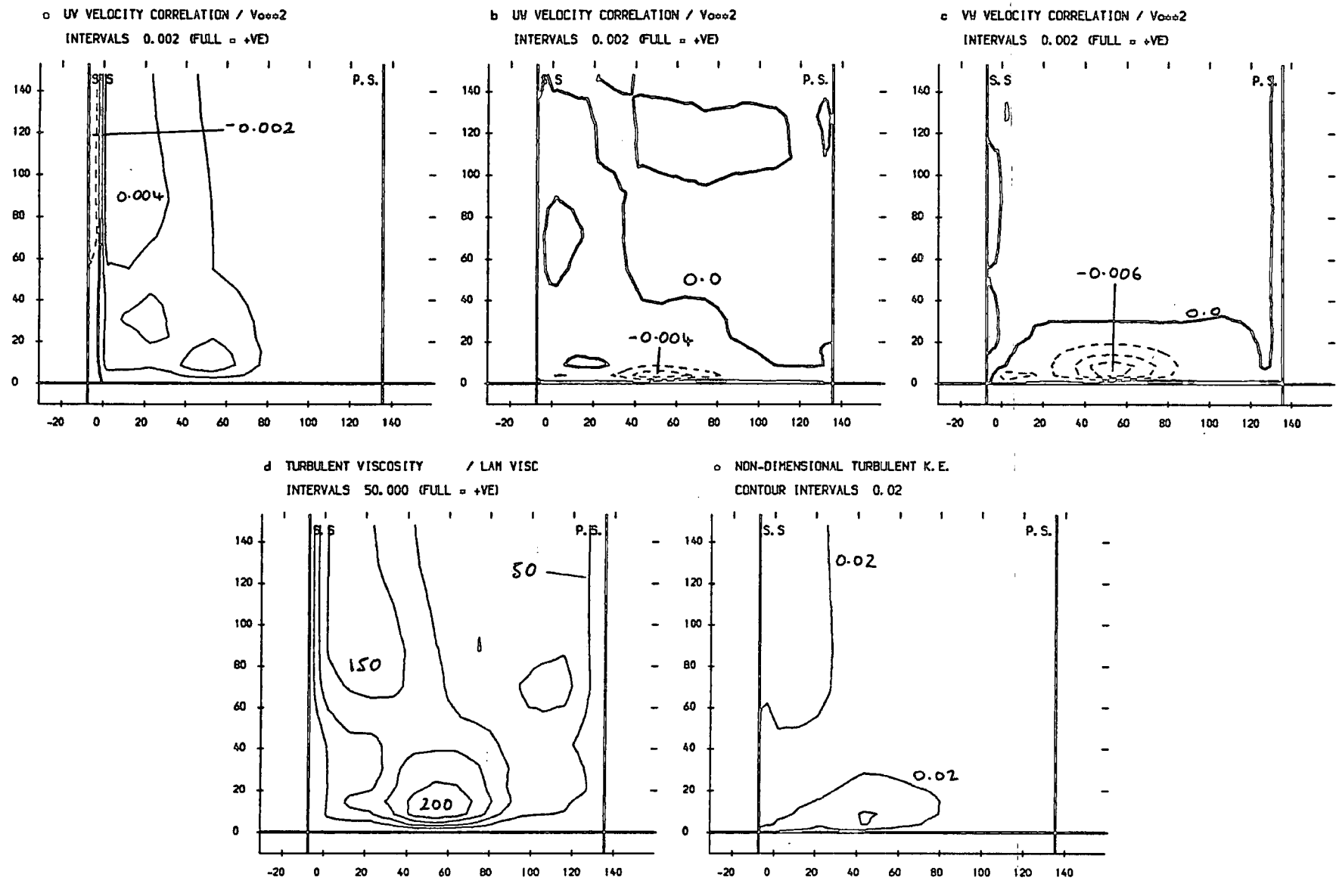


FIGURE 8.18 (a-f) : Area Plots For Slot 5

# One Equation Turbulence Model Results (Turbulent Flowfield)

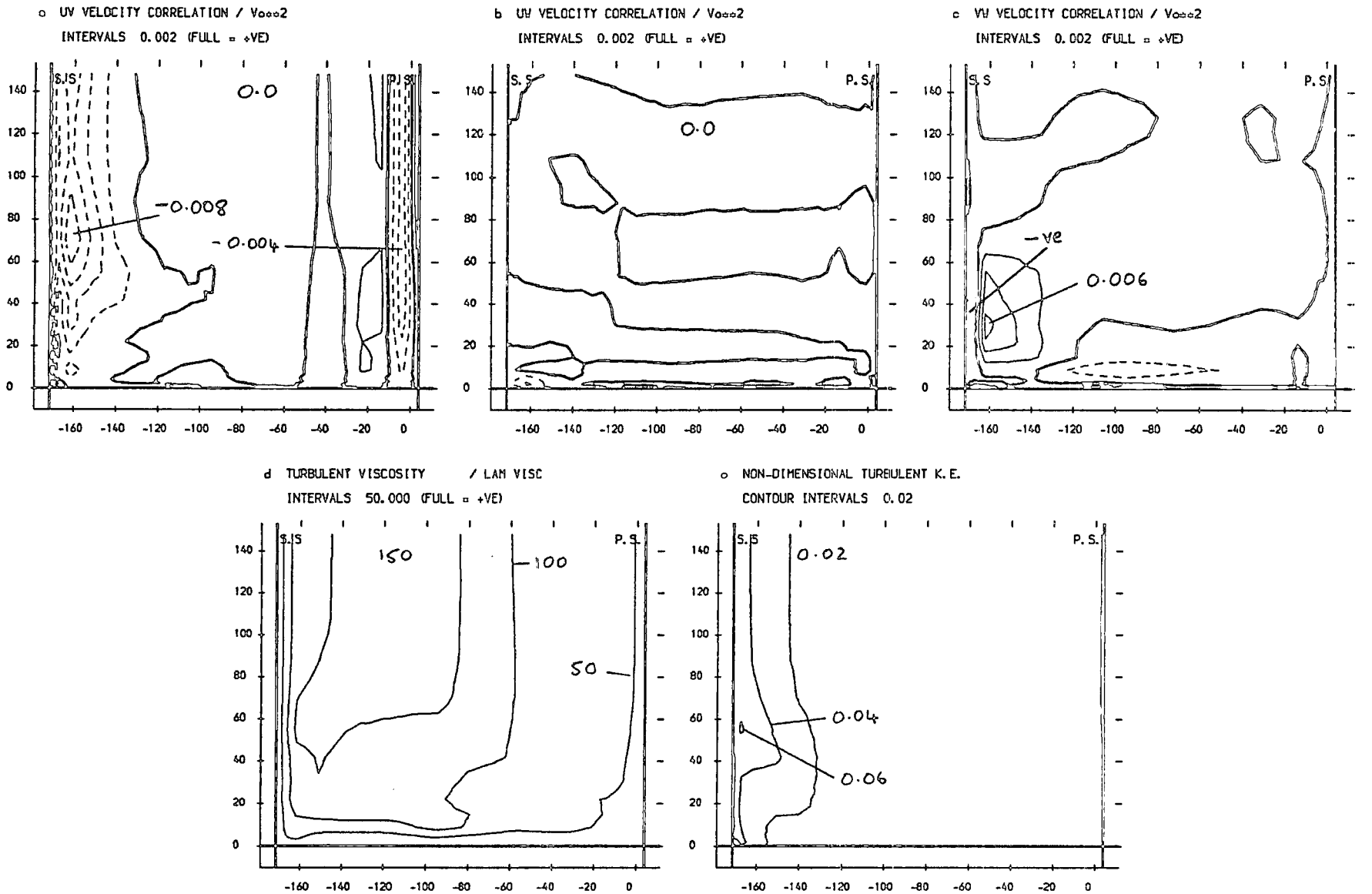


FIGURE 8.19 (a-e) : Area Plots For Slot 8

One Equation Turbulence Model Results (Turbulent Flowfield)

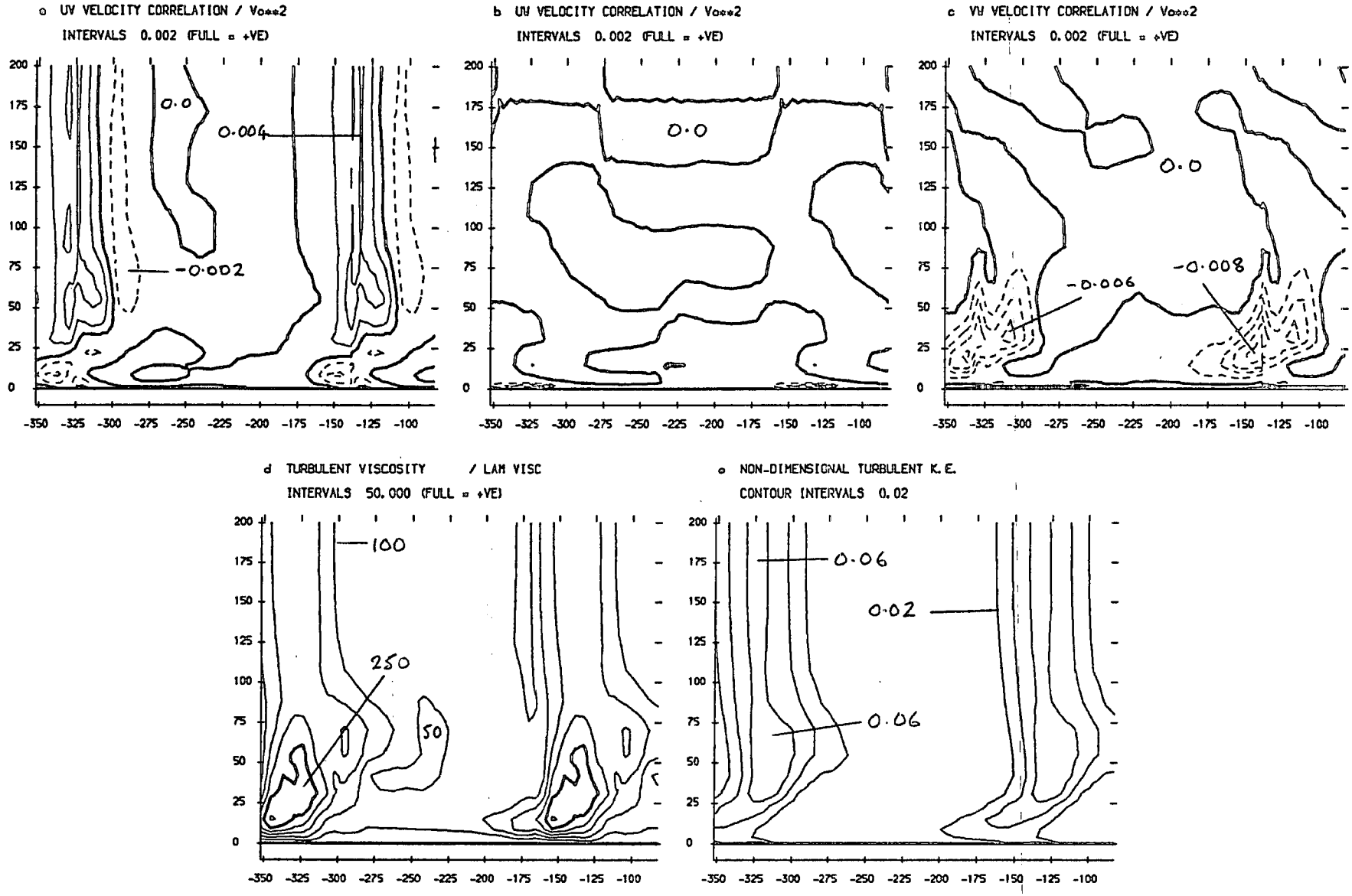


FIGURE 8.20 (a-e) : Area Plots For Slot 10

# K-Epsilon/Mixing Length Hybrid Turbulence Model Results

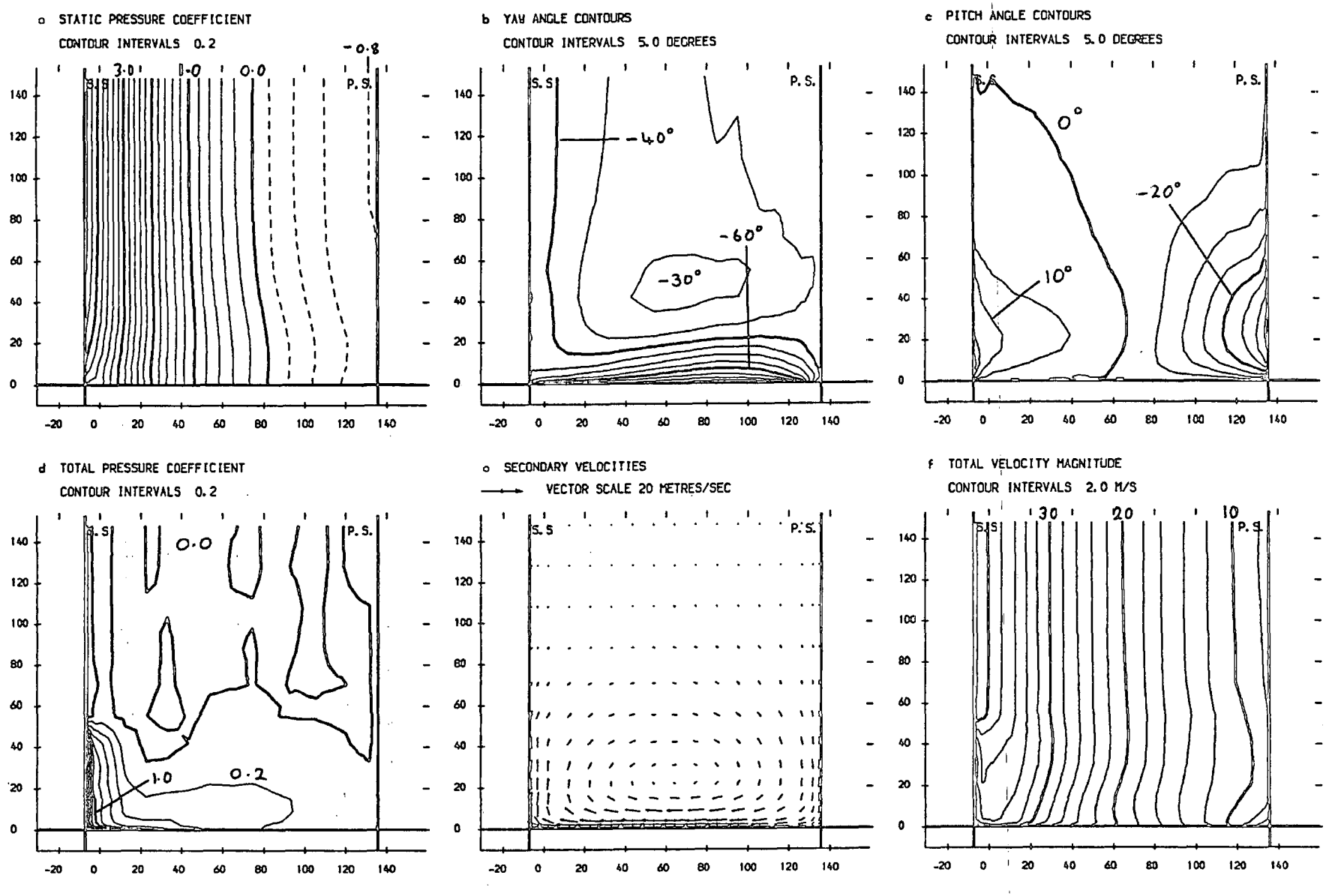


FIGURE 8.21 (a-f) : Area Plots For Slot 5

K-Epsilon/Mixing Length Hybrid Turbulence Model Results

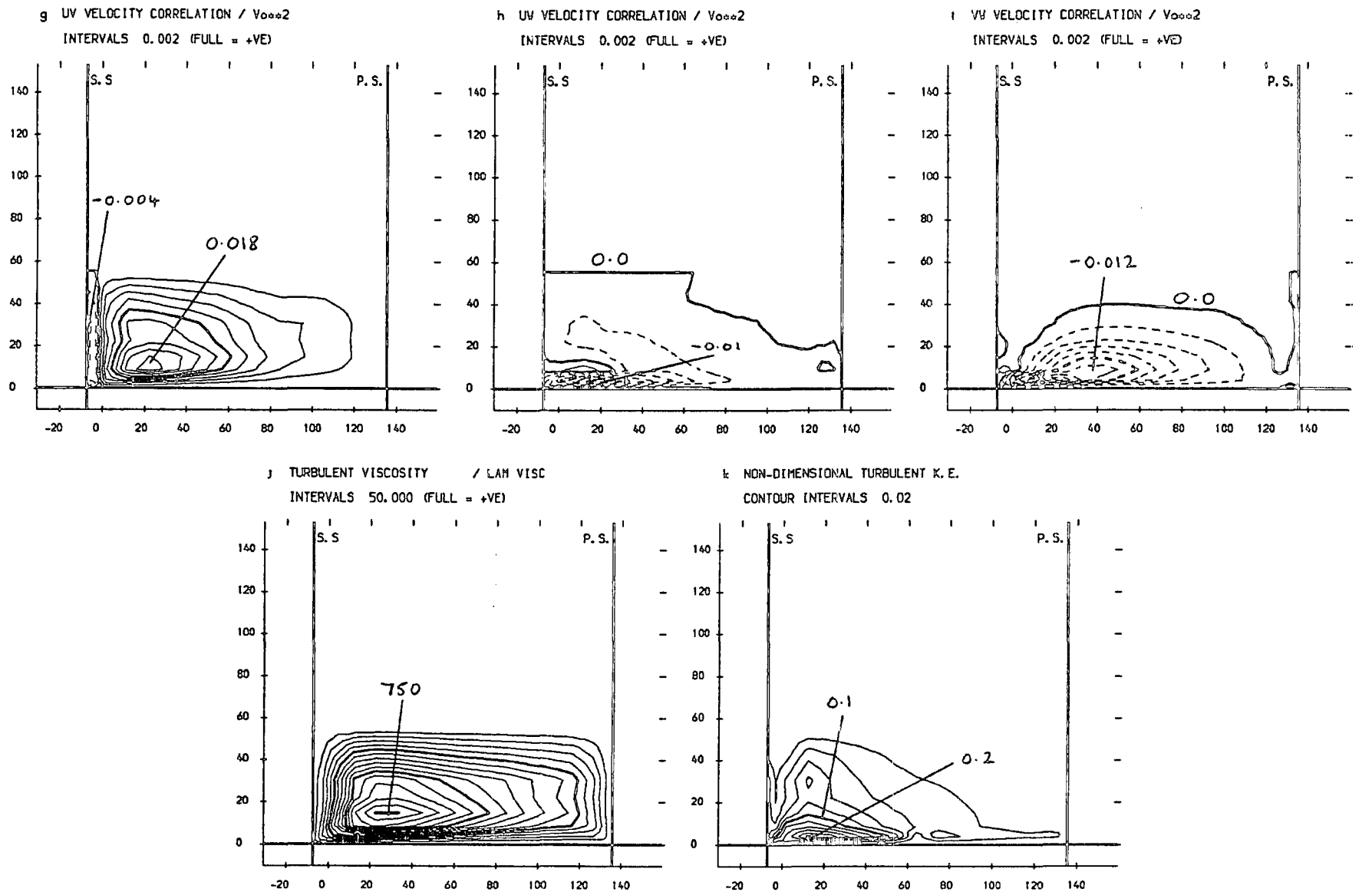


FIGURE 8.21 (g-k) : Area Plots For Slot 5

# K-Epsilon/Mixing Length Hybrid Turbulence Model Results

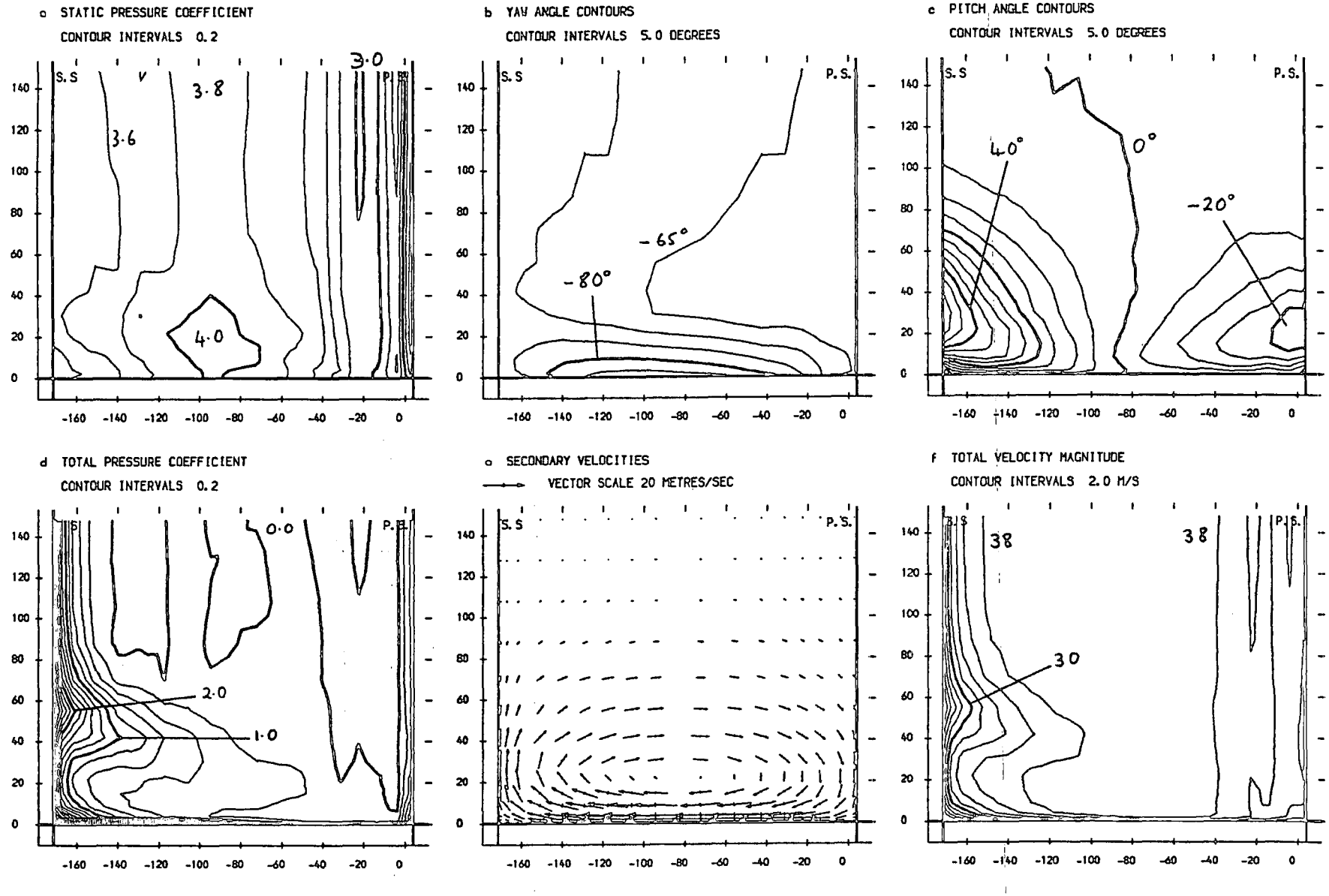


FIGURE 8.22 (a-f) : Area Plots For Slot 8

K-Epsilon/Mixing Length Hybrid Turbulence Model Results

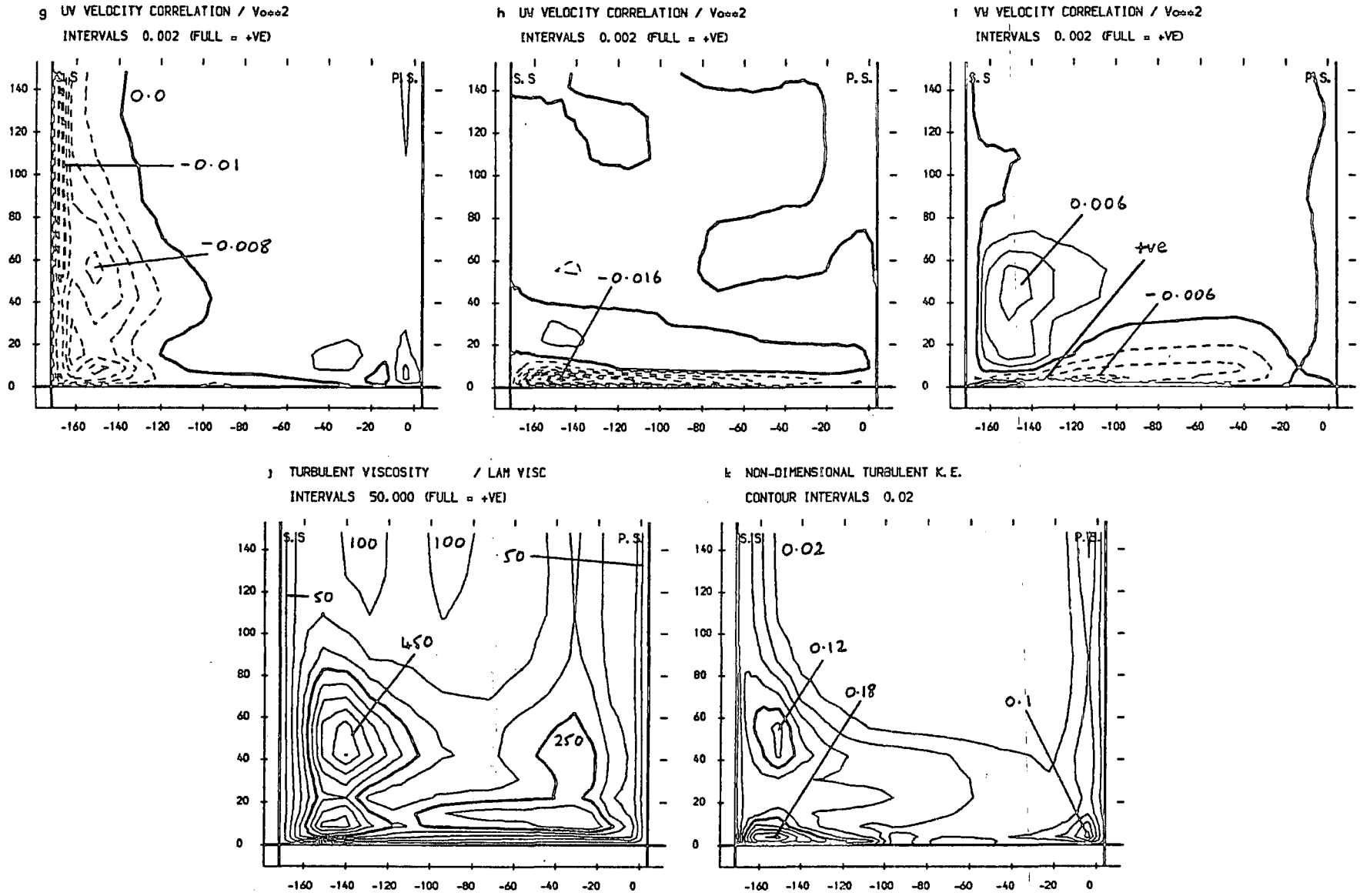


FIGURE 8.22 (g-k) : Area Plots For Slot 8

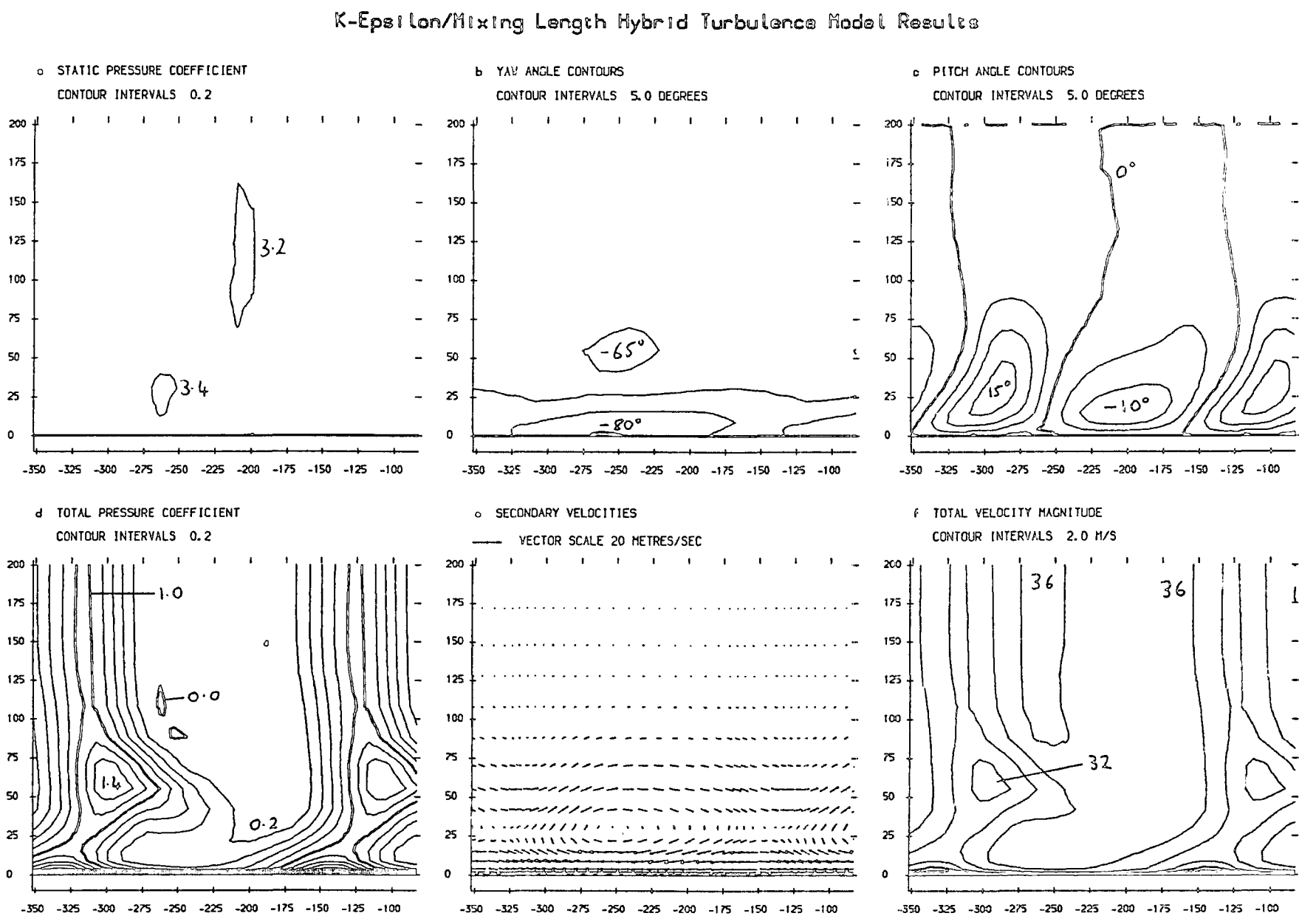


FIGURE 8.23 (a-f) : Area Plots For Slot 10

# K-Epsilon/Mixing Length Hybrid Turbulence Model Results

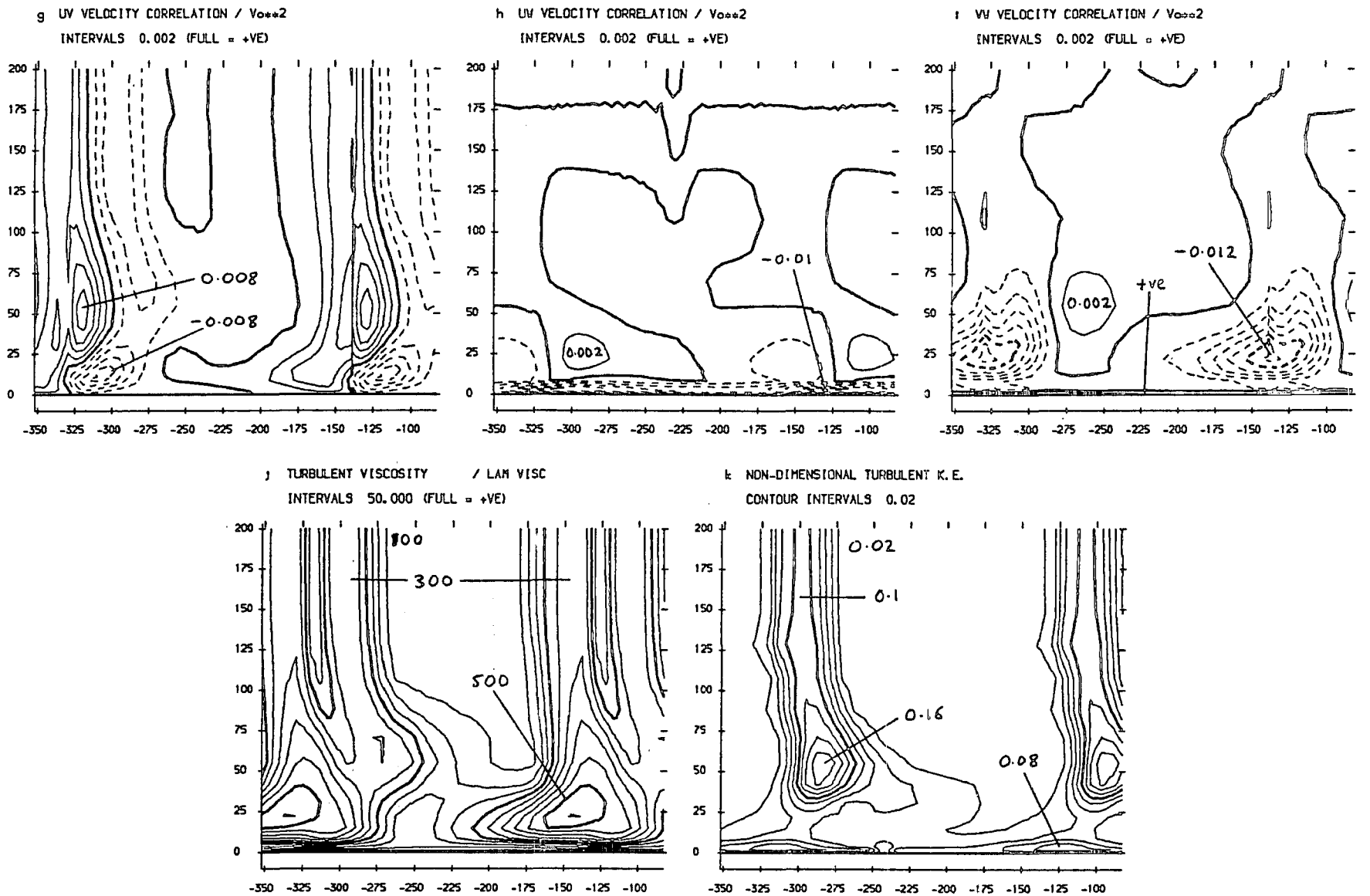


FIGURE 8.23 (g-k) : Area Plots For Slot 10

# Chapter 9
# Discussion

## 9.0 Introduction

This chapter presents a discussion of the experimental and modelling results presented in this thesis, with the aim of providing a coherent view of the conclusions which may be derived from them.

## 9.1 Experimental Results

Some additional pressure probe traverses of the flow in the Durham turbine cascade without a turbulence grid ('JAW' test case) have been made to add to the data presented by Walsh (1987). A traverse at slot 7 (87% Cax) revealed the secondary loss core just becoming detached from the endwall. The loss contours show that high losses form in the region where the passage vortex separates from the suction surface, and also in the suction surface/endwall corner where a counter vortex forms. The mass averaged losses show that rapid loss generation occurs in the final 20-30% of axial chord, which is in accord with the results of other workers (e.g. Langston *et al* (1977)).

Traverses at slots 9 (116% Cax) and 11 (152% Cax) coupled with Walsh's traverse at slot 10 (128% Cax), provide detailed information concerning the flow development downstream of the cascade. These results show that as the flow proceeds downstream, the static pressure over the traverse plane becomes more even, and the high loss zones mix with the surrounding fluid to become broader and less intense. The over-turning on the endwall is observed to become less severe due to the growth of the counter vortex situated between successive passage vortices, which has its origin in the suction surface/endwall corner. In contrast the under-turning further away from the endwall remains fairly constant as the flow proceeds downstream. Radial velocities however reduce considerably, due to the interaction between passage vortices from successive passages.

The mass averaged secondary kinetic energy is observed to decay steadily downstream of the cascade, and the mixed out loss (calculation described by Moore and Adhye (1985)) is well represented by the sum of loss and secondary kinetic energy at a given axial plane. Also the mixed out secondary loss is observed to reduce slightly as the flow proceeds downstream. This suggests that the normal Reynolds stresses could be acting to produce mean flow energy from turbulent kinetic energy, thus offsetting some of the turbulent deformation work, and the reversible pressure work term described by Moore *et al* (1986) is acting to convert secondary kinetic energy to primary kinetic energy. The sum of these two mechanisms must then be sufficient to exceed slightly the rate at which the growth of an endwall boundary layer is producing extra loss.

Measurements have also been presented of the flow in the same turbine cascade, but with a turbulence generating grid mounted upstream ('JGC' test case). The results show that changing the inlet freestream turbulence intensity from 1.4% to 4.5% promoted earlier transition of the suction surface boundary layer. This eliminated the laminar separation bubble which had previously been observed on the suction surface, leading to slightly increased profile loss. However the effect of the change in inlet freestream turbulence level upon the development of the secondary flows and losses was found to be very small. This may be because the secondary loss core fluid originates in the endwall boundary layer at inlet to the cascade, where the turbulence levels are likely to be less effected by the freestream intensity. Also significant turbulence generation occurs within the secondary flow, leading to much higher turbulence levels than those present in the freestream.

The introduction of the turbulence grid also resulted in a thinner endwall boundary layer at inlet to the cascade. This was because a 'jet' flow occurred near to the endwall through the turbulence grid, which was then slowed by growth of the endwall boundary layer to yield the observed profile at inlet. The thinner inlet boundary layer was found to result in less secondary kinetic energy generation within the blade row. However, apart from this, the secondary flows and losses were remarkably unchanged by the

different inlet conditions.

Slightly less secondary loss was observed in the 'JGC' test case. This may seem surprising at first sight, but could result from the way in which the secondary losses are calculated, by subtracting the midspan loss and inlet loss from the total loss measured downstream. Since the higher inlet turbulence promoted earlier transition of the suction surface boundary layer, more 'profile loss' was subtracted from the total loss measured at slot 10 in the 'JGC' test case. The separation line running up the suction surface divides it into a region in which a two-dimensional boundary layer grows, and a region which is swept by the passage vortex. This latter region is then in contact with highly turbulent fluid, and thus the growth of a turbulent suction surface boundary layer is likely to start earlier below the passage vortex separation line, than it does above it. Any additional loss resulting from this over and above the undisturbed suction surface boundary layer loss, is then accounted for as secondary loss.

Despite the similarity between secondary losses measured at slot 10 for the 'JAW' and 'JGC' test cases, the mixed out secondary loss was observed to be smaller in the latter case. This was because the thinner inlet boundary layer profile resulted in the generation of less secondary kinetic energy to be mixed out. Thinning of the endwall boundary layer also resulted in a smaller horseshoe vortex, situated closer to the leading edge. The fact that the secondary flows and losses remained largely unchanged despite this, suggests that the horseshoe vortex is not a very significant factor in the process of passage vortex generation.

Hot-wire anemometry traverses of the flowfield with a turbulence grid placed upstream of the cascade ('JGC' test case) showed that high turbulence levels are associated with the secondary flow. Comparison with the results of Gregory-Smith *et al* (1988) reveals similar levels, which suggests that the higher inlet turbulence in this test had little bearing upon the turbulence development within the secondary flow. Within the blade passage, significant positive $\overline{u'v'}$ correlation was found to be associated with the cross-passage velocity gradient and the turbulent secondary flow. Downstream however,

the correlation was observed to have changed sign over much of the passage vortex, in keeping with the velocity gradients within it.

At slot 10 (128% Cax) the turbulence activity was observed to be concentrated within the secondary flow, with fairly low values within the wake. This agrees with the results of Gregory-Smith *et al* (1988) who observed the wake turbulence to decay rapidly downstream of their cascade, whilst that within the passage vortex was maintained. In general high turbulence energy was found to be associated with the secondary loss core, and regions where separation lines on the endwall and suction surface feed loss into the main flow. At slot 8 (97% Cax), high streamwise turbulence was observed all over the suction surface. Also the surface pressure coefficient measurements indicate that there is significant deceleration near to the suction surface over the final 20% of axial chord, particularly within 10% span of the endwall. This streamwise deceleration coupled with high streamwise turbulence could be a significant factor behind the rapid rise in loss which is normally observed in the latter half of turbine rotor cascades.

The endwall flow has been traversed with a rotatable single wire probe. At slot 5 (55% Cax) results showed that the flow has almost constant total velocity down to 0.25% span from the endwall, but is highly skewed with the under-turning reducing by 5° for each millimetre moved away from the endwall. Also freestream turbulence levels were found to be present near to the endwall on the pressure side of the passage, but on the suction side the flow was more turbulent. This lends some support to the results of Harrison (1989) who observed a laminar flow over much of the endwall on the pressure side of the passage within his turbine cascade. However, if such a boundary layer exists here it must be extremely thin. Measurements of the flow at slot 8 (97% Cax) indicate that although the total velocity is still almost constant up to $1mm$ from the endwall, the skew is very much reduced with the flow direction only changing by 1° for each millimetre moved radially. In the suction surface/endwall corner the velocity reduces sharply, due to the counter vortex there. The endwall flow was observed to be generally more turbulent than at slot 5, which also supports Harrison's results, as he

observed transition of the endwall flow on the pressure side of the passage, occurring as the trailing edge was approached.

Downstream of the cascade the endwall flow was observed to be more turbulent, and a more usual type of boundary layer starts to develop. Mass averaging of the turbulent kinetic energy over the traverse plane, reveals that only 16% of the loss may be accounted for directly as turbulent kinetic energy. This is in accord with the results of other workers (e.g. Moore *et al* (1986) 23%, Zunino *et al* (1987) 10%, Gregory-Smith *et al* (1988) 17%). It is thought that this indicates that the dissipation of turbulence by molecular viscosity almost matches its rate of generation, thus preventing a large accumulation of turbulent kinetic energy.

The rates at which the turbulent Reynolds stresses transfer mean flow kinetic energy to turbulent kinetic energy, and the rate of viscous dissipation of mean flow kinetic energy have been calculated at slot 10. The results indicate that the turbulent effects are generally two orders of magnitude greater than that due to molecular viscosity. By far the largest rates are produced by the normal stresses, but these act to extract energy from the mean flow in some places, and return turbulent kinetic energy to the mean flow in others. Thus their net effect is much smaller than their large local effects, but is still found to be significant. This may indicate the inadaquacy of a Boussinesq eddy viscosity model (which cannot model normal stresses) particularly within the blade passage where the normal rates of strain are large.

Comparing the results calculated from the Durham data with those of Moore *et al* (1986) shows general agreement, except for the term $\overline{u'^2}\frac{\partial \overline{U}}{\partial x}$ which they found to be significant. However their measurement plane was closer to the trailing edge (10% Cax) than slot 10 (28% Cax), so streamwise gradients might be greater due to the flow being less mixed in their case. The mass averaged rate of turbulent deformation work was found to account for 25% of the rate of loss production downstream of the cascade (as indicated by pressure probe measurements of the 'JAW' test case). However two terms which Moore *et al* found to contribute 60% of the total rate in their work,

were not accounted for here. Also the downstream rate of loss production might be less in the 'JGC' test case than the 'JAW' test case as less secondary kinetic energy was developed. Hence the value for the total deformation work which was calculated seems reasonable. Thus it appears that downstream of the cascade loss is produced principally by the turbulent Reynolds stresses, and that direct viscous action has only a relatively small effect.

Calculations of eddy viscosities at slot 10 from the experimental shear stress measurements, indicate that downstream of the cascade an isotropic eddy viscosity is a reasonable model for the $\overline{u'v'}$ and $\overline{u'w'}$ stresses. Peak values of eddy viscosity of 2000 times the molecular viscosity were found to be associated with the secondary loss core.

A short spectral survey of the flowfield revealed no dominant frequencies in the energy spectrum, except for a low frequency organ resonance within the wind tunnel. No evidence was found for the low frequency peak observed by Gregory-Smith *et al* (1988) to be associated with the passage vortex downstream of their cascade. This might be because of the smaller suction surface diffusion in this test, and the absence of the associated laminar separation bubble.

The invariance of the secondary loss between the 'JAW' and 'JGC' test cases when significant variation in secondary kinetic energy was observed seems a little surprising. It would seem logical that the secondary loss would depend upon the strength of the secondary flow. It could be that most secondary loss is produced near to the endwall and suction surface. The effect of the inlet boundary layer might be to determine how much secondary kinetic energy is initially imparted to the endwall boundary layer. This is then rolled up into a core, and is convected up the suction surface. Thus most of the change in secondary kinetic energy occurs within this core, and the levels close to much of the endwall and suction surface are little changed by the differing inlet boundary layer thickness. However, the mechanisms of secondary loss production within the cascade are not entirely clear. It seems likely that the suction surface flow will undergo earlier transition close to the endwall due to the higher turbulence in the endwall boundary layer,

and the presence of the turbulent secondary flow. This will contribute some loss to the secondary loss downstream of the cascade. Also it seems likely that the deceleration of the suction surface flow within the last 20% of axial chord, is a major contributor to the loss production process. In particular the steeper deceleration in the endwall region caused by the presence of the passage vortex, and the more turbulent flow which it introduces to the suction surface, will tend to result in more suction surface loss production close to the endwall. This is particularly true of the region where the passage vortex separates from the suction surface since there the flow is very turbulent.

The above discussion of secondary loss production mechanisms within the cascade is speculative, and other processes may also have significant effects. In particular the high Reynolds stresses measured within the secondary flow away from the passage walls may also be a significant factor in the loss production process. Further experimental investigation would be required to determine the relative contributions of the various possible secondary loss production mechanisms.

## 9.2 Modelling Results

The experimental measurements of the mean flowfield in the Durham cascade with no turbulence grid ('JAW' test case) which were reported by Walsh (1987), have been used to test three Navier-Stokes solution techniques. The results indicated that it is possible to obtain accurate numerical solutions of the three-dimensional pressure driven effects. However, the use of first order spatial accuracy in discretisation coupled with inexpert grid generation (the resulting mesh was highly non-uniform) was found to produce very large numerical errors which completely destroyed the solution accuracy. Also the use of excessive second order smoothing was found to be equally damaging to the quality of the prediction. The application of second order spatial accuracy, coupled with careful consideration of the discretisation so as to avoid numerical loss production, was found to be capable of producing very accurate predictions of the mean flowfield. This particular code (which is due

to Moore and Moore (1985)) was thus used in further tests.

The quality of the solutions obtained has been found to be very sensitive to the turbulence model which is used within the calculation procedure. Seemingly arbitrary changes to the turbulence model were found to produce significantly different mean flow predictions. In particular, the mobility of the passage vortex centre, which experimentally is observed to move towards and up the suction surface, appears to be greatly effected by the turbulence modelling. This suggests that considerable caution should be exercised when applying simple turbulence models to such a complex flow.

The general development of the secondary flow can be modelled with relatively few grid points (a calculation mesh of 47 axial, 25 tangential, and 17 radial points was used here to model half the cascade span). However the required density of points is likely to be dependent upon the formal spatial accuracy of the algorithm, and thus may be different for other codes. Despite the generally good flow predictions, numerical problems were observed in the trailing edge region when using this 'coarse' mesh. The use of a finer calculation mesh with 60 axial and 36 tangential points was shown to help reduce the numerical loss production in the trailing edge region, and also different turbulence models can have a significant effect upon this flow.

Specification of different regions of the flowfield as laminar was found to have some effect upon predictions of the secondary flows and losses. In particular specification of the blade boundary layers as laminar in the region where they were known to be laminar, produced much improved predictions of the profile loss. This also produced some increase in the predicted secondary loss, since turbulent blade boundary layers were retained within $40mm$ of the endwall which were than accounted for as 'secondary' rather than 'profile' loss. Also specification of the flow close to the endwall as laminar within the blade passage, was found to increase the predicted secondary kinetic energy and passage vortex migration, generally achieving better agreement with experiment. As discussed previously, there is some experimental evidence for such a laminar flow on the endwall within the blade passage. This suggests that there is a real need for models of transition in order to predict accurately

the secondary flow effects, as well as for the prediction of blade profile losses.

The mixing length turbulence model which is incorporated within the most recent version of the Moore's program, appears to produce good predictions of the secondary loss. It is also possible to deduce from the results obtained, that a large proportion of this secondary loss is generated within the blade boundary layers and wake, downstream of 80% axial chord. Unfortunately it is not possible to determine the accuracy of this prediction with the available experimental data.

The results of these initial tests indicated that very accurate solution of the Navier-Stokes equations in three dimensions is now possible using a 'state of the art' finite volume solution technique. Code authors are now producing techniques which produce sufficiently low levels of numerical error, for the turbulence modelling to be the most limiting part of the solution accuracy. These techniques therefore offer the realistic possibility of accurately assessing the performance of different turbulence models for three-dimensional flows, and should thus aid their development.

The Navier-Stokes solver of Moore and Moore (1985) has also been used to predict the flow in the Durham turbine cascade with a turbulence grid placed upstream ('JGC' test case). The code was run with three different turbulence models and comparisons made with experiment for predictions of the mean flow and the turbulent Reynolds stresses.

The mixing length turbulence model was found to predict quite accurately the reduced secondary kinetic energy resulting from the thinner inlet boundary layer in this case. It also appears to produce reasonable predictions for the secondary loss. Forcing the endwall flow within the blade passage to be laminar, was found to be more significant here than it was in the 'JAW' test case. Apparently higher over-turning was produced on the endwall, which appeared to help the passage vortex to migrate towards the suction surface.

Comparison of predictions of shear stress produced by the mixing length model, with those measured experimentally, showed that the mixing length model generally fails to identify the magnitude of the turbulent stresses

within the secondary flow. This explains why the mass averaged secondary kinetic energy is not observed to decay enough downstream of the cascade in the predictions. The apparently realistic loss growth downstream is then produced by too much endwall boundary layer growth and/or the mixing out of too deep a velocity deficit within the wake. This is not a realistic model of the loss production downstream of the cascade.

Within the cascade the contribution of the Reynolds stresses within the separated three-dimensional secondary flow to the loss production process is not known. Thus it is not possible to determine the accuracy of the mixing length model prediction of most secondary loss production within the suction surface boundary layer in the final 20% of axial chord. As mentioned in the discussion of the experimental results, the interaction of the passage vortex with the suction surface boundary layer may indeed be a significant factor in the process of secondary loss generation. However, whether the mixing length turbulence model can be expected to predict accurately such a process in which the normal Reynolds stresses are likely to be important is questionable particularly for significantly different blade shapes. Even within one blade row the mixing length model might be expected to have difficulty in coping with the varied flow regimes, such as accelerating flow, decelerating flow, and swirling flow.

A one equation model of turbulence which solves a transport equation for the turbulent kinetic energy, and specifies a dissipation length scale algebraically, has been used to model the 'JGC' test case. The mean flow prediction produced by this model was found to be less accurate than that resulting from application of the mixing length model. The secondary kinetic energy was under-predicted, and the correspondingly weak passage vortex did not migrate as it is observed to do in the experimental results. However the model has not been implemented for as long a period as the mixing length model, and so may be expected to benefit from 'fine tuning' of its constants. Interestingly, this model predicts too little secondary loss and this significant change in prediction with the application of a different turbulence model might be considered to direct further suspicion at the foundations of

the mixing length model's secondary loss predictions.

Comparison with the experimental turbulence data shows that too much turbulent kinetic energy is predicted to be produced on the suction surface. This might be because the model does not take account of the effects of the passage curvature, which tends to keep losses low on the suction surface where the flow accelerates. In contrast, on the endwall the model predicts much less $\overline{u'w'}$ correlation than the mixing length model. Despite the large prediction of turbulent kinetic energy on the suction surface the observed generation of turbulent kinetic energy, and the associated high stresses within the secondary flow, are not predicted. Downstream of the cascade the model predicts too much turbulent kinetic energy within the wake. Although significant decay of the wake turbulence is predicted between slots 9 and 11, in accord with the results of Gregory-Smith *et al* (1988) who showed rapid decay of wake turbulence to be a feature of the downstream flow, too much turbulence is still present at slot 10.

Thus it seems that this turbulence model needs further development before it can be considered to be an acceptable replacement for the mixing length model. The inclusion of a transition modelling capability as is available within the one equation model is also worthy of development, as it is felt that this is one of the major requirements for future extensions of predictive capabilities.

The final turbulence model which was tested in this work is a hybrid of the mixing length model for the boundary layers and a standard two equation $K - \epsilon$ model elsewhere. The use of the mixing length model in the near wall regions is intended to avoid the large numbers of grid points which are required within boundary layers by $K - \epsilon$ models. This would be very costly for a three-dimensional calculation.

Comparison of results with experiment again reveals a poor prediction of the mean flow. As with the one equation model the passage vortex was predicted to be too weak, and did not migrate as it is observed to do in reality. The prediction of secondary loss was found to be reasonable, but this is not surprising as the mixing length model was used in the boundary layer regions

where most of this is predicted to be produced. A striking improvement which is produced by the two equation model solution is the prediction of turbulent kinetic energy which compares much better with experiment. The solution of a transport equation for the length scale appears to identify the turbulence generation within the secondary flow. This was also observed by Zunino *et al* (1988) who tested turbulence models against their experimental data. They showed excellent predictions of turbulent kinetic energy by the standard $K-\epsilon$ turbulence model. However their test used the experimentally measured velocity distributions rather than those emerging from a solution coupled to the turbulence model. Also their measurement locations are such that they only showed comparisons up to the passage throat, whereas they point out that significant turbulence development is likely to occur on the suction side of the passage downstream of this position. Even in these conditions however, they concluded that the turbulence models could only be considered to give a qualitative agreement with the experimental measurements.

The increased predictions of turbulent viscosity within the secondary flow by the $K-\epsilon$ model result in much larger stresses there. However, as the loss at slot 10 is little bigger than that predicted by the mixing length model, it appears that these stresses do not produce much loss. The turbulence levels within the wake also appear to be over-predicted by the $K-\epsilon$ model, as observed with the one equation model. However the $K-\epsilon$ model predicts even larger values within the wake at slot 9, although these decay rapidly to become comparable with results of the one equation model by slot 11.

In general the results of the $K-\epsilon$ model appear to be encouraging, and development of a hybrid $K-\epsilon$/one equation model with transition prediction seems to be an attractive intermediate step before launching into the realm of full Reynolds stress models. Indeed there appears to be a requirement for further experimental work in order to identify the level of modelling which is required for meaningful predictions of aerodynamic loss. It may be that most loss is produced in the blade boundary layers within the blade passage, and that accurate modelling of the Reynolds stresses within the swirling three-dimensional secondary flows is not really necessary. However this may not

be the case, and the generality of a model which relies upon a Boussinesq eddy hypothesis within such a highly curved duct is in any case questionable. Leschziner (1989) suggests that in such circumstances it is necessary to solve for individual components of the Reynolds stress tensor in order to adaquately model the anisotropy producing effects of the strong curvature. Although the development of such models is likely to be a rather long and difficult process, this must surely be one of the most important aims of developments in the future.

# Chapter 10
# Conclusions and Recommendations for Further Work

## 10.0 Introduction

This chapter presents separately the main conclusions of the experimental and modelling work presented in this thesis. Recommendations for further work using the experimental facilities, and directions for further modelling developments are then discussed.

## 10.1 Experimental Conclusions

This thesis presents results of experimental investigations of the flow in a large scale, low speed, linear cascade of high turning turbine rotor blades. The results obtained with only natural tunnel freestream turbulence at inlet ('JAW' test case) have shown that:

a) The flow develops rapidly in the final 20-30% of axial chord, and this is accompanied by significant loss generation.

b) The endwall counter vortex is a significant feature of the downstream flow, where it tends to reduce the over-turning near to the endwall.

c) Downstream of the cascade radial velocities mix out quite rapidly.

d) The mixed out loss is observed to be fairly constant in the downstream flow, despite the growth of an endwall boundary layer. This suggests that secondary kinetic energy is being converted to primary kinetic energy as the flow proceeds downstream.

Measurements have also been made of the turbulent flow in the same turbine cascade but with a turbulence generating grid mounted upstream ('JGC' test case). This raised the freestream turbulence from 1.4% to 4.5%, and also resulted in a thinner endwall boundary layer at inlet to the cascade. The results show that:

a) Raising the freestream turbulence intensity promoted earlier transition of the suction surface boundary layer, resulting in slightly increased profile loss.

b) Raising the freestream turbulence intensity in the range tested, has very little effect upon the secondary flows and losses which develop.

c) Thinning the endwall boundary layer at inlet makes no significant change to the net loss produced by the cascade. However the resulting secondary kinetic energy is considerably reduced by this change, and hence the mixed out loss is also smaller.

d) High turbulent kinetic energy is associated with the passage vortex, and the regions in which separation lines on the endwall and suction surface feed loss into the main flow. Significant $\overline{u'w'}$ shear stress is also located near the suction surface separation line.

e) Within the blade passage the $\overline{u'v'}$ shear stress shows negative values within the loss core due to the high cross-passage velocity gradient. These change to positive values downstream of the cascade where the velocity gradients due to the passage vortex and wake are dominant.

f) Just upstream of the trailing edge, high streamwise turbulence was observed right across the suction surface. The surface pressure measurements also indicate that the flow near to the suction surface is decelerating in this region. Thus the mechanism $\overline{u'^2}\frac{\partial \overline{U}}{\partial x}$ on the suction surface, may be a significant contributor to the more rapid rate of loss production which is normally observed in the latter half of turbine rotor cascades.

g) The new endwall boundary layer which forms within the blade passage away from the suction surface is extremely thin. The flow further from the surface has almost constant speed, but is highly skewed. Freestream turbulence levels are present on the pressure side of the passage close to the endwall, and a thin laminar flow may exist in this region. However on the suction side of the passage and downstream of the cascade, the endwall flow is turbulent.

h) The frequency spectrum of the turbulence shows no dominant fre-

quencies where the turbulence is high.

i) Downstream of the cascade a fairly isotropic eddy viscosity is seen in the loss core.

j) There are significant contributions to the loss generation process by the Reynolds normal stresses, which cannot be allowed for by a Boussinesq eddy viscosity model.

## 10.2 Modelling Conclusions

The flowfield of the cascade has been extensively modelled with the three-dimensional Navier-Stokes solution technique of Moore and Moore (1985). Comparisons between the modelling and experiment have shown that:

a) Very accurate solution of the governing equations may be obtained with a 'state of the art' finite volume calculation procedure.

b) The second order spatial accuracy of the algorithm permits good solutions for the secondary flow to be obtained with a calculation mesh of 20000 points. However, a finer mesh is required to restrict numerical errors in the trailing edge region to a similar degree.

c) The quality of the secondary flow predictions is very sensitive to the model used to simulate the effects of the turbulent Reynolds stresses. Too much turbulent stress modelling results in an under-prediction of secondary kinetic energy, and prevents the vortex from migrating towards and up the suction surface.

d) The mixing length turbulence model predicts that most secondary loss is produced within the blade boundary layers and wake, downstream of 80% axial chord. It is not known how realistic this prediction is.

e) Within the separated, three-dimensional, secondary flows, the mixing length model, and a one equation turbulence model, do not identify the magnitude of the turbulent stresses which are present. Thus these models cannot model the loss production in the downstream flow correctly.

f) A $K - \epsilon$ model of turbulence appears to predict the generation of

turbulent kinetic energy within the secondary flow reasonably well. However too much turbulence is predicted within the wake.

g) The ability of simple turbulence models to predict accurately the aerodynamic loss within such a varied and complex flowfield is questionable. In particular the application of a Boussinesq eddy viscosity hypothesis within such a highly curved duct, cannot properly account for the effects of the high normal rates of strain which are present. Great effort should therefore be directed at the development of more sophisticated models of the turbulent Reynolds stresses.

## 10.3 Recommendations for Further Work

On the experimental side, there are clearly several pieces of work which are a natural extension of the work described in this thesis. Firstly a traverse at slots 5 and 8 with a pressure probe would allow existing software to calculate the rate of turbulent deformation work within the separated shear layers. This would clearly indicate the importance of the Reynolds stresses within the secondary flow as a loss production mechanism. The use of surface mounted film gauges on the endwall could identify the presence of any laminar patches there.

The modelling results suggest that the $\overline{v'w'}$ shear stress is important for the secondary flow, and Moore *et al* (1986) showed this to be true for the flow downstream of their cascade. Hence measurements of this stress would be valuable. Such measurements could be obtained with a third traverse of the x-probe technique (probe set at different yaw angle and a new analysis program) or alternatively with a triple wire or rotatable single wire probe. Traverses very close to the suction surface using pressure probes and hot-wires or laser doppler anemometry, would also be very valuable in order to determine its role in the production of secondary loss. It is clear that the flow develops rapidly between slots 5 and 8. Detailed traverses of the mean and turbulent flowfields between these two locations would provide a useful extension to the data, increasing its value as a case with which to test and

set up turbulence models.

The turbulence effects which are present within stator cascades are still a little unclear. There is some contrast between the results of Bailey (1980), who observed very low turbulence energy in the secondary flow region of a cascade of inlet guide vanes, and Sharma *et al* (1985) who detected significant turbulence downstream of the first stator in a one and a half stage model turbine. It is possible that the lower turning of nozzle guide vanes, and their higher acceleration, results in much less turbulence production than is typical of rotor cascades. Hence a detailed investigation of the turbulent flowfield in a cascade of nozzle guide vanes would provide both a useful contribution to knowledge, and a valuable data set for the evaluation of turbulence models.

On the modelling side the most urgent requirements now appear to be for better turbulence models, and for models of transition. The development of more sophisticated models is a formidable problem, but should be aided by the high accuracy of modern Navier-Stokes solvers. Despite the success of the code authors in controlling numerical errors, the modelling of trailing edge flows still appears to present some problems. Validation of models over a wide variety of cases should be undertaken in order to assess their predictive capabilities in this area.

Developments in grid generation techniques, and more stable algorithms should continue to contribute to solution accuracy for some time to come. Also as computing power continues to increase, models of three-dimensional unsteady flow, and blade row interaction are likely to appear. These developments may be particularly accelerated if transputer technology is complemented by the development of highly sophisticated parallelising compilers. Such a combination would completely revolutionise supercomputing, and thus have profound repercussions for computational fluid dynamics.

The results in this thesis show that current technology is capable of accurately predicting the pressure driven effects of secondary flow generation. This suggests that some progress might be made by applying such calculation techniques to different endwall geometries. Thus an interesting project could

consist of the design of endwalls with a three-dimensional Navier-Stokes solver, and testing of the predictions in an experimental facility. The value of such work would however be greatly enhanced if it was extended to radial geometries, as the radial pressure gradients are likely to have a significant bearing upon the geometry of a successful design.

The effects of skew in the endwall boundary layer have been shown by Walsh (1987) to have a profound effect upon the development of the secondary flows and losses. Thus it may be possible to gain some advantage by ejecting endwall coolant flow at an angle so as to introduce positive skew into the endwall boundary layer. The application of a specially modified Navier-Stokes solver could usefully determine the feasibility of such a suggestion.

# References


**Ainley, D.G., Mathieson, G.C.R., (1951)**
*'An Examination of the Flow and Pressure Losses in Blade Rows of Axial-Flow Turbines'*,
ARC R&M, No. 2891.

**Anderson, J.D., (1986)**
*'Introduction to Computational Fluid Dynamics'*,
VKI Lecture Series 1986-01.

**Arts, T., (1984)**
*'Secondary Flows and Endwall Boundary Layers in Axial Turbomachines'*,
VKI-LS 1984-05, 'Secondary Flows and Endwall Boundary Layers in Axial Turbomachines'.

**Atkins, M.J., (1987)**
*'Secondary Losses and Endwall Profiling in a Turbine Cascade'*,
Proc. I Mech E, Conf. 'Turbomachinery - Efficiency Prediction and Improvement', Paper C255/87.

**Bailey, D.A., (1980)**
*'Study of Mean and Turbulent Velocity Fields in a Large-Scale Turbine Vane Passage'*,
Trans. ASME, J. Eng. Power, 102, pp 88-97.

**Bains, W.P. Peterson, E.G., (1950)**
*'An Investigation of Flow Through Screens'*,
Trans. ASME, p 467.

**Belik, L., (1975)**
*'Secondary Losses in a Turbine Blade Cascade with Low Aspect Ratio and Large Deflection'*,
Proc. $6^{th}$ Conf. on Steam Turbines of Large-Power Output, Plzen, Czechoslavakia.

**Belik, L., (1977)**
*'Three-Dimensional and Relaminarisation Effects in Turbine Blade Cascades - An Experimental Study'*,
JSME-ASME Joint Gas Turbine Conference, Paper 37.

**Binder, A., Romey, R., (1983)**
*'Secondary Flow Effects and Mixing of the Wake Behind a Turbine Stator'*,
Trans. ASME, J. Eng. Power, 105, p40.

**Birch, N.T., (1989a)**
*'Predictions of the Durham Low-Speed Turbine Cascade using the ANSI-3D Code'*,
Private Communication.

**Birch, N.T., (1989b)**
*'Turbulence Modelling Options in the CFD System - A Status Report'*,
Private Communication.

**Boletis, E., (1984)**
*'Experimental Research on Secondary Flows in Annular Turbine Cascades at VKI'*,
VKI-LS 1984-05.

**Briley, W.R., McDonald, H., (1977)**
*'Solution of the Multi-Dimensional Compressible Navier-Stokes Equations by a Generalised Implicit Method'*,
J. Comp. Physics, 24, p372.

**Bruun, H.H., Khan, M.A., Al-Kayiem, H.H., Fardad, A.A., (1988)**
*'Velocity Calibration Relationships for Hot-Wire Anemometry'*,
J. Phys. E: Sci. Instrum., 21, p 225.

**Came, P.M., Marsh, H., (1974)**
*'Secondary Flow in Cascades: Two Simple Derivations for the Components of Vorticity'*,
J. Mech. Eng. Sci., 16, p 391.

**Chew, J.W., Birch, N.T., (1987)**
*'Comparison Between Numerical Solutions and Measurements for a High-Speed Turbine Blade'*,
Proc. IMechE Conf. 'Turbomachinery - Efficiency Prediction and Improvement', Paper C268/87.

**Chew, Y.T., Ha, S.M., (1988)**
*'The Directional Sensitivities of Crossed and Triple Hot-Wire Probes'*,
J. Phys. E: Sci. Instrum, 21, pp 613-620.

**Chima, R.V., (1985)**
*'Inviscid and Viscous Flows in Cascades with an Explicit Multi-Grid Algorithm'*,
AIAA J., 23, p1556.

**Choi, D., Knight, C.J., (1988)**
*'Computation of Three-Dimensional Viscous Linear Cascade Flows'*,
AIAA J., 26, p1477.

**Cleak, J.G.E., Gregory-Smith, D.G., Birch, N.T., (1989)**
*'Three-Dimensional Laminar and Turbulent Flow Modelling in an Axial Turbine Cascade : A Comparison with Experiment'*,
Submitted to : Computers and Fluids.

**Cohen, H., Rogers, G.F., Saravanamuttoo, H.I., (1972)**
*'Gas Turbine Theory'*,
Published by : Longmans.

**Davis, R.L., Hobbs, D.E., Weingold, H.D., (1988)**
*'Prediction of Compressor Cascade Performance Using a Navier-Stokes Technique'*,
Trans. ASME, J. Turbomachinery, 110, p 520.

**Dawes, W.N., (1983)**
*'Efficient Implicit Algorithm for the Equations of 2-D Viscous Compressible Flow : Application to Shock-Boundary Layer Interaction'*,
Int. J. Heat and Fluid Flow, 4, p17.

**Dawes, W.N., (1986)**
*'A Numerical Method for the Analysis of 3D Viscous Compressible Flow in Turbine Cascades ; Application to Secondary Flow Development in a Cascade With and Without Dihedral'*,
ASME Paper No. 86-GT-145.

**Dawes, W.N., (1987)**
*'Application of a Three-Dimensional Viscous Compressible Flow Solver to a High Speed Centrifugal Compressor Rotor - Secondary Flow and Loss Generation'*,
Proc. IMechE Conf. 'Turbomachinery - Efficiency Prediction and Improvement', Paper C261/87.

**Delaney, R.A., (1982)**
*'Time Marching Analysis of Steady Transonic Flow in Turbomachinery Using the Hopscotch Method'*,
ASME Paper No. 82-GT-152.

**Denton, J.D., (1975)**
*'A Time Marching Method for Two- and Three-dimensional Blade-to-Blade Flow'*,
ARC R&M 3775.

**Denton, J.D., (1985a)**
*'The Calculation of Fully Three Dimensional Flow Through Any Type of Turbomachine Blade Row'*,
AGARD-LS-140, '3D Computation Techniques Applied to Internal Flows in Propulsion Systems', Paper 9.

**Denton, J.D., (1985b)**
*'Solution of the Euler Equations for Turbomachinery Flows Part 1 : Basic Principles and Two Dimensional Applications'*,
NATO ASI Series E : Applied Sciences - No. 97A, 'Thermodynamics and Fluid Mechanics of Turbomachinery', p283.

**Denton, J.D., (1987)**
*'Review of Numerical Methods for Flow Field Computation'*,
Lecture notes received in private communication.

**Denton, J.D., Cumpsty, N.A., (1987)**
*'Loss Mechanisms in Turbomachines'*,
Proc. I Mech E, Conf. 'Turbomachinery - Efficiency Prediction and Improvement', Paper C260/87.

**Dishart, P.T., Moore, J., (1989)**
*'Tip Leakage Losses in a Linear Turbine Cascade'*,
ASME Paper no. 89-GT-56.

**Dodge, P.R., (1977)**
*'Numerical Method for 2D and 3D Viscous Flows'*,
AIAA J., 15, p961.

**Dominy, R.G., Harding, S.C., (1989)**
*'An investigation of Secondary Flows in Nozzle Guide Vanes'*,
Unpublished Work.

**Dunham, J., (1970)**
*'A Review of Cascade Data on Secondary Losses in Turbines'*,
J. Mech. Eng. Sci., 12, p 48.

**Dunham, J., (1986)**
*'The Role of Flow Field Computation in Improving Turbomachinery'*,
AIAA $15^{th}$ Congress of the International Council of the Aeronautical Sciences, ICAS-86-3.7.3.

**Gaugler, R.E., Russell, L.M., (1984)**
*'Comparison of Visualised Turbine Endwall Secondary Flows and Measured Heat Transfer Rates'*,
Trans. ASME, J. Eng. Gas Turbines and Power, 106, p 168.

**Glynn, D.R., (1982)**
*'Calculation of Secondary Flows in Cascades Including Effects of Bernoulli Surface Distortion'*,
Int. J. Heat and Fluid Flow, 3, p 73.

**Glynn, D.R., Marsh, H., (1980)**
*'Secondary Flow in Annular Cascades'*,
Int. J. Heat and Fluid Flow, 2, p 29.

**Gopalakrishnan, S., Bozzola, R., (1972)**
*'Computation of Shocked Flows in Compressor Cascades'*,
ASME Paper 72-GT-31.

**Gostelow, J.P., (1984)**
*'Cascade Aerodynamics'*,
Pub. Pergamon Press.

**Graves C.P., (1985)**
*'Secondary Flows and Losses in Gas Turbines'*,
Ph.D. Thesis, Durham University.

**Gregory-Smith, D.G., (1982)**
*'Secondary Flows and Losses in Axial Flow Turbines'*,
Trans. ASME, J. Eng. Power, 104, p 819.

**Gregory-Smith, D.G., (1984)**
*'Secondary Flow Theory in Straight and Annular Cascades'*,
VKI-LS 1984-05.

**Gregory-Smith, D.G., (1989)**
*'A Comparison of Three Calculation Codes for the Flow in a Turbine Cascade'*,
Private Communication.

Gregory-Smith, D.G., Graves, C.P., (1983)
*'Secondary Flows and Losses in a Turbine Cascade'*,
AGARD CP-351, 'Viscous Effects in Turbomachines', Paper no. 17.

Gregory-Smith, D.G., Graves, C.P., Walsh, J.A., (1987)
*'Growth of Secondary Losses and Vorticity in an Axial Turbine Cascade'*,
ASME Paper no. 87-GT-114.

Gregory-Smith, D.G., Okan, M.B., (1989)
*'Estimation of Secondary Flows and Losses in Axial Flow Turbines'*,
Private communication.

Gregory-Smith, D.G., Walsh, J.A., Graves, C.P., Fulton, K.P., (1988)
*'Turbulence Measurements and Secondary Flows in a Turbine Rotor Cascade'*,
Trans. ASME, J. Turbomachinery, 110, pp 479-485.

Hah, C., (1984)
*'A Navier-Stokes Analysis of Three-Dimensional Turbulent Flows Inside Turbine Blade Rows at Design and Off-Design Conditions'*,
Trans. ASME, J. Eng. Gas Turbines and Power, 106, p421.

Hah, C., Leylek, J.H., (1987)
*'Numerical Solution of Three-Dimensional Turbulent Flows for Modern Gas Turbine Components'*,
ASME Paper No. 87-GT-84.

Hanjalic, K., Launder, B.E., (1972)
*'A Reynolds Stress Model of Turbulence and its Application to Thin Shear Flows'*,
J.Fluid Mech., 52, p609.

Harrison, S., (1989)
*'Secondary Loss Generation in a Linear Cascade of High Turning Turbine Blades'*,
ASME Paper no. 89-GT-47.

Hawthorne, W.R., (1951)
*'Secondary Circulation in Fluid Flow'*,
Proc. Royal Soc. London, Series A, 206, p 374.

**Hebert, G.J., Tiederman, W.G., (1989)**
*'Comparison of Steady and Unsteady Flows in a Turbine Stator Cascade'*,
ASME Paper no. 89-GT-79.

**Hinze, J.O., (1975)**
*'Turbulence'*,
Published by McGraw-Hill, Second Edition.

**Hodson, H.P., Dominy, R.G. (1988)**
*'An Investigation into the Effects of Reynolds Number and Turbulence upon the Calibration of 5-hole Cone Probes'*,
Proc. $9^{th}$ Symp. on Measuring Techniques for Transonic and Supersonic Flow in Cascades and Turbomachines, Imperial College Report No. TPS/88.008.

**Horlock, J.H., Laksminarayana, B., (1973)**
*'Secondary Flows: Theory, Experiment, and Application in Turbomachinery Aerodynamics'*,
Ann. Review Fluid Mechanics, 5, p 247.

**Jennions, I.K., Stow, P., (1985a)**
*'A Quasi Three-Dimensional Turbomachinery Blade Design System : Part I - Throughflow Analysis'*,
Trans. ASME, J. Eng. Gas Turbines and Power, 107, p 301.

**Jennions, I.K., Stow, P., (1985b)**
*'A Quasi Three-Dimensional Turbomachinery Blade Design System : Part II - Computerized System'*,
Trans. ASME, J. Eng. Gas Turbines and Power, 107, p 308.

**Johnston, J.P., (1960)**
*'On the Three-Dimensional Turbulent Boundary Layer Generated by Secondary Flow'*,
Trans. ASME, J. Basic Eng., 82, p233-248.

**Jørgensen, F.E., (1971)**
*'Directional Sensitivity of Wire and Fiber-Film Probes : An Experimental Study'*,
DISA Information, No. 11.

**Kirtley, K.R., Warfield, M., Laksminarayana, B, (1986)**
*'A Comparison of Computational Methods for Thre-Dimensional, Turbulent Turbomachinery Flows'*,
AIAA Paper 86-1599.

**Langston, L.S., (1980)**
*'Crossflows in a Turbine Cascade Passage'*,
Trans. ASME, J. Eng. Power, 102, p 866.

**Langston, L.S, Nice, M.L., Hooper, R.M., (1977)**
*'Three-Dimensional Flow Within a Turbine Cascade Passage'*,
Trans. ASME, J. Eng. Power, pp 21-28.

**Launder, B.E., Reece, G., Rudi, W., (1975)**
*'Progress in the Development of a Reynolds Stress Turbulence Closure'*,
J. Fluid Mech., 68 p537.

**Lawrenz, M., (1984)**
*'Calculation of 3D Viscous Flows in Annular Cascades Using Parabolised Navier-Stokes Equations'*
VKI-LS 1984-05, 'Secondary Flows and Endwall Boundary Layers in Axial Turbomachines'.

**Leschziner, M.A., (1989)**
*'Modelling Turbulent Recirculating Flows by Finite-Volume Methods - Current Status and Future Directions'*,
Int. J. Heat and Fluid Flow, 10, p186.

**Majola, O.O., (1974)**
*'A Hot-Wire Method for Three-Dimensional Shear Flows'*,
DISA Information, No. 16, pp 11-14.

**Marchal, Ph., Sieverding, C.H., (1977)**
*'Secondary Flows Within Turbomachinery Bladings'*,
AGARD-CP-214, 'Secondary Flows in Turbomachines', Paper no. 11.

**Marsh, H., (1976)**
*'Secondary Flow in Cascades: The Effect of Compressibility'*,
ARC R&M No. 3778.

**McNally, W.D., Sockol, P.M., (1985)**
*'Review - Computational Methods for Internal Flows with Emphasis on Turbomachinery'*,
Trans. ASME, J. Fluids Eng., 107, p6.

**Moore, J., (1985)**
*'Performance Evaluation of Flow in Turbomachinery Blade Rows'*,
AGARD-LS-140, '3D Computation Techniques Applied to Internal Flows in Propulsion Systems'.

FIGURE 4.3 : Turbulence Grid Viewed From the Tunnel Side

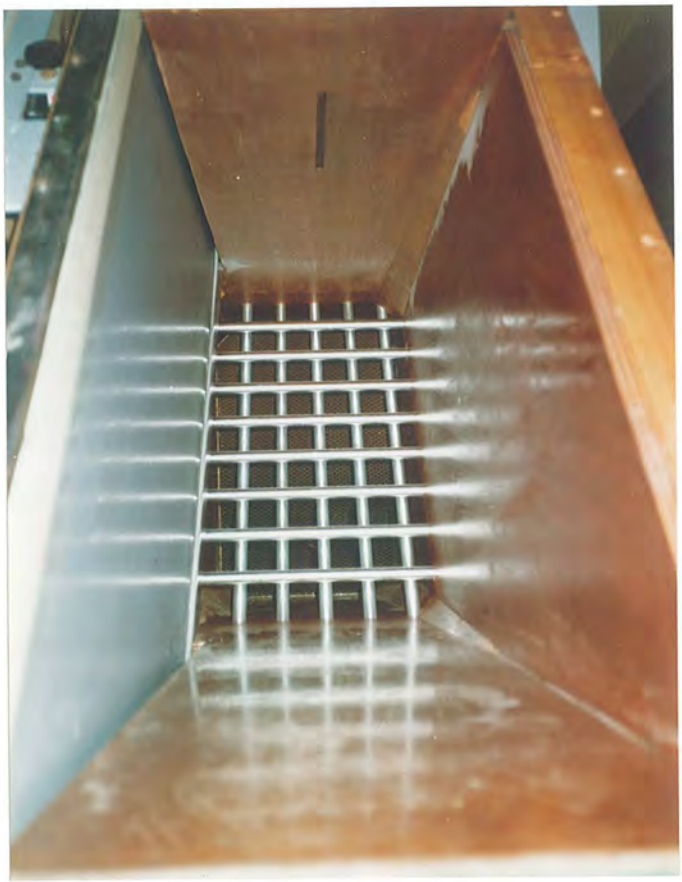

Moore, J., Adhye, R.Y., (1985)
*'Secondary Flows and Losses Downstream of a Turbine Cascade'*,
Trans. ASME, J. Eng. Gas Turbines and Power, 107, p961.

Moore, J., Moore, J.G., (1979)
*'A Calculation Procedure for Three-Dimensional Viscous Compressible Duct Flow, Part 1 : Inviscid Flow Considerations'*,
Trans. ASME, J. Fluids Eng., 101, p415.

Moore, J., Moore, J.G., (1985)
*'Performance Evaluation of Linear Turbine Cascades Using Three-Dimensional Viscous Flow Calculations'*,
Trans. ASME, J. Eng. Gas Turbines and Power, 107, p969.

Moore, J., Schaffer, D.M., Moore, J.G., (1986)
*'Reynolds Stresses and Dissipation Mechanisms Downstream of a Turbine Cascade'*,
ASME Paper no. 86-GT-132.

Moore, J., Smith, B.L., (1984)
*'Flow in a Turbine Cascade : Part 2 - Measurements of Flow Trajectories by Ethylene Detection'*,
Trans. ASME, J. Eng. Gas Turbines and Power, 106, p 409.

Moore, J.G., (1985a)
*'An Elliptic Calculation Procedure for 3D Viscous Flow'*,
AGARD-LS-140, '3D Computation Techniques Applied to Internal Flows in Propulsion Systems'.

Moore, J.G., (1985b)
*'Calculation of 3D Flow Without Numerical Mixing'*,
AGARD-LS-140, '3D Computation Techniques Applied to Internal Flows in Propulsion Systems'.

Morgan, S., (1984)
*'Low Aspect Ratio Turbine Design at Rolls-Royce'*,
VKI-LS 1984-05.

Northall, J.D., Moore, J.G., Moore, J., (1987)
*'Three-Dimensional Viscous Flow Calculations for Loss Prediction in Turbine Blade Rows'*,
Proc. IMechE Conf. 'Turbomachinery - Efficiency Prediction and Improvement', Paper C267/87.

Norton, R.J.G., Thompkins, W.T., Haimes, R., (1984)
*'Implicit Finite Difference Schemes with Non-Simply Connected Grids - A Novel Approach'*,
AIAA Paper 84-0003.

Oka, S., Kostić, Ž., (1972)
*'Influence of Wall Proximity on Hot-Wire Velocity Measurements'*,
DISA Information, No. 13, pp 29-33.

Patankar, S.V., Spalding, D.B., (1972)
*'A Calculation Procedure for Heat, Mass and Momentum Transfer in Three-Dimensional Parabolic Flows'*,
Int. J. Heat and Mass Transfer, 15, pp1787-1806.

Perdichizzi, A., (1989)
*'Mach Number effects on Secondary Flow Development Downstream of a Turbine Cascade'*,
ASME Paper no. 89-GT-67.

Perry, A.E., (1982)
*'Hot-Wire Anemometry'*,
Published by OUP.

Pouagare, M., Delaney, R.A., (1986)
*'Study of Three-Dimensional Viscous Flow in an Axial Compressor Cascade Including Tip Leakage Effects Using a SIMPLE - Based Algorithm'*,
Trans. ASME, J. Turbomachinery, 108, p51.

Pratap, V.S., Spalding, D.B., (1976)
*'Fluid Flow and Heat Transfer in Three-Dimensional Duct Flows'*,
Int. J. Heat and Mass Transfer, 19, p1183.

Priddy, W.J., Bayley, F.J., (1988)
*'Turbulence Measurements in Turbine Blade Passages and Implications for Heat Transfer'*,
Trans. ASME, J. Turbomachinery, 110, p 73.

Roach, P.E., (1987)
*'The Generation of Nearly Isotropic Turbulence by means of Grids'*,
Int. J. Heat and Fluid Flow, 8, pp 88-91.

**Sato, T., Aoki, S., Nagayama, T., (1986a)**
*'Extensive Verification of the Denton New Scheme From the User's Point of View: Part 1 - Calibration of Code Control Variables'*,
Trans. ASME, J. Turbomachinery, 108, pp162-169.

**Sato, T., Aoki, S., Nagayama, T., (1986b)**
*'Extensive Verification of the Denton New Scheme From the User's Point of View: Part 2 - Comparison of Calculated and Experimental Results'*,
Trans. ASME, J. Turbomachinery, 108, pp170-179.

**Schaub, U.W., Sharp, C.R., Basset, R.W., (1964)**
*'An Investigation of the Three-Dimensional Flow Characteristics of a Non-Nulling Five-Tube Probe'*,
Report No. LR-393, Division of Mechanical Engineering, National Research Laboratories, Ottawa, Canada.

**Senoo, Y., (1958)**
*'The Boundary Layer on the Endwall of a Turbine-Nozzle Cascade'*,
Trans. ASME, 80, p 1711.

**Shang, J.S., Buning, P.G., Hankey, W.L., Wirth, M.L., (1980)**
*'Performance of a Vectorised Three-Dimensional Navier-Stokes Code on the CRAY-1 Computer'*,
AIAA J., 9, p1073.

**Sharma, O.P., Butler, T.L., Joslyn, H.D., Dring, R.P., (1985)**
*'Three-Dimensional Unsteady Flow in an Axial Flow Turbine'*,
J. Propulsion, 1, p 29.

**Sieverding, C.H., (1985a)**
*'Axial Turbine Performance Prediction methods'*,
NATO ASI Series E: Applied Sciences, 'Thermodynamics and Fluid Mechanics of Turbomachinery', No. E97B, p 737.

**Sieverding, C.H., (1985b)**
*'Recent Progress in the Understanding of Basic Aspects of Secondary Flows in Turbine Blade Passages'*,
Trans. ASME, J. Eng. Gas Turbines and Power, 107, pp 248-252.

**Sjolander, S.A., (1975)**
*'The Endwall Boundary Layer in an Annular Cascade of Turbine Nozzle Guide Vanes'*,
Technical Report no. ME/A 75-4, Carlton University, Canada.

Squire, H.B., Winter, K.G., (1951)
*'The Secondary Flow in a Cascade of Aerofoils in a Nonuniform Stream'*,
J. Aero. Sci., 18, p 271.

Stow, P., (1985)
*'Turbomachinery Blade Design Using Advanced Calculation Methods'*,
NATO ASI Series E: Applied Sciences - No. 97A, 'Thermodynamics and Fluid Mechanics of Turbomachinery', p923.

Stow, P., Northall, J., Birch, N., (1987)
*'Navier-Stokes Methods for Turbomachinery Blading Design'*,
Private Communication.

Swaminathan, M.K., Rankin, G.W., Sridhar, K., (1986)
*'A note on the Response Equations for Hot-Wire Anemometry'*,
Trans. ASME, J. Fluids Eng., 108, p 115.

Turner, J.R., (1957)
*'An Investigation of the End-Wall Boundary Layer of a Turbine-Nozzle Cascade'*,
Trans. ASME, 79, p 1801.

Walsh, J.A., (1987)
*'Secondary Flows and Inlet Skew in Axial Flow Turbine Cascades'*,
Ph.D. Thesis, Durham University.

Walsh, J.A., Gregory-Smith, D.G., (1987)
*'The effect of Inlet Skew on the Flows and Losses in a Turbine Cascade'*,
Proc. I Mech E, Conf. 'Turbomachinery - Efficiency Prediction and Improvement', Paper C275/87.

Wills, J.A.B., (1962)
*'The Correction of Hot-Wire Readings for Proximity to a Solid Boundary'*,
J. Fluid. Mech., 12, pp 388-396.

Wolf, H., (1961)
*'Die Randverluste in Geraden Schaufelgittern'*,
Wiss. Z. Tech. Hochsch. Dresden, 10.
RAE Translation no. 1336, 1968.

Wu, C.H., (1952)
*'A General Theory of Three-Dimensional Flow in Subsonic and Supersonic Turbomachines of Axial, Radial and Mixed Flow Types'*,
Trans. ASME, p1363.

Yavuzkurt, S., (1984)
*'A Guide to Uncertainty Analysis of Hot-Wire Data'*,
Trans, ASME, J. Fluids Eng., 106, p 181.

Zunino, P., Ubaldi, M., Satta, A., (1987)
*'Measurements of Secondary Flows and Turbulence in a Turbine Cascade Passage'*,
ASME Paper no. 87-GT-132.

Zunino, P., Ubaldi, M., Satta, A., Enrico, P., (1988)
*'A Comparison Between Measurements and Turbulence Models in a Turbine Cascade Passage'*,
ASME Paper no. 88-GT-226.

# Appendix A
# Rotatable Single Wire Probe Technique

## A.0 Introduction

This appendix gives details of the method used to obtain flow measurements from a single wire rotated in a plane parallel to the endwall.

## A.1 Analysis Of The Response Of A Hot-Wire

For a hot-wire in the $x-y$ plane (Figure A.1) the velocity vector can be resolved into three components, two of which, $u$ and $v$ are themselves in the $x-y$ plane. If the angle of the wire to the $y-$axis is $\alpha$, then the components are :-

a) Velocity component perpendicular to the wire in the $x-y$ plane

$$V_L = U\cos\alpha + V\sin\alpha \qquad (A.1)$$

b) Velocity component along the wire in the $x-y$ plane

$$V_M = -U\sin\alpha + V\cos\alpha \qquad (A.2)$$

c) Velocity component normal to the wire and the $x-y$ plane

$$V_N = W \qquad (A.3)$$

Due to the conduction effects of the probe supports, the effective cooling velocity is not merely the sum of the components perpendicular to the wire, but may be expressed as :-

$$V_{eff}{}^2 = V_L{}^2 + k^2 V_M{}^2 + h^2 V_N{}^2 \qquad (A.4)$$

where $k$ and $h$ are factors dependent upon probe geometry.

This response equation was proposed by Jørgensen (1971). He tested DISA single wire probes and gold plated wire probes, for their response over a wide range of angles. The values he measured for $k$ and $h$ which are most appropriate for the probes used here are shown below :-

**Table A.1 : Wire Response Factors**

| Probe | $k$ | $h$ |
|---|---|---|
| DANTEC 55P14 | 0.286 | 1.086 |
| DANTEC 55P04 | 0.119 | 1.043 |
| 'Ideal Wire' | 0.000 | 1.000 |

Although it might seem that it would be possible to measure these responses for each individual wire, in practise an extremely accurate calibration facility is required, with very careful data recording. It is far simpler therefore, to use those values tabulated above. Care should be taken however, when trying to apply results obtained for single wires to x-wires or triple wires, as the prong geometry influences the response (Chew and Ha (1988)).

Substituting individual velocity components into the response equation gives :-

$$\begin{aligned} V_{eff}^2 &= (U\cos\alpha + V\sin\alpha)^2 + k^2(-U\sin\alpha + V\cos\alpha)^2 + h^2W^2 \\ &= (\cos^2\alpha + k^2\sin^2\alpha)U^2 + (\sin^2\alpha + k^2\cos^2\alpha)V^2 \\ &\quad + \sin 2\alpha(1-k^2)UV + h^2W^2 \end{aligned} \tag{A.5}$$

Following Hinze (1975), we split each velocity into a mean and fluctuating part :-

$$U = \overline{U} + u' \qquad V = \overline{V} + v' \qquad W = \overline{W} + w' \tag{A.6}$$

where $\overline{u'}, \overline{v'}, \overline{w'} = 0$ by definition.

Thus

$$\begin{aligned} V_{eff}^2 &= (\cos^2\alpha + k^2\sin^2\alpha)(\overline{U}+u')^2 + (\sin^2\alpha + k^2\cos^2\alpha)(\overline{V}+v')^2 \\ &\quad + \sin 2\alpha(1-k^2)(\overline{U}+u')(\overline{V}+v') + h^2(\overline{W}+w')^2 \end{aligned} \tag{A.7}$$

Define :-

$$\nu = \frac{\sin^2\alpha + k^2\cos^2\alpha}{cos^2\alpha + k^2\sin^2\alpha}$$

$$\mu = \frac{\sin 2\alpha\,(1-k^2)}{\cos^2\alpha + k^2\sin^2\alpha} \qquad (A.8)$$

$$\phi = \frac{h^2}{\cos^2\alpha + k^2\sin^2\alpha}$$

Then we may write :-

$$V_{eff}^2 = \overline{U}^2(\cos^2\alpha + k^2\sin^2\alpha)\left\{1 + \frac{2u'}{\overline{U}} + \frac{u'^2}{\overline{U}^2} + \nu\left[\frac{\overline{V}^2 + 2\overline{V}v' + v'^2}{\overline{U}^2}\right]\right.$$
$$\left. + \mu\left[\frac{\bar{U}\bar{V} + \overline{V}u' + \overline{U}v' + u'v'}{\overline{U}^2}\right] + \phi\left[\frac{\overline{W}^2 + 2\overline{W}w' + w'^2}{\overline{U}^2}\right]\right\} \qquad (A.9)$$

A binomial expansion is used to obtain the square root of $(A.9)$, assuming that the axis system is aligned to the flow, such that $\overline{U} > \overline{V}$ and $\overline{U}^2 \gg \overline{V}^2$ (similarly for $\overline{U}$ and $\overline{W}$), and that third and higher order correlations of fluctuating terms are very small compared with the second order correlations. This yields the following equation :-

$$V_{eff} = \overline{U}\sqrt{(\cos^2\alpha + k^2\sin^2\alpha)}\left\{1 + \frac{u'}{\overline{U}} + \left[\frac{\nu}{2} - \frac{\mu^2}{8}\right]\left[\frac{\overline{V}^2 + 2\overline{V}v' + v'^2}{\overline{U}^2}\right]\right.$$
$$\left. + \frac{\mu}{2}\left[\frac{\overline{V} + v'}{\overline{U}}\right] + \frac{\phi}{2}\left[\frac{\overline{W}^2 + 2\overline{W}w' + w'^2}{\overline{U}^2}\right]\right\} \qquad (A.10)$$

Evaluating the mean of $(A.10)$ gives :-

$$\overline{V}_{eff} = \overline{U}\sqrt{(\cos^2\alpha + k^2\sin^2\alpha)}\left\{1 + \left[\frac{\nu}{2} - \frac{\mu^2}{8}\right]\left[\frac{\overline{V}^2 + \overline{v'^2}}{\overline{U}^2}\right]\right.$$
$$\left. + \frac{\mu}{2}\frac{\overline{V}}{\overline{U}} + \frac{\phi}{2}\left[\frac{\overline{W}^2 + \overline{w'^2}}{\overline{U}^2}\right]\right\} \qquad (A.11)$$

Squaring $(A.11)$ and making the same assumptions as when expanding $(A.9)$ yields

$$\overline{V}_{eff}^2 = \overline{U}^2(\cos^2\alpha + k^2\sin^2\alpha)\left\{1 + \nu\left[\frac{\overline{V}^2 + \overline{v'^2}}{\overline{U}^2}\right] - \frac{\mu^2\overline{v'^2}}{4\overline{U}^2} + \frac{\mu\overline{V}}{\overline{U}} + \phi\left[\frac{\overline{W}^2 + \overline{w'^2}}{\overline{U}^2}\right]\right\} \tag{A.12}$$

Evaluating the mean of $(A.9)$ gives :-

$$\overline{V}_{eff}^2 = \overline{U}^2(\cos^2\alpha + k^2\sin^2\alpha)\left\{1 + \frac{\overline{u'^2}}{\overline{U}^2} + \nu\left[\frac{\overline{V}^2 + \overline{v'^2}}{\overline{U}^2}\right] + \mu\left[\frac{\bar{U}\bar{V} + \overline{u'v'}}{\overline{U}^2}\right] + \phi\left[\frac{\overline{W}^2 + \overline{w'^2}}{\overline{U}^2}\right]\right\} \tag{A.13}$$

As

$$V_{eff} = \overline{V}_{eff} + v_{eff}{}' \Longrightarrow V_{eff}^2 = \overline{V}_{eff}^2 + 2\overline{V}_{eff}v'_{eff} + \overline{v'^2_{eff}} \tag{A.14}$$

Therefore

$$\overline{V_{eff}^2} = \overline{V}_{eff}^2 + \overline{v'^2_{eff}} \quad since \quad \overline{v'_{eff}} = 0 \quad by \quad definition. \tag{A.15}$$

Thus

$$\overline{v'^2_{eff}} = \overline{V_{eff}^2} - \overline{V}_{eff}^2 = \quad equations \quad (A.13) - (A.12) \tag{A.16}$$

Therefore

$$\left(\sqrt{\overline{v'^2_{eff}}}\right)^2 = (\cos^2\alpha + k^2\sin^2\alpha)\left[\overline{u'^2} + \frac{\mu^2\overline{v'^2}}{4} + \mu\overline{v'u'}\right] \tag{A.17}$$

Equations $(A.11)$ and $(A.17)$ represent the mean and r.m.s. responses of a wire placed at an angle $\alpha$ to the $y$-axis.

## A.2 Rotatable Method for Flow Measurement

If mean voltage $\overline{E}$ and r.m.s. voltage $\sqrt{\overline{e'^2}}$ (A.C. coupled) are measured for a wire set at various angles to the flow, using a linearised system, then the corresponding mean and r.m.s. velocities are obtained by simply dividing by the wire sensitivity S, obtained from calibration.

Consider the case of the turbulence data, for which the equations may be written in matrix form :-

$$\begin{pmatrix} 1 & \frac{\mu^2(\alpha_1)}{4} & \mu(\alpha_1) \\ 1 & \frac{\mu^2(\alpha_2)}{4} & \mu(\alpha_2) \\ 1 & \frac{\mu^2(\alpha_3)}{4} & \mu(\alpha_3) \\ \vdots & \vdots & \vdots \\ 1 & \frac{\mu^2(\alpha_n)}{4} & \mu(\alpha_n) \end{pmatrix} \times \begin{pmatrix} \overline{u'^2} \\ \overline{v'^2} \\ \overline{u'v'} \end{pmatrix} = \begin{pmatrix} \frac{\overline{v_1'^2}}{(\cos^2\alpha_1 + k^2\sin^2\alpha_1)} \\ \frac{\overline{v_2'^2}}{(\cos^2\alpha_2 + k^2\sin^2\alpha_2)} \\ \frac{\overline{v_3'^2}}{(\cos^2\alpha_3 + k^2\sin^2\alpha_3)} \\ \vdots \\ \frac{\overline{v_n'^2}}{(\cos^2\alpha_n + k^2\sin^2\alpha_n)} \end{pmatrix} \qquad (A.18)$$

If more than three results are recorded, i.e. $n > 3$, then these simultaneous linear equations may be solved by a least squares method. This was implemented using a Numerical Algorithms Group subroutine F04AMF.

## A.3 Calculation Of Confidence Intervals

We may represent equation $(A.18)$ as a general matrix equation :-

$$\mathbf{A}\,\mathbf{X} = \mathbf{B} \qquad (A.19)$$

for $n$ equations in 3 unknowns.
Having obtained a least squares solution $\mathbf{X}$, the computed values of the input velocities which satisfy this solution are

$$\mathbf{S} = \mathbf{A}\,\mathbf{X} \qquad (A.20)$$

then the residuals for each angle may be calculated

$$\mathbf{r} = \mathbf{B} - \mathbf{S} \qquad (A.21)$$

where $\mathbf{r}$ is a vector of rank $n$.
The error of the fit is given by

$$E = \frac{\sum_{i=1}^{n} r_i^2}{n - q} \qquad (A.22)$$

where $q$ is the number of unknowns in the original system of equations. In this case $q = 3$.

The matrix $\mathbb{S}_{\mathbf{inv}} = (\mathbb{A}^{\mathrm{T}}\,\mathbb{A})^{-1}$ is diagonal. For each diagonal element $\mathbb{S}_{ii}$ $(i = 1, q)$ a confidence interval to the solution vector may be calculated such that

$$C.I._i = \sqrt{E} * \sqrt{\mathbb{S}_{ii}} * t \qquad (A.23)$$

where $t$ is a statistical parameter obtained from tables, and depends upon the number of degrees of freedom, and the limit chosen. For three degrees of freedom, and 99% confidence, t = 4.54.

## A.4 Mean Velocity Equation

Equation $(A.11)$ cannot be solved in the same way as equation $(A.17)$, since it is non-linear. An elimination method of solution was adopted initially to solve the equations. In order to obtain information on the accuracy of the method, it was decided to perform a least squares solution as described for the turbulence data, but based upon the concept of an ideal wire. For an ideal wire with $k = 0$ and $h = 1$, equation $(A.11)$ reduces to :-

$$\overline{V}_{eff} = \overline{U}\cos\alpha + \overline{V}\sin\alpha + \frac{1}{2\cos\alpha}\frac{\overline{W^2}}{\overline{U}} \qquad (A.24)$$

which is linear. It was found that the results of solving this equation with a least squares method, were very similar to the results of solving equation $(A.11)$ with an elimination method. This is because the non-linearity of equation $(A.11)$ is extremely small. Hence it was decided to simply adopt the ideal wire solution for mean velocity measurements, and only use gold-plated wires (DANTEC 55P04) which are closer to 'ideal'.

All equations were solved in a coordinate system approximately aligned with the flow direction in order to ensure the validity of the binomial expansion used to obtain equation $(A.10)$. Having solved for the flow in these coordinates, the solutions could then be rotated to cascade coordinates for storage.

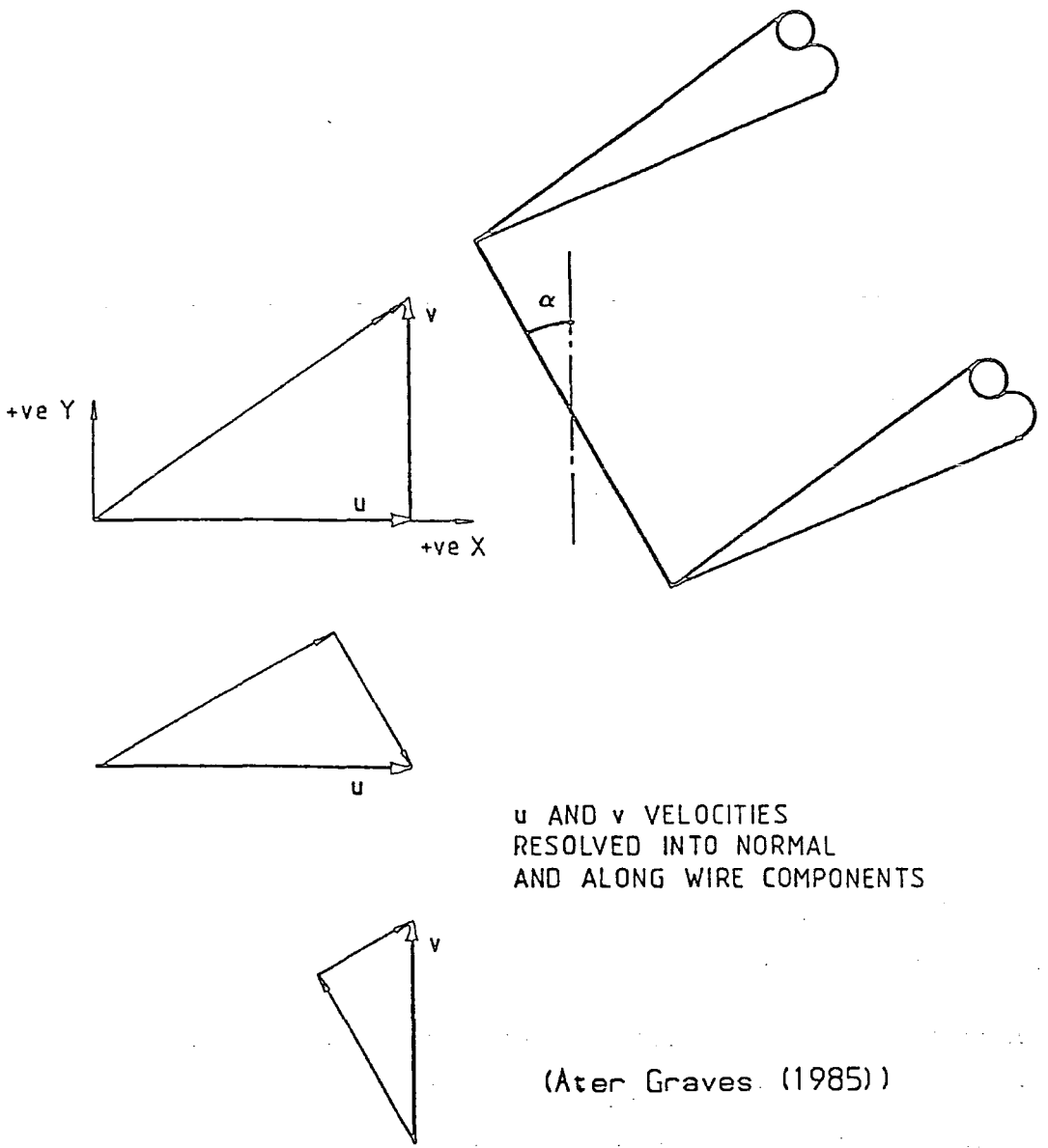


FIGURE A.1 : Hot-Wire Velocity Components

# Appendix B
# Estimation of Change in Shear Stress from Slot 8 to Slot 10

## B.0 Introduction

This appendix gives details of a rough assessment of the change in $\overline{u'v'}$ shear stress which might be expected between slots 8 and 10. The assessment is based on consideration of the shear stress transport equation, evaluating Reynolds stress terms from the hot-wire measurements for the 'JGC' test case, and velocity gradients calculated from measurements of the 'JAW' test case.

## B.1 Shear Stress Transport Equation

The shear stress transport equation may be written as

$$\begin{aligned}\frac{D}{Dt}(\overline{u_i'u_j'}) = &-\left[\overline{u_j'u_l'}\frac{\partial \overline{U_i}}{\partial x_l} + \overline{u_i'u_l'}\frac{\partial \overline{U_j}}{\partial x_l}\right] && Production\\ &+\overline{\frac{p'}{\rho}\left(\frac{\partial u_i'}{\partial x_j}+\frac{\partial u_j'}{\partial x_i}\right)} && Redistribution\\ &-\frac{\partial}{\partial x_l}\left[\overline{u_i'u_j'u_l'} - \nu\frac{\partial \overline{u_i'u_j'}}{\partial x_l} + \overline{\frac{p'}{\rho}(\delta_{jl}u_i' + \delta_{il}u_j')}\right] && Diffusion\\ &-2\nu\overline{\frac{\partial u_i'}{\partial x_l}\frac{\partial u_j'}{\partial x_l}} && Dissipation\end{aligned} \tag{B.1}$$

Neglecting the redistribution, diffusion, and dissipation terms, and considering $i = 1$, and $j = 2$ gives the following equation:-

$$\begin{aligned}-\frac{D}{Dt}(\overline{u'v'}) \simeq &\ \overline{u'v'}\frac{\partial \overline{U}}{\partial x} + \overline{v'^2}\frac{\partial \overline{U}}{\partial y} + \overline{v'w'}\frac{\partial \overline{U}}{\partial z}\\ &+\overline{u'^2}\frac{\partial \overline{V}}{\partial x} + \overline{u'v'}\frac{\partial \overline{V}}{\partial y} + \overline{u'w'}\frac{\partial \overline{V}}{\partial z}\end{aligned} \tag{B.2}$$

The substantive derivative on the left hand side may be approximated as

$$\frac{D}{Dt}(\overline{u'v'}) \simeq \overline{U}\frac{\partial \overline{u'v'}}{\partial x} \simeq \frac{\overline{U}}{\Delta x}\Delta(\overline{u'v'}) \tag{B.3}$$

Assuming that the $\overline{V}\frac{\partial}{\partial y}$ and $\overline{W}\frac{\partial}{\partial z}$ terms are small, and that the values remain constant over the streamwise distance from slot 8 to slot 10.

Values for terms on the right hand side of equation (B.2) may be evaluated, if it is assumed that the velocity gradients are little changed between the 'JAW' and 'JGC' test cases. Figure B.1 shows plots of the partial velocity gradients in hot-wire coordinates, determined from a traverse of slot 8 presented by Walsh (1987). Values for the Reynolds stresses (except for $\overline{v'w'}$ which must be ignored) may be read from the contour plots in Figure 7.14. Summing terms for a point in the loss core at coordinate (-120,40) gives:-

$$\frac{\Delta(\overline{u'v'})}{V_0^2} = -0.096 \qquad (B.4)$$

The dominant term in the calculation for this point is $\overline{v'^2}\frac{\partial \overline{U}}{\partial y}$. At the point (-140,70) near the suction surface separation line, the change is:-

$$\frac{\Delta(\overline{u'v'})}{V_0^2} = -0.1 \qquad (B.5)$$

with the dominant term here being due to $\overline{u'v'}\frac{\partial \overline{V}}{\partial y}$.

Although this analysis is very approximate, and makes several assumptions, it does suggest that the data is consistent and that the observed change of -0.04 is believable.

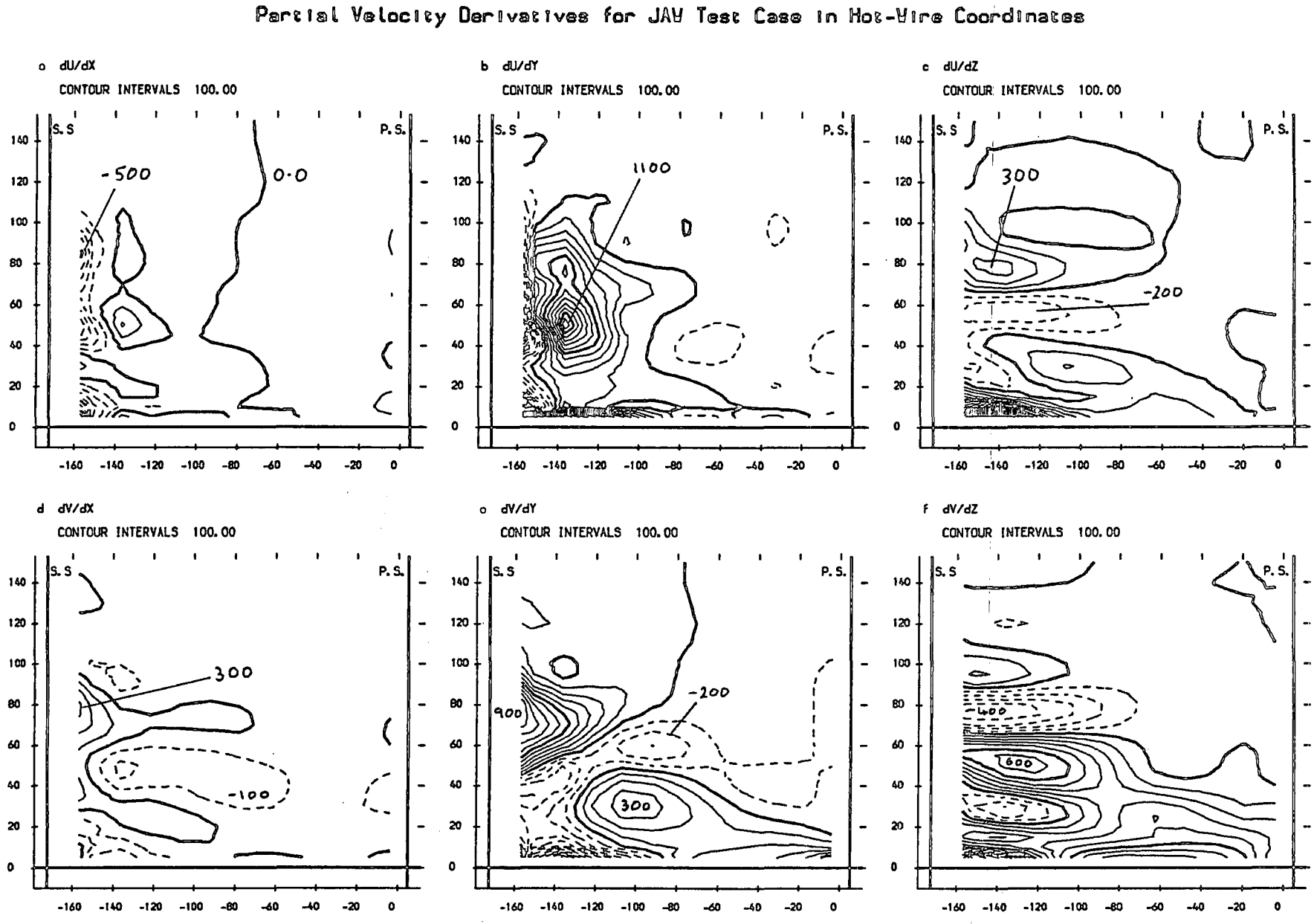


FIGURE B.1 (a-f) : Area Plots For Slot 8

# Appendix C
# Partial Velocity Derivatives

This appendix presents contour plots of partial velocity derivatives at slot 10. The derivatives were evaluated from bi-cubic spline surfaces which were fitted to the data as discussed in Chapter 7. The five hole probe traverse of slot 10 for the 'JGC' test case was used to evaluate all derivatives, as although the hot-wires do provide information about velocities over the traverse plane, a total pressure traverse is also required by the calculation procedure to determine axial gradients. This is done via the incompressible Helmholtz equation, and the method has been described by Gregory-Smith *et al* (1987) who developed it to calculate vorticity from experimental traverses.

The partial derivatives are presented in both cascade coordinates (axial, tangential, radial) and the 'hot-wire' coordinates in which the Reynolds stresses were measured. The hot-wires were aligned with the midspan streamwise direction for each tangential location, and so the coordinates $x, y, z$ are in fact 'streamwise, cross-passage, and radial' in this case. It was necessary to calculate the partial velocity derivatives in hot-wire coordinates, as one of the components of the Reynolds stress tensor was not measured, preventing evaluation of its components in cascade coordinates. The resulting contour plots of partial velocity derivatives are presented in Figure C.1.

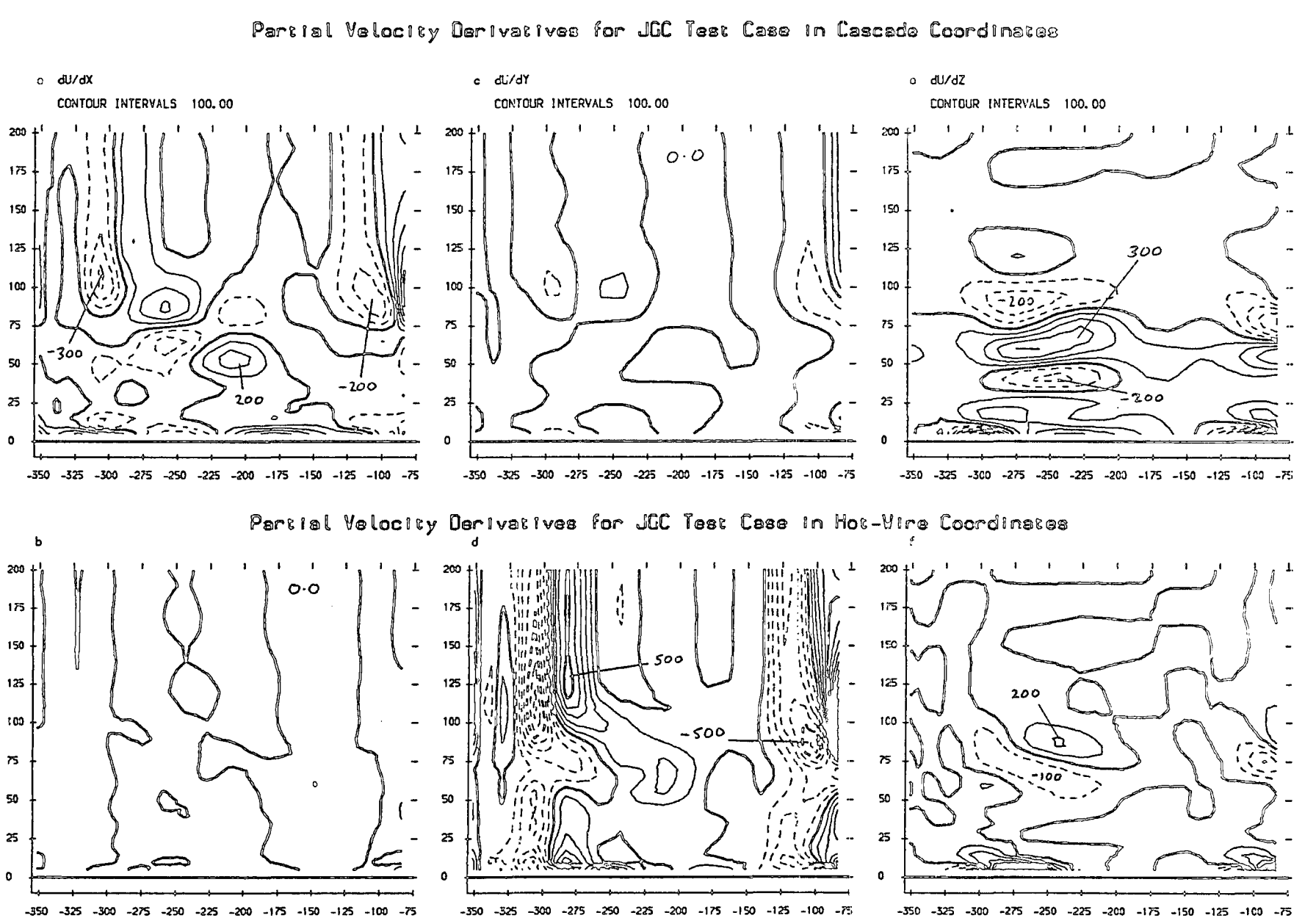


FIGURE C.1 (a-f) : Area Plots For Slot 10

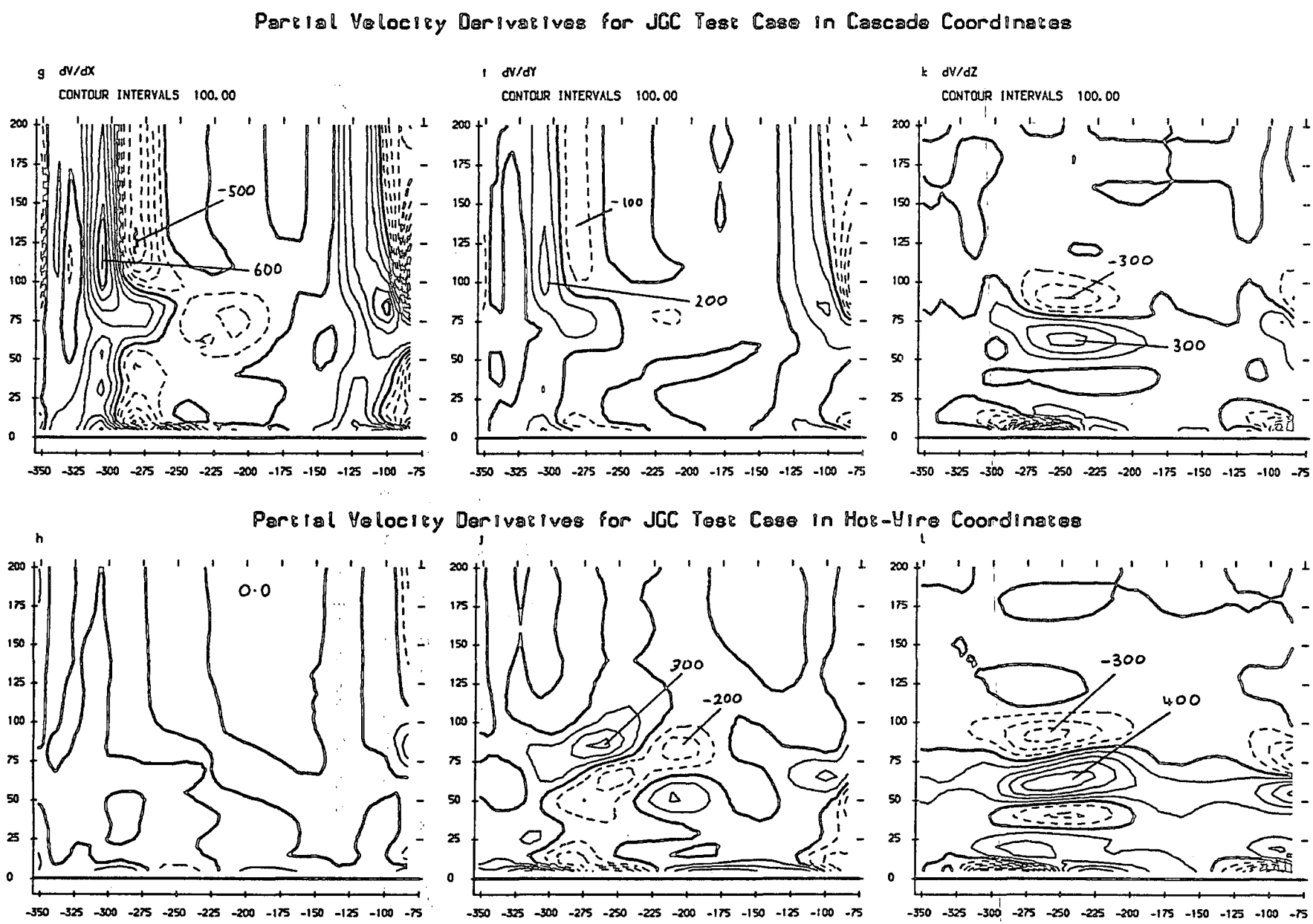


FIGURE C.1 (g-l) : Area Plots For Slot 10

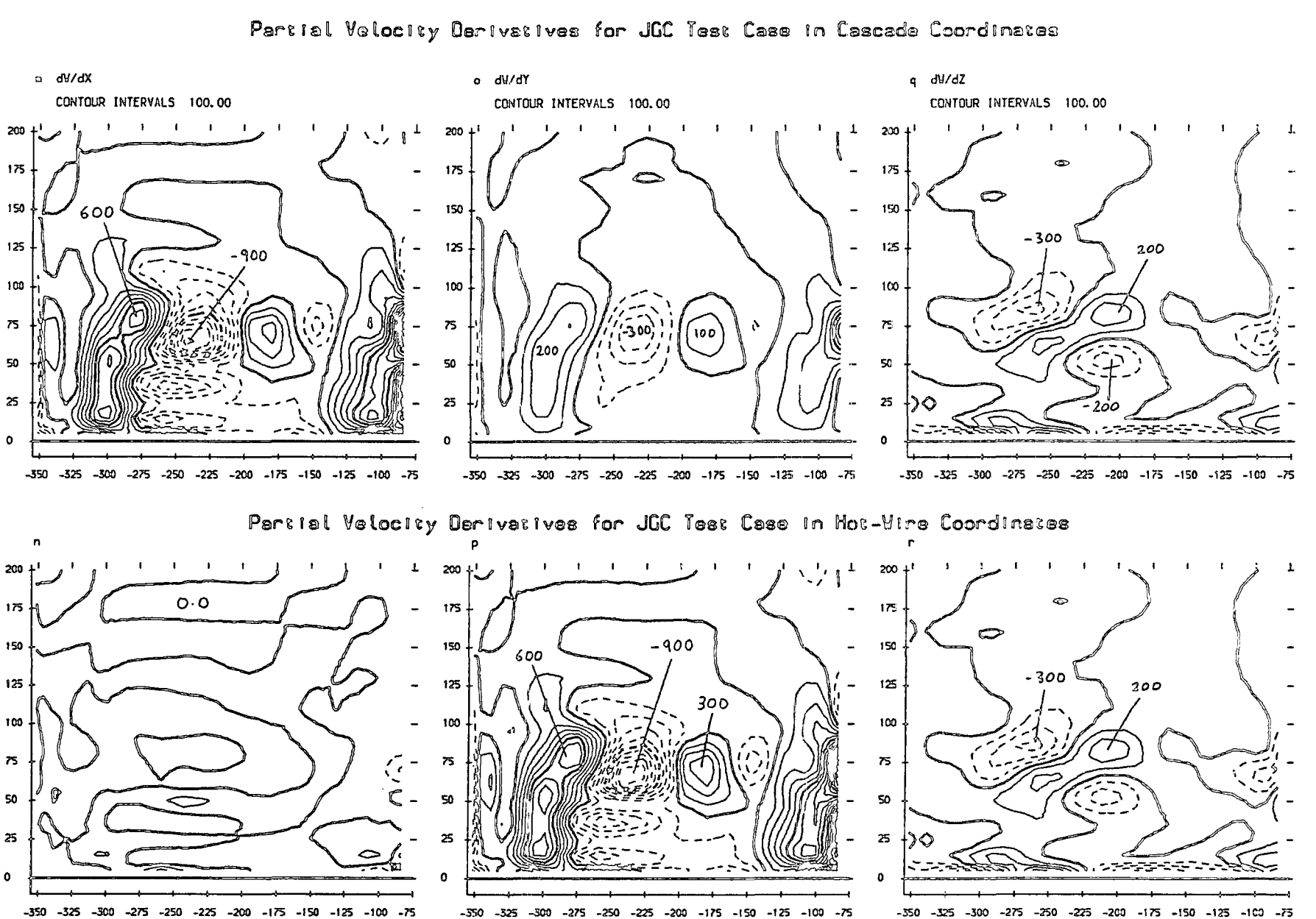


FIGURE C.1 (m-r) : Area Plots For Slot 10